NON-LINEAR FINITE ELEMENT-BASED MATERIAL CONSTITUTIVE LAW FOR ZERO SLUMP STEEL FIBER REINFORCED CONCRETE PIPE STRUCTURES

by

ALENA MIKHAYLOVA

Presented to the Faculty of the Graduate School of

The University of Texas at Arlington in Partial Fulfillment

of the Requirements

for the Degree of

DOCTOR OF PHILOSOPHY

THE UNIVERSITY OF TEXAS AT ARLINGTON

DECEMBER 2013

Acknowledgements

I would like to sincerely express my gratitude to Dr. Abolmaali who has been my advisor and a wonderful mentor throughout this journey, who provided impeccable guidance, motivation and understanding. I would also like to extend my gratitude to my doctoral committee members, Dr. Shih-Ho Chao, Dr. Pranesh Aswath, Dr. Matthys and Dr. Siamak Ardekani for their time to serve on this committee and their invaluable guidance on improving my work.

I would also like to thank the members of the Center for Structural Engineering Research (CSER). Over the years many of them became my friends, and the memories of this wonderful time and people I will hold dear to my heart for many years.

I would also like to acknowledge the sponsors of the project for providing financial support, Bekaert Corporation and American Concrete Pipe Association. In addition thanks to Hanson Plant and Precast, Rinker-Concrete Pipe Product, Northern Concrete Pipe and Sherman Dixie for providing their facilities and resources. I would also like to express my gratitude to the Department of Civil Engineering at The University of Texas at Arlington for their support and assistance.

Finally, I would like to express my deepest gratitude to my husband and a dearest friend, Yuri. Your patience, understanding, support and unconditional love were undeniably uplifting throughout this time.

November 20, 2013

Abstract

NON-LINEAR FINITE ELEMENT-BASED MATERIAL CONSTITUTIVE LAW FOR ZERO SLUMP STEEL FIBER REINFORCED CONCRETE PIPE STRUCTURES

Alena Mikhaylova, PhD

The University of Texas at Arlington, 2013

Supervising Professor: Ali Abolmaali

This study presents a comprehensive investigation of performance and behavior of steel-fiber reinforced concrete pipes (SFRCP). The main goal of this study is to develop the material constitutive model for steel fiber reinforced concrete used in dry-cast application. To accomplish this goal a range of pipe sizes varying from 15 in. (400 mm) to 48 in. (1200 mm) in diameter and fiber content of 0.17%, 0.25%, 0.33%, 0.5%, 0.67% and 83% by volume were produced. The pipes were tested in three-edge bearing condition to obtain the load-deformation response and overall performance of the pipe. The pipes were also subjected to hydrostatic joint and joint shear tests to evaluate the performance of the fiber-pipe joints for water tightness and under differential displacements, respectively. In addition, testing on hardened concrete was performed to obtain the basic mechanical material properties. High variation in the test results for material testing was identified as a part of experimental investigation.

A three-dimensional non-linear finite element model of the pipe under the three edge bearing condition was developed to identify the constitutive material relations of fiber-concrete composite. A constitutive model of concrete implementing the concrete

plasticity and continuum fracture mechanics was considered for defining the complex non-linear behavior of fiber-concrete. Three main concrete damage algorithms were examined: concrete brittle cracking, concrete damaged plasticity with adaptive meshing technique and concrete damaged plasticity with visco-plastic regularization. The latter was identified as the most robust and efficient to model the post-cracking behavior of fiber reinforced concrete and was used in the subsequent studies.

The tension stiffening material constitutive law for composite concrete was determined by converging the FEM solution of load-deformation response with the results of experimental testing. This was achieved by iteratively modifying the non-linear material model of concrete properties in tension until the load-deformation response matched the one of experimental testing. Based on the results of finite element simulations the mathematical expressions for the material constitutive law for concrete composite were obtained using the least squares approach.

Internal moments, shear and thrust forced developed in the pipe under the three-edge bearing were determined. In addition, finite element model of pipe-soil interaction was developed to determine the deflections of the pipe under a range of backfill heights. A part of this research was a qualitative evaluation of fiber distribution in concrete pipe using statistical approach. The study revealed that the variation of fiber distribution varies with the fiber content in concrete.

This study has resulted in the development of a stand-alone performance based specification (ASTM C1765-13) for steel fiber reinforced concrete pipes, which has been approved in 2013.

Table of Contents

List of Illustrations

List of Tables

Chapter 1

Introduction

1.1. Background

Concrete pipes constitute the vast majority of today's infrastructure to convey water, applicable to storm water drainage, sewers and irrigation in transportation and agriculture. The first concrete pipes were discovered in the nineteenth century and have been a part of development of any civilized society. Over the years the technological and market developments had triggered demand for increased production rate and quality of concrete pipe by using more economical methods. Reinforcement with steel wires and automatization brought new advancements to the concrete pipe industry allowing concrete pipes to carry higher loads and sustain larger deformations without a collapse. The increased load carrying capacity and durability characteristics of reinforced concrete pipes make them invaluable in applications of higher strength demands, such as bridge overpasses in highways and railways or increased depth of pipe burial. Concrete pipes are categorized as rigid systems which mainly rely on inherent strength to carry the imposed loads, whereas flexible pipe systems rely on the strength of surrounding soil.

Although conventional reinforcement of concrete pipes satisfies all strength requirements imposed by modern infrastructure demand, production of reinforced concrete pipe, as we know it today, is a labor intensive process which involves steel cage machines and the equipment operators to produce the cages, including manual labor for bending and placement of the reinforcement into molding forms. In addition, corrosion of a steel cage has been a concern in installed conventionally reinforced concrete pipes (RCP) in cracked condition which may lead to durability issues and strength deterioration.

For the past decades studies have considered the use of steel fibers in concrete structures (Gopalaratnam and Shah 1986, Narayanan and Darwish 1987) to enhance the

behavior of structural elements, improve their shear strength and reduce cracking due to shrinkage and creep. In addition, the use of steel fibers may allow a reduction or complete elimination of flexural or shear resisting steel reinforcement (Swamy 1981 and Jindal 1984).

Although a significant amount of research has been done in the area of steel fiber reinforced concrete structures, the majority of studies are applicable to the wet-cast type production, where the concrete possesses high workability and fluidity.

This study is concerned with the application of steel fiber to precast concrete pipe structures in a dry-cast environment. Dry-cast production environment is a common practice for the production of precast underground structures, such as concrete pipes, culvert boxes and manholes, due to its efficiency. This type of production allows an immediate reuse of the molding forms without the need to wait for concrete hardening (unlike the production of wet-cast structures). Concrete structures produced in a dry-cast environment are able to support their own weight immediately upon removal of the mold. In addition, the dry-cast concrete products have an early strength gain which allows them to be shipped to the site commonly at the age of 3 to 7 days after production.

The addition of fibers into a concrete mix allows complete elimination of the conventional steel cage in concrete pipe while still providing comparable strength and durability of the structure (Abolmaali et. al 2012) . This technology has gained popularity in Europe and has successfully been implemented into mass production for the past ten years.

Steel fiber reinforced concrete pipes (SFRCP) however are relatively new to the U.S.A. concrete pipe industry. Little is known in regards to their behavior or approaches in the design of SFRCP.

Currently, there are two design philosophies applicable to RCP that have been defined by the American Concrete Pipe Association (ACPA) based on Marston-Spangler approach: direct design and indirect design methods (*Concrete pipe handbook 1958)*. The former is based on the comparison of the pipe strength under the three-edge bearing loading and the calculated field strength of a buried pipe; whereas the latter is based on determination of the internal forces exerted on the installed pipe and estimation of the physical parameters necessary to support those loads.

The design limits of SFRCP or any other structure are dictated by the requirements to provide safety, economy, strength and aesthetic appearance. The above criteria are commonly achieved by performing the elastic analysis to determine the internal forces developed in the structure under a given loading condition and calculating the amount of reinforcing steel or size of the member. Although design of the structures performed in accordance with current code provisions should guarantee the safety, in the events of natural disasters or catastrophic failures economic losses necessitate for a more detailed analysis. Often it is impossible or unjustifiably costly to perform experimental testing on a large scale structures to determine the behavior of the system subjected to a combination of forces. In these situation the Nonlinear Finite Element Analysis (FEA) can become a powerful tool in determining the complex response of structures under various loading conditions.

The material constitutive relations of concrete in uniaxial compression and tension are required to design a structure that satisfy the strength, serviceability and safety requirements. In addition, material properties in biaxial tension and compression are often necessary to accurately simulate the behavior of the structure using FEA.

The strength of the SFRCP, in general, depends on pipe's geometry (diameter and wall thickness), fiber type and its content in concrete, steel fiber-concrete matrix

interfacial bond and concrete mechanical properties, which in turn depend on proportions of the concrete constituents (cement, fly ash, fine and coarse aggregates, water, water-to-cement ratio, admixtures)

The complex behavior of steel-fiber concrete structure is dictated by a composite action of the steel fiber and concrete matrix. The fiber-concrete material behavior is characterized by a reduction of load carrying capacity and increased rate of deformation after attaining the ultimate load, which often corresponds to a formation of the first crack. This type of response can be described as strain softening behavior which occurs in both tension and compression. Strain softening occurs in reinforced concrete structures and is commonly used for defining the material model in FEA. A variety of models have been proposed to characterize the constitutive material law of reinforced concrete (Lubliner 1989, Taqieddin 2008,), fewer models are available that deal with steel fiber reinforced concrete (Lee et al. 2012, De La Fuente et al. 2012). For both types of reinforcement models based on theory of plasticity and fracture mechanics are utilized.

In general, the material model can be obtained by the means of experimental testing. For large scale concrete structures this is done by taking samples of fresh concrete from the in-field conditions to further investigate the properties of hardened concrete by testing specimens for compressive and flexural strengths as well as modulus of elasticity, Poisson's ratio and other basic parameters of mechanical properties of the material.

For the concrete structures produced in a wet-cast environment material samples taken from the field normally closely represent the actual properties of concrete that is possessed by the structure. Contrary, for the dry-cast underground structures material samples produced in the field do not necessarily represent the material properties experienced by the structure. The material properties of concrete pipes are dictated by a

manufacturing process which involves machine compaction process to densify the material by means of internal vibration or mechanical compaction with the rotary heads of equipment; whereas the concrete sample produced for the purpose of determining the mechanical properties of the material are hand compacted. As a result, there is an undeniable difference in the density, number of voids and alignment of fibers in a pipe and its material sample specimen, leading to the differences in the strength threshold. Consolidation technique can be identified as one of the issues in standard practice of material testing for zero-slump concrete.

A comprehensive investigation on steel fiber reinforced concrete pipes is undertaken in this study. The investigation consists of experimental testing and analytical analysis. The experimental program includes production of SFRCP with a range of diameters and fiber content and subjecting the pipes to the three-edge bearing test in order to determine the overall behavior of fiber-pipes. In addition, the joints of SFRCP were tested for hydrostatic water tightness and resistance to differential displacement through joint shear test. The experimental investigation also included material testing to determine the basic mechanical properties and the fiber distribution study on select pipe specimens. A complete three-dimensional non-linear finite element model is developed using the FEA software ABAQUS to determine the material constitutive law model of the fiber reinforced concrete material. Using the verified finite element model, location of the first crack initiations are determined and confirmed with experimental testing. In addition, the pipe-soil interaction model is considered to determine the maximum backfill height applicable to the most common pipe diameters. And finally, the internal forces developed along the pipe circumference are determined herein.

The current research have contributed to the development of the performance based specification ASTM C1765 applicable to the steel fiber reinforced concrete pipes.

1.2. Scope and Objectives

The development of the material tension stiffening model for zero-slump steel fiber reinforces concrete is in the forefronts of this research. The goal of identifying the material constitutive law should be set with consideration of the complexity of material nonlinearity, variation of the properties from one specimen to another, the scattered distribution of experimental data associated with the manufacturing specifics and the variation in testing techniques. The material model should be selected such that the structure replicates the behavior observed during the experimental testing.

Thus, the objectives of this study can be identified as follows:

- Conduct experimental testing on full scale steel fiber reinforced concrete pipes to determine behavior of the pipe and its strength depending on the fiber content.
- Obtain load-deformation response under the three edge bearing condition loaded monotonically for a representative sample of SFRCP for each fiber dosage. Once the load-deformation envelopes have been found, an averaged response for each diameter pipe and fiber content should be determined.
- Conduct experimental testing on hardened steel fiber reinforced concrete to determine compressive and tensile strengths of the material.
- Develop the finite element model to simulate the three edge bearing loading conditions. Identify an appropriate algorithm and failure criterion for defining the elasto-plastic material model of damaged steel fiber reinforced concrete.
- Once the appropriate algorithm is defined, using the FEM determine the material constitutive relationship law experienced by the steel fiber reinforced concrete pipes.

- Determine the regression model of tension-stiffening behavior obtained from FEM.
- Once the material model is found, determine internal forced developed in the pipe under the three edge bearing test.
- Develop pipe-soil interaction model for SFRCP under various backfill heights to obtain the deflection and maximum backfill height to cause the first crack.
- In addition, fiber distribution is to be conducted to determine the variation of steel fiber in concrete pipe depending on the fiber volume fraction and type of fiber.

1.3. Literature Review

The literature review for the current research can be separated into two different categories: experimental studies on steel fiber reinforced concrete and SFRC pipes, and analytical studies of steel fiber reinforced concrete pipes. In the first category the discussion will be made on advances in the area of steel fiber reinforced concrete pipes and their design approaches, as well as the properties of steel fiber reinforced concrete. Whereas in the second part of literature review the discussion will be concerned with the available models on steel fiber reinforced concrete and general finite element analysis of concrete pipes.

1.3.1. Steel Fiber Reinforced Concrete

Over the years steel fiber has been used increasingly in reinforced concrete structures. Concrete is a heterogeneous material which consists of cement, fly ash, water, aggregates and sometimes admixtures. It is economical as compared to steel and possesses high strength in compression, which makes it invaluable in structural application, however the brittle nature of the material requires it to be compensated by addition of reinforcement into the concrete. The first developments in utilizing fibers in

concrete took place in early 1960' by Romuldi and Mandel (1964) and in Denmark by Krenchel (1964). Numerous studies on behavior of steel fiber reinforced concrete have been conducted since then. Among the studies are Gopalaratnam and Shah (1987), who reported that the fibers affect mechanical properties of concrete, especially the ability of concrete to resist tensile and fatigue stresses

When the fibers are present the stresses in concrete matrix can be transferred to fibers through interfacial shear or bond between the fiber and matrix. The interfacial bond between the two materials is provided by surface roughness of the fibers or it deformed configuration. Steel fibers are very effective in arresting the crack and preventing it further propagation. The aspect ratio (ratio of the fiber length to its diameter) and tensile strength are also important factors in composite concrete to resist cracking. Long fibers with higher aspect ratios in general can provide larger interfacial surface area with the concrete matrix increasing pullout resistance, however Swamy and Mangat (1974) reported that the fiber having an aspect ratio higher than 100 cause bundling and uneven distribution in the concrete mix.

Anchorage system is important in providing the mechanism to prevent a pullout of fibers from concrete matrix. Shah et al. (1978) in his work had demonstrated that the stress-strain responses of cementitious material is greatly affected by the shape and the aspect ratio of the fibers, and the fiber content, Figure 1-1.

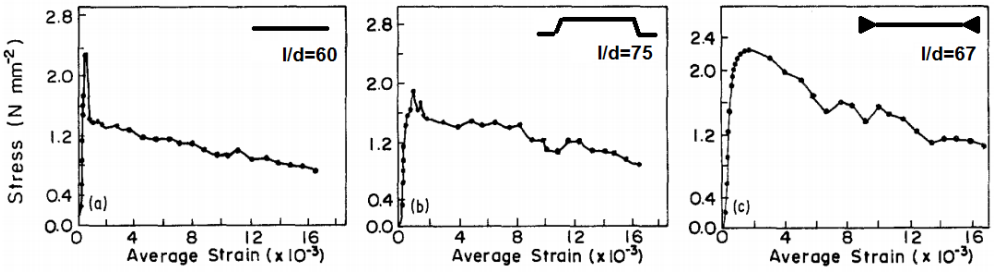

Figure 1-1 Stress strain curves for steel fiber mortar in tension (Shah et al. 1978)

The increase of fiber content in concrete , however, has no significant effect on the ultimate compressive strength of the fiber composite. But the post-failure behavior in compression is highly dependent on the fiber volume content, as was shown by Fanella and Naaman (1985) and later confirmed by Nataraja (1999). The compressive stress-strain curves obtained for the steel fiber reinforced concrete with different fiber volume fraction are shown in Figure 1-2. Fiber-concrete with higher fiber content experiences larger strains at the peak stress as compared to unreinforced concrete. It also should be noted that the residual stress is greater at the end of the loading cycle for concrete with higher fiber volumes.

Similar effect was observed in regards to the aspect ratio of fibers, also conducted by Fanella and Naaman (1985) and is illustrated in Figure 1-3. The post cracking behavior experiences higher strains at the ultimate compressive stress residual stresses for concretes having fibers with larger aspect ratios.

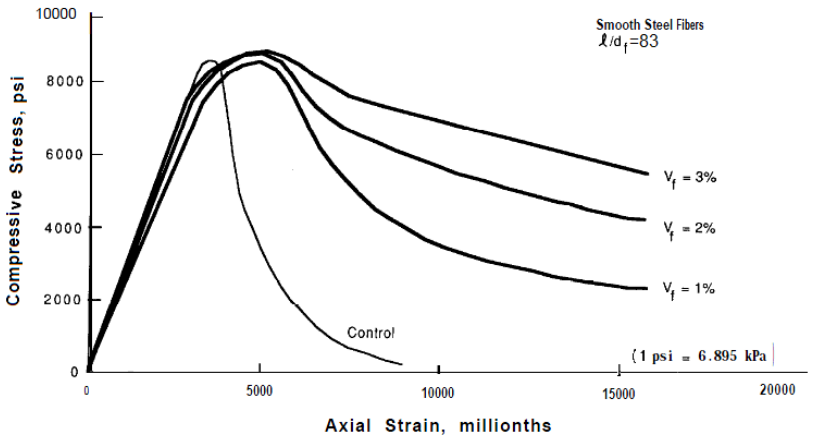

Figure 1-2 Influence of the fiber content on the compressive stress-strain response (Fanella and Naaman 1985)

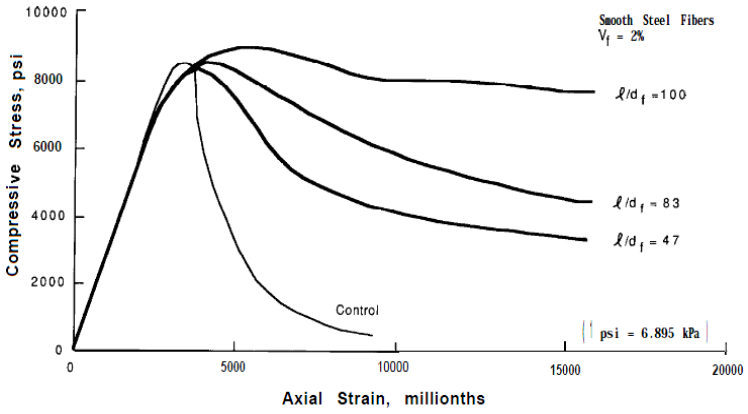

Figure 1-3 Influence of aspect ratio of fibers on the compressive stress-strain curve (Fanella and Naaman 1985)

The fiber in concrete also enhances the flexural strength (Johnston 1974) and the toughness in structural members as the fiber content increases. However the effect of it varies depending on the type of fiber, its shape and characteristics of the mechanical properties (Johnston and Skarendahl 1992). Typical stress-strain responses for steel fiber reinforced and polypropylene fibers were shown in work of Naaman (2007), Figure

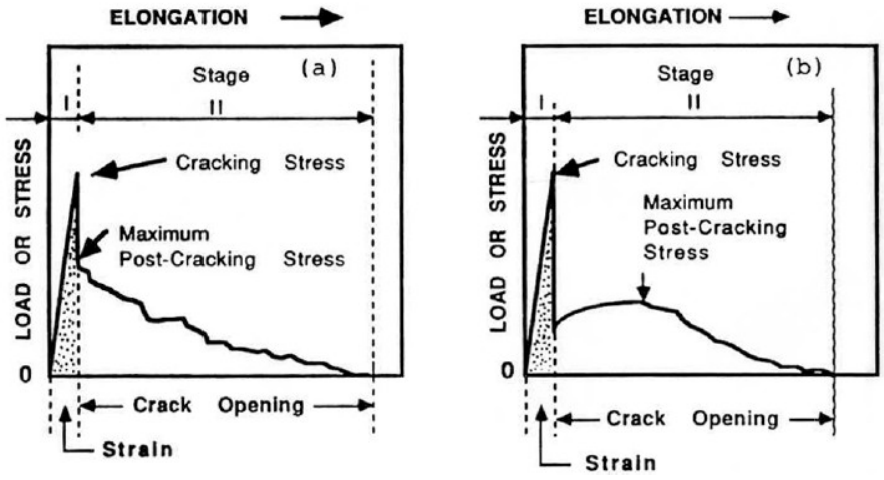

Figure 1-4 Typical elongation response in tension of fiber reinforced concrete (a) steel fiber; and (b) polypropylene fiber l/d

Most of the fiber reinforced concretes exhibits strain softening behavior in tension after cracking, that is when the stress gradually reduced as the strain increases.

Flexural toughness under the statics load is defined as the area under the load deformation curve in flexure which is characterized by the amount of energy absorbed to completely separate the specimen (ACI 544.1R). Strengthening effect also depends on the relative proportions of the water and cement as well as the grading of the aggregates. Increasing the amount of fiber in concrete has an effect of workability of concrete, as it decreased with the increase of fiber, thus the appropriate adjustment need to be made to the concrete mix.

Current research considers the use of deformed galvanized steel fibers with an aspect ratio of 65 and tensile strength 225 ksi and fiber fraction ranging between 0.17% and 0.83% by volume.

1.3.2. Application of Steel Fibers to Precast Concrete Pipes

The use of steel fibers in precast concrete pipes as the primary reinforcement has gained popularity in Europe and successfully been implemented into mass production. The existing European EN 1916-02 standard for concrete pipes and fittings include performance-based design guidelines for steel fiber reinforced concrete pipes. Among other existing specifications that provide SFRCP provisions, French NF P16-345-2 (2003), Belgium NBN–B21-106 (2004), Italian UNI EN 1916 (2004), Netherlands NEN 7126 (2004), Spain UNE 127916 (2004), NBR 8890 are all the equivalents of EN1916 standard

The EN 1916 performance-based specification is based on the concept of minimum crushing load (F_n) under "*crushing test*" also known as *three-edge bearing test*. The load is applied uniformly along the crown-line of the pipe while the pipe is supported by two longitudinal strips. The pipe is loaded in a sequence shown in Figure 1-5: the load

is applied until it reaches F_c, which is a proof load and it should be a factor of 1.5 away from the specified crushing load $F_{n,}$ (or $0.67F_n$). The crushing load is specified by the EN1916 standard depending on the strength class and diameter of the pipe. The proof load is maintained for a minute without the pipe showing any noticeable damage. The pipe then is continued to be loaded until it reaches its ultimate load (F_u), which typically coincide with formation of the first crack. The ultimate load should be higher than the crushing load (F_n). After the sustained load has dropped to 95 % or less of Fu, the pipe is completely unloaded and then reloaded to 0.67 F_n which is again held for one minute.

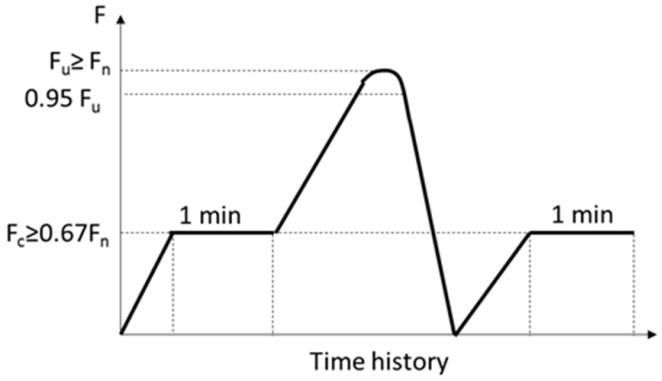

Figure 1-5 Loading time history for steel fiber reinforced concrete pipes in accordance with EN1916 specification

The loading history of the SFRCP is similar to that of RCP but having more stringent requirements for acceptance. Unlike fiber reinforced pipes, RCP are allowed to be cracked at proof load, moreover, there is no unloading-reloading cycle present for RCP, which is mainly conducted for verification of the fiber-concrete anchorage and residual strength after cracking.

Similar provisions were recently developed for SFRCP as a part of research work described herein. The performance-based ASTM C1765 covers guidelines for SFRC pipes design ranging between 12 in (300 mm) to 48 in. (1200 mm) in diameter and is

based on the results of studies conducted by Abolmaali et al. (2012). Table 1-1 shows the values of the strength criteria that the pipe has to satisfy for acceptance, depending on the chosen strength class and the pipe diameter. D-load is the load normalized over length (ft.) and internal diameter (ft.) of the pipe.

Table 1-1 ASTM C1765 Strength requirements for SFRCP

Pipe Class	**D_{serv} (lbs/ft./ft.)**	**D_{test} (lbs/ft./ft.)**
I	800	1200
II	1000	1500
III	1350	2000
IV	2000	3000
V	3000	4500

The loading history for the SFRCP required by ASTM C1765 is illustrated in Figure 1-6. The pipe at service load should remain uncracked under the three-edge bearing condition.

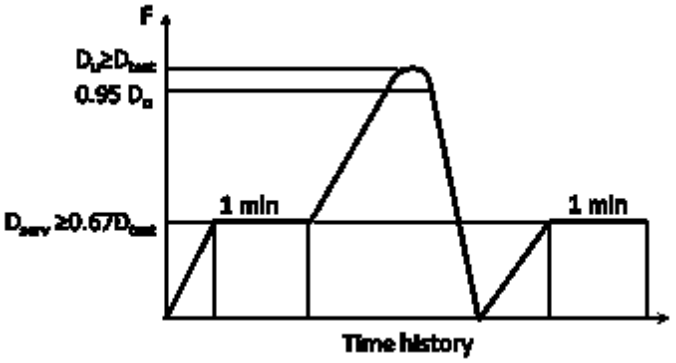

Figure 1-6 ASTM C1765 loading history for SFRCP

These provisions are similar to the ones described in EN 1916 with the exceptions of values that define D-test (or crushing) load.

Overall, the literature on application of steel fiber to precast concrete pipes is limited, however majority of the studies considered the use of fiber in pipes up to 33 in. (800 mm) in diameter. De La Fuente et al. (2011) in his studies determined that the upper boundary of steel fiber application in concrete pipes is limited to pipes with 42 in. (1000 mm) as distinctive reinforcement.

Among the studies reported, Haktanir et al. (2006) investigated the effects of steel fibers and mineral fillers on the water-tightness of concrete pipes. It was found that tests revealed that addition of mineral fillers that pass No. 100 sieve and reinforcement of concrete pipe with steel fiber overall improved water tightness of the pipe due to reduced internal cracking.

Another experimental study conducted by Haktanir et al. (2007) compared SFRCP to conventionally RCP of 20 in (500 mm) diameter under three-edge-bearing test. The SFRCP with fiber dosage of 44 lb/yd^3 (25 kg/m^3) and 66 lb/yd^3 (40 kg/m^3) were considered; RC-80/60-BN and ZP-308 fibers with lengths of 2.36 in (60 mm) and 1.18 in (30 mm), respectively, were used for each fiber dosage. It was concluded that fibers with higher aspect ratio have a more prominent effect on pipe performance than shorter fibers, providing higher strength at the same fiber dosage.

Experimental and numerical study related to SFRCP was done by de la Fuente (2011). In this study eighteen pipes with a diameter of 24 in. (600 mm) and a fiber dosages of 16, 34, and 68 lb/yd^3 (10, 20 and 40 kg/m^3) were produced and tested for crushing load according to UNE-EN1916. He determined that the pipes with 68 lb/yd^3 (40 kg/m^3) show hardening after global cracking and overall steel fibers can provide strength comparable to RCP.

De Figueiredo (2008) in his studies evaluated the crushing tests of EN1916, where unloading and reloading stages for the pipe are present and NBR 8890, when the

load is applied continuously. He compared the load-deformation responses(Figure 1-7) for the two different loading modes and determined that the reloading cycle of SFRCP does not affect the residual strength of pipes.

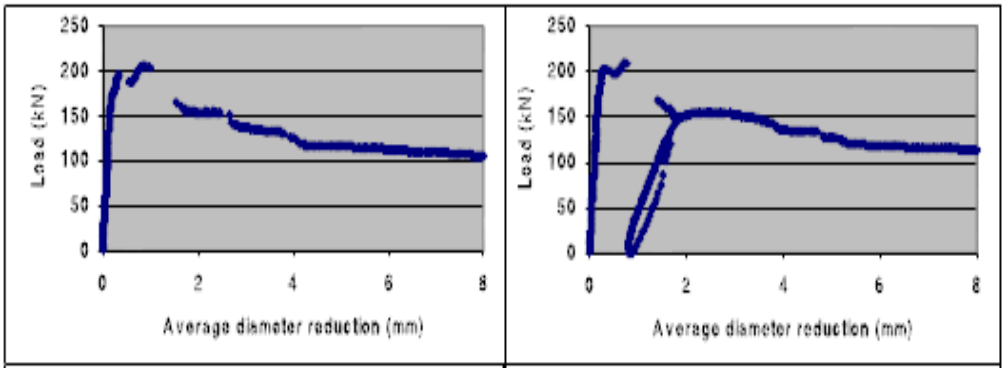

Figure 1-7 Load-deflection curves obtained for continuous and cycled tests for 33 in. (800 mm) pipe with 34 lb/yd^3 (20 kg/m^3) fiber content (De Figueiredo)

In another study, De La Fuente et. Al. (2012) determined the relationship between the fiber content and ultimate strength in the 42 in.(1000 mm) diameter pipe by applying regression. He also determined from the experiment that the minimum amount of fiber required to attain class C60 for 24 in. (600 mm) pipe is 55 lb/yd^3 (31 kg/m^3); and for the pipe of 42 in. (1000 mm) in diameter fiber amount of 64 lb/yd^3 (38 kg/m^3) should be used.

The suitability of steel fibers as substitution for conventional reinforcing in precast concrete pipes is in its developing stages in the United States. Among few studies conducted, MacDonald and Trangsrud (2004) considered the use of fibers in precast application. In their experiments they used steel fiber with rectangular cross-section and enlarged and bent ends. Fiber volumes of 0.25%, 0.5% and 0.75% were considered. In this studies increase of ultimate strength with increase of fiber volume was observed. In addition, the minor increase in ultimate load was noted for the pipes tested at the age of 5

days as compared to 2 days, however this was attributed to concrete maturity rather than effect of fiber.

The performance-based specification ASTM C 1765 developed for SFRCP in the United States is a leap forward towards increasing the use of steel fiber in concrete application and expanding the range of reinforced concrete pipe nomenclature, making them more durable, stronger and more competitive on today's market.

1.3.3. Numerical Models for Steel Fiber Reinforced Concrete

Modeling the mechanical behavior of reinforced concrete still remains a main challenge in the area of structural engineering due to the multi-dimensional non-linearities of reinforced concrete material and plasticity during the process of cracking. Variety of models have been proposed to characterize the non-linear behavior of reinforced concrete.

In general, concrete cracking can be distinguished in three different levels as suggested by Wittman (1983): micro-cracking, which can only be visible through electron microscope and where the crack forms within the cement paste; meso-cracking, which can be observed with conventional microscope and it occurs due to the bond slip between the cement paste and the aggregates; and finally macro-crack, which is visible without any special equipment.

The numerical models of concrete fracture were first introduced in late 1960s by Ngo and Scordelis (1967) in which the discrete crack approach was used and later by Rashid (1968) using a smeared crack technique. The former is based on fracture mechanics and was developed on a principle of capturing the dominant crack initiation and propagation, and the latter on the other hand adopts the idea of concrete inherent heterogeneity which is represented by microscopic cracks which coalesce into macro-cracks upon stress application.

The model of smeared cracking is possible due to the introduction of damage into material model in terms of stiffness deterioration over a given volume. The concept of smeared cracking is based on the crack band model in which the cracking strain of an element equals to the crack opening divided by the length of fracture zone with length l_p (Bazant and Oh 1983). Before the crack initiation, where crack initiation is defined by a combination of stresses satisfying a certain criterion, concrete material is modeled as isotropic. However after crack initiation the stress-strain is represented by the orthotropic material law which implements the material stiffness degradation normal to the crack direction, that is called tension –stiffening (Borst et al. 2004) and is introduced by a descending branch of the stress-strain relationship.

This method however has several drawbacks: Rots and Blaauwendraad (1985) described that the straining of the cracked element imposes the condition that the adjacent element should also experience some strain which causes stress-locking, that is when the element is being in elastic region and cannot change its length, while the cracked element is in its plastic range. Another major shortcomings of the smeared crack approach is that the exact location of the crack inside the element is unknown and due to the crack band width approach the refinement of the mesh may lead to the problems in the solution convergence.

Plasticity alone cannot properly model the non-linear softening behavior due to damage propagation of concrete in tension or compression, at the same time fracture mechanics is only capable of modeling the weakening of materials due to development of micro-cracks. The model combining the two approaches was proposed by Lubliner (1988) and later modified by Lee and Fenves (1998) introducing concrete damaged plasticity which is based on the principle of the smeared cracking. The main characteristics of this model allow to describe the behavior of concrete in terms of strain

hardening, limited tensile strength and non-associative flow rules. The model of concrete damage requires definition of the damage rate. The damage rules vary for concrete models proposed by different researchers, some of them implement the effective stress which accounts for reduction of the area due to the crack formation and is larger than the Cauchy stress (Kachanov 1985). The advantage of this approach is that the stiffness degradation can be decoupled from the plastic deformation by linearizing the evolution equation for the yield surface (Lee and Fenves 1998). However it is not simple to obtain the plasticity parameters needed for the model calibration with experimental tests.

When the crack width or spacing of cracks is a major goal, the discrete crack approach would be beneficial in modeling the concrete behavior. The discrete crack is modeled by defining the tensile strength criterion where the node once reaching the failure stress is split into two nodes and the tip of the crack is propagated to the next node. The process is repeated allowing to visualize the crack propagation through the concrete continuum.

The discrete crack model, however, also has some disadvantages. Since the crack tip propagates only along the boundaries of the elements, the results are highly sensitive to the mesh size. The constant change in mesh topology by remeshing of the crack tip region can alleviate the problem, however at the expense of the computational costs (Borst 2004). There were several techniques developed to overcome the above shortcomings. One of the techniques involves introduction of the interfacial element with a nearly zero thickness along the boundaries of elements where the crack is expected to occur. The dummy stiffness is assigned to that element which is set to zero upon crack initiation (Rots and Blaauwendraad 1985). This method however makes the modeling of cracking at unknown locations rather difficult.

Another method which addresses the mesh sensitivity in discrete crack approach is extended finite element model (XFEM) which was introduced by Fries and Belytschko (2000). The XFEM is based on enriching the region of the location where the crack is expected to appear. This is done by enriching the polynomial approximation space such that non-smooth solution is modeled independent of the mesh This allows an arbitrary crack formation within the enriched region as the crack imposes displacement discontinuity.

In this study, two main approaches of discrete and smeared cracking are considered. The smeared crack in form of concrete damaged plasticity is adopted for further structural pipe behavior investigation.

.

Chapter 2

Pipe Production and Testing

2.1. General

The experimental program consisted of full scale structural pipe and small scale material testing. The full scale pipe testing was mainly conducted in accordance with ASTM C497 at the Hanson plant facility in Grand Prairie, Texas (Rinker-Cemex's pipes, were tested at the location of their production.). The small scale specimens produced at Northern Concrete Pipe and Sherman-Dixie were delivered by truck to the Grand Prairie location. They were then transported to The University of Texas' civil engineering laboratory for testing. Full scale pipes and small scale specimens from Rinker-Cemex plant were tested at their facility.

Structural pipe testing consisted of ASTM standard tests that are currently accepted for RCP and include: the D-load test, Hydrostatic Joint test and Joint Shear test. Small scale material testing consisted of the flexural beam test, compressive cylinder strength test and direct tension test, also known as "dogbone test".

A total of ninety seven (97) SFRCP were produced at the four production sites with diameters ranging from 15 in. (400 mm) to 48 in. (1200 mm). In addition a total of fifteen (15) RCP and 4 plain concrete pipes (PCP) with diameters of 24 in. (600 mm) and 36 in. (900 mm) were produced. A summary of the total pipe count produced at each plant is presented in Table 2-1.

Both ATSM C76 B and C walls were produced and tested, where the wall B is found as (diameter (in.))/12+1 and wall C is found as (diameter (in.))/12+1.75; thus 24 in. (600 mm) with wall B pipe has a wall thickness of 3 in. (76 mm) and wall C has a thickness of 3.75 in. (95 mm).

Table 2-1 Summary of a pipes produced at each plant

Test Site	Number of SFRCP	Number of RCP	Number of PCP	Sizes (in.)	Wall Thickness
HANSON	49	5	-	15,24,30,33,36,42,48	B,C
RINKER-CEMEX	16	2	1	24,36	B
NORTHERN CONCRETE PIPE	21	6	-	24,36,48	B,C
SHERMAN DIXIE	11	2	3	24,36,48	B,C

Fiber volumes ranging from 0.17% to 0.83% with increment of 0.17 % were used. The lower ranges of the fiber content was used for small diameter pipes. For example, typical 24 in. (600 mm) diameter pipe specimens were produced with 0.17%, 0.25 %, 0.33%, and 0.5% fiber fraction and typical 36 in. (900 mm) diameter pipes had 0.5%, 0.67%, and 0.83% fiber content by volume. For the largest diameter pipe 48 in. (1200 mm) tested, 0.67% and 0.83%fiber volumes were considered. Pipe joint lengths produced were 4 ft. (1.2 m), 6ft. (1.8 m) and 8 ft. (2.4 m). To ensure repeatability at least two test specimens for each pipe diameter and fiber dosage were produced. During the production of SFRCP, each plant stopped their production of RCP to accommodate this project.

2.2. Materials

2.2.1. Steel Fiber

Steel fibers RC-65/35-CN were mainly used in the project, a few test specimens with RC-80/60-CN were also produced for comparison. Steel fiber RC-65/35-CN is a galvanized cold drawn wire with nominal tensile strength of 225 ksi (1550 N/mm^2) with straight profile and hooked ends, 1.378 in. (35 mm) total length and an aspect ratio of sixty five (65). Aspect ratio represents the ratio of total length to diameter of the fiber (Figure 2-1). RC-65/35-CN steel fibers are shipped in a pallet of sixty sacks with each

bag weighing 44 lbs (20 kg). Steel fibers RC-80/60-CN have a nominal tensile strength of 152 ksi (1050 N/mm^2) with straight profile and hooked ends, 2.362 in. (60 mm) total length and an aspect ratio of eighty (80).

Figure 2-1 Dramix RC-65/35-CN glued steel fibers

2.2.2. Concrete Mix

Each plant kept their original concrete mix design used for production of RCP with some adjustment in water content. The water amount was adjusted to compensate for the presence of steel fiber which increase demand of moisture due to the increased surface area in concrete components. Local aggregates and other materials were used in the mix design for SFRCP production. Proportions and amounts for each plant are presented in Table A- 1 through Table A- 2 of Appendix A.

Designation for each test specimen was given depending on the mix to distinguish between the tests as follows:

Plant - Pipe Diameter (in.)-Wall Type - Fiber Content by volume (%)-Fiber Type-Test Number;

Plants were denoted as: HAN for *Hanson Pipe and Precast*; SHD for *Sherman-Dixie* plant; NCP for *Northern Concrete Pipe* plant and RNK- Rinker Materials;

Fiber type is denoted as: 65/35 – for Dramix RC-65/35-CN and 80/60 – for Dramix RC-80/60-CN;

Test number: T1 for test 1 and T2 for test 2, etc.

2.3. Production

2.3.1. Mixing Procedure

In all of the production plants, steel fibers were added directly into the mixer or through a conveyer belt along with aggregates before the water was added to assist in uniform distribution and separation of fibers. This method has been practiced successfully in Europe for many years with pipes currently in service.

(a) (b)

Figure 2-2 (a) Fiber introduction into the mix; and (b) fiber distribution

2.3.2. Production Plants

Four production sites in diverse geographical locations were selected. These locations include Hanson Pipe and Precast (Texas), Rinker-Cemex (Florida), Northern Concrete Pipe (Michigan), and Sherman Dixie (Kentucky). The selection of different regions ensured that steel fiber reinforced concrete pipes were produced using various aggregate types available to each region and different mix designs specific to each production site. At each production site the SFRCP were produced using the same materials and mix proportions (except for water) as that used to produce RCP. Water

amounts were adjusted based on fiber dosage in the concrete mix. All four plants used dry-cast production.

2.3.2.1. Hanson Pipe and Precast

The Hanson plant is located in Grand Prairie in the northern region of Texas. With its large facility, the plant produces a wide variety of precast concrete products ranging from pressure pipes to box culverts. This plant is conveniently located in close proximity to the University of Texas at Arlington and is only twelve miles away. All initial mixing, production and testing were conducted at the Hanson plant.

Production of pipes at this plant employs Packerhead equipment that uses a high speed rotating roller head (Figure 2-3 (a)) to form the inside surface of the pipe. This is a semi-automated process in which speed of the rotating head is controlled by an operator.

(a) (b)

Figure 2-3 a) Roller head, (b) formation of inner surface of the pipe

The head forms the inside diameter of the pipe by moving upwards, while the concrete mix is fed in from above (Figure 2-3 (b)). The outside surface of the pipe is formed with a three piece jacket that is placed on a rotating table (Figure 2-4). The forms are moved to a curing area upon completion of compaction where the three piece jackets are stripped from the pipes

Figure 2-4 Three piece jacket on rotating table

The curing area is an allocated space within the production facility. Curing is accomplished by covering the pipes with vinyl curtains. Temperature and humidity are controlled with low pressure steam, which accelerates the rate of hydration. Pipes are cured overnight and then moved to the yard for storage.

It should be noted that the Packerhead equipment was the most challenging of the production processes for manufacturing steel fiber reinforced pipes. The dynamic motion of the de-jacketing process, which commonly occurs within 30 seconds of the final Packerhead pass, would render the pipe incapable of standing up. To alleviate this problem, the water content in the mix was reduced to make it dryer which in turn improved the ability of the fresh pipe to stand up without collapse. The reduction of water did help, however, the excessive dryness contributed to degradation of the compressive strength of the concrete pipe, which is linked to the lack of adequate water needed for the hydration process. Thus, water was added back, but the de-jacketing was delayed from 30 seconds to 1 minute. This was the best solution when the three piece jacket of the Packerhead process was used.

2.3.2.2. Rinker Material –Cemex

The Rinker-Materials' facility is located in Apopka, Florida. This plant employs a fully automated production system using VIHY Mastermatic RC 180 equipment manufactured by Pedershaab. The inside diameter of a pipe is formed with a rising core and the concrete is consolidated using internal vibration of the core and compactor rotor system. The outside surface of the pipe is formed with descending jackets (Figure 2-5). After compaction, the pipes are stripped from the top and transported to a curing kiln via a moving floor or kiln car.

Figure 2-5 Pedershaab Equipment

2.3.2.3. Northern Concrete Pipe

The Northern Concrete Pipe plant is located in Lansing, Michigan and makes precast concrete pipes, manholes and catch basins and other products.

This plant employs Hawkeye equipment with a rising core (Figure 2-6(a)) and descending jackets. Vibration in the jackets consolidates the concrete to form a pipe. After the compaction concrete pipes are stripped and moved to a curing area. The curing area, shown in Figure 2-6(b), utilizes draped curtains where temperature and moisture is controlled with low pressure steam.

(a) (b)

Figure 2-6 (a) Hawkeye rising core and (b) curing room

2.3.2.4. Sherman-Dixie

Finally, the Sherman Dixie plant uses the EXACT 2500 modular, fully automated system by Schlüsselbauer (Figure 2-7 (a)), which operates with the same concept of core vibration. Modules include a cage-master that places the reinforcing cage into the headers, and a casting mold quick change system. Pipes are stripped from the top and then transported by an electric cart to the kiln (Figure 2-7(b)) for curing.

(a) (b)

Figure 2-7 (a) Photograph of EXACT 2500 and (b) curing room

2.3.3. Production Methodology

The first trial of pipe production was conducted at the Hanson plant. A total of four successful SFRCP with 15 in. (400 mm) in diameter, wall B and a fiber content by volume of 0.33% were produced. The initial batch was designed based on information obtained from Haktanir et al. (2007). However this design was not suitable for the Packerhead production method. Upon opening the jackets a crack formed along the joint (Figure 2-8). More over once the forms were removed the pipe had a complete collapse and slid down the form with some of the pipe wall still sticking to the form. A mold release admixture "Rapid Release" was added to the mix in an attempt to resolve the issue. Forms were also sprayed with a form releasing agent. This helped prevent the pipe from excessive sticking to the wall, however it did not solve the problem of crack formation at the initial opening of the jacket and the collapse of the pipe.

(a) (b)

Figure 2-8 (a) Crack formation at initial opening; (b) pipe is standing after 30 sec settling

Consequently, it was decided to use the original mix design practiced at this plant for production of 15 in. (400 mm) RCP. The original Hanson's mix formula worked well and the pipes were able to stand. At a fiber content of 0.33% by volume the surface looked pretty smooth with some fibers visible at the surface. The inside surface looked rough with fibers sticking out which is likely due to the friction effect of the rotating roller head. Some of the joints were crooked but for the most part pipes looked satisfactory. The finished product is shown in Figure 2-9, with joints being repaired using regular procedures of cementing and brushing to obtain a smoother surface.

Other common size pipes with a diameter of 24 in. (600 mm), 30 in. (750 mm), 33 (850 mm), 36 in. (900 mm) and 48 in. (1200 mm) having wall B were produced at this plant. Original mix designs were used to produce SFRCP with adjustment of water content to achieve the pipe aesthetics. Production of pipes with smaller diameters 24 in. (600 mm), 30 in. (750 mm), 33 (850 mm) did not experience problems in the process of making the pipe or in regards to the pipe appearance.

Figure 2-9 First SFRCP with 15 in. diameter lined up for testing

Test results showed that it was more challenging to produce larger diameter pipes of 36 in. (900 mm) and 48 in. (1200 mm) using the Packerhead equipment. Having a larger diameter and length of 8 feet would make it harder for the pipe to support its own weight without the reinforcing cage that typically plays the role of a core support in RCP. Ultimately the concrete mix was optimized to the point where the pipes were able to stand on their own, but it came with a cost of the pipe appearance and joint quality. The mix seemed to be overly dry and the surface of the pipes was a little rough. Some areas of the pipe were not well compacted, especially close to the groove of the pipe. Some of the pipe specimens experienced shrinkage cracking during curing along the joint length which rendered the pipe unsuitable for testing. These pipes overall showed lower three-edge bearing strengths without reaching Class III of ASTM C76 even with higher dosages of fiber. The above results can be explained by the specifics of the production method and dryer mix which did not allow for full hydration of the cement. Poor compaction of the dryer concrete in larger diameters also contributed to lower strength.

Pipe production by means of vibrational compaction of concrete did not experience any challenges. Pipes with diameters of 24 in. (600 mm), 36 in. (900 mm) and 48 in. (1200 mm)in. were produced at the Sherman-Dixie and Northern Concrete Pipe plants, and 24 in. (600 mm) and 36 in. (900 mm) at the Rinker-Cemex plant. The original mix designs at each plant were used for production of SFRCP with the water content adjusted based on the amount of fiber in the mix. The typical surface of SFRCP looked smooth, as shown in Figure 2-10.

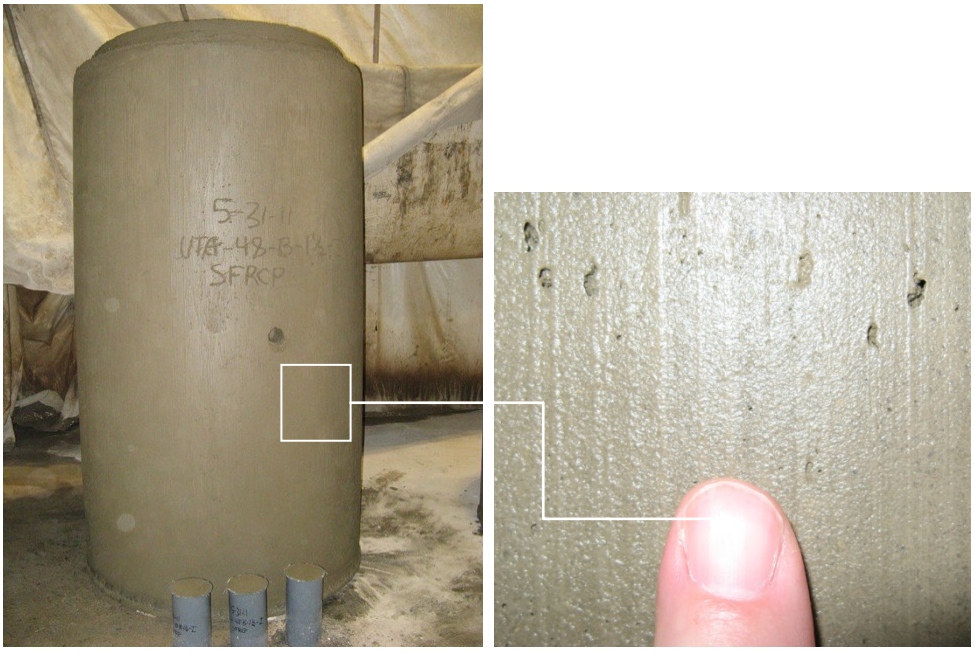

Figure 2-10 Typical finish of the SFRC pipe, here NCP-48-B-8-66

Production of pipe that employs vibrational methods of concrete consolidation was less challenging as compared to the Packerhead process. The finished product looked more aesthetic and the joints had fewer defects. Even for larger diameter pipes this method is an effective way to produce cageless SFRC pipes.

2.4. Test Set Up and Procedures

2.4.1. D-Load ASTM C497

The three-edge bearing test, also known as a D-Load test, was conducted according to ASTM C497 testing procedures. The purpose of this test is to determine the transverse load strength of the pipe and to classify it according to ASTM C76 strength classes. With the exception of the Rinker-Cemex (the Rinker-Cemex SFRCP were tested at their own facility also in accordance with ASTM C497), pipes that were produced at other sites were delivered to Grand Prairie, TX and tested at the Hanson facility.

The testing rack for a three-edge-bearing test consists of two closely spaced bearing strips and the upper loading strip. The pipe is loaded along its length through the upper strip. The spacing between the lower bearing strips can be easily adjusted depending on the pipe size and is verified with a measuring tape. Pipes ranging from 12 in. to 120 in. in diameter can be tested on this rack.

Pipes were instrumented to record the deformations in vertical and horizontal directions using *Cable-Extension Displacement Sensors* (CDS) attached to the inner surface of the pipe at invert and springline, as shown in Figure 2-11. The deformation history synchronized with the applied load was transmitted to the data acquisition system with a frequency of two data points per second.

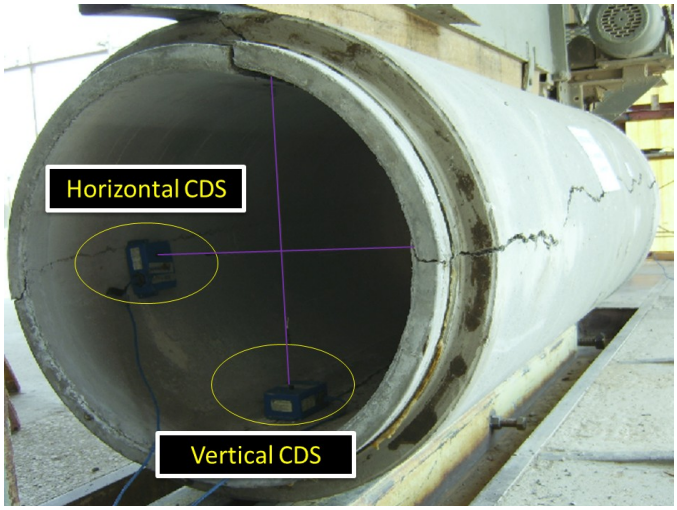

Figure 2-11 Pipe instrumentation

Load was applied incrementally at a maximum rate of 7500 lbf/linear foot of pipe per minute until it reaches service load and then its ultimate strength. As the pipe reaches its ultimate strength, the first crack appears at the interior surface along the crown and invert and then at the exterior surface of the springlines. After reaching its ultimate, deformation starts increasing and no more load is taken by the pipe. The test continued

until the vertical deformation of the pipe reached 5% of its diameter, up to this time parameters were recorded and crack sizes measured up till the completion of the test. The testing was stopped beyond this point to avoid loss of equipment.

The three-edge bearing tests at the Rinker-Cemex facility was conducted in the same manner with the exception that the test was stopped once the pipes reached its ultimate strength. Only displacement history was recorded for this location.

2.4.2. Hydrostatic Test ASTM C443

Hydrostatic joint test is a quality control test for acceptance of pipes with flexible watertight joints, such as rubber gaskets, where water infiltration is a concern. Two sections of pipes are assembled together through a properly designed rubber gasket. Gaskets are fitted to the joint in a proper manner as shown in Figure 2-12.The joint is then plugged with watertight bulkheads at each end as shown in Figure 2-13.

Figure 2-12 Equalizing the gasket for pipe installation

Pipes are placed in a maximum deflected position with one side deflected to ½ in. on one of the sides, as shown in Figure 2-13. The pressure gage is attached to the joint at a horizontal level to measure pressure in the pipe. The assemblage is then filled with water to the exclusion of air and subjected to a pressure of 13 psi for 10 minutes. Pipes were tested immediately upon filling with water with no soaking time.

Figure 2-13 Hydrostatic test setup at deflected ½" position

2.4.3. Joint Shear Test ASTM C497

This test is a "proof-of-design" of a pipe joint which evaluates structural capability of the joint to withstand the differential load. The assemblage of a joint is done per ASTM C497 and as illustrated in Figure 2-14. Pipes are connected with installed rubber gaskets, without water in the assemblage and bulkheads on either end. One of the pipes is supported at both ends, while the other pipe is only supported at the far end of the joint with its spigot resting on a bell of the supported pipe. Load is applied to a suspended pipe at a distance of 1 in.(25.4 mm) from the bell of the supported pipe, as shown in Figure 2-14.

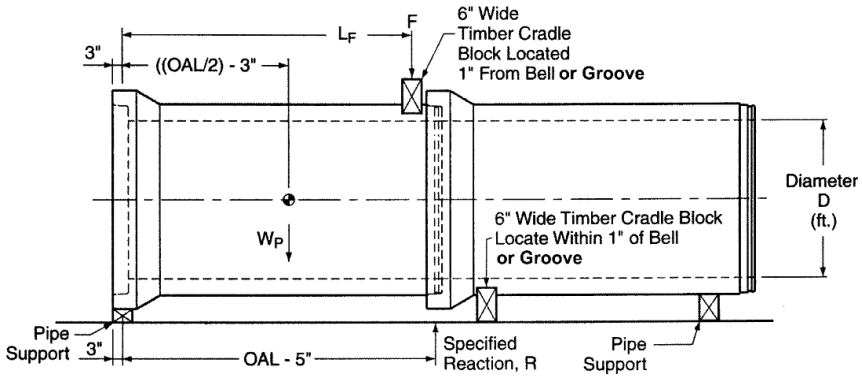

Figure 2-14 Joint shear test pipe setup (ASTM C497)

First, the required additional force (F) should be calculated beforehand. This force determines the estimate of acceptance criteria for the joint. Additional required force (F) is applied at a rate of 56 lb/sec per foot of pipe diameter and is calculated as follows:

$$F = \frac{((OAL) - 5")R - ((OAL/2) - 3")W_p}{L_F}\ (lbs) \tag{2-1}$$

$$R = 4000lbs \times Internal\ \ Diameter\ in\ Feet$$

Here, R - is the required total load on the joint, R=4000*3ft=12000 lb (for 36" diameter pipe); F-additional test force, Wp – nominal weight of a test pipe. Each pipe is measured on a scale before assembling the joint to obtain the weight of each pipe.

Additional required load (F) depends on the installed dimensional parameters: OAL –overall length of the pipe, and LF – distance from the point of load application to the mid-length of the bell. Values are provided in Table 2-2.

Table 2-2 Parameters for calculating the required addition load

Specimen	**Pipe designation**	**Weight of the pipe, lbs (kg)**	**OAL, in. (m)**	**Distance of force application, in. (m)**
#1	HAN-36-C-0.83	5280 (2395)	99.5 (2.53)	89.25 (2.27)
#2	HAN-36-C-0.5	5230 (2372)	99.5 (2.53)	88.38 (2.24)

If the applied load exceeds the additional required load by 2%, pipe is deemed to pass. For the case of SFRCP, load was taken all the way up until the joint failed in order to determine the ultimate shear capacity of the joint.

2.5. Test Results and Discussions

2.5.1. D-Load ASTM C497

A total of 116 pipes were tested for this project, which include RCP, PCP and SFRCP with RC-65/35-CN and RC-80/60/BN fibers. For each tested SFRCP diameter, conventionally reinforced pipes (RCP) were tested for comparison. Here, discussion of the D-load test results is divided based on the production plant and then the results of each plant were compared to each other. Figure 2-15 presents a summary of the normalized over pipe diameter and length (D-load) test results of SFRCP ranging from 15 in.(375 mm) to 48 in. (1200 mm) in diameter, reinforced with Dramix RC-65/35-CN type fiber for all the four plants.

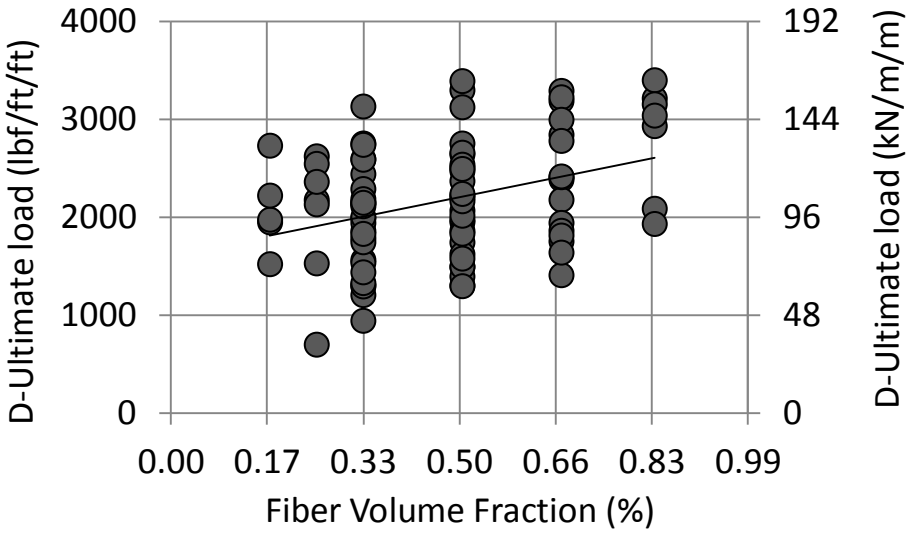

Figure 2-15 Summary of D-load test results for all plants

This chart shows the values of D-ultimate load, which represents the total load applied to a pipe per each foot of length and per each foot of diameter of the pipe (lb/ft/ft). This load is shown along the vertical axis as a function of fiber volume fraction.

Overall the D-Ultimate load has a positive trend with increase of steel fiber content, however the variation in the test results is relatively high. The variation in the test

results can be attributed to the difference in mix designs for each plant as well as variation between the design for different pipe diameters. The graphs shown in Figure 2-16 (a) and (b) and Figure 2-17 (a) and (b) show the D-load test results obtained from each plant.

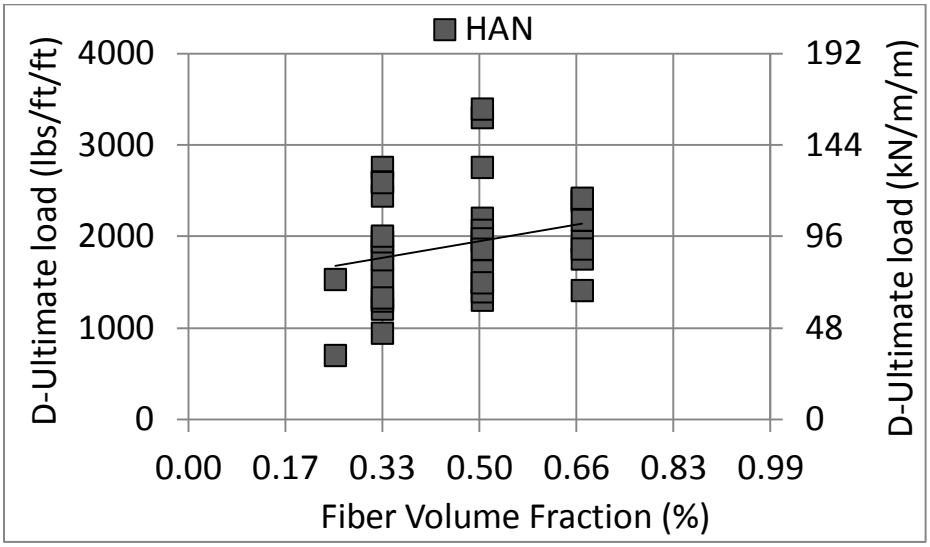

(a)

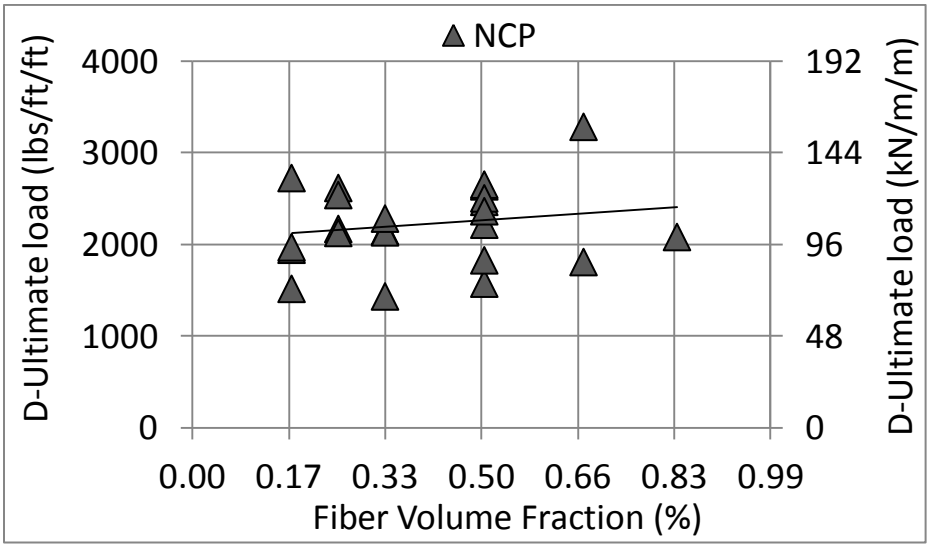

(b)

Figure 2-16 Summary of D-load test results by plant

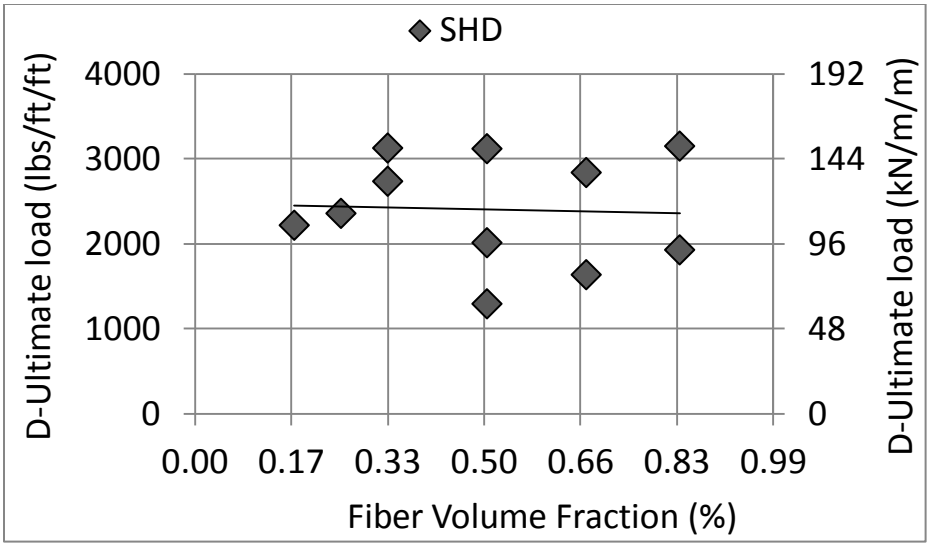

(a)

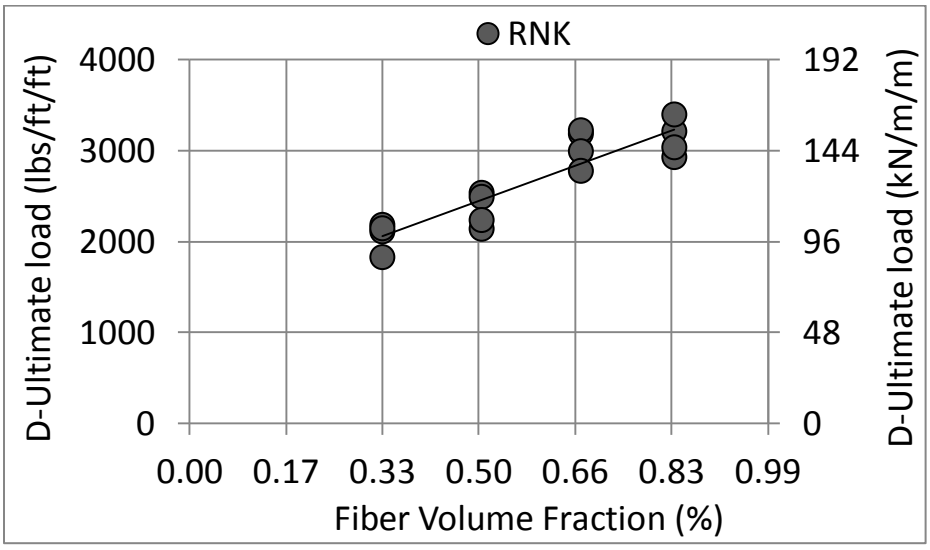

(b)

Figure 2-17 Summary of D-load test results by plant

The data on charts Figure 2-16 (a), (b) and Figure 2-17 (b) show the positive trend in D-ultimate load with increase of fiber content for Hanson, Rinker-Cemex and Northern Concrete Pipe plants. However the test results for Sherman-Dixie plant (Figure 2-17 (a) doesn't show any trend as the fiber content increases remaining nearly constant.

The complete load-deformation responses for all tested pipes are presented in Figure B-1 through Figure B- 49 of Appendix B.

2.5.1.1. SFRCP strength

A total of four pipes with 15 in. (375 mm) diameter and fiber content of 0.33% were the first SFRC trial pipes that were produced and tested successfully. Two of the pipes passed Class III and two of the four pipes passed Class IV of ASTM C76 D-ultimate load. Although, such an excessive amount of fiber in a small diameter pipe would not be practical, subsequent tests and fiber dosages were adjusted based on the obtained knowledge.

A total of thirty three SFRCP with a diameter of 24 in. (600 mm) were tested. Twenty four out of thirty three pipes (73%) satisfied Class III of ASTM C76 D-ultimate load. It is evident from the graph that 0.17% of steel fiber is not sufficient. However 0.25% of steel fiber would suffice to reach Class III, while 0.33% and 0.5% would also work. At a dosage of 0.67% pipes would meet Class IV of ASTM C76 requirements. It is apparent from the chart, that increasing the amount of fiber from 0.25% to 0.5% does not have a great effect on the capacity of a pipe while 0.25% or 0.33% seems to be more reasonable from an economical point of view.

For 30 in. (750 mm) SFRCP, 67% of the D-ultimate loads were between Class III and Class IV and 33% between Class II and Class III, but closer to Class III.

Out of the total of the thirty five SFRCP specimens with 36 in. (900 mm) diameter that were tested, twenty pipes (57%) surpassed Class III and fifteen pipes (43%) did not meet the Class III requirements. It should be noted that all fifteen pipes that did not meet strength requirement of Class III were produced with a Packerhead process. There can be several reasons for having lower values of three-edge bearing strength in larger diameter pipes, such as compaction process difference, amount of cement and types of

aggregate used at this location. These factors can be adjusted accordingly to achieve the desired strength. The problem does not extend to smaller diameter pipes. The variability in fiber dosage for reaching the ultimate D-load for a given pipe class is highly dependent on the quality of concrete and curing time. Indeed, this is similar to the variability observed in precast plants with D-load tests when conventional RCP is produced.

A total of seven (7) pipe with 48 in. (1200 mm) in diameter and fiber volume fractions of 0.5%, 0.67% and 0.83% were tested in three-edge bearing. One (1) pipe with 0.67% fiber fraction attained Class I strength, four pipes (57%) with fiber content of 0.5%, and 0.67% by volume satisfied Class II strength requirements and two pipes (28%) satisfied Class III requirements of ASTM C76 ultimate load.

All the above pipes were manufactured with the concrete mix intended to produce at least Class III strength requirements, however a range of the produced SFRC piped fell below the intended strength class. The concrete mix design should be adjusted accordingly to produce the desired strength class. In addition, the amount of steel fiber in the concrete mix should be considered not only from the economical viability standpoint, but also from the aspect of post-cracking behavior of the pipe. Pipes with lower content have a higher rate strength reduction after macro cracking as compared to pipes with higher fiber content, as shown in Figure 2-18.

The graph shows stiffness degradation which happens right after the macro-crack formation. Pipe with fiber content of 0.17% has a higher rate of stiffness degradation once the pipe is cracked as compared to pipes with 0.25% and 0.33% fiber content. With increase in fiber volumes from 0.17% to 0.25%, the stiffness degradation rate decreases which shows the sign of improved ductility. Pipe with 0.33% fiber content shows strain softening after the crack followed by strain hardening, slightly recovering its stiffness. This trend was observed for the majority of tested pipe diameters.

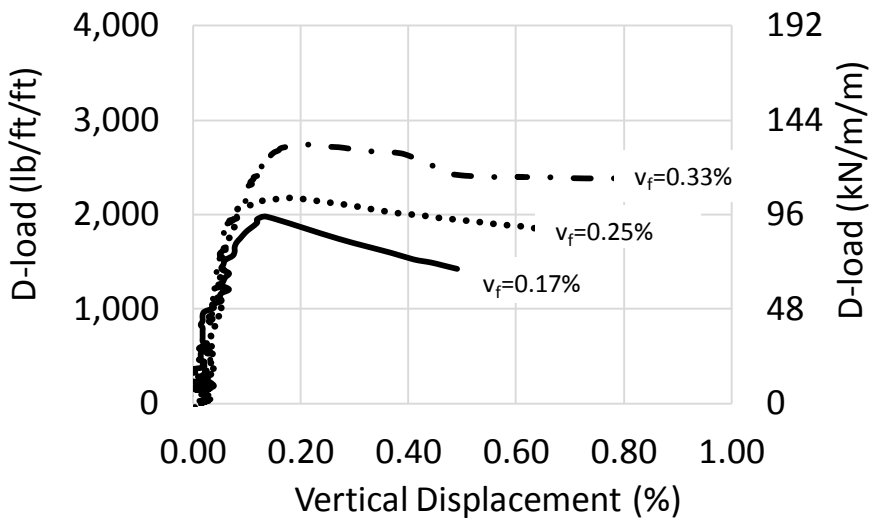

Figure 2-18 Post-cracking stiffness reduction for 24 in. (600 mm) SFRCP

The amount and performance of fiber is essential for concrete post-cracking behavior not only at large deformation, but immediately after the cracking. Once the stage of the load transfer from concrete to fiber is complete, initial stiffness will experience partial recovery.

2.5.1.2. Crack size and failure mode

The crack formation and pattern (along with the capacity of SFRCP to withstand crack opening) is discussed next. Figure 2-19 shows photographs of typical SFRCP and RCP specimens that were tested for comparison at the same age.

(a) (b)

(c) (d)

Figure 2-19 Typical crack patterns: (a), (c)-SFRCP, (b), (d)-RCP

Figure 2-19 (a) and (c) and Figure 2-20 show SFRCP specimens which undergo a unique one-line crack pattern exclusive to the crown, invert, and springlines. Figure 2-19 (b) and (d) show the crack patterns at failure for the RCP, which are distinctly different than those of SFRCP. Also, circumferential cracks are formed along the circumference of the cross section of RCP at the crown, and shear combined with debonding cracks are present at the crown along the pipe joint length. Larger diameter RCP show multiple crack lines at the springlines. Since SFRCP do not experience these

types of crack patterns, shear and debonding type failure modes are excluded by using steel fibers as replacements for the steel wire mesh.

Figure 2-20 Typical crack pattern for SFRCP with bell

The crack lines at the springlines along the joint length are limited to one crack for the SFRCP. This pattern, in fact, was typical for all SFRC pipe sizes and fiber dosages with the exception of pipes with bell, Figure 2-20.

For D-load testing of SFRCP, failure was defined when vertical deformation reached 5% of the pipe's internal diameter. Typically, the measured crack opening in any of the pipes at this deformation level did not exceed ½ in (13 mm).

A comparison graph of the load-deformation plots and crack sizes at the ultimate load for RCP and SFRCP is shown in Figure 2-21. The peak load for SFRCP represents the ultimate load and nearly coincides with a formation of the macro-crack in concrete. The crack at ultimate is a hairline crack visible by a visual inspection. Once a crack appears at the surface, a sudden drop in load on load-deformation plot is observed. Load continues dropping with deformation and cracks growing at crown, invert and springlines. This trend is observed for all pipe sizes and fiber contents.

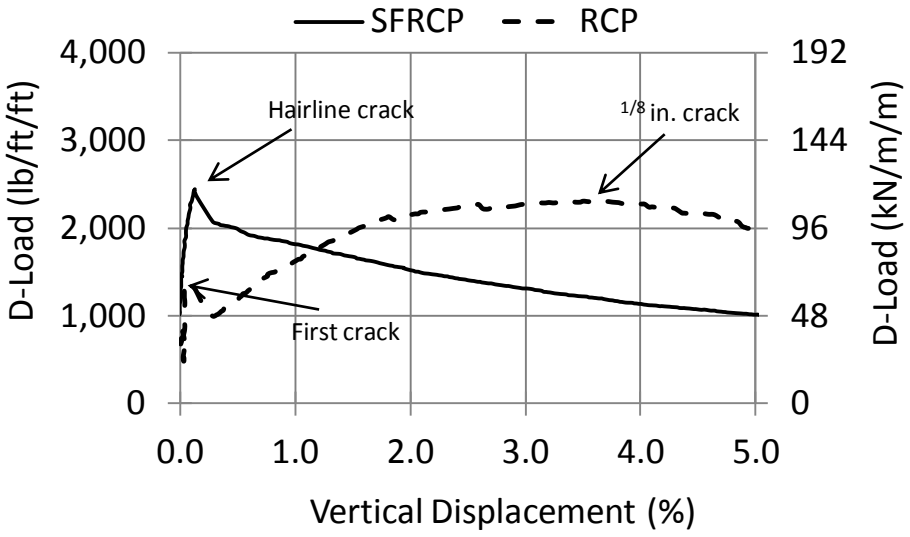

Figure 2-21 Load–displacement curve comparison in 24 in. (600 mm) RCP and SFRCP

In RCP the macro-crack appears at a lower value of load compared to SFRCP. An appearance of the crack is accompanied by a slight drop in load-carrying capacity on the graph. Upon cracking the load is transferred to the steel cage which resists tensile stresses, while compressive stresses are still resisted by both concrete and the steel cage. Transfer of load from concrete to steel cage is signified by increase in load-carrying capacity on the load-deformation plot. The load increases until it reaches its maximum (steel cage yielding) followed by decrease in load. Comparing the size of a crack at 5% pipe's deformation, both RCP and SFRCP experience about the same crack opening. It should be noted that for SFRCP there is a hairline crack at ultimate load, while in RCP the opening at ultimate load is about 1/8 in. Therefore SFRCP remains uncracked at service load with the first crack appearing only upon reaching its ultimate capacity.

Figure B- 50 through Figure B- 54 show typical crack openings at failure for test specimens which were measured at 5% deformation of internal pipe diameter. It was found that crack size does not exceed ½ inches (13 mm) for any size of the pipe at this

deformation. These figures show that SFRCP are capable of undergoing large vertical and horizontal displacements without a collapse.

The test revealed that the fiber dosage of RC-65/35-CN affected the three-edge bearing strength of the pipe, as well as its toughness. The pipe toughness is defined by an area under the D-load-deformation curve at 5% deformation for the three-edge bearing test. The larger area under the curve indicates higher toughness, consequently increased ductility of the structure and the ability to absorb more energy under applied stress conditions before fracturing, in this case, before the collapse of the pipe.

The calculated toughness was normalized over the length and diameter of the pipe to obtain uniform toughness parameters independent of the pipe size. The graph on Figure 2-22 shows how fiber content in concrete influences the toughness of the pipe under the three-edge bearing test for different SFRCP diameters. The figure shows that toughness increases with increased amount of steel fiber content in the concrete mix.

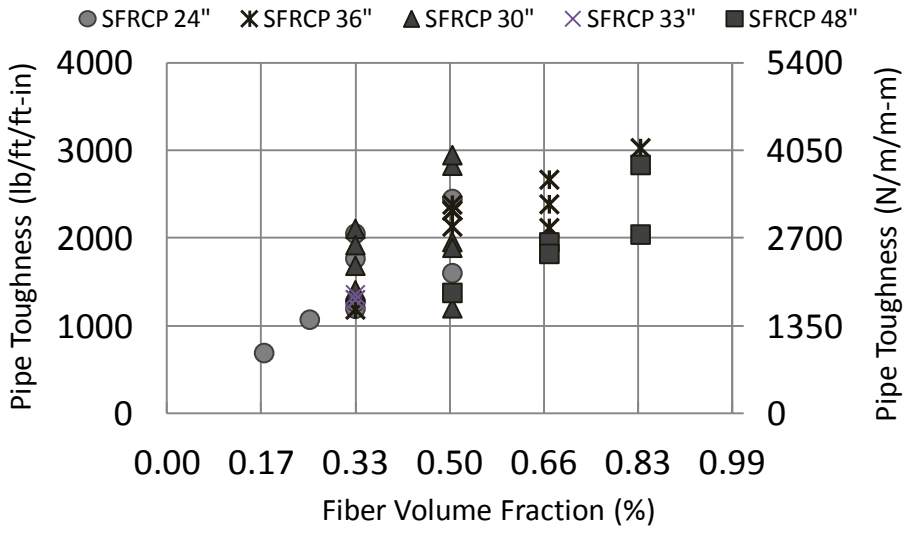

Figure 2-22 Effect of fiber dosage on pipe toughness for SFRCP

Toughness is directly correlated with ductility and strength of the pipe, which is shown in Figure 2-23. This graph demonstrates the relationship between the normalized

toughness and the D-ultimate load. It can be seen that as the toughness increases, the strength of the pipe under the three-edge bearing also increases.

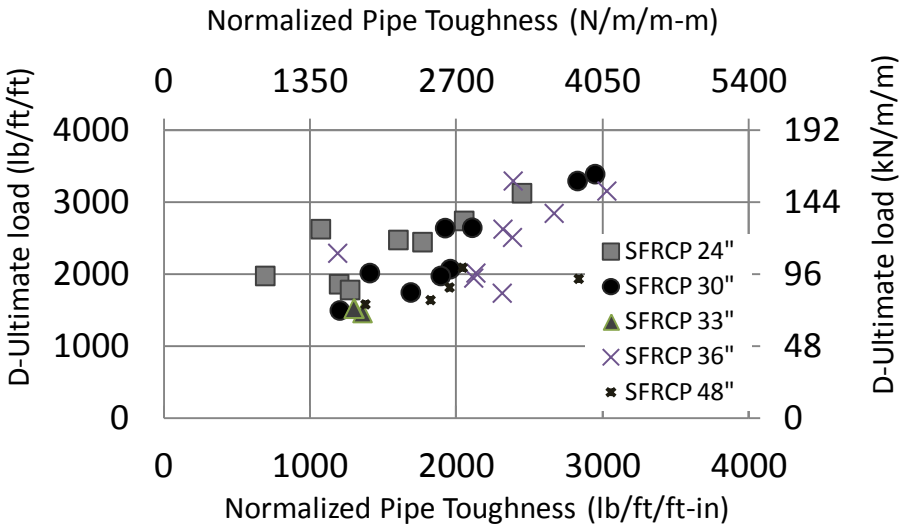

Figure 2-23 Toughness vs. D-ultimate load relationship

The toughness values and the corresponding D-ultimate test results for all tested pipes are presented in Table 2-3.

Table 2-3 SFRCP D-ultimate and pipe toughness for Hanson plant

Pipe designation	Fiber (v_f), (%)	D-ult., (lb/ft/ft)	Toughness D-load (lb/ft/ft-in.)
Hanson Pipe and Precast			
HAN-24-B-44-65/35-T1	0.33	2440	1770
HAN-24-B-44-65/35-T2	0.33	1855	1200
HAN-30-B-44-65/35-T2	0.33	1740	1690
HAN-30-B-44-65/35-T3	0.33	2010	1410
HAN-30-B-66-65/35-T1	0.5	2065	1960
HAN-30-B-66-65/35-T2	0.5	1970	1895
HAN-30-B-66-65/35-T3-	0.5	1490	1205
HAN-30-C-44-65/35-T1	0.33	2640	2110
HAN-30-C-44-65/35-T2	0.33	2635	1925
HAN-30-C-66-65/35-T1	0.5	3290	2830
HAN-30-C-66-65/35-T2	0.5	3385	2950

Table 2- 3 Continued

Pipe designation	Fiber (v_f), (%)	D-ult., (lb/ft/ft)	Toughness D-load (lb/ft/ft-in.)
Hanson Pipe and Precast			
HAN-33-B-44-65/35-T1	0.33	1455	1360
HAN-33-B-44-65/35-T2	0.33	1515	1305
HAN-33-B-44-65/35-T3	0.33	1515	1300
HAN-36-B-66-65/35-T1	0.5	1730	2315
HAN-36-B-88-65/35-T1	0.67	1940	2120
Northern Concrete Pipe			
NCP-24-B-22-65/35-T3	0.17	1970	695
NCP-24-B-33-65/35-T2	0.25	2620	1075
NCP-24-B-44-65/35-T1	0.33	1775	1275
NCP-24-B-66-65/35-T1	0.5	2470	1605
NCP-36-C-44-65/35-T1	0.33	2285	1190
NCP-36-C-66-65/35-T1	0.5	2620	2320
NCP-36-C-66-65/35-T2	0.5	2505	2385
NCP-36-C-88-65/35-T1	0.67	3290	2390
NCP-48-B-66-65/35-T2	0.5	1575	1380
NCP-48-B-88-65/35-T1	0.67	1810	1955
NCP-48-B-110-65/35-T1	0.83	2085	2045
Sherman-Dixie			
SHD-24-C-33-65/35-T1	0.25	2360	724
SHD-24-C-44-65/35-T1	0.33	2735	2055
SHD-24-C-66-65/35-T1	0.5	3120	2450
SHD-36-C-66-65/35-T1	0.5	2010	2135
SHD-36-C-88-65/35-T1	0.67	2840	2670
SHD-36-C-110-65/35-T1	0.83	3150	3030
SHD-48-B-88-65/35-T1	0.5	1635	1825
SHD-48-B-110-65/35-T1	0.83	1930	2838

2.5.2. Hydrostatic Joint Test ASTM C443

The hydrostatic joint testing of structural pipe was conducted at the Hanson Pipe and Precast facility in Grand Prairie and Houston plants in Texas. The Hanson facility in Grand Prairie produces tongue and grove on a daily basis and only occasionally the

production allows for bell and spigot type joints. Due to specifics of production schedule, the initial testing was done on tongue and groove pipes using a flexible mastic gasket “RAM-NEK”. The pipe of 30 in. (750 mm), wall B and fiber fraction of 0.5% was filled with water and attempted to be pressurized. However leakage started immediately from the joints and within the body, Figure 2-24. The test was repeated unsuccessfully using O-ring rubber gaskets. Thus, tongue and groove pipes were deemed to be unsuitable for hydrostatic pressure. A set of bell and spigot pipes were produced at Hanson plant in Houston using Hawkeye equipment, which produces mainly wall C.

Figure 2-24 Hydrostatic testing on tongue and groove pipes using RAM-NEK

Hydrostatic ASTM C443 tests were done on five specimen joints produced at the Hanson plant in Houston. Three of the pipes with 30 in. (750 mm) diameter wall C and a fiber volume fraction of 0.33, 0.55 and 0.66% were delivered for testing to the Grand Prairie plant. Figure 2-25 shows a typical setup for hydrostatic testing.

A summary of the specimens tested is shown in Table 2-4. Specimen #1 with fiber content of 0.33% by volume showed some seepage from a pinhole eventually forming a drip in the body of one joint of the pipe, as shown in Figure B- 55.

Figure 2-25 Hydrostatic test setup in Grand Prairie, TX

Specimen#2 with fiber content of 0.33% by volume was holding the pressure of 13 psi until the last minute without showing any leakage or seepage.

Table 2-4 Hydrostatic test matrix

Specimen	Pipe designation	Test age (days)	Rubber gasket type
#1	HAN-30-C-0.33	7	PG-JKP
#2	HAN-30-C-0.33	9	PG -JKP
#3	HAN-30-C-0.5	13	PG-JKP
#4	HAN-36-C-0.83	8	PG -JKP
#5	HAN-36-C-0.5	10	PG-JKP

In the final minute the joint of one of the bulkheads started leaking and dripping for the duration of the test. Specimen #3 with fiber content of 0.5% by volume started leaking from the joints immediately and lasted for the duration of the test, Figure B- 56. Specimens #4 and #5 were tested at the Hanson plant in Houston. The pipe with fiber content of 0.83% by volume for specimen #4 started having seepage shortly after the beginning of the test. For the duration of testing, the pipe developed minor seepage in seven locations within the body of the pipe, Figure B- 57. One of the bulkhead-pipe joints had minor leakage throughout the test.

After the test was completed the joint was disassembled for further examination. During visual observation of the joint an uneven surface due to presence of fiber was detected, as shown in Figure B- 58. The area surrounding the imperfection was wet and may have caused the joint seepage. Specimen #5 was tested successfully without showing any seepage.

In conclusion, pipes with higher fiber dosage are more prone to body leakage than the pipes having lower volumes of fiber. Preparation of the joint for the assemblage, such as mortar leveling, may be needed to prevent joint leakage. In addition, presoaking for a period of up to 24 hours, as allowed per the ASTM C497, may be required to seal micro cracks within the body.

2.5.3. Joint Shear Test ASTM C497

Joint shear test was conducted per ASTM C497 on two pipe specimens with diameters 36 in. (900 mm), wall C and a fiber content of 0.5% by volume and 0.83% at the Hanson plant in Houston. Both specimens exceeded the required additional load; results of the test are presented in Table 2-5. The joints have enough shear capacity to sustain the load exceeding almost 2.5 times the required shearing strength in the joint

Table 2-5 Joint shear test matrix

Specimen	Pipe designation	Test age (days)	Required additional joint load, (lbf)	Applied additional joint load, (lbf)
#1	HAN-36-C-0.83	23	9940	23614
#2	HAN-36-C-0.5	23	10065	25552

Both specimens exhibited failure in a brittle manner without signs of crack initiation and propagation. The tongue of the supported pipe remained intact while the groove, which the shearing joint force was applied to, failed, as shown in Figure B- 59 through Figure B- 61 of Appendix B..

Chapter 3

Testing for Mechanical Properties of Zero-Slump Steel Fiber Reinforced Concrete

3.1. Production

Material testing was conducted at the UTA Civil Engineering Laboratory. Once cured, the small scale specimens were delivered from the Hanson facility to the testing site at UTA. Testing was conducted at 3, 7 and 28 days in accordance with ASTM C39 standard.

Small scale specimens were produced in the field along with pipes made from the same mix as the structural pipes. Fresh concrete mix left from pipe production was dumped into the wheelbarrow and delivered to the site for the specimen fabrication. The concrete was a dry-cast mix with low or zero slump, without a flow. This required the use of a shake table and a plunger to provide proper concrete consolidation. Specimens were fabricated according to ASTM C31 procedures and cured the same way as the concrete pipes, in a designated curing area, Figure 3-1 .

Beam specimens were formed in 6x6x22 (in.) standard steel molds in three lifts without rodding, but using a vibrational table. Two beam specimens were produced for each mix. Specimens produced using the Hanson concrete mix would typically have a rougher surface with numerous defects and geometric imperfections as compared to the specimens produced at the other plant.

Concrete compaction issues at the Hanson facility could be attributed to the dryer concrete mix than the other plants. Specimens had to be consolidated for a longer time period on a vibration table and with increased number of plunger passages. Concrete beams produced from the other three facilities were smoother, with fewer defects and better geometric tolerances.

Figure 3-1 Specimen curing

Cylinder specimens with 4x8 (in.) and 6x12 (in.), depending on the available molds at the plant, standard sizes were molded in plastic cylinders forms in three lifts using plunger and a vibrating table, without rodding. For each SFRCP, three compressive cylinders were produced to be tested at the ages of 3, 7 and 28 days. In general, specimens had a smooth surface with only few combs and defects.

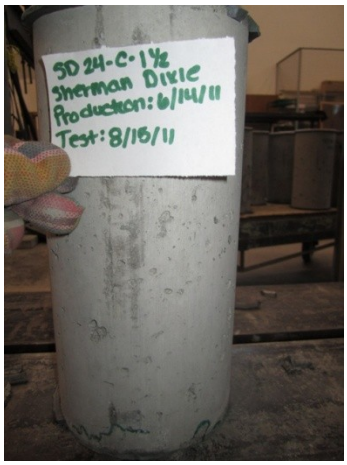

Figure 3-2 Typical finish of SFRC cylinder specimen

The number of specimens for the direct tension test was limited to the number of available molds, but typically two direct tension test specimens per mix were produced to ensure consistency of the test. The molds for this test are made of a high density polyethylene and were manufactured at the UTA machine shop (Figure 3-3). The specimens have a unique dog-bone shape with a thickness of 4 in. (102 mm). Dog-bone specimens were formed with 5 layers of concrete interchanged by 4 layers of nineteen gauge galvanized steel mesh. Steel mesh is cut to shape in advance to fit the dog-bone mold and is placed at each end of the specimen after a layer of concrete is compacted. Steel mesh is embedded into the specimen as reinforcement to prevent crack initiation in undesired locations, such as a sudden geometry change.

Figure 3-3 Direct tension test specimen mold on left and steel mesh reinforcing

3.1.1. Compression Cylinder Strength ASTM C39

Compressive cylinder tests were conducted to determine the compressive strength of the fiber reinforced concrete and the influence of steel fiber on its properties, the mode of failure and the rate of straining of the concrete specimen. Specimens were analyzed separately for each plant to distinguish between mix designs. Then compressive strengths for all plants were compared.

Figure 3-4 Capping cylinder specimens

Concrete cylinder specimens were first prepared for testing. Each end of the specimen was capped with a sulfur-based compound to create a smooth and leveled surface (Figure 3-4). Sulfur caps were applied at least one day before testing. Testing was done in accordance with ASTM C39 “Standard Test Method for Compressive Strength of Cylindrical Concrete Specimens”. Cylinders are centered in the compression-testing machine and loaded until complete failure. The setup of the test is shown in Figure 3-5

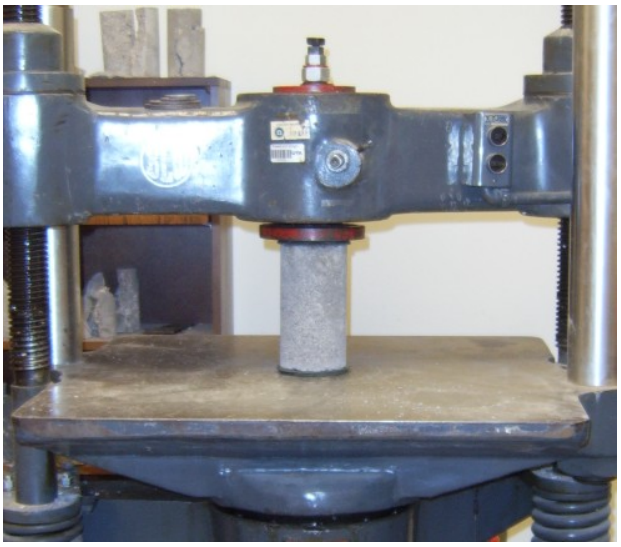

Figure 3-5 Compressive test setup

The compressive strength of concrete is calculated by dividing the maximum load at failure by the cross-sectional area of the specimen. A minimum of three cylinders were tested at the same age and the average strength is reported.

3.1.2. Flexural Beam Test ASTM C1609

The flexural beam test is useful in determining modulus of rupture, modulus of elasticity and the stress-strain relationship in the elastic region. This test is performed to evaluate the flexural performance of the fiber reinforced concrete using parameters derived from the load-deflection curve. The curve is obtained by testing a simply supported beam under third point loading using a closed-loop servo-controlled testing system. For this study the influence of steel fiber on modulus of rupture, modulus of elasticity and the relationship between compressive and tensile strength will be established through the strength ration (η).

Beams with sizes 6×6×22 (width×depth×length) (in.) were used for the third-point bending test. The test was conducted in accordance with ASTM 1609 “Flexural Performance of Fiber Reinforced Concrete” specification

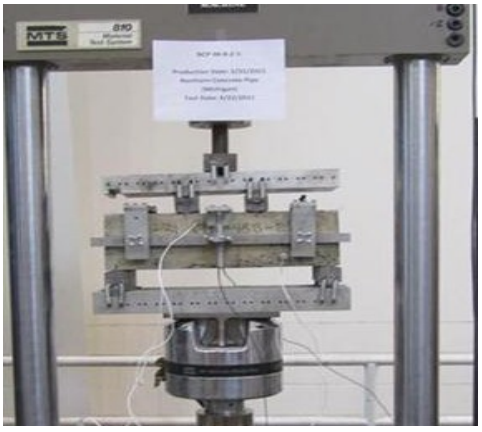

Figure 3-6 Flexural test setup

The test setup is shown in Figure 3-6. The setup consists of electronic transducers to measure vertical deflection of the beam upon loading. The transducers are

located at the mid-span and attached by means of a rectangular jig which is clamped to the specimen directly over the supports on each side. The average of the two measurements from the transducers represents the net deflection. This test provides methods for determining the first peak, peak loads and the corresponding flexural tensile stress which is calculated as:

$$f_t = \frac{PL}{b \cdot d^2} \quad (3\text{-}1)$$

3.1.3. Direct Tension Test

The direct tension test is a displacement controlled test where displacement at predefined rate is applied to the specimen and the strain is measured. Although the direct tension test is not considered to be a standardized test, it is very useful in obtaining the direct relationship between stress and strain. Testing was done using an MTS machine with the setup shown in Figure 3-7. Two electronic transducers are attached on each side of the specimen to measure axial displacement. The tensile displacement is applied at a rate of 0.005 in./min, which is identical to the deformation rate of the flexural beam test.

Figure 3-7 Direct tension test setup

Displacement data from the transducers and the loading is transmitted to a data acquisition system, and the average of two displacement transducers is taken in deformation calculations. Stress is obtained by dividing the load at each increment over the cross-sectional area within the gage of the specimen, and the strain is calculated by dividing the average deformation by the gage length.

3.2. Test Results and Discussions

3.2.1. Compression Cylinder Strength ASTM C39

A total of 139 compression specimens were tested per ASTM C39 at ages: 1, 3, 7 and 28 days, and fiber contents of 0.17%, 0.25%, 0.33%, 0.5%, 0.67% and 0.83% by volume. Compression test results were analyzed based on average compressive strength, strain and failure mode. Compressive strengths test results are presented in Table C-1 through Table C-4 of Appendix C.

Figure 3-8 shows concrete compressive strengths of cylinders as a function of fiber dosage and is distinguished by the plant. The results of 106 specimens are reported here, excluding the compressive strength tests conducted at the age of older than 28 days. An average value of compressive strength at an average day of 7 days was 7010 psi. The graph shows that there is no apparent trend in the fiber dosage – compressive strength relationship. Therefore, the amount of fiber in the mix, as shown in Figure 3-8, does not affect the compressive strength of the concrete, which was also confirmed in previous studies by other researchers (Naaman 2007, Natarja et al. 1999). The variation in results of compressive strength can be attributed to the difference in the mix design for different plants. Concrete compressive strength is a function of the type of cement and its amount in the concrete mix, as well as the origin of the aggregates, type of fly ash and other material variables.

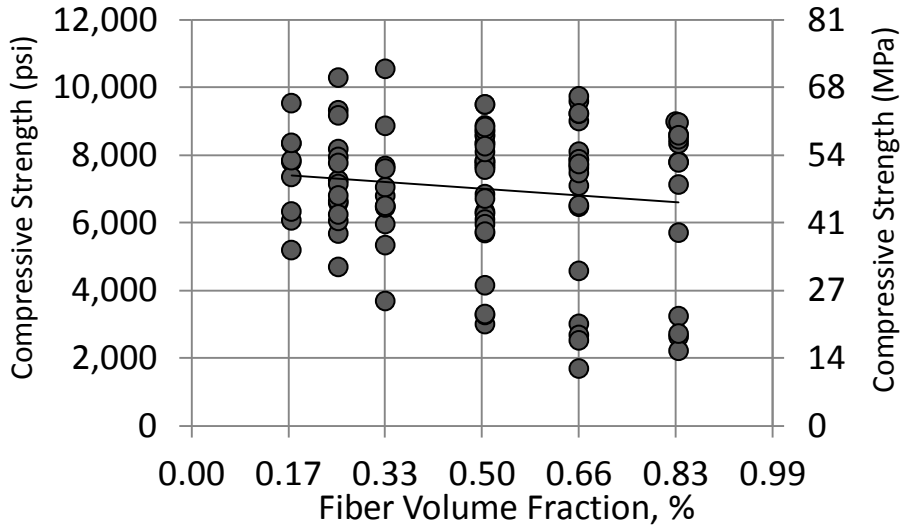

Figure 3-8 Effect of fiber content on compressive strength for all plants

The results of compressive strength tests for cylinders produced at Northern Concrete Pipe are shown in Figure 3-9. The compressive strength results shows a slight upward trend with increase of fiber volumes, however with a high variation in results.

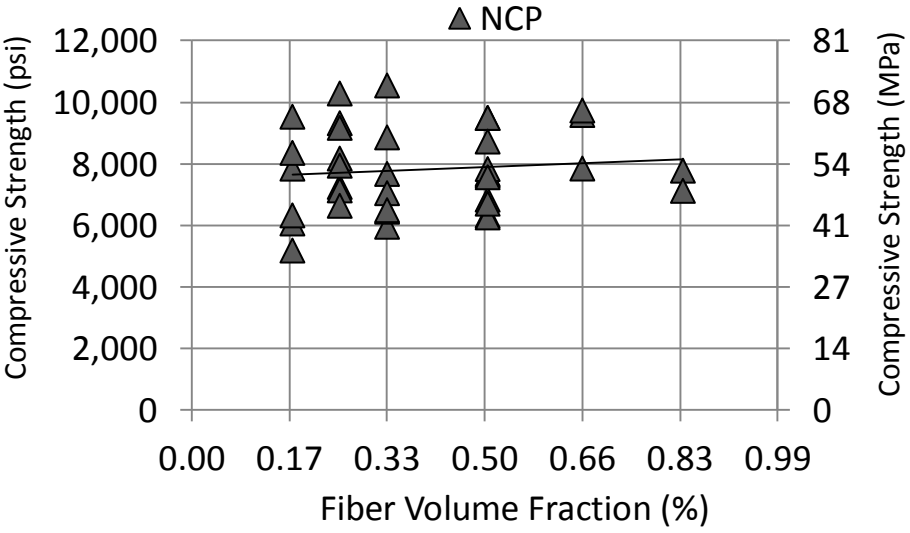

Figure 3-9 Effect of fiber content on compressive strength for Northern Concrete plant

However the average compressive strength of 7810 psi for this plant is the highest out of all plants, which could be attributed to higher cement content in the mix as compared to other plants (refer to Table A-1 through Table A-16 for mix design information).

The cylinders produced at Sherman-Dixie plant also had a higher range of compressive strength values with the average of 7742 psi. The variation of the test results for this plant is lower than for the other two plants. There is a slight positive trend in compressive strength with increase in fiber content.

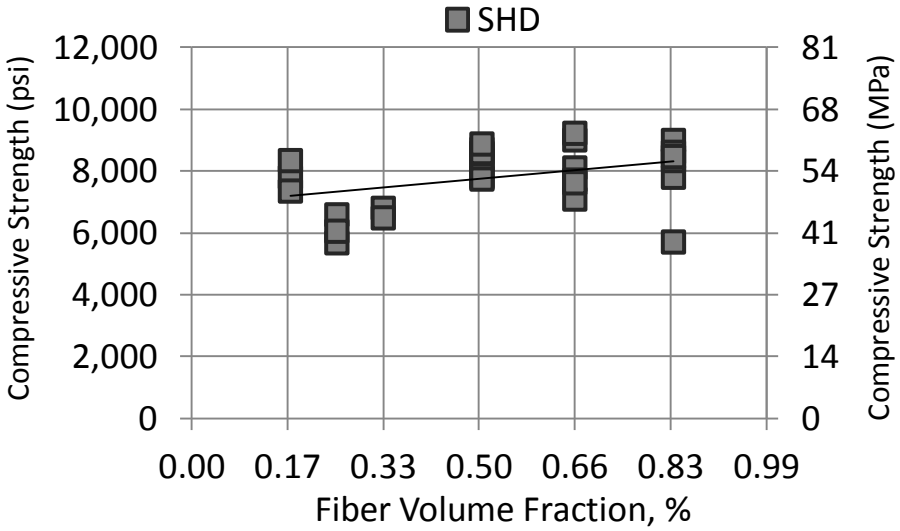

Figure 3-10 Effect of fiber content on compressive strength for Sherman-Dixie plant

Compressive strength test results of concrete cylinders for Hanson plant are shown in Figure 3-11 and has an average strength of 5484 psi. The overall trend is negative with decrease of compressive strength as the fiber content increases. Moreover, cylinders produced at Hanson plant have the highest variation in test results as compared to other plants. A lower value of compressive strength at Hanson could be a result of production specifics at this plant for a Packerhead process, which requires the mix to be dryer than the mixes at other plants which may result in the lack of water needed for proper hydration. In addition the original concrete mix at Hanson plant contains less

cement which contributes to the lower values of compressive strength of concrete. Also many cylinders produced at Hanson plant were for the trial mix-design in a search for the optimum water content which inevitably contributed to high variation in test results.

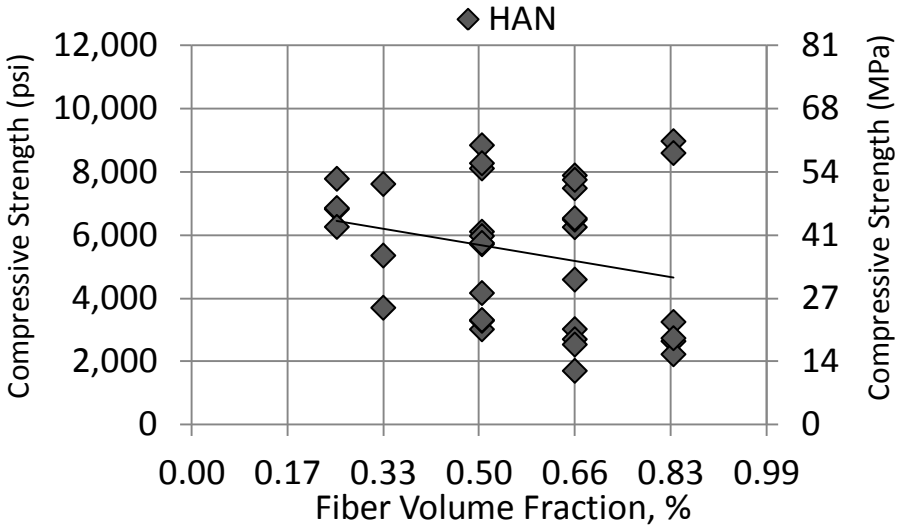

Figure 3-11 Effect of fiber content on compressive strength for Hanson plant

Fifty eight out of 139 cylinders were measured for an axial strain due to compressive stress. The average value for axial strain was 0.038 in./in. at the peak load, as shown in Figure 3-12, which is almost ten times higher than the typical strain of plain concrete. The strain measurement was done by recording the displacement of testing machine and is not accurate, however the overall trend from this relationship can be observed. Although an overall trend of compressive strain is not apparent, looking at the trends separately for each plant shows that results for cylinders produced at Sherman-Dixie and Northern Concrete pipe plants have a slight upward trend in strains as the fiber content increases, whereas Hanson plant shows strong downward trend.

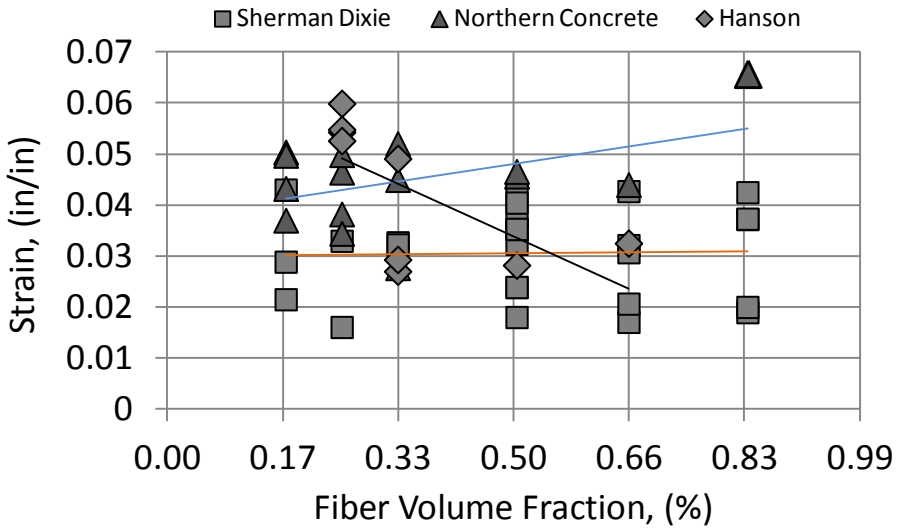

Figure 3-12 Effect of fiber content on concrete strain in compression

The specimen has the capacity to sustain higher loads by experiencing larger deformation, therefore higher strains. The influence of the amount of fiber in the mix on compressive strength is not apparent from the strain-fiber content relationship, but it has a slight upward trend on stress-strain relationship curve with a slight upward trend in compressive stress as the specimen strains more, as shown in Figure 3-13.

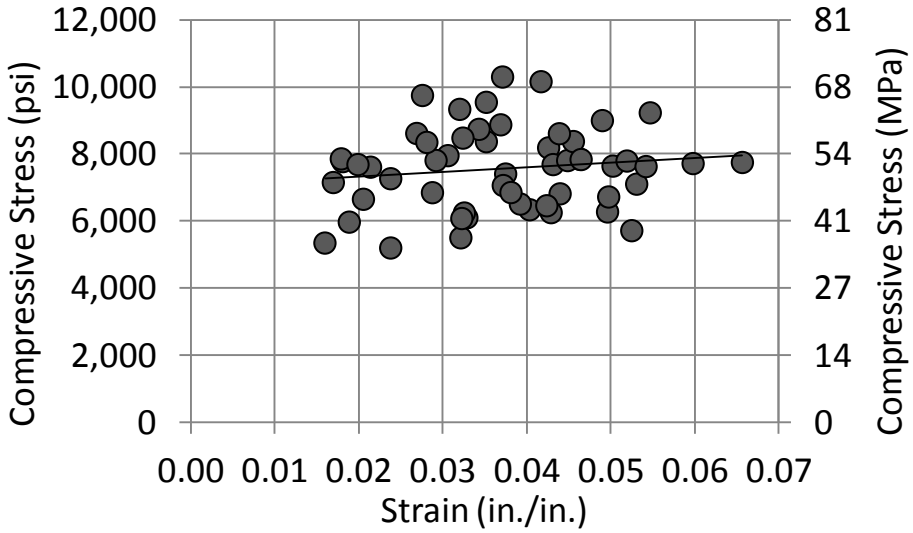

Figure 3-13 Effect of fiber content on compressive strength for Hanson plant

Failure modes of SFRC cylinders are shown in Figure C-1 through Figure C-16 of Appendix C. A plain concrete cylinder's typical failure is brittle failure, characterized by side fractures and chipping off. Concrete having lower volumes of steel fiber failed in a brittle like manner with complete splitting of the specimen, as shown in Figure C-7. Cylinders from the Hanson plant had more failures by chipping off (Figures C-13 and C-14) than the cylinders from the other plants. Typical failure of SFRC cylinders is a diagonal fracture of the cylinder without formation of cones. Columnar vertical cracking is also characteristic of SFRC cylinders.

3.2.2. Flexural Beam Test ASTM C1609

Beam failure modes, modulus of rupture and strength ratio coefficients were considered for analysis in beam testing. Table D-1 summarizes beam test results and includes tensile strength (f_t), which represents modulus of rupture; strength ratio (η), which represents ratio of tensile strength to a square root of compressive strength; and steel fiber reinforced concrete modulus of elasticity (E), which represents stiffness of the material. Compressive strength (f_c) is obtained through compressive cylinder testing and presented in this table for the tensile strength ratio calculation. For each of the parameters, the influence of steel fiber dosage on modulus of rupture, stiffness, strength ratio and load-deformation behavior is evaluated.

Three main types of load-deformation curves can be distinguished for steel fiber reinforced concrete, as shown in Figure 3-14. The shapes of the curves can be distinguished as: sharp drop of load carrying capacity and subsequent stiffness recovery; transitional with two peaks, where first peak generally has a lower value and an insignificant drop in load carrying capacity after the crack and is followed by a higher peak; and finally, smooth curve without prominent sharp drops in load carrying capacity.

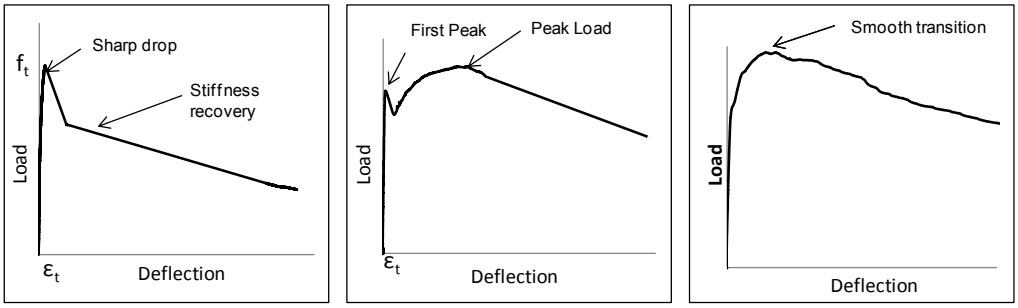

(a) (b) (c)

Figure 3-14 Typical load-deformation curves (a) with sharp drop, (b) transitional with two peaks, (c) smooth

Three specimens with fiber content of 0.17% were tested, two of them were produced at Northern Concrete Pipe and one at the Sherman-Dixie plants. All three specimens went through a load-deformation exhibiting a sharp drop in load carrying capacity after the first crack, Figure D-1, D-3 and D-5. Ultimate flexural stress coincides with formation of a macro-crack in the specimen and corresponds to the load in a range of 7,000-10,000 lbs. The specimen partially recovers its stiffness once the load transfer from concrete to fibers is complete.

Two specimens with fiber content 0.25% produced at Northern Concrete Pipe and the Sherman Dixie plants were tested. Similar to the specimens with 0.17% fiber content, these specimens undergo a sharp drop with a subsequent partial stiffness recovery, Figure D-7 and Figure D-10. The specimen produced at the Sherman-Dixie plant gains some strength after reaching deformation of about 0.015 in. having another peak followed by a gradual stiffness degradation at a lower rate.

A total of seven beam specimens with fiber content of 0.33% were tested. Three beams were produced at Hanson plant, one at Sherman-Dixie and three at Northern Concrete Pipe plants. The specimens produced at Sherman-Dixie and Hanson plants went through a load-deformation curve with a sharp drop after reaching the first crack.

Beams were able to gain some strength reaching a new peak of load followed by a gradual decrease, shown in Figures D-11 through D-24. Specimens from the Northern Concrete Pipe plant experienced loss of strength after the first crack without further strength recovery only with a slight decrease of stiffness degradation rate. Absence of strength recovery at the Northern concrete pipe as compared to the other two plants could be attributed to a difference in compaction of the concrete specimen and to differences in concrete mix.

When the steel fiber content reaches 0.5% by volume concrete behavior changes from brittle to a more ductile-like behavior. Both Sherman-Dixie and the Hanson plants' specimens follow a transitional load-deformation curve having a drop of only 3-18 percent, as opposed to a 30-50 percent drop for lower dosages, Figures D-25 through D-42. The peak load at first crack did not change drastically with the increase of fiber dosage, however the specimen gains significant strength after the first crack initiation, acting almost like steel with the presence of strain hardening region. Flexural strength of the specimen is increased and reached a new peak corresponding to its ultimate strength. Specimens from Northern Concrete Pipe did not have significant gain in strength post cracking and they behaved similar to the specimen with content 0.25% having a sharp drop followed by slight strength recovery.

Seven specimens were tested with fiber content of 0.67% by volume and four specimens with content of 0.83% by volume. All specimens exhibited more ductile-like behavior having transitional and smooth load-deformation curves. The range of ultimate was between 8000 to 11000 lbs for fiber content of 0.67% by volume and between 11000 to 15000 lb for fiber content of 0.83% by volume. Specimens with content of 0.83% by volume behaved as a composite material having a smooth load-deformation curve.

Crack pattern represents failure modes from which types of failure modes can be distinguish in the specimens, whether it is a flexural, shear or a combination type of failures. Vertical crack indicates flexural type of failure which typically occurs when the specimen doesn't have enough bending capacity. A shear type crack is typically an inclined crack which occurs in close proximity from supports or load application, where sudden change in load is present.

For specimens with steel fiber content of 0.17% by volume and 0.25% the vertical crack is characteristic for the majority of specimens; a typical crack pattern is shown in Figures D-2, D-4 and D-6. This type of failure is peculiar to plain concrete beams when the specimen experiences abrupt loss of load carrying capacity after the first crack followed by complete collapse in a brittle manner, whereas, a SFRC beam is capable of undergoing large deformation beyond the first crack without collapse.

As fiber content increases to 0.33% by volume, some of the specimens have a pronounced inclined crack (Appendix D), others had a combination of inclined cracks followed by straight cracking. The SFRC beams with fiber dosage had a similar failure pattern as a beam with 0.33%, with more specimens having inclined cracks.

At higher steel fiber content of 0.67% and 0.83% by volume, beams experience failure with a combined crack pattern. Shear type cracking predominates failure of the beam, since higher volumes of steel fiber enhance flexural tensile strength of the beam excluding pure flexural type cracking.

Addition of steel fiber influences load-deformation response of the beam specimen as well the modulus of rupture. The modulus of rupture represents concrete flexural tensile strength at a moment of the first crack of 6x6 (in.) concrete crossection based on third point loading and is calculated as:

$$f = \frac{PL}{b \cdot d^2} \tag{3-2}$$

where P – total peak load from MTS reading, [lbf];

L – the span length, [in];

b – the average width of the specimen at the fracture, [in];

d – the average depth of the specimen at the fracture, [in].

The graph shown in Figure 3-15 represents an average tensile strength of beam specimens as a function of fiber dosage. There is a strong upward trend in tensile strength as fiber dosage increases. The higher the amount of steel fiber in concrete, the higher its tensile strength is for all plants. Overall, beam specimens produced at the Northern Concrete Pipe plant exhibited higher values of tensile strength as compared to the beams produced at Sherman-Dixie and Hanson plants. Variation in tensile strength between the plants can be attributed to the differences in concrete mix at a particular plant.

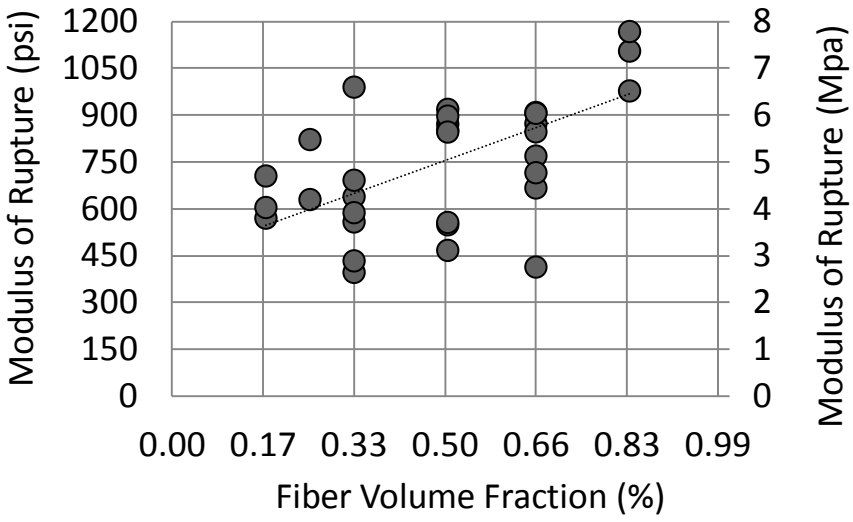

Figure 3-15 Effect of steel fiber content on modulus of rupture of the beam specimen

Tensile strength ratio, which is a ratio of modulus of rupture and square root of compressive strength, is also affected by the presence of fiber in concrete tending to be higher with increase of fiber content, as shown in Figure 3-16. The average value of

strength ratio is η=9.35, which lies in a typical range for concrete between $8\sqrt{f_c}$ and $12\sqrt{f_c}$ The relationship has a slight upward trend with increase in fiber content which is explained by higher tensile strength values of concrete specimen at higher fiber volumes and is dependent on compressive strength of the concrete. This ratio decreases as compressive strength increases.

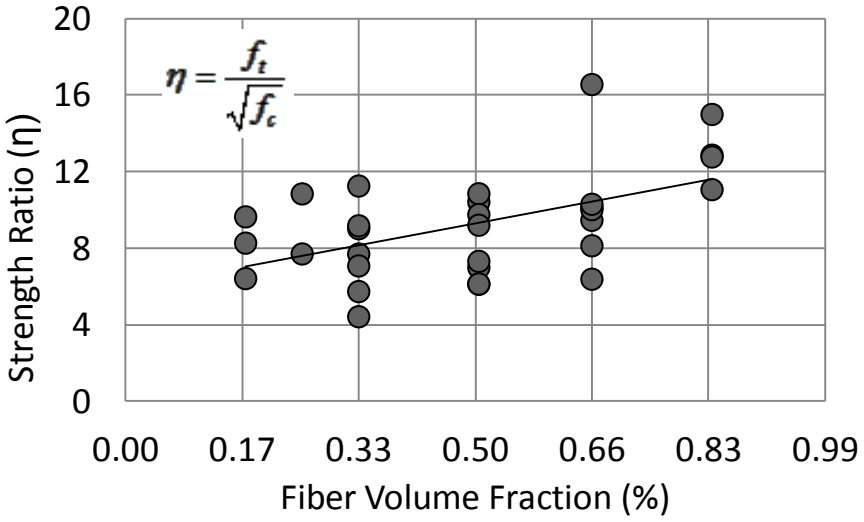

Figure 3-16 Effect of steel fiber content on modulus of rupture of the beam specimen

The effect of steel fiber on initial slope of SFRC beams was also evaluated and is shown in Figure 3-17. The initial slope of load-deformation plot was found for flexural beam test and it represents the initial stiffness of fiber-concrete specimen.

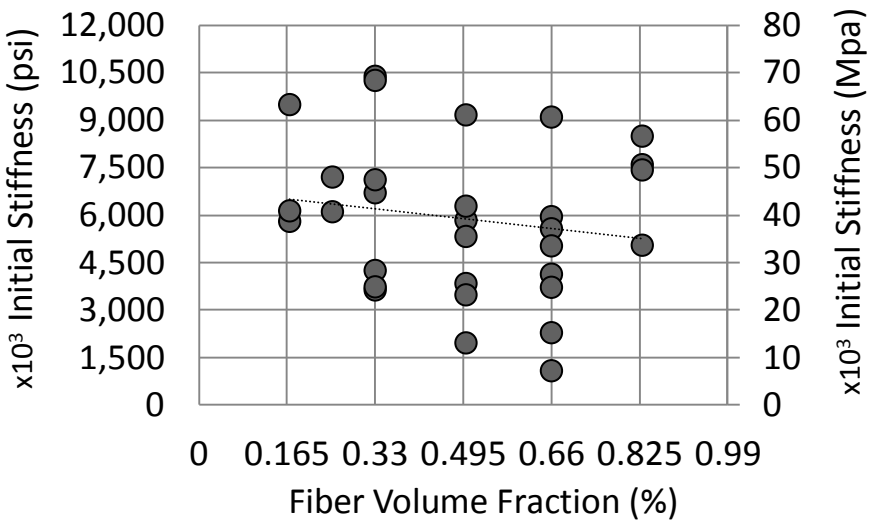

Figure 3-17 Effect of steel fiber content on initial stiffness of the beam specimen

It shows that there is a slight downward trend in stiffness as the fiber content increases. Although no distinct conclusion can be made on the effect of steel fiber on initial stiffness of beam specimen due to the inconsistencies in the consolidation between different specimens, the initial stiffness of fiber-concrete composite should largely depend on the stiffness of concrete matrix (Gao et al. 1997).

Steel fiber reinforced concrete toughness (T_{150}) and relative strength ratio ($R_{T,150}$) for each tested beam is shown in Table D-2 for fiber contents ranging from 0.17% to 0.83%. The relative strength ratio for flexural beam specimen is calculated in accordance with ASM C1609 and it shows contribution of fibers to the flexural strength of concrete beam specimen. The effect of steel fiber content on relative flexural strength ratio is presented in Figure 3-18 and it shows a positive correlation with increase of steel fiber volumes.

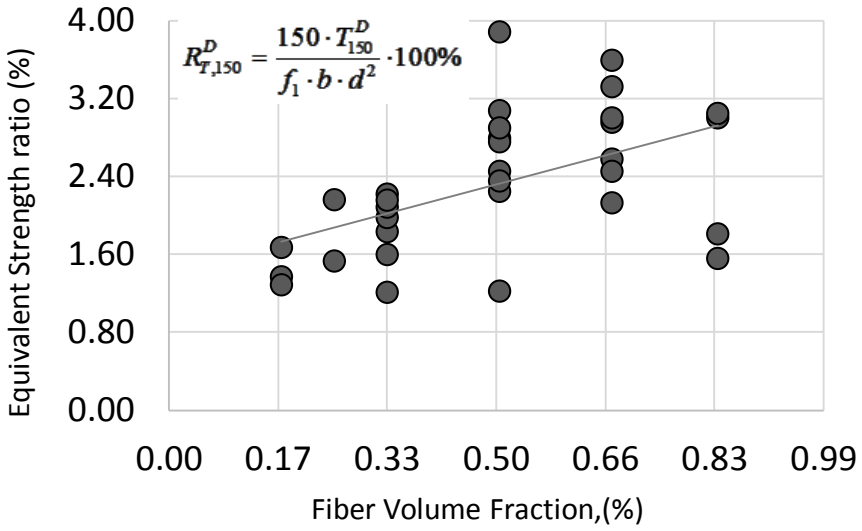

Figure 3-18 Effect of steel fiber content on equivalent strength ratio of the beam where T150 – toughness at L/150 deformation; f1 – first peak load; b and d – width and depth of the beam respectively.

The relationship between the fiber content and beam toughness is shown in Figure 3-19 and has an overall upward trend, that is toughness is increasing with increase in fiber content. Toughness is represented by an area under the load-deformation curve up to the point of a net deflection of L/150 of the span length. The increase in toughness is indicative of the ductility enhancement of concrete with increased fiber dosage. The results of calculated toughness for the flexural beam test is shown in Table D-2 of Appendix D. Beams produced at the Sherman-Dixie plant overall exhibit higher toughness values as compared to the beams produced at the Hanson and Northern Concrete plants.

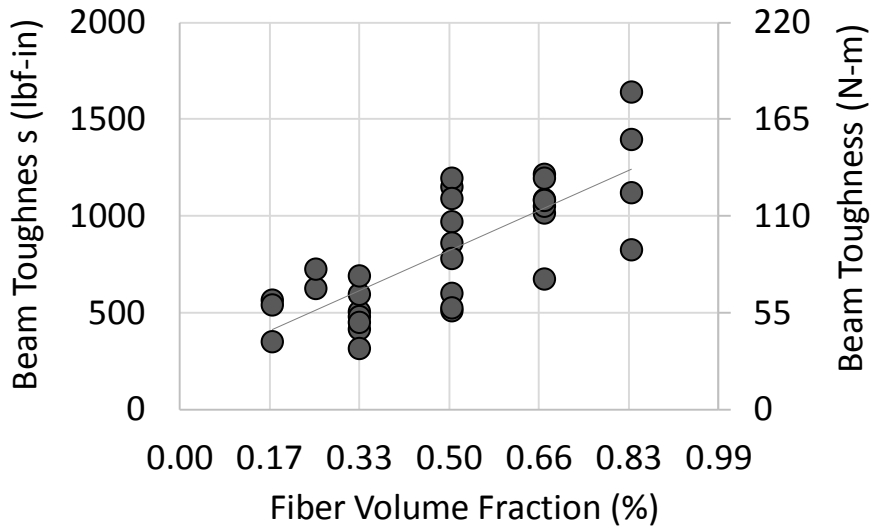

Figure 3-19 Effect of fiber volume fraction on toughness of the beam specimen

The presence of fiber has significant influence on the behavior of the beam. After the first crack, the concrete loses its ability to resist any load, which is characterized by a sudden drop on the load-deformation plot, which is then followed by load redistribution; fibers are engaged in carrying the load, which is reflected by a change in stiffness on the curve with the rate of stiffness degradation decreasing. Addition of steel fiber enables the beam not only to prevent the beam from collapse in a brittle manner, but also enhances the strength of the beam by increasing the load carrying capacity before the first crack appears. In addition, at a higher fiber contents, (somewhere above 0.5% by volume), material tends to behaves as a composite and it becomes harder to distinguish between the stages of concrete failure and a moment when the load is transferred to fibers.

Next graph (Figure 3-20) shows the correlation between the toughness of the beam and the D-ultimate strength of the pipe.

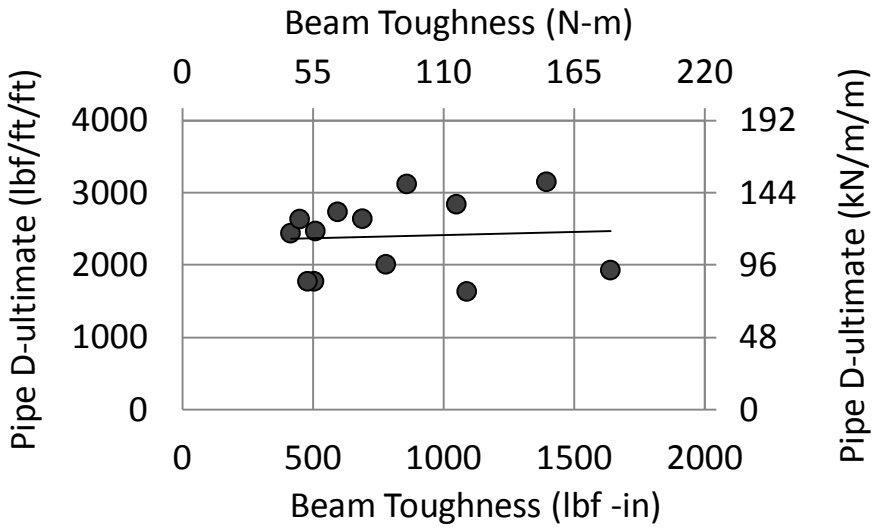

Figure 3-20 Effect of fiber amount on equivalent residual concrete strength

From the Figure 2-23 the apparent positive correlation was demonstrated between the normalized toughness of the pipe and its D-ultimate strength. From the graph in Figure 3-20 it can be seen that there is no distinct correlation between the beam toughness and the pipe D-ultimate load. The data is randomly scattered without any pattern. However, in reality we would expect to see positive correlation between the beam toughness and the pipe strength. Higher material toughness of the steel fiber reinforced concrete would indicate the ability of the pipe to absorb more energy without collapse. No correlation however is found on the above figure, which can be attributed to the compaction differences between the pipe and the beam specimens. Manufactured pipes in general are machine-consolidated, whereas the beam specimens are compacted by hand, which contributes to the variability on compaction from one specimen to another.

3.2.3. Direct Tension Test

The direct tension test is a relatively difficult test to conduct as compared to flexural beam test or compressive cylinder test. Mold geometry specifics require more

intensive labor in forming the specimens to insure good compaction of the dry-cast concrete. Sudden changes in geometry of the specimen make it difficult to reach certain areas. Ultimately, geometry discontinuities become a weak point during the testing procedure. In addition, it requires a high precision in equipment installation to insure proper reading of the data. Figure 3-21 shows a photograph of specimen placement in a proper position and instrumentation mounting.

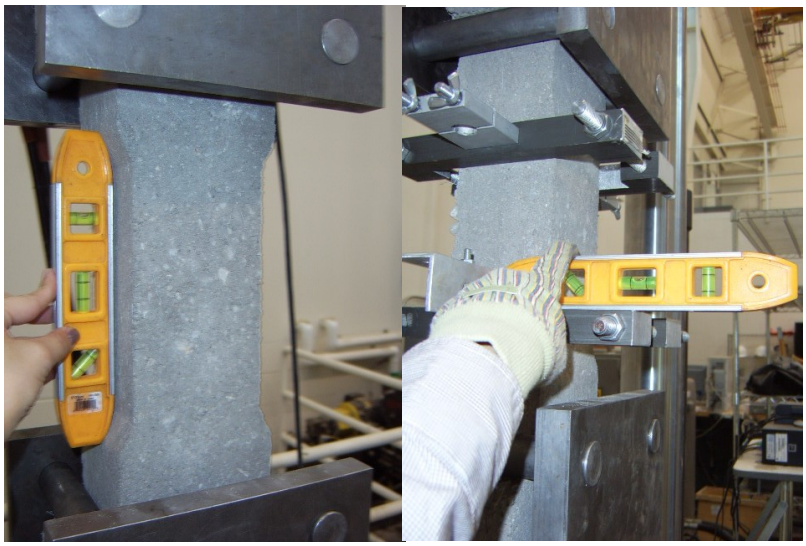

Figure 3-21 Insuring instrumentation precision

For the data to be valid, the crack should form within the gage length of the placement of electrical displacement transducers, as shown on Figure 3-22. When the crack is formed outside the gage length (as shown in Figure 3-23), the data acquisition of axial displacement gets interrupted. This test can be very useful in determining the elastic properties of the fiber reinforced concrete, such as Youngs modulus, tensile strength and the corresponding strain.

All direct tension test specimens were produced at the Hanson plant. A total of 20 specimens were tested, however only six of them were usable for data analysis. Stress-strain data was obtained from load-deformation history of the direct tension, where

stress is obtained by dividing a load over the area of the specimen within the gage (which is 16 in^2); the strain is obtained by dividing the displacement over the length of the gage.

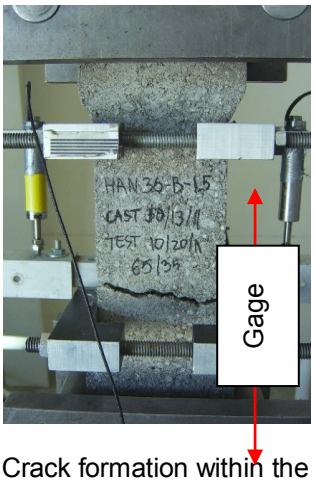

Figure 3-22 Crack formation within the gage length

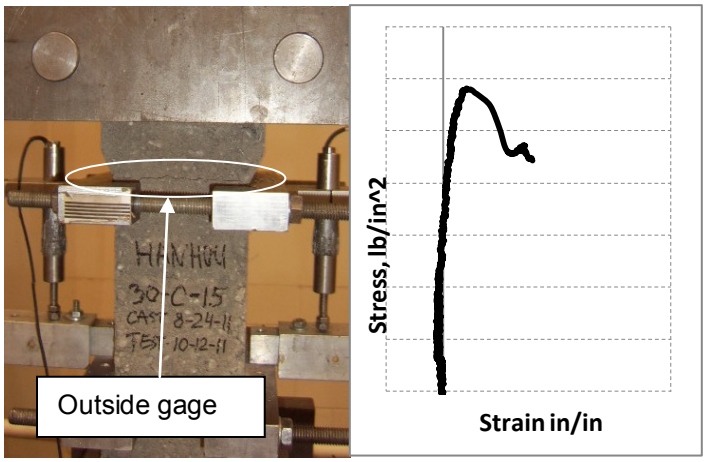

Figure 3-23 Crack formation outside the gage length

A typical stress-strain curve is shown on Figure 3-24 and is characterized by a sharp drop of load after the first crack with a subsequent gain of stiffness.

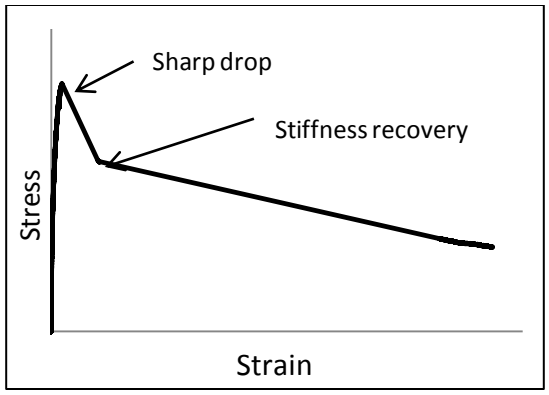

Figure 3-24 Typical stress-strain curve for direct tension test

Three (3) specimens with fiber content of 0.33% by volume were successfully tested; stress-strain curves were obtained. All three specimens exhibited similar behavior during the test. The tensile strength, which corresponds to the peak stress on the diagram, varied from 200 psi to 330 psi for the specimens.

Test #1 specimen, which is denoted as HAN30-8-B-44(1)-T1, reached the stress of approximately 330 psi before the appearance of the first crack, followed by a loss of stiffness by almost 200 psi and reached a strain of 0.0025 until it regained the ability to support some load reaching 165 psi at a stain of 0.004 followed by gradual decrease in stiffness.

Specimen for test #2 was produced from the same mix as specimen of test#1 and showed similar behavior (Figure E-3). After reaching peak strength of 200 psi, it drops 130 psi and reached a strain of 0.0025, than it regained the stiffness reaching a new peak of 110 psi and strain of 0.013 followed by a gradual decrease in stiffness.

The third specimen with fiber content of 0.33% by volume, had a similar sharp drop in strength from 270 psi by 140 points, Figure E-5. After reaching 0.0018 strain value, degradation of stiffness decreases, however it does not go through another peak like it was for test #1 and test #2, rather gradually decreases.

Specimens with steel fiber content of 0.5% and 0.67% by volume did not show adequate tensile strength reaching only 68 psi and 125 psi and respectively, both reached a strain of 0.007 before stiffness started degrading. Low values of tensile strength could have resulted from poor concrete compaction in the specimen or mix design issues. Load-deformation plots for these two specimens exhibited a ductile-like behavior with a smooth curve; Figures E-9 and E-11 show no sharp drop in strength.

Specimens with fiber content of 0.83% by volume, produced at the Hanson plant in Houston, showed relatively high strength as compared to other direct tension test specimens, reaching 580 psi. The typical curve is shown in Figure E-13 and has a sharp drop in strength and subsequent partial stiffness recovery after reaching a strain of 0.001. Higher strength can be explained by the difference in mix design and compaction specific to the Hanson plant in Houston which incorporates Hawkeye equipment for pipe production. This type of production allows for concrete to have more water content than in a Packerhead process. Higher amounts of water make concrete more workable which results in a better compaction of the specimens with a reduced number of voids and imperfections, which otherwise would contribute to a lower strength.

3.2.4. Comparison of Beam and Direct Tension Test Results

Both direct tension and flexural beam tests are used for determination of modulus of rupture of steel fiber reinforced concrete. Flexural beam test allows determining the peak rupture stress and can give a stress-strain relationship up to the first crack, where linear elastic behavior is valid. However it is relatively difficult to find the relation between stress and strain in non-linear region of the graph, when material behaves inelastically. Direct tension is, in turn, a convenient method for determination of the direct relationship between the stress and strain. Table 3-1 shows the comparison of

the two tests, showing the values of the flexural tensile strength obtained with flexural beam test and the tensile stress obtained with the direct tension test.

Table 3-1 Comparison of tensile strength obtained for beam and dog-bone specimens

Steel Fiber lb/yd^3 (%)	Flexural Beam	Direct Tension	Factor
	f_r (psi)	f_t (psi)	f_r / f_t
0.33	690	330	2.1
0.33	432	210	2.1
0.33	430	276	1.6
0.83	977	580	1.7

Overall the ratios of tensile strengths obtained from the flexural beam test are about twice the values of the strengths obtained from the direct tension test for the same fiber content. The tensile strength obtained by means of the flexural beam test exceeds the tensile strength obtained with the direct tension test. More tests need to be conducted and compared to correlate the two tests.

Load-deformation plots can give an idea of the specimen behavior, both direct tension test and flexural beam tests can be used to find the ultimate tensile strength of the specimen. However the tensile strength from the direct tension test, as described in the previous paragraph, have strength values that are nearly twice as low as the strength obtained with flexural beam test. Nevertheless from comparison of the load-deformation response for either of the tests it becomes possible to see if these tests are comparable. For this reason, a direct tension test's stress-strain curve and load-deformation curve from flexural beam tests are compared, shown in Figures E-1 through E-8. The patterns of the stress-strain curve for the direct tension test closely replicate the load-deformation plot obtained with the flexural beam test. For a fiber content of 0.33% by volume, both

specimens experience a sharp drop once the specimen reaches the ultimate load followed by a change in stiffness after some deformation, as shown in Figure E-1 through E-4. Specimens with a fiber content of 0.67% and 0.83% by volume exhibit ductile like behavior in both tests. From the above, we can conclude that either test is suitable for determining the load-deformation plot as well as for evaluation of post-cracking behavior of the specimen. However, one needs to keep in mind that tensile strength obtained with a direct tension test needs to be multiplied by a factor to compare the tensile strengths results obtained with the flexural beam test.

Chapter 4

Initial Non-Linear Finite Element Analysis

4.1. Introduction

This chapter describes the development stages of a suitable model to simulate the behavior of steel fiber reinforced concrete pipe. The finite element model (FEM) development was based on the three-edge bearing experimental test known as a "D-Load test." Although traditional analysis of the pipe systems has employed two-dimensional FEM analysis due its intrinsic plane strain elasticity behavior, 3-D modeling is adopted here to incorporate the effect of Poisson's ratio along the pipe length on its response. This more accurately predicts the actual response of the pipe systems (Abolmaali and Kararam 2011). A three dimensional model was built for each standard pipe size included into the experimental program. Initial model was built to a full scale having a length equal to a total length of the pipe tested. Three dimensional solid elements with geometric and material non-linearities were used. The presence of steel fibers in concrete was modeled through introduction of tension stiffening in concrete material definition obtained with direct tension test. The model also included a loading strip 5 in. x 5 in. (127 mm x 127 mm) for displacement application to the pipe and two rectangular support strips 5 in. x5 in. (127 mm x 127 mm) along the span of the pipe to create a three-edge bearing condition. Loading was applied through incremental displacement application along the loading strip up to the point when the pipe reaches 5% vertical deformation of its internal diameter.

Two different material models for reinforced concrete were used as a first trial in obtaining the appropriate material model for fiber reinforced concrete: (1) concrete brittle cracking and (2) concrete damaged plasticity. Both models use explicit analysis scheme which is based on the incremental procedure where the stiffness matrix is updated

depending on geometry and material changes for each increment known as Updated Lagrangian. In this scheme, the next load or displacement increment is applied to the system with a new stiffness matrix to obtain the subsequent internal equilibrium of the system. The proposed two models were capable of accurately predicting the first crack load in the three-edge bearing loading conditions, crack formation and propagation and stress distribution across the pipe section. Finite element model verification was performed for model validation by comparing the results of load-deformation obtained with FEM to that of the experimental testing.

4.2. Concrete Brittle Cracking

4.2.1. Elements

Eight-noded isoparametric solid elements with hourglass control and reduced integration algorithm were used to model the pipe. Reduced integration uses a lower-order integration to form the element stiffness which reduces computational time. They also referred to as uniform strain or centroidal strain elements with hourglass control. Centroidal strain formulation reduces the amount of effort required to compute the gradient matrix. This cost savings also extends to strain and element nodal force calculations because of the anti-symmetric property of the gradient matrix (Manual ABAQUS 6.12). These elements use linear interpolation in each direction and called first-order elements, shown in Figure 4-1.

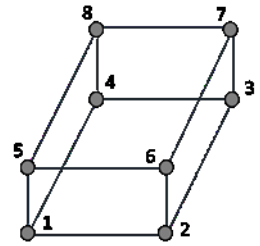

Figure 4-1 Eight-noded linear brick with reduced integration

First order elements are shown to yield accurate results in non-linear analysis involving large deformations and plasticity without significantly sacrificing computational time as compared to the second order brick elements.

First-order, reduced integration elements are susceptible to hourglassing when subjected to stress/displacement analyses. This happens due to the elements having only one point of integration and during the analysis they can be distorted in such a way that the calculated strains at that location become zero. In this case mesh will get significantly distorted.

An optimized mesh comprised of hexahedral or quadrilateral elements can provide adequate accuracy without significant computational costs as compared to triangular or tetrahedral elements. This is due to a better convergence rate of hexahedral elements and low mesh orientation sensitivity. However, the triangles and tetrahedral elements are less sensitive to initial element shape, whereas the first-order quadrilateral and hexahedral perform better if their shape is approximately rectangular (Manual ABAQUS 6.12).

4.2.2. Boundary Conditions

Supports were defined by application of boundary conditions to the system. In the case of the three-edge bearing test the two lower strips are fixed at the bottom to prevent any rotational or translation degrees of freedom. Also for highly non-linear or large deformation problems in explicit scheme the solution may lead to an unsymmetrical stiffness matrix due to severe changes in geometry. This, in turn, can lead to an unsymmetrical deformation of the system, even though the system is modeled to be fully symmetric. To avoid the distortion in the deformed shape of the system additional boundary conditions were introduced along the sides of the loading strip to prevent translation in x-direction.

4.2.3. Surface Interactions

Interactions between the loading strip and a pipe and support strips and a pipe were modeled through a tie constraint. This type of constraint would be valid here as the contact between the two instances is can be considered insignificant. In other words, the solution of the pipe-loading strip or pipe-support strips interaction will not have a significant effect on the overall load-deformation behavior of the pipe. The tie constraint was applied over a line along the pipe span and at the bottom surface of the loading strip.

4.2.4. Velocity-Controlled Loading

Load application to simulate the three-edge bearing test was accomplished by applying the velocity along the loading strip with a predefined speed to obtain the final deformation. The rate of the load application in terms of velocity was chosen such that the rate of the applied velocity chosen ensured a quasi-static solution. The details of boundary conditions, loading and system constraints are shown in Figure 4-2.

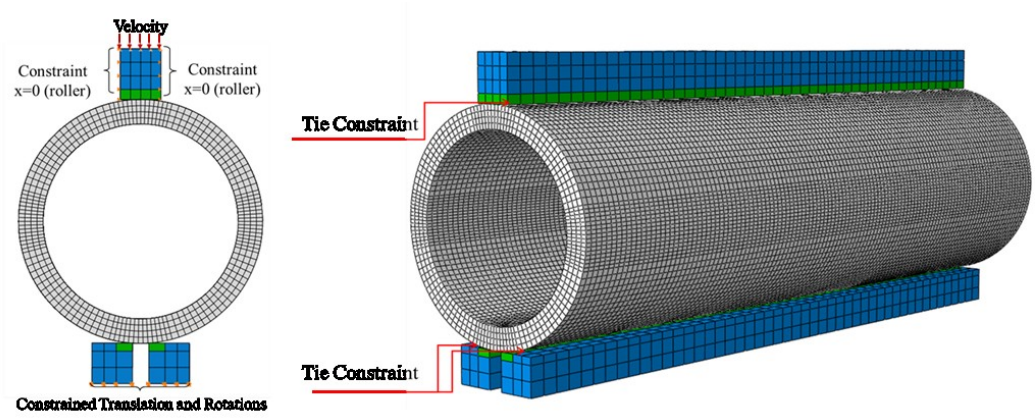

Figure 4-2 Load and Boundary Condition for the ASTM C497 FEM model

Thus, to obtain a displacement of 1.2 inches (30.5 mm) in a 24 inches (600 mm) diameter pipe, velocity varying linearly from 0 to 0.48 in/sec over the time period of 5 sec was applied. The velocity was imposed on top of the loading strip in single step

incrementally by increasing its amplitude from 0 to 1 over the time period varying from 0 to 5 sec.

In large load-displacement analyses the system becomes unstable once the crack in the section occurs and it might become difficult to avoid inertia effect when analysis is dynamic. Application of displacement-controlled loading with the velocity ensures gradual displacement of the nodal region of the pipe without inducing significant inertia effects. The loading rate with the velocity of 0.48 in/sec is slow enough to produce quasi-static response of the structure.

4.2.5. Selection of Time Period

The total time period of the explicit solution was chosen based on the perturbation analysis. Eigenvalues of the system, hence its natural frequencies of vibration were extracted from the analysis. Figure 4-3 shows major modes of the structure, which represent eigenvectors. It was determined that the lowest value of the eigenvalues of the system was f=9.4 sec^{-1}, which corresponds to a natural time period of T=0.1 sec, shown in Figure 4-3 (a). Other modes had higher natural frequencies of f= 14.9 sec^{-1}, f= 18.2 sec^{-1} and f= 28.5 sec^{-1} for mode shapes shown in Figures 4-3 (b), (c) and (d), respectively.

To determine an appropriate integration time for the explicit analysis, the lowest value of the system's eigenvalues need to be considered as the first approach in determining quasi-static solution. Higher rates of the load application are determined first and then gradually decreased until the solution can be considered quasi-static; that is the appropriate time acceleration from its natural time scale to produce static loading results, despite running the analysis in the dynamic scheme.

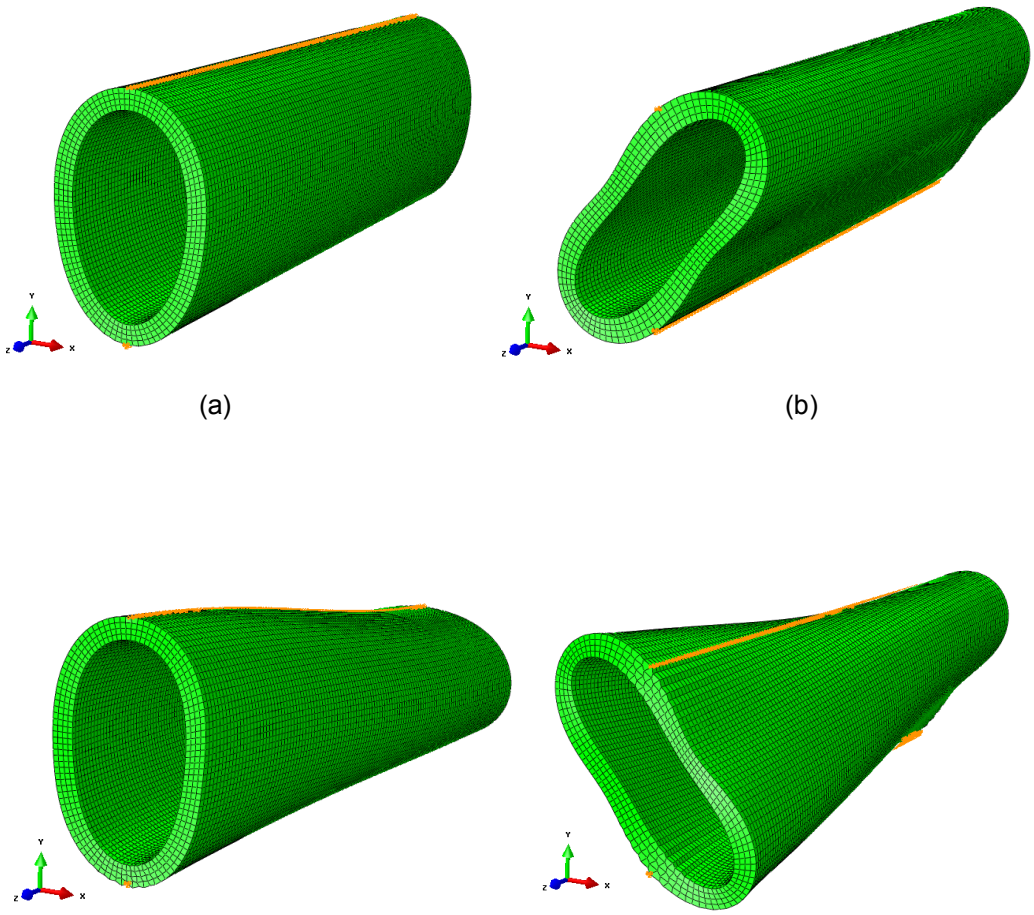

(a) (b)

(c) (d)

Figure 4-3 Eigenvectors and eigenvalues: (a) Mode 1, f=9.4 sec^{-1}

(b) Mode 2, f=14.9 sec^{-1}, (c) Mode 3, f=15.9 sec^{-1}, (d) Mode 4, f=18.2 sec^{-1}

To increase the likelihood of a quasi-static result the total time of a step should be a factor of at least of 10 to 50 times slower than the time corresponding to the fundamental frequency. Therefore, as a first attempt a time period of T=1 sec was used for perform the first the model run. With the time step equal to 1 sec the analysis results exhibited dynamic response of the structure having high fluctuations in the post-cracking

load-deformation behavior. The appropriate time period was found to be T=5 sec to produce quasi-static solution. The typical load-deformation responses from both dynamic and quasi-static solutions are shown in Figure 4-4.

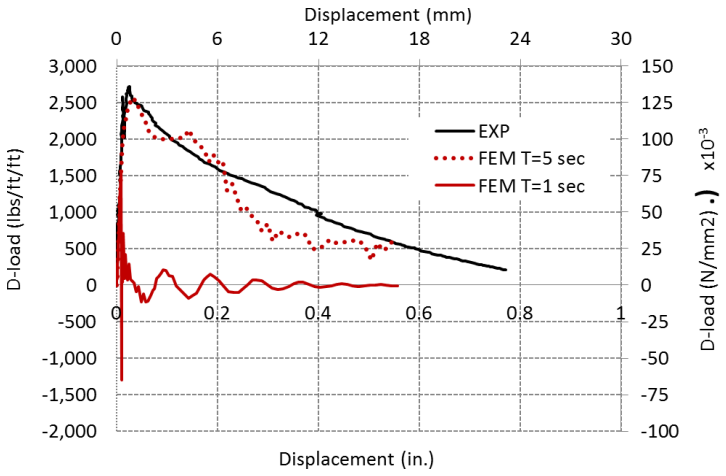

Figure 4-4 Load-deformation response of FEM in comparison to experimental results for 24-B-0.5 using Brittle Cracking algorithm

The load-deformation response obtained with FEM for a step time of T=1 sec exhibits dynamic behavior once the load is applied to the structure. However, once the time period is increased to T=5 sec, effect of inertia is minimal and the solution can be considered quasi-static. Therefore time period of a minimum 5 seconds should be used for dynamic analysis.

4.2.6. Mass scaling

In dynamic explicit analysis the computational cost is highly dependent on the time period and element size. Element size, in turn, defines the stable time of an increment (eq. 5.1). Using mass scaling enables accelerate the analysis without artificially increasing the loading rate. In general, the stable time increment is related to material density through:

$$\Delta t = \frac{L^e}{c_d} \qquad (5.1)$$

where L^e is the characteristic element length; c_d is the dilatational wave speed of the material. In turn, the dilatational wave speed for linear-elastic material with Poisson's ratio equal to zero is given by:

$$c_d = \sqrt{\frac{E}{\rho}} \tag{5.2}$$

Increasing the mass density of the material reduces the wave speed (eq.5.2). Smaller wave speed of the material increases the stable time increment, thus, as the mass scale increases, the solution time decreases due to larger stable increment. However using mass scaling can decrease the quality of the results because the dynamic effects of the increased mass density become more prominent. Therefore care should be exercised when mass scaling is used to accelerate the analysis speed. To verify the factor of mass scaling so the accuracy of the results is not sacrificed, a ratio of kinetic energy to the internal energy of the system should be checked. Kinetic energy in the system should be small as compared to the internal energy of the entire system. Typically kinetic energy (KE) value should not exceed 8-10% of the system's internal energy (IE). Figure 4-5 shows the variation of kinetic and internal energies when a mass scaling of zero and mass scaling of 1000 are used.

Kinetic energy with no mass scaling (Figure 4-5 (a)) exhibits quasi-static response with kinetic energy almost zero throughout the step. Kinetic energy, when the mass scaling of 1000 was used (which is an extreme case, Figure 4-5 (b)), is more than 20% of the entire internal energy of the system at any given step increment. This indicates that the mass scaling of 1000 is very high which may lead to unrealistic or inaccurate results. Kinetic energy histories shown in Figure 4-5 (c)) for the analysis with the aforementioned mass densities were compared.

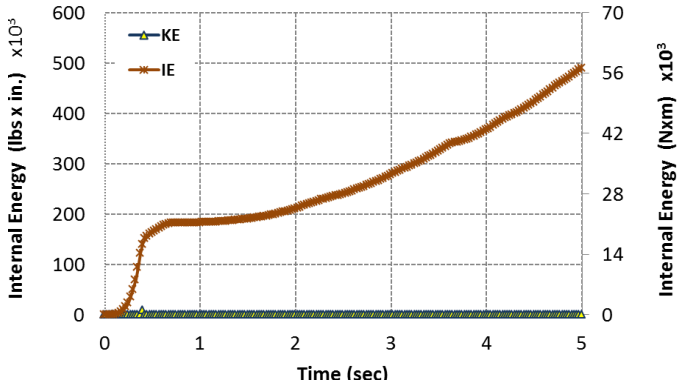

(a)

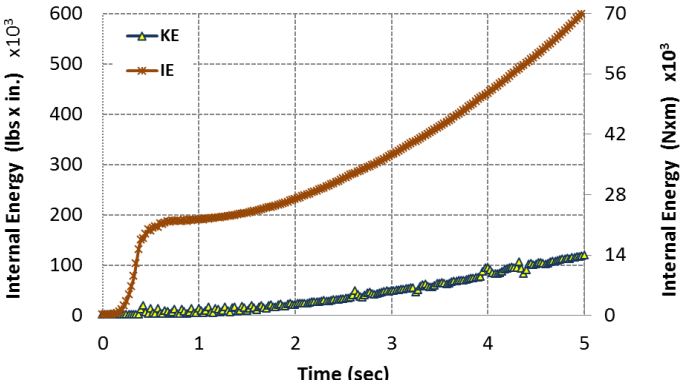

(b)

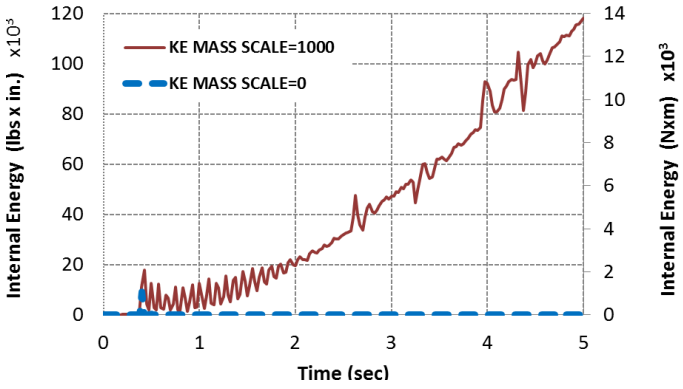

(c)

Figure 4-5 Comparison of the ratios of kinetic to internal energy for the cases

(a) mass scaling of zero and (b) mass scaling of 1000

Kinetic energy history for the mass density of 1000 has oscillations inherent of dynamic type loading, whereas for the zero mass scaling kinetic energy remains almost constant. For both cases an event of crack initiation can still be observed with the sudden jump followed by the drop in kinetic energy.

The mass scaling factor can be applied to the whole model (pipe and loading strips) or it can be applied only to a certain region. The choice should be made based on the region that affects stable time increment the most. This can be a minimum element size in the model or region with the maximum deformation of the elements which can lead to reduction in a stable time increment or non-convergence of the solution. For this model the scaling of the mass density was applied to concrete pipe region only due to the pipe having finer mesh and larger distortions in the elements.

4.2.5. Material Properties and Behavior

4.2.5.1. Elastic properties.

Material properties for the linear behavior of concrete and steel were defined using known standard properties. Concrete material with the following elastic properties were assigned to the pipe model: modulus of elasticity of 4,000,000 psi (27,580 MPa) , mass density of 0.00025 pci (2400 kg/m^3), Poisson's ratio of 0.22. In the explicit analysis scheme the compressive strength of concrete is assumed to have an unlimited strength. This assumption is reasonable when the concrete failure is dominated by cracking due to tension failure. Elastic properties of steel with mass density of 490 pcf (7850 kg/m^3), modulus of elasticity of 29,000,000 psi (200,000 MPa) and Poisson's ratio of 0.3, were assigned to the loading and the support strips. Both load and support strips were assumed to exhibit linear elastic behavior.

4.2.5.2. Inelastic Properties.

Tension stiffening. The post-failure behavior for the strain across cracks was modeled with tension stiffening. The strain-softening behavior was defined through post-failure stress as a function of strain across the crack by means of a post-failure stress-strain relation. The approximation of tension stiffening depends on the density of reinforcement, the size of the concrete aggregates, and the mesh regeneration.

Generalized tension stiffening model for reinforced concrete is illustrated in Figure 4-6. Once the stress reaches the failure point, the strain-softening reduces the stress linearly to zero at a total strain of about 10 times the strain at failure for reinforced concrete (Lubliner et al.,1989). However the value of strain for steel fiber reinforced concrete was calibrated due to the difference in behavior.

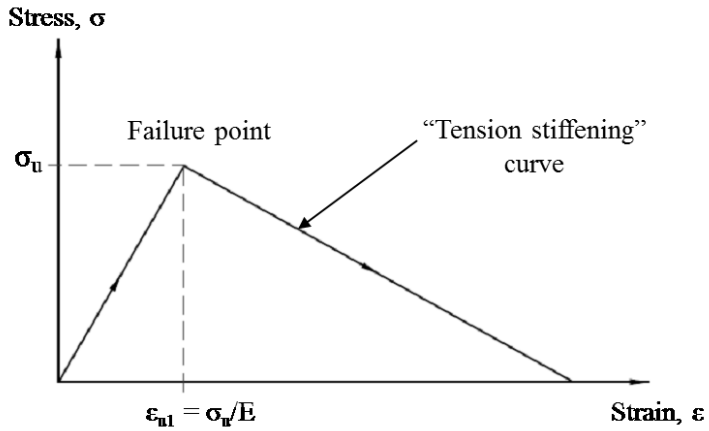

Figure 4-6 Tension stiffening model

Tension stiffening model was obtained from the direct tension test. The stress-obtained from the laboratory testing with direct tension test, as discussed previously in Chapter 2, was in disagreement with the cracking load obtained through the flexural beam test. However, for the modeling purposes, it was assumed that the relationship between stress and stain remains in the same proportion as it was obtained from the test.

The values of stress were multiplied by a factor such that the cracking stress obtained with direct tension test matches cracking stress obtained from the four point bending beam test. Strain values were similarly multiplied by the same factor to preserve proportion between stress and strain for non-linear behavior. These calibrated values were used as initial tension stiffening model for steel fiber concrete.

The final values of tension stiffening model after calibration used in the 30-B-0.5 steel fiber reinforced concrete pipe FEM model are presented in Table 4-1.

Table 4-1 Tension stiffening model for 24-B-0.5 SFRCP

Post-cracking stress psi (MPa)	**Post-cracking strain, in/in (mm/mm)**
0	0
334 (2.30)	0.0000835
180 (1.24)	0.00212
104 (0.717)	0.0197

Element removal. Brittle failure criterion allows for removal of an element from the mesh when any local direct cracking strain reaches failure strain. Element removal helps to avoid severe distortion of the element which can lead to difficulties in the solution convergence and premature calculation abruption. Care should be exercised when implementing element removal, as setting the failure strain of the element to relatively low values can result in lower post-failure strength of the system (Manual ABAQUS 6.12). The failure strain of the element was determined to be suitable at 15% - 20% deformation for the concrete to obtain adequate strength.

Brittle shear retention. Crack initiation is generally dominated by Mode I fracture, whereas post-failure behavior is accompanied by both Mode I and Mode II when failure occurs due to both tension which is acting normal to crack and due to shear aligned in

the plane of the crack. Shear retention can be modeled as a function of strain across the growing crack and expressed in a power law form:

$$G_c = \rho(e_{nn}^{ck})G \qquad (5.1)$$

were G_c is post-cracking shear modulus and G is shear modulus of uncracked concrete section; c^{ck}_{nn} crack opening strain (Manual ABAQUS 6.12). Shear retention values describe shear carrying capacity of steel fiber reinforced concrete after cracking.

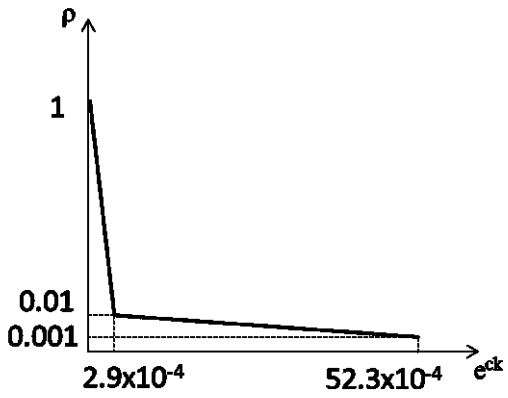

Figure 4-7 Post-cracking shear retention model

The shear retention was modeled with two segments as shown in Figure 4-7. As there was no experimental test done on shear retention, the values to define brittle shear were used from previously conducted studies (Manual ABAQUS 6.12)

4.3. Typical FEM Results Obtained with Brittle Cracking

4.3.1. Load-Deformation Response

Typical results of the analysis using *brittle cracking* algorithm are discussed in this section. Typical load-deformation curves in Figure 4-8 were obtained for the 24 inch pipe by varying strain values for brittle failure of the element. Lower values of failure strain resulted in a more sudden drop in stiffness after the crack, whereas higher values give more gradual stiffness degradation.

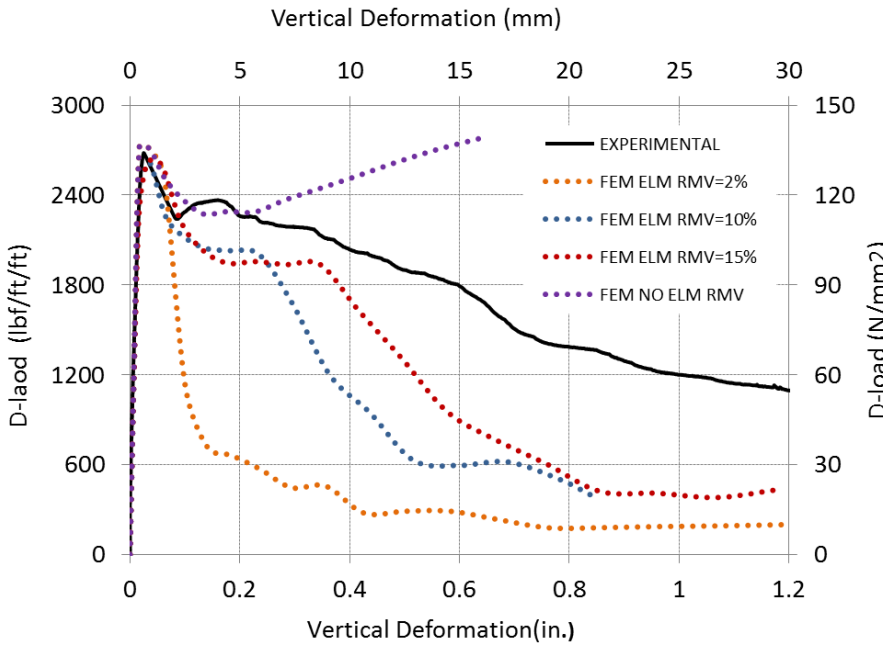

Figure 4-8 Load-deformation behavior for *brittle cracking* algorithm

As shown in Figure 4-9(a), the applied displacement produced a compressive stress at the crown of the pipe wall along the line of load application, above the neutral axis (external section). Below the neutral axis (internal section) the applied displacement produced tensile stress at the crown of the pipe. Similarly, for the invert maximum principal stresses were produced at the internal side of the section, whereas minimum principal stresses developed on the outside of the section of the invert.

As the displacement of pipe increases (Figure 4-9(b)) springlines develop maximum principal stresses as the external wall of the pipe and minimum principal stresses in the internal wall. Thus, as the stresses progress along the crown, invert and the springlines four plastic hinges form along the pipe creating a unique four line cracking. These stress patterns were similar to those observed during the experimental three-edge bearing test.

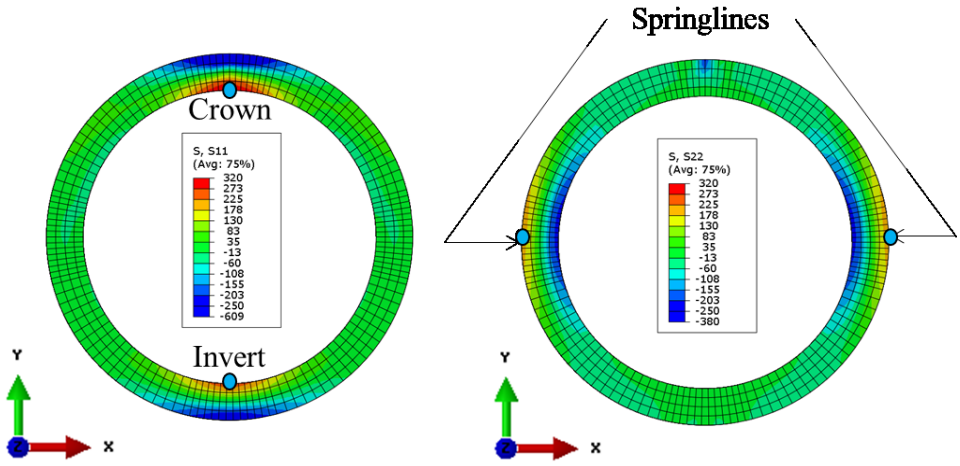

(a) (b)

Figure 4-9 Typical FEM stress contours; (a) *principal stresses* at crown and invert and (b) principal stresses at springlines.

4.3.3. Crack Formation

The *brittle crack* model has an advantage of giving visualization of the crack opening. When any of the local stresses in the element reached the failure stress defined by the stiffness model, crack initiates in the pipe. As the strain in the element increases and reaches the failure strain (was defined 10-15%) the element is removed from the mesh. First elements reaching the failure strain are generally located in the regions of the maximum principal stresses, hence at crown, invert and springlines. For the invert and crown, the longitudinal cracks began at the internal surface (tension zone) of the pipe wall and propagated outward in a radial direction to the external surface (compression zone). For the springline, the longitudinal cracks started at the external surface (tension zone) of the pipe wall and propagated inward in a radial direction to the internal surface (compression zone). The typical crack formation for the *brittle crack* model is shown in Figure 4-10.

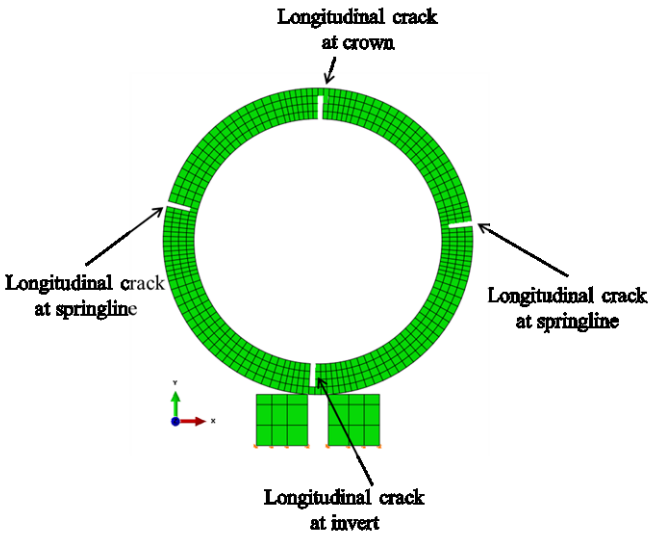

Figure 4-10 Typical FEM crack results X – Y plane view

4.3.2. Deformation of the Pipe

Typical deformed shape of the pipe cross section under the three edge bearing load condition is shown in Figure 4-11. The FEM results exhibited adequate deformation about centerline with a loss of circular shape in the cross-section. The deformation of the pipe was symmetrical about vertical axis having an eigenvector of Mode 1.

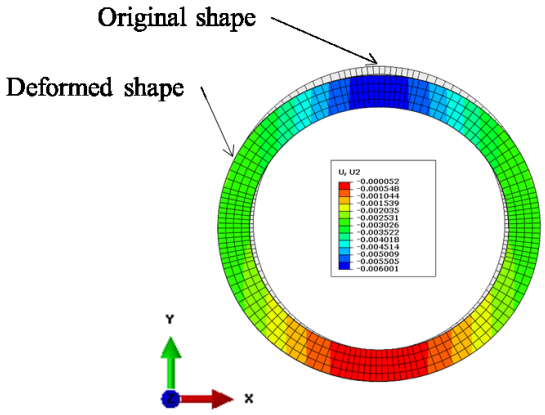

Figure 4-11 Typical FEM deformation results of pipe deformed shape after loaded (Magnified 150 times);

4.3.3. Comparison of FEM-based Ultimate Pipe Strength and Experimental Results

A total of four FEM models were developed for 30 inch pipe to predict the first crack and determine the ultimate pipe strength The results of ultimate load and the corresponding vertical deformation obtained with FEM analysis were compared with those from the experimental testing for the same diameter.

Results of the finite element analysis are shown in Table 4-2 and –had a good correlation with experimental results.

Table 4-2 Comparison of experimental and FEM results

Pipe	**Experimental three-edge bearing test results**		**FEM three-edge bearing test results**	
	D-ult	Disp	D-ult	Disp
30-B-44 #1	2010	-0.0548	2035	-0.0234323
30-B-44 #2	1691	-0.02017	1646	-0.0161324
30-C-44	2590	-0.0337	2511	-0.0129827
30-C-66	3293	-0.10859	3290	-0.0401091

D-ultimate load obtained with FEM closely match the values of test results. Stress-strain relationship was magnified on average by the factor of 2.4 for 30 in. (750 mm) pipe with fiber content of 0.33% by volume and by a factor of 6.6 for 30 in pipe with a fiber content of 0.5% by volume. However more direct tension tests need to be conducted to account for all ranges of fiber dosages and consistency of the results in the FEM model.

Overall, the direct tension test is an appropriate method to use in FEM first crack prediction in a structural pipe. Some calibration in strain might be needed to obtain more accurate values of the vertical deformation.

Post-failure properties of concrete in the form of “tension stiffening” in FEM showed a good agreement with the experimental results in crack propagation as shown in Figure 4-12. By means of the numerical model it was possible to predict the load at the first crack, crack propagation and the final pattern. However FEM results could not predict the measured crack size.

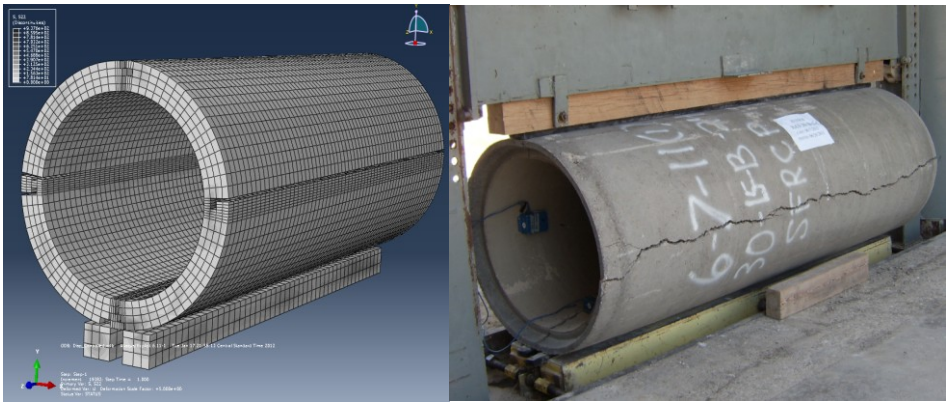

Figure 4-12 Comparison of crack pattern of FEM with experimental results

Chapter 5

Development of Material Constitutive Law for Steel Fiber Reinforced Concrete

5.1. Introduction

Identifying the correct tension stiffening model in finite element analysis for fiber reinforced concrete has been one of the challenges in order to determine crack initiation, ultimate strength of the system and its structural behavior. Generally the material properties of wet cast concrete can be found through standard material testing, such as ASTM C39 to determine compressive strength, ASTM C1609 to find flexural strength of concrete or direct tension test of a dogbone specimen. However present work and other studies on dry-cast fiber reinforced concrete (Wilson and Abolmaali 2013, and Wilson 2013) had shown that there is a high variation in the results for the flexural beam and compression cylinder tests. Moreover, the material mechanical properties of the vertically cast steel fiber concrete pipes are distinct from those of determined in the beam or direct tension specimens. The material in pipes is machine-compacted which densifies it and significantly reduces the voids and imperfections in dry-cast fiber-concrete matrix as compared to the beam and dogbone specimens which are hand-compacted. Inconsistencies in the hand-compacted specimens as well as differences in the material constituents are reflected in the high variation of the load-deformation and stress-strain relationship for the beam and dogbone specimens, respectively.

Finite element analysis have been used to obtain the more accurate material tension-stiffening model for steel-fiber concrete in machine compacted pipes. Traditionally, pipe structures have been analyzed using two-dimensional model taking advantage of its intrinsic plane strain condition. In present work a three-dimensional model was adopted for the pipe analysis which incorporates the Poisson's ratio effect.

This improves the accuracy of predicting the strength and behavior of the results as was shown in the work of Abolmaali and Kararam (2011). The finite element based material constitutive law was obtained by calibrating the material model parameters to converge the solution for load-deformation response with the experimental results.

The model of a pipe with a total length of one inch to facilitate the computational efficiency was used. The appropriate boundary conditions to restrain translations were applied as described later in this chapter. The boundary conditions were defined to simulate the three-edge bearing loading condition. The model included a mesh with the eight-noded isoparametric reduced integration and hourglass control solid elements. The mesh density was calibrated (H-convergence) for optimization and convergence of the solution at a reasonable computational cost without sacrificing accuracy of results. The displacement controlled incremental loading was applied to simulate the load and obtain the post-failure response of the pipe.

5.2. Concrete Damaged Plasticity

5.2.1. Analysis Algorithm

Crack initiation and propagation is one of the significant aspects in concrete damage. Finding an appropriate model to capture first crack and its growth defines one of the challenges in failure analysis of concrete structures. Concrete is one of the materials that exhibit strain softening which causes the loss of strength under applied stresses. Strain softening which can be viewed as loss of cohesion occurs in both pure compression and pure tension. Microscopic cracks continuously forming under the applied stresses until the free surfaces of the cracks form a macro-crack that causes softening mechanism. Material models are generally based on classical theory of plasticity which includes yield criterion, flow rule and the hardening rule. The major two

damage mechanisms in concrete structure are compressive damage and tensile cracking. The latter is rather an external manifestation of damage in the material.

In incremental theory of plasticity elastic-plastic decomposition of the total strain rate without stiffness degradation will be given by:

$$\dot{\varepsilon} = D^{-1}\sigma + \dot{\varepsilon}^{p} \tag{5-1}$$

where D is the undamaged elastic stiffness and ε^{p} is the plastic component of the total strain and σ is a Cauchy stress. Damage in tension and compression are defined by two equivalent plastic strains:

$$\tilde{\varepsilon}^{p} = \begin{bmatrix} \tilde{\varepsilon}_{t}^{p} \\ \tilde{\varepsilon}_{c}^{p} \end{bmatrix} \tag{5-2}$$

Plastic strain variables increase with tension and compression damage. Based on continuum damage theory, the stress is governed by effective stress which can be expressed in terms of undamaged stiffness:

$$\tilde{\sigma} = E_{0}(\varepsilon - \varepsilon^{p}) \tag{5-3}$$

When the isotropic stiffness degradation damage is considered, then the above expression for effective stress will take form:

$$\tilde{\sigma} = (1 - d)E_{0}(\varepsilon - \varepsilon^{p}) \tag{5-4}$$

where E_0 is initial elastic stiffness; *d*- degradation variable which represents degradation of elastic stiffness. Tension post-failure behavior is described through strain softening mechanism whereas compression exhibits initial hardening followed by softening. A schematic representation of the tension and compression stress-strain responses are shown in Figure 5-1 (a) and (b) respectively.

Under uniaxial tension the stress is allowed to be linear following stiffness E_0 until it reaches (σ_{t0}) cracking stress. This point is onset of micro-cracks and beyond this point macro-cracks start developing with the softening behavior in stress-strain response.

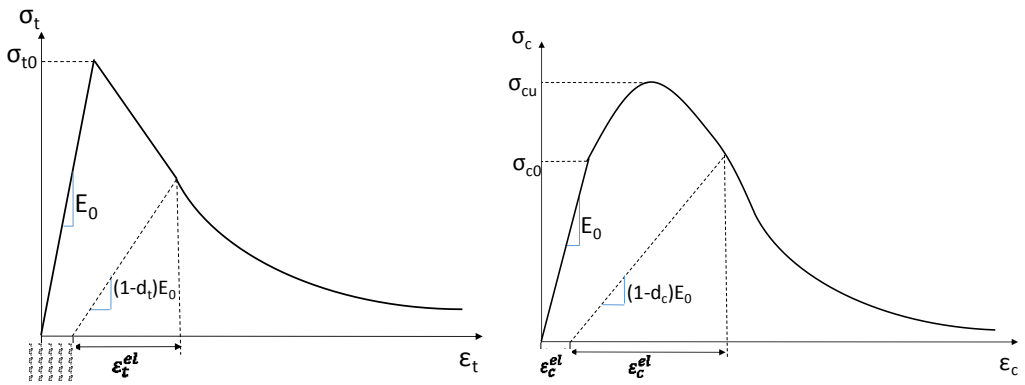

(a) (b)

Figure 5-1 Concrete material model for (a) tension; (b) compression

Unlike uniaxial tension, compression stress-strain response follows linear relationship until it reaches compressive strength (σ_{c0}) followed by compression hardening. Beyond the ultimate stress material is experiencing strain softening with a subsequent decrease in compressive strength.

Stiffness Degradation. It is practical to assume stiffness degradation in concrete since cementitious materials experience micro-cracking during the loading stages which lead to development of free surfaces and loss of cohesion. This process is the most appropriate to apply when concrete structures are subjected to cyclic loading (Lee and Fenves, 1998). In previous studies it was shown that when subjected to reverse loading condition structures experience stiffness recovery when tensile loading changes to compression sealing tensile micro-cracks. However, as the load changes from compression to tension, once crushing micro-cracks developed, there will be no stiffness recovery. If concrete specimen is unloaded at any point of strain softening, the unloading path will be going through $(1-d_t)\cdot E_0$ stiffness for tension response and $(1-d_c)\cdot E_0$ for compression response, where d_t and d_t are tension and compression damage variables, respectively, that vary from zero (for undamaged concrete) to 1 (for full loss of strength).

These parameters are assumed to be dependent of plastic strains, temperature and field variables:

$$d_t = d_t\left(\tilde{\varepsilon}_t^{pl}, \theta, f_i\right); \quad 0 \le d_t \le 1 \tag{5-5}$$

$$d_c = d_c\left(\tilde{\varepsilon}_c^{pl}, \theta, f_i\right); \quad 0 \le d_c \le 1 \tag{5-6}$$

Yield Criterion. Material models of Mohr-Coulomb and Drucker-Prager were used in the framework of concrete damaged plasticity yield criterion for concrete and other geomaterials and can be expressed in general form:

$$F(\sigma) = c \tag{5-7}$$

where F(σ) is a function of the stress components and c is a constant describing cohesion. When $c=f_{c0}$ the equation describes initial yield surface, whereas the full failure surface is defined when *c* reaches its maximum. In general strain softening requires that the cohesion decreases once the failure surface has been reached (Lubliner, 1989). The failure surface can be well described by Equation 5-7, in which $F(\sigma)$ has a form :

$$F(\sigma) = \frac{1}{1-\alpha}\left[\sqrt{3J_2} + \alpha I_1 + \beta\langle\sigma_{max}\rangle - \gamma\langle\sigma_{max}\rangle\right] \tag{5-8}$$

where α, β and γ are dimensionless constants. It should be noted that when $\sigma_{max} = 0$ in biaxial tension, the above expression becomes the Drucker-Prager criterion, then parameter α can be found by comparing yield stresses in the initial biaxial (f_{b0}) and uniaxial (f_{c0}) compression:

$$\begin{pmatrix} f_{\mathrm{b0}} \\ f_{\mathrm{c0}} \end{pmatrix} = \begin{pmatrix} 1-\alpha \\ 1-2\alpha \end{pmatrix} \tag{5-9}$$

which yields

$$\alpha = \begin{pmatrix} \frac{f_{\mathrm{b0}}}{f_{\mathrm{c0}}} - 1 \\ 2\,\frac{f_{\mathrm{b0}}}{f_{\mathrm{c0}}} - 1 \end{pmatrix} \tag{5-10}$$

From experiments it was found that $\frac{f_{b0}}{f_{c0}}$ lie between 1.10 and 1.16, giving a value α between 0.08 and 0.12. Similarly, with a known constant α, the value of β is found to be:

$$\beta = (1-\alpha)\frac{f_{b0}}{f_{c0}} - (1+\alpha) \tag{5-11}$$

The parameter γ corresponds to triaxial state of stress with $\sigma_{max}<0$. According to Lubliner et al., if meridians are designated as tensile meridian for $\sigma_1>\sigma_2=\sigma_3$ and compressive meridian for $\sigma_1=\sigma_2>\sigma_3$ on the yield surface, then for tension

$$\sigma_{max} = \frac{1}{3}(I_1 + 2\sqrt{3J_2}) \tag{5-12}$$

and compression:

$$\sigma_{max} = \frac{1}{3}(I_1 + \sqrt{3J_2}) \tag{5-13}$$

In the case of triaxial stress ($\sigma_{max}<0$) the meridian equations take the form of:

Tension Meridian

$$(2\gamma+3)\sqrt{3J_2} + (\gamma+3\alpha)I_1 = (1-\alpha)f_c \tag{5-14}$$

Compressive Meridian

$$(\gamma+3)\sqrt{3J_2} + (\gamma+3\alpha)I_1 = (1-\alpha)f_c \tag{5-15}$$

where f_c is critical stress in uniaxial compression corresponding to the yield stress for the yield surface and to ultimate stress for failure surface. If a constant K is defined to be:

$$\rho = \frac{\gamma+3}{2\gamma+3} \tag{5-16}$$

then γ can be found

$$\gamma = \frac{3(1-K)}{2K-1} \tag{5-17}$$

Typical values for *K* were found to range from 0.64 (Schickert and Winkler) to about 0.8 (Mills and Zimmerman).

With the all parameters determined, the yield surface for the plane stress condition will take the form of Equation 5-18 and is shown in Figure 5-2

$$F(\sigma) = \frac{1}{1-\alpha}\left[\sqrt{3J_2} + \alpha I_1 + \beta\langle\sigma_{max}\rangle\right] \tag{5-18}$$

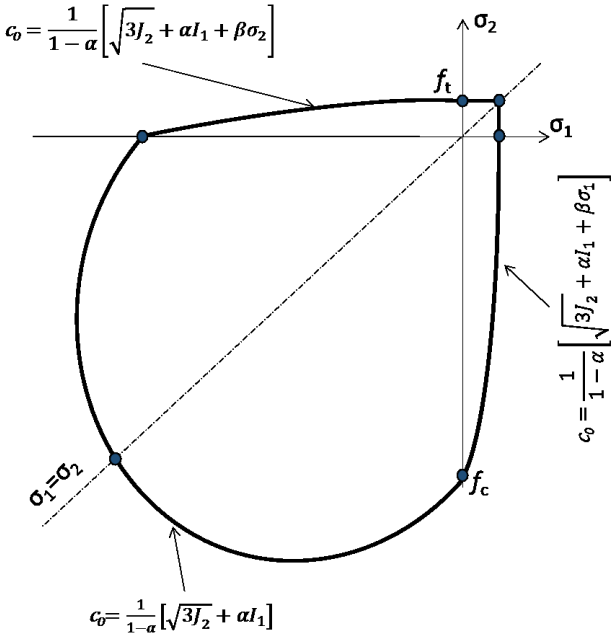

Figure 5-2 Initial yield function for plane stress condition

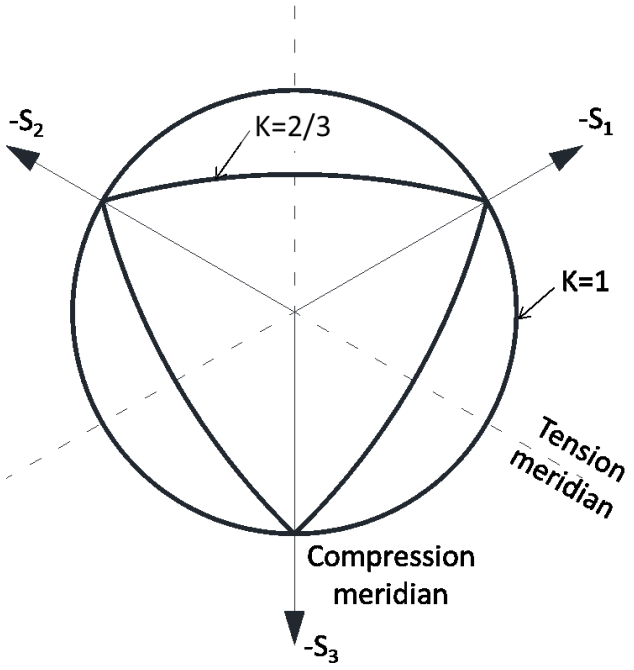

Figure 5-3 Yield surface in deviatoric plane

Plastic flow for concrete damaged plasticity model assumes non-associated plastic flow for dilatancy evaluation of the . The flow rule defines the relationship between direction of the plastic flow and strain rate:

$$\dot{\varepsilon}^p = \dot{\lambda}\frac{\partial \Phi}{\partial \bar{\sigma}} \tag{5-19}$$

where λ is a non-negative function, also known as the plastic consistency parameter; Φ is a scalar plastic flow potential which is defined by modified Drucker-Prager hyperbolic function:

$$\Phi = \sqrt{(\varepsilon \cdot \sigma_{t0} \tan\psi)^{\,2} + \bar{q}^2} - \bar{p}\tan\psi \tag{5-20}$$

where $\bar{p} = -\frac{1}{3}trace(\bar{\sigma})$ is hydrostatic pressure stress;

$\bar{q} = \sqrt{\frac{3}{2}(\bar{S}:\bar{S})}$ is Von Mises equivalent effective stress;

$\bar{S} = \bar{\sigma} + \bar{p}I$ is the effective stress deviator

$\psi(\theta, f_i)$ – dilation angle measured in p-q plane at high confining pressures;

$\sigma_{t0}(\theta, f_i) = \sigma_t\ (at\ \varepsilon_t^{pl} = 0)$ – uniaxial tensile stress at failure;

$\epsilon(\theta, f_i)$ – eccentricity, defines the rate at which the function approaches the asymptote.

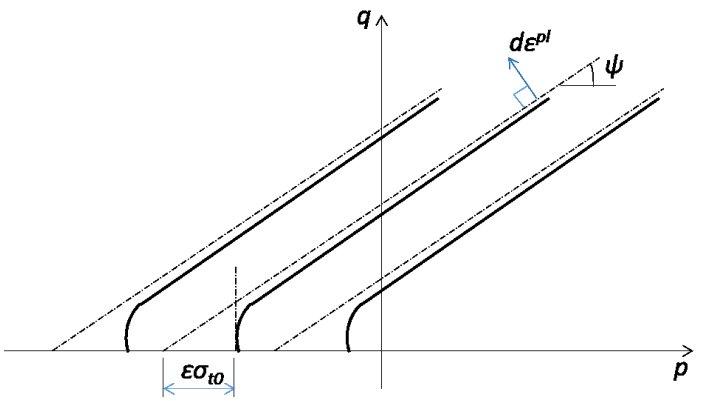

Figure 5-4 Hyperbolic flow potential in the p-q plane

The default value of eccentricity is $\epsilon = 0.1$, at this value material dilation angle remains unchanged with a range of confining pressures, however higher values for eccentricity mean that the dilation angle increases rapidly with the reduction of the confining pressure. It is suggested to avoid using values of eccentricity lower than the suggested value as it may lead to difficulties in solution convergence (Hibbitt, 1997).

5.2.2. Element Type

Eight-noded isoparametric solid elements with hourglass control and reduced integration were used to model the pipe. See for Section 4.2.1 of Chapter 4 for details. A typical meshed pipe model is shown in Figure 5-5. The two-element thickness was used for the pipe length to ensure the adequate Poisson's effect.

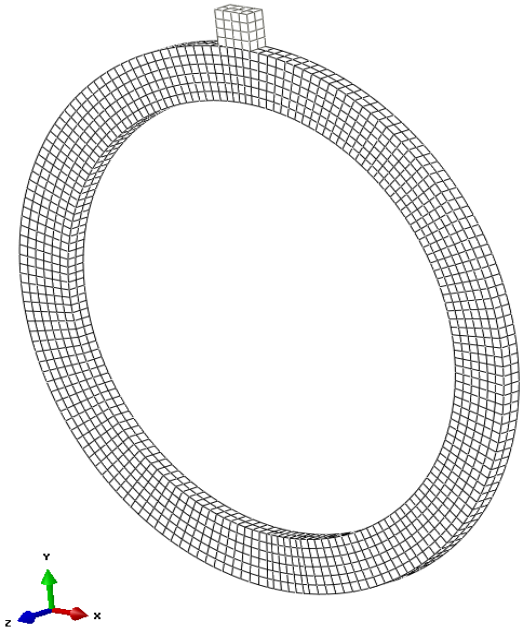

Figure 5-5 Typical mesh for the pipe model

The details of the mesh for each pipe model are presented in Table 5-1.

Table 5-1 Total number of elements and nodes for the models

Pipe Designation	Number of Nodes	Number of Elements in Wall Thickness	Total Number of Elements
24-B-0.17-II	3687	2096	6
24-B-0.25-III	3687	2096	6
24-C-0.25-III	1782	1782	6
24-B-0.33-III	3687	2096	6
24-C-0.33-III	1782	1782	6
24-C-0.5-IV	1782	1782	6
30-B-0.33-III	3771	2144	6
30-C-0.33-III	4395	2552	7
30-B-0.5-III	3771	2144	6
30-B-0.5-IV	3771	2144	6
33-B-0.33-I	4149	2360	6
36-C-0.25-III	5745	3394	7
36-C-0.33-III	5745	3394	8
36-C-0.5-III	5745	3394	8
36-B-0.67-III	5064	2944	7
36-C-0.67-IV	5745	3394	8
36-C-0.83-IV	5745	3394	8
48-B-0.50-II	7554	4466	8
48-B-0.67-II	7554	4466	8
48-B-0.67-II	7554	4466	8

5.2.3. Material Properties Definition

5.2.3.1. Elastic Properties

Concrete material with the following elastic properties were assigned to the pipe model: Modulus of Elasticity of 4,000,000 psi (27,580 MPa) , mass density of 0.00025 pci (2400 kg/m^3). The Poisson's ratio of 0.22 was considered for the analysis to account for present of steel fibers. It was shown that presence of steel fibers have marginal effect on compressive strength of concrete, thus it was reasonable to assume that the stress-strain evolution in compression for fiber concrete can be approximated as that of the plain concrete. Compression softening model was used from experimental testing conducted by (Gribniak, 2012). Stress-strain in compression remains linear-elastic until it reaches compressive strength. Non-linear behavior is defined in inelastic material properties domain

5.2.3.2. Inelastic Properties

Non-linear behavior of steel fiber concrete was modeled with tension stiffening constitutive law using a preliminary estimated model obtained from direct tension test. The values have been iteratively calibrated until the finite element based load-deformation response converged with those of experimental tests.

Plasticity parameters

The following plasticity parameters used in the analysis:

Dilation angle $\psi=38^0$

Eccentricity $\epsilon = 0.1$

Ratio of biaxial and uniaxial compression $f_b/f_{c0}=1.16$

Ratio of the second invariant on the tensile meridian to that on the compressive meridian for any given value of the pressure invariant p such that the maximum principal stress is negative K=0.667

Viscosity Parameter μ =(0.0002-0.0008) is used to avoid difficulties in convergence. Higher values were used for the material model with stiffness degradation. Solution convergence difficulties are pertinent to the material exhibiting softening behavior. Application of viscosity parameter to the constitutive equations is based on Duvaut-Lions regularization which allows the stresses to be outside the yield surface.

Compressive strength

Compression cylinder tests (ASTM C39) have shown that the presence of steel fibers only marginally affects the compressive strength of concrete and failure mode, thus it would be reasonable to assume the plastic stress-strain evolution in compression for modeling the steel fiber reinforced concrete. The values for compressive strength of concrete was taken from the work of Jankowiak et al. (2005); the same values of compression envelop were used for all models.

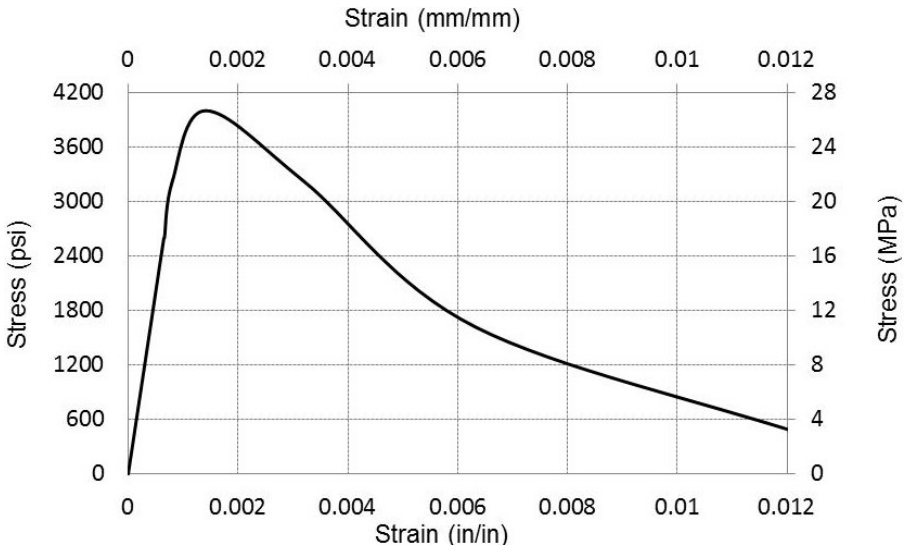

Figure 5-6 Material constitutive law of concrete in compression

Once the concrete reaches its compressive strength, hardening takes place at about 2700 psi until it reaches its ultimate; strain softening behavior is followed .

Tensile behavior

To define tension stiffening model for steel fiber concrete stress-strain envelop obtained from direct tension tests were used as a first approximation. Since the complete stress-strain relationship was available for 30-B-0.33-III pipe, the FEM model for that size pipe was developed to implement the tension stiffening as a first calibration point. The values were calibrated such that the load-deformation curves of the FEM model converged with the experimental test results.

5.2.3. Boundary Conditions

Displacement-controlled loading to produce 5% vertical deformation of the pipe's diameter was applied over the time period of t=1 sec in order to capture the post-cracking behavior. The post-failure response of steel-fiber concrete pipe is characterized by the increase in displacement without any increase in load which is indicative of the strain softening behavior.

Boundary conditions (B.C.) restraining translation in z-direction were applied along both faces of the pipe to ensure plane strain condition (Figure 5-17 (a)). Roller restraint in x-directions was imposed on the loading strip in order to limit the pipe movement strictly in vertical plane (Figure 5-7 (b)).

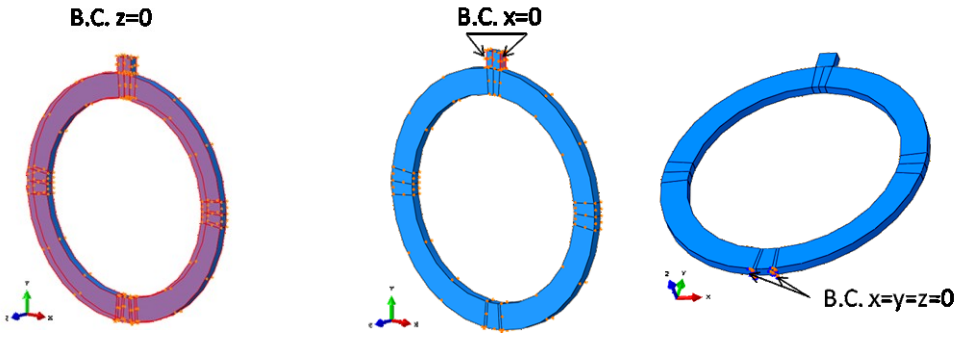

(a) (b) (c)

Figure 5-7 Boundary conditions applied to the model

Finally, bearing supports were simulated by applying boundary conditions restricting translations in x, y and z-directions.

5.3. Concrete Damaged Plasticity with Adaptive Meshing Technique

During the displacement application in a plastic range, the pipe structure experiences large deformations which can lead to severe mesh distortion and interruption in the analysis. In the dynamic explicit analysis algorithm there are several techniques to control mesh distortion applicable to the reduced integration three-dimensional elements. One of the techniques that were used in this study is concrete damaged plasticity in the explicit solution scheme using adaptive remeshing. Application of this technique enables the mesh to regenerate itself at regular intervals the mesh quality. In general Lagrangian analysis is performed when the nodes move with dependence on the material points, in this case mesh can distort severely with high strain gradients. Lagrangian adaptive mesh domain can be used with quasi-static problems having large deformations. Eulerian domain however is used mostly to analyze the steady state problems which involve material flow. In this case mesh remains fixed, whereas material is allowed to move independently through the mesh. Arbitrary Lagrangian-Eulerian (ALE) method is a combination of the two for which constraints of the mesh motion are only at free boundaries, whereas the rest of the material is allowed to flow through the mesh independently. The adaptive remeshing was applied to the model by defining the free boundaries regions along with the adaptive mesh domain. The free boundaries of the mesh are defined by the Lagrangian boundary regions which restrict movement of the mesh in the direction normal to the surface of the boundary region. This region coincided with the boundary conditions restricting the translation of the nodes in z-direction, as shown in Figure 5-7.

The system was subjected to a low-rate ramp displacement controlled loading to minimize the dynamic effect of inertia forces associated with the analysis. Displacement was applied in form of velocity to produce 5% vertical deformation of the pipe diameter. The total duration of the loading of t=10 sec was selected based on the eigenvalue frequency analysis such that it exceeds at least twice the natural frequency of the system. The details of the analysis are described in Section 4.2.5 of Chapter 4.

The parameters for the material plastic model in the explicit analysis scheme used:

Dilation angle $\psi=38^0$

Eccentricity $\epsilon = 0.1$

Ratio of biaxial and uniaxial compression $f_b/f_{c0}=1.16$

Ratio of the second invariant on the tensile meridian to that on the compressive meridian K=0.667

Viscosity Parameter μ =0

Mass scaling with a factor of 20 was employed in the analysis to increase the stable time increment thus reducing the total number of increments.

5.3.1. Load-Deformation obtained with FEM using Adaptive Mesh Technique

The model using adaptive meshing technique was capable of accurately modeling load-deformation response of the pipe up to the first crack. An example of the full load-deformation responses for 24-B-44-III obtained with FEM and experimental testing are shown in Figure 5-8. It can be seen that the dynamic based explicit solution can accurately predict the first crack in the pipe and thus the ultimate load. However post-failure response exhibits response of somewhat a dynamic nature as the crack propagates through the section of the pipe. But in general, post-cracking behavior of load-deformation closely follows that of the experimental testing.

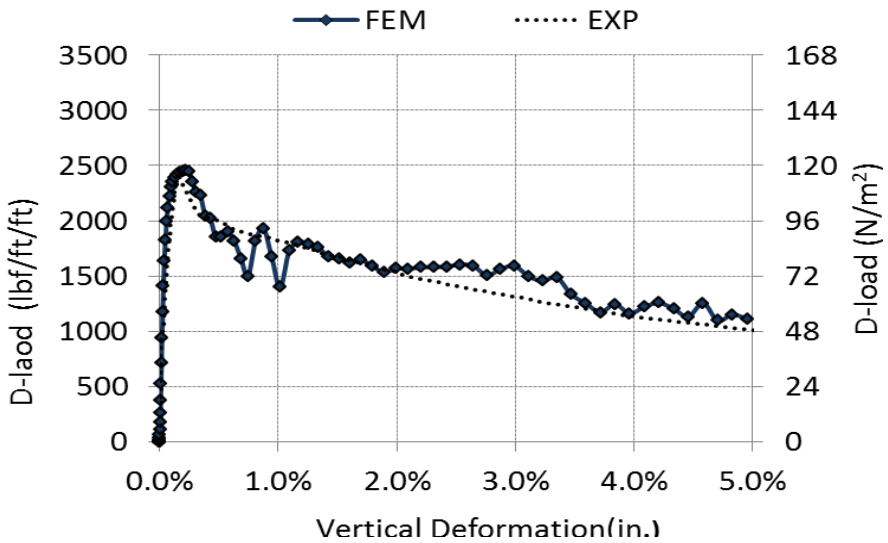

Figure 5-8 Comparison of FEM-based load-deformation response

with the results of experimental testing for 24-B-44-III

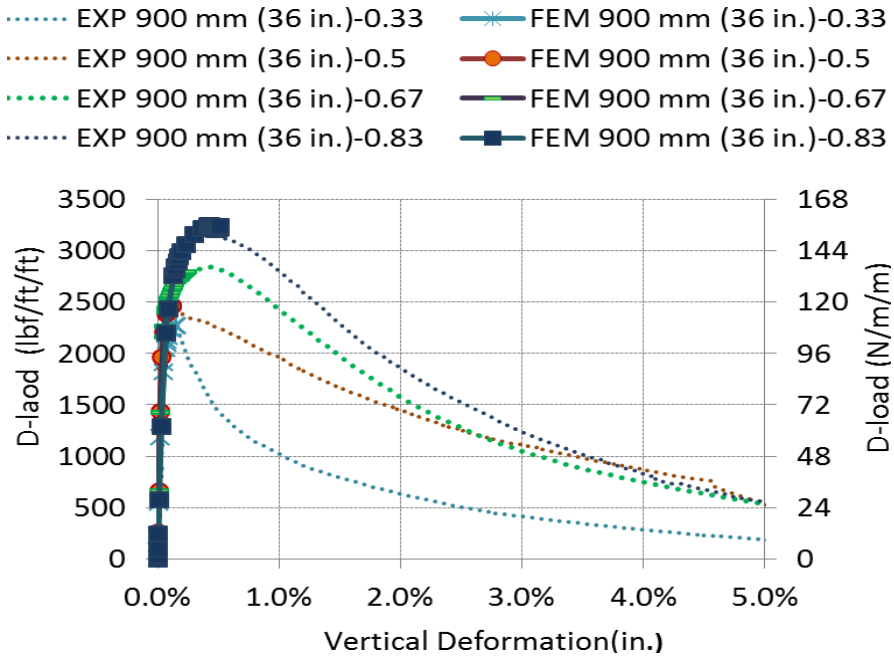

Figure 5-9 Comparison of FEM-based load-deformation response with experimental

results for the 36 in. (900 mm) SFRCP for fiber fractions

varying from 0.33 to 0.83 in volume.

The load from the finite element model was obtained by estimating the reaction forces at the supports; the vertical displacement was obtained for the nodal degree of freedom at the crown. Figure 5-9 shows the FEM analysis results for load-deformation response of 36 inch pipe with various fiver volume fractions. The prediction of the first crack with FEM agrees with the experimental test results.

5.3.2. Material constitutive law obtained with FEM using Adaptive Mesh Technique

Material constitutive law obtained from the dynamic explicit model with adaptive meshing technique for the critical regions is illustrated in Figure 5-10. The analysis had shown that the first crack occurs at the crown followed by the invert and springlines. This is consistent with the results observed during the experimental testing. Through the displacement application process the elements experience higher levels of strain at the crown as compared to the invert and springlines.

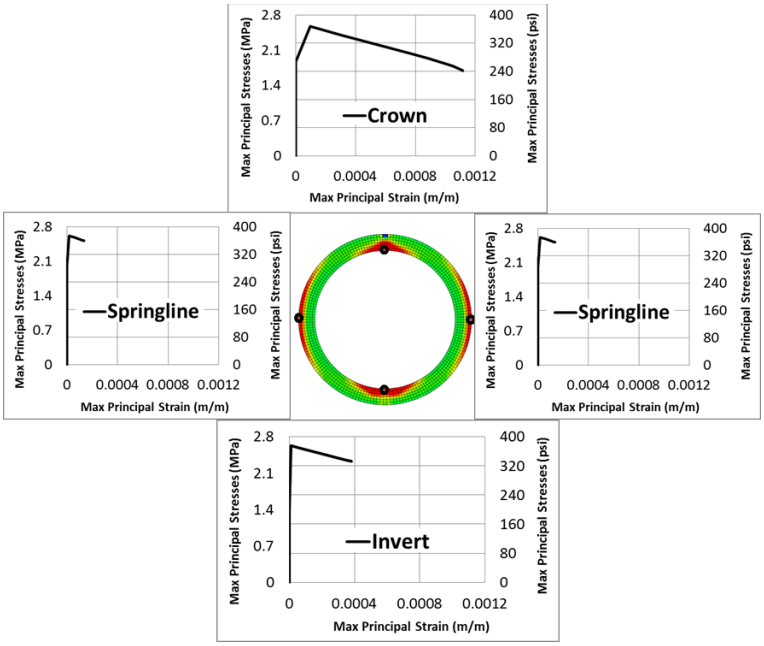

Figure 5-10 Maximum principal stress-strains at 5% deformation and stress contours at ultimate stress

Although the adaptive meshing technique is effective in determining behavior of the pipe, the cracking load and the load-deformation response, this process is computationally expensive in the dynamic explicit scheme. The dynamic nature of load-deformation response calls for increase in the total integration time from 10 seconds that was used for the analysis to improve the quasi-static solution. This will further increase computational time, which is not economical. Therefore, another model will be considered.

5.4. Development of the Material Model

A model with concrete damaged plasticity using implicit static analysis was considered for further modeling of the behavior of the pipe structure. The plasticity parameters for the material model used:

Dilation angle $\psi=38^0$

Eccentricity $\epsilon = 0.1$

Ratio of biaxial and uniaxial compression $f_b/f_{c0}=1.16$

Ratio of the second invariant on the tensile meridian to that on the compressive meridian K=0.667

Viscosity Parameter μ =0.0002 and 0.0008. Higher values of viscoplastic regularization were used for the model of pipes exhibiting behavior with steeper negative slope (typical for the lower bounds of fiber volume fractions) in the load-deformation response to correct for higher instabilities in the system during the plastic straining.

In addition, for the models representing the pipes with low steel fiber volume fraction stiffness damage was used. The stress-strain relationship of the scalar damaged elasticity is governed by:

$$\bar{\sigma} = (1-d)D_0^{el}:(\varepsilon - \varepsilon^{pl}) \tag{5-21}$$

where D_0^{el} is the undamaged elastic stiffness of the material, and *d* represents the scalar stiffness degradation variable. The latter can vary from zero, representing the undamaged material, to one, which is a fully damaged material.

In the presence of damage the Cauchy stress is no longer representative of the stresses and it is substituted by an effective stress. The effective stress represents the external loads acting over the effective area, which is the uncracked portion of the section. The following values for the tension stiffness degradation were used:

Table 5-2 Stiffness damage variable for the corresponding plastic strains

Damage Variable	Plastic Strain
0	0
0.2	0.001
0.4	0.006
0.8	0.01
0.9	0.02
0.98	0.03
0.99	0.08

The stiffness damage parameters were applied, as mentioned before, to the SFRC pipe models with the lower bounds of the steel fiber content and which exhibited more pronounced loss of stiffness in the post-failure behavior. The models included pipes: 24-B-0.17-II, 24-C-0.25-III, 36-C-0.25-III, 36-C-0.33-III and 48-B-0.5-III.

5.4.1. Obtaining Load-Deformation Curves with FEM

To obtain the behavior and the load-deformation response for each representative case of the experimentally tested SFRC pipe (i.e. test for 24 inch pipe with wall B and steel fiber volume fraction of 0.17 was repeated three times) an average of the load-deformation plots for the repeated tests was found. An average of the repeated

three-edge bearing tests can be assumed to be a representative load-deformation response for that group of pipes. Figure 5-11 shows an example of the curve average for 24-B-0.33-III pipe (see Appendix F for all cases.).

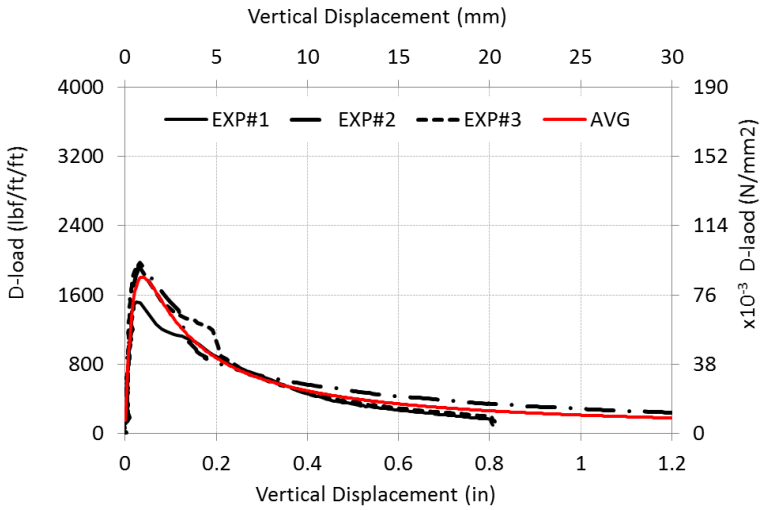

Figure 5-11 Average load-deformation curve for the repeated tests for 24-B-0.17-II

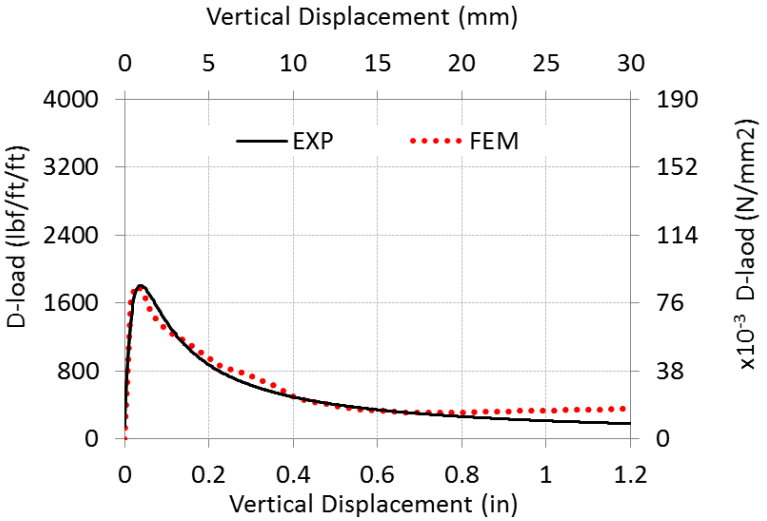

Figure 5-12 Finite element-based load-deformation response in comparison with an averaged experimentally obtained curve for 24-B-0.17-II

The curve of an averaged load-deformation response was utilized for the calibration of the finite element model in order to determine the material constitutive law for the steel fiber reinforced concrete pipe. Each curve for load-deformation response obtained with FEM was matched to that of an averaged experimentally derived curves. An example of the FEM in comparison to experimental load-deformation response is shown in Figure 5-12 (see Appendix G for all cases).

5.4.2. Obtaining Stress-Strain Curves with FEM

Once the model was calibrated, the element maximum and minimum principal stresses and the corresponding strains were extracted for the critical regions of the cross-section: at the crown, invert and springlines.

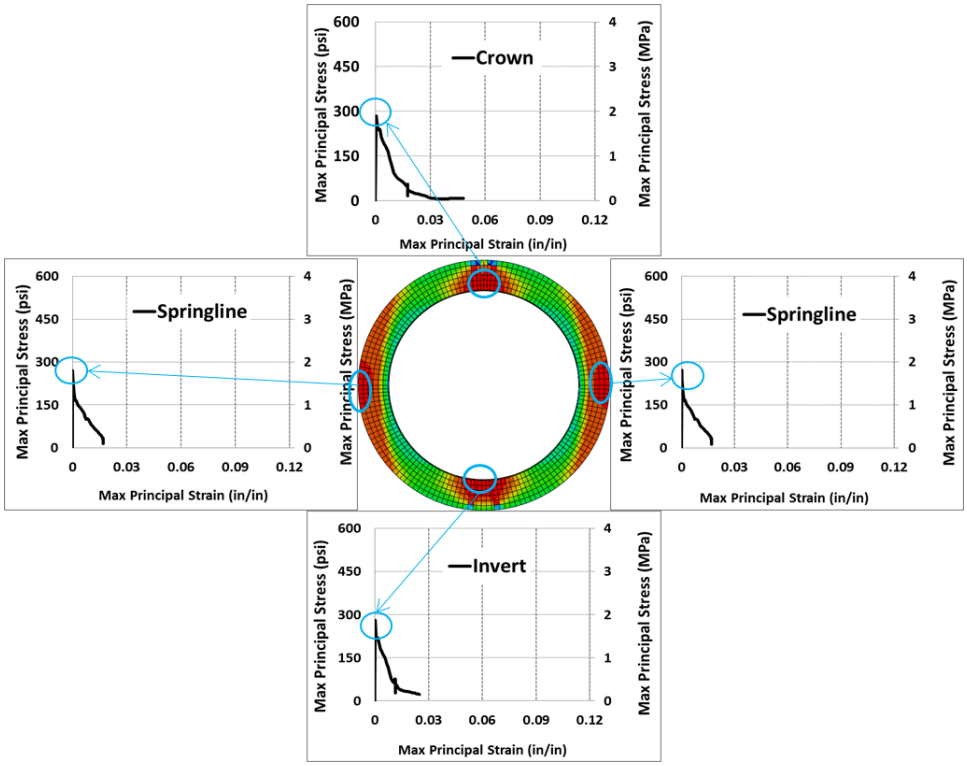

Figure 5-13 Maximum (tensile) principal stress and strains at 5% deformation and stress contours at ultimate stress in the 24-B-0.17-II SFRCP

The material constitutive law for the critical locations in 24-B-0.17-II (lower bound of steel fiber volume fraction content) and 24-B-0.33-III (upper bound of steel fiber volume fraction content) are shown in Figure 5-13 and Figure 5-14, respectively.

For the SFRCP with the lower fiber volume fraction (Figure 5-13) the crown goes through the complete stress-strain envelope with the stress going almost to zero after cracking. The section regions at invert and springlines go through smaller strains as compared to crown as the deformation reaches 5%. On the other hand, for SFRCP with the higher fiber volume (Figure 5-14) fraction the springlines undergo full plastic deformation whereas the crown and invert experience almost only half of the plastic strain experienced at springlines.

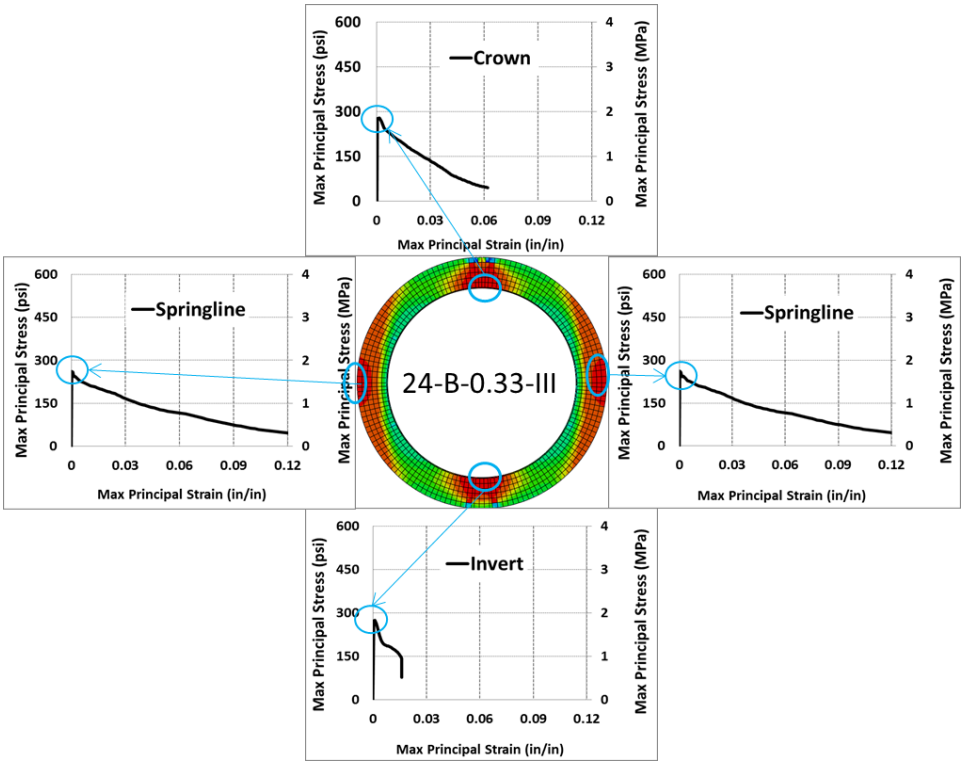

Figure 5-14 Maximum (tensile) principal stress and strains at 5% deformation and stress contours at ultimate stress in the 24-B-0.33-III SFRCP

Total strain versus time increment are plotted on Figures 5-15 and 5-16 for the SFRCP 24-B-0.17-II and 24-B-0.33-III, respectively. It shows that for the 24-B-0.17-II pipe strain at the crown are higher than the strains at invert and springlines at any time increment. And the strains at the springlines are slightly higher than those at the invert. However at the final time increment (t=1 sec), when the vertical deformation reaches 5% of the pipe diameter, the strains at the invert surpass the strains at springlines.

A different pattern is observed for the pipes with higher fiber volume fractions. The crown undergoes the highest strains up to the point of t=0.25 sec, which corresponds to 1.25% deformation or 0.3 in. (7.62 mm) in 24 in. (600 mm) pipe. Passed this point the springlines experience higher strain rate as compared to other locations and become the highest by the end of deformation. Crown continues to strain at approximately the same rate and the invert strains at almost a constant rate.

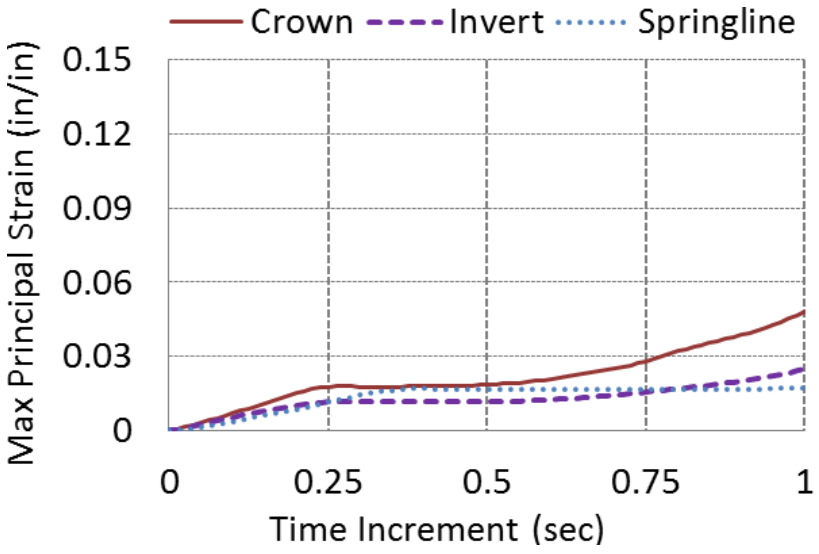

Figure 5-15 Maximum (tensile) principal strains versus time increment for the critical locations in the 24-B-0.17-III SFRCP.

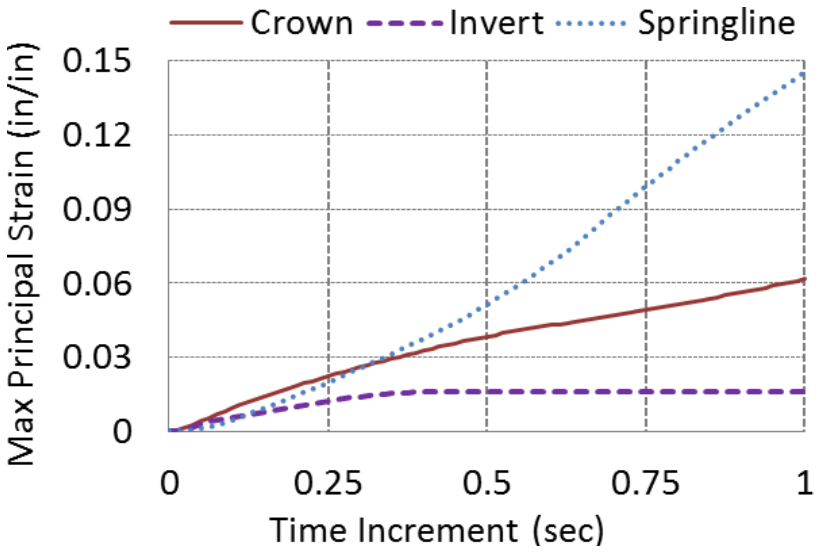

Figure 5-16 Maximum (tensile) principal strains versus time increment for the critical locations in the 24-B-0.33-III SFRCP.

The incremental stress contours that illustrate yielding of concrete for the 24-B-0.17-II and 24-B-0.33-III are shown in Figure 5-17 and Figure 5-18, respectively. It can be seen that for lower dosages of fiber the section yields fully at t=0.1 sec which corresponds to vertical displacement of 0.6%. On the other hand, the section of the pipe with higher fiber volume fraction (Figure 5-18) yields at a slower rate having smaller deformation of 0.5% at time t=0.1 sec.

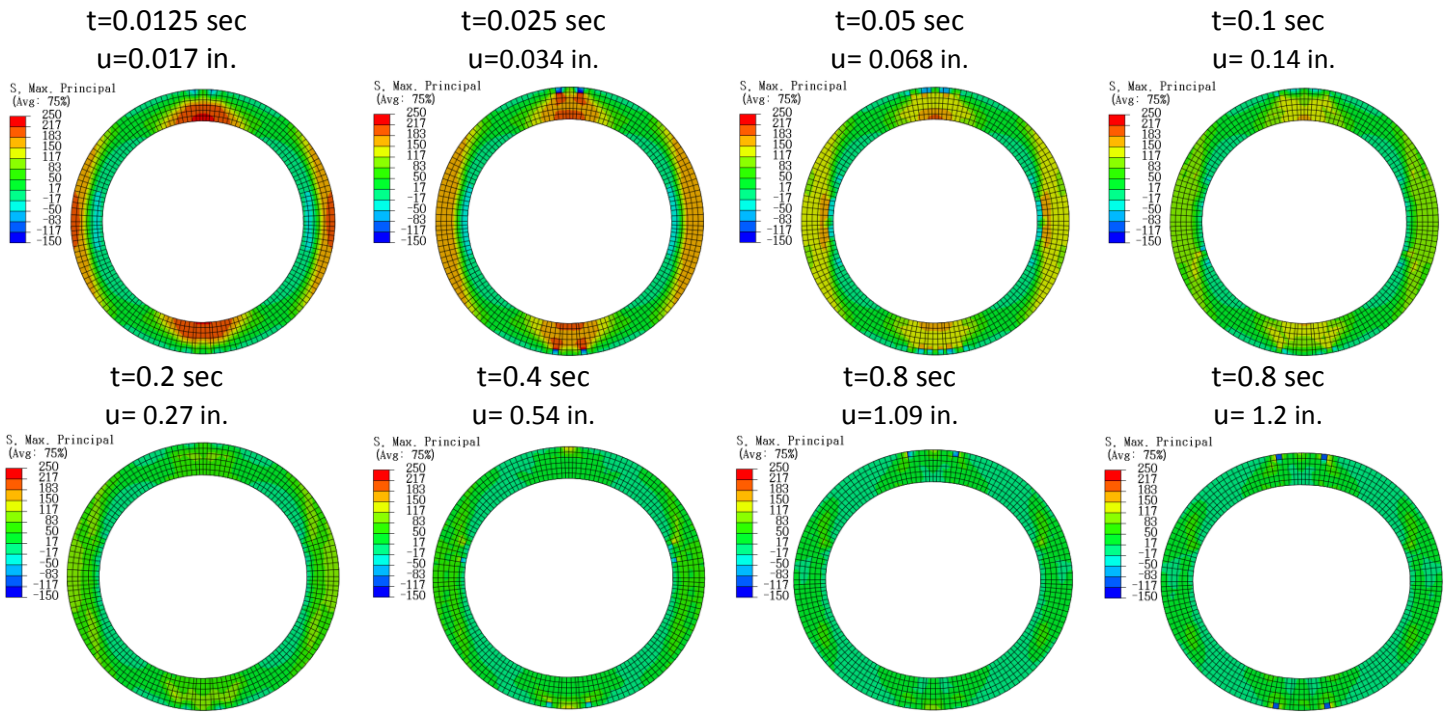

Figure 5-17 Principal stress contours and vertical displacement in a pipe with low fiber volume fraction (24-B-0.17-II)

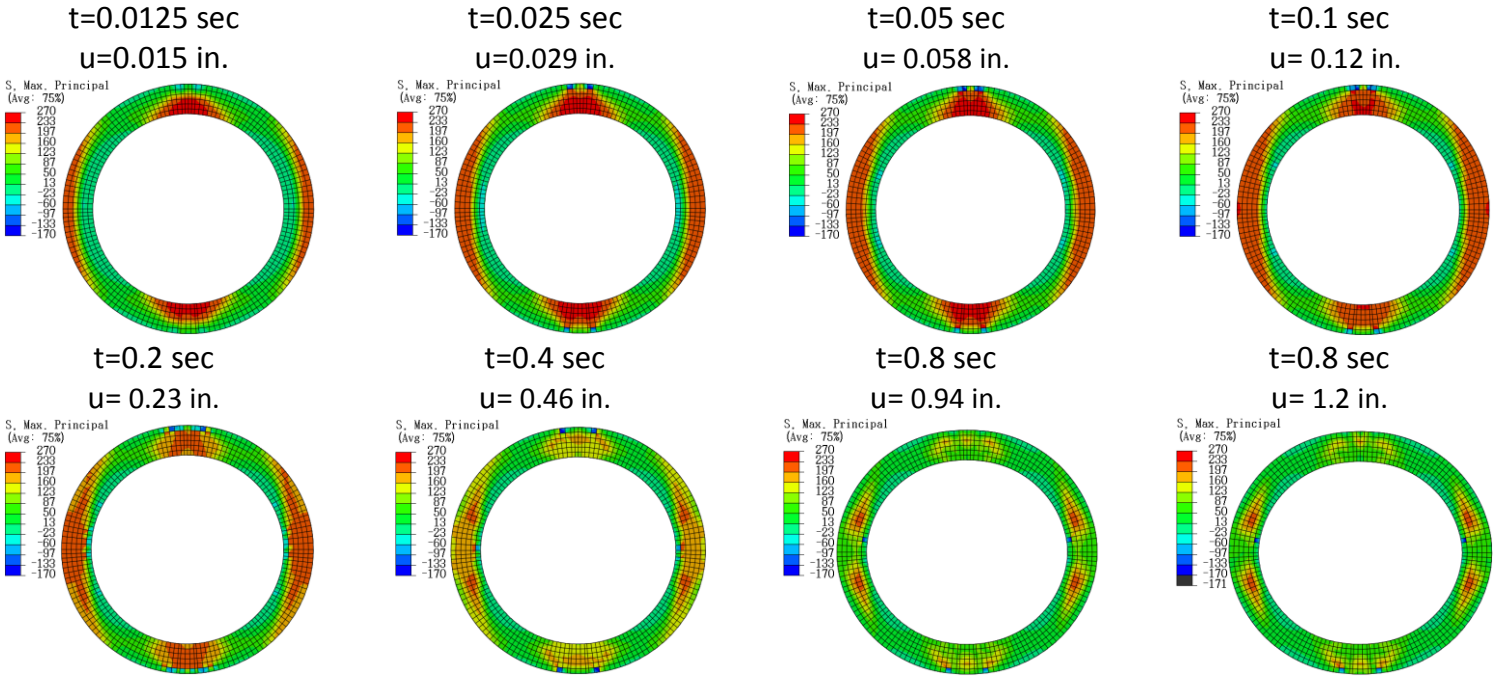

Figure 5-18 Principal stress contours and vertical displacement in a pipe with low fiber volume fraction (24-B-0.33-III)

A typical minimum principal stress versus strain for the critical regions, is shown in Figure 5-19. It can be seen that for all locations the compressive stresses are within elastic range with higher strains at springlines and lower at crown and invert. These pattern are typical for all pipe diameters and fiber dosages (see Appendix G for all cases).

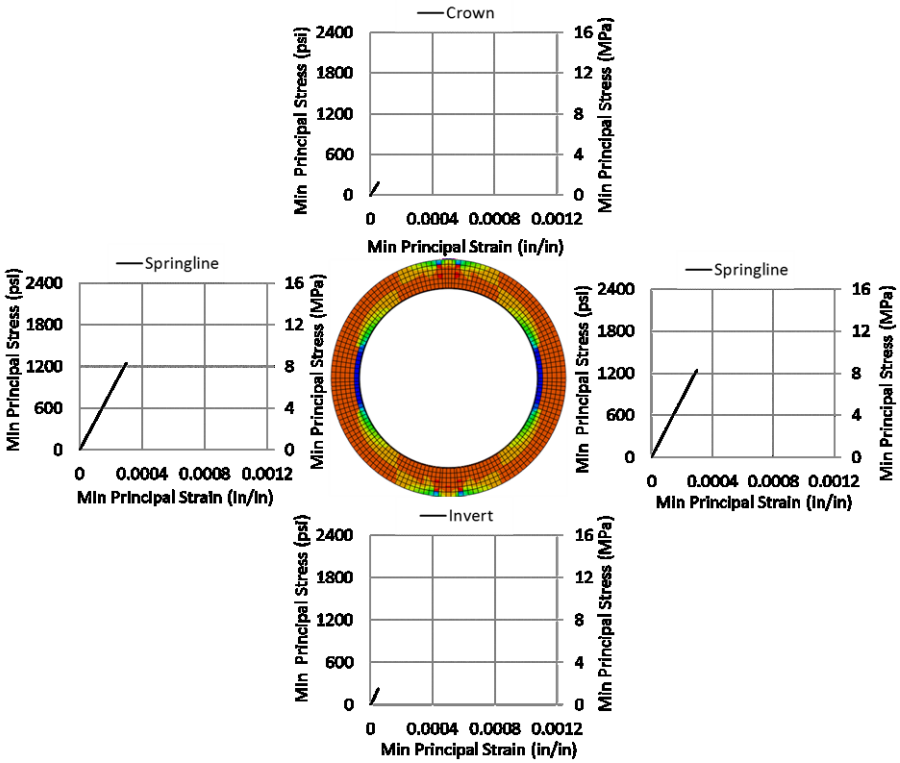

Figure 5-19 Minimum (compressive) principal stress-strain relationships at 5% deformation and stress contours at ultimate stress in the 24-B-0.17-II SFRCP.

5.4.3. Fitting Equation for the Tension Stiffening Model

For each case of the tension stiffening model a curve fitting was performed using the least squares approach coupled with Newtonian iterations (Bathe, 1996). This method is based on minimizing the sum of the squared errors. The errors are the residuals which represent the difference between the observed value and the fitted value.

The fitted equation undergoes several iteration processes until the best fit is obtained, determined based on the sum of squared errors. The fitted equations of the tension stiffening model and the corresponding coefficient of determinations are presented in Table 5-3.

Table 5-3 Fitted equations for the material constitutive laws for the

Pipe Diameter (in.)	***Wall Type***	***Fiber Volume Fraction, V_f***	***Pipe Designation (D_{id}-Wall-V_f-Strength Class)***	***Coefficient of Determination, R^2***
24	***B***	***0.17***	***24-B-0.17-II***	**0.97**
$\sigma = \frac{-0.0824\sin(-25.8\varepsilon)}{1.28\times10^{-6}+0.00527\varepsilon+\varepsilon^2}$				
24	***B***	***0.25***	***24-B-0.25-III***	**0.96**
$\sigma = 304 + 2.02\times10^3\varepsilon - 1.49\times10^3\sqrt{\varepsilon} - (3041.01\times10^{-7})^{3.3\times10^6\times\varepsilon^2}$				
24	***B***	***0.25***	***24-C-0.25-III***	**0.99**
$\sigma = 1.14 + \frac{\varepsilon^{0.116}}{0.00222+32.6\varepsilon^2}$				
24	***B***	***0.33***	***24-B-0.33-III***	**0.99**
$\sigma = 250e(-13.5\varepsilon - 6.34\varepsilon^{(2.53\times10^3\varepsilon)})$				
24	***B***	***0.33***	***24-C-0.33-III***	**0.98**
$\sigma = 4.58\times10^3\varepsilon + 1.93\times10^3\sqrt{\sqrt{\varepsilon}} - 4.79\times10^3\sqrt{\varepsilon}$				
24	***B***	***0.5***	***24-C-0.5-IV***	**0.98**
$\sigma = 4.84\times10^3\varepsilon + 2.2\times10^3\sqrt{\sqrt{\varepsilon}} - 5.32\times10^3\sqrt{\varepsilon}$				

Table 5-3 - *Continued*

30	***B***	***0.33***	***30-B-0.33***	**0.91**
$\sigma = \frac{12.3\varepsilon^{7.88\times10^{-9}} - 31.4\varepsilon}{-0.0476 + \varepsilon + e(-4.25\times10^{4}\varepsilon)}$				
30	***C***	***0.33***	***30-C-0.33-III***	**0.98**
$\sigma = 2203.6\times10^{-7^{(1+\varepsilon-(9.22\times10^{3}\varepsilon)^{(\frac{5.16\times10^{-6}}{\varepsilon})}}}$				
30	***B***	***0.5***	***30-B-0.5-III***	**0.95**
$\sigma = 5.1\times10^{3}\varepsilon + 2.55\times10^{3}\sqrt{\sqrt{\varepsilon}} - 5.97\times10^{3}\sqrt{\varepsilon}$				
30	***B***	***0.5***	***30-B-0.5-IV***	**0.92**
$\sigma = \frac{2.04\times10^{5}\varepsilon}{0.0191 + 391\varepsilon + 1.12\times10^{4}\varepsilon^{2})}$				
33	***B***	***0.5***	***33-B-0.5-II***	**0.96**
$\sigma = 226e(-23.9\varepsilon - 8.150.329^{(4.21\times10^{4}\varepsilon)})$				
36	***C***	***0.25***	***36-C-0.25-III***	***0.98***
$\sigma = \frac{279}{e(86\varepsilon + \frac{8.07\times10^{-5}}{\varepsilon} - 456\varepsilon^{2})}$				
36	***C***	***0.33***	***36-C-0.33-III***	***0.97***
$\sigma = \frac{-0.0824\sin(-25.8\varepsilon)}{1.38\times10^{-6} + 0.00527\varepsilon + \varepsilon^{2}}$				
36	***C***	***0.5***	***36-C-0.5-III***	***0.91***
$\sigma = 1.23\times10^{5}\varepsilon + 260\varepsilon^{0.00118} - 1.81\times10^{5}\varepsilon^{3} - 1.28\times10^{5}\varepsilon\times0.666^{\varepsilon}$				

Table 5-3 - *Continued*

36	***B***	***0.67***	***36-B-0.67-III***	***0.98***
$\sigma = 4.91\sin(-73.7\varepsilon) + 335\varepsilon^{(0.000676+4.5\varepsilon)}$				
36	***C***	***0.67***	***36-C-0.67-III***	***0.94***
$\sigma = 6.21 + \frac{-6.79\varepsilon}{-1.04\times10^{-6} - \varepsilon^2 - 0.0183\varepsilon}$				
36	***C***	***0.83***	***36-C-0.83-III***	***0.96***
$\sigma = \frac{12.9 - 17.1\varepsilon}{0.0341 + \varepsilon + 0.0441^{(1.73\times10^8\varepsilon^2)}} - 12.5$				
48	***B***	***0.5***	***48-B-0.5-II***	***0.98***
$\sigma = \frac{2.7}{0.00654 + \varepsilon + \varepsilon^2 + \varepsilon^{(3.95\times10^3\varepsilon)}}$				
48	***B***	***0.67***	***48-B-0.67-III***	***0.94***
$\sigma = 3.87\times10^3\varepsilon + 17.9\sqrt{(2.83\times10^3\sqrt{\sqrt{\varepsilon}} - 3.34\times10^3\sqrt{\varepsilon}}$				
48	***B***	***0.83***	***48-B-0.83-III***	***0.97***
$\sigma = 5.45\times10^3\varepsilon + 3.33\times10^3\sqrt{\sqrt{\varepsilon}} - 7.46\times10^3\sqrt{\varepsilon}$				

5.4.4. Internal Forces in the Pipe

Internal forces, particularly shear, thrust and moment were obtained for each model along the circumference of the pipe section. The typical distribution of force components for shear and thrust at the time of first crack are illustrated in Figure 5-20. The maximum thrust is experienced by the crown and springlines, whereas maximum shear occurs at approximately 15 degrees from the crown and is zero at springlines.

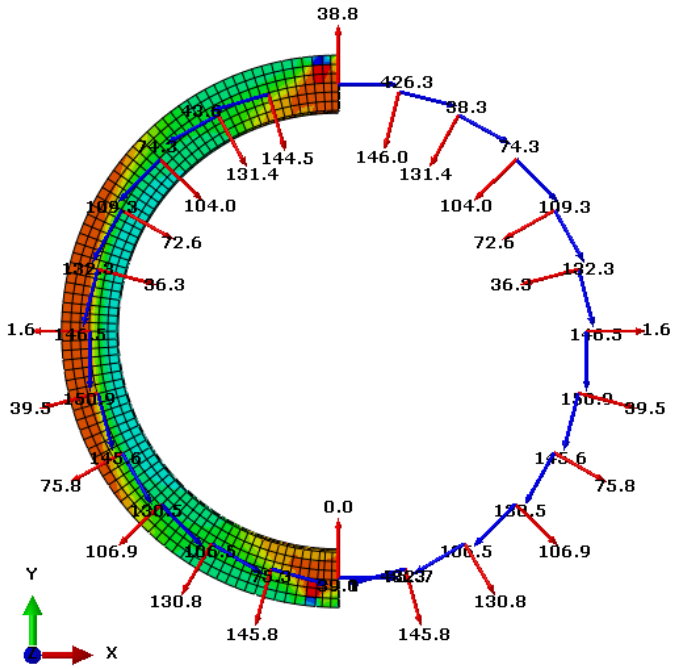

Figure 5-20 Distribution of shear and trust forces along the pipe circumference at first crack initiation

The thrust forces along the pipe circumference in Figure 5-21 and shear and moment forces in Figure 5-22 (a), (b) show a graphical representation of internal forces at deformation of 5% (see Appendix H for all cases).

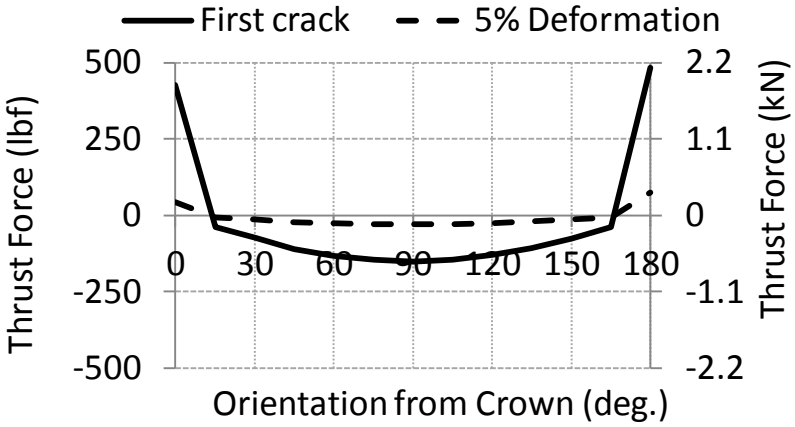

Figure 5-21 Internal forces with support and strips

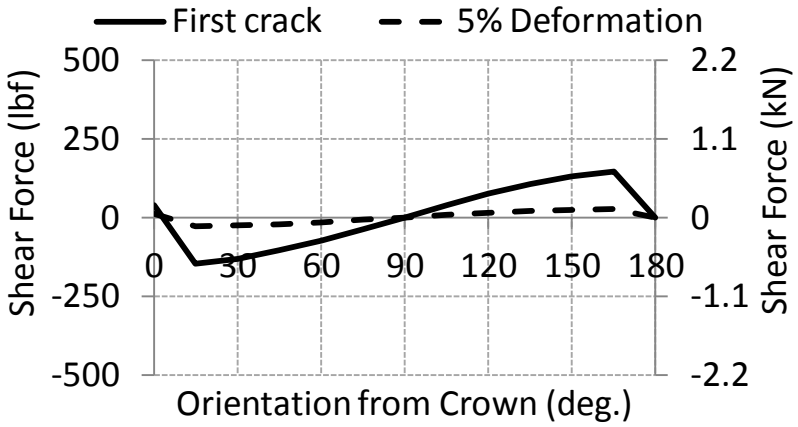

(a)

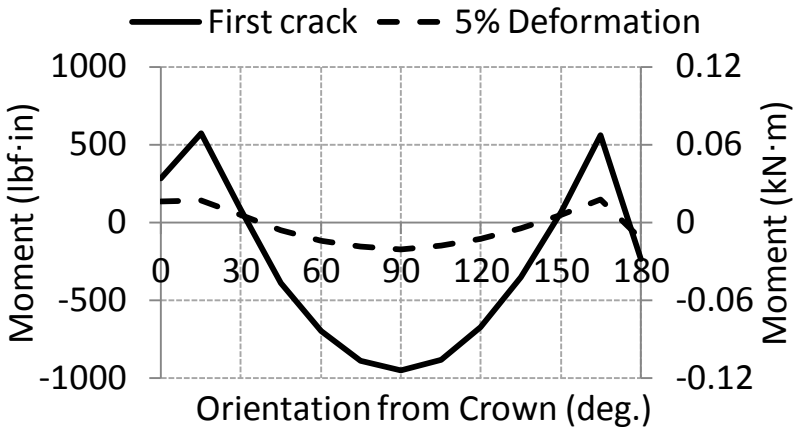

(b)

Figure 5-22 Internal forces with support and strips

The forces at the first crack are the highest and reduce with increase in deformation. This happens due to the redistribution of forces and release of energy as the crack propagates through the section.

The forces in Figure 5-21 and Figure 5-22 (a) and (b) were obtained for the model having two lower bearing strips and the top loading strip (Figure 5-23 (a)). From the graphs it is apparent that the applied boundary conditions affect the distribution of the force components in the regions of crown and 15 degrees from the crown and invert, which is approximately corresponds to the width of the strips. The spikes in the internal

forces are inevitable due to the effect of the boundaries at supports. The effect of the restraints can be alleviated by eliminating the upper strip and applying a line displacement along the pipe length (Figure 5-23 (b)).

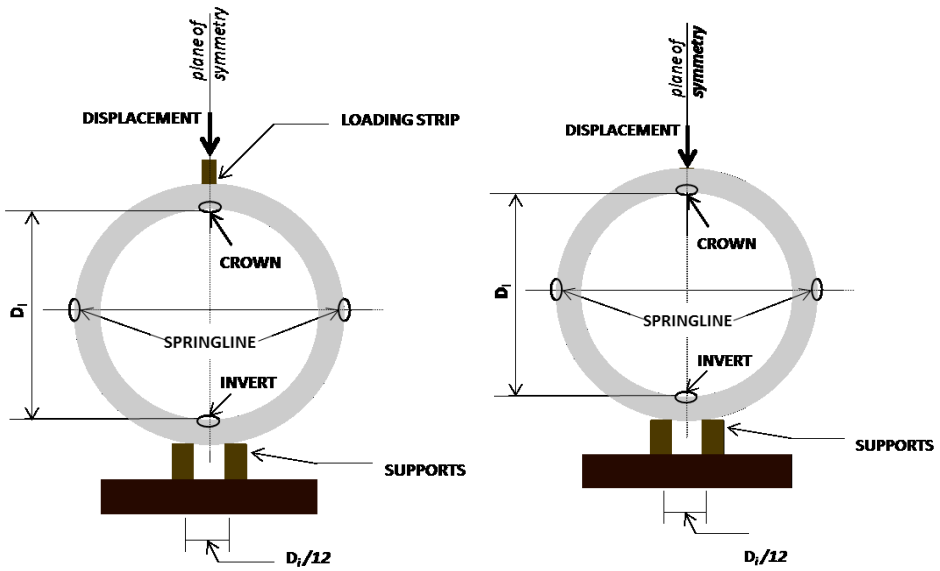

(a) (b)

Figure 5-23 ASTM C497 three-edge bearing test configuration

(a) with loading strip and (b) without loading strip

The internal forces for the model without the upper loading strip are shown in Figure 5-24 (a), (b) and (c). In the absence of the strip the thrust forces at crown become zero and maximum shear forces occur at the crown and invert, rather than at 15 degrees from crown. The maximum moment occurs at crown, springlines and at 15 degrees from the invert, which is an effect of the lower bearing strips. The maximum bending moment produces the tensile stresses at the extreme fibers of the pipe wall at crown, invert and the springlines which causes plastic hinges at those locations creating four-line cracking.

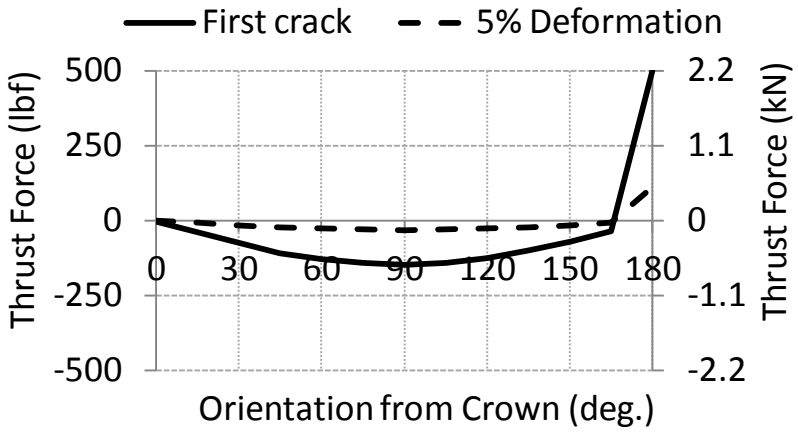

(a)

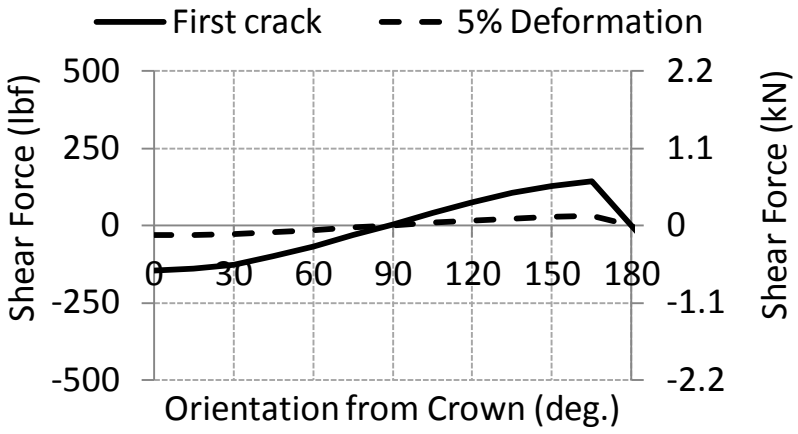

(b)

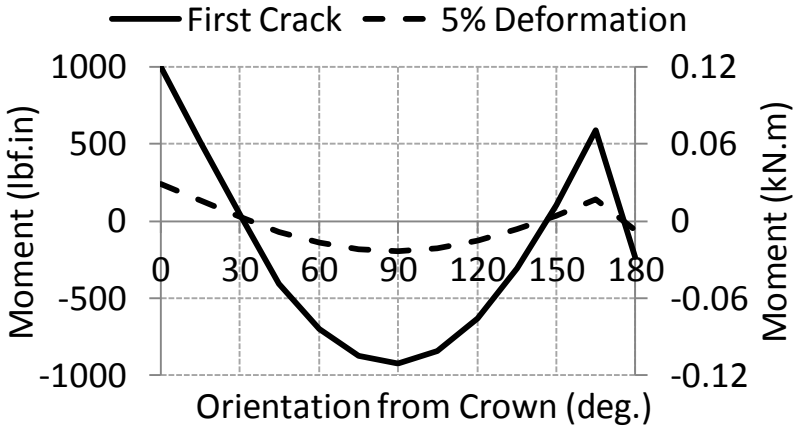

(c)

Figure 5-24 Internal forces with support and without loading strip

Another case of the pipe model without the loading strip having a single support at the bottom was considered (Figure 5-25). The internal forces for this case are plotted in Figure 5-26. Thrust forces are zero at crown and invert and a maximum at springlines. Shear forces are maximum at crown and invert and are zero at springlines; and the moments are maximum at crown, invert and springlines. Moments at crown and invert are the highest in the section, thus the first crack is expected at these locations. This is coherent with the observations during the experimental testing.

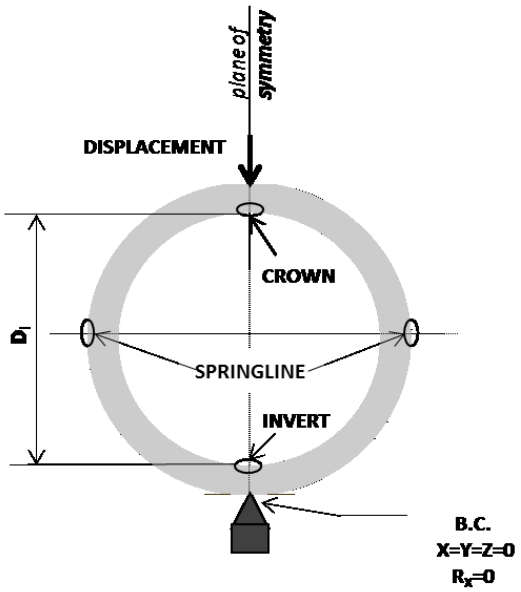

Figure 5-25 internal forces with support and without loading strip

Also the results of the latter configuration are consistent with the work of Heger (1963), where the stresses and internal forces were calculated for the case of reinforced concrete pipe with ordinary (cage) reinforcement for the three-edge bearing condition.

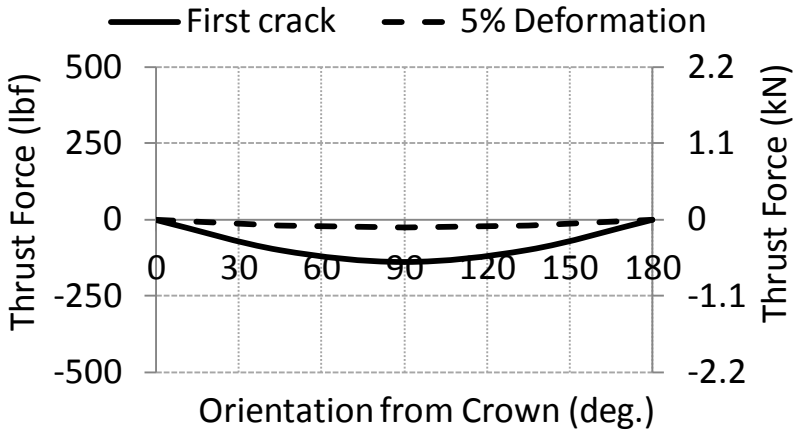

(a)

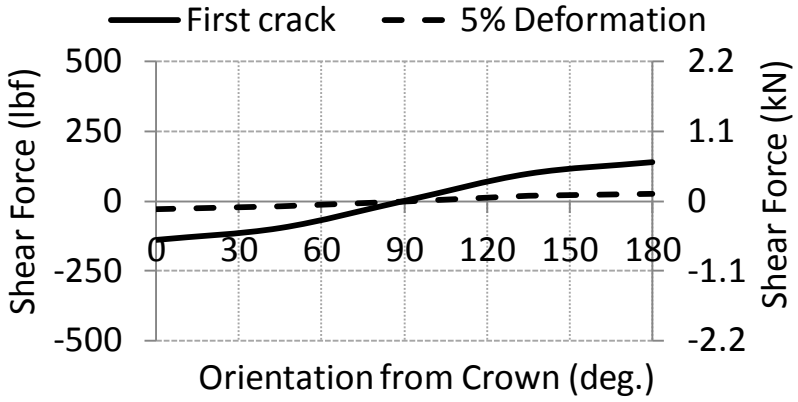

(b)

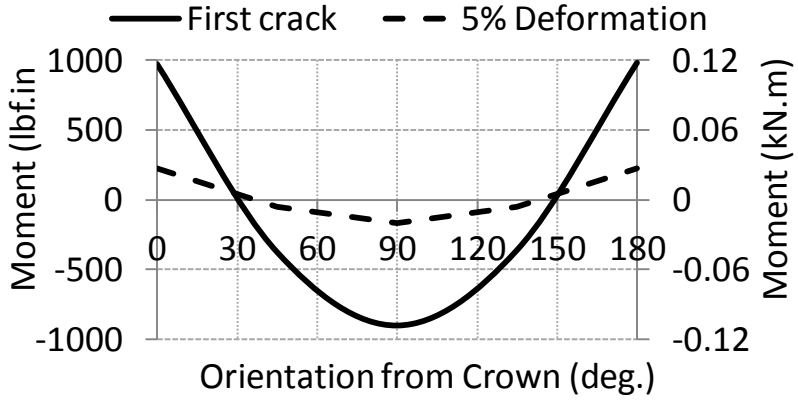

(c)

Figure 5-26 internal forces without supports and without loading strip

5.5. Finite Element Modeling of Pipe-Soil Trench Installation

5.5.1. Modeling overview

In this chapter, the pipe-soil interaction in the trench installation was modeled to simulate the behavior in the pipe and stresses developed under the weight of soil. The elements used were three-dimensional eight-noded solid elements (see Section 4.2.1) for the pipe and three-dimensional hexagonal elements for the soil. A model with a length of one foot was used for computational efficiency.

The model included both geometric and material non-linearities. The interaction between the pipe and the soil was modeled with node-to-surface contact which allowed for stress transfer between the two surfaces. The model of the surrounding soil was partitioned to distinguish between the properties of compacted soil for bedding and backfill soil. The geometric configuration of the model is illustrated in Figure 5-27.

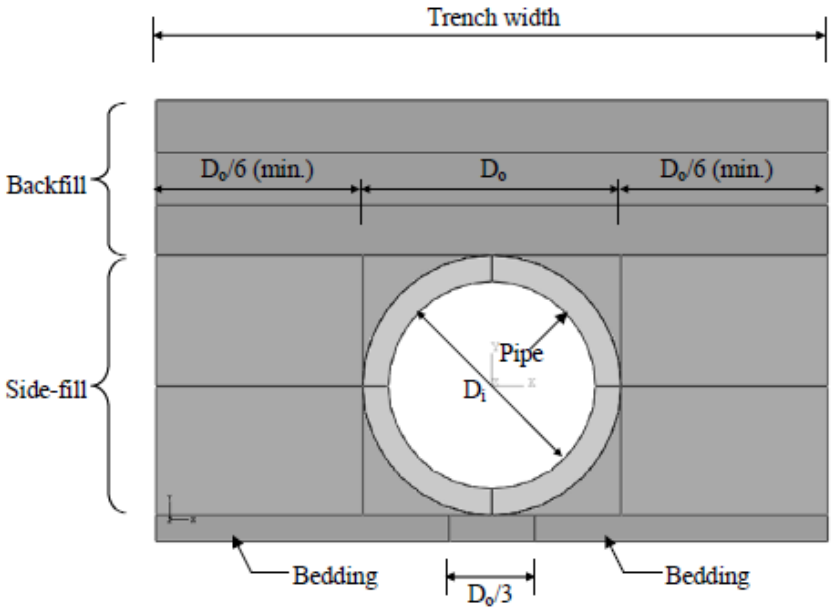

Figure 5-27 Geometric dimensions of a trench installation FEM model

Mesh for the soil model was generated using the swept meshing technique to produce primarily hexahedral elements, but allowing some triangular prisms in transition regions and around the circular pipe geometry, Figure 5-28.

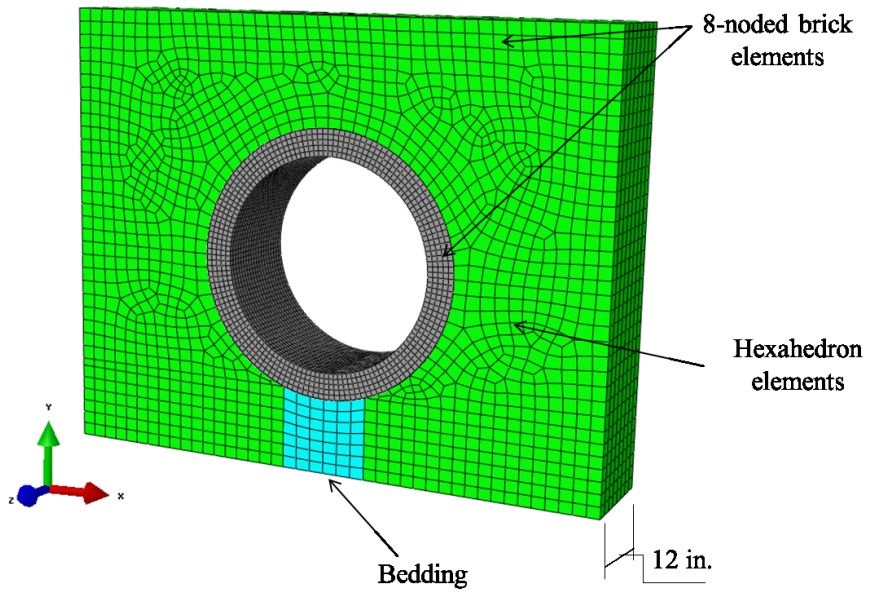

Figure 5-28 FEM model meshing for the pipe and soil with 1 ft. of backfill

5.5.2. Material properties and behavior

The concrete damaged plasticity algorithm was used to define SFRCP material model beyond the elastic range. The elastic material properties used to define concrete elasticity are: Modulus of Elasticity of 4,000,000 psi (27,580 MPa), mass density of 0.00025 pci (2400 kg/m^3), and Poisson's ratio 0.22. The appropriate tension and compression stiffening material models for the pipe sizes under considerations were defined accordingly with the properties defined in Section 5.2.3.

There are four standard installations depending on compaction level of the underlying soil. The standard Type 2 installation was used to model the trench condition for the steel fiber reinforced concrete pipe which calls for 90% compaction of Category 1

soil (gravelly sand) or 95% compaction of Category II soil (sandy silt), in accordance with Concrete Hand Book (1958).

The material properties for the backfill soil were used as follows: soil density 0.000127 pci (1360 kg/m^3), Elastic Modulus 58,000 psi (400 MPa), Poisson's ratio of 0.35; friction angle of 42^0 and cohesion yield stress of 10 psi (0.069 MPa). The bedding soil represents a compacted state of soil and has the following parameters: soil density 0.000186 pci (1420 kg/m^3), Elastic Modulus of 304,579 psi (2100 MPa), Poisson's ratio of 0.19; friction angle of 19^0 and cohesion yield stress of 286 psi (1.97 MPa).

The Mohr-Coulomb plasticity model was used for the surrounding soil. The failure criterion is defined by Equation 5-22:

$$\tau = c - \sigma \tan \varphi \qquad (5\text{-}22)$$

where *s* is the shear stress; σ - normal stress on plane of shearing (negative in compression); c –cohesion and φ-normal stress angle of friction.

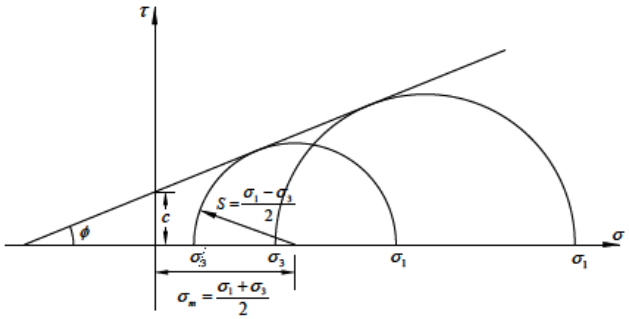

Figure 5-29 The Mohr-Coulomb failure envelope

The failure criteria can be represented in terms of the maximum (σ_1) and minimum (σ_3) principal stresses, shown in Figure 5-29.

The Mohr-Coulomb model is based on the assumption of the failure under maximum shear stresses which depend on the normal stress. The failure occurs when

the shear stress reaches its critical value and it depends linearly on the normal stress acting in the same plane.

5.5.3.Boundary conditions

The boundary conditions to simulate the constraints imposed by the trench installation were applied in the locations as illustrated in Figure 5-30.

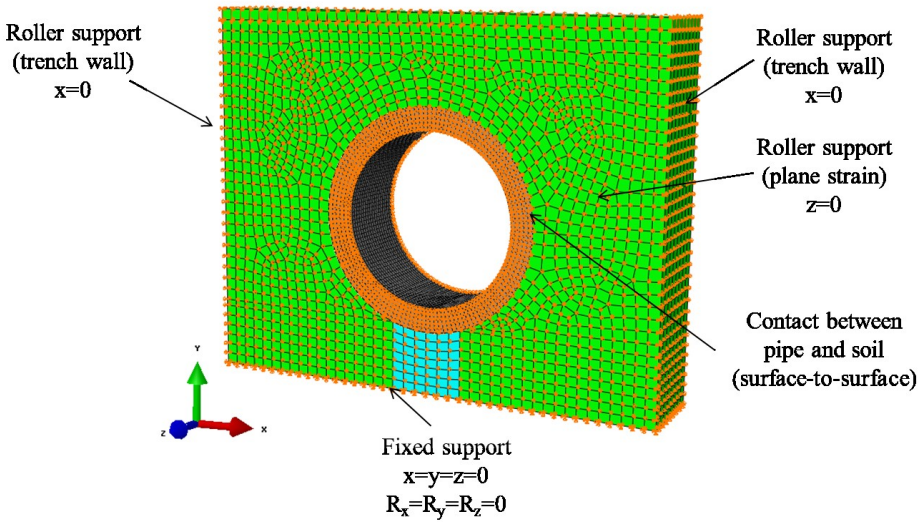

Figure 5-30 Boundary conditions and for the pipe and soil with 1 ft. of backfill

The roller supports along the sides restraining translation in x-direction and roller support along the front and back face of the pipe with constrained translation in z-directions were applied. The bottom of the trench was constrained in translational and rotational degrees of freedom. These conditions simulate the trench installation by allowing the soil movement in y-direction under the gravity forces inducing stresses in the buried pipe and underlying soil.

Two the most common pipe diameters, 24 in. (600 mm) and 36 in. (900 mm) with 0.33% and 0.5% fiber volume fraction, respectively, were considered for the pipe-soil interaction simulation. An effect of the common range of the fill height on 24 in. (600 mm) and 36 in. (900 mm) SFRCP were studied in terms of stress distribution. The study cases of the models are presented in Table 5-4.

Table 5-4 Cases for the pipe-soil interaction study

Pipe Internal Diameter in. (mm)	**Wall Thickness in. (mm)**	**Fiber Dosage V_f (%)**	**Pipe Cracking Stress psi (MPa)**	**Backfill Height ft. (m)**
24 (600)	3 (76) (Type B)	0.33	350 (2.41)	5 (1.5)
				8 (2.4)
				11 (3.4)
				15 (4.5)
				25 (7.6)
				35 (10.7)
36 (900)	4 (100) (Type B)	0.5	380 (2.62)i	5 (1.5)
				8 (2.4)
				11 (3.4)
				15 (4.5)
				25 (7.6)
				35 (10.7)

5.5.4. Results of the Finite Element simulation

Results of simulation are discussed next. As was shown in Table 5-4, SFRCP with diameters of 24 in. (600 mm) and 36 in. (900 mm) and fiber volume fractions of 0.33

and 0.5%, respectively, were considered. The trench installation with fill heights of 5 ft., 8 ft., 11 ft., 15 ft., 25ft. and 35 ft. was simulated. Maximum principal stresses and the corresponding strains evaluated at the crown for each of the fill heights are plotted in Figure 5-31 and Figure 5-32 for 24 in. (600 mm) and 36 in (900 mm) pipes, respectively. The stress-strain relationship is exhibiting linear relationship up until the point of the first crack. Once crack has initiated at 350 psi (2.41 MPa) for 24 in. (600 mm) pipe, stresses no longer increase, concrete is straining due to the growth of the crack. From the numerical simulation it was found that the pipe with the tensile stress of 350 psi may sustain the fill height of maximum 10 feet without cracking.

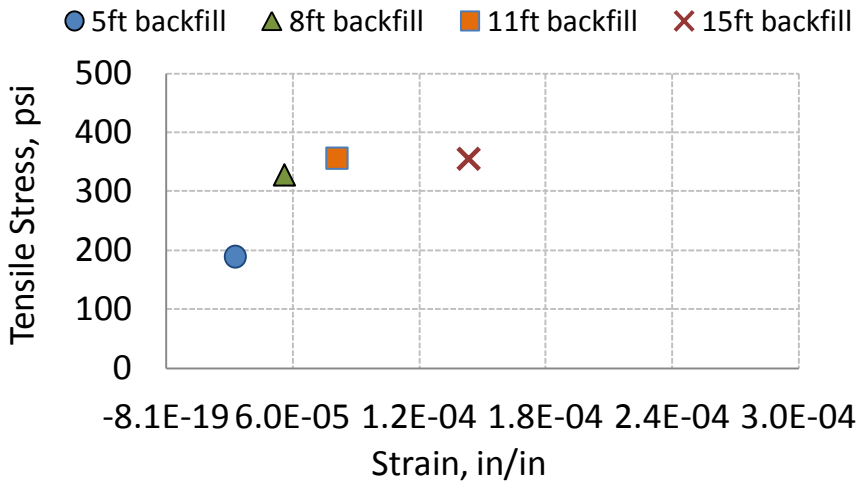

Figure 5-31 Maximum principal stress-strain relationship at crown for 24 in. (600 mm) SFRCP with V_f =0.33%

Similar trend was observed for 36 in (900 mm) diameter SFRCP. Having the cracking stress of 380 psi (2.62 MPa) the first crack in this diameter pipes appears at the fill height of 8 feet which is a lower value as compared to 24 in. (600 mm) with lower limits for the cracking stress.

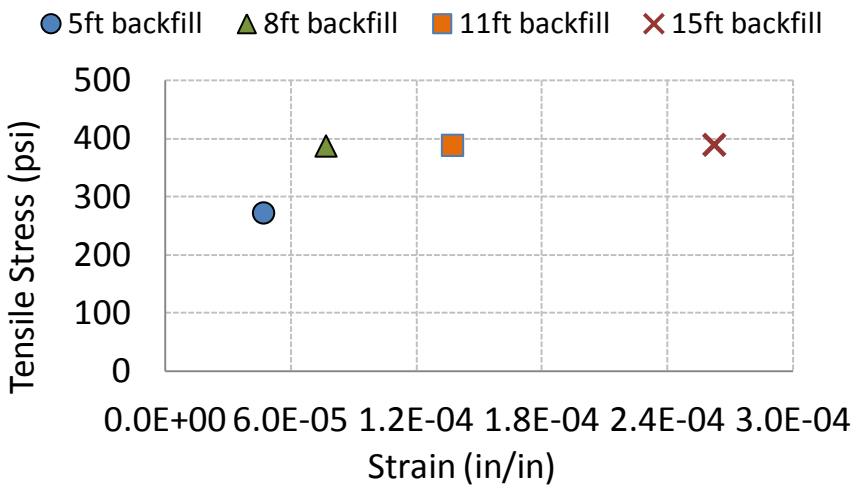

Figure 5-32 Maximum principal stress-strain relationship at crown

for 36 in. (900 mm) SFRCP with V_f =0.50%

The fill height was plotted against pipe vertical deformation in Figure 5-33 and Figure 5-34 for 24 in. (600 mm) and 36 in. (900 mm) SFRCP, respectively. For the fill heights of 5 ft. (1.5 m) through 25 ft. (7.6 m) both pipes goes through the similar deformation.

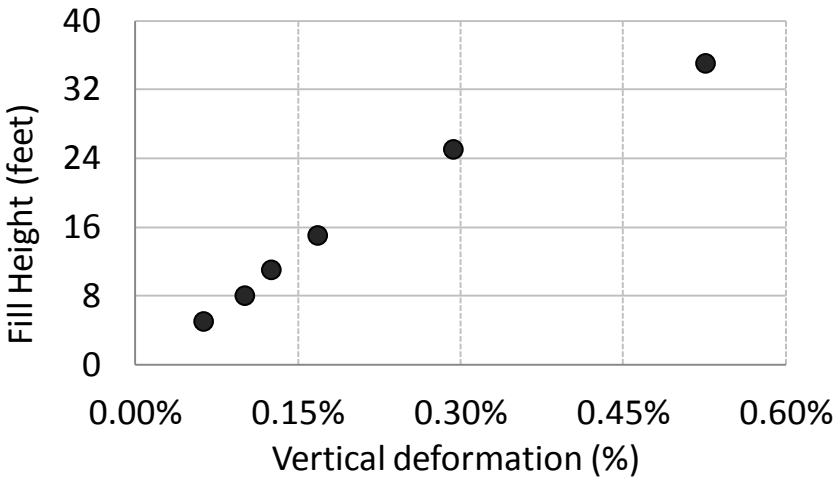

Figure 5-33 Effect of fill height on vertical deformation

in 24 in. (600 mm) SFRCP with V_f =0.33%

However, for the fill height of 35 ft. (10.7 m) the 36 in. (900 mm) diameter pipe exhibit larger deformation as compared to 24 in. (600 mm) diameter pipe. Smaller diameter pipes exhibit a shell action in resisting the bending load which helps which results in a higher rigidity of the structure to resist deformation. On the other hand, pipe with larger diameters act as beams at the crown and the invert regions which allows the pipes to have higher deformations.

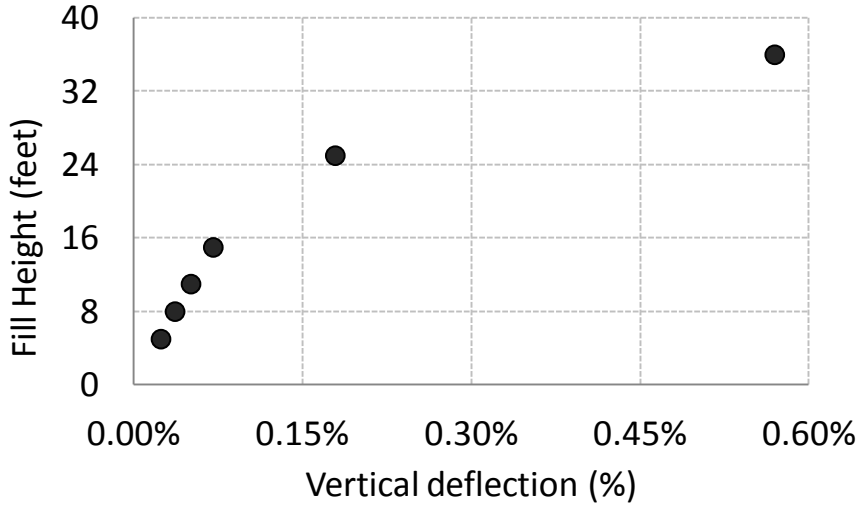

Figure 5-34 Effect of fill height on vertical deformation

in 36 in. (900 mm) SFRCP with V_f =0.50%

Chapter 6

Steel Fiber Distribution Study within Concrete Pipe Specimen

6.1. Introduction

Steel fiber reinforced study was conducted as a part of NSF - East Asia and Pacific Summer Institutes (EAPSI) program at the Kyungpook National University in South Korea. The goal of this study is to quantitatively evaluate the distribution of fibers within the specimen and to investigate the effect of its variation on structural behavior of the pipe. As discussed in previous chapters, the results of experimental testing have shown a high variation in the flexural strength of steel fiber reinforced concrete specimens as well as the strength of concrete pipes when subjected to the three-edge bearing condition.

Fiber orientation and the uniformity of distribution within concrete matrix play an important role in the ability of fibers to transfer stresses across the crack. Uniformity of fiber distribution cannot be guaranteed since it is affected by numerous factors during the pipe production, such as concrete workability, concrete composition, fiber volume fraction, time of concrete mixing and pipe production methods. The ability of fibers to distribute evenly within the matrix also depends on fiber characteristics such as length, diameter, anchoring system (hooked or twisted) and form of fiber in which it is introduced to the mix (loose or glued). Inconsistent dispersion of fibers within structural member will inevitably lead to decreased flexural strength and variation in the test results from specimen to specimen.

There are several studies related to steel fiber distribution investigation. In the study by Dupont and Vandewalle (2004) a derivation of an expression to predict the number of fibers crossing a rectangular section was introduced using “so-called” orientation factor. To verify the derived formulation, the results of computed number of

fibers were compared with that obtained by counting number of fibers in the cross-section. Although the model has shown to be accurate in predicting the number of fibers in a section within an acceptable margins of error, this study did not make an attempt to correlate the fiber distribution and mechanical properties of the material. However another study conducted by Glodkowska and Kobaka (2013) was concerned with both statistical-based model of fiber distribution in fine aggregate concrete and the effect of fiber addition on mechanical properties of fiber-concrete, such as compressive strength, dynamic modulus of elasticity, split tensile strength and other parameters. Images of the statistical model of fiber distribution within rectangular specimen were compared to the images of the actual section of a tested specimens, showing a good agreement. Several other techniques are available for evaluating the fiber orientation, including image analysis (Guild and Summerscales, 1993), AC-impedance spectroscopy and image analysis by Ozyurt et al. (2001.). One of the studies conducted by Kang et al. (2011) used image analysis to determine the influence of fiber orientation on the tensile strength of a specimen. It was determined that the placement direction of fiber-concrete, transverse or longitudinal, significantly affects the flexural strength of the composite.

6.2. Materials

The current investigation on distribution of fibers in concrete matrix is based on the image processing technique which is done on the segmented core specimens extracted from the structural pipe. A total of four pipes with different content of fiber dosages and two types of fiber (three pipes with v_f=0.17%, 0.33%, 0.50 % and RC-65/35-CN fiber and one pipe with v_f=0.33% with FS7 fiber) were considered for the study. The pipes produced at Hanson plant in Grand Prairie, Texas were denoted as 24-B-0.17 (RC-65/35-CN), 24-B-0.33 (RC-65/35-CN), 30-B-0.5 (RC-65/35-CN) and 24-B-0.33 (FS7), where the first number stands for the pipe's internal diameter in inches, followed by the

wall type (B) defined in accordance with ASTM C76 and fiber volume fraction (v_f); the fiber type is indicated in the parentheses.

6.2.1. Fiber

The fibers Bekaert RC-65/35-CN are glued galvanized cold-drawn deformed steel wires with an aspect ratio (L/D) of 60, a length of 1.378 in. (35 mm) and a tensile strength of 195 ksi (1,345 MPa), shown in Figure 6-1 (a).

The fibers Maccaferri FS7 are non-galvanized cold-drawn deformed steel wire with an aspect ratio (L/D) of 60, a length of 1.299 in. (33 mm) and a tensile strength of 180 ksi (1,200 MPa), shown in Figure 6-1 (b).

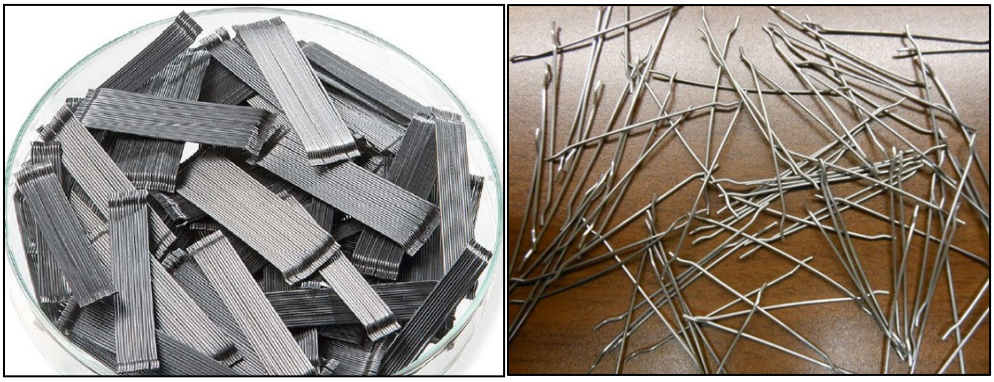

(a) (b)

Figure 6-1 Steel fiber: (a) RC-65/35-CN and; (b) FS7

Although the main focus of this study was on RC-65/35-CN type of fiber distribution, the non-galvanized FS7 fibers used for comparison.

6.2.2. Concrete mix

Cylindrical samples of 3.68 in. (94 mm) in diameter were cored directly from the pipe wall and were subjected to the compressive strength test and fiber dispersion investigation. The height of the cylinders represent the wall thickness in the pipe and varies with its diameter.

The composition of concrete mixes used for production of the pipe specimens is presented in Table 6-1 with an average compressive strength of concrete 5 ksi (35 MPa).

Table 6-1 Concrete mix proportions of steel fiber reinforced concrete

24" Mix Proportions, (per 1 yard^3), SSD	**Mix#1**	**Mix#2**	**Mix#3**
Type I/II Cement, (lbs)	545	545	540
Class F Fly Ash (lbs.)	136	138	151
Crushed Limestone 3/8" (lbs.)	1897	1920	1954
Crushed Limestone 5/8" (lbs.)	N/A	N/A	N/A
Mfg. Sand (lbs.)	N/A	N/A	N/A
Natural Sand (lbs.)	1500	1455	1481
Water (lbs.)	245	250	250
Admix Axim (ozs./cwt.)	3.0	3.0	3.0
Plasticizer (oz/yard)	N/A	N/A	N/A
W/C Ratio	0.36	0.37	0.36
Fiber dosage (lbs.)	0.17	0.33	0.50

6.3. Methodology

The study focuses on the quantitative analysis of steel fiber distribution through statistical analysis of variation of fiber dispersion within the length and the thickness of a pipe. The analysis will delve into determining the influence of amount of fiber on variation of distribution as well as the type of fiber used.

For each of the pipe specimens (with the exception of 30-B-0.5 pipe) six core samples were taken out in three locations along the pipe length, at the bell, mid-length and spigot, two for each location (Figure 6-2). For the 30-B-0.5 pipe with v_f=0.5% fiber

the cores were only taken at the bell and mid-length due to the length of the pipe being shorter as compared to the rest of the pipes.

(a) (b)

Figure 6-2 Location of the sampling from the pipe (a); and core samples for 24-B-0.33 SFRCP with RC-65/35-CN fiber (b)

A total of twenty two core samples were extracted from the steel fiber reinforced concrete pipes and delivered to laboratory in South Korea for further testing. One core sample from each pipe taken from the mid-length was tested for compressive strength; the remaining samples were subjected to fiber distribution study.

To conduct the fiber distribution investigation each specimen was sectioned horizontally into three equal segments with a diamond band saw, as shown in Figure 6-3 (a). Although a higher number of sections per core is desirable, only three segments could be partitioned due to the size and geometry of the specimen. Three segments representing the near region of the outside wall (O.D.), mid- thickness (M) and inside wall (I.D.) were considered, where “D” stands for diameter. Each core specimen was given a designation by numbering it from 1 to 18. Segments belonging to the same core were given identical numbers, letters were added to distinguish between locations in the wall (O.D., M., and I.D.). The complete designation of the specimens is presented in Table 6-2. The specimens denoted as C1 through C4 are the cylinders tested in compression.

(a) (b)

Figure 6-3 Specimen sectioning into segments: (a) diamond band saw box; and (b) core samples divided into three segments

A high resolution image of each surface of the segments was taken using SLR Canon 50 D camera with EF 28-135mm f/3.5-5.6 IS lens and a standard flash. Each image was preprocessed by adjusting the brightness, contrast, exposure and RGB colors to improve the object recognition.

Table 6-2 Pipe designation and numbering of segmented core specimens

Pipe designation	Bell		Middle		Spigot	
	#1	#2	#1	#2	#1	#2
24-B-0.17(RC-65/35-CN)	1	2	C1	3	4	5
24-B-0.25 (RC-65/35-CN)	6	7	C2	8	9	10
24-B-0.25 (FS7)	11	12	C3	13	14	15
30-B-0.5 (RC-65/35-CN)	16	17	-	-	18	C4

The images of a typical cut are shown in Figure 6-4. The steel fibers are clearly visible on the image due to the reflected light applied by exposing the object to a camera flash. Some of the grey areas present on the image of fibers were subjected to correction to produce bright areas.

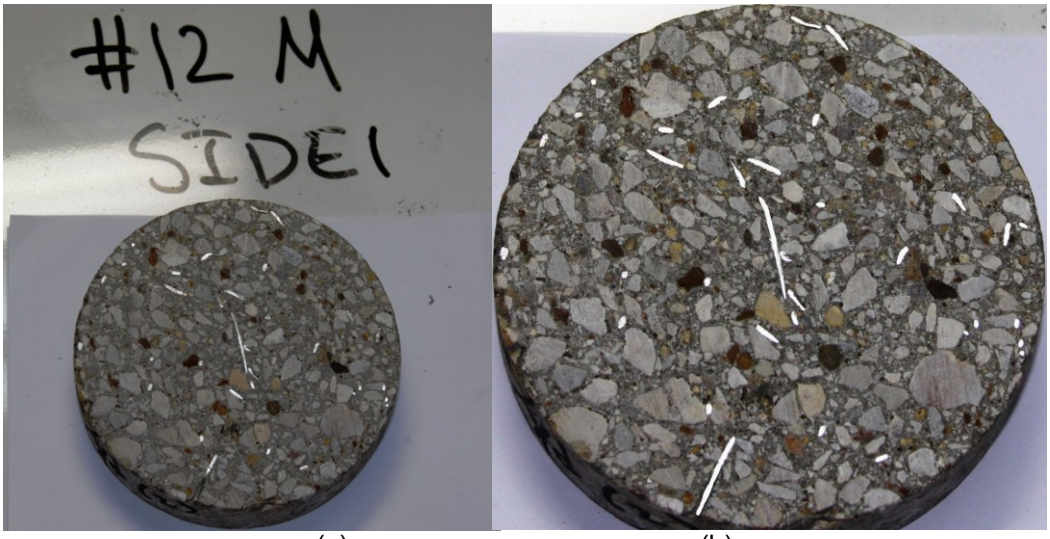

(a) (b)

Figure 6-4 Typical image of a segment surface: (a) raw image;

and (b) after image adjustments

After making adjustments the images were processed with a digital image analysis program called Pixcavator. The program is based on capturing a cluster of bright objects (fibers) surrounded by darker pixels (concrete matrix). The bright objects are evaluated, and location, the shape roundness, size, perimeter and the area of each object are determined, expressed in pixels. An image of each side of the segment was subjected to the digital analysis.

A typical program interface used for the image processing is shown in Figure 6-5. The light objects are shown in green-colored contours, while the shadows and dark inclusions represent darker objects and enclosed by the red-colored contours. The illustration of the image in Figure 6-5 shows a typical example of an image analyzed without a preprocessing. The fibers along with other bright inclusions are recognized as bright objects, thus preprocessing of the image is essential in obtaining acceptable results. All the information related to the detected objects, such as coordinates of the centroids, size and length and perimeter of the objects is shown next to the image.

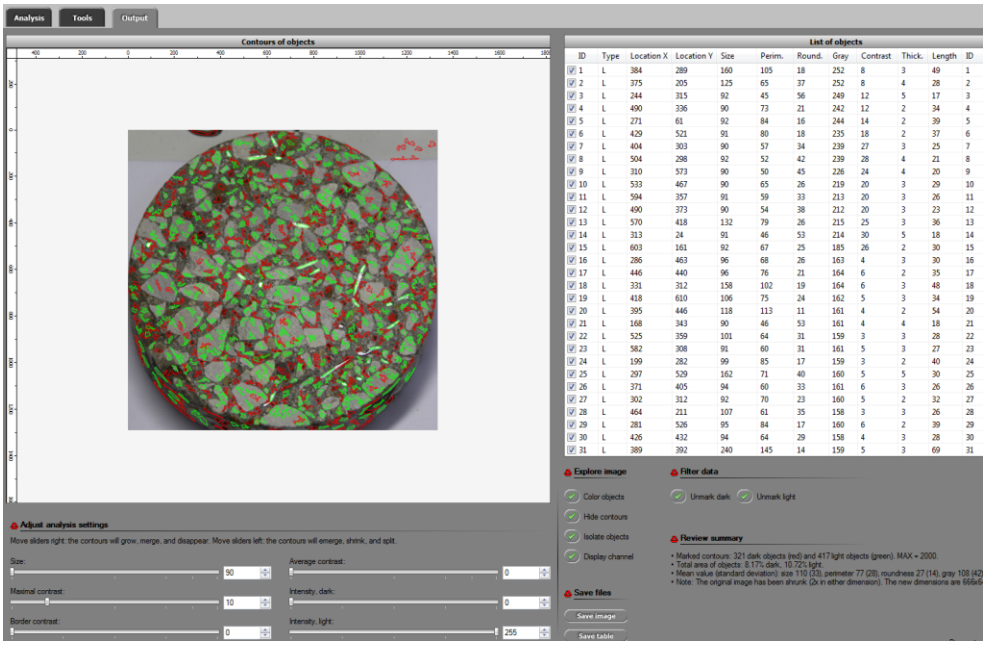

Figure 6-5 Image processing software interface

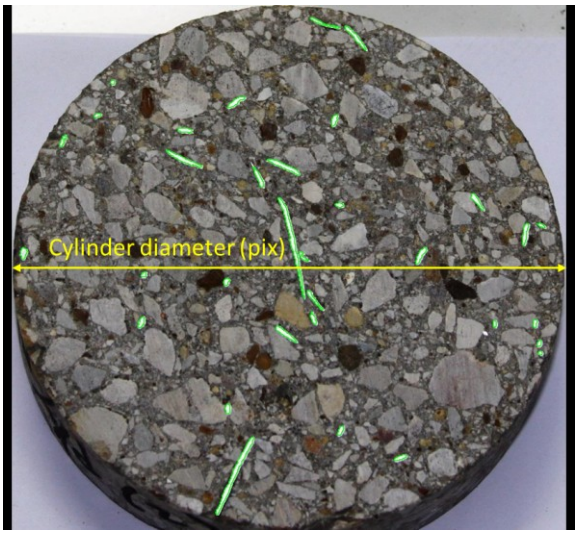

Figure 6-6 Typical image after preprocessing and analysis

An output of an image statistics for each side of the segment was extracted for further analysis. Since the location of each fiber within the specimen is known, the fiber distribution within a single surface can be quantified.

Fiber area fraction was estimated for each side of the segmented surface as a ratio of the fiber area to the total area of the composite section:

$$a_f = \frac{A_f}{A_c} * 100\ (\%) \quad (6\text{-}1)$$

where A_f is total fiber area on the image in pixels^2 and A_c is a total area of the segment (pixels^2). Knowing the width and the height of an image (not necessarily equal) in pixels the total area of the segment can be found:

$$A_c = \frac{\pi d^2}{4}\ (pix^2) \quad (6\text{-}2)$$

Since the height and the width of the image is not always equal, an average of the two dimensions was regarded as the circle diameter.

6.4. Results

A summary of the values for the fiber area fraction averages and its standard deviations along with the D-load strengths averages and its standard deviations are presented in Table 6-3.

Table 6-3 Fiber distribution and corresponding D-load strength averages

Pipe Designation	**Fiber Volume Fraction v_f (%)**	**Avg. Fiber Area Fraction a_f (%)**	**Standard Deviation of Fiber Area Fraction**	**Average D-load Results lbf/ft/ft (kN/m/m)**	**Standard Deviation of D-load**
24-B-0.17 (RC-65/35-CN)	0.17	0.346	0.2131	1970 (2.93)	0
24-B-0.33 (RC-65/35-CN)	0.33	0.371	0.1729	2201 (3.28)	463 (0.69)
24-B-0.33 (FS7)	0.33	1.029	0.4544	2026 (3.02)	497 (0.74)
30-B-0.5 (RC-65/35-CN)	0.50	0.796	0.3199	2440 (3.63)	723 (1.08)

The data suggests that pipe specimen with FS7 fiber has the highest standard deviation in fiber area fraction. Also the pipe with the lowest fiber area fraction (0.17 %) has higher standard deviation than the specimen with v_f=0.33 % for the same fiber type.

The high variation in the specimen with FS7 fibers is caused by the cluster of fibers in the pipe specimen. The core specimen was extracted from the region of fiber clustering to examine the clustering more closely. The image of the cored sample obtained from 24-B-0.33 is shown in Figure 6-7.

Figure 6-7 Fiber clustering in 24-B-0.33 (FS7) specimen

To obtain more accurate results on fiber distribution variation in representative sample, it is recommended the cores are to be taken in more location within the pipe.

A total of 108 images have been pre-processed and analyzed. The results of the image analysis for all segments are summarized in Appendix I, where images of the segment surfaces, length and area of the fibers, and the areas of the total segment surface are provided. The fiber area fraction average distribution charts along the pipe length –bell, middle and spigot are presented in Figure 6-8 and Figure 6-9.

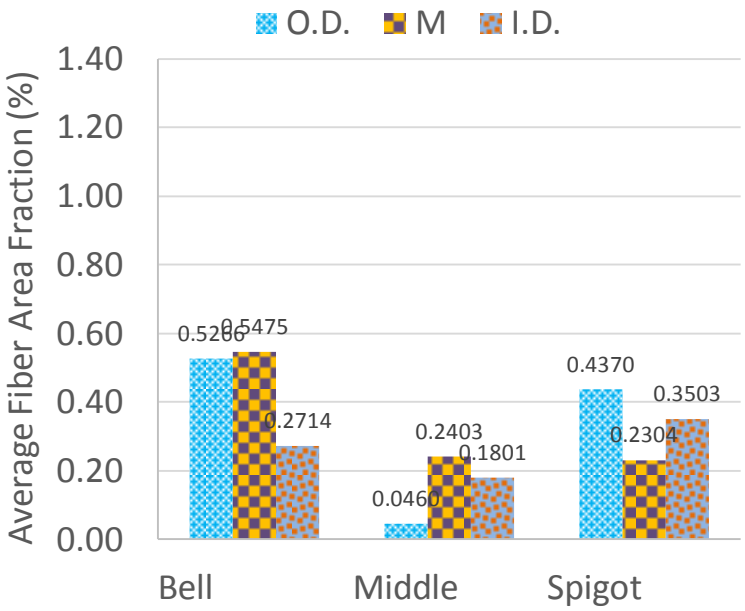

(a)

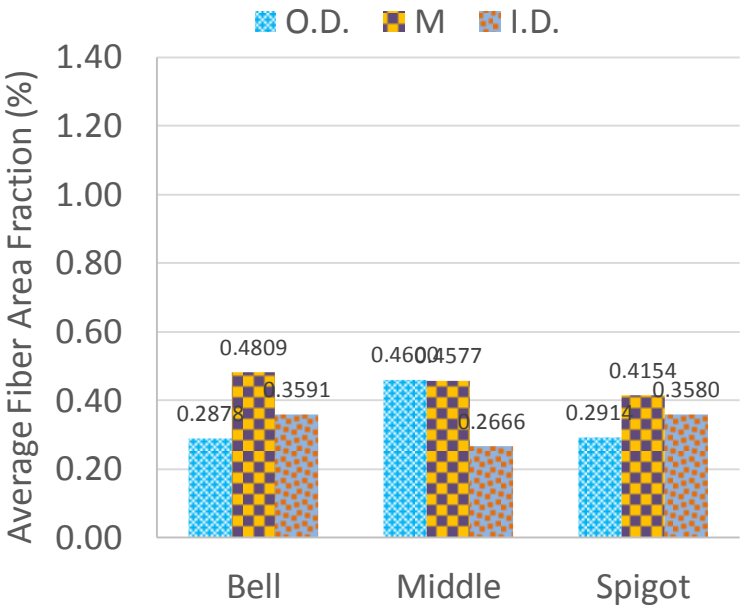

(b)

Figure 6-8 Variation of average fiber distribution within wall layers and along the pipe:

(a) Specimen 24-B-0.17 (RC-65/35-CN); (b) Specimen 24-B-0.33 (RC-65/35-CN)

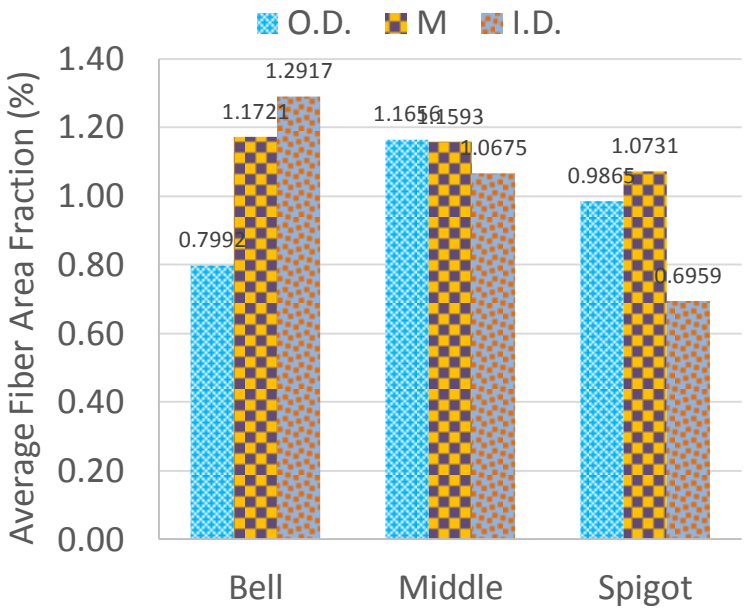

(a)

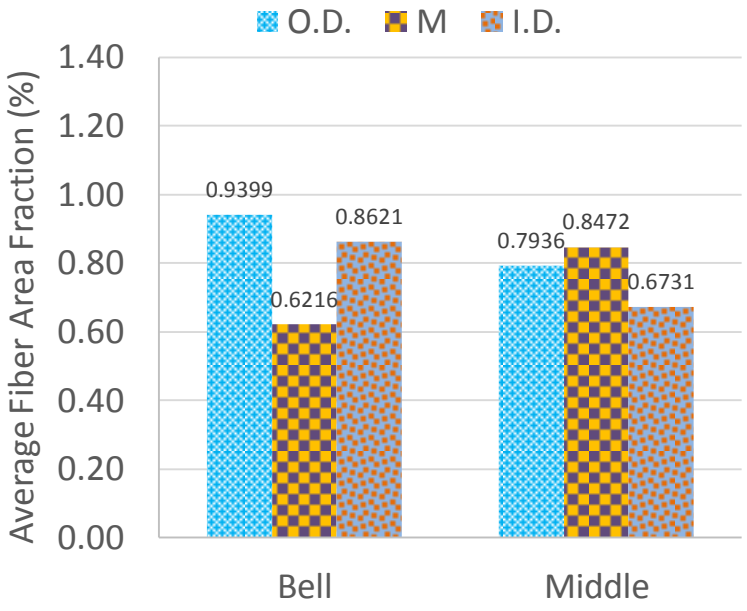

(b)

Figure 6-9 Variation of average fiber distribution within wall layers and along the pipe:

(a) Specimen 24-B-0.33 (FS7); (b) Specimen 30-B-0.50 (RC-65/35-CN)

Pipe with the lowest fiber content (0.17 %) has higher fiber distribution variation along the length of the pipe as compared to other pipes. The fiber area fractions are higher at the bell and spigot and lower in the midsection of the pipe. The data suggests that for the pipe with the lowest fiber dosage variation in fiber distribution is the highest across the wall thickness (I.D, M and O.D.). For higher fiber volume fractions variation in fiber density within the pipe length and the wall thickness is not significant.

The fiber distribution by specimen and along the pipe length is shown in Figure 6-10. The average area fraction is the highest for the 24-B-0.33 with FS7 type fibers which is due to the clustering of the fibers in the representative sample.

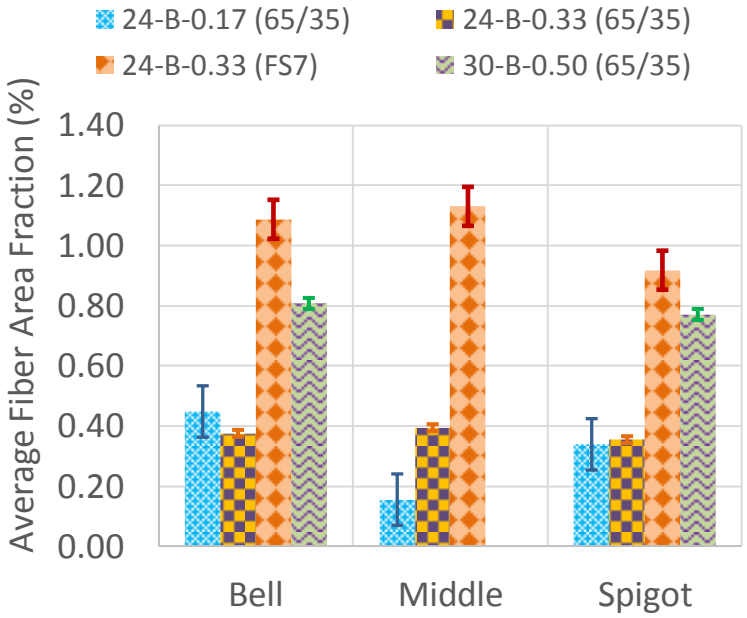

Figure 6-10 Variation of average fiber distribution and standard error along the pipe by specimen:

Standard error bars for the average fiber area fractions along the pipe length are also indicated. The highest standard error of distribution is observed for the sample of 24-B-0.17 (RC-65/35-CN) pipe with the lowest fiber content. Pipes with 0.33 and 0.5 fiber

volume fractions and RC-65/35-CN fiber type have fairly uniform distribution along the length of the pipe.

Based on the above observations a statistical analysis is performed to verify the assumptions regarding the uniformity of fiber distribution.

6.5. Statistical analysis

6.5.1. Test for Variance Equality of Two Population with Different Fiber Content

In this test the variances of two populations are verified for equality in samples taken from 30-B-0.5 and 24-B-0.33 pipes. This test allows to determine whether the variation of steel fiber distribution is affected by the amount of fiber in concrete. The F-test is conducted for Sample 1 (v_f= 0.50%) with n_1=18 observations in 30 in. (750 mm) pipe and Sample 2 (v_f=0.33%) with n_2=30 observations in 24 in. (600 mm) pipe.

A two-sided test with a confidence level of 90% is conducted for the following hypothesis:

H_0: $\sigma_1^2=\sigma_2^2$

H_1: $\sigma_1^2\neq\sigma_2^2$

Decision rule - conclude H_0 if:

$$F\left(\frac{\alpha}{2};\ n_1-1, n_2-1\right) \leq \frac{s_1^2}{s_2^2} \leq F\left(\left(1-\frac{\alpha}{2}\right);\ n_1-1, n_2-1\right) \qquad (6\text{-}3)$$

Mean value of *Sample 1*:

$$\bar{x}=\frac{\sum x_i}{n_1}=0.796 \qquad (6\text{-}4)$$

and sample variance:

$$s_1^2=\frac{\sum(x_i-\bar{x})^2}{n_1-1}=0.09669 \qquad (6\text{-}5)$$

Mean value of *Sample 2*:

$$\bar{y}=\frac{\sum y_i}{n_2}=0.372 \qquad (6\text{-}6)$$

and sample variance:

$$s_2^2 = \frac{\sum(y_i - \bar{y})^2}{n_2 - 1} = 0.029894 \quad (6\text{-}7)$$

Critical value: $F\left(\frac{\alpha}{2};\ n_1 - 1, n_2 - 1\right) = F(0.05;\ 29, 17) = 2.1537$ (6-8)

$$F\left(\left(1 - \frac{\alpha}{2}\right);\ n_1 - 1, n_2 - 1\right) = F(0.95; 29; 017) = 0.4643 \quad (6\text{-}9)$$

Test value: $\frac{s_1^2}{s_2^2} = \frac{0.09669}{0.02989} = 3.23$ (6-10)

The F-test value is greater than F-critical value, thus reject H_0 hypothesis. The two population of SFRCP with different fiber content do not have the same variances of fiber distribution. Thus, the next test of hypothesis will determine whether the variance of population 1 (30-B-0.5) is larger than the variance of population of 2 (24-B-0.5). Both populations have the same fiber type RC-65/35-CN.

6.5.2. Comparison of Variances of Two Population with Different Fiber Content

In this test the variances of two populations are compared for the samples taken from *30-B-0.50* and *24-B-0.33* pipes to evaluate whether the variance of sample with higher amount of fiber in larger pipe diameter is greater than the variance of the sample with lower fiber content in smaller pipe diameter. The F-test is conducted for Sample 1 (v_f= 0.50%) with n_1=18 observations in 30 in. (750 mm) pipe and Sample 2 (v_f=0.33%) with n_2=30 observations in the 24 in. (600 mm) pipe.

A one-sided test with 95% confidence level is conducted for the hypothesis:

H_0: $\sigma_1^2 = \sigma_2^2$

H_1: $\sigma_1^2 > \sigma_2^2$

Decision rule - conclude H_0 if:

$$\frac{s_1^2}{s_2^2} \geq F(\alpha;\ n_1 - 1, n_2 - 1) \quad (6\text{-}11)$$

conclude H_1 if:

$$\frac{s_1^2}{s_2^2} < F(\alpha;\ n_1 - 1, n_2 - 1) \tag{6-12}$$

Mean value of *Sample 1*:

$$\bar{x} = \frac{\sum x_i}{n_1} = 0.796 \tag{6-13}$$

and sample variance:

$$s_1^2 = \frac{\sum (x_i - \bar{x})^2}{n_1 - 1} = 0.09669 \tag{6-14}$$

Mean value of *Sample 2*:

$$\bar{y} = \frac{\sum y_i}{n_2} = 0.372 \tag{6-15}$$

and sample variance:

$$s_2^2 = \frac{\sum (y_i - \bar{y})^2}{n_2 - 1} = 0.029894 \tag{6-16}$$

Critical value: $F(\alpha;\ n_1 - 1, n_2 - 1) = F(0.05;\ 29, 17) = 2.1537$ (6-17)

Test value: $\frac{s_1^2}{s_2^2} = \frac{0.09669}{0.02989} = 3.23$ (6-18)

The F-test value is greater than F-critical value, thus conclude H_0 – variance of 30 in. (750 mm) SFRCP with v_f=0.50% is greater than the variance of 24 in. (600 mm) SFRCP with v_f=0.33%.

6.5.3. Test for Variance Equality of Two Population with Same Fiber Content but Different Fiber Type

In this test the variances of two populations are verified for equality in samples taken from 24-B-0.33 SFRCP with v_f=0.33% and fiber types FS7 (Sample 1) and RC-65/35-CN (Sample 2). This test allows to determine whether the variance of steel fiber distribution is affected by the type of fiber in concrete. The F-test is conducted for Sample 1 with n_1=30 and Sample 2 with n_2=30 observations in the 24 in. (600 mm) pipe.

A two-sided test with a confidence level of 90% is conducted for the following hypothesis:

H_0: $\sigma_1^2=\sigma_2^2$

H_1: $\sigma_1^2\neq\sigma_2^2$

Decision rule - conclude H_0 if:

$$F\left(\frac{\alpha}{2};\ n_1-1, n_2-1\right) \leq \frac{s_1^2}{s_2^2} \leq F\left(\left(1-\frac{\alpha}{2}\right);\ n_1-1, n_2-1\right) \quad (6\text{-}19)$$

Mean value of *Sample 1*:

$$\bar{x}=\frac{\sum x_i}{n_1}=1.029 \quad (6\text{-}20)$$

and sample variance: $$s_1^2=\frac{\sum(x_i-\bar{x})^2}{n_1-1}=0.20651 \quad (6\text{-}21)$$

Mean value of *Sample 2*:

$$\bar{y}=\frac{\sum y_i}{n_2}=0.372 \quad (6\text{-}22)$$

and sample variance: $$s_2^2=\frac{\sum(y_i-\bar{y})^2}{n_2-1}=0.02989 \quad (6\text{-}23)$$

Critical value: $$F\left(\frac{\alpha}{2};\ n_1-1, n_2-1\right)=F(0.05;\ 29, 29)=1.8924 \quad (6\text{-}24)$$

$$F\left(\left(1-\frac{\alpha}{2}\right);\ n_1-1, n_2-1\right)=F(0.95; 29; 29)=0.5284 \quad (6\text{-}25)$$

Test value: $$\frac{s_1^2}{s_2^2}=\frac{0.09669}{0.02989}=6.91 \quad (6\text{-}26)$$

The test F value is larger than F-critical value, thus reject H_0 hypothesis - the variances of the two tests are not the same.

6.5.4. Comparison of Variances of Two Population with Different Fiber Content

In this test the variances of two populations are compared for the samples taken from *24-B-0.33* pipes with v_f=0.33% and fiber types FS7 (Sample 1) and RC-65/35-CN

(Sample 2) to evaluate whether the variance of sample with FS7 fibers is larger than the variance of the sample with RC-65/35-CN fibers for the same fiber content. The F-test is conducted for Sample 1 (FS7) with n_1=30 and Specimen 2 (RC-65/35-CN) with n_2=30 observations in the 24 in. (600 mm) pipe.

A one-sided test with a confidence level of 95% is conducted for the hypothesis:

H_0: $\sigma_1^2 \geq \sigma_2^2$

H_1: $\sigma_1^2 < \sigma_2^2$

Decision rule - conclude H_0 if: $\frac{s_1^2}{s_2^2} \geq F(\alpha;\ n_1 - 1, n_2 - 1)$ (6-27)

conclude H_1 if: $\frac{s_1^2}{s_2^2} < F((\alpha;\ n_1 - 1, n_2 - 1)$ (6-28)

Mean value of *Sample 1*:

$$\bar{x} = \frac{\sum x_i}{n_1} = 1.029 \quad (6\text{-}29)$$

and sample variance:

$$s_1^2 = \frac{\sum (x_i - \bar{x})^2}{n_1 - 1} = 0.20651 \quad (6\text{-}30)$$

Mean value of *Sample 2*:

$$\bar{y} = \frac{\sum y_i}{n_2} = 0.372 \quad (6\text{-}31)$$

and sample variance:

$$s_2^2 = \frac{\sum (y_i - \bar{y})^2}{n_2 - 1} = 0.029894 \quad (6\text{-}32)$$

Critical value: $F(1 - \alpha;\ n_1 - 1, n_2 - 1) = F(0.95;\ 29, 29) = 1.85$ (6-33)

Test value: $\frac{s_1^2}{s_2^2} = \frac{0.20651}{0.02989} = 6.908$ (6-34)

The F-test value is greater than F-critical value, thus conclude H_0 – variance of SFRCP with SF7 type fibers is greater than the variance of SFRCP with RC-65/35-CN type fibers.

6.5.5. Test of Variances of Two Population for Equality of Fiber Distribution in Pipe Wall

Similarly the variances of fiber distribution within wall thickness of the same pipe will be tested for the hypothesis of equal variances. In this test the variances of two populations for the samples taken from the bell section of 24-B-0.17 pipe with v_f=0.17% and RC-65/35-CN fiber type will be compared for the outside diameter and mid-diameter segments This test allows determining whether the distribution of the fiber varies with the depth of the pipe wall. The F-test is conducted for Sample 1 (O.D.) with n_1=4 observations and Sample 2 (M.D.) with n_2=4 observations.

A two-sided test with a confidence level 90% is conducted for the hypothesis:

H_0: $\sigma_1^2=\sigma_2^2$

H_1: $\sigma_1^2\neq\sigma_2^2$

Decision rule - conclude H_0 if:

$$F\left(\frac{\alpha}{2};\ n_1-1, n_2-1\right) \leq \frac{s_1^2}{s_2^2} \leq F\left(\left(1-\frac{\alpha}{2}\right);\ n_1-1, n_2-1\right) \quad (6\text{-}35)$$

Variance of *Sample 1*: $s_1^2 = 0.0495$

Variance of *Sample 2*: $s_2^2 = 0.00513$

Critical value: $F\left(\frac{\alpha}{2};\ n_1-1, n_2-1\right) = F(0.05;\ 3, 3) = 9.28$ (6-36)

$$F\left(\left(1-\frac{\alpha}{2}\right);\ n_1-1, n_2-1\right) = F(0.95; 4; 4) = 0.1078 \quad (6\text{-}37)$$

Test value: $\frac{s_1^2}{s_2^2} = \frac{0.0495}{0.00513} = 9.65$ (6-38)

The test F value is larger than F-critical value, thus reject H_0 hypothesis - the variances of the two tests are statistically not the same. Although the average fiber distribution appears to be close for the indicated depths of the pipe wall, the variances of two distributions are not the same, since the standard deviations for the two locations are distinct from each other (O.D.=0.22 and M.D.=0.07).

6.5.6. Test of Variances of Two Population for Equality within the Pipe Length

The variances of fiber distribution within the same layer of the wall thickness and along the length of same pipe will be tested for the hypothesis of equal variances. In this test the variances of two populations for the samples taken from the bell and mid-length sections of 24-B-0.17 pipe with v_f=0.17% and RC-65/35-CN fiber type will be compared for the mid-depth (M.D.) diameter. This test allows determining whether the distribution of the fiber varies within the length of the pipe. The F-test is conducted for Sample 1 (Bell) with n_1=4 observations and Sample 2 (Mid-length) with n_2=4 observations.

A two-sided test with a confidence level of 90% is conducted for the hypothesis:

H_0: $\sigma_1^2=\sigma_2^2$

H_1: $\sigma_1^2\neq\sigma_2^2$

Decision rule - conclude H_0 if:

$$F\left(\frac{\alpha}{2};\ n_1-1, n_2-1\right) \leq \frac{s_1^2}{s_2^2} \leq F\left(\left(1-\frac{\alpha}{2}\right);\ n_1-1, n_2-1\right) \quad (6\text{-}39)$$

Variance of *Sample 1*: $s_1^2 = 0.00513$

Variance of *Sample 2*: $s_2^2 = 0.01524$

Critical value: $F\left(\frac{\alpha}{2};\ n_1-1, n_2-1\right) = F(0.05;\ 3, 3) = 9.28 \quad (6\text{-}40)$

$$F\left(\left(1-\frac{\alpha}{2}\right);\ n_1-1, n_2-1\right) = F(0.95; 3; 3) = 0.1078 \quad (6\text{-}41)$$

Test value: $\frac{s_1^2}{s_2^2} = \frac{0.01524}{0.00513} = 2.97 \quad (6\text{-}42)$

The test F value is larger than F-critical value, thus reject H_0 hypothesis - the variances of the two tests statistically are not the same.

Fiber distribution within concrete matrix is not uniform. Non-uniformity of the distribution increases when the lower fiber volume fractions are used and becomes more uniform with higher fiber volume fractions. In addition, fiber average area fraction is

higher and more consistent throughout the length in mid-layers of the pipe's wall whereas variation in fiber densities for outer and inner layers are less uniform. Outer and inner layers play an important role in resisting the first crack formation at the springlines (outer) and crown and invert (inner), while the mid-layers are active in resisting the crack growth as the load increases.

Chapter 7

Summary, Conclusions and Future Work

7.1. Summary

This study presents a comprehensive experimental and analytical investigation of steel-fiber reinforced concrete pipes (SFRCP) performance and behavior introduced for the first time in the US. The material constitutive model development of steel fiber reinforced concrete is one of the primary goal of this research.

As a part of experimental investigation various pipe sizes were produced which included 15 in. (400 mm), 24 in. (600 mm), 30 in. (750 mm), 33 in. (850 mm), 36 in. (900 mm) and 48 in. (1200 mm) diameters pipes. The pipe production was conducted at four different geographical regions within the country to allow for variabilities in pipe production methods and the local material properties. All the produced pipes were delivered to the Hanson Concrete Pipe and Precast facility for further testing. Steel fibers RC-65/35-CN which are the galvanized deformed cold drawn wire were used for pipe reinforcement by varying the volume fraction content. The fiber content in the produced pipe varied from 0.17% to 0.83% by volume. The structural behavior of the pipe was analyzed by subjecting each pipe to the three-edge bearing test and obtaining the load-deformation response. Each pipe was loaded monotonically to produce 5% deformation in vertical plane. The crack sizes were measured at the end of loading cycle. For each tested SFRCP a conventionally reinforced concrete control pipe (RCP) was tested. In addition, a sample of test pipes were subjected to hydrostatic joint and joint shear tests to assess the joints for water tightness and differential displacement resistance. Material testing was also conducted on hardened concrete to determine the basic material properties.

Analytical investigation consisted of development of a three-dimensional finite element model of the fiber-reinforced concrete pipe using non-linear solution in ABAQUS software. The concrete damaged plasticity algorithm was used to define the plastic behavior of concrete after cracking.

Several approaches to modeling elasto-plastic constitutive relations were undertaken in this study to simulate the behavior of steel fiber reinforced concrete pipes under monotonic loading. The plasticity theory coupled with fracture mechanics approach was introduced into the model to define the complex cracking mechanism in fiber concrete composite. Non-associative plasticity flow rule was implemented to describe the irreversible plastic damage of concrete. A tension damage variable was used to model the stiffness degradation after cracking. The strain softening concept was implemented to model the tensile material behavior, and the strain hardening with subsequent strain softening model was used to define the compressive behavior of the fiber-concrete composite. Three major relations in forms of *concrete brittle cracking* using dynamic explicit approach, *concrete damaged plasticity with adaptive meshing* technique in explicit scheme and *concrete damaged plasticity with visco-plastic regularization* in implicit integration scheme were considered.

The model implementing concrete damaged plasticity with visco-plastic regularization was identified as the most robust in defining the behavior of steel fiber reinforced concrete pipes due to its computational efficiency and optimized accuracy.

The material constitutive law of the fiber concrete material was determined with the finite element model by converging the load-deformation responses of FEM and experimental testing. To compare the FEM results with experimental testing, The experiment-based curves were averaged for each diameter pipe and fiber content. The values of stress and strain of the material tension stiffening model then were iteratively

modified until the envelopes of load-deformation of FEM matched the one from experimental testing. The mathematical expressions for the tension stiffening material models were obtained for each tested fiber-concrete pipe.

Once the material model of SFRC was established, internal forces in the pipe, such as moments, shear and thrust were determined for every case of the fiber content.

In addition, the simulation of the pipe under various backfill heights for 24 in (600 mm) and 36 in. (900 mm) diameter pipes was performed. The concrete damaged plasticity algorithm was implemented for concrete non-linear behavior definition. A Mohr-Coulomb failure criterion was used for soil plasticity. The pipe-soil interaction was used by introducing a hard contact between the surfaces of the pipe and soil. The maximum height of the backfill and deformation of the pipe under the weight of the soil were determined for different cases of the fiber content.

The findings of these studies have resulted in development of a stand-alone performance based specification (ASTM C1765-13) for steel fiber reinforced concrete pipes, which has been approved in 2013.

7.2. Conclusions

7.2.1. Experimental Testing

The following conclusions can be made based on the D-load test results:

- The steel fibers have adequate strength, stiffness, and ability to withstand large crack widths without a pullout.

- The steel fiber reinforced concrete pipes are capable of undergoing large deformations under the three-edge bearing condition with crack widths in excess of ½ in. (13 mm) without collapse.

- The crack sizes for SFRCP observed at ultimate load are mostly hairline cracks.

- At large deformation exceeding 5%, the typical failure of random fibers is both due to fracture by yielding and pull out (loss of bond). Thus, fiber anchorage system and tensile strength play an important role in preventing pull out and enhancing the behavior of the pipe with respect to strength, stiffness, and crack width tolerance.

- The crack formation pattern is unique to SFRCP regardless of fiber content or the pipe size which undergoes a one-line cracking along the joint length exclusive to crown, invert, and springlines. Unlike RCP the steel fiber reinforced concrete pipes do not experience shear or debonding failure.

- A minimum fiber content of 0.25% and 0.5% by volume is recommended for 24 (600 mm) and 36 in. (900 mm) diameter pipes, respectively, to achieve at least ASTM C1765 Class III strength when using RC-65/35-CN fibers.

- The load-deformation graphs reveal that after the cracking occurs, stiffness initially starts declining with a negative slope which then, with increase in deformation, approaches almost a zero slope and remained nearly constant. This phenomenon explains the capability of the SFRCP to undergo large lateral and vertical deformation without a collapse.

- Stiffness on the load-deformation curve in the elastic range for SFRCP is comparable to that observed in RCP. The data suggests that addition of

fibers has only a marginal effect on to the initial stiffness of SFRCP in which stiffness is mainly governed by initial stiffness of concrete.

- In the present specification the SFRCP remains uncracked at service load (D_{serv}-as described in Chapter 1) ; and the first crack in SFRCP approximately coincides with ultimate load of the pipe.

- Pipes with lower fiber content have a higher rate of stiffness reduction after initiation of the crack as compared to the pipes with higher fiber fractions.

- The toughness in SFRCP increases with increase of fiber content in concrete. Thus, SFRCP with higher fiber volume fraction exhibit a more ductile behavior.

- This study suggest that SFRCP can be successfully implemented into mass production with a minimal modification to the existing manufacturing process and mix design.

Hydrostatic joint test, which is an acceptance test for the pipes with flexible watertight joints, such as rubber gaskets, was performed on selected steel-fiber reinforced concrete pipes. Five pipe specimens with diameter of 30 in. (750 mm) and fiber volume of 0.33%, 0.50% and 0.83% were subjected to the test by applying internal hydrostatic pressure of 13 psi (89.6 kPa) for duration of 10 min. The conclusions based on the conducted tests are as follows:

- Pipes with higher fiber content are more prone to leakage than the pipes having lower volumes of fiber. Thus, it is recommended to to presoak SFRCP for a period of up to 24 hours, as allowed per the ASTM C497, before

performing hydrostatic joint test to allow for sealing of micro cracks in the concrete body.

Two sets of pipe specimens with diameter of 36 in. (900 mm) and fiber fraction by volume of 0.5% and 0.83 % were subjected to Joint Shear test, which is a “proof-of-design” of a pipe joint to evaluate structural capability of the joint to withstand the differential displacement. The following conclusions were made based on the test observations:

- The SFRCP joints are capable of withstanding differential load and meet the ASTM C497 test requirements.

Compressive cylinder strength test was conducted on a total of 139 specimens at ages: 1, 3, 7 and 28 days, and fiber fractions by volume of 0.17, 0.25, 0.33, 0.50, 0.67 and 0.83 %.

- An average value of compressive strength of cylinders at the age of 28 days was at 6740 psi (46.5 MPa).
- There is no significant influence of fiber content on the compressive strength of concrete was found, which also agrees with other studies on steel fiber reinforced concrete.
- The values of strain increase at ultimate compressive strength with the increase of fiber content in concrete.

- Steel fiber reinforced concrete in dry-cast application exhibit high variation in the results of the compressive strength test for different fiber dosages which is inherent of the cylinder molding process as well as the material itself.

Flexural beam test on steel fiber reinforced concrete were performed in accordance with ASTM C1609. For each test load-midspan deformation was obtained and analyzed for the influence of fiber content on beams mode failures, flexural strength, residual load and toughness. Based on the test results, the conclusions are as follows:

- Three main types of load-deformation curves can be distinguished in steel fiber reinforced concrete: curve with sharp drop in stiffness after the first crack which is inherent to the beams with low fiber volume fractions (0.17-0.25 %); transitional with two peaks, in which the first peak generally lower than the second peak and characterized by initial small drop and subsequent stiffness recovery reaching the second peak. This type of behavior is pertinent to beams with fiber content in mid-range (0.33-0.5%). Finally, the smooth curve in beams with fiber fraction range between 0.5% and 0.83 %, where there is no apparent drop in stiffness, as it was observed in beams with lower fiber fractions, and the load-deformation curve exhibits ductile-like (metallic) behavior.

- Failure modes for beam cracking can be distinguished between the brittle failure, which is characterized by flexural vertical crack; semi-brittle with the initiated flexural crack followed by an inclined crack; and ductile failure characterized by an inclined crack which is pertinent to shear failures. The modes of failure vary from brittle to ductile with the increase of fiber volume fractions in concrete from 0.17% to 0.83%. Ductile metallic type failure is predominant in beams with 0.67% atnd 0.83% of fiber by volume.

- Toughness in beams increases with an increase of fiber amount in concrete. The increase in toughness is indicative of the ductility enhancement of concrete by added fiber.

- The residual strength (residual load on the load-deformation curve at L/150 deformation) is larger in beams with greater amounts of fiber volumes.

- No correlation was found between the beam strength and the pipe D-load strength, which is indicative that the properties of materials found from beam specimen do not represent the actual material behavior experienced by the structural pipe. However, the overall trend with regards to the strength variation with changes in fiber volume fraction in beams agrees with that of structural pipe.

A total of twenty direct tension specimens were tested, only four out of the total were tested successfully giving satisfactory results for stress-strain relationship.

- The cracking stress obtained with the direct tension test was almost twice lower than that obtained with the flexural beam test.
- Direct tension test is not practical in application to the dry-cast steel fiber reinforces concrete.

Based on the fiber distribution study, the following conclusions can be drawn:

- The variance of fiber distribution for the pipe with lower fiber volume fraction is greater than the variance of the pipe with higher fiber content.
- The standard deviation of fiber distribution for the pipe with Maccaferri FS7 fiber was higher than for the pipes with Bekaert RC-65/35-CN type fiber.

7.2.2. Finite Element Modeling

- Concrete damaged plasticity with visco-plastic regularization was found to be the most suitable for simulating the behavior of fiber-composite pipes and can be implemented for variety of pipe loading configurations

- The finite element model showed a good agreement in predicting the first crack formation locations which occurred at crown, invert and springlines.

- Tensile damage parameters for the steel fiber reinforced concrete pipe model with lower range of steel-fiber content under monotonic loading should be incorporated to account for a premature damage of the concrete section.

- Finite element analysis showed that if a rectangular strip is used in the model for application of the displacement the results will lead to a non-zero values of trust forces at the crown.

- Boundary conditions significantly affect the distribution of moment, shear and thrust forces at the critical locations in the pipe at the crown, invert and springlines creating the sudden changes in those forces along application points of boundary conditions.

- The tension stiffening model of steel fiber reinforced concrete is in general is represented by an exponential function.

- It was found that the maximum bending moments occur at the crown and springlines; maximum shear is developed at crown and invert and is zero at

springlines; and the thrust force is zero at crown and invert and is at its maximum at springlines.

- When modeling soil-pipe interaction, the minimum height of the backfill to produce cracking was found to be 11 ft. (3.35 m) and 8 ft.(2.43 m) in 24 in. (600 mm) SFRCP with 0.33% and 36 in. (900 mm) SFRCP with 0.5% fiber volume fraction, respectively.

7.3. Future work

Based on the conducted studies the following future wok is recommended to improve the design and understanding of the behavior of steel fiber reinforced concrete pipes.

In the present study SFRCPs with diameters ranging from 24 in. (380 mm) to 48 in. (1200 mm) were investigated. It is recommended that the range of pipe diameters with adjustment of fiber volume fraction is expanded.

Effect of a short term monotonic loading was considered during the experimental program. Further study concerning long term performance of buried pipes is required to investigate pipe performance under a long-term sustained loading and corrosive environment.

Another study that would be beneficial to the area of steel-fiber reinforced concrete pipes is investigation of the suitability of the SFRC pipes to a trenchless tunneling where the jacking forces at the joints will be of a major concern.

The tests results of material properties for flexural beam strength and direct tension suggest that the current methods are not suitable for determining the tensile properties of steel-fiber concrete properties pertinent the structural pipe. Other methods are recommended to be developed for testing tensile material properties.

The current model of SFRCP considers homogeneous isotropic material model which greatly simplifies the definition of fiber in concrete. A model which incorporates material imperfections through introduction of discontinuities into material constitutive law will improve the results of simulation.

Appendix A

Concrete Mix Designs for All Plants

Table A- 1 Hanson mix design 15 in. (400 mm) diameter pipe

Concrete constituents, SSD (per yd^3)	**Mix#1**
Type I/II Cement, (lbs)	424
Class F Fly Ash (lbs.)	140
Crushed Limestone 3/8" (lbs.)	1315
Crushed Limestone 5/8" (lbs.)	N/A
Mfg. Sand (lbs.)	N/A
Natural Sand (lbs.)	2035
Water (lbs.)	200
Admix Sika PI100 (fl.oz/100lbs)	2.5
Admix Sika Rapid (fl.oz/100lbs)	3
Plasticizer (oz/yard)	N/A
W/C Ratio	0.35
Fiber dosage	0.33%

Table A- 2 Hanson mix design 24 in. (600 mm) diameter pipe

Concrete constituents, SSD (per yd^3)	**Mix#1**	**Mix#2**	**Mix#3**	**Mix#4**	**Mix#5**
Type I/II Cement, (lbs)	424	424	424	380	380
Class F Fly Ash (lbs.)	140	140	140	125	125
Crushed Limestone 3/8" (lbs.)	1450	1450	1450	1450	1450
Crushed Limestone 5/8" (lbs.)	N/A	N/A	N/A	N/A	N/A
Mfg. Sand (lbs.)	950	950	950	960	960
Natural Sand (lbs.)	950	950	950	957	957
Water (lbs.)	200	200	200	167	167
Admix Sika PI100 (fl.oz/100lbs)	2.5	2.5	2.5	12.6	12.6
Admix Sika Rapid (fl.oz/100lbs)	3	3	3	N/A	N/A
Plasticizer (oz/yard)	N/A	N/A	N/A	N/A	N/A
W/C Ratio	0.35	0.35	0.35	0.33	0.33
Fiber dosage	0.33%	0.5%	0.67%	0.33%	0.67%

Table A- 2 Continued

Concrete constituents, SSD (per yd^3)	Mix#6	Mix#7	Mix#9	Mix#10
Type I/II Cement, (lbs)	495	495	553	553
Class F Fly Ash (lbs.)	163	163	138	138
Crushed Limestone 3/8" (lbs.)	1450	1450	1908	1908
Crushed Limestone 5/8" (lbs.)	N/A	N/A	N/A	N/A
Mfg. Sand (lbs.)	853	853	N/A	N/A
Natural Sand (lbs.)	853	853	1501	1501
Water (lbs.)	242	242	242	242
Admix Sika PI100 (fl.oz/100lbs)	2.5	2.5	9.7	9.7
Admix Sika Rapid (fl.oz/100lbs)	3	3	N/A	N/A
Plasticizer (oz/yard)	N/A	N/A	4	4
W/C Ratio	0.37	0.37	0.35	0.35
Fiber dosage	0.33%	0.5%	0.25%	0.33%

Table A- 3 Hanson mix design 30 in (750 mm) diameter pipe

Concrete constituents, SSD (per yd^3)	Mix#1	Mix#2	Mix#3	Mix#4
Type I/II Cement, (lbs)	552	552	432	432
Class F Fly Ash (lbs.)	138	138	106	108
Crushed Limestone 3/8" (lbs.)	1908	1908	924	924
Crushed Limestone 5/8" (lbs.)	N/A	N/A	920	916
Mfg. Sand (lbs.)	N/A	N/A	748	752
Natural Sand (lbs.)	1501	1501	748	760
Water (lbs.)	242	242	204	204
Admix Sika PI100 (fl.oz/100lbs)	18	18	N/A	N/A
Admix Sika Rapid (fl.oz/100lbs)	N/A	N/A	N/A	N/A
Plasticizer (oz/yard)	4	4	N/A	N/A
W/C Ratio	0.35	0.35	0.38	0.38
Fiber dosage	0.5%	0.33%	0.33%	0.5%

Table A- 4 Hanson mix design 33 in. (850 mm) diameter pipe

Concrete constituents, SSD (per yd^3)	Mix#1	Mix#2
Type I/II Cement, (lbs)	404	400
Class F Fly Ash (lbs.)	103	102
Crushed Limestone 3/8" (lbs.)	1774	1774
Crushed Limestone 5/8" (lbs.)	N/A	N/A
Mfg. Sand (lbs.)	N/A	N/A
Natural Sand (lbs.)	1496	1452
Water (lbs.)	184	214
Admix Sika PI100 (fl.oz/100lbs)	N/A	N/A
Admix Sika Rapid (fl.oz/100lbs)	N/A	N/A
Plasticizer (oz/yard)	N/A	N/A
W/C Ratio	0.36	0.43
Fiber dosage	0.33%	0.5%

Table A- 5 Hanson mix design 36 in. (900 mm) diameter pipe

Concrete constituents, SSD (per yd^3)	Mix#1	Mix#2	Mix#3
Type I/II Cement, (lbs)	380	461	461
Class F Fly Ash (lbs.)	125	150	150
Crushed Limestone 3/8" (lbs.)	1300	1170	1170
Crushed Limestone 5/8" (lbs.)	370	580	580
Mfg. Sand (lbs.)	880	791	791
Natural Sand (lbs.)	880	790	790
Water (lbs.)	200	200	200
Admix Sika PI100 (fl.oz/100lbs)	2.5	2.5	2.5
Admix Sika Rapid (fl.oz/100lbs)	3	3	3
Plasticizer (oz/yard)	N/A	N/A	N/A
W/C Ratio	0.40	0.33	0.33
Fiber dosage	0.33%	0.33%	0.5%

Table A- 6 Hanson mix design 48 in (1200 mm) diameter pipe

Concrete constituents, SSD (per yd^3)	Mix#1
Type I/II Cement, (lbs)	424
Class F Fly Ash (lbs.)	140
Crushed Limestone 3/8" (lbs.)	875
Crushed Limestone 5/8" (lbs.)	875
Mfg. Sand (lbs.)	763
Natural Sand (lbs.)	763
Water (lbs.)	190
Admix Sika PI100 (fl.oz/100lbs)	2.5
Admix Sika Rapid (fl.oz/100lbs)	2.5
Plasticizer (oz/yard)	N/A
W/C Ratio	0.33
Fiber dosage	0.67%

Table A- 7 Rinker mix design for 24 in. (600 mm) diameter pipe

Concrete constituents, SSD (per yd^3)	Mix#1	Mix#2	Mix#3	Mix#4	Mix#5
Type I/II Cement, (lbs)	404	401	402	403	400
Class F Fly Ash (lbs.)	103	102	102	101	101
Crushed Limestone 3/8" (lbs.)	1774	1732	1740	1742	1741
Crushed Limestone 5/8" (lbs.)	N/A	N/A	N/A	N/A	N/A
Mfg. Sand (lbs.)	N/A	N/A	N/A	N/A	N/A
Natural Sand (lbs.)	1496	1463	1456	1457	1457
Water (lbs.)	184	215	214	213	213
Admix Rheofit (fl.oz/100lbs)	4.1	4.1	4.1	4.1	4.1
W/C Ratio	0.36	0.43	0.42	0.42	0.43
Fiber dosage	0.33%	0.33%	0.5%	0.67%	0.83%

Table A- 8 Rinker mix design for 36 in. (900 mm) diameter pipe

Concrete constituents, SSD (per yd^3)	Mix#1	Mix#2	Mix#3	Mix#4
Type I/II Cement, (lbs)	404	402	403	400
Class F Fly Ash (lbs.)	103	102	101	101
Crushed Limestone 3/8" (lbs.)	1774	1740	1742	1741
Crushed Limestone 5/8" (lbs.)	N/A	N/A	N/A	N/A
Mfg. Sand (lbs.)	N/A	N/A	N/A	N/A
Natural Sand (lbs.)	1496	1456	1457	1457
Water (lbs.)	184	214	213	213
Admix Rheofit (fl.oz/100lbs)	4.1	4.1	4.1	4.1
W/C Ratio	0.36	0.42	0.42	0.43
Fiber dosage	0.33%	0.5%	0.67%	0.83%

Table A- 9 Sherman-Dixie mix design 24 in. (600 mm) diameter pipe

Concrete constituents, SSD (per yd^3)	Mix #1	Mix #2	Mix #3	Mix #4
Type I/II Cement, (lbs)	538	526	537	530
Class F Fly Ash (lbs.)	140	135	136	133
Crushed Limestone 3/8" (lbs.)	1487	1469	1460	1473
Crushed Limestone 5/8" (lbs.)	N/A	N/A	N/A	N/A
Mfg. Sand (lbs.)	N/A	N/A	N/A	N/A
Natural Sand (lbs.)	1873	1859	1871	1885
Water (lbs.)	230	230	235	242
Axim Navitas 33-BASF(ozs./cwt.)	2	2	2	2
W/C Ratio	0.34	0.35	0.35	0.36
Fiber dosage	0.17%	0.25%	0.33%	0.5%

Table A- 10 Sherman-Dixie mix design for 36 in. (900 mm) diameter pipe

Concrete constituents, SSD (per yd^3)	Mix #1	Mix #2	Mix #3
Type I/II Cement, (lbs)	534	528	539
Class F Fly Ash (lbs.)	138	139	140
Crushed Limestone 3/8" (lbs.)	1496	1459	1469
Crushed Limestone 5/8" (lbs.)	N/A	N/A	N/A
Mfg. Sand (lbs.)	N/A	N/A	N/A
Natural Sand (lbs.)	1861	1867	1889
Water (lbs.)	235	240	248
Axim Navitas 33-BASF(ozs./cwt.)	2	2	2
W/C Ratio	0.35	0.36	0.36
Fiber dosage	0.5%	0.67%	0.83%

Table A- 11 Sherman-Dixie mix design for 48 in. (1200 mm) diameter pipe

Concrete constituents, SSD (per yd^3)	Mix #1	Mix #2	Mix #3
Type I/II Cement, (lbs)	525	531	530
Class F Fly Ash (lbs.)	138	137	130
Crushed Limestone 3/8" (lbs.)	1457	1470	1475
Crushed Limestone 5/8" (lbs.)	N/A	N/A	N/A
Mfg. Sand (lbs.)	N/A	N/A	N/A
Natural Sand (lbs.)	1882	1892	1878
Water (lbs.)	205	215	240
Axim Navitas 33-BASF(ozs./cwt.)	2	2	2
W/C Ratio	0.31	0.32	0.36
Fiber dosage	0.5%	0.67%	0.83%

Table A- 12 Northern Concrete Pipe mix design 24 in. (600 mm) diameter pipe

Concrete constituents, SSD (per yd^3)	Mix #1	Mix #2	Mix #3	Mix #4	Mix #5
Type I/II Cement, (lbs)	553	545	599	545	540
Class F Fly Ash (lbs.)	138	136	90	138	151
Crushed Limestone 3/8" (lbs.)	1907	1897	1934	1920	1954
Crushed Limestone 5/8" (lbs.)	N/A	N/A	N/A	N/A	N/A
Mfg. Sand (lbs.)	N/A	N/A	N/A	N/A	N/A
Natural Sand (lbs.)	1500	1500	1477	1455	1481
Water (lbs.)	245	245	250	250	250
Admix Axim (ozs./cwt.)	3	3	2.9	3	3
Plasticizer (oz/yard)	N/A	N/A	N/A	N/A	N/A
W/C Ratio	0.35	0.36	0.36	0.37	0.36
Fiber dosage	0.17%	0.17%	0.25%	0.33%	0.5%

Table A- 13 Northern Concrete Pipe mix design 36 in. (900 mm) diameter pipe

Concrete constituents, SSD (per yd^3)	Mix #1	Mix #2	Mix #3	Mix #4
Type I/II Cement, (lbs)	588	540	581	691
Class F Fly Ash (lbs.)	91	147	76	97
Crushed Limestone 3/8" (lbs.)	1557	1987	1911	1907
Crushed Limestone 5/8" (lbs.)	N/A	N/A	N/A	N/A
Mfg. Sand (lbs.)	N/A	N/A	N/A	N/A
Natural Sand (lbs.)	1494	1407	1477	1453
Water (lbs.)	245	245	250	295
Admix Axim (ozs./cwt.)	2.9	2.9	3	3
Plasticizer (oz/yard)	N/A	N/A	N/A	N/A
W/C Ratio	0.36	0.36	0.38	0.37
Fiber dosage	0.25%	0.25%	0.33%	0.33%

Table A- 13 Continued

Concrete constituents, SSD (per yd^3)	Mix #5	Mix #6	Mix #7
Type I/II Cement, (lbs)	545	569	599
Class F Fly Ash (lbs.)	141	89	99
Crushed Limestone 3/8" (lbs.)	1889	1597	2034
Crushed Limestone 5/8" (lbs.)	N/A	N/A	N/A
Mfg. Sand (lbs.)	N/A	N/A	N/A
Natural Sand (lbs.)	1505	1422	1375
Water (lbs.)	240	240	240
Admix Axim (ozs./cwt.)	3	3.1	2.9
Plasticizer (oz/yard)	N/A	N/A	N/A
W/C Ratio	0.35	0.36	0.34
Fiber dosage	0.5%	0.5%	0.67%

Table A- 14 Northern Concrete Pipe mix design for 48 in. (1200 mm) diameter pipe

Concrete constituents, SSD (per yd^3)	Mix #1	Mix #2	Mix #3
Type I/II Cement, (lbs)	579	588.5	549
Class F Fly Ash (lbs.)	104	101	136
Crushed Limestone 3/8" (lbs.)	1931	1914	1893
Crushed Limestone 5/8" (lbs.)	N/A	N/A	N/A
Mfg. Sand (lbs.)	N/A	N/A	N/A
Natural Sand (lbs.)	1437	1474	1481
Water (lbs.)	240	240	240
Admix Axim (ozs./cwt.)	3	2.9	3
Plasticizer (oz/yard)	N/A	N/A	N/A
W/C Ratio	0.35	0.35	0.35
Fiber dosage	0.33%	0.33%	0.5%

Table A- 14 Continued

Concrete constituents, SSD 48 in. (1200 mm), per yd3	Mix #4	Mix#5	Mix#6
Type I/II Cement, (lbs)	540.5	578	590
Class F Fly Ash (lbs.)	148	110	101
Crushed Limestone 3/8" (lbs.)	2211	2005	1883
Crushed Limestone 5/8" (lbs.)	N/A	N/A	N/A
Mfg. Sand (lbs.)	N/A	N/A	N/A
Natural Sand (lbs.)	1471	1347	1478
Water (lbs.)	265	265	265
Admix Axim (ozs./cwt.)	2.9	2.9	3
Plasticizer (oz/yard)	N/A	N/A	N/A
W/C Ratio	0.38	0.39	0.38
Fiber dosage	0.5%	0.67%	0.83%

Table A- 15 Fiber volume fraction conversion table

Steel fiber dosage (lbs per yd^3)	Fiber volume fraction
22	0.17 %
33	0.25 %
44	0.33 %
66	0.50 %
88	0.67 %
110	0.83 %

.

Appendix B

Results of Experimental Pipe Testing

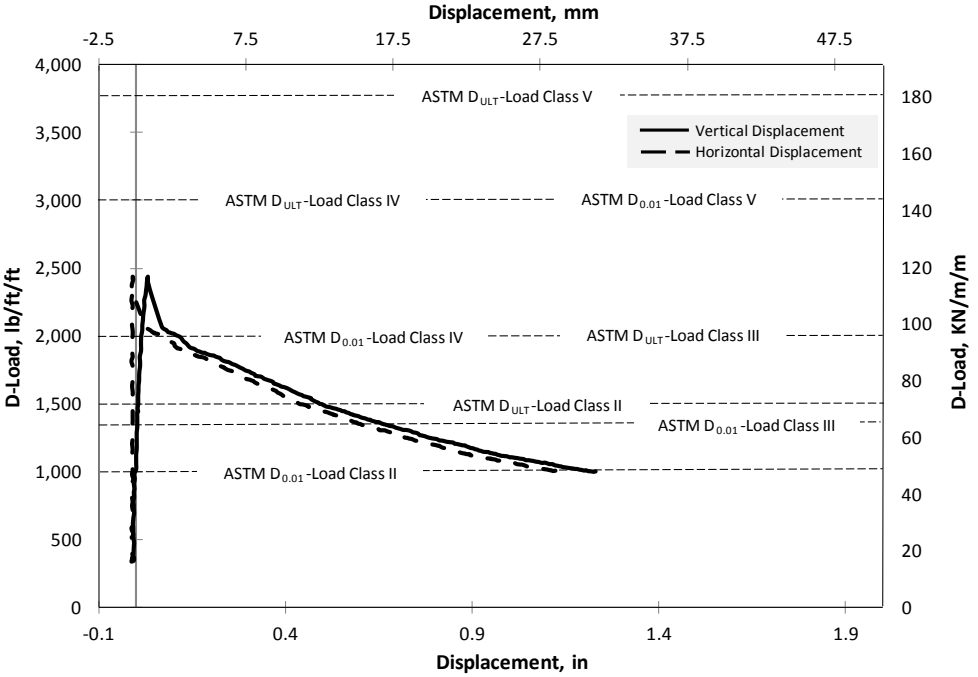

Figure B- 1 D-load versus displacement for HAN-24-B-0.33-65/35-T1

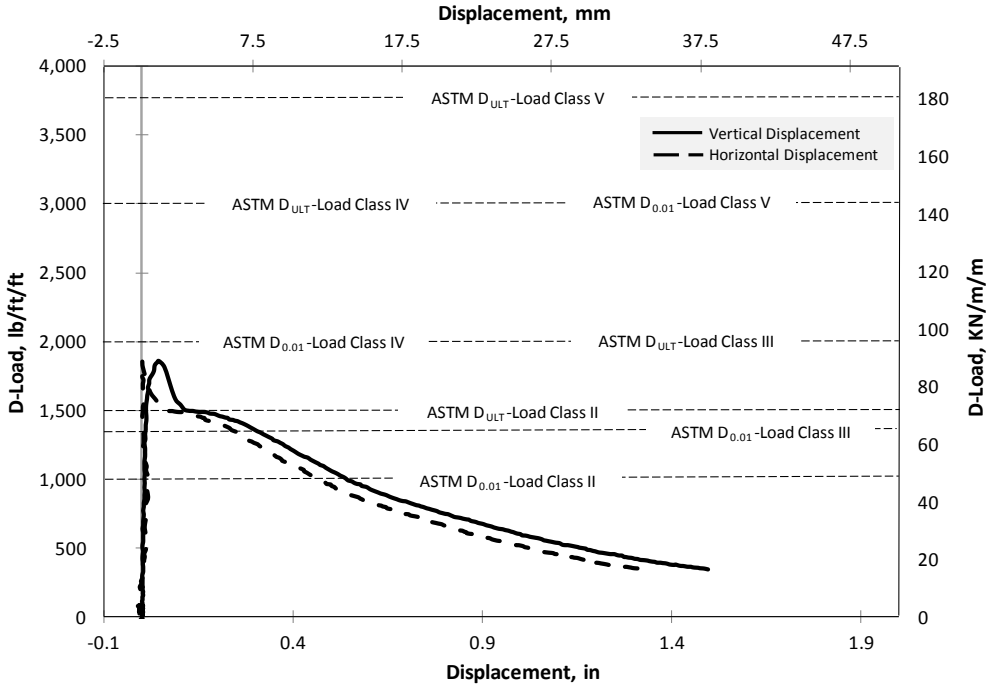

Figure B- 2 D-load versus displacement for HAN-24-B-0.33-65/35-T2

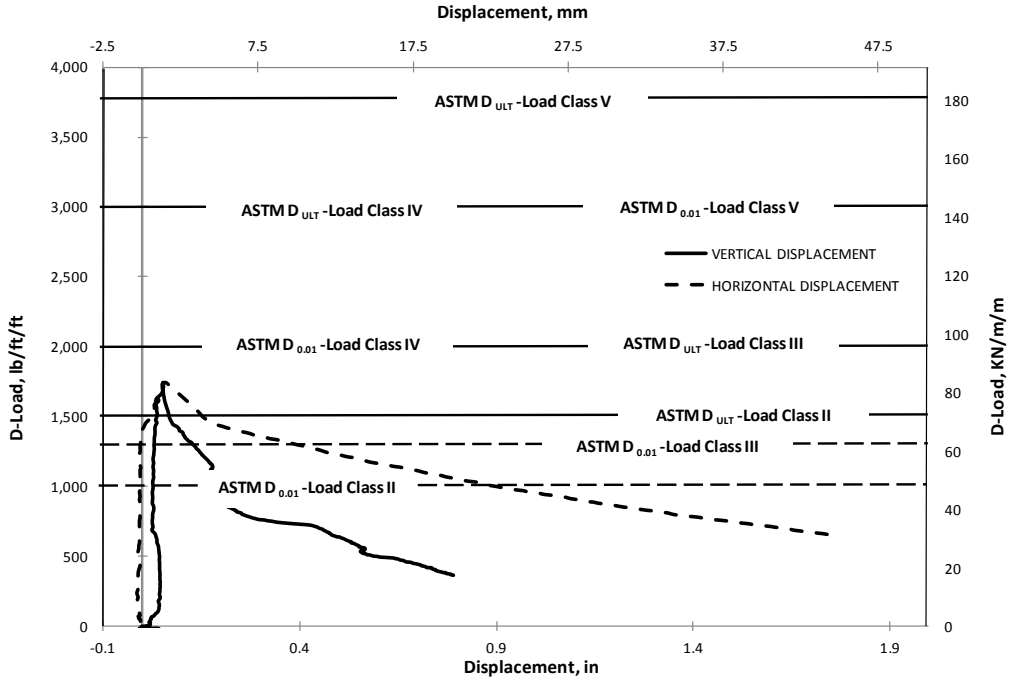

Figure B- 3 D-load versus displacement for HAN-30-B-0.33-65/35-T2

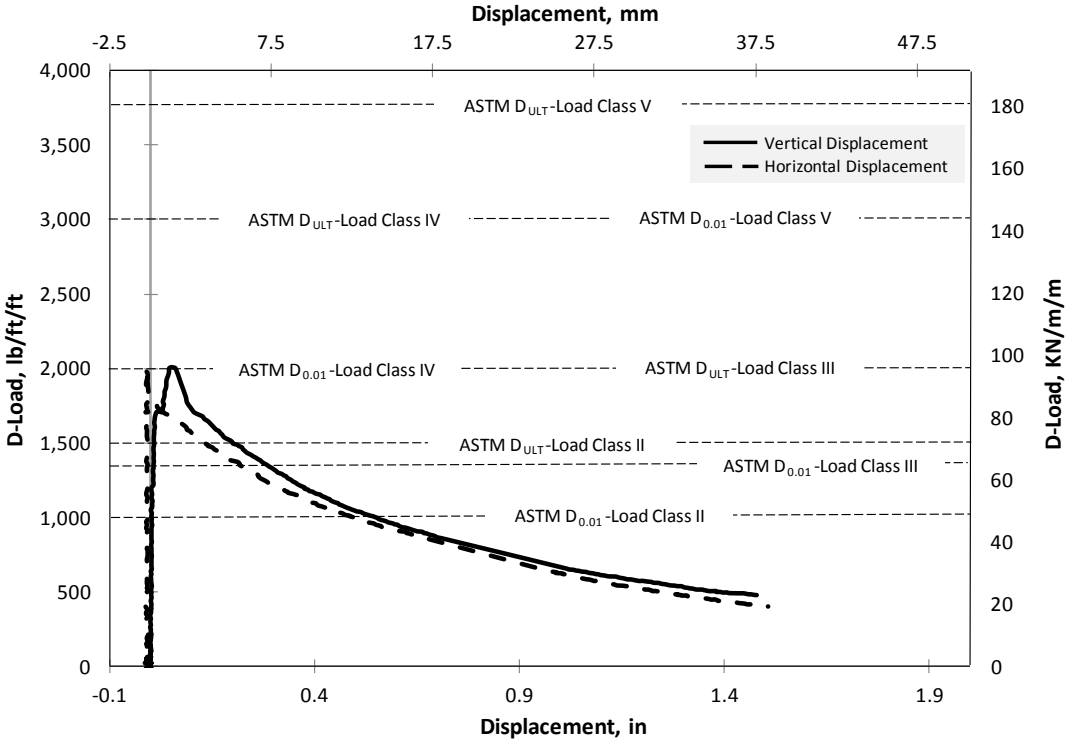

Figure B- 4 D-load versus displacement for HAN-30-B-0.33-65/35-T3

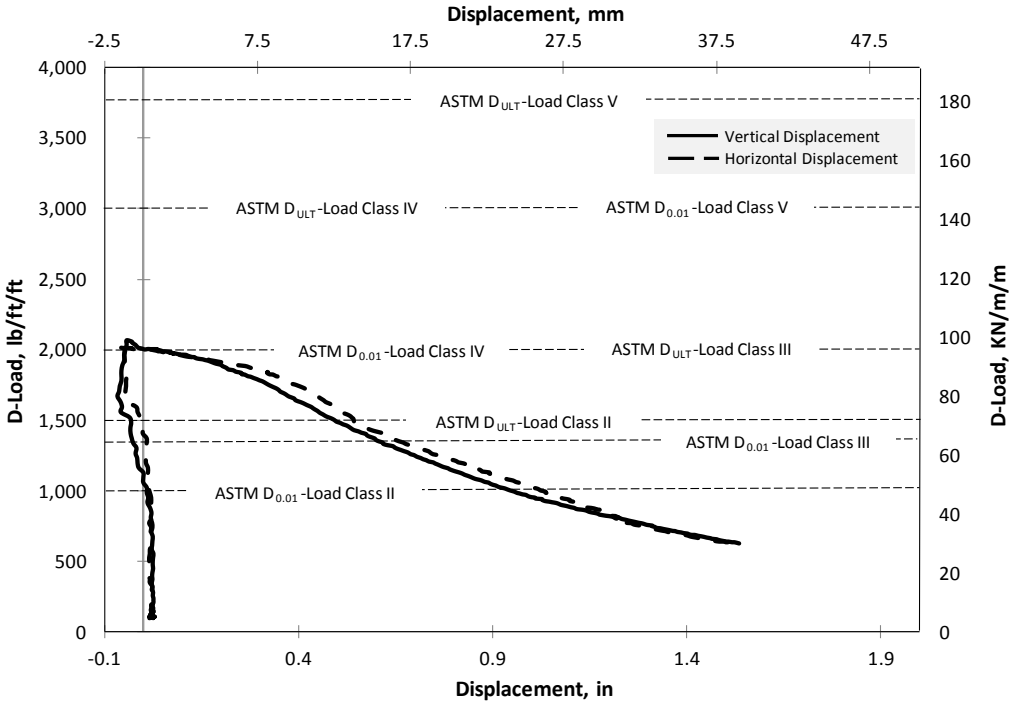

Figure B-5 D-load versus displacement for HAN-30-B-0.5-65/35-T1

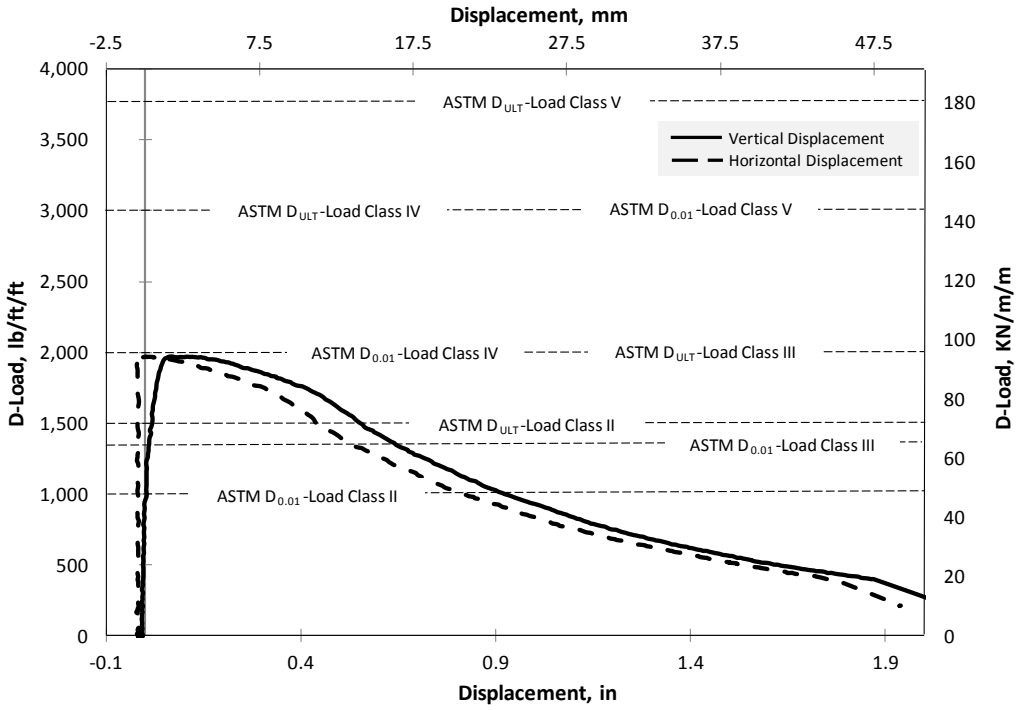

Figure B- 6 D-load versus displacement for HAN-30-B-0.5-65/35-T2

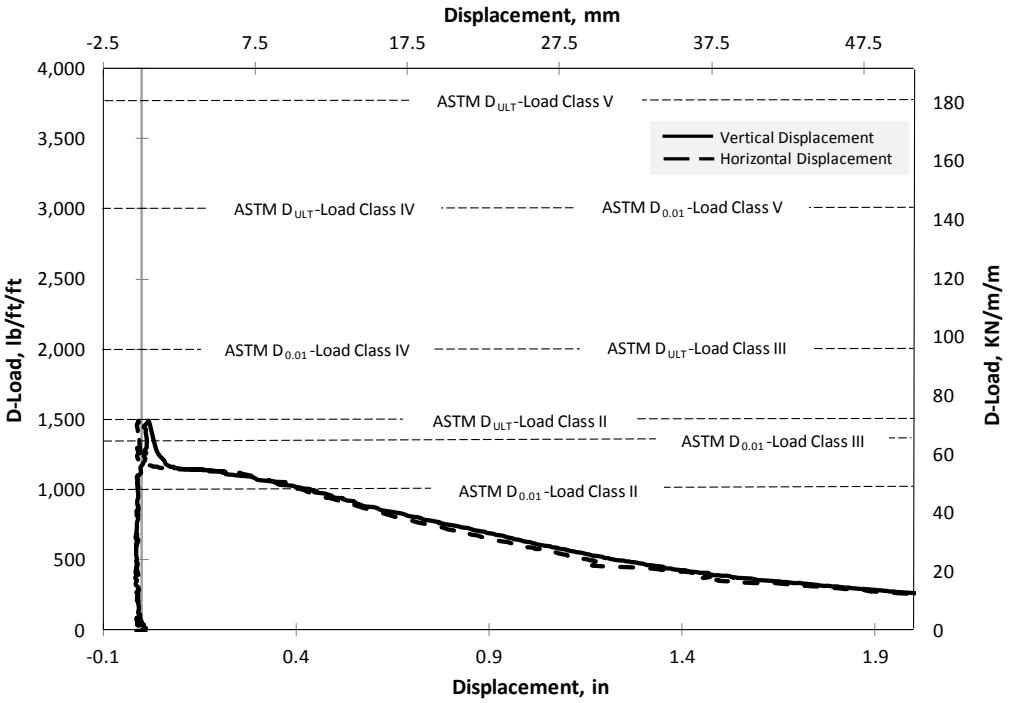

Figure B-7 D-load versus displacement for HAN-30-B-0.5-65/35-T3

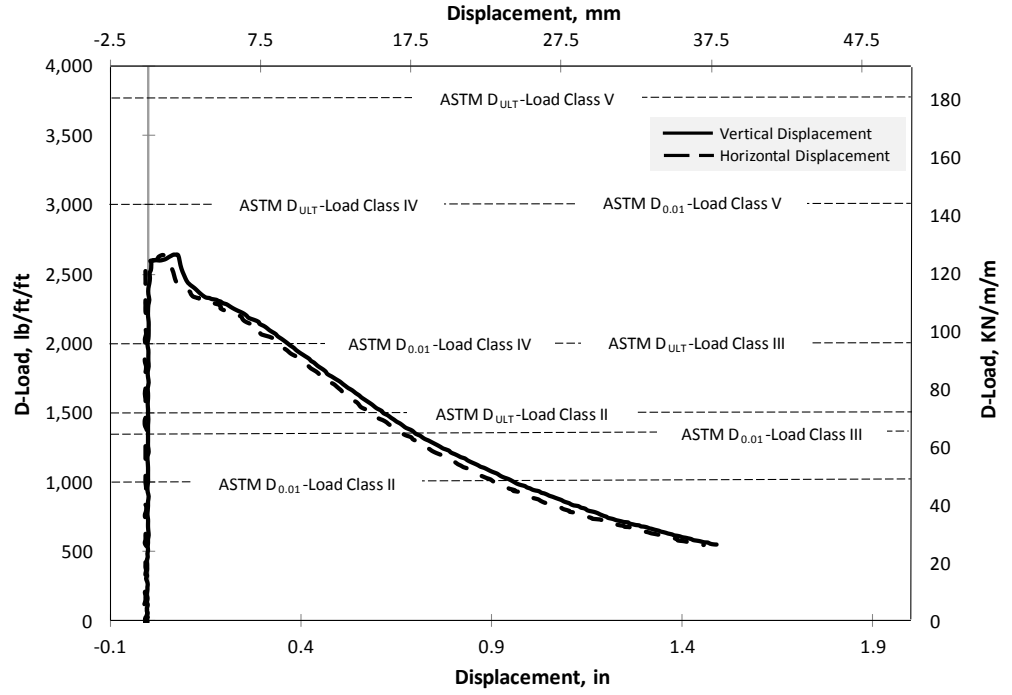

Figure B- 8 D-load versus displacement for HAN-30-C-0.33-65/35-T1

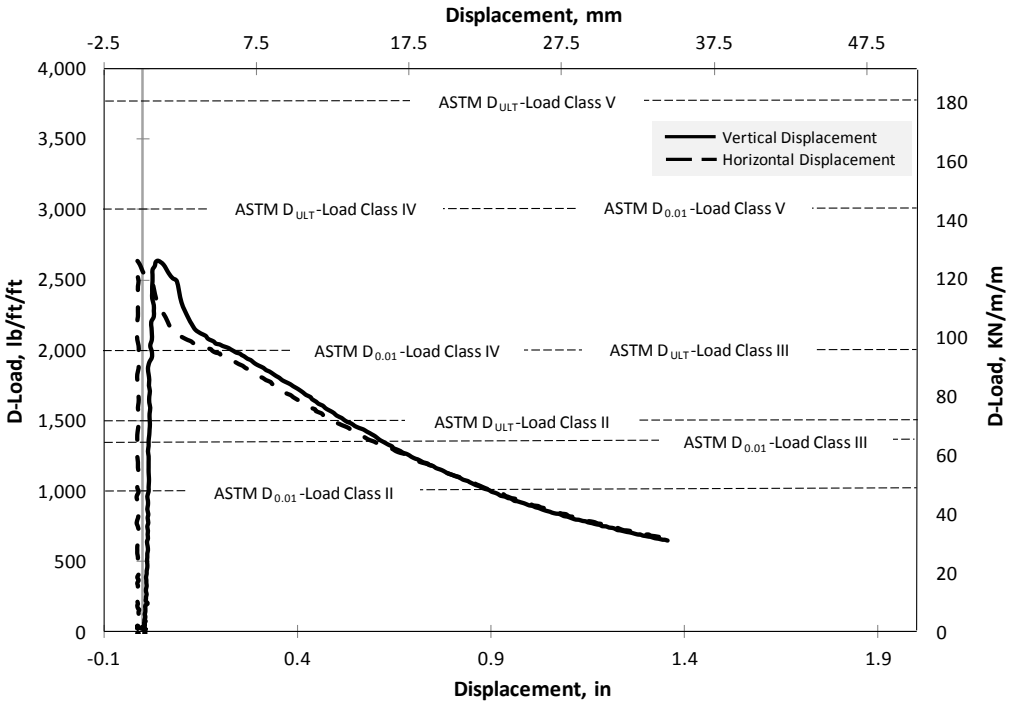

Figure B- 9 D-load versus displacement for HAN-30-C-0.33-65/35-T2

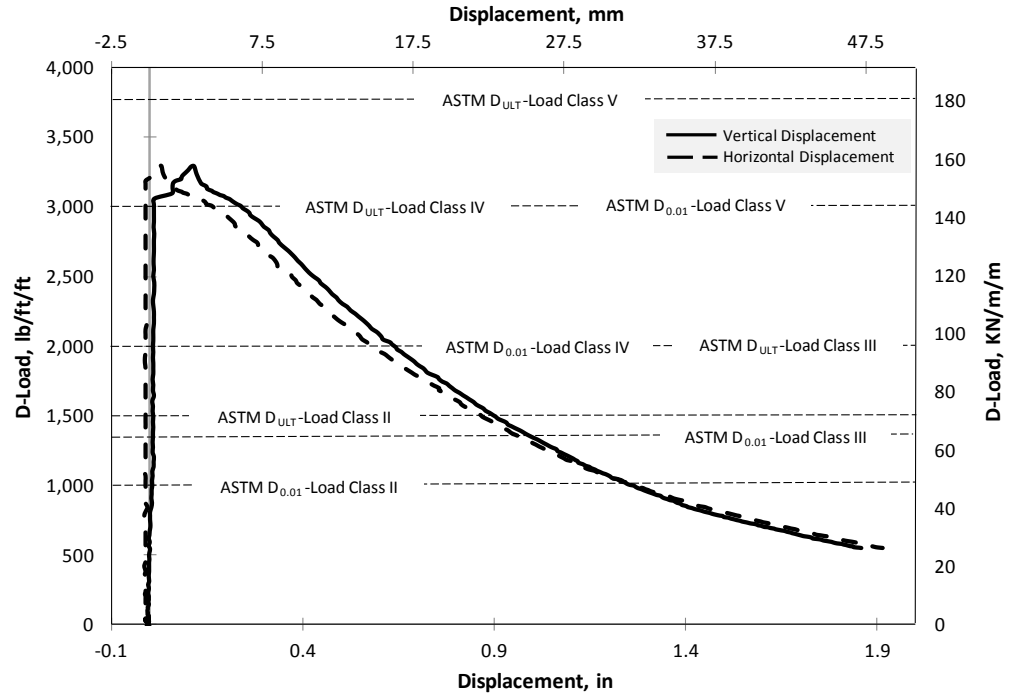

Figure B- 10 D-load versus displacement for HAN-30-C-0.5-65/35-T1

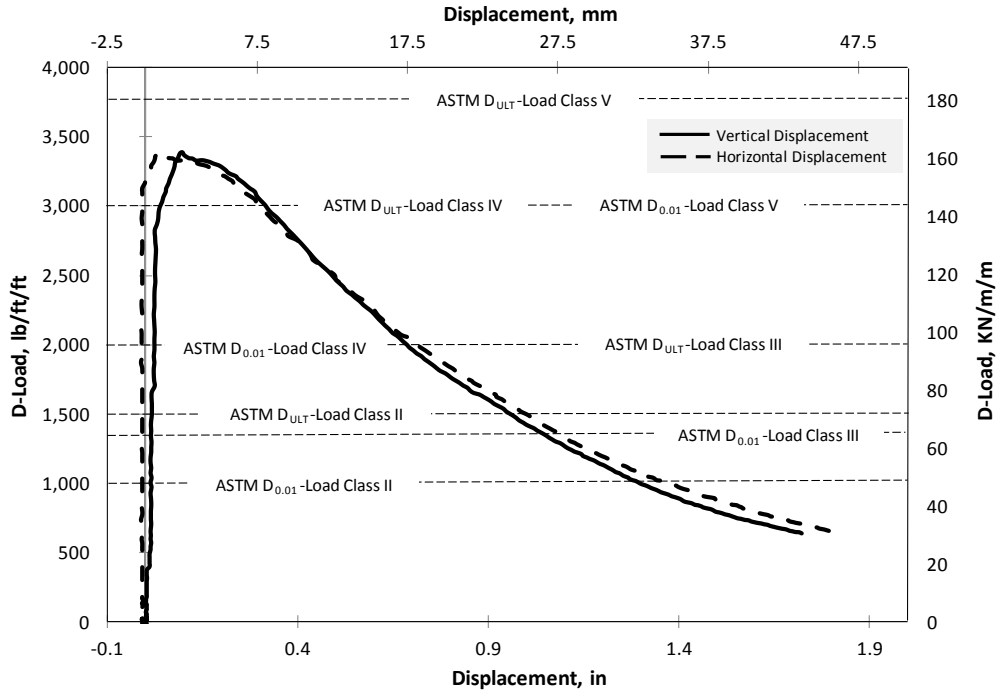

Figure B- 11 D-load versus displacement for HAN-30-C-0.5-65/35-T2

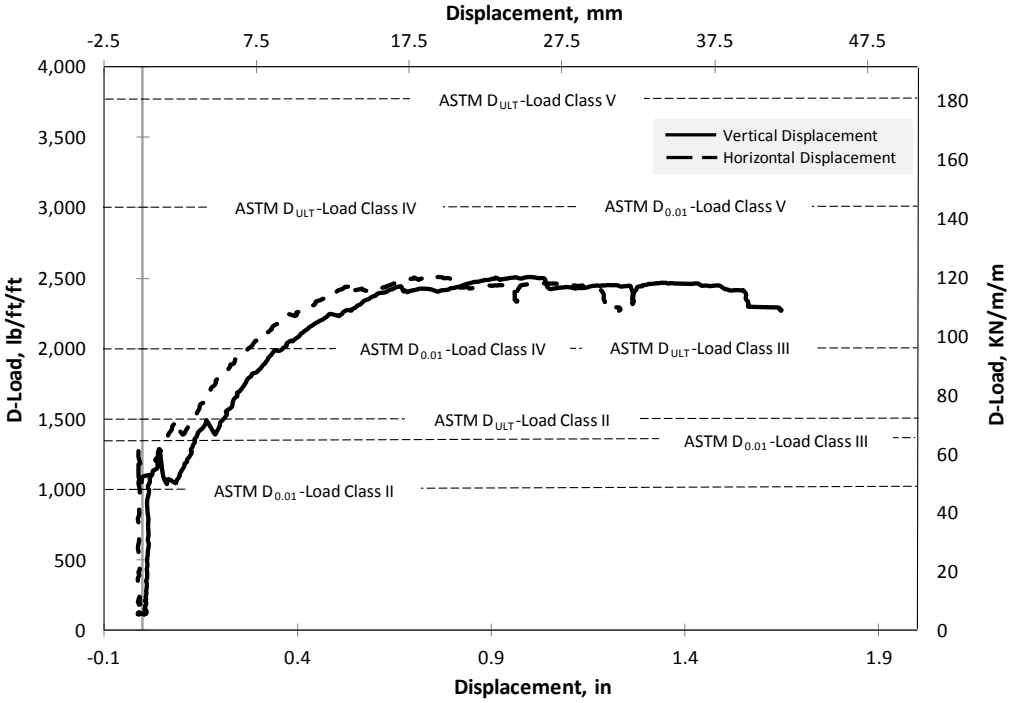

Figure B- 12 D-load versus displacement for HAN-30-B-RCP-T1

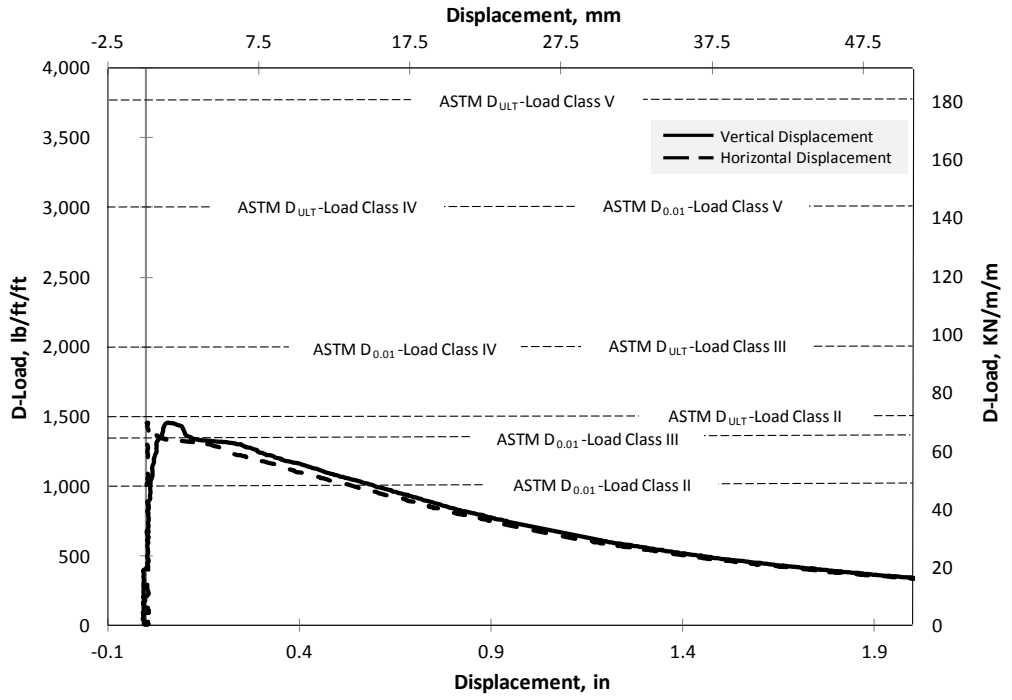

Figure B- 13 D-load versus displacement for HAN-33-B-0.33-80/60-T1

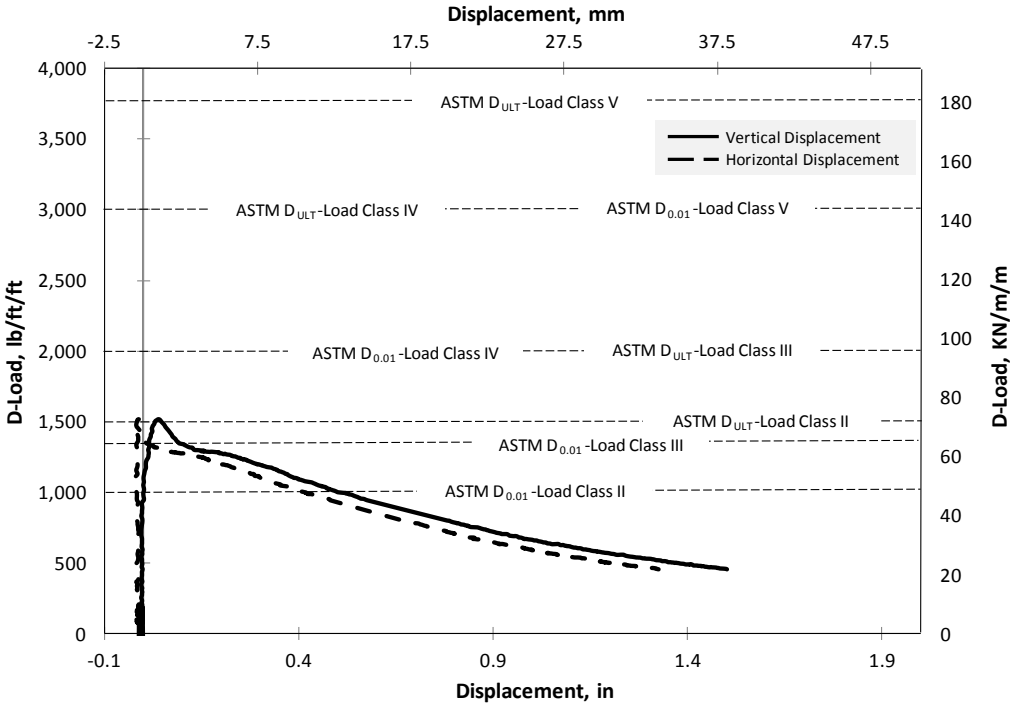

Figure B- 14 D-load versus displacement for HAN-33-B-0.33-65/35-T2

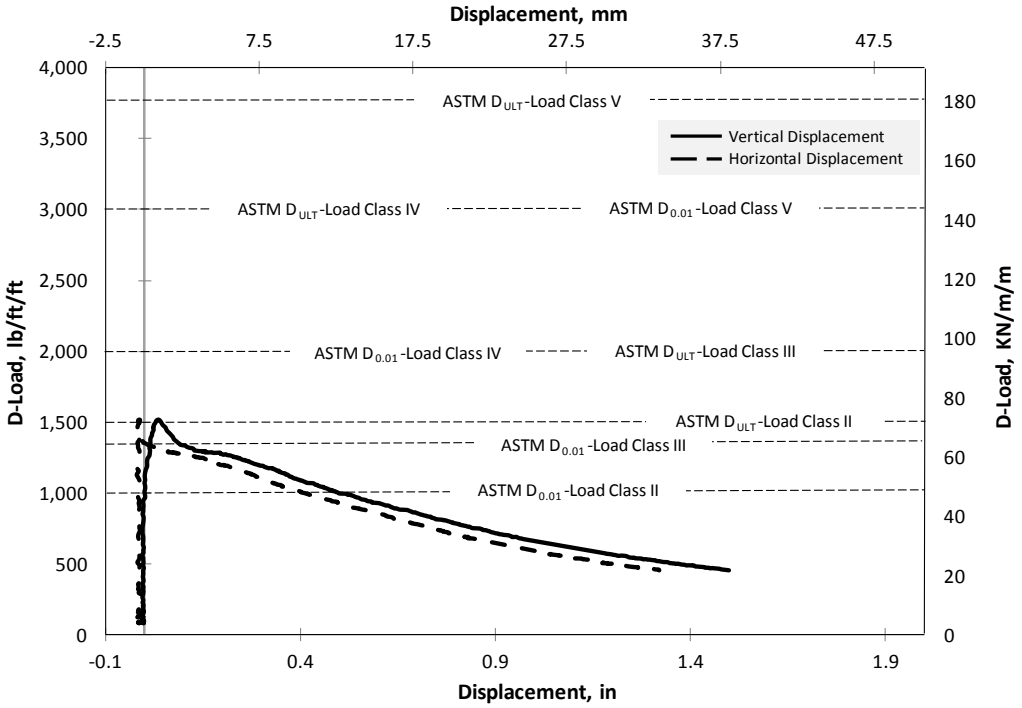

Figure B- 15 D-load versus displacement FOR HAN-33-B-0.33-65/35-T3

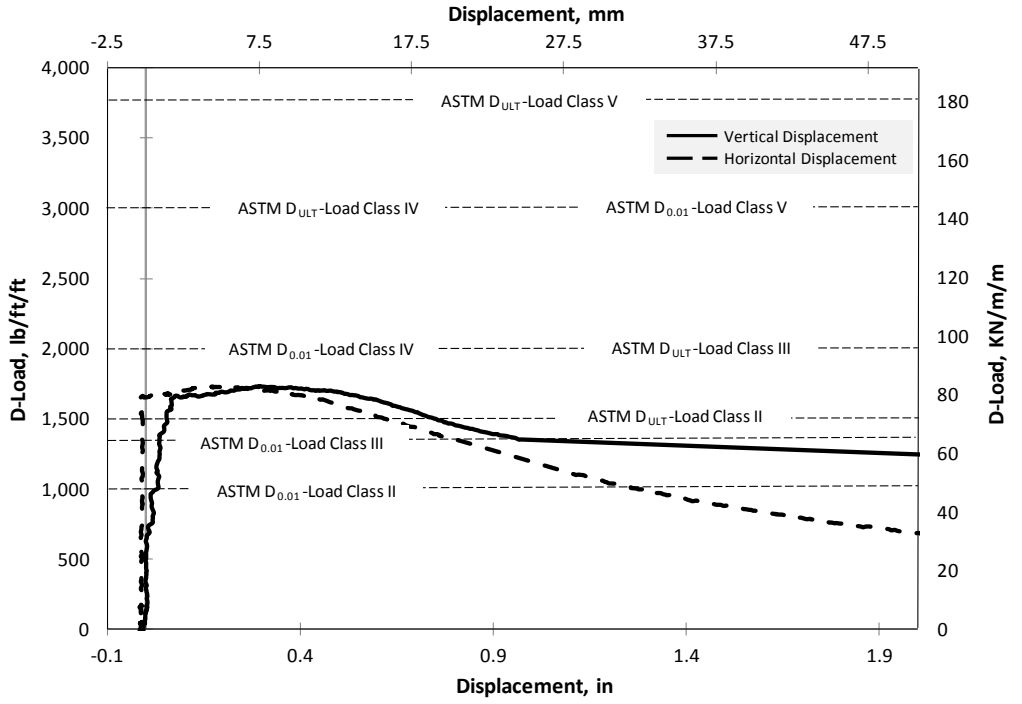

Figure B- 16 D-load versus displacement for HAN-36-B-0.5-80/60-T1

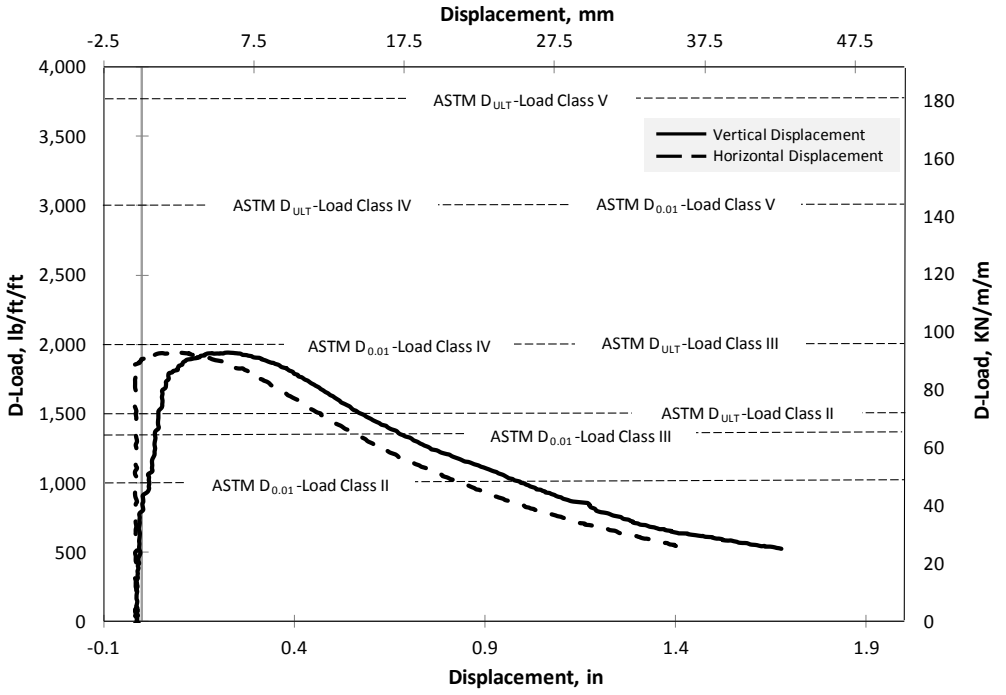

Figure B- 17 D-load versus displacement for HAN-36-B-0.67-65/35-T1

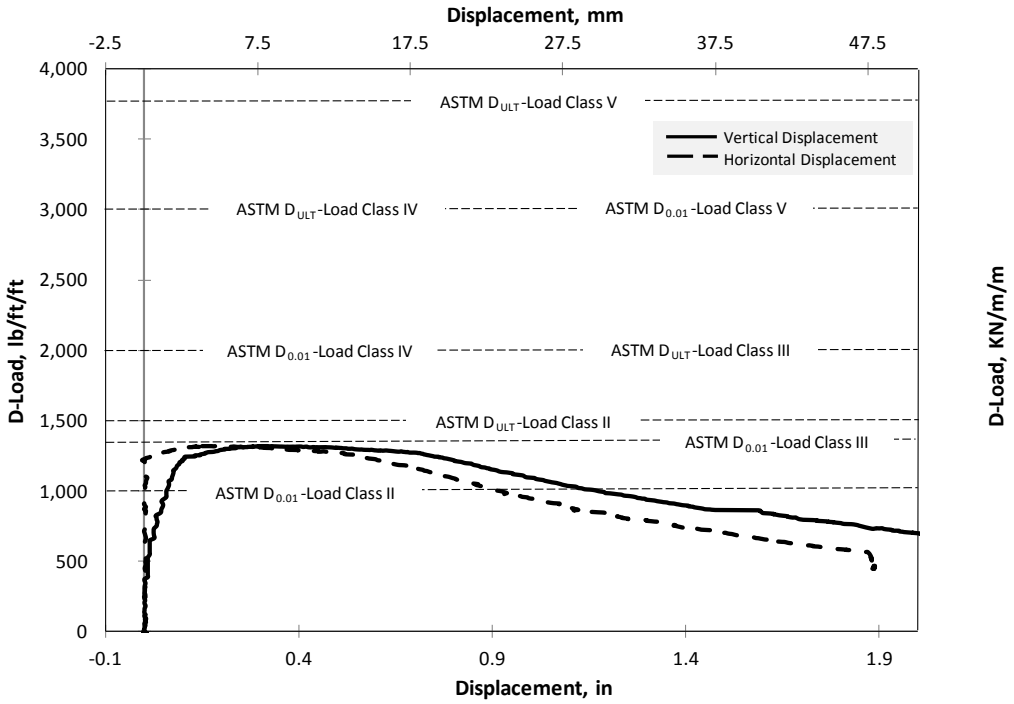

Figure B- 18 D-load versus displacement for HAN-48-B-0.67-80/60-T1

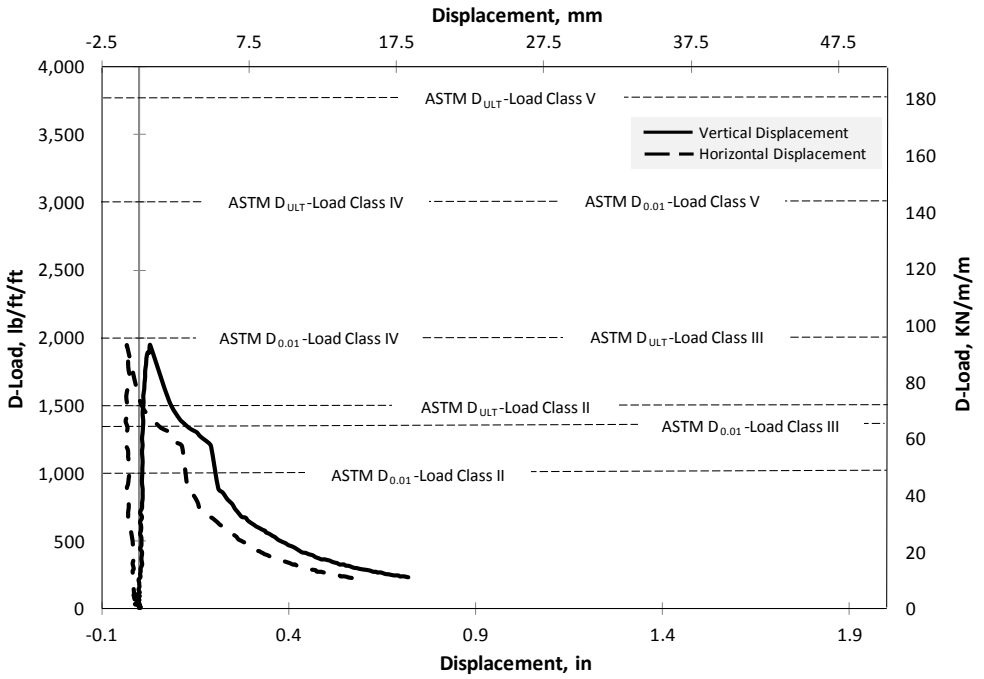

Figure B- 19 D-load versus displacement for NCP-24-B-0.17-65/35-T1

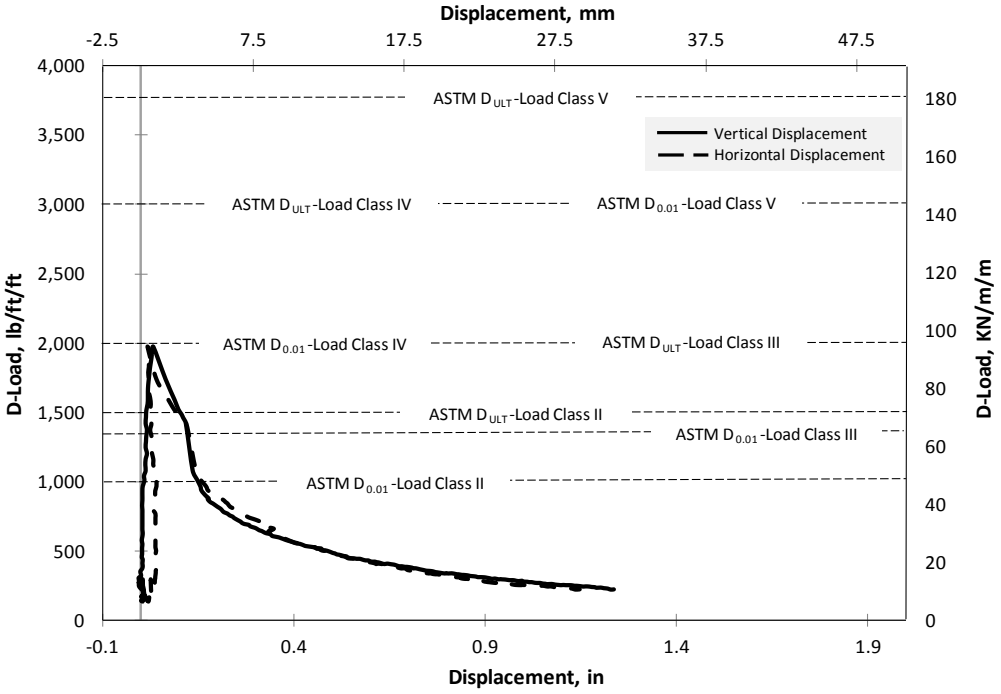

Figure B- 20 D-load versus displacement for NCP-24-B-0.17-65/35-T3

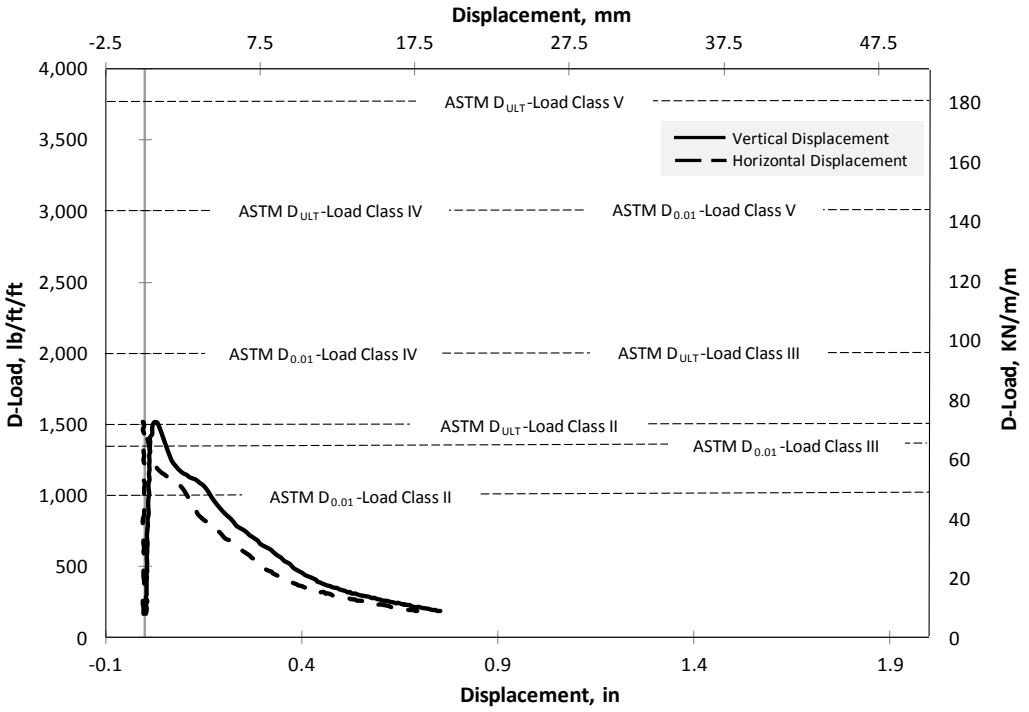

Figure B- 21 D-load versus displacement for NCP-24-B-0.17-65/35-T4

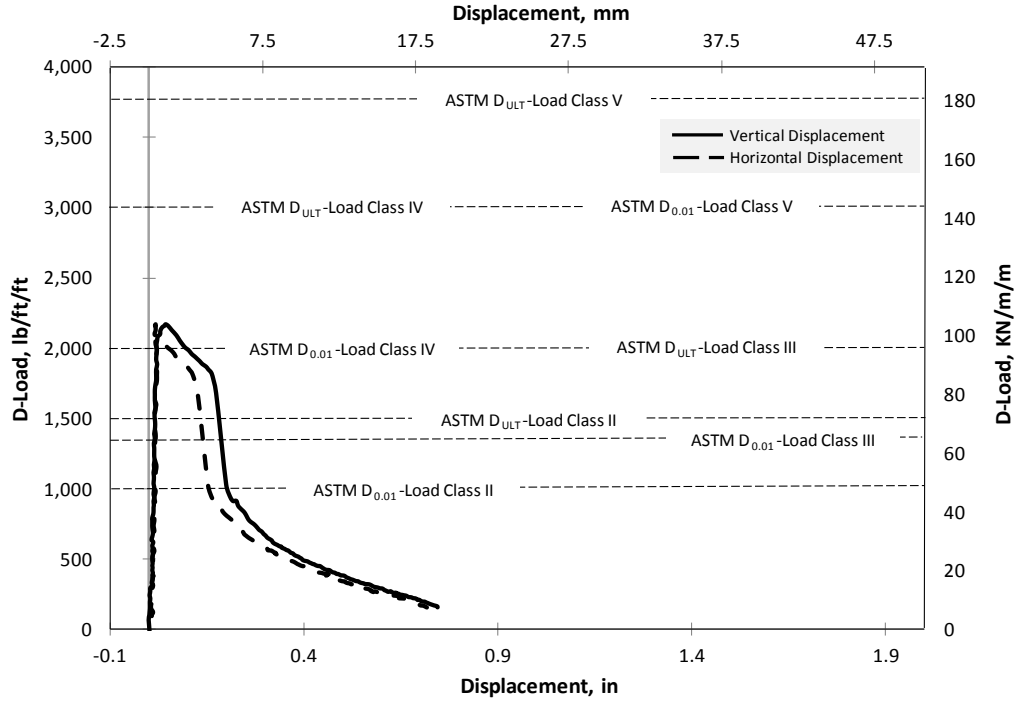

Figure B- 22 D-load versus displacement for NCP-24-B-0.25-65/35-T1

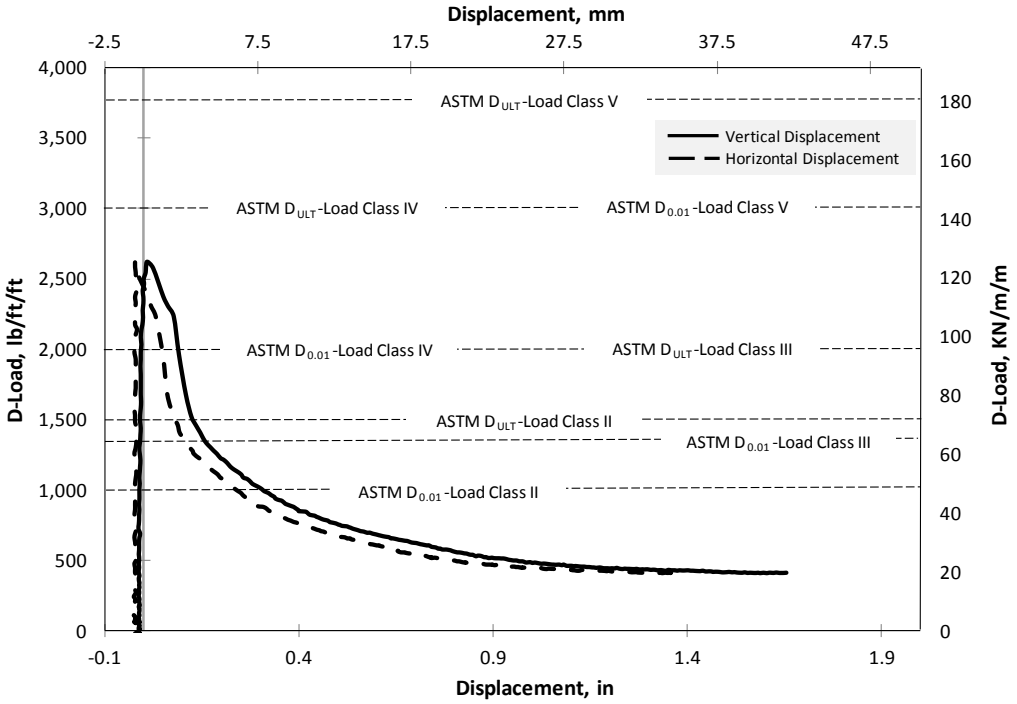

Figure B- 23 D-load versus displacement for NCP-24-B-0.25-65/35-T2

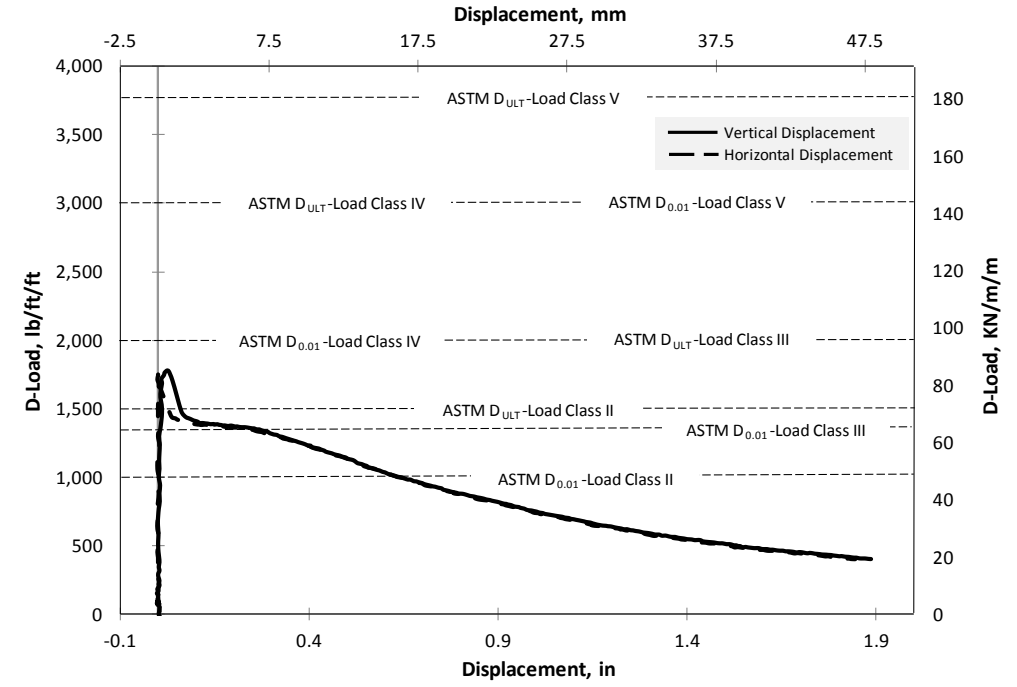

Figure B- 24 D-load versus displacement for NCP-24-B-0.33-65/35-T1

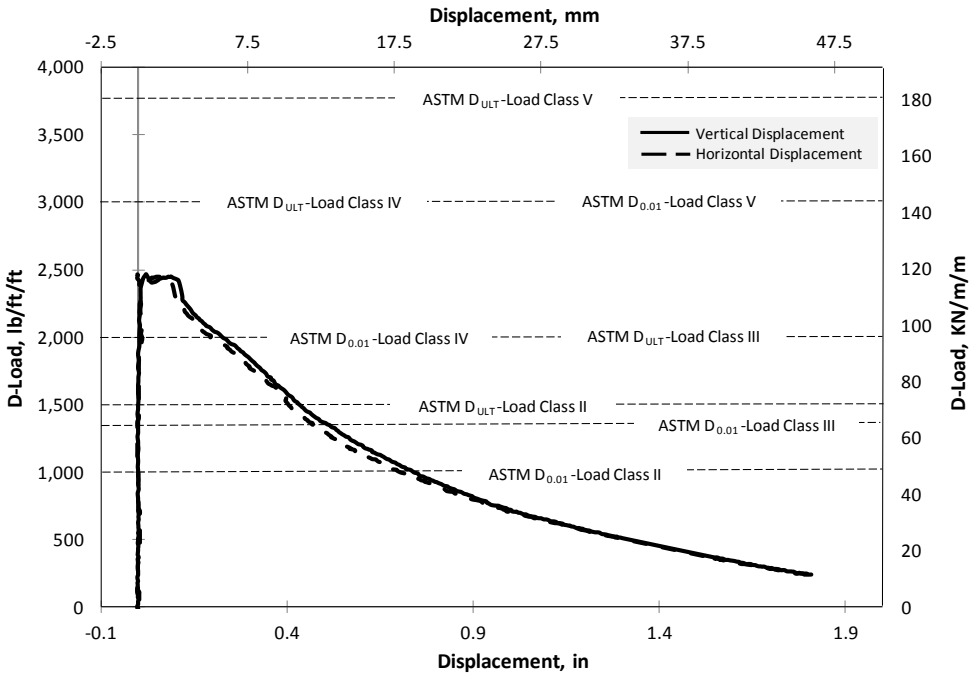

Figure B- 25 D-load versus displacement for NCP-24-B-0.5-65/35-T1

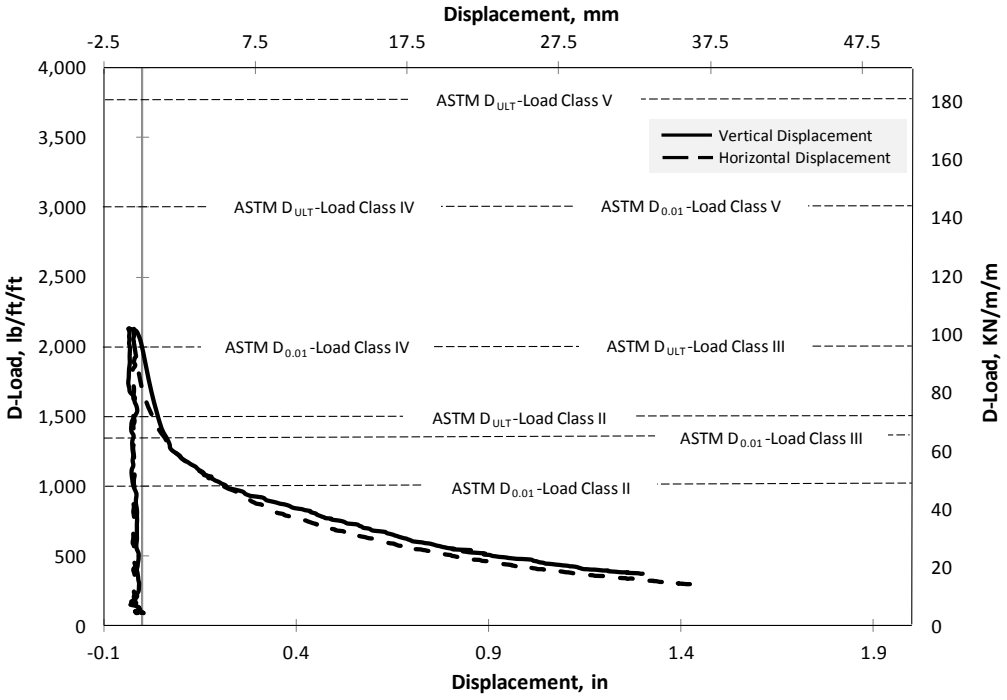

Figure B- 26 D-load versus displacement for NCP-36-C-0.25-65/35-T1

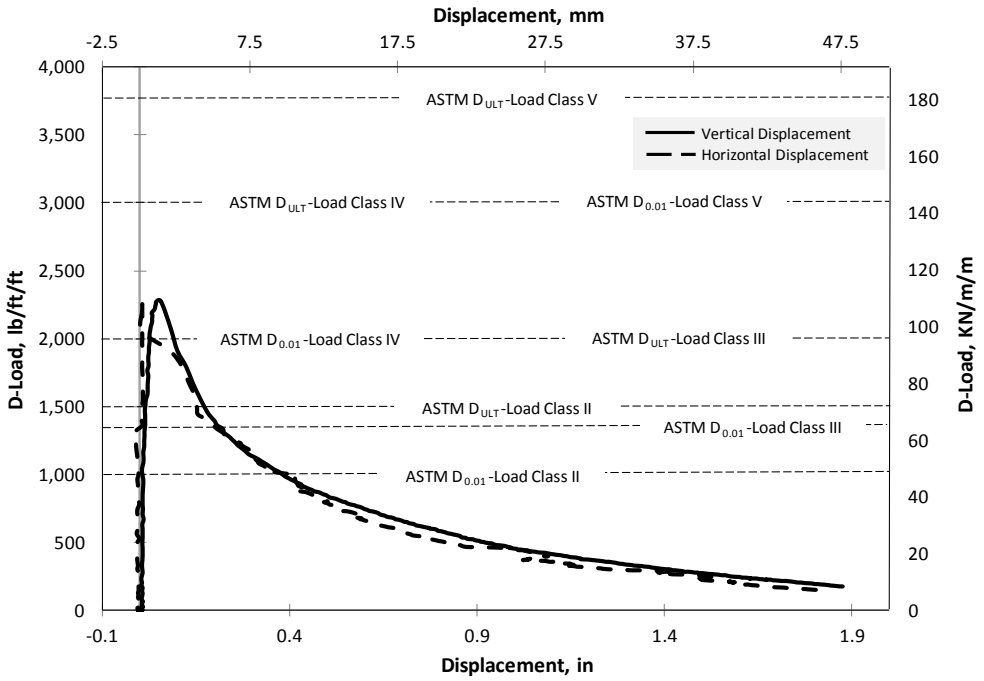

Figure B- 27 D-load versus displacement for NCP-36-C-0.33-65/35-T1

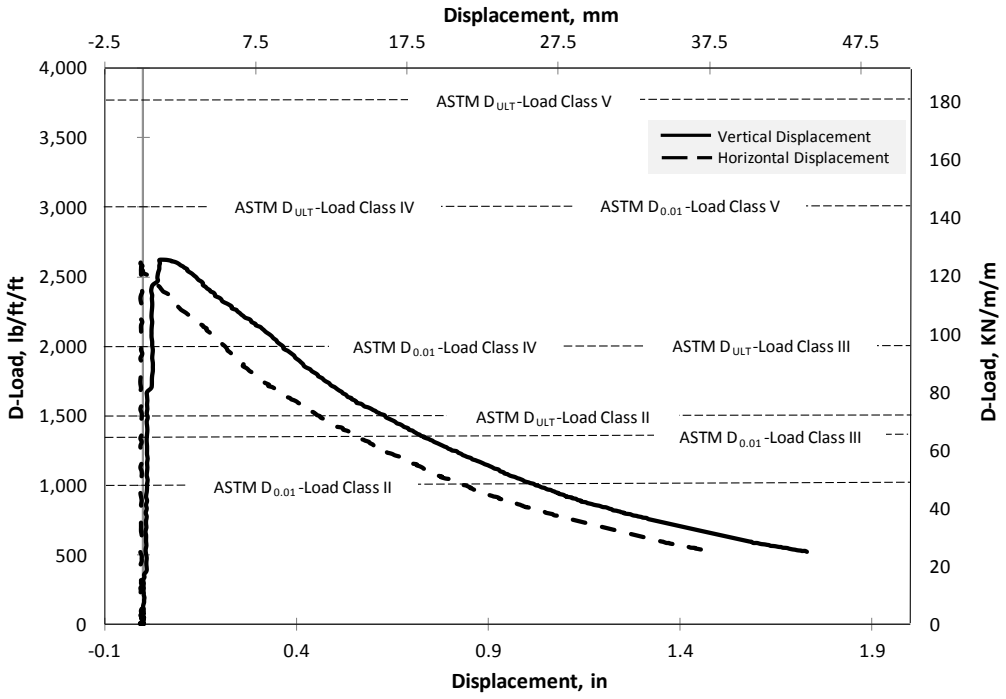

Figure B- 28 D-load versus displacement for NCP-36-C-0.5-65/35-T1

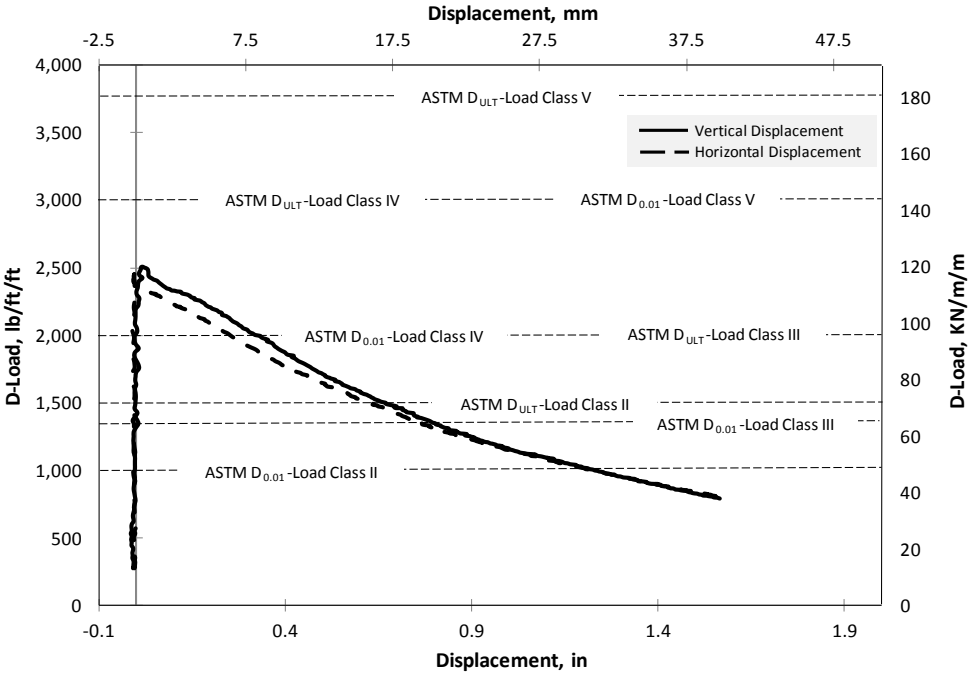

Figure B- 29 D-load versus displacement for NCP-36-C-0.5-65/35-T2

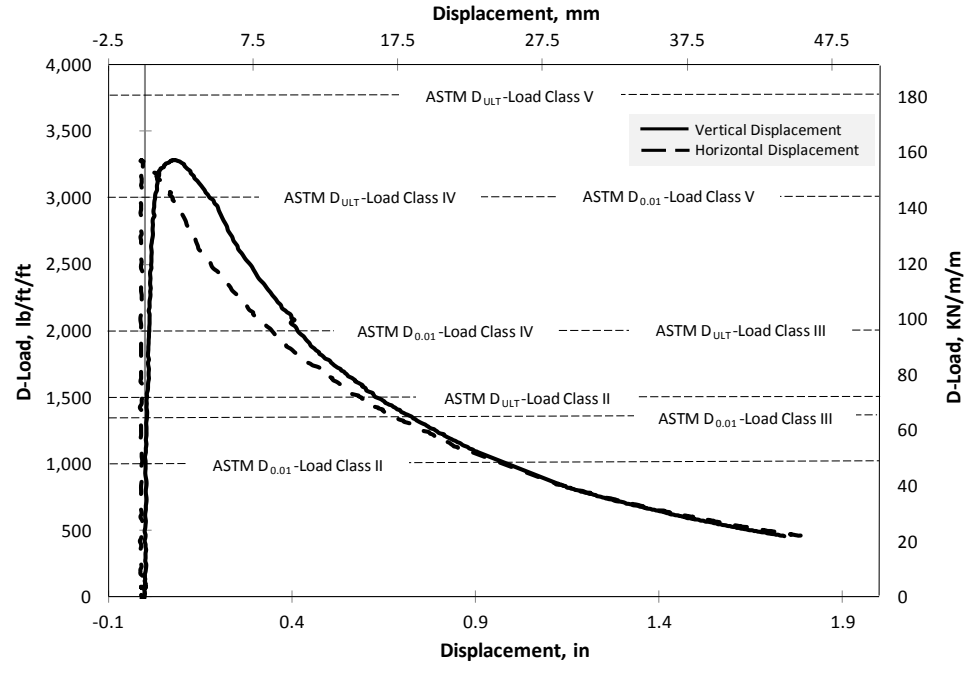

Figure B- 30 D-load versus displacement for NCP-36-C-0.67-65/35-T1

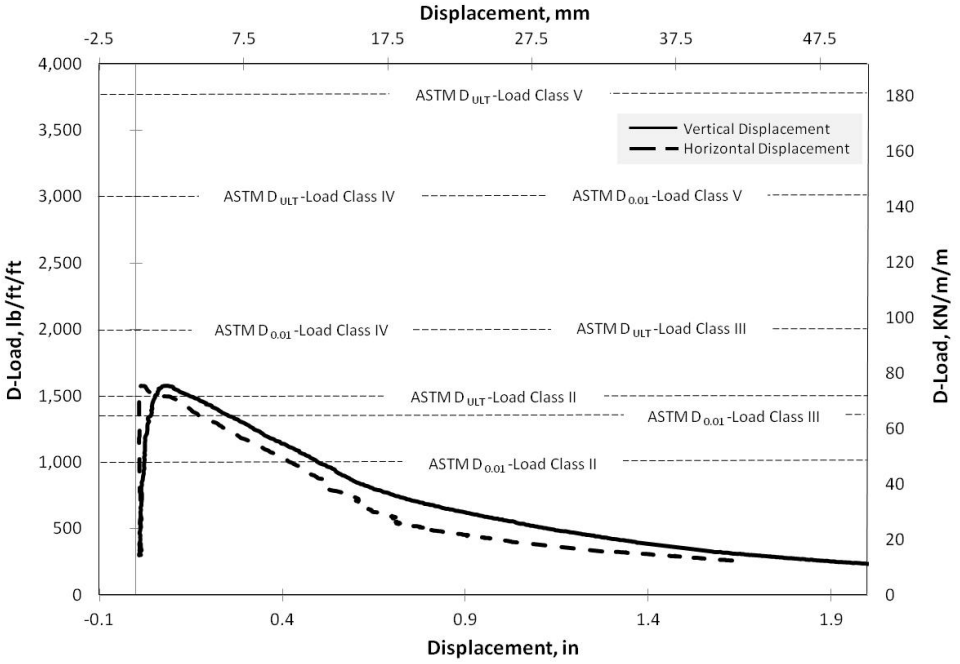

Figure B- 31 D-Load versus displacement for NCP-48-B-0.5-65/35-T1

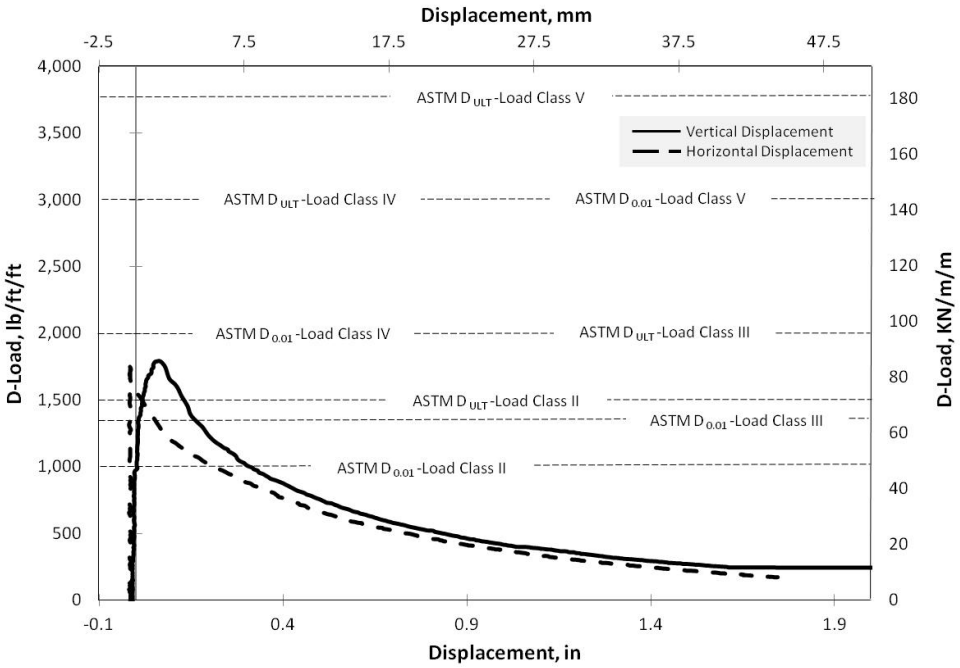

Figure B- 32 D-Load versus displacement for NCP-48-B-0.5-65/35-T2

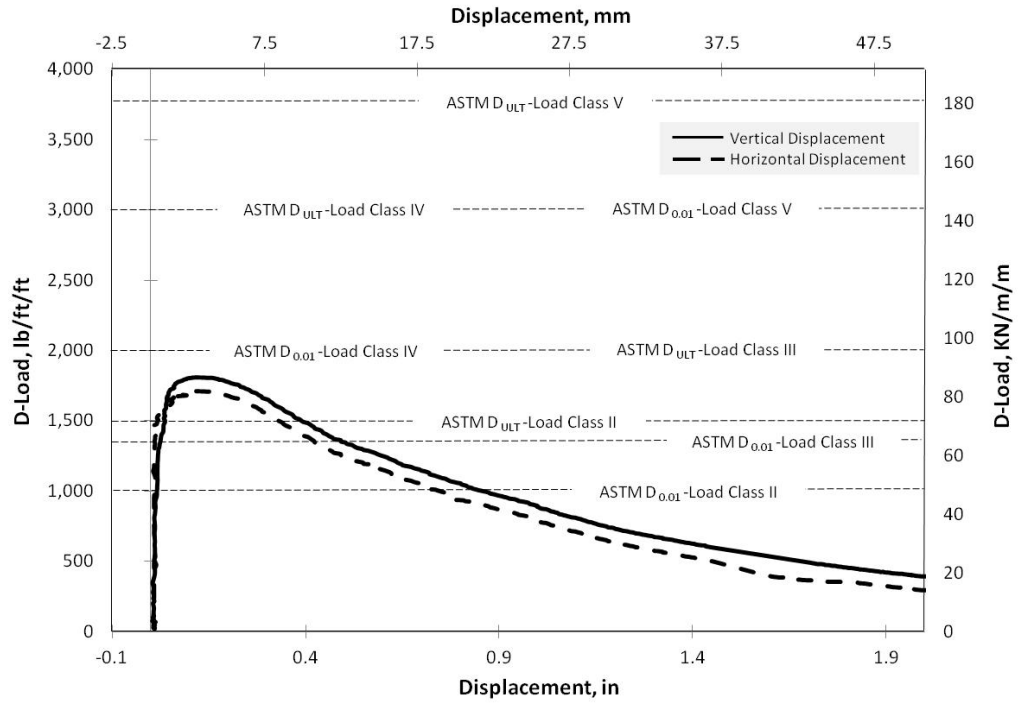

Figure B- 33 D-load versus displacement for NCP-48-B-0.67-65/35-T1

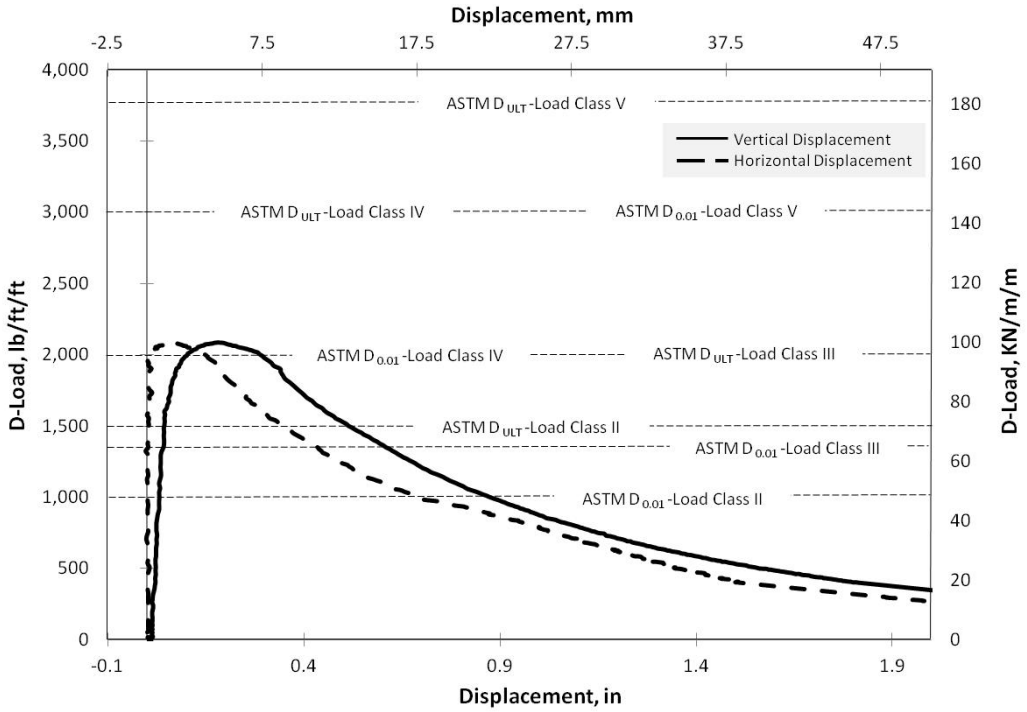

Figure B- 34 D-LOAD versus displacement for NCP-48-B-0.83-65/35-T1

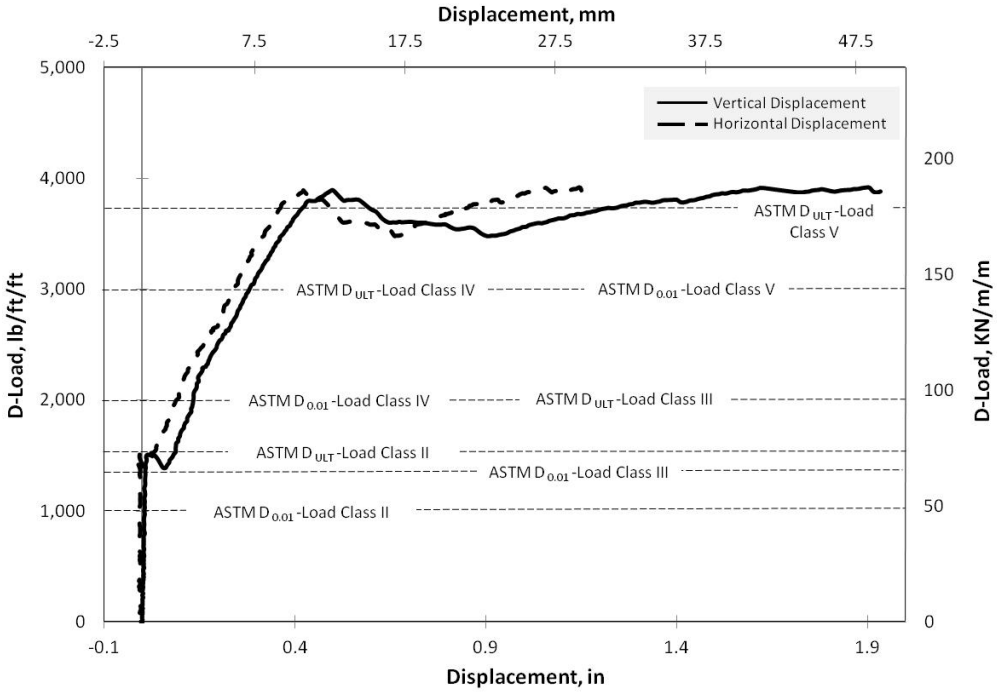

Figure B- 35 D-load versus displacement for NCP-24-B-RCP-T1

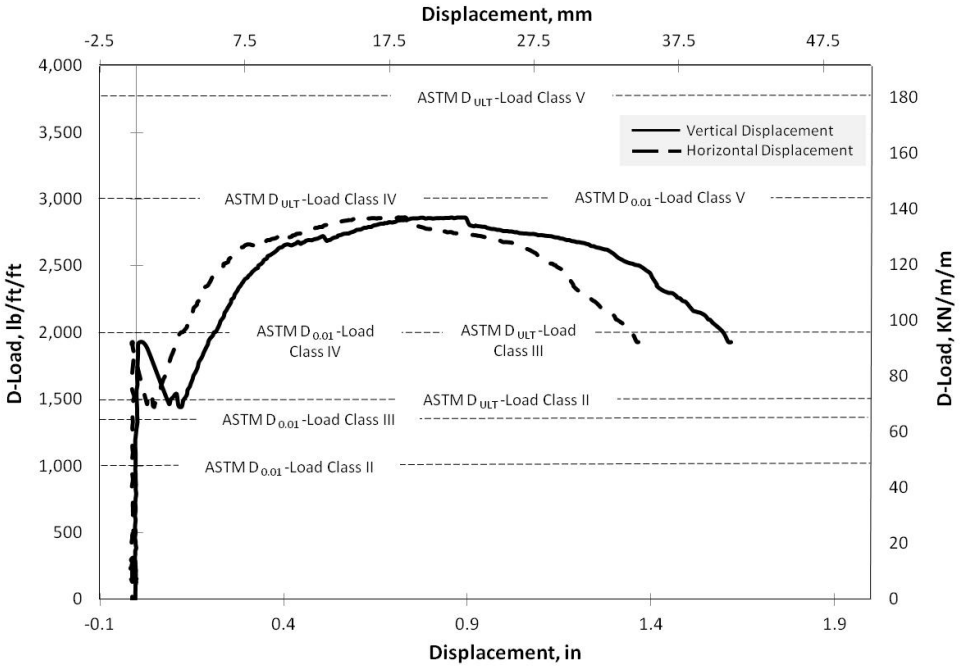

Figure B- 36 D-load versus displacement for NCP-24-B-RCP-T2

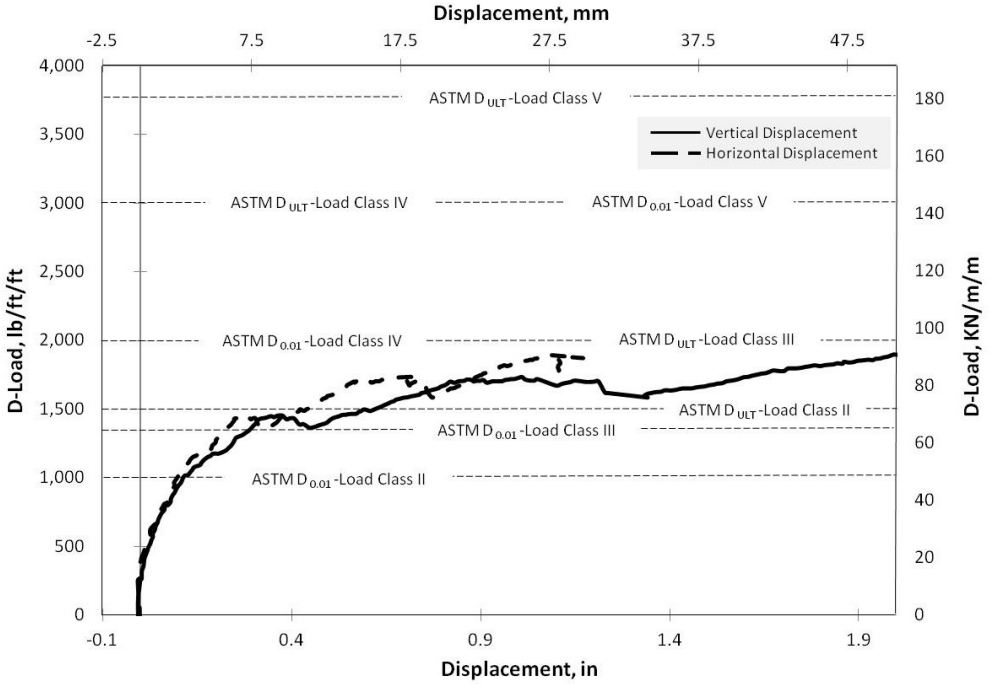

Figure B- 37 D-load versus displacement for NCP-24-B-RCP-T3

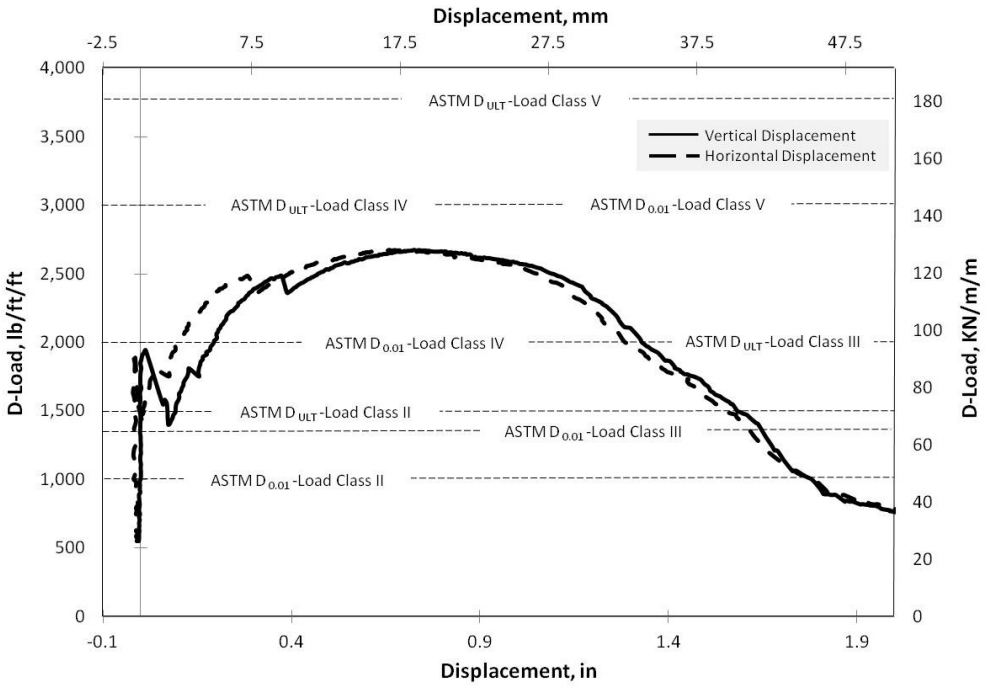

Figure B- 38 D-load versus displacement for NCP-24-B-RCP-T4

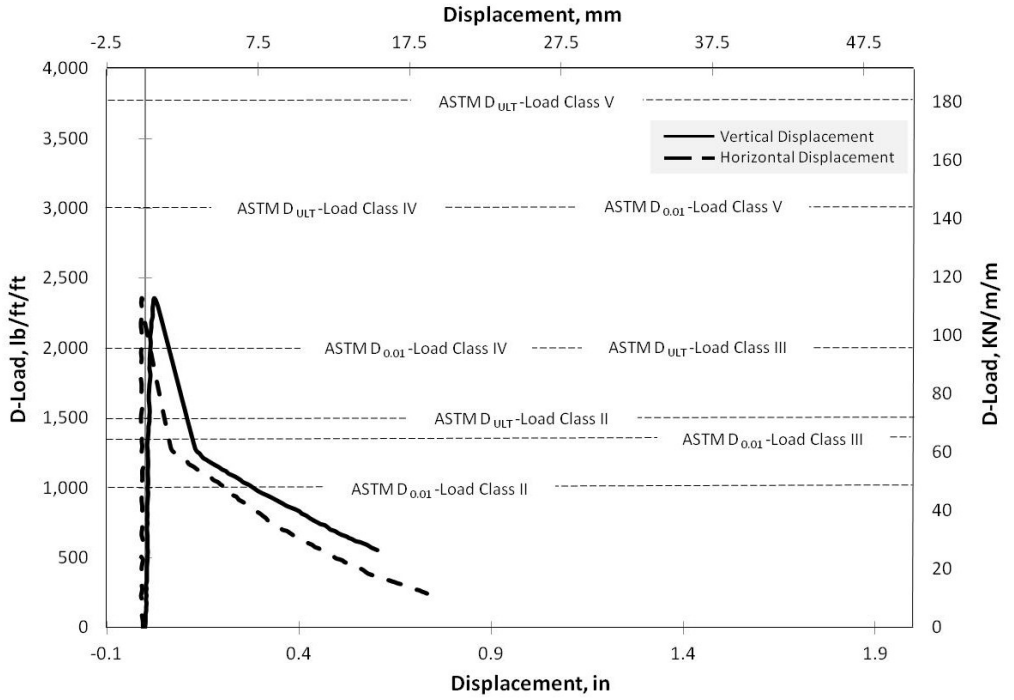

Figure B- 39 D-load versus displacement for SHD-24-C-0.25-65/35-T1

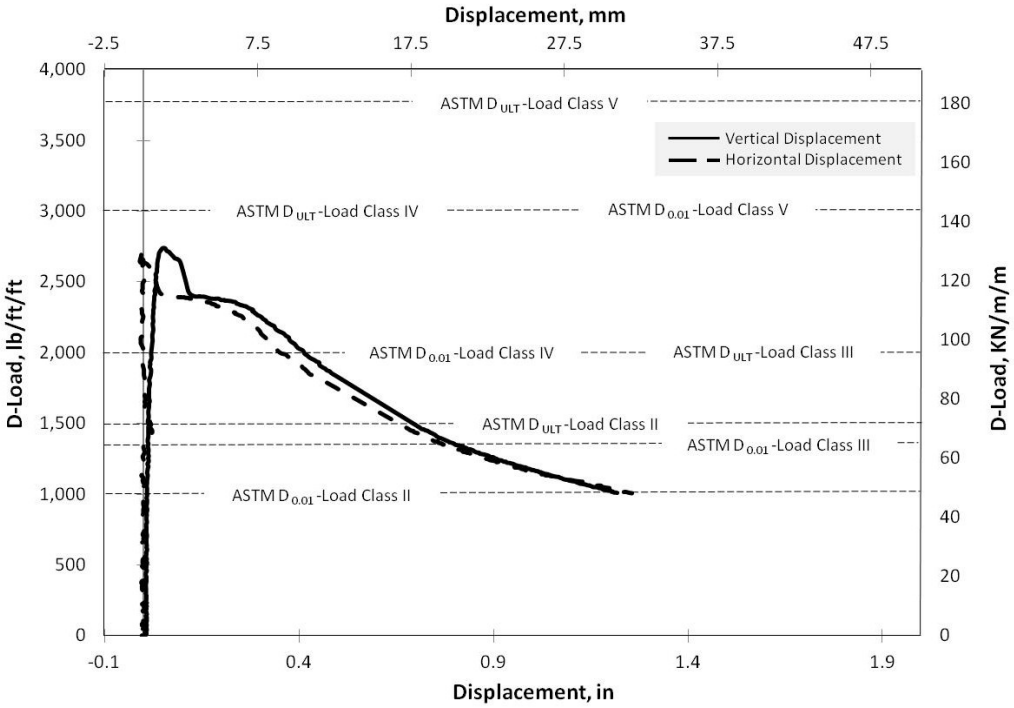

Figure B- 40 D-load versus displacement for SHD-24-C-0.33-65/35-T1

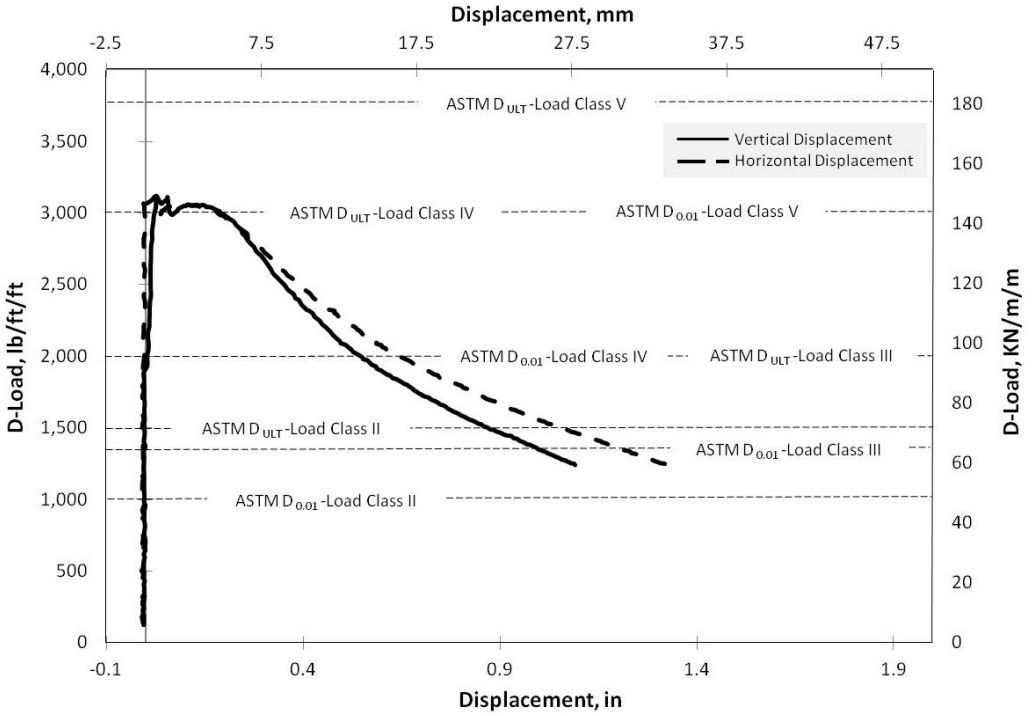

Figure B- 41 D-load versus displacement for SHD-24-C-0.5-65/35-T1

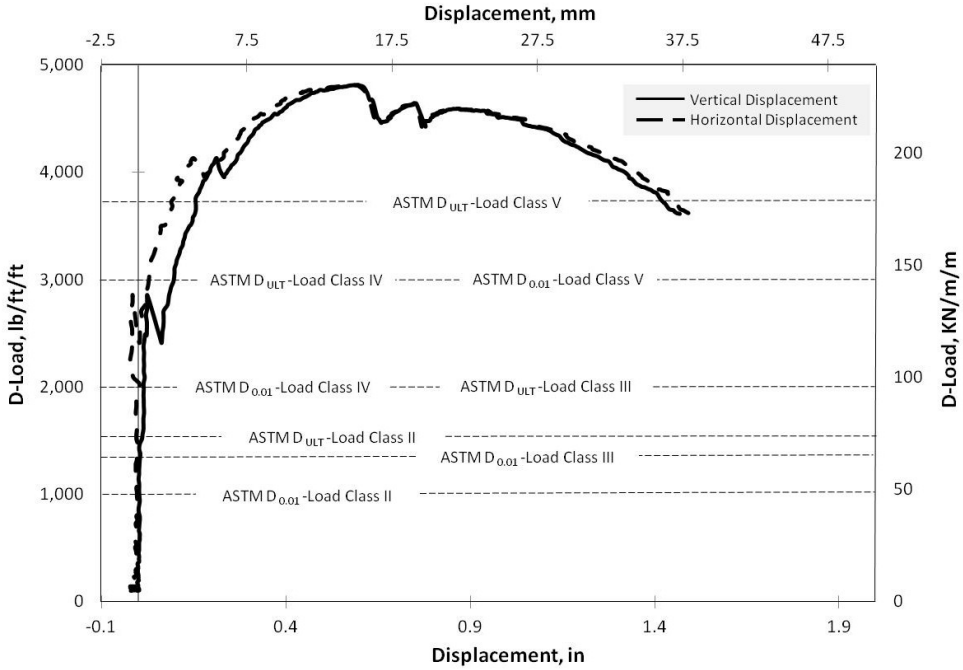

Figure B- 42 D-load versus displacement for SHD-24-C-RCP-T1

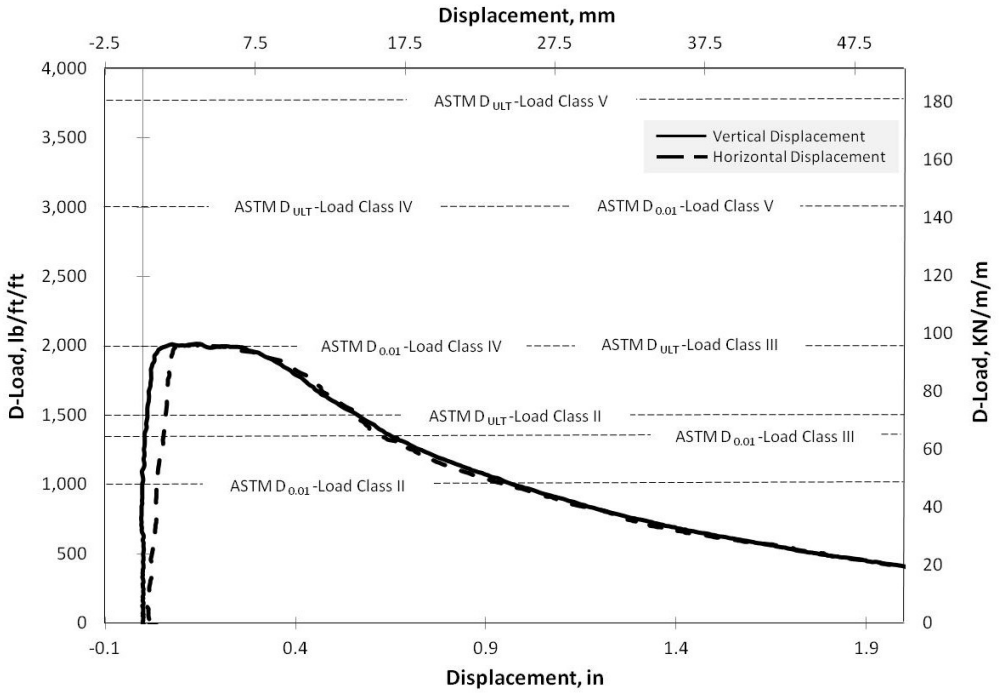

Figure B- 43 D-load versus displacement for SHD-36-C-0.5-65/35-T1

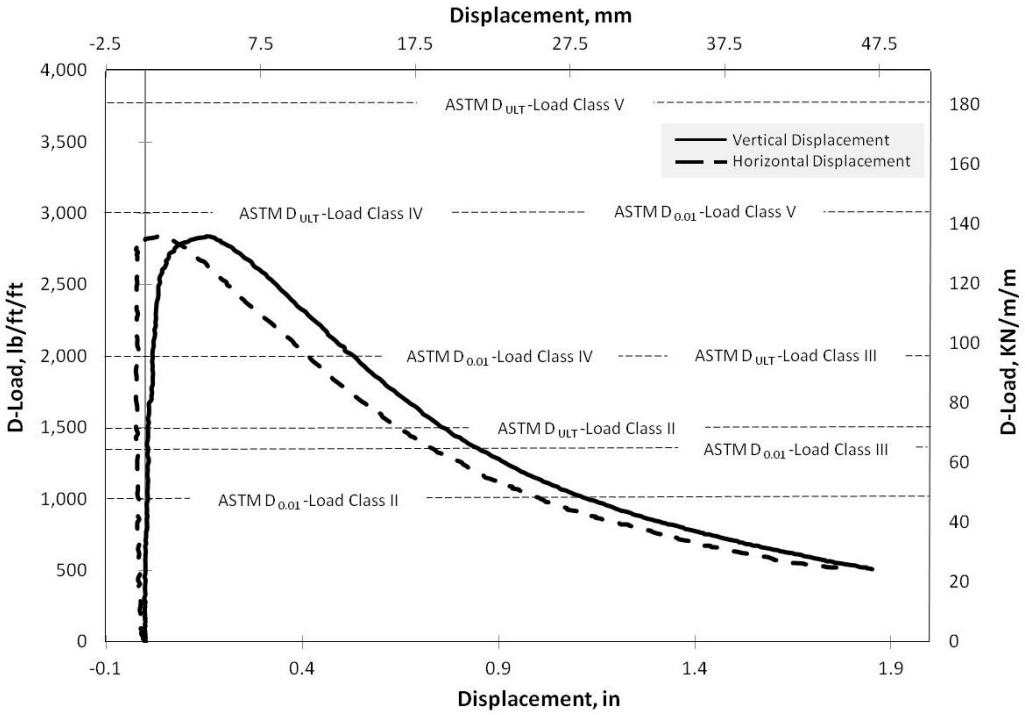

Figure B- 44 D-load versus displacement for SHD-36-C-0.67-65/35-T1

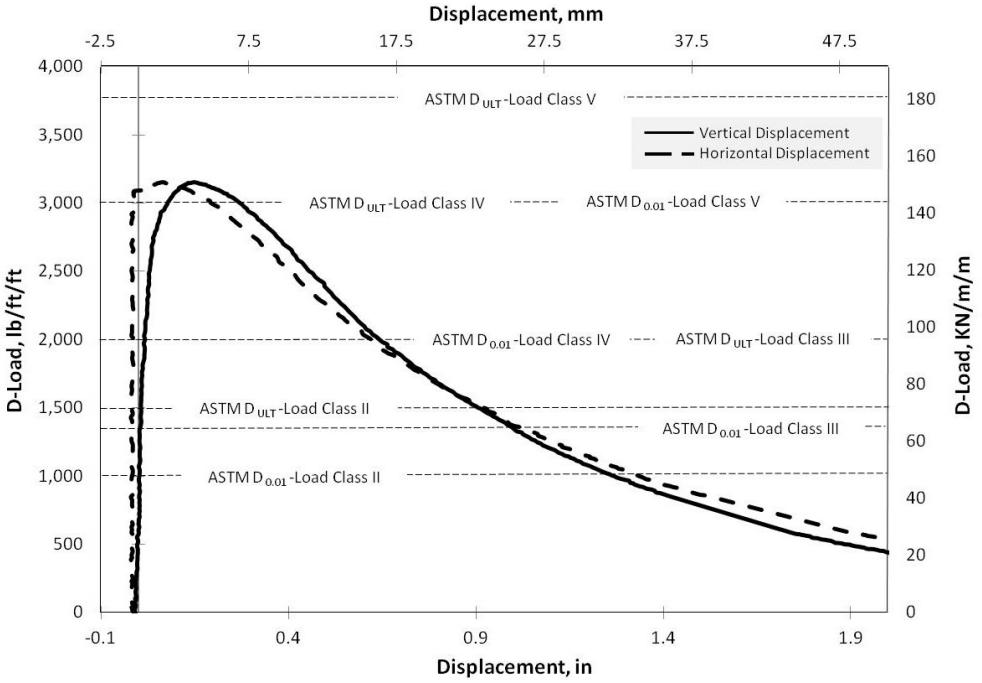

Figure B- 45 D-load versus displacement for SHD-36-C-0.83-65/35-T1

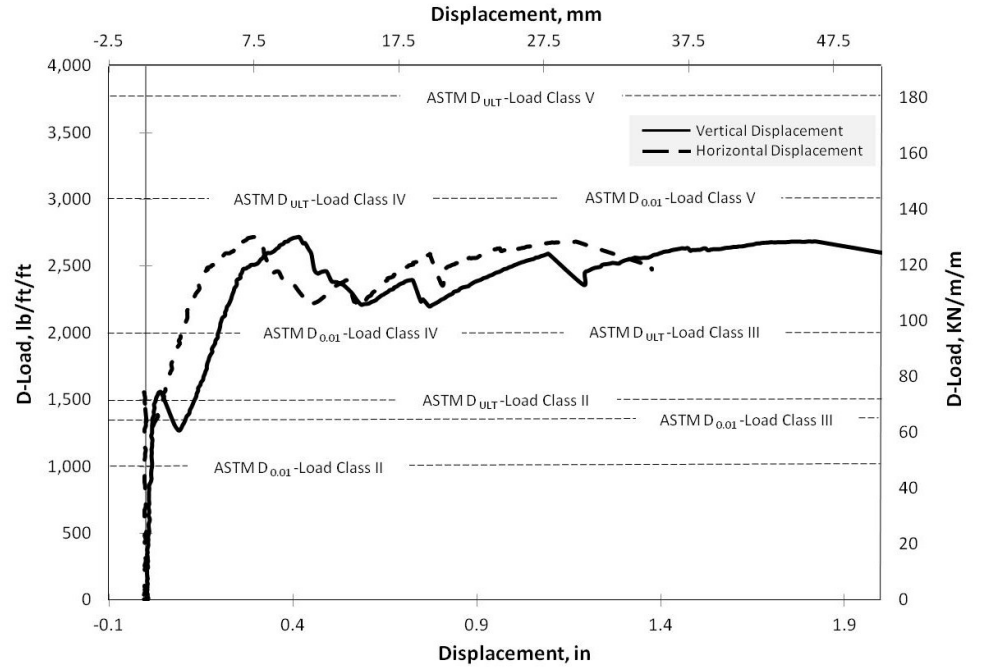

Figure B- 46 D-load versus displacement for SHD-36-C-RCP-T1

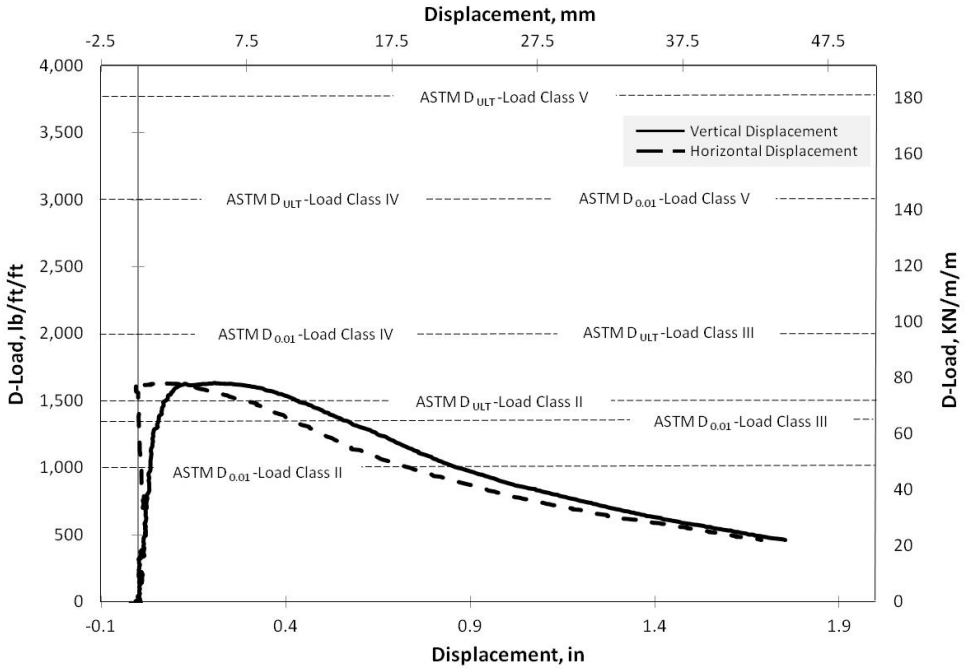

Figure B- 47 D-load versus displacement for SHD-48-B-0.67-65/35-T1

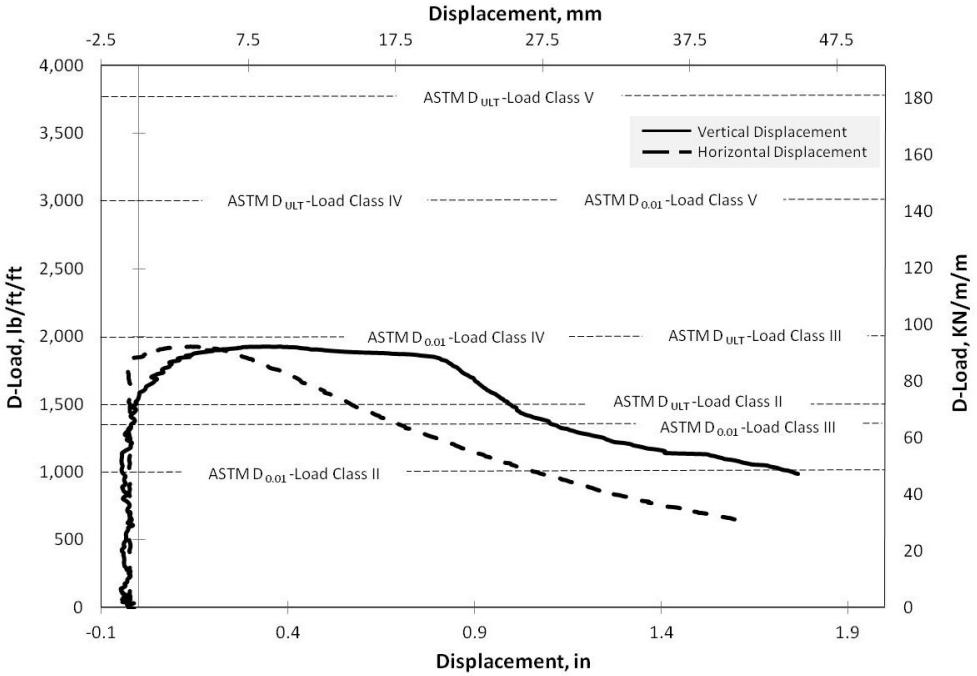

Figure B- 48 D-load versus displacement for SHD-48-B-0.83-65/35-T1

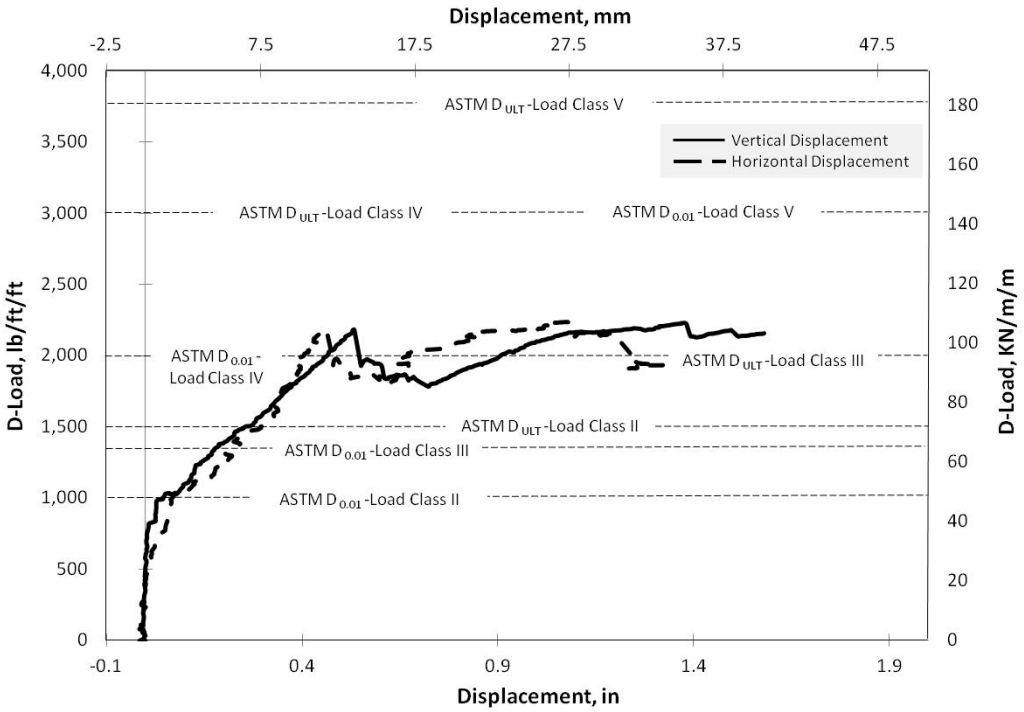

Figure B- 49 D-load versus displacement for SHD-48-B-RCP-T1

Figure B- 50 SFRCP 24 in. (600 mm) with 0.33% fiber fraction at 2.5 in deformation

Figure B- 51 SFRCP 24 in. (600 mm) with 0.33% fiber fraction at large deformation

Figure B- 52 Typical crack opening for 24 in. (600 mm) SFRCP at 5% deformation

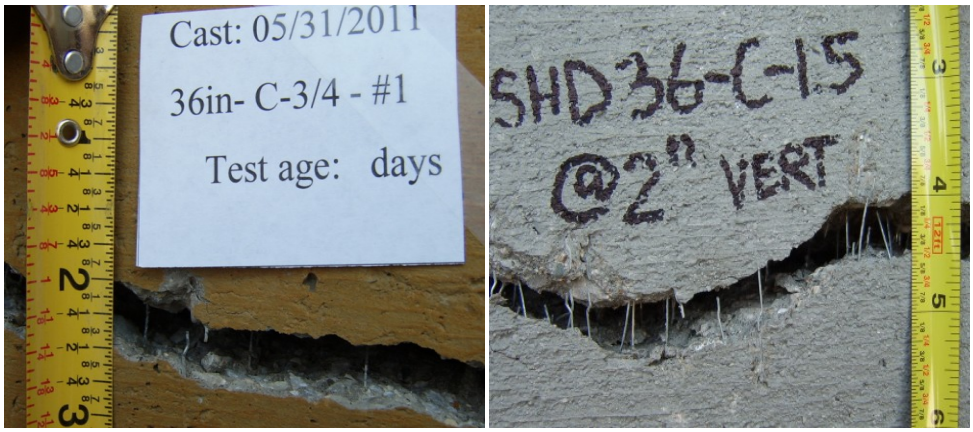

Figure B- 53 Typical crack opening for 36 in. (900 mm) SFRCP at 5% deformation

Figure B- 54 Typical crack opening for 48 in. (1200 mm) SFRCP at 5% deformation

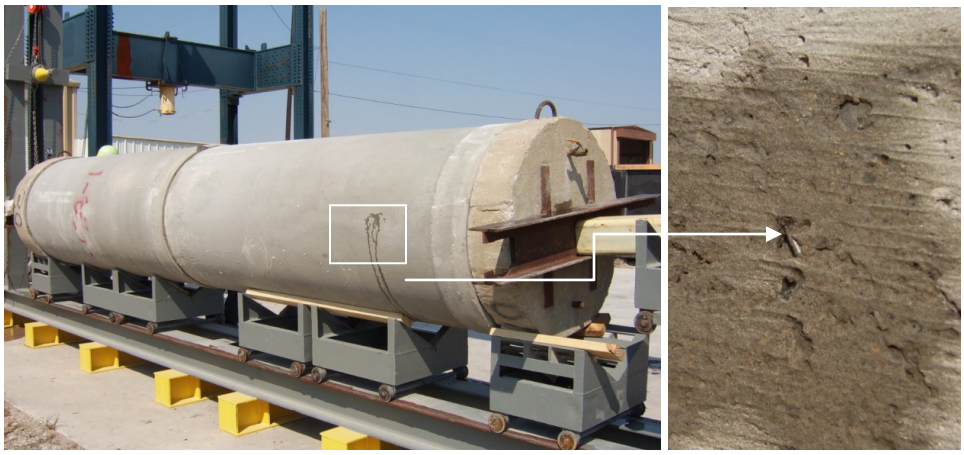

Figure B- 55 Specimen 1 for HAN-30-C-0.33 SFRCP minor seepage from a pinhole

Figure B- 56 Specimen 3 for HAN-30-C-0.5 SFRCP dripping from the body and joints

Figure B- 57 Specimen 4 for HAN-36-C-0.83 SFRCP seepage

developed at seven locations

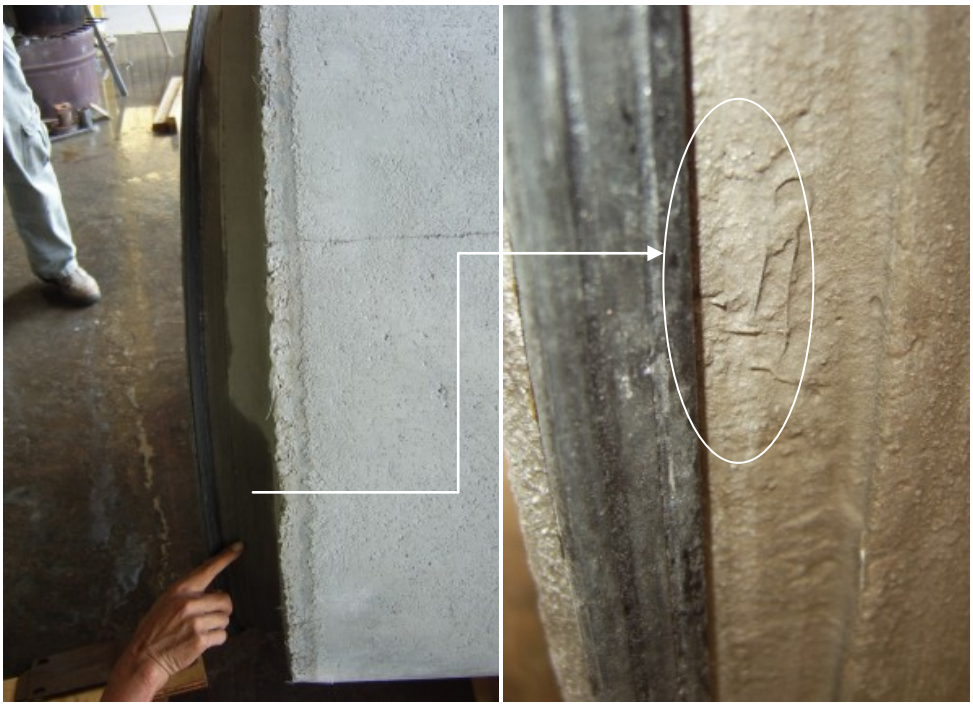

Figure B- 58 Specimen 4 for HAN-36-C-0.83 joint leaking location

Figure B- 59 Specimen #1 joint shear differential failure

Figure B- 60 Specimen #1 joint shear joint failure pattern

Figure B- 61 Specimen #2 joint shear failure pattern

Appendix C

Results of Compressive Cylinder Testing

Table C- 1 Sherman Dixie compressive cylinder with RC-65/35-CN fiber strength results

(1 psi=6895 Pa)

Test age (days)	Cylinder designation	Stress (psi)	Average stress (psi)	Strain
>28	SHD24-8-C-RCP-T1	6,075	6,088	0.009733
>28	SHD24-8-C-RCP-T2	6,101		0.00945
>28	SHD24-8-C-0.17-T1	7,287	7,329	0.010433
>28	SHD24-8-C-0.17-T2	6,843		0.009883
>28	SHD24-8-C-0.17-T3	7,856		0.011383
>28	SHD24-8-C-0.25-T1	5,680	5,761	-
>28	SHD24-8-C-0.25-T2	6,045		0.009283
>28	SHD24-8-C-0.25-T3	5,559		0.008667
>28	SHD24-8-C-0.33-T1	6,303	6,101	0.0099
>28	SHD24-8-C-0.33-T2	5,899		0.008017
>28	SHD24-8-C-0.5-T1	7,690	7,719	0.009717
>28	SHD24-8-C-0.5-T2	7,271		0.01
>28	SHD24-8-C-0.5-T3	8,195		0.01075
>28	SHD36-8-C-0.5-T1	7,322	7,685	0.0103
>28	SHD36-8-C-0.5-T2	7,686		0.011033
>28	SHD36-8-C-0.5-T3	8,048		0.011033
>28	SHD48-8-B-0.5-T1	7,967	7,860	0.012017
>28	SHD48-8-B-0.5-T2	8,360		0.011917
>28	SHD48-8-B-0.5-T3	7,254		0.011017
>28	SHD36-8-C-0.67-T1	6,543	7,716	0.010933
>28	SHD36-8-C-0.67-T2	8,101		-
>28	SHD36-8-C-0.67-T3	8,503		0.012467
>28	SHD48-8-B-0.67-T1	7,173	7,662	0.0147
>28	SHD48-8-B-0.67-T2	7,110		0.0102
>28	SHD48-8-B-0.67-T3	8,704		0.013383
>28	SHD36-8-C-0.83-T1	5,216	7,271	0.0096
>28	SHD36-8-C-0.83-T2	8,483		0.0122
>28	SHD36-8-C-0.83-T3	8,114		0.0116
>28	SHD48-8-B-0.83-T1	7,291	7,703	0.011717
>28	SHD48-8-B-0.83-T2	7,848		0.014133
>28	SHD48-8-B-0.83-T3	7,970		0.012567

Figure C- 1 Typical failure mode of SHD cylinder with 0.17%

Figure C- 2 Typical failure mode of SHD cylinder with 0.25%

Figure C- 3 Typical failure mode of SHD cylinder with 0.33%

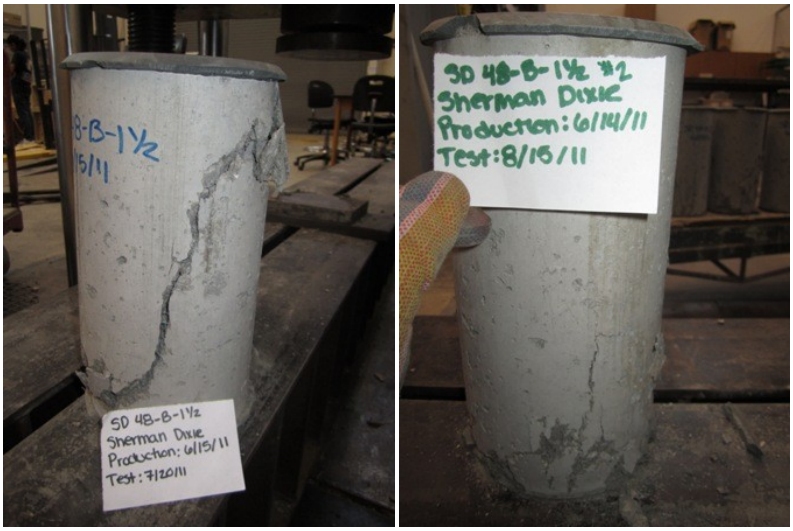

Figure C- 4 Typical failure mode of SHD cylinder with 0.5%

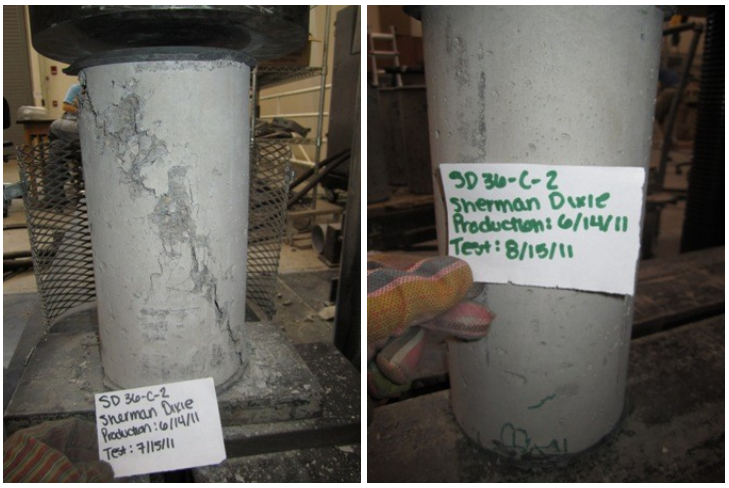

Figure C- 5 Typical failure mode of SHD cylinder with 0.67%

Figure C- 6 Typical failure mode of SHD cylinder with 0.83%

Table C- 2 Northern Concrete Pipe compressive cylinder with RC-65/35-CN fiber strength results (1 psi=6895 Pa)

Test age (days)	Cylinder Designation	Stress (psi)	Average stress (psi)	Strain
7	NCP24-8-B-RCP-T1	5,494	6,970	0.0369
45	NCP24-8-B-RCP-T2	5,748		0.0082
65	NCP24-8-B-RCP-T3	9,673		0.014417
7	NCP24-8-B-0.17-T1	7,850	6110	-
45	NCP24-8-B-0.17-T2	5,587		0.012317
7	NCP24-8-B-0.17-T4	5,193		-
45	NCP24-8-B-0.17-T5	5,805		0.00895
7	NCP24-8-B-0.25-T1	7,260	7,935	
45	NCP24-8-B-0.25-T2	7,692		0.01065
7	NCP24-8-B-0.25-T4	7,143		0.034317
7	NCP36-8-C-0.25-T1	7,945	7,950	-
45	NCP36-8-C-0.25-T2	6,146		0.009317
66	NCP36-8-C-0.25-T3	9,763		0.011633
7	NCP24-8-B-0.33-T1	5,965	5965	

Table C-2 Continued

Test age (days)	Cylinder Designation	Stress (psi)	Average stress (psi)	Strain
7	NCP36-8-C-0.33-T1	7,681		-
45	NCP36-8-C-0.33-T2	7,056		-
72	NCP36-8-C-0.33-T3	5,897		0.009767
7	NCP48-8-B-0.33-T1	6,504	8,642	-
45	NCP48-8-B-0.33-T2	8,868		-
66	NCP48-8-B-0.33-T3	10,554		-
7	NCP24-8-B-0.5-T1	7,636	5965	-
72	NCP24-8-B-0.5-T3	5,686		0.009517
7	NCP36-8-C-0.5-T1	7,681	7,568	-
45	NCP36-8-C-0.5-T2	6,269		-
72	NCP36-8-C-0.5-T3	8,754		0.010883
7	NCP48-8-B-0.5-T1	6,847	7,045	-
7	NCP48-8-B-0.5-T4	7,573		-
45	NCP48-8-B-0.5-T5	6,716		-
7	NCP36-8-C-0.67-T1	7,856	8,578	-
45	NCP36-8-C-0.67-T2	8,863		0.01155
65	NCP36-8-C-0.67-T3	9,014		0.011383
7	NCP48-8-B-0.83-T1	7,787	7,460	-
45	NCP48-8-B-0.83-T2	7,132		-

Figure C- 7 Typical failure mode of NCP cylinder with 0.17

Figure C- 8 Typical failure mode of NCP cylinder with 0.25

Figure C- 9 Typical failure mode of NCP cylinder with 0.33

Figure C- 10 Typical failure mode of NCP cylinder with 0.5

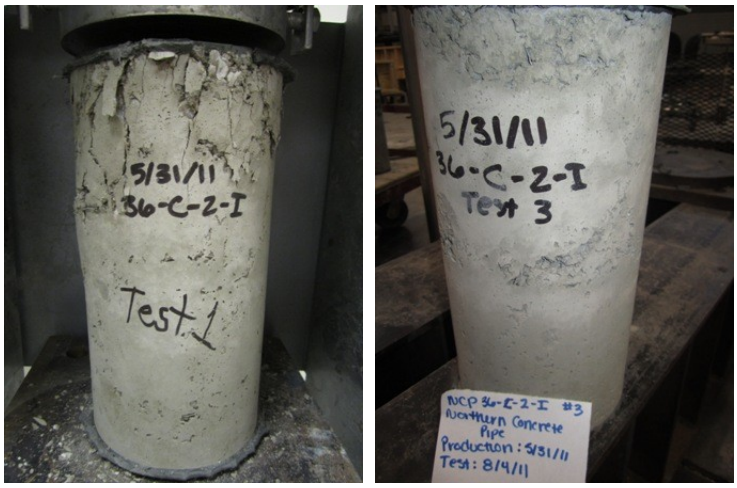

Figure H- 1 Typical failure mode of NCP cylinder with 0.67

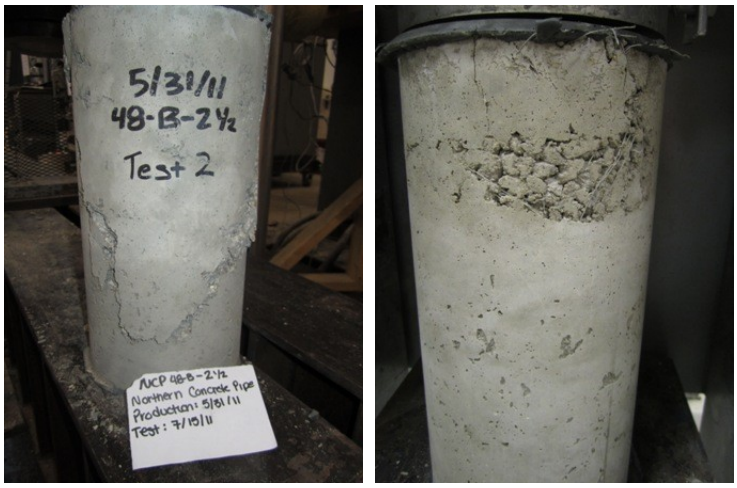

Figure C- 11 Typical failure mode of NCP cylinder with 0.83

Table C- 3 Hanson compressive cylinder with RC-65/35-CN and 80/60 fiber strength (1 psi=6895 Pa)

Test age (days)	Cylinder designation	Fiber type	Stress (psi)	Average stress (psi)	Strain
8	HAN33-8-B-0.33-T1	65/35	1,985	1,435	-
8	HAN33-8-B-0.33-T2	65/35	960		-
8	HAN33-8-B-0.33-T3	65/35	1,360		-
15	HAN33-8-B-0.33-T4	65/35	1,728	1,860	-
15	HAN33-8-B-0.33-T5	65/35	1,712		-
15	HAN33-8-B-0.33-T6	65/35	2,149		-
8	HAN33-8-B-0.5-T1	65/35	3,503	2,680	-
8	HAN33-8-B-0.5-T2	65/35	2,009		-
8	HAN33-8-B-0.5-T3	65/35	2,531		-
15	HAN33-8-B-0.5-T4	65/35	1,226	1,970	-
15	HAN33-8-B-0.5-T5	65/35	2,529		-
15	HAN33-8-B-0.5-T6	65/35	2,162		-
43	HAN24-8-B-0.25-T1	65/35	5,534	5,715	0.0082
43	HAN24-8-B-0.25-T2	65/35	6,637		0.0089
43	HAN24-8-B-0.25-T4	65/35	4,974		0.0076

Table C- 3 Continued.

Test age (days)	Cylinder designation	Fiber type	Stress (psi)	Average stress (psi)	Strain
42	HAN24-8-B-0.33-T1	65/35	6,958	5920	0.0098
45	HAN24-8-B-0.33-T5	65/35	3,796		
45	HAN24-8-B-0.33-T6	65/35	7,006		
14	HAN30-8-C-0.33-T1	65/35	4,760	4,760	0.0131
14	HAN30-8-C-0.5-T1	65/35	5,489	5,489	0.0136
14	HAN30-8-C-0.67-T1	65/35	5,665	5,665	0.0138
27	HAN36-6-B-0.5-T1	80/60	3,004	3,193	-
27	HAN36-6-B-0.5-T2	80/60	3,274		-
27	HAN36-6-B-0.5-T3	80/60	3,301		-

Table C- 4 Hanson Cylinder Results Cont.

Test age (days)	Cylinder designation	Fiber type	Stress (psi)	Average stress (psi)	Strain
27	HAN36-6-B-0.67-T1	80/60	1,690	2,351	-
27	HAN36-6-B-0.67-T2	80/60	3,011		-
20	HAN48-8-B-0.83-T1	65/35	3,239	2,694	-
20	HAN48-8-B-0.83-T2	65/35	2,629		-
20	HAN48-8-B-0.83-T3	65/35	2,215		-
15	HAN48-8-B-0.67-T1	80/60	2,683	2,603	-
15	HAN48-8-B-0.67-T2	80/60	2,523		-
15	HAN48-8-B-0.83-T1	65/35	2,723	2,723	-
14	HAN36-6-B-0.5-T4	80/60	4,152	5,269	-
14	HAN36-6-B-0.5-T5	80/60	5,957		-
14	HAN36-6-B-0.5-T6	80/60	5,697		-
14	HAN36-6-B-0.5-T7	65/35	5,739	5,739	-

Table C- 4 Continued.

Test age (days)	Cylinder designation	Fiber type	Stress (psi)	Average stress (psi)	Strain
14	HAN36-6-B-0.67-T3	65/35	6,475		
14	HAN36-6-B-0.67-T4	65/35	6,522	5,859	-
14	HAN36-6-B-0.67-T5	65/35	4,578		-
16	HAN42-8-C-0.5-T1	65/35	8,097		-
16	HAN42-8-C-0.5-T2	65/35	8,835	8,399	-
16	HAN42-8-C-0.5-T3	65/35	8,266		-
16	HAN42-8-C-0.67-T1	65/35	7,474		-
16	HAN42-8-C-0.67-T2	65/35	7,879	7,697	-
16	HAN42-8-C-0.67-T3	65/35	7,740		-
16	HAN42-8-C-0.83-T1	65/35	8,966	8,777	-
16	HAN42-8-C-0.83-T2	65/35	8,589		-

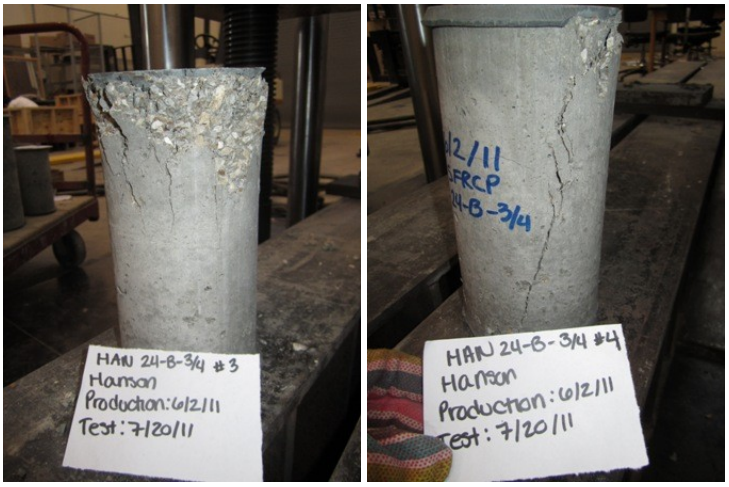

Figure C- 12 Typical failure mode of HAN cylinder with 0.25%

Figure C- 13 Typical failure mode of HAN cylinder with 0.33%

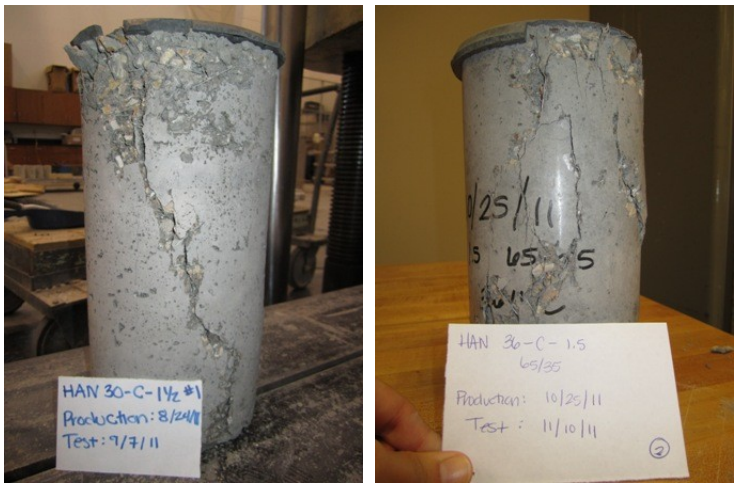

Figure C- 14 Typical failure mode of HAN cylinder with 0.5%

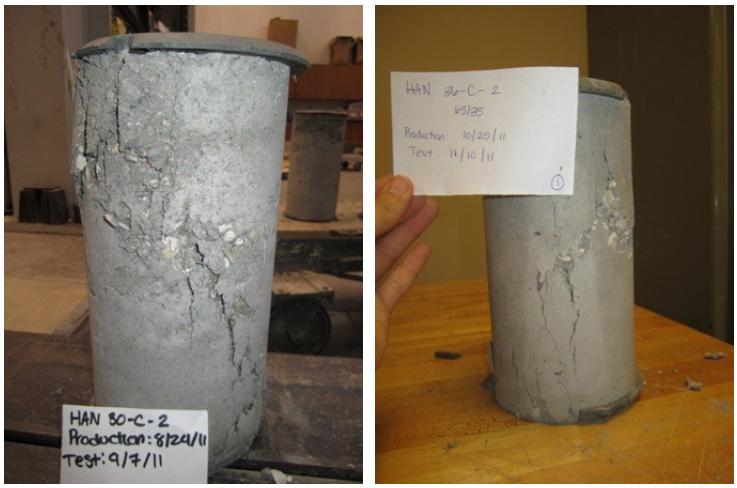

Figure C- 15 Typical failure mode of HAN cylinder with 0.67%

Appendix D

Results of Flexural Beam Testing

Table D- 1 Summary of test results for beam flexural strength

(1 psi=6895 Pa)

Beam designation	Flexural Strength (psi)	Compressive Strength (psi)	Strength Ratio (η)
SHD24-8-C-0.17-T1	568.7	7,833	6.43
SHD24-8-C-0.25-T1	602.8	6,109	7.71
SHD24-8-C-0.33-T1	628.2	6,644	7.71
SHD24-8-C-0.5-T1	637.5	8,291	7.00
SHD36-8-C-0.5-T1	556.5	8,247	6.13
SHD48-8-B-0.67-T1	586.3	8,408	6.39
SHD36-8-C-0.67-T1	851.0	8,071	9.47
SHD48-8-B-0.67-T1	917.2	8,187	10.14
SHD36-8-B-0.83-T1	976.2	7,771	11.07
SHD48-8-B-0.83-T1	1166.4	8,206	12.88
NCP24-8-B-0.17-T1	703.8	7,226	8.28
NCP24-8-B-0.17-T2	820.4	7,226	9.65
NCP36-8-C-0.25-TI	988.4	8,296	10.85
NCP24-8-B-0.33-T1	869.9	5,965	11.26
NCP24-8-B-0.33-T2	547.4	5,965	7.09
NCP48-8-B-0.33-T1	412.0	8,642	4.43
NCP24-8-B-0.5-T1	871.4	6,982	10.43
NCP24-8-B-0.5-T2	907.3	6,982	10.86
NCP48-8-B-0.83-T1	1295.9	7,460	15.00
NCP48-8-B-0.83-T2	1103.9	7,460	12.78
HAN24-8-B-0.33-T1	395.0	1,912	9.03
HAN30-8-B-0.33-T1	690.0	5,645	9.18
HAN30-8-B-0.33-T2	431.9	5,645	5.75
HAN30-8-C-0.67-T1	665.3		
HAN48-8-B-0.67-T1	845.2	2,603	16.57
HAN36-6-B-0.5-T1	554.9	5,739	7.33
HAN36-6-B-0.5-T2	465.4	5,739	6.14
HAN36-6-B-0.5-T1	767.6	5,859	10.03
HAN36-8-C-0.5-T1	895.6	8,399	9.77
HAN36-8-C-0.5-T2	844.4	8,399	9.21
HAN36-8-C-0.67-T1	904.4	7,697	10.31
HAN36-8-C-0.67-T2	714.2	7,697	8.14

Table D- 2 Estimated parameters obtained from flexural beam test

Beam designation	Fiber dosage	First Peak Strength, (psi)	Toughness, in-lbf	Equivalent Strength ratio, %
NCP24-8-B-0.17-T1	0.17	235	565	1.7
NCP24-8-B-0.17-T2	0.17	274	540	1.4
SHD24-8-C-0.17-T1	0.17	189	350	1.3
NCP 36-8-C-0.25-T1	0.25	329	725	1.5
SHD24-8-C-0.25-T1	0.25	201	625	2.2
HAN24-8-B-0.33-T1	0.33	130	415	2.2
HAN30-8-B-0.33-T1	0.33	230	690	2.1
HAN30-8-B-0.33-T2	0.33	145	450	2.2
NCP24-8-B-0.33-T1	0.33	290	505	1.2
NCP24-8-B-0.33-T2	0.33	182	480	1.8
NCP48-8-B-0.33-T1	0.33	137	315	1.6
SHD24-8-C-0.33-T1	0.33	209	595	2
HAN36-6-B-0.5-T1	0.5	170	600	2.5
HAN36-6-B-0.5-T2	0.5	155	525	2.3
HAN36-8-C-0.5-T1	0.5	290	1150	2.8
HAN36-8-C-0.5-T2	0.5	270	1195	3.1
NCP24-8-B-0.5-T1	0.5	290	510	1.2
NCP24-8-B-0.5-T2	0.5	300	970	2.2
SHD24-8-C-0.5-T1	0.5	214	860	2.8
SHD36-8-C-0.5-T1	0.5	187	780	2.9
SHD48-8-B-0.5-T1	0.5	195	1090	3.9

Table D-2 Continued

Beam designation	Fiber dosage	First Peak Strength, (psi)	Toughness, in-lbf	Equivalent Strength ratio, %
HAN30-8-C-0.67-T1	0.67	220	674	2.1
HAN36-6-B-0.67-T1	0.67	255	1085	2.9
HAN36-8-C-0.67-T1	0.67	235	1215	3.6
HAN36-8-C-0.67-T2	0.67	235	1015	3
HAN48-8-B-0.67-T1	0.67	250	1195	3.3
SHD36-8-C-0.67-T1	0.67	283	1050	2.6
SHD48-8-B-0.67-T1	0.67	306	1080	2.5
NCP48-8-B-0.83-T1	0.83	430	1120	1.8
NCP48-8-B-0.83-T2	0.83	368	825	1.6
SHD36-8-C-0.83-T1	0.83	323	1395	3
SHD48-8-B-0.83-T1	0.83	374	1640	3

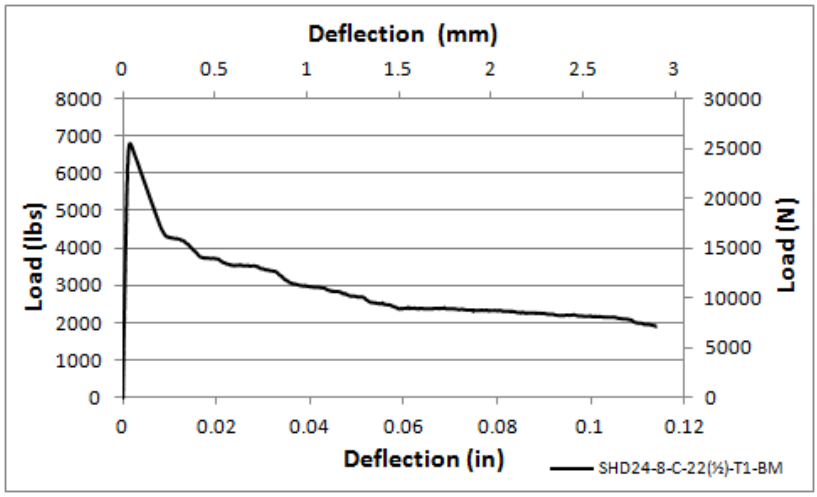

Figure D- 1 Deflection vs. Load graph for SHD-24-C-0.17-T1

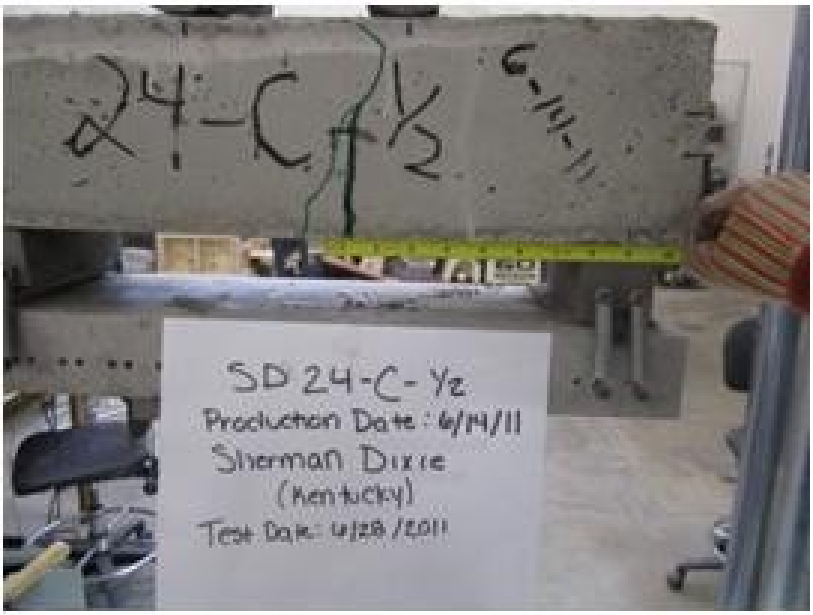

Figure D- 2 Crack pattern of SHD-24-C-0.17-T1

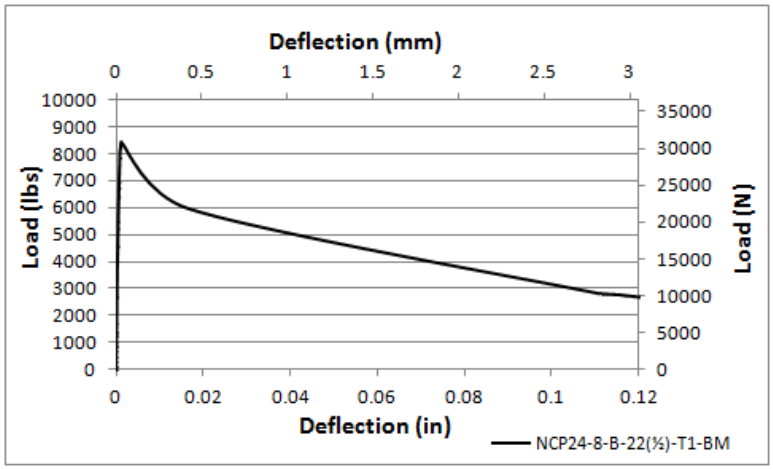

Figure D- 3 Deflection vs. Load graph for NCP-24-B-0.17-T1

Figure D- 4 Crack picture for NCP-24-B-0.17-T1

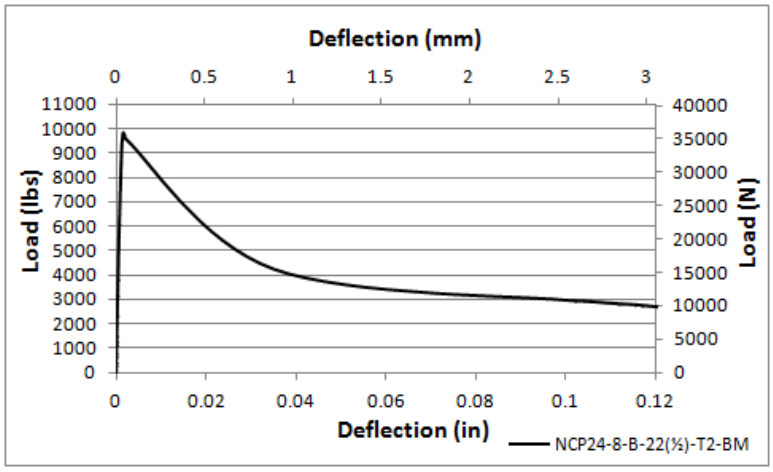

Figure D- 5 Deflection vs. Load graph for NCP-24-B-0.17-T2

Figure D- 6 Crack pattern for NCP-24-B-0.17-T2

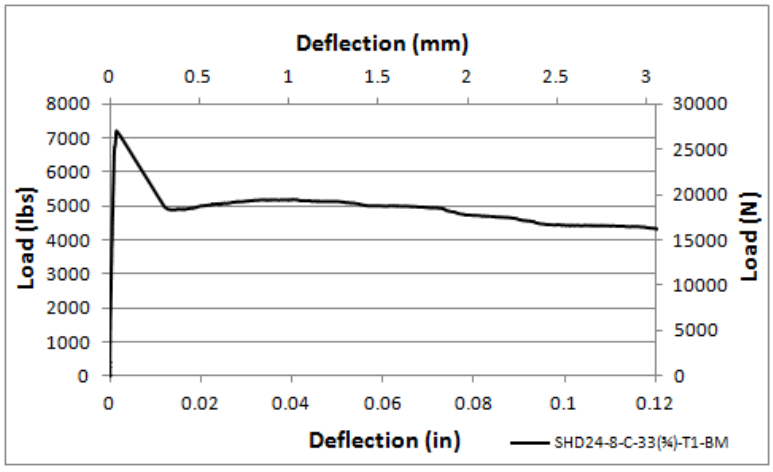

Figure D- 7 Deflection vs. Load graph for SHD-24-C-0.25-T1

Figure D- 8 Crack pattern of SHD-24-C-0.25-T1

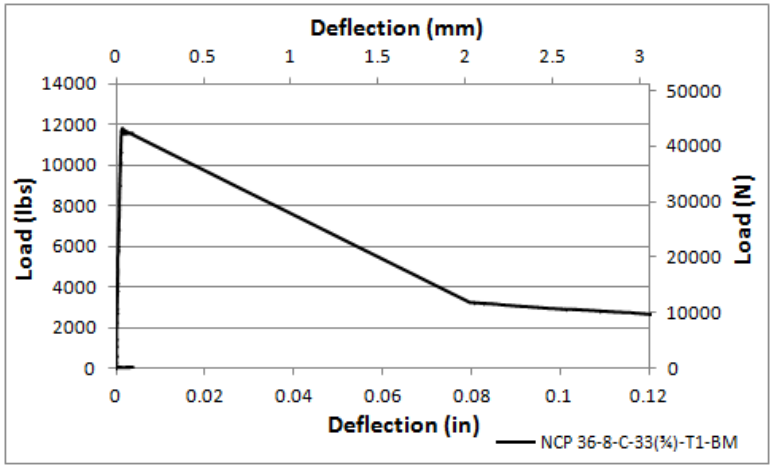

Figure D- 9 Deflection vs. Load graph for NCP-36-C-0.25-T1

Figure D- 10 Crack pattern for NCP-36-8-C-0.25-T1

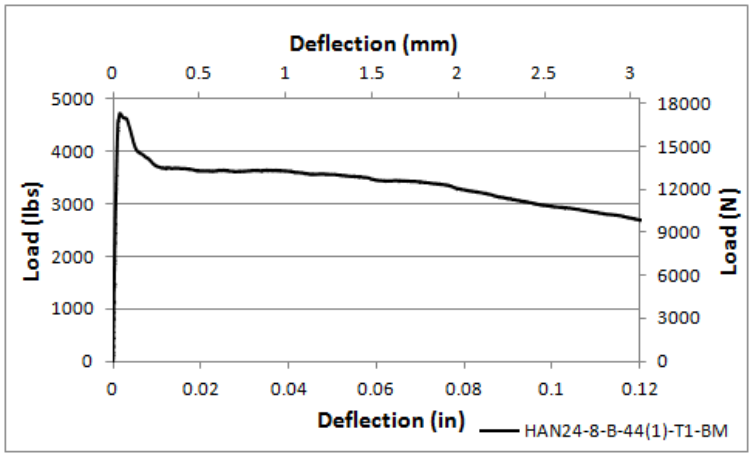

Figure D- 11 Deflection vs. Load graph for HAN-24-8-B-0.33-T1

Figure D- 12 Crack pattern of HAN-24-8-B-0.33-T1

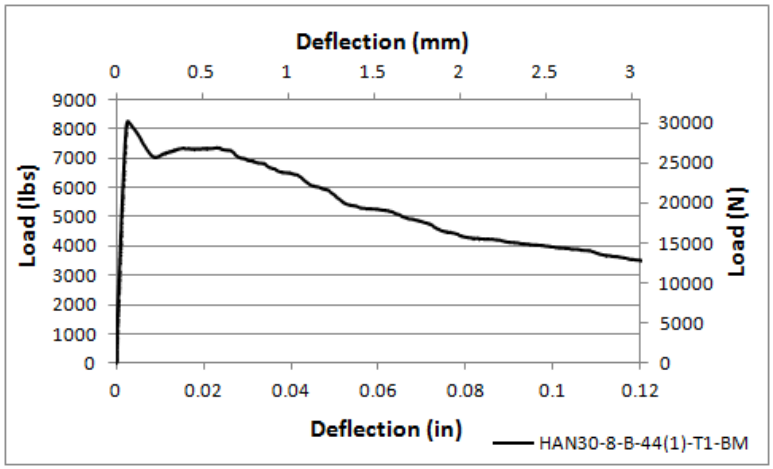

Figure D- 13 Deflection vs. Load graph for HAN-30-B-0.33-T1

Figure D- 14 Crack pattern of HAN-30-B-0.33-T1

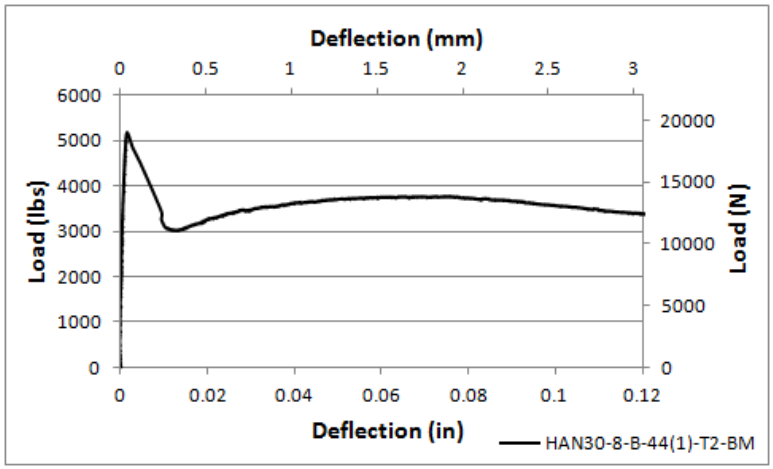

Figure D- 15 Deflection vs. Load graph for HAN-30-B-0.33-T2

Figure D- 16 Crack pattern of HAN-30-B-0.33-T2

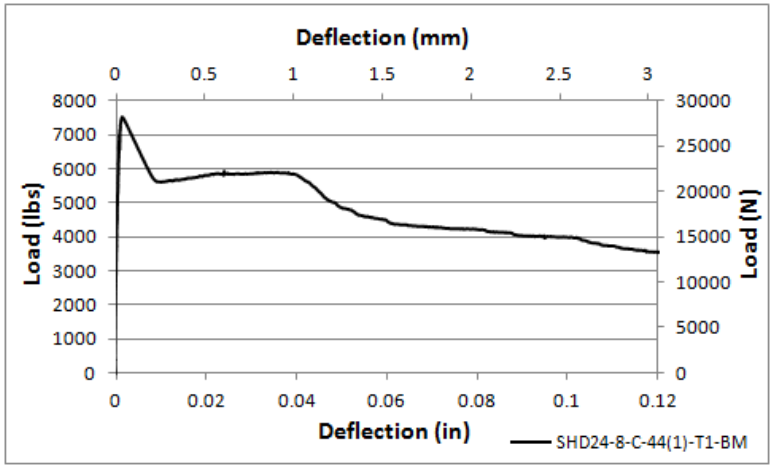

Figure D- 17 Deflection vs. Load graph for SHD-24-C-0.33-T1

Figure D- 18 Crack pattern of SHD-24-C-0.33-T1

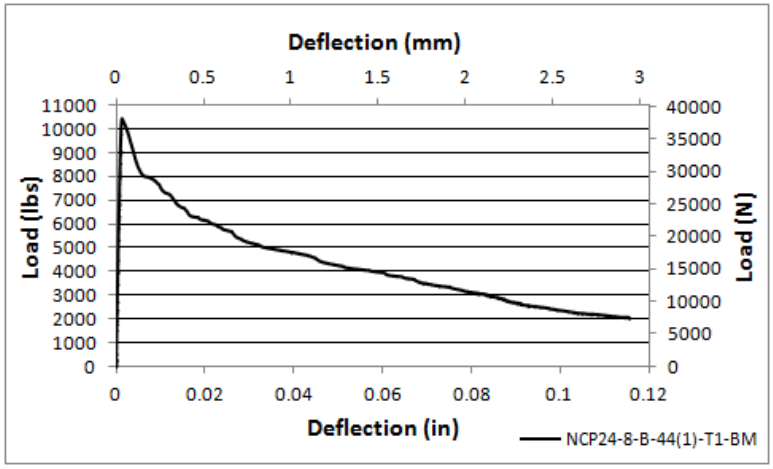

Figure D- 19 Deflection vs. Load graph for NCP-24-B-0.33-T1

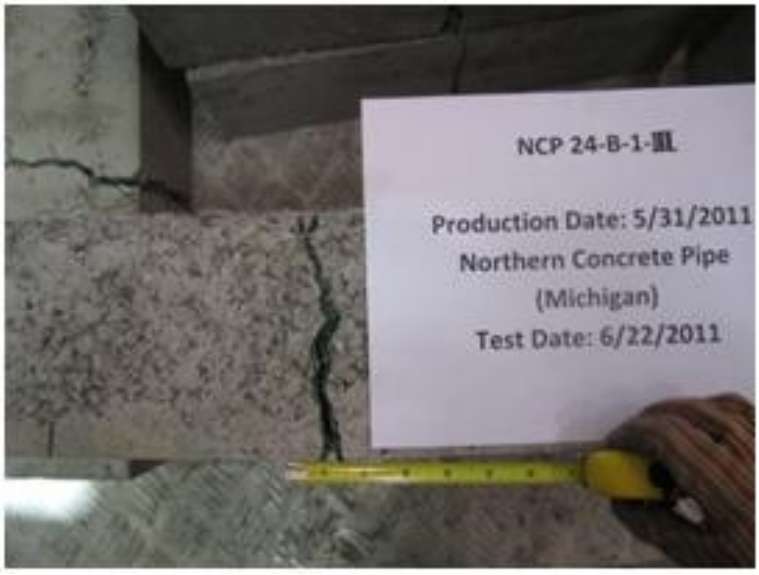

Figure D- 20 Crack pattern for NCP-24-B-0.33-T1

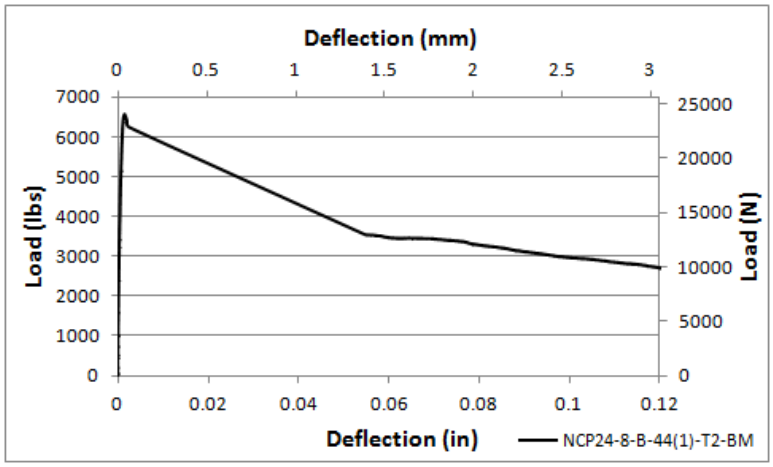

Figure D- 21 Deflection vs. Load graph for NCP24-8-B-0.33-T2-BM

Figure D- 22 Crack pattern for NCP24-8-B-0.33-T2-BM

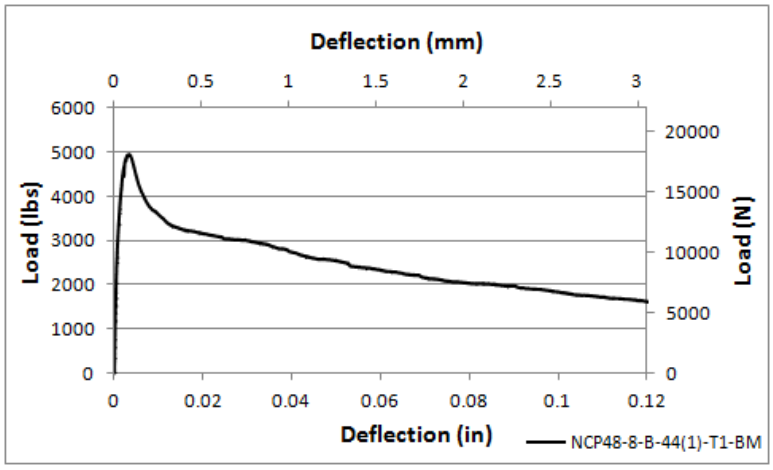

Figure D- 23 Deflection vs. Load graph for NCP48-8-B-0.33-T1-BM

Figure D- 24 Crack pattern for NCP48-8-B-0.33-T1-BM

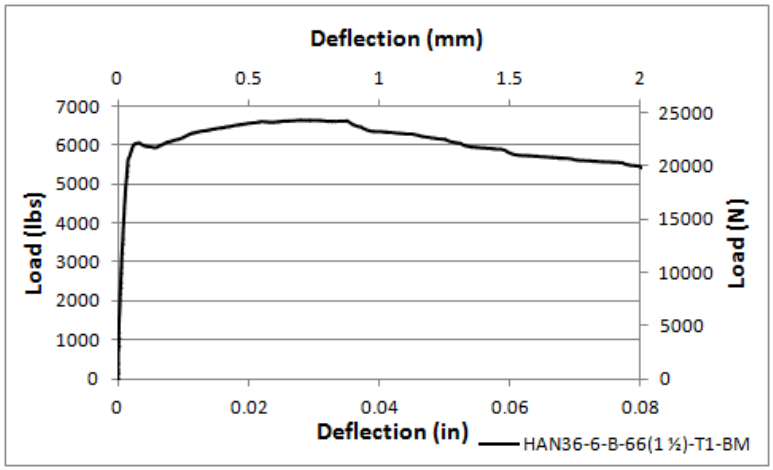

Figure D- 25 Deflection vs. Load graph for HAN36-6-B-0.5-T1-BM

Figure D- 26 Crack pattern of HAN36-6-B-0.5-T1-BM

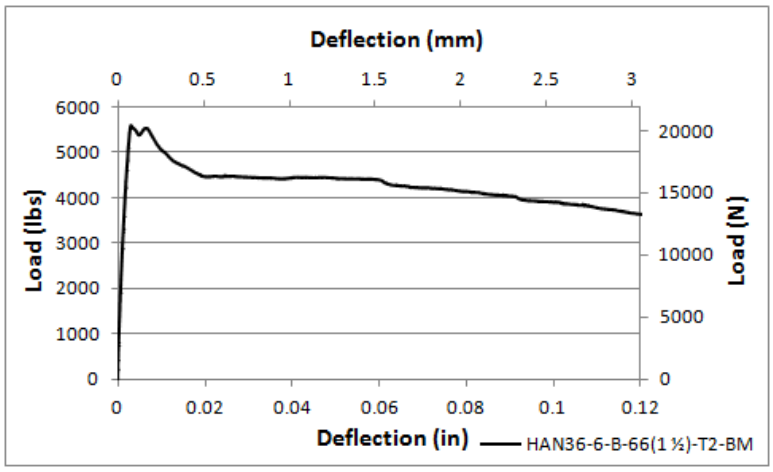

Figure D- 27 Deflection vs. Load graph for HAN36-6-B-0.5-T2-BM

Figure D- 28 Crack pattern of HAN36-6-B-0.5-T2-BM

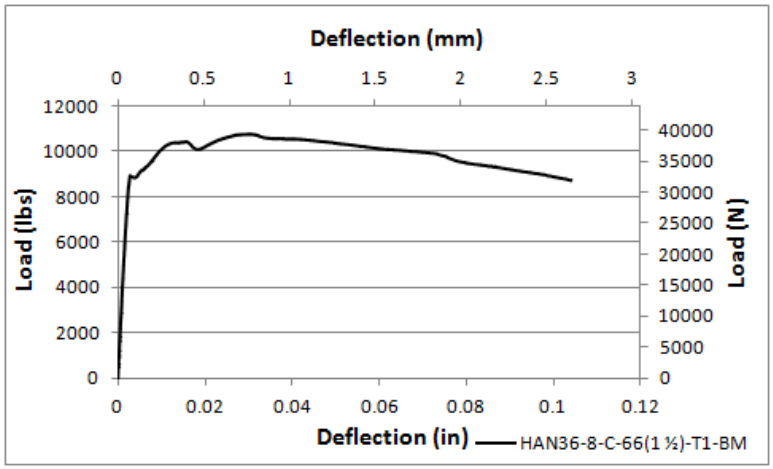

Figure D- 29 Deflection vs. Load graph for HAN36-8-C-0.5-T1-BM

Figure D- 30 Crack pattern of HAN36-8-C-0.5-T1-BM

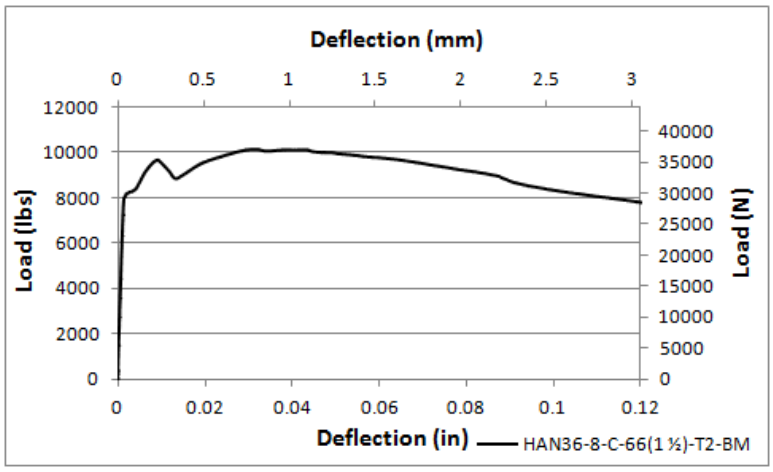

Figure D- 31 Deflection vs. Load graph for HAN36-8-C-0.5-T2-BM

Figure D- 32 Crack pattern of HAN36-8-C-0.5-T2-BM

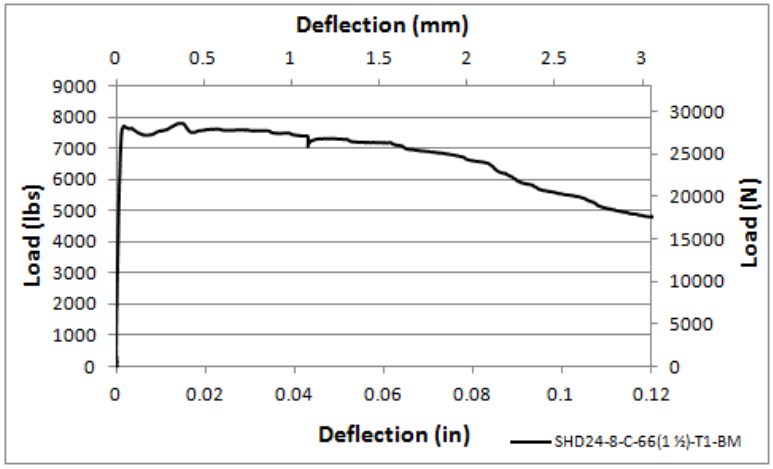

Figure D- 33 Deflection vs. Load graph for SHD24-8-C-0.5-T1-BM

Figure D- 34 Crack pattern for SHD24-8-C-0.5-T1-BM

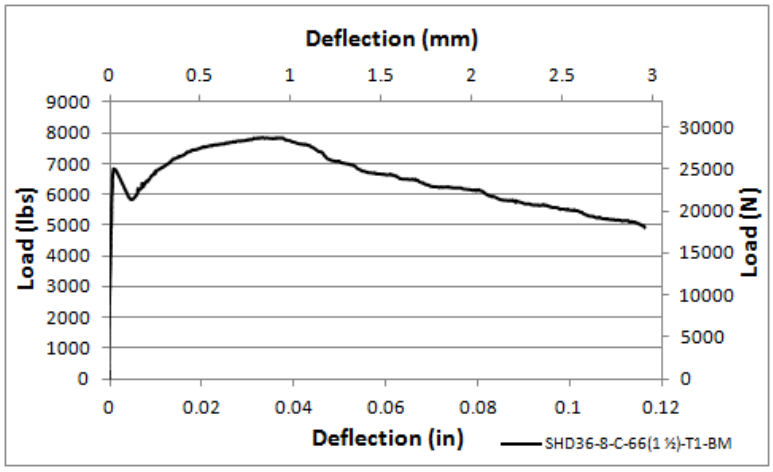

Figure D- 35 Deflection vs. Load graph for SHD36-8-C-0.5-T1-BM

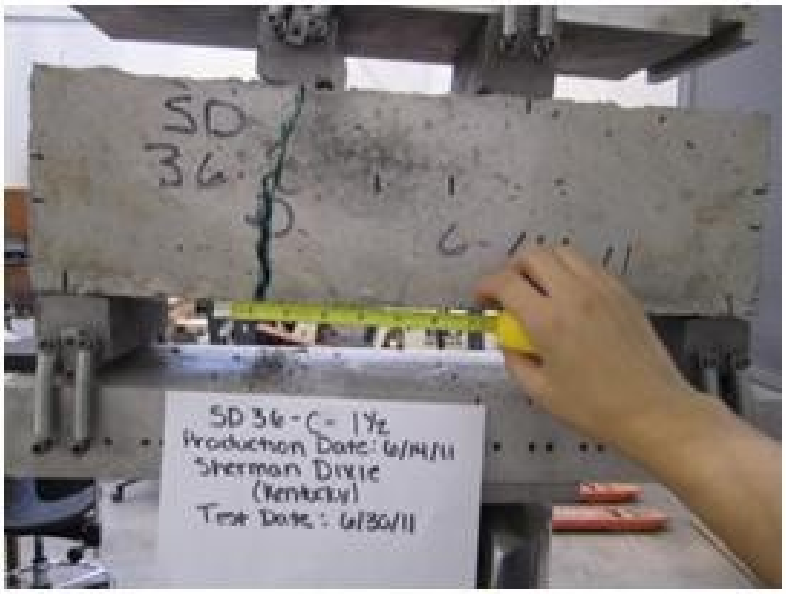

Figure D- 36 Crack pattern for SHD36-8-C-0.5-T1-BM

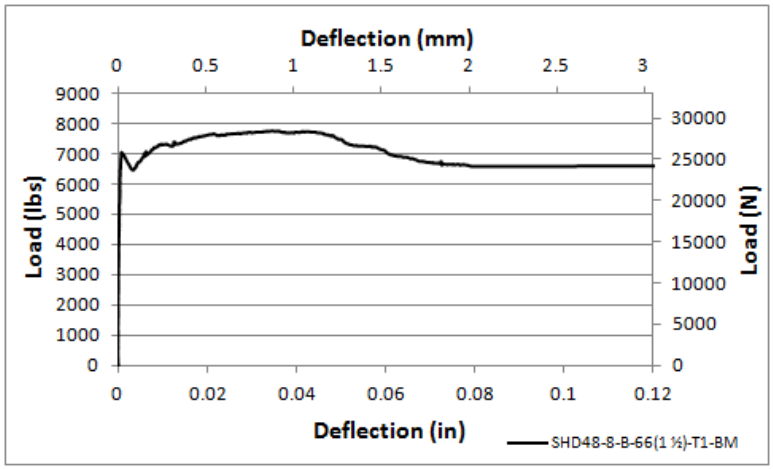

Figure D- 37 Deflection vs. Load graph for SHD48-8-B-0.5-T1-BM

Figure D- 38 Crack pattern for SHD48-8-B-0.5-T1-BM

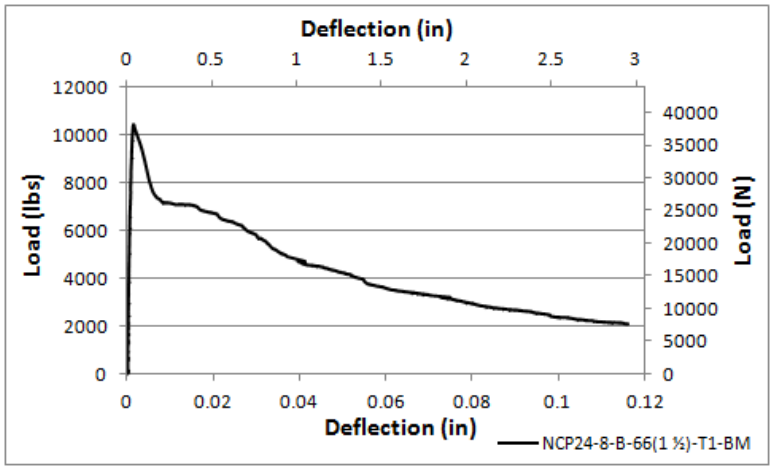

Figure D- 39 Deflection vs. Load graphs for NCP24-8-B-0.5-T1-BM

Figure D- 40 Crack pattern for NCP24-8-B-0.5-T1-BM

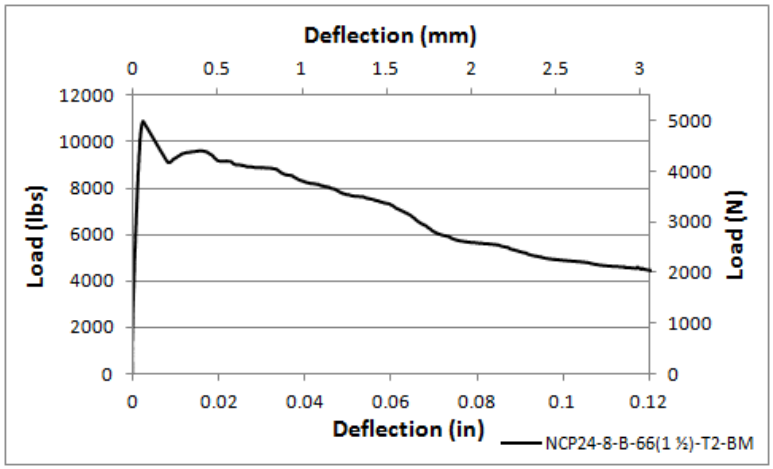

Figure D- 41 Deflection vs. Load graph for NCP24-8-B-0.5-T2-BM

Figure D- 42 Crack pattern for NCP24-8-B-0.5-T2-BM

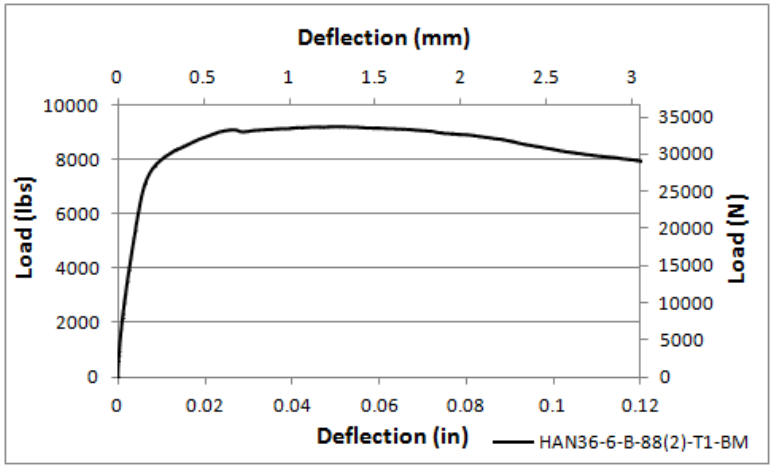

Figure D- 43 Deflection vs. Load graph for HAN36-6-B-0.67-T1-BM

Figure D- 44 Crack pattern of HAN36-6-B-0.67-T1-BM

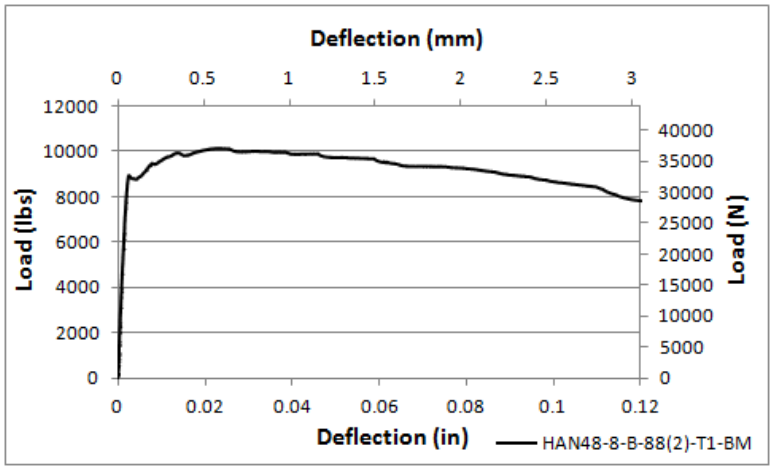

Figure D- 45 Deflection vs. Load graph for HAN48-8-B-0.67-T1-BM

Figure D- 46 Crack pattern of HAN48-8-B-0.67-T1-BM

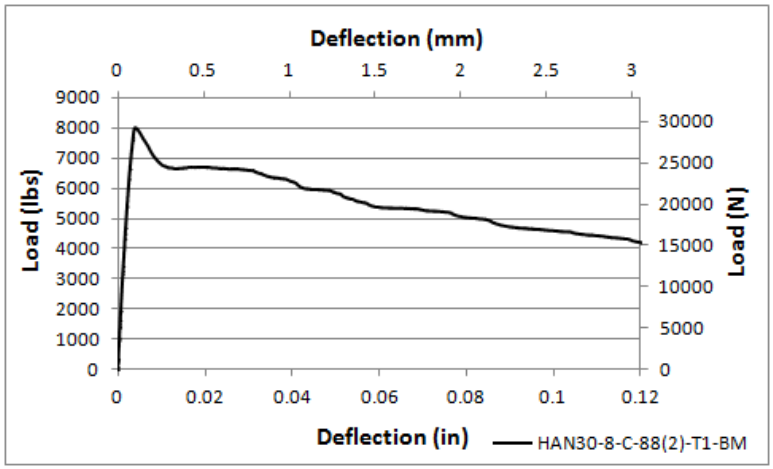

Figure D- 47 Deflection vs. Load graph for HAN30-8-C-0.67-T1-BM

Figure D- 48 Crack pattern of HAN30-8-C-0.67-T1-BM

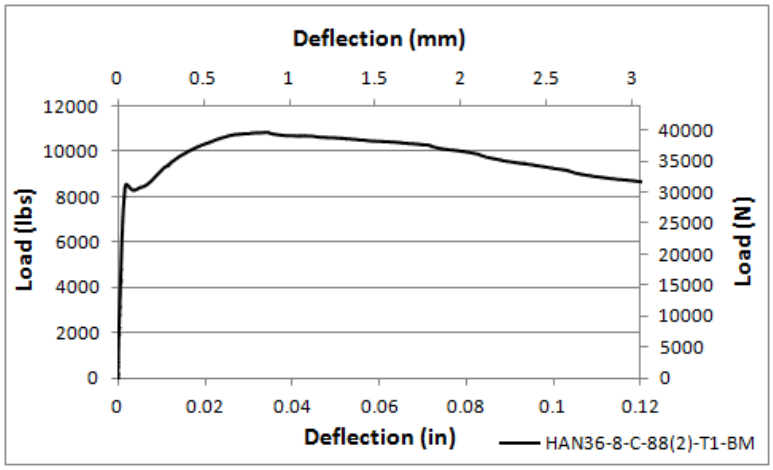

Figure D- 49 Deflection vs. Load graph for HAN36-8-C-0.67-T1-BM

Figure D- 50 Crack pattern of HAN36-8-C-0.67-T1-BM

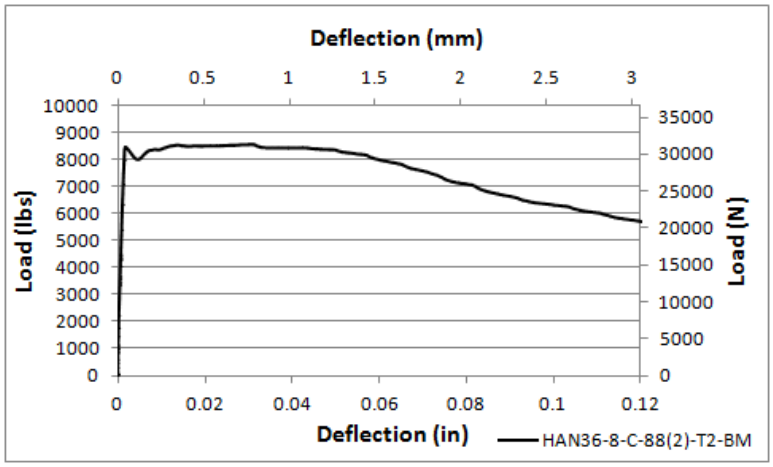

Figure D- 51 Deflection vs. Load graph for HAN36-8-C-0.67-T2-BM

Figure D- 52 Crack pattern of HAN36-8-C-0.67-T2-BM

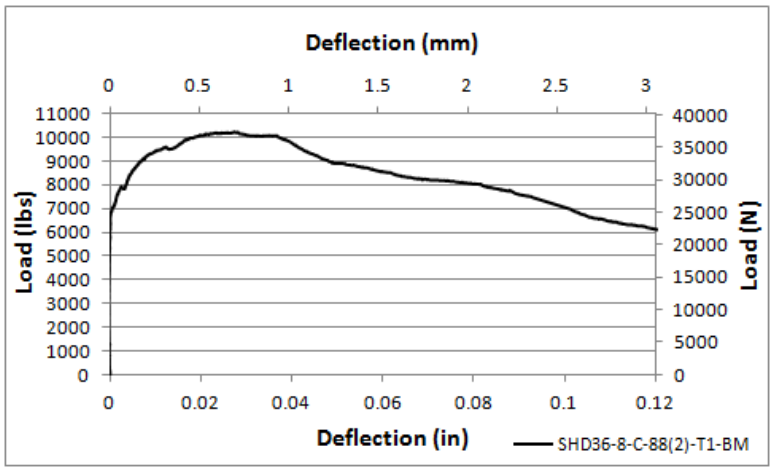

Figure D- 53 Deflection vs. Load graph for SHD36-8-C-0.67-T1-BM

Figure D- 54 Crack pattern for SHD36-8-C-0.67-T1-BM

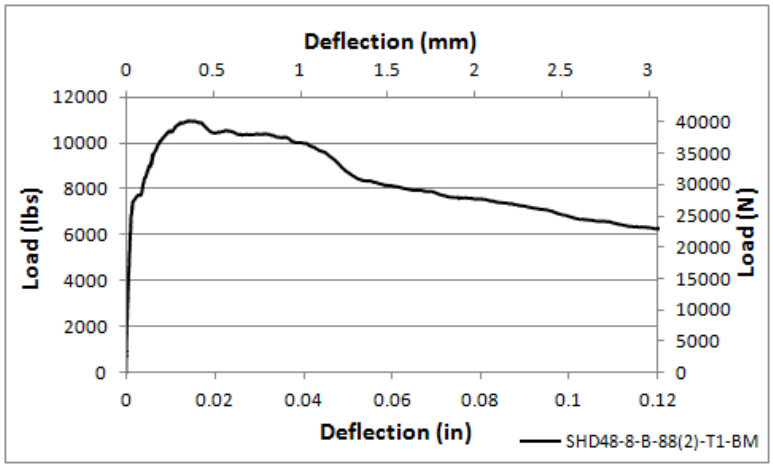

Figure D- 55 Deflection vs. Load graph for SHD48-8-B-0.67-T1-BM

Figure D- 56 Crack pattern for SHD48-8-B-0.67-T1-BM

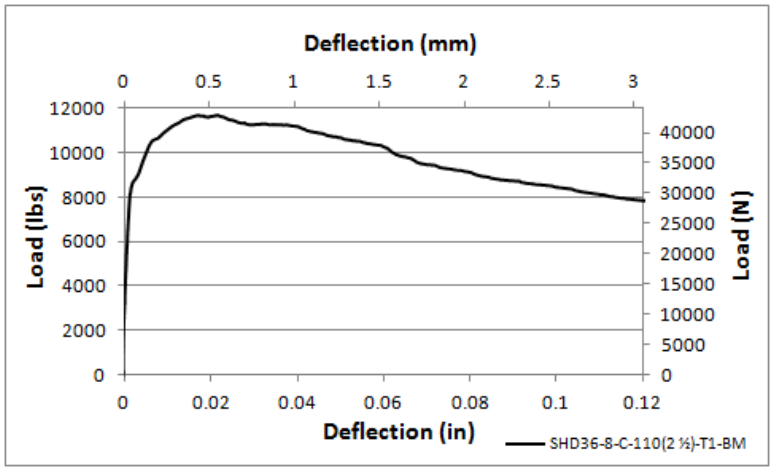

Figure D- 57 Deflection vs. Load graph for SHD 36-8-C-0.83-T1-BM

Figure D- 58 Crack pattern for SHD 36-8-C-0.83-T1-BM

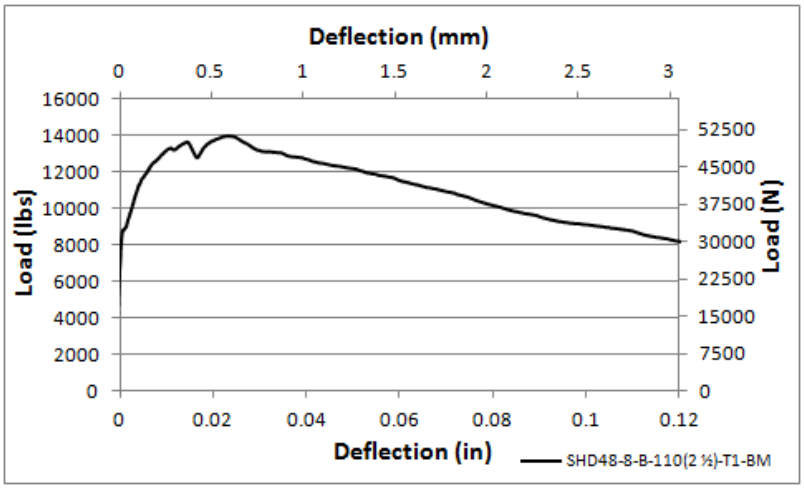

Figure D- 59 Deflection vs. Load graph for SHD48-8-B-0.83-T1-BM

Figure D- 60 Crack pattern for SHD48-8-B-0.83-T1-BM

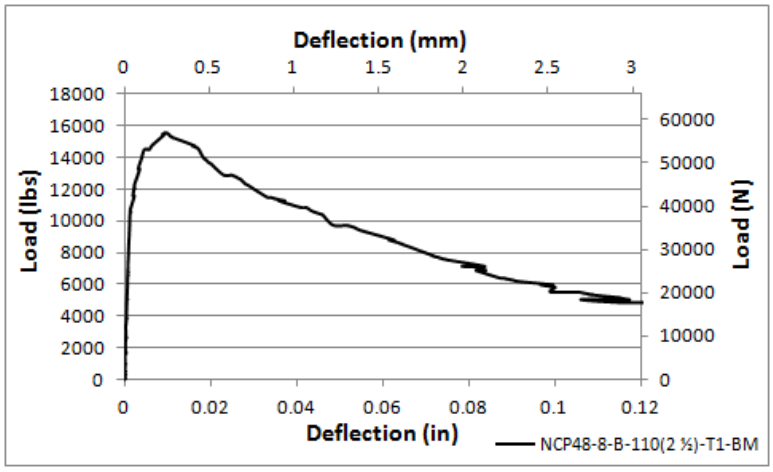

Figure D- 61 Deflection vs. Load graph for NCP48-8-B-0.83-T1-BM

Figure D- 62 Crack pattern for NCP48-8-B-0.83-T1-BM

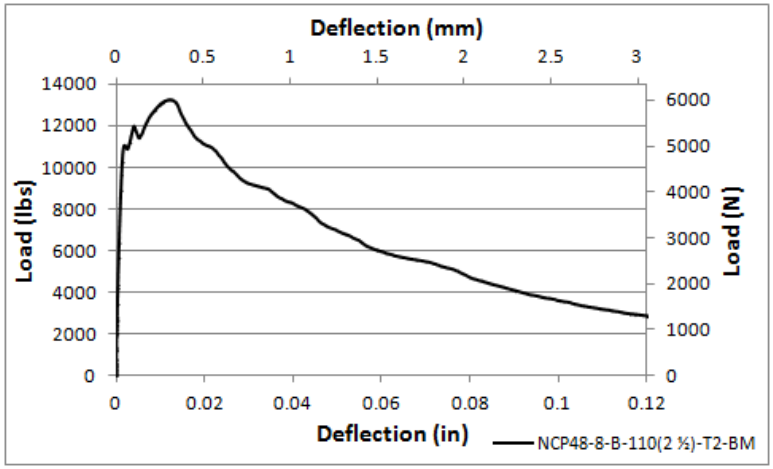

Figure D- 63 Deflection vs. Load graph for NCP48-8-B-0.83-T2-BM

Figure D- 64 Crack pattern for NCP48-8-B-0.83-T2-BM

Appendix E

Results of Direct Tension Testing

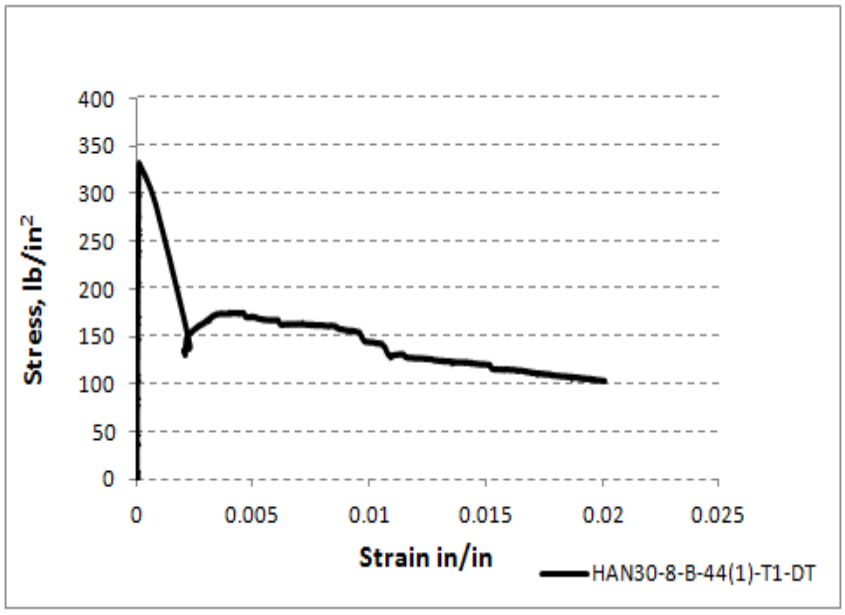

Figure E- 1 Strain-Stress diagram for HAN30-8-B-44(1)-T1-DT

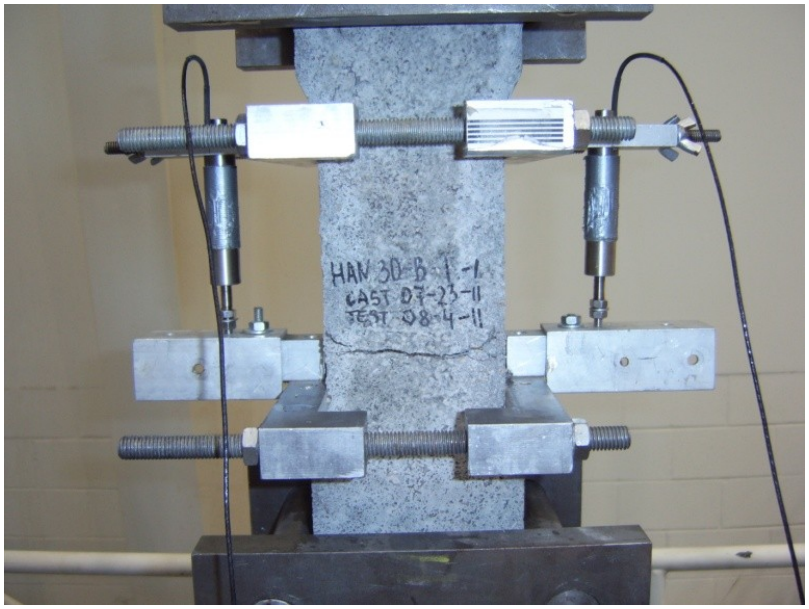

Figure E- 2 Crack formation of HAN30-8-B-44(1)-T1-DT

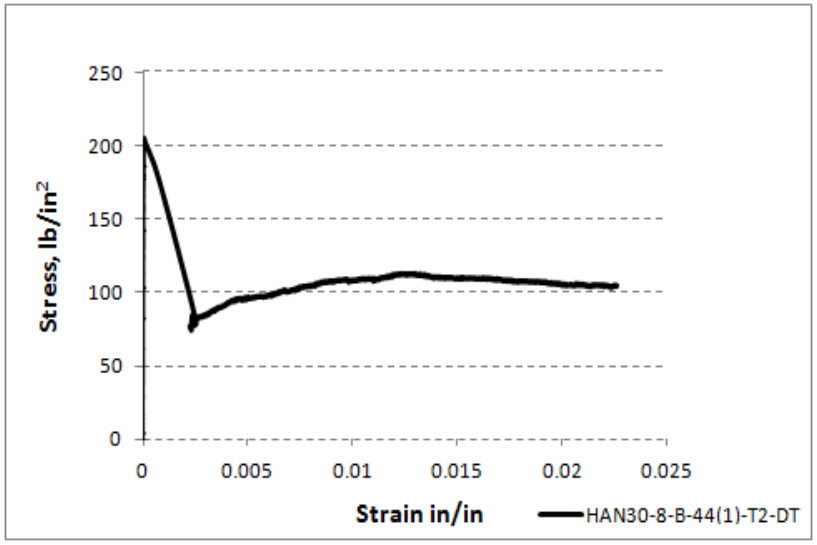

Figure E- 3 Strain-Stress diagram for HAN30-8-B-44(1)-T2-DT

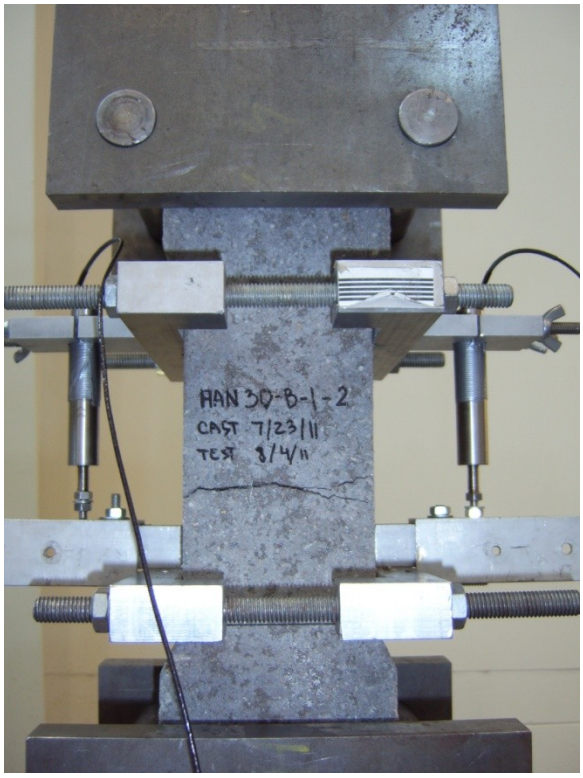

Figure E- 4 Crack formation of HAN30-8-B-44(1)-T2-DT

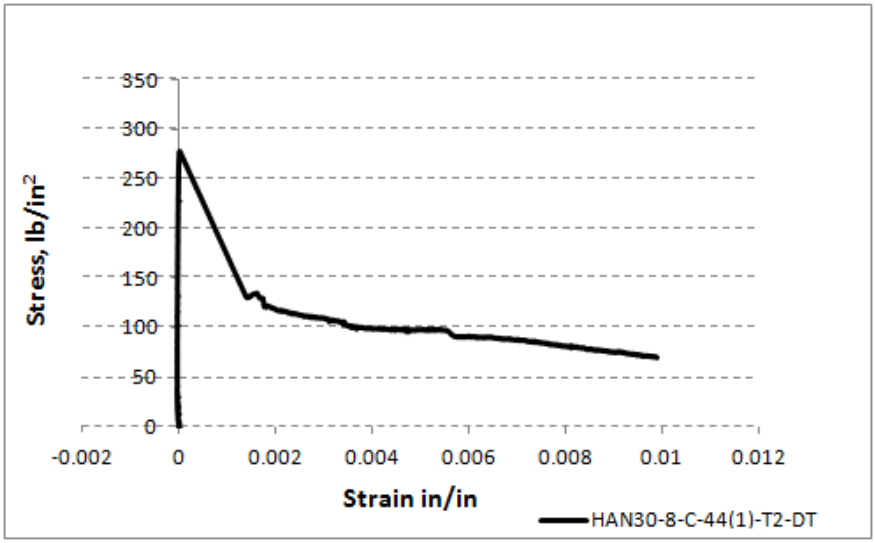

Figure E- 5 Strain-Stress diagram for HAN30-8-C-44(1)-T2-DT

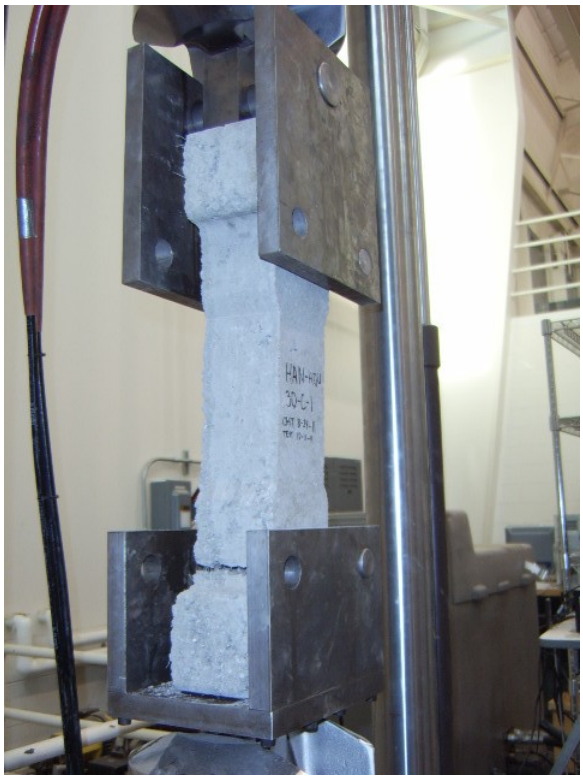

Figure E- 6 Crack formation of HAN30-8-C-44(1)-T2-DT

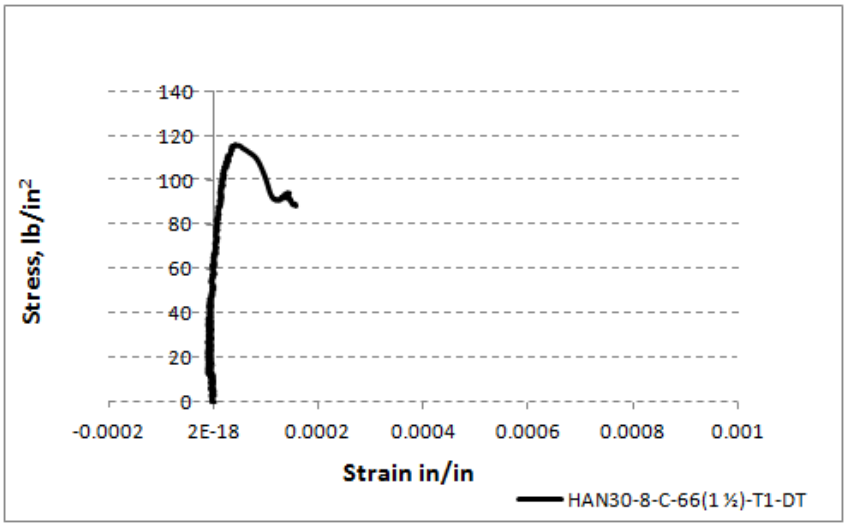

Figure E- 7 Strain-Stress diagram for HAN30-8-C-66(1 ½)-T1-DT

Figure E- 8 Crack formation of HAN30-8-C-66(1 ½)-T1-DT

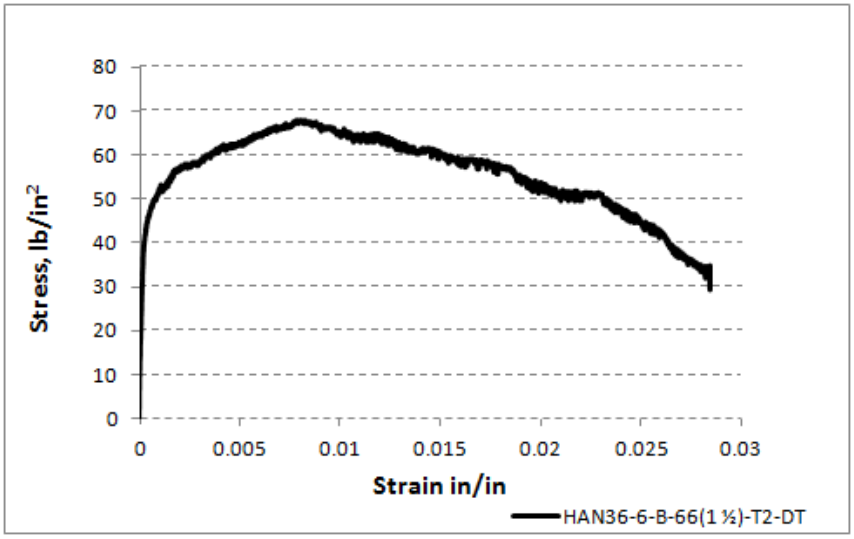

Figure E- 9 Strain-Stress diagram for HAN36-6-B-66(1 ½)-T2-DT

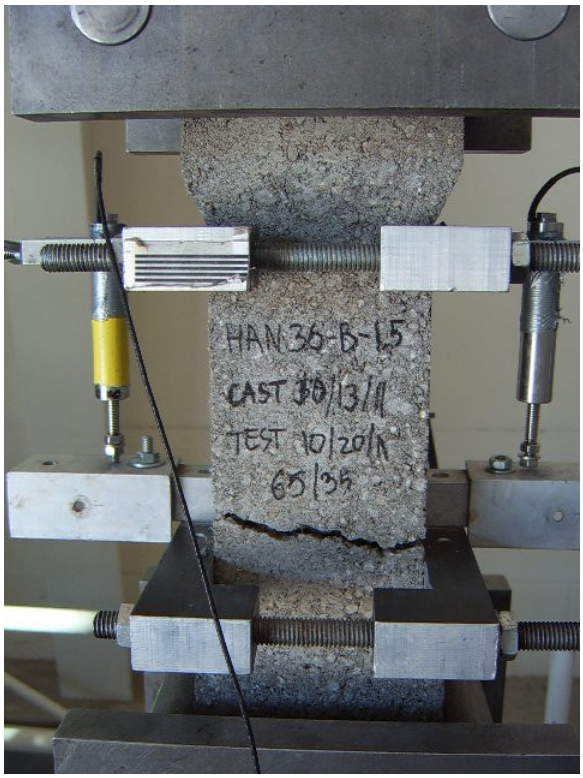

Figure E- 10 Crack formation of HAN36-6-B-66(1 ½)-T2-DT

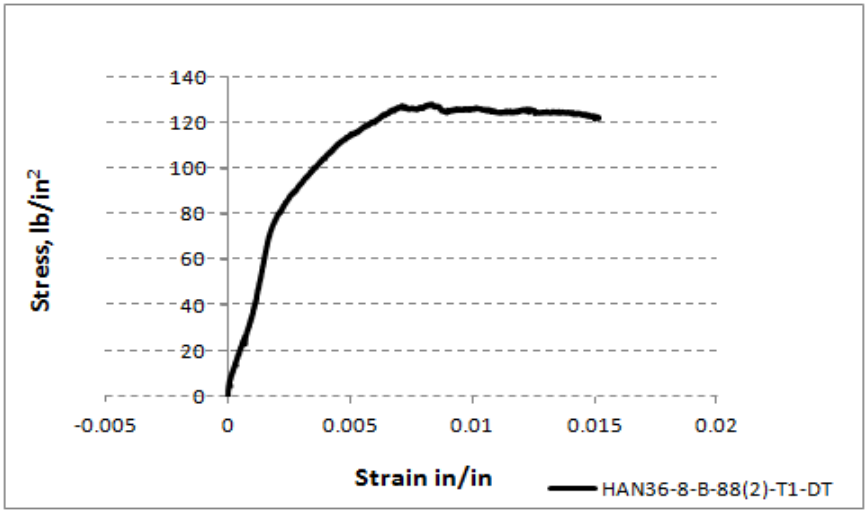

Figure E- 11 Strain-Stress diagram for HAN36-8-B-88(2)-T1-DT

Figure E- 12 Crack formation of HAN36-8-B-88(2)-T1-DT

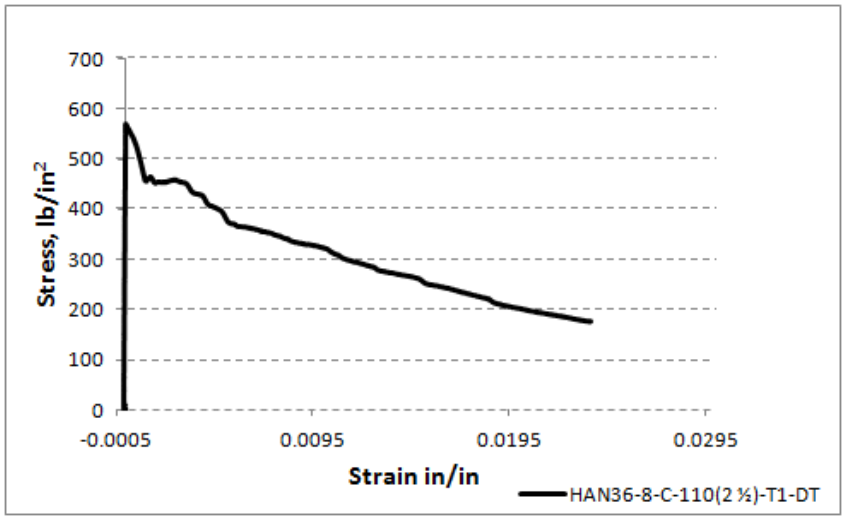

Figure E- 13 Strain-Stress diagram for HAN36-8-C-110(2 ½)-T1-DT

Figure E- 14 Crack formation of HAN36-8-C-110(2 ½)-T1-DT

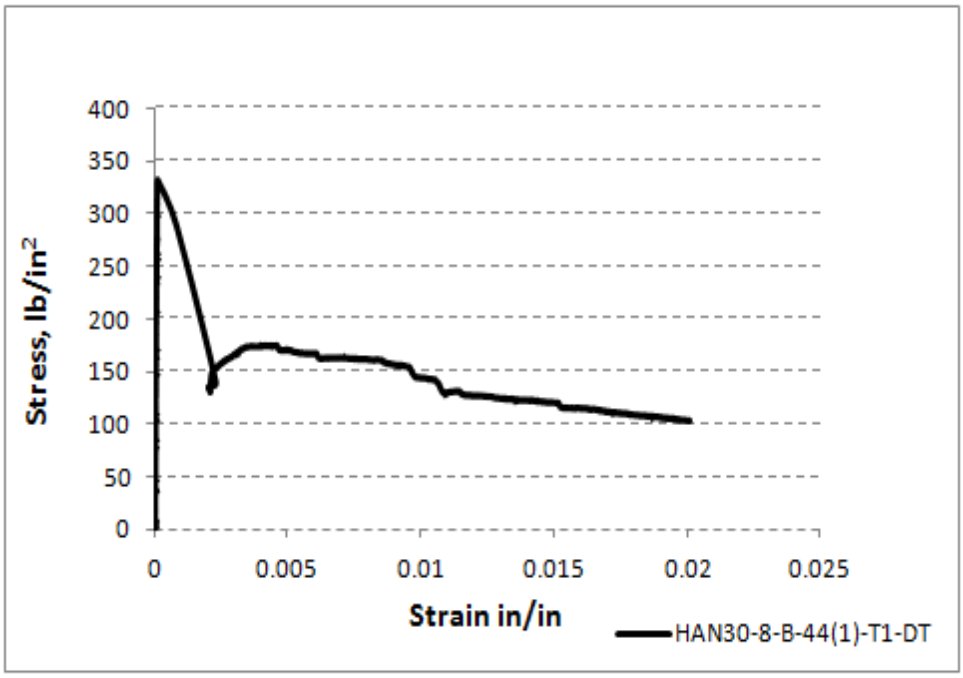

Figure E- 15 Direct Tension Results for HAN30-8-B-44(1)-T1-DT

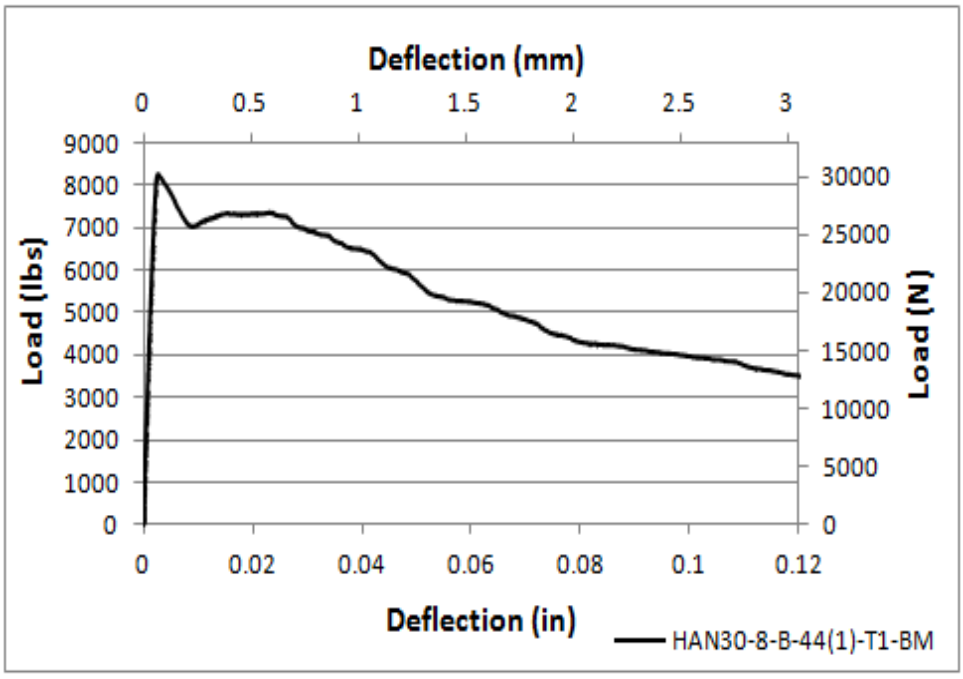

Figure E- 16 Beam Results for HAN30-8-B-44(1)-T1-BM

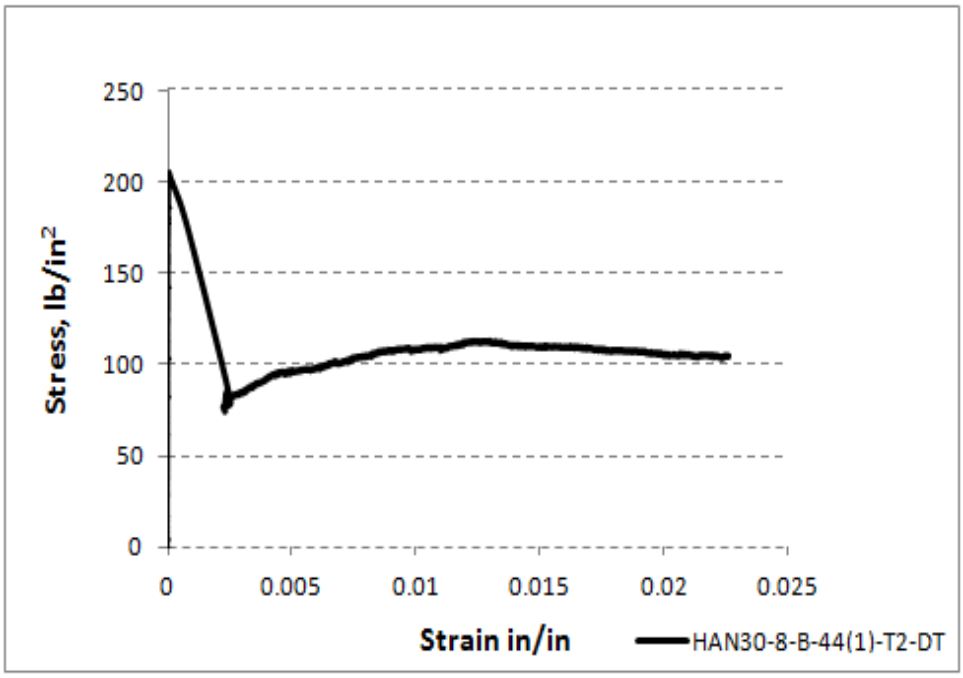

Figure E- 17 Direct Tension Results for HAN30-8-B-44(1)-T2-DT

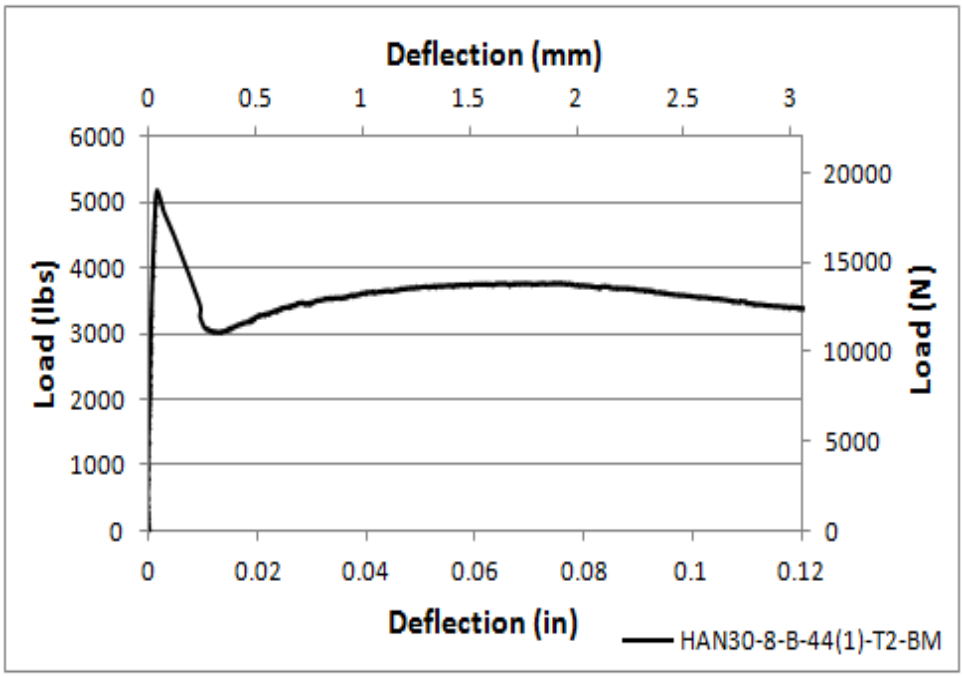

Figure E- 18 Beam Results for HAN30-8-B-44(1)-T2-BM

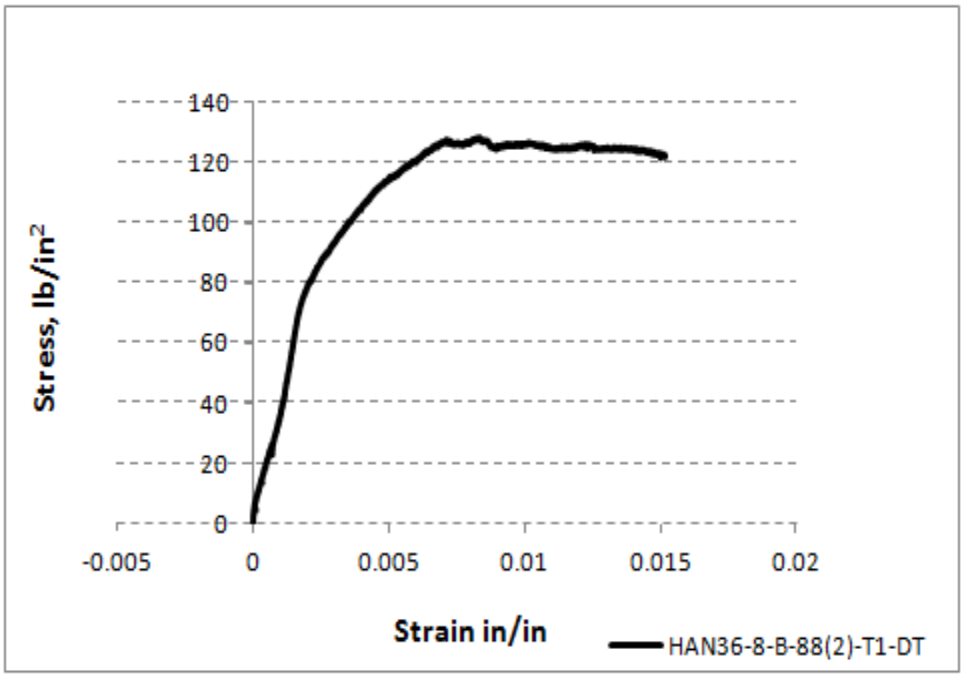

Figure E- 19 Direct Tension Results for HAN36-8-B-88(2)-T1-DT

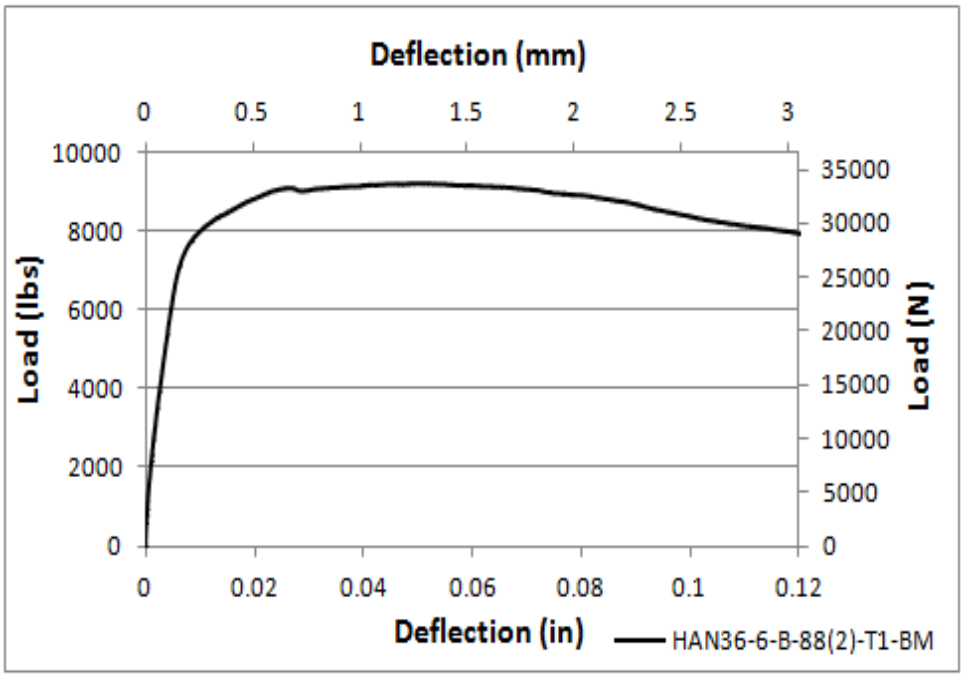

Figure E- 20 Beam Results for HAN36-6-B-88(2)-T1-BM

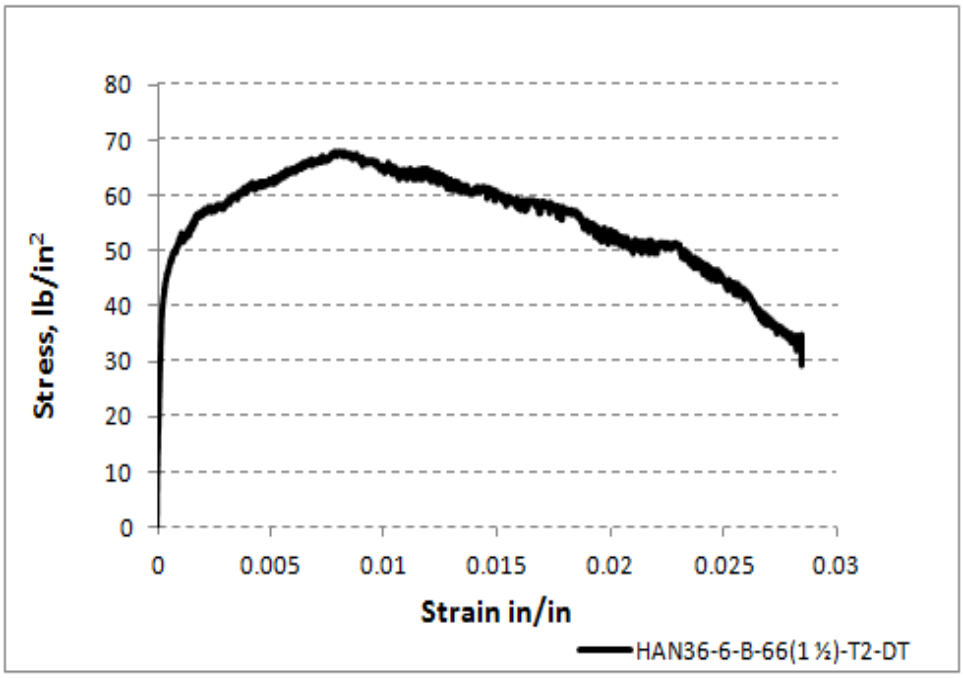

Figure E- 21 Direct Tension Results for HAN36-6-B-66(1 ½)-T2-DT

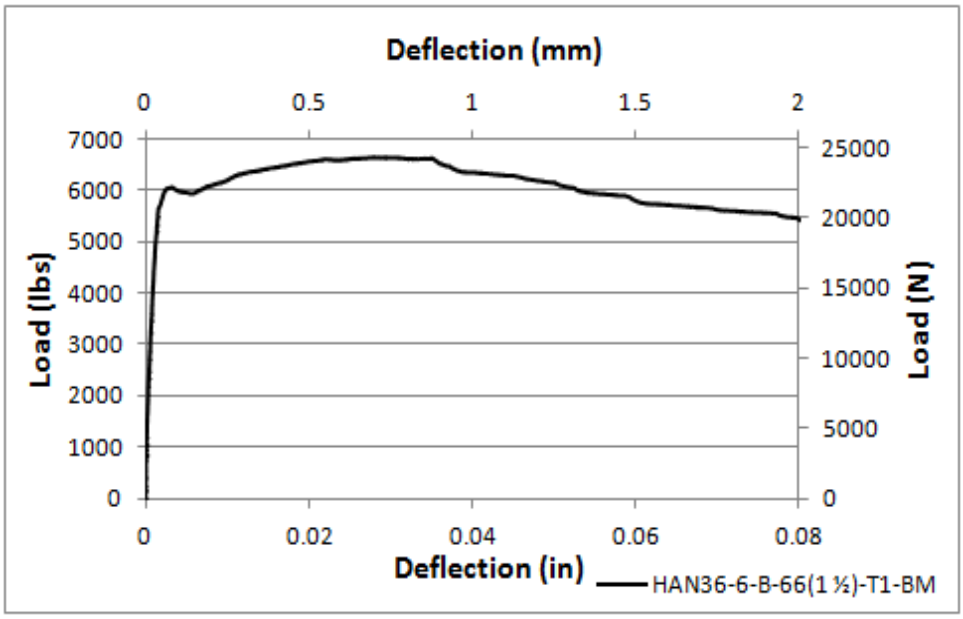

Figure E- 22 Beam Results for HAN36-6-B-66(1 ½)-T1-BM

Appendix F

Comparison of Predicted Load-Deformations Obtained with Finite Element Method and an Average of Experimental Test Results in Steel Fiber Reinforced Concrete Pipes

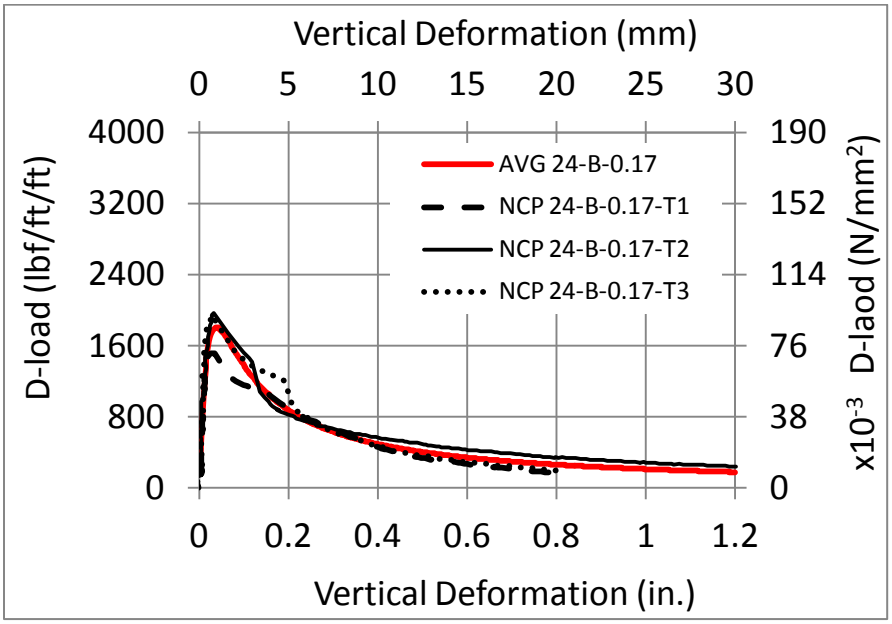

(a)

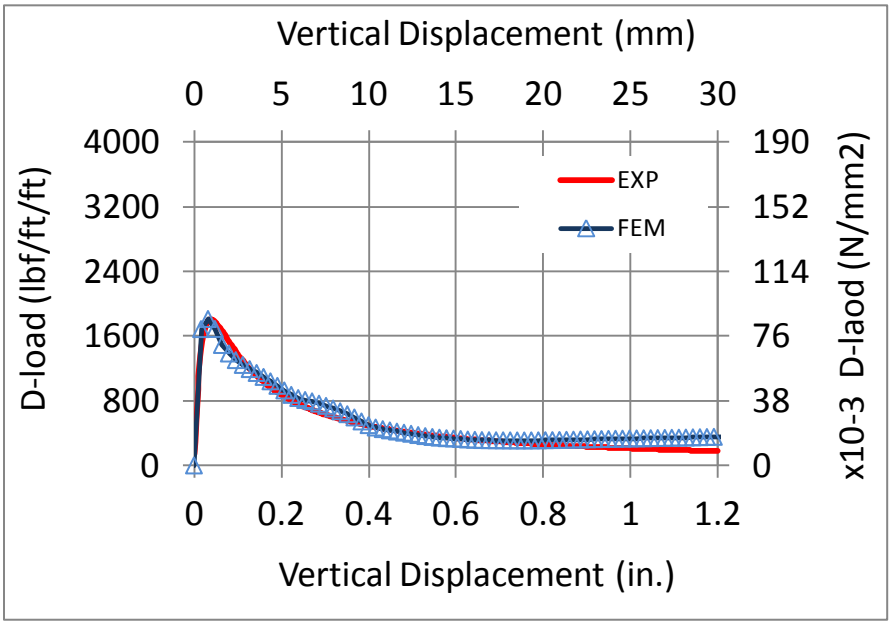

(b)

Figure F- 1 Load-deformation relationship (a) experimental average (b) FEM match to experimental average for 24-C-0.17-II SFRCP

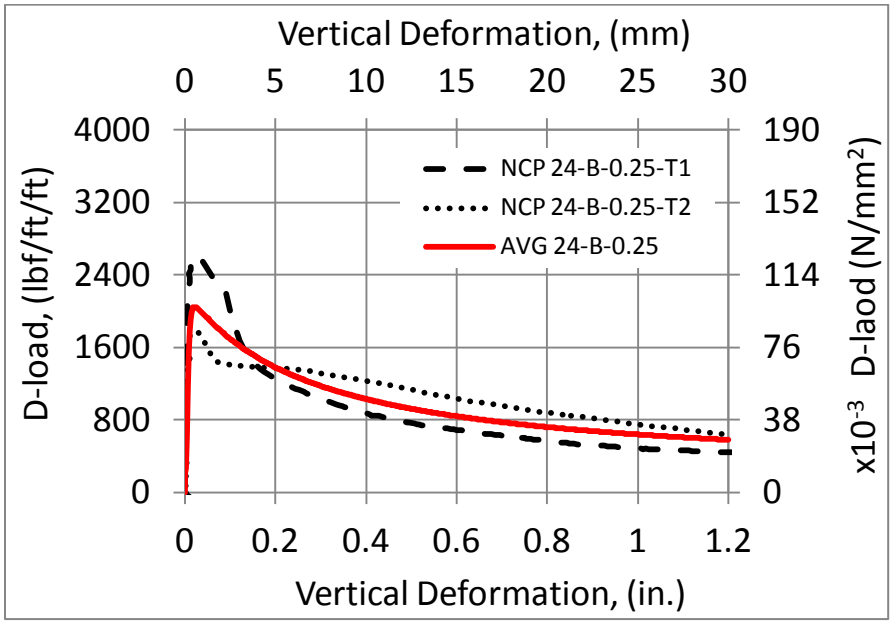

(a)

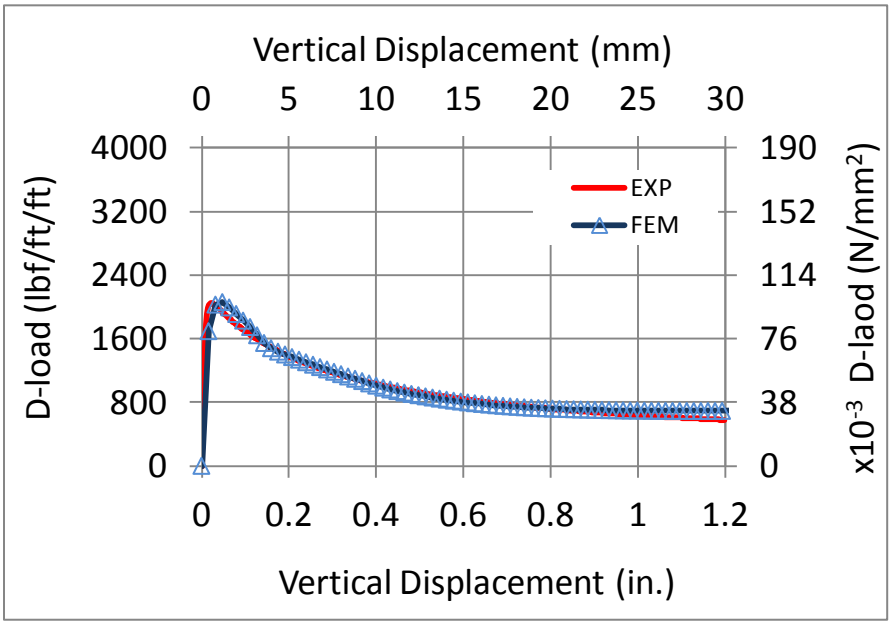

(b)

Figure F- 2 Load-deformation relationship (a) experimental average (b) FEM match to experimental average for 24-B-0.25-III SFRCP

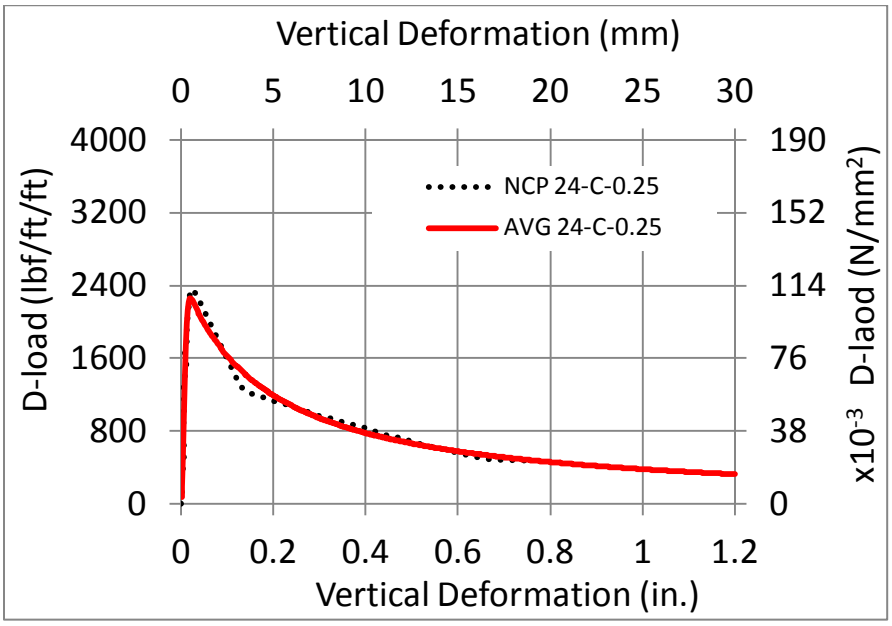

(a)

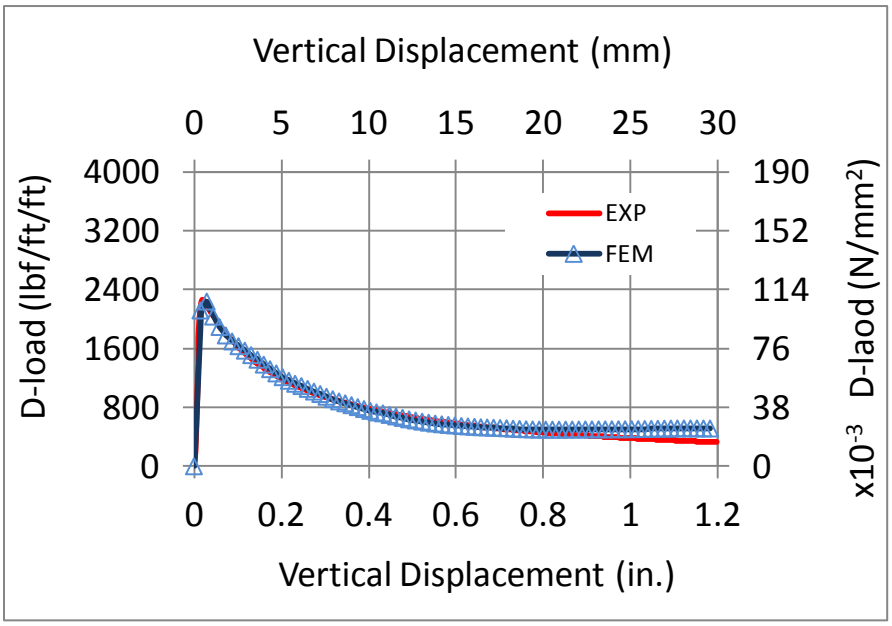

(b)

Figure F- 3 Load-deformation relationship (a) experimental average (b) FEM match to experimental average for 24-C-0.25-III SFRCP

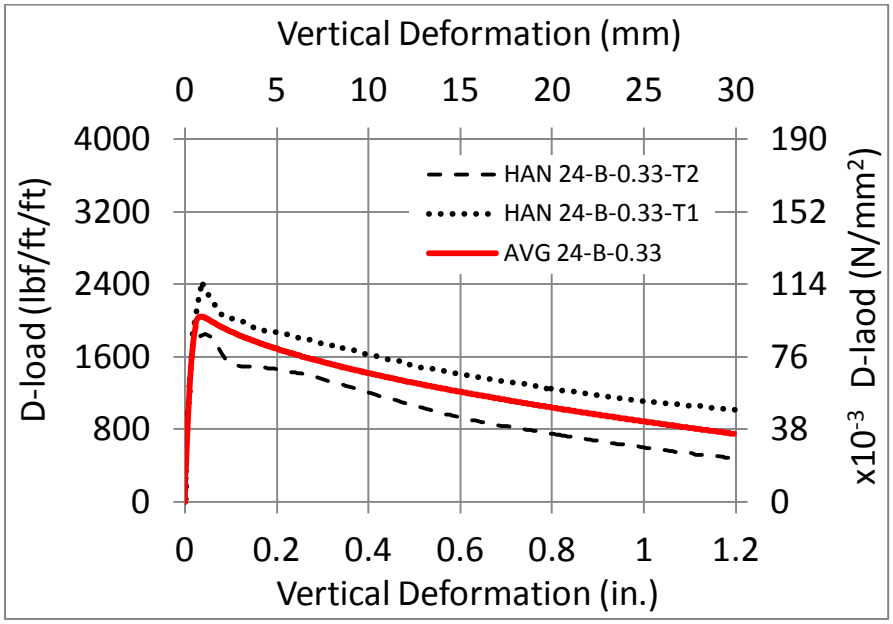

(a)

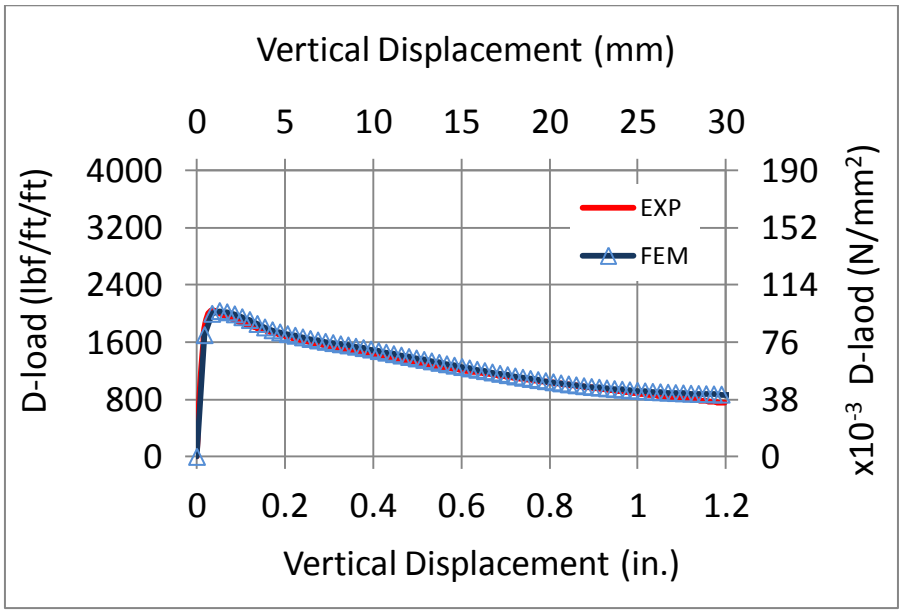

(b)

Figure F- 4 Load-deformation relationship (a) experimental average (b) FEM match to experimental average for 24-B-0.33-III SFRCP

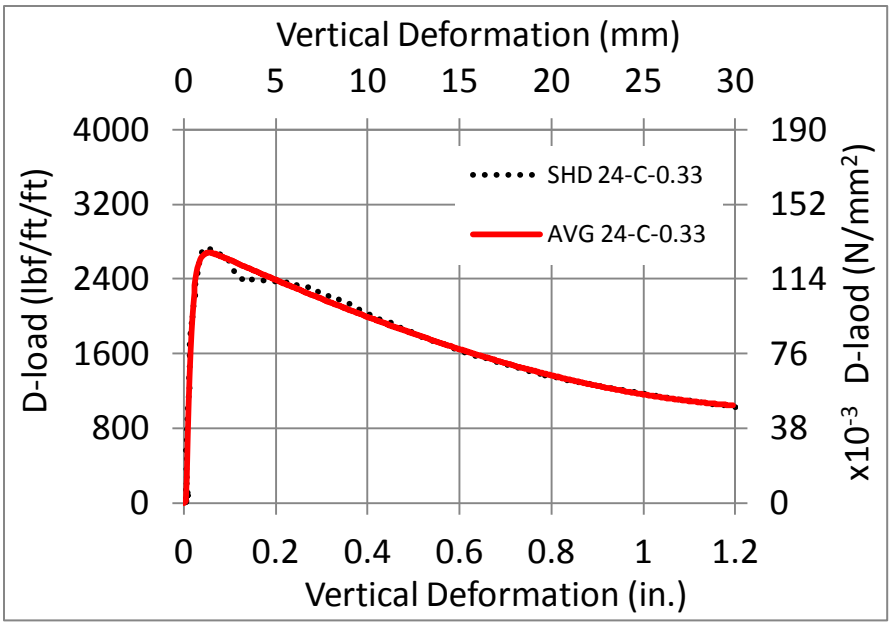

(a)

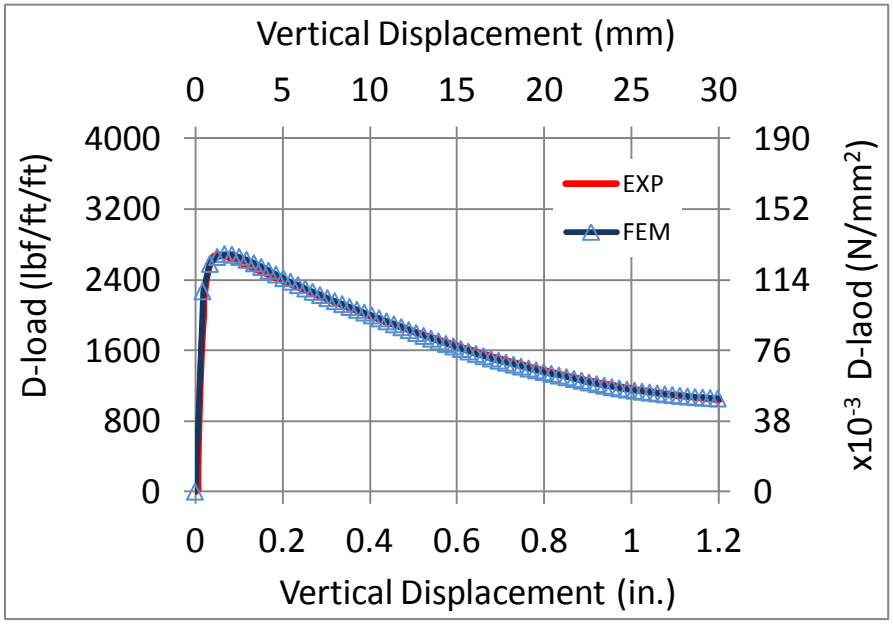

(b)

Figure F- 5 Load-deformation relationship (a) experimental average (b) FEM match to experimental average for 24-C-0.33-III SFRCP

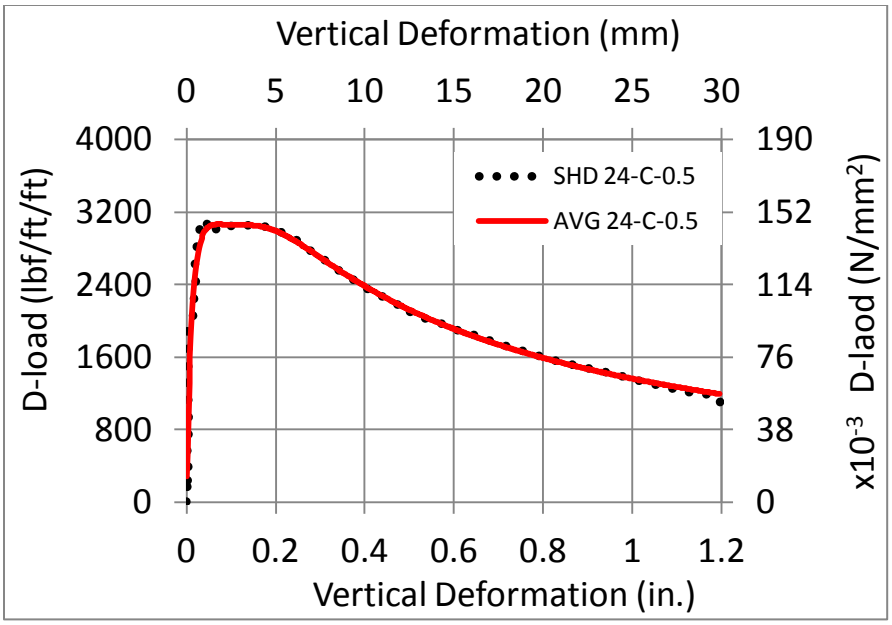

(a)

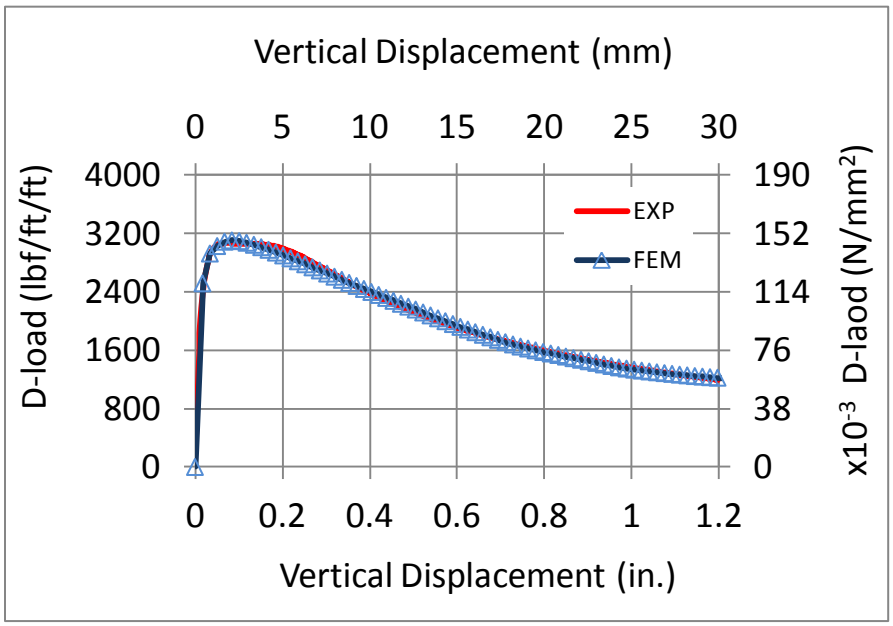

(b)

Figure F- 6 Load-deformation relationship (a) experimental average (b) FEM match to experimental average for 24-C-0.50-IV SFRCP

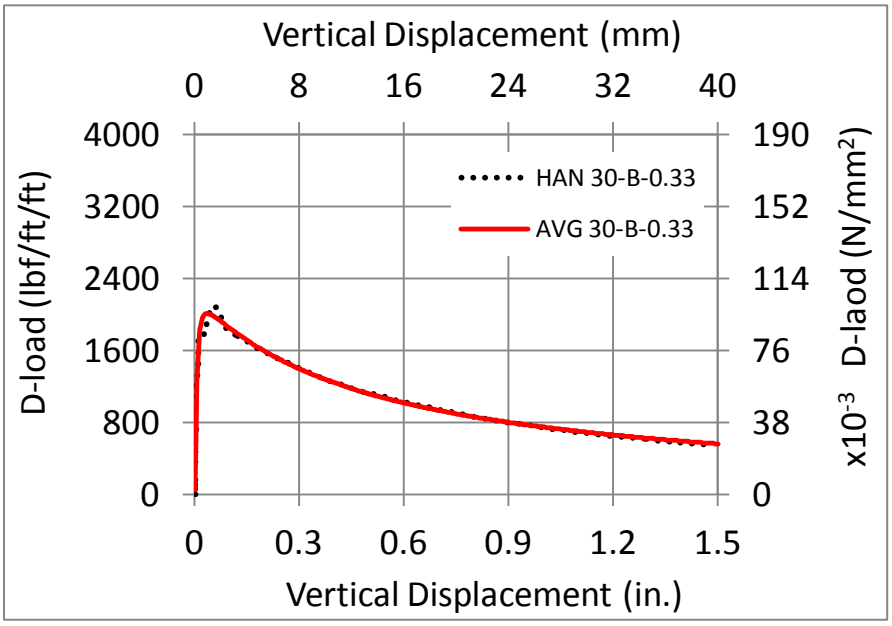

(a)

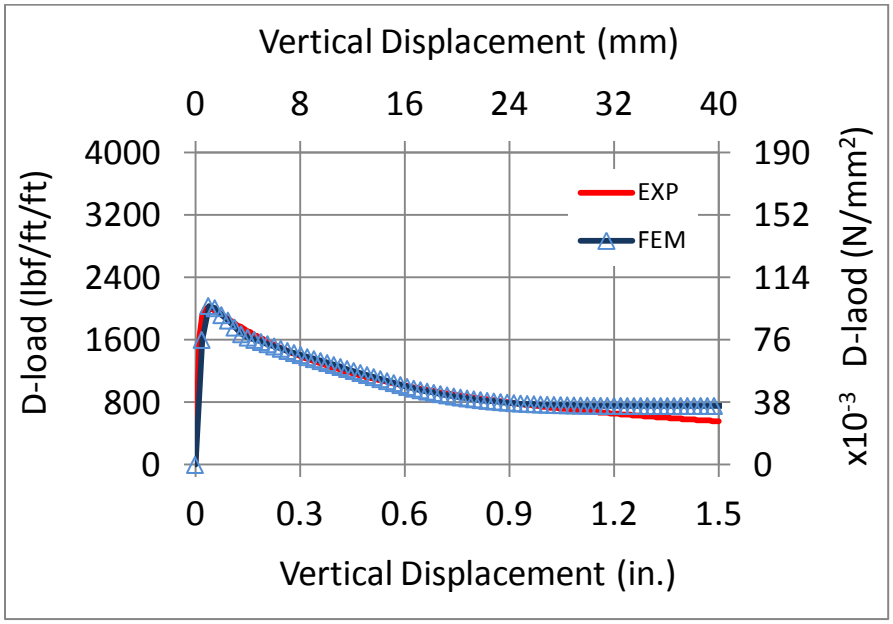

(b)

Figure F- 7 Load-deformation relationship (a) experimental average (b) FEM match to experimental average for 30-B-0.33-III SFRCP

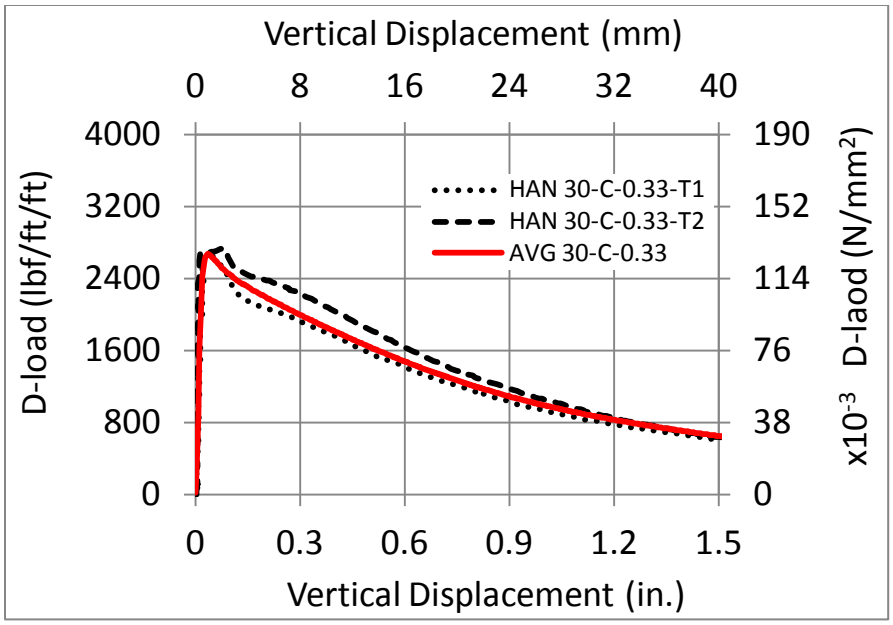

(a)

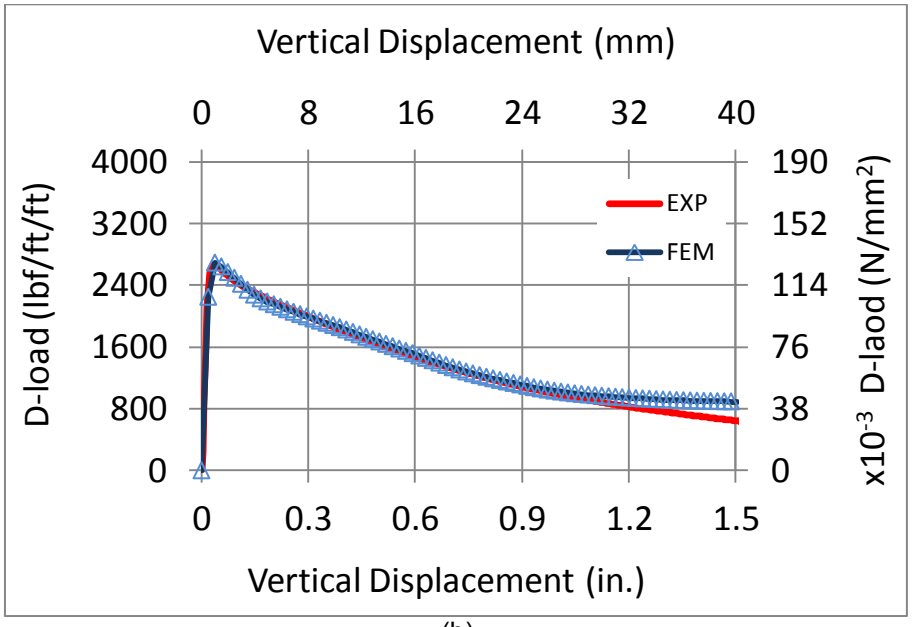

(b)

Figure F- 8 Load-deformation relationship (a) experimental average (b) FEM match to experimental average for 30-C-0.33-III SFRCP

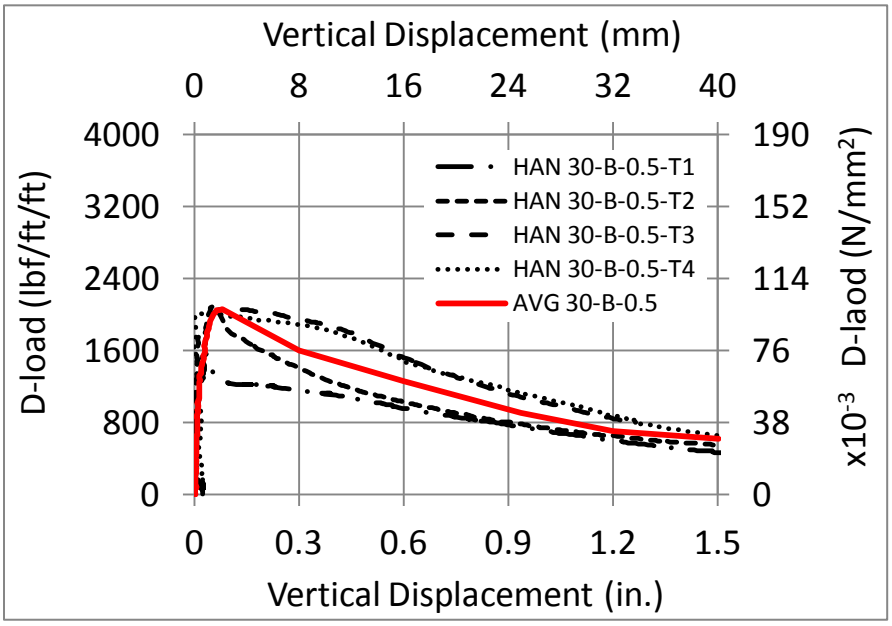

(a)

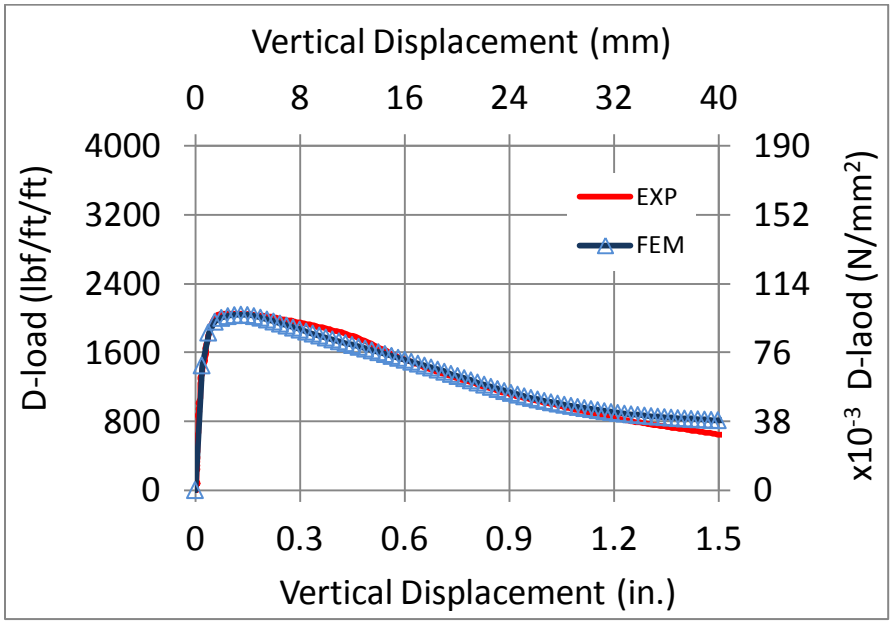

(b)

Figure F- 9 Load-deformation relationship (a) experimental average (b) FEM match to experimental average for 30-B-0.50-III SFRCP

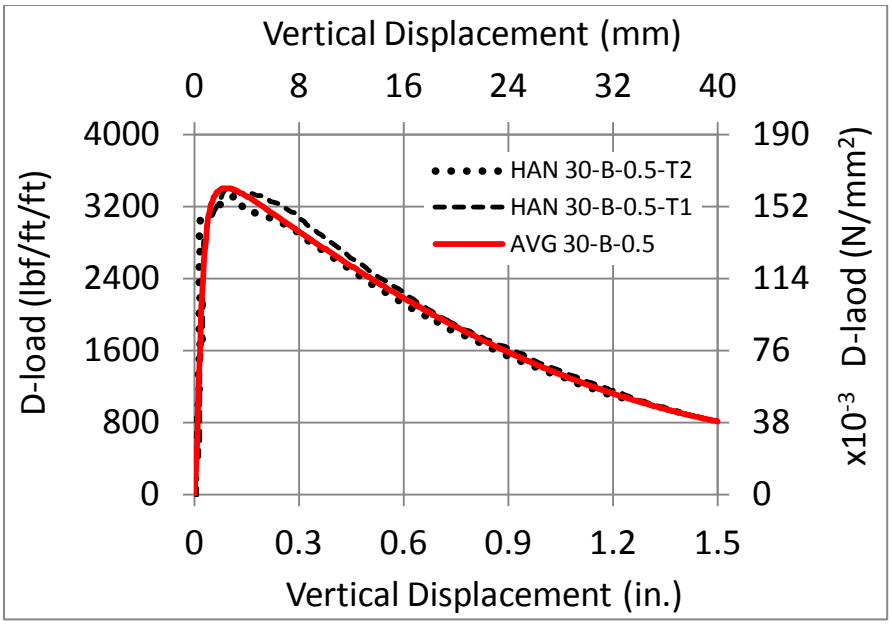

(a)

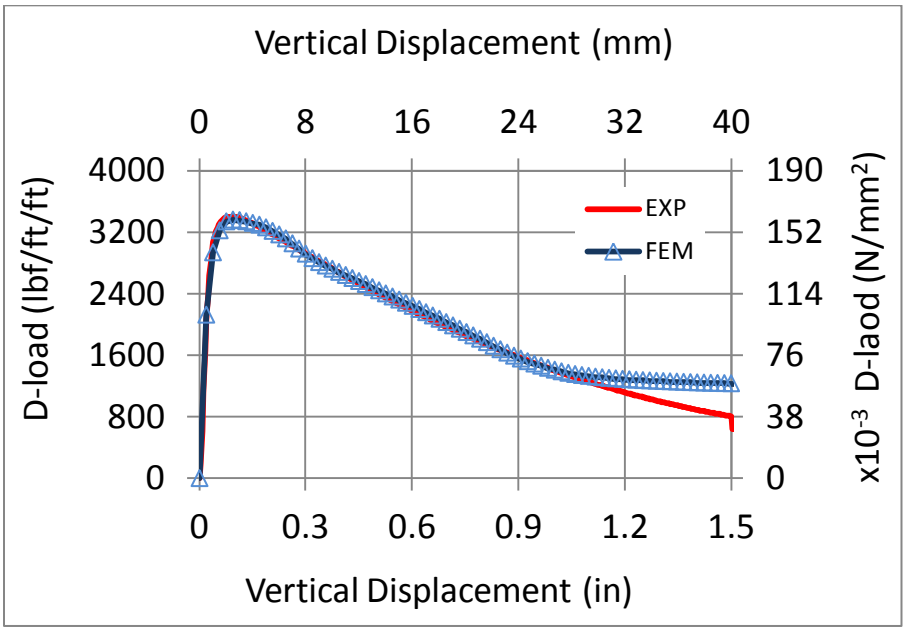

(b)

Figure F- 10 Load-deformation relationship (a) experimental average (b) FEM match to experimental average for 30-B-0.50-IV SFRCP

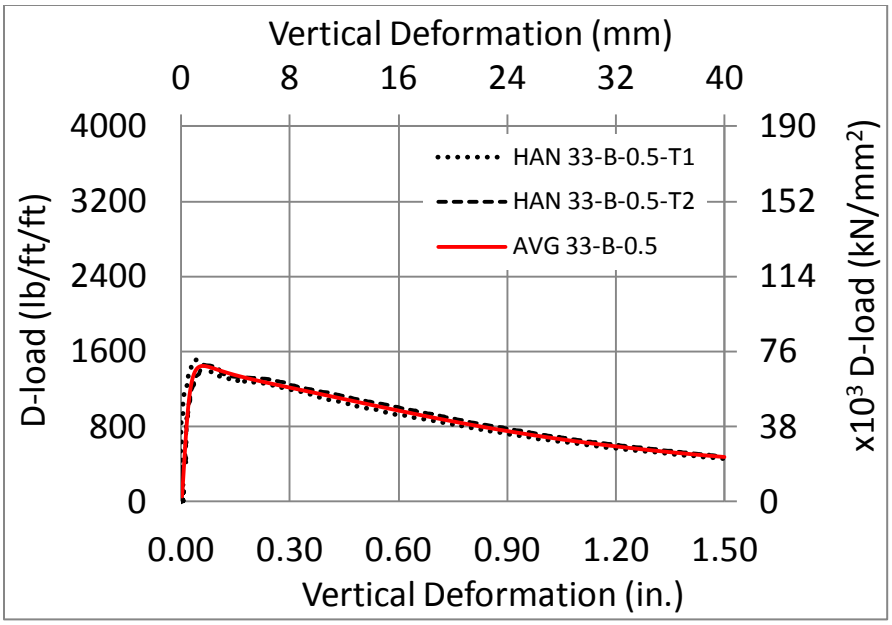

(a)

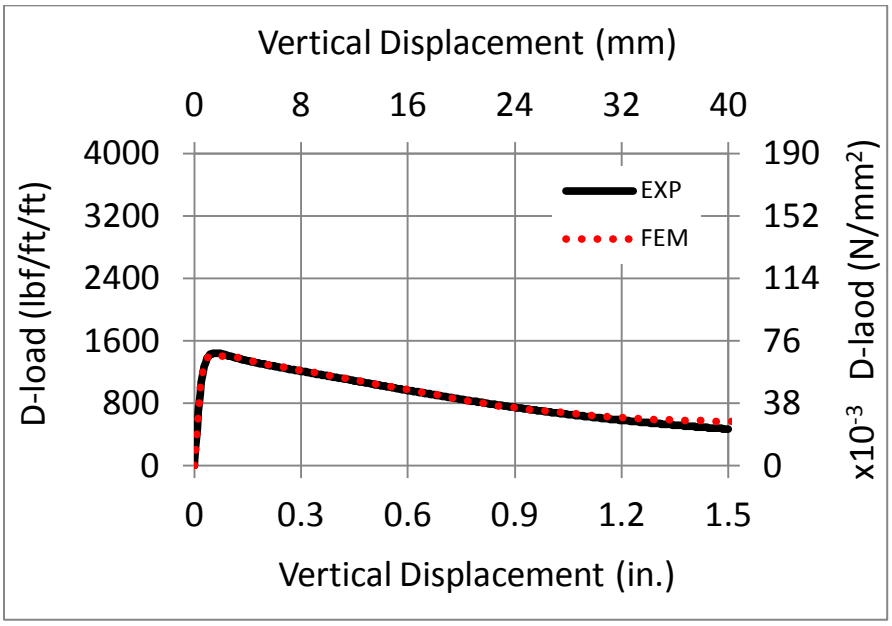

(b)

Figure F- 11 Load-deformation relationship (a) experimental average (b) FEM match to experimental average for 33-B-0.33-I SFRCP

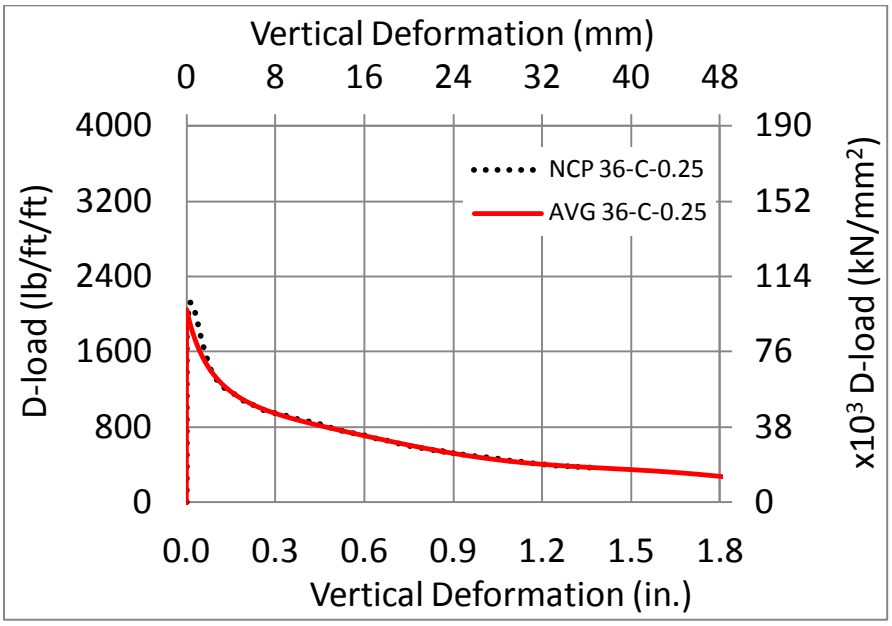

(a)

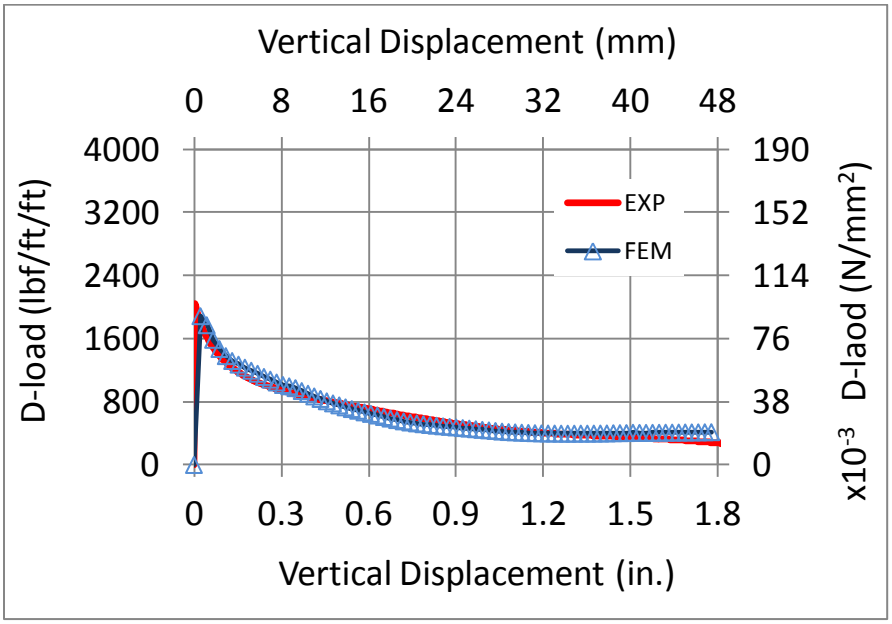

(b)

Figure F- 12 Load-deformation relationship (a) experimental average (b) FEM match to experimental average for 36-C-0.25-III SFRCP

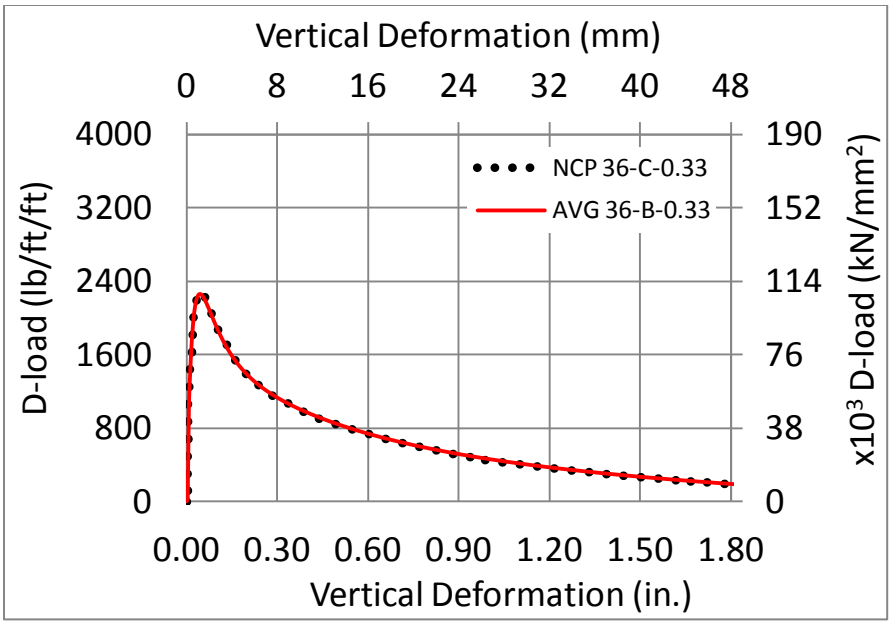

(a)

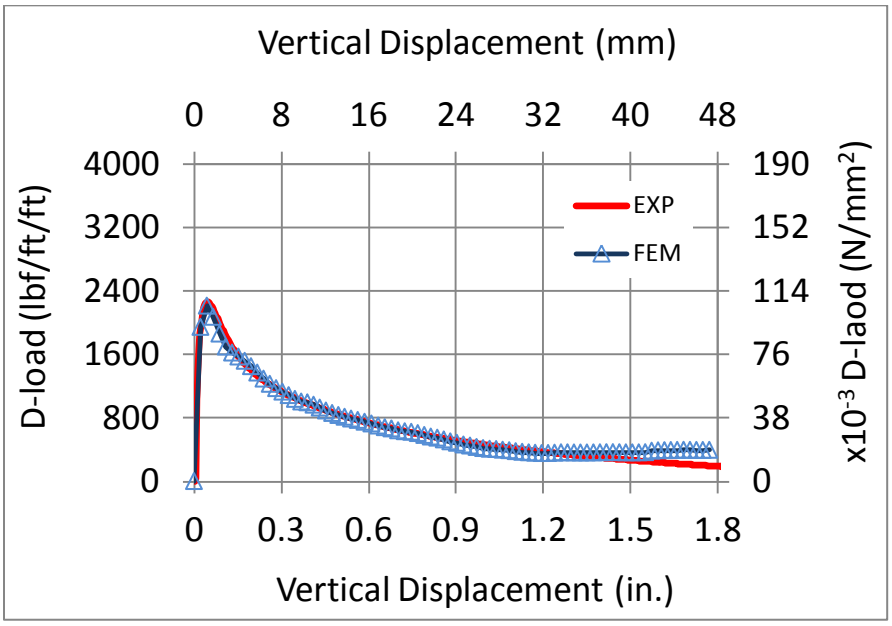

(b)

Figure F- 13 Load-deformation relationship (a) experimental average (b) FEM match to experimental average for 36-C-0.33-III SFRCP

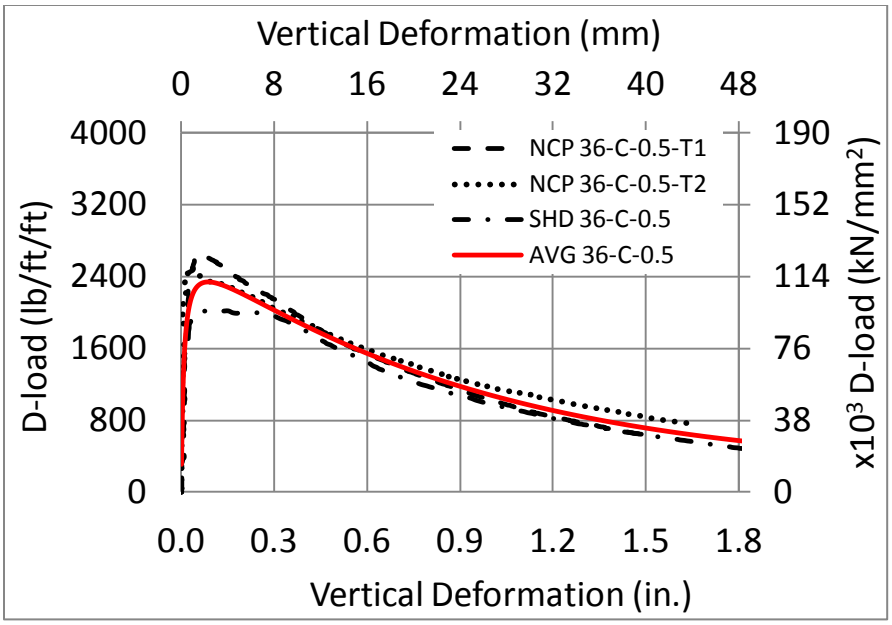

(a)

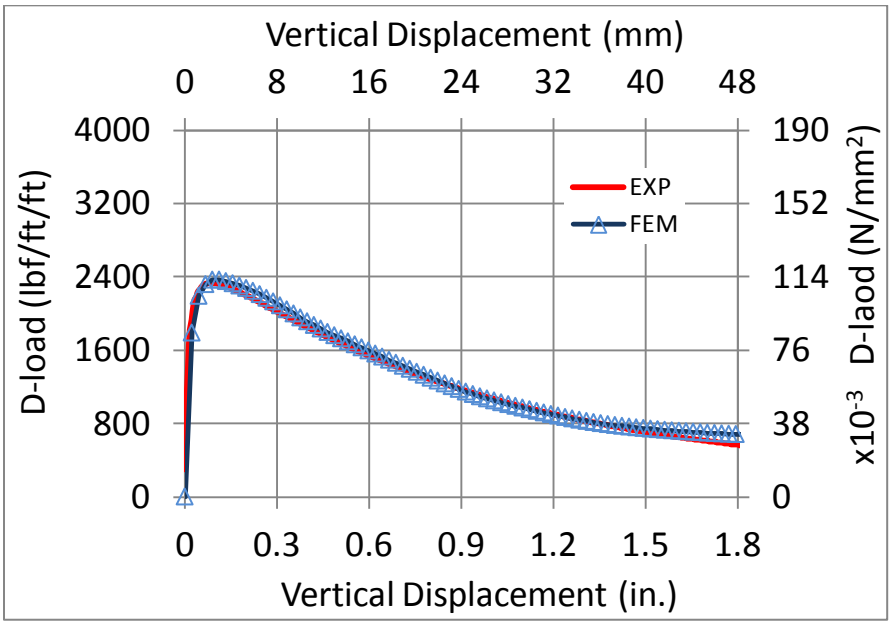

(b)

Figure F- 14 Load-deformation relationship (a) experimental average (b) FEM match to experimental average for 36-C-0.50-III SFRCP

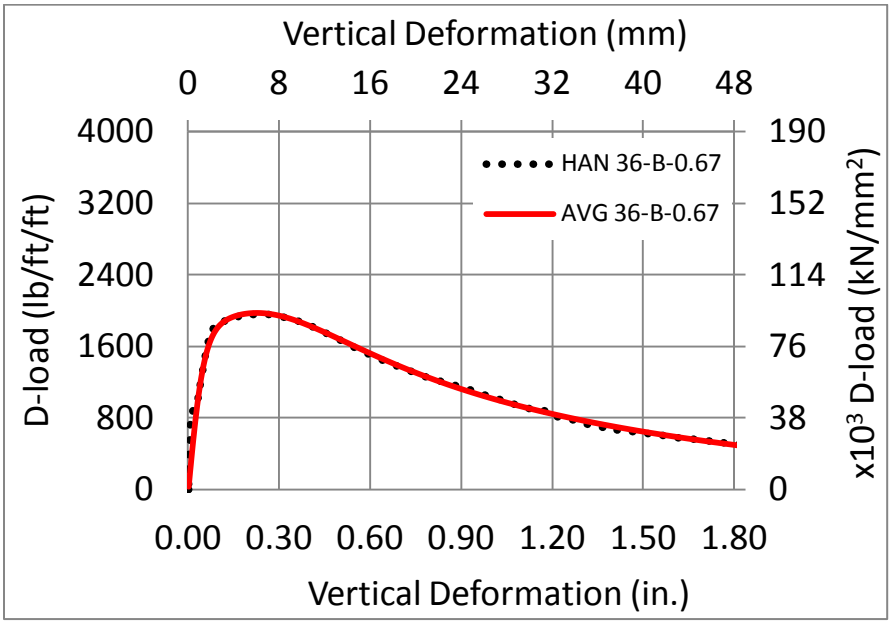

(a)

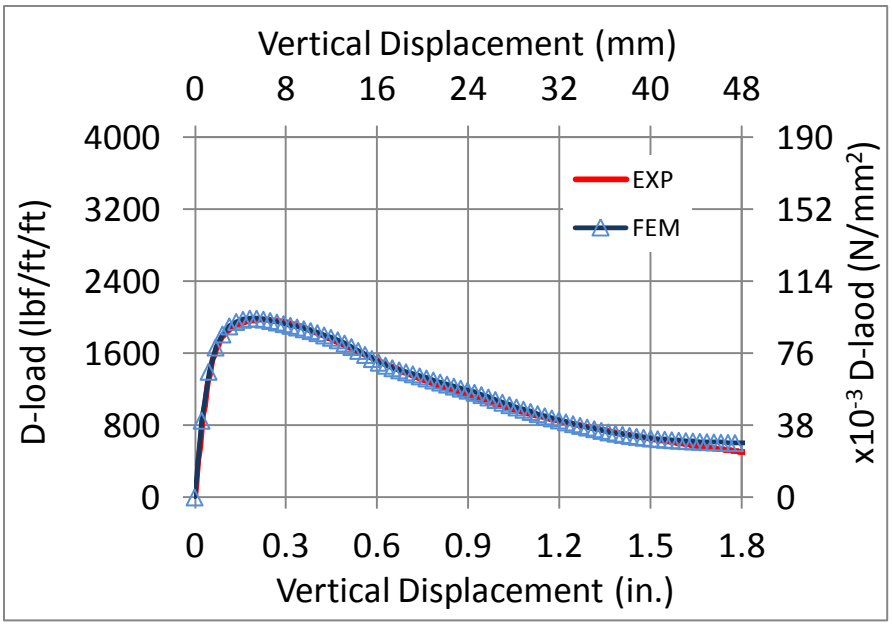

(b)

Figure F- 15 Load-deformation relationship (a) experimental average (b) FEM match to experimental average for 36-B-0.67-III SFRCP

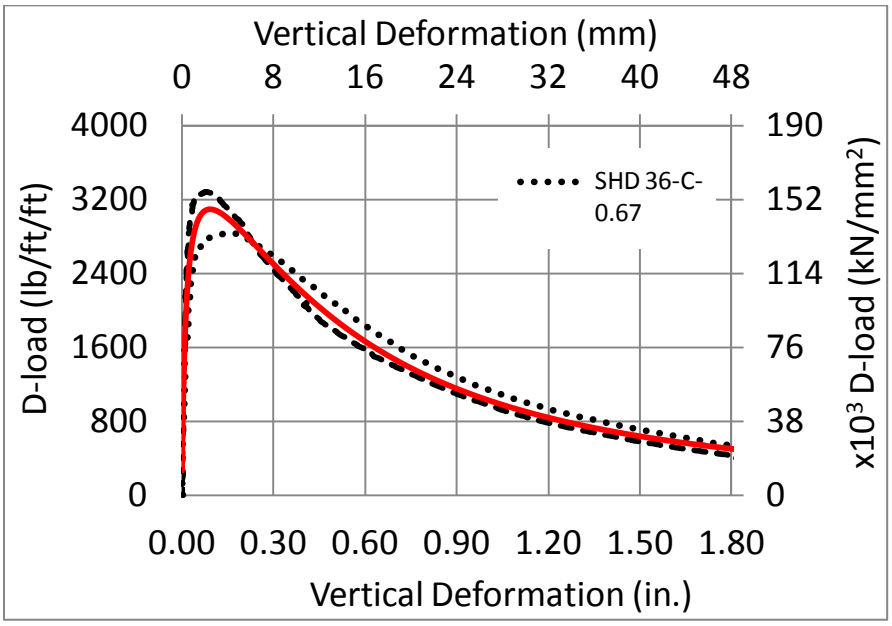

(a)

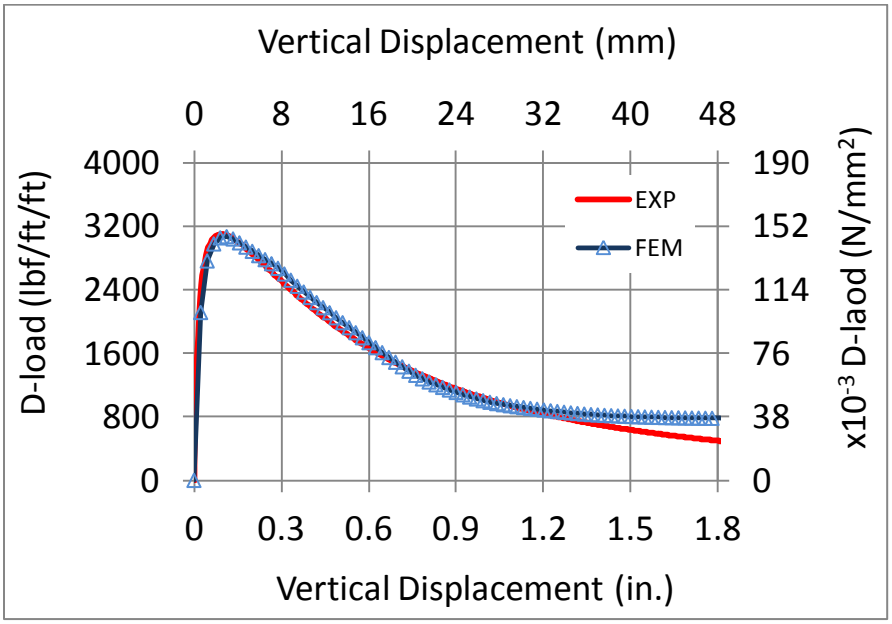

(b)

Figure F- 16 Load-deformation relationship (a) experimental average (b) FEM match to experimental average for 36-C-0.67-IV SFRCP

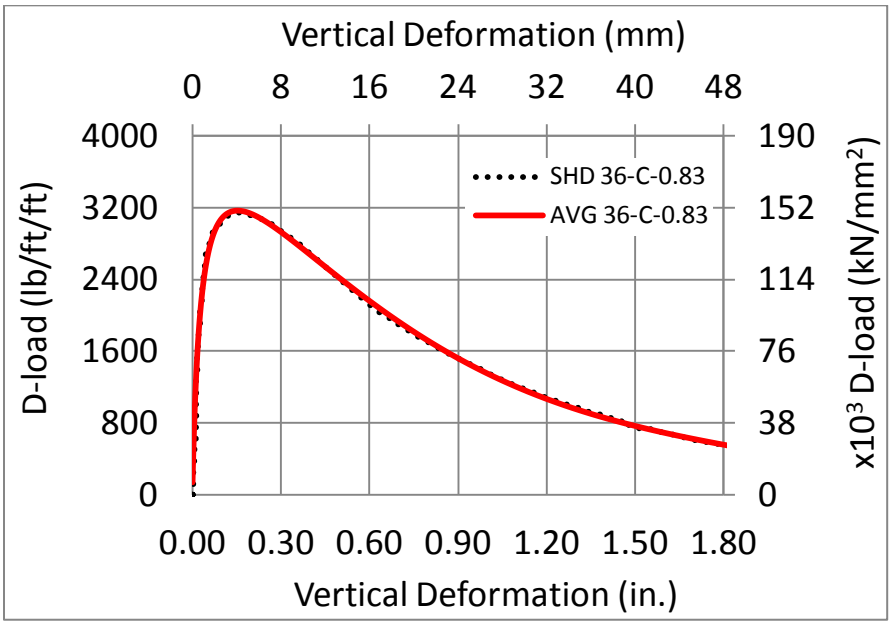

(a)

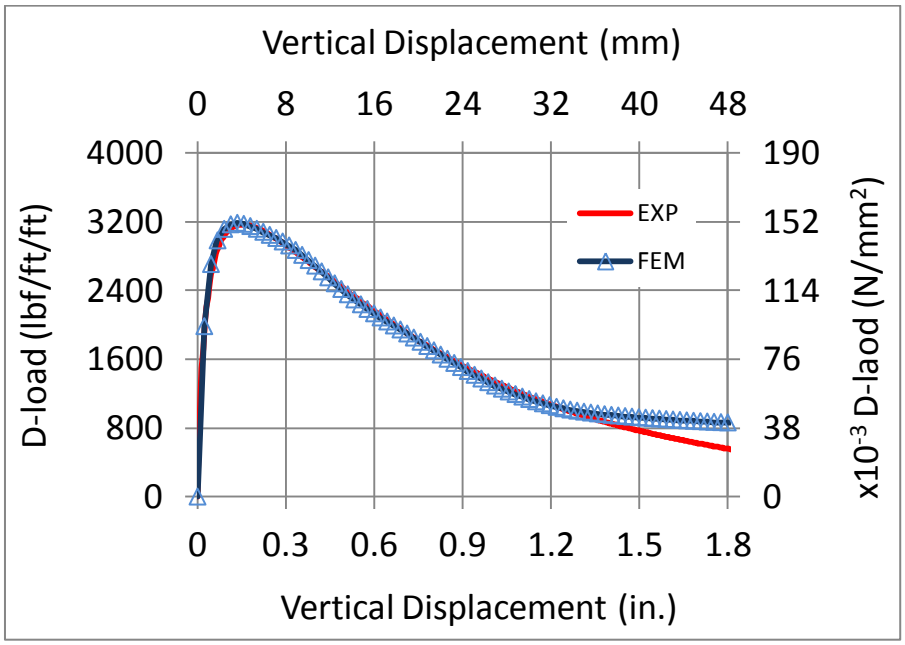

(b)

Figure F- 17 Load-deformation relationship (a) experimental average (b) FEM match to experimental average for 36-C-0.83-IV SFRCP

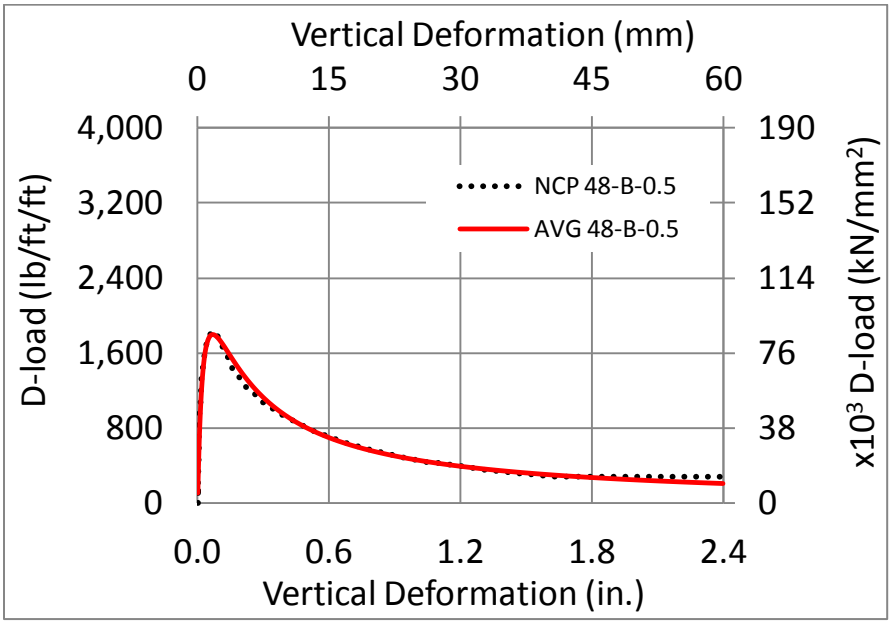

(a)

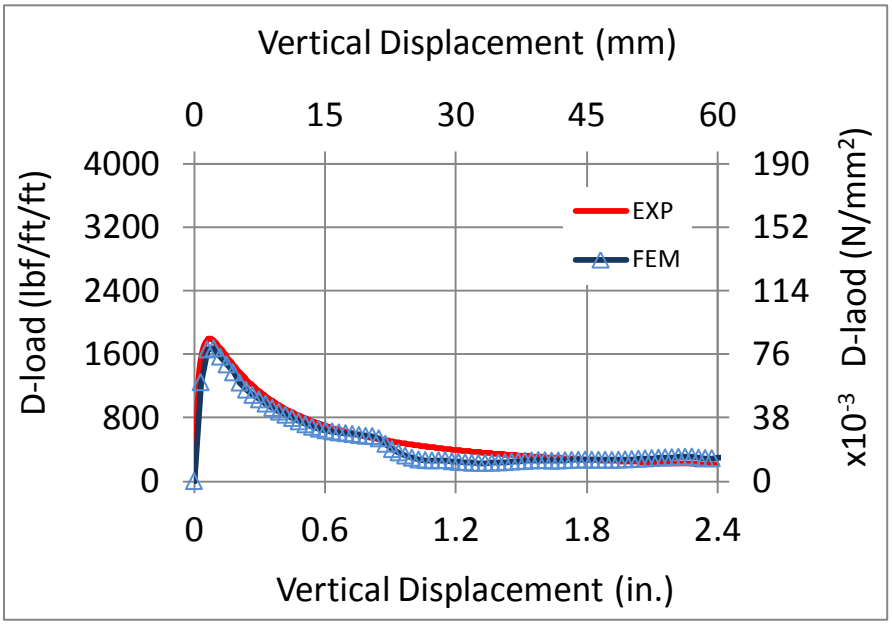

(b)

Figure F- 18 Load-deformation relationship (a) experimental average (b) FEM match to experimental average for 48-B-0.5-II SFRCP

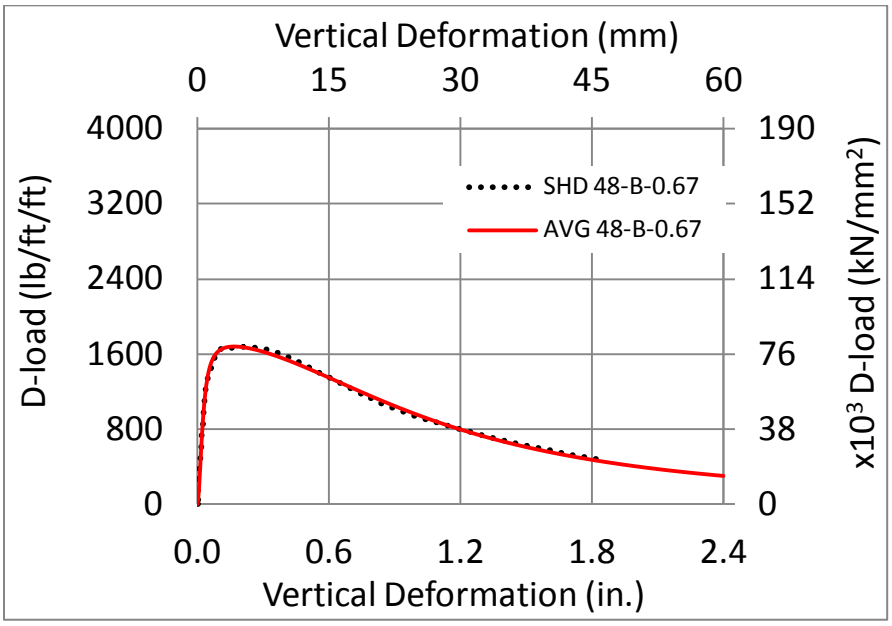

(a)

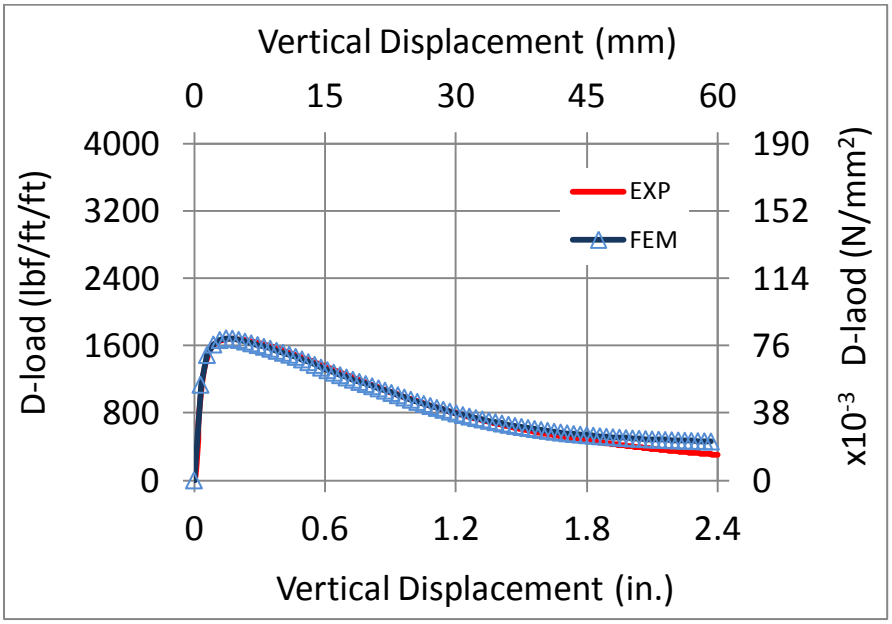

(b)

Figure F- 19 Load-deformation relationship (a) experimental average (b) FEM match to experimental average for 48-B-0.67-II SFRCP

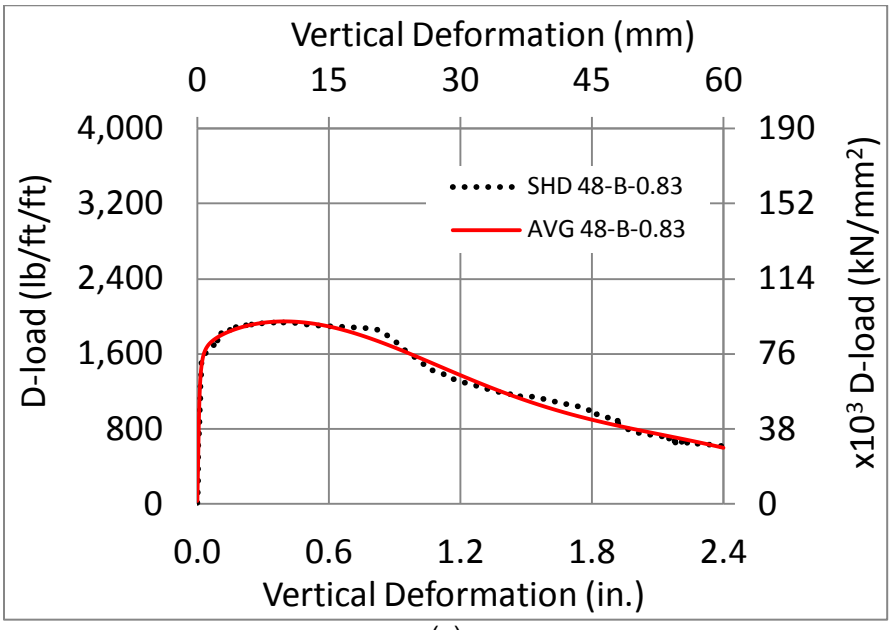

(a)

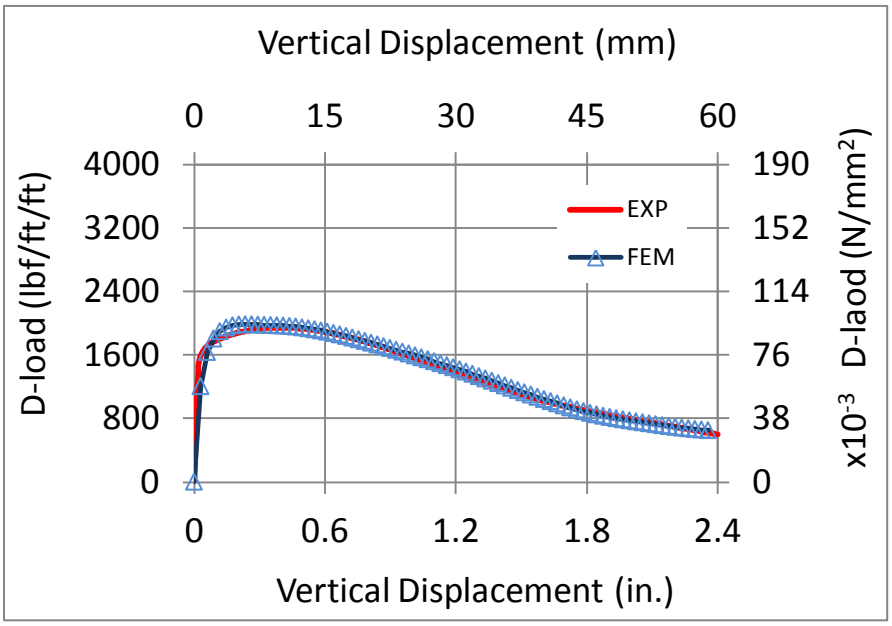

(b)

Figure F- 20 Load-deformation relationship (a) experimental average (b) FEM match to experimental average for 48-B-0.83-III SFRCP

Appendix G

Stress-Strain Relationships in the Critical Regions Obtained with Finite Element Analysis

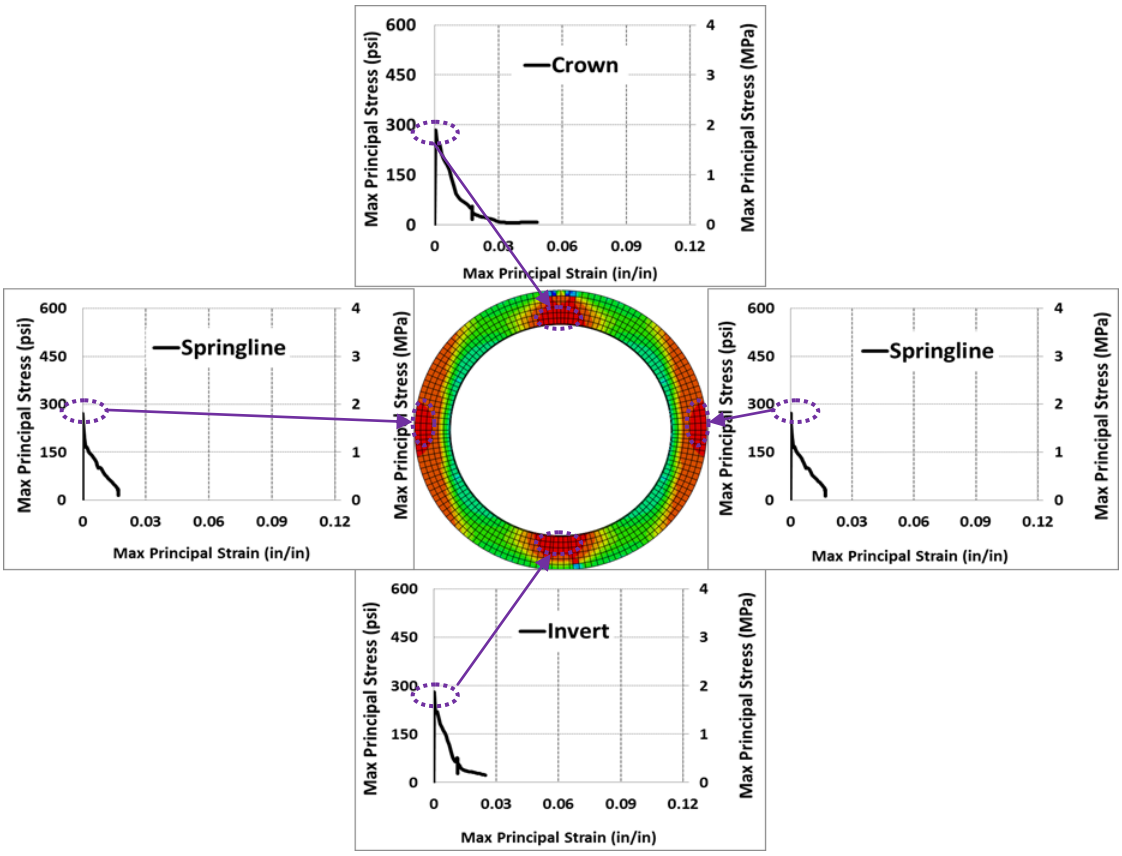

Figure G- 1 Maximum principal stress-strain relationship and stress distribution contours at ultimate stress in FEM 24-B-0.17-II Steel Fiber Reinforced Concrete Pipe

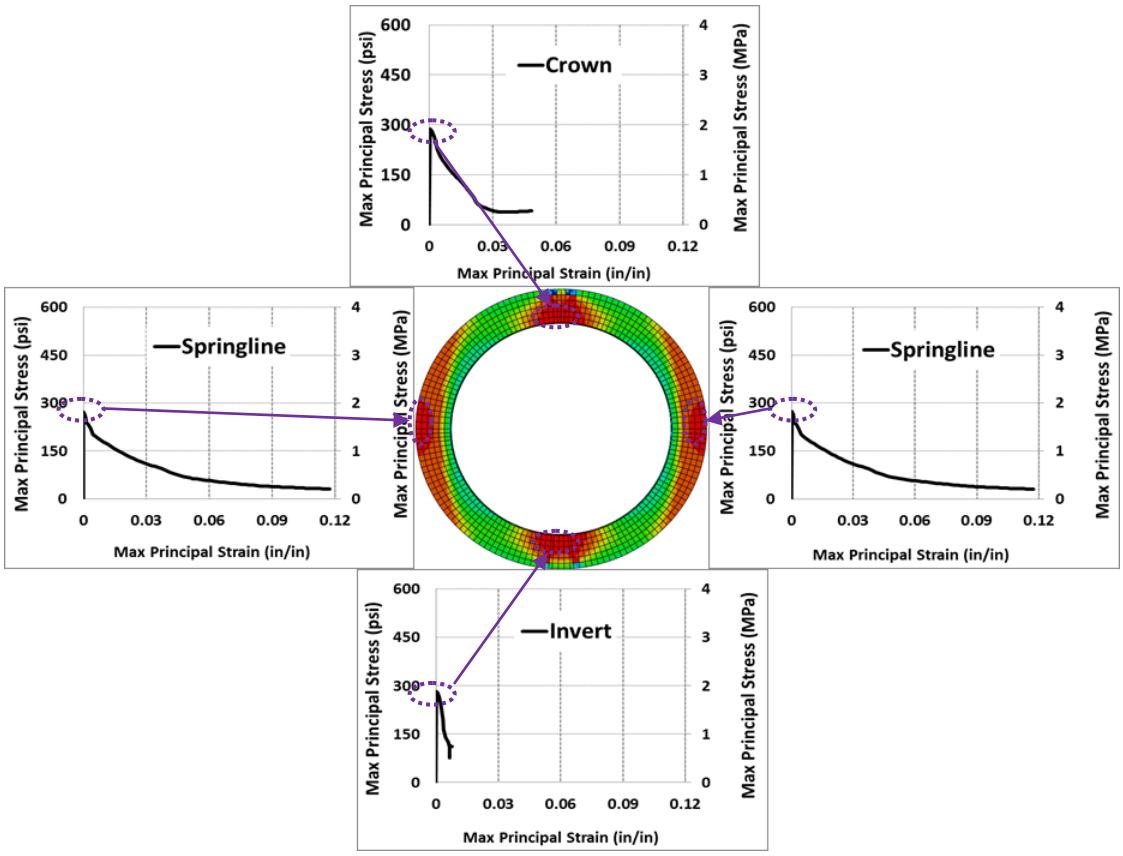

Figure G- 2 Maximum principal stress-strain relationship and stress distribution contours at ultimate stress in FEM 24-B-0.25-III Steel Fiber Reinforced Concrete Pipe

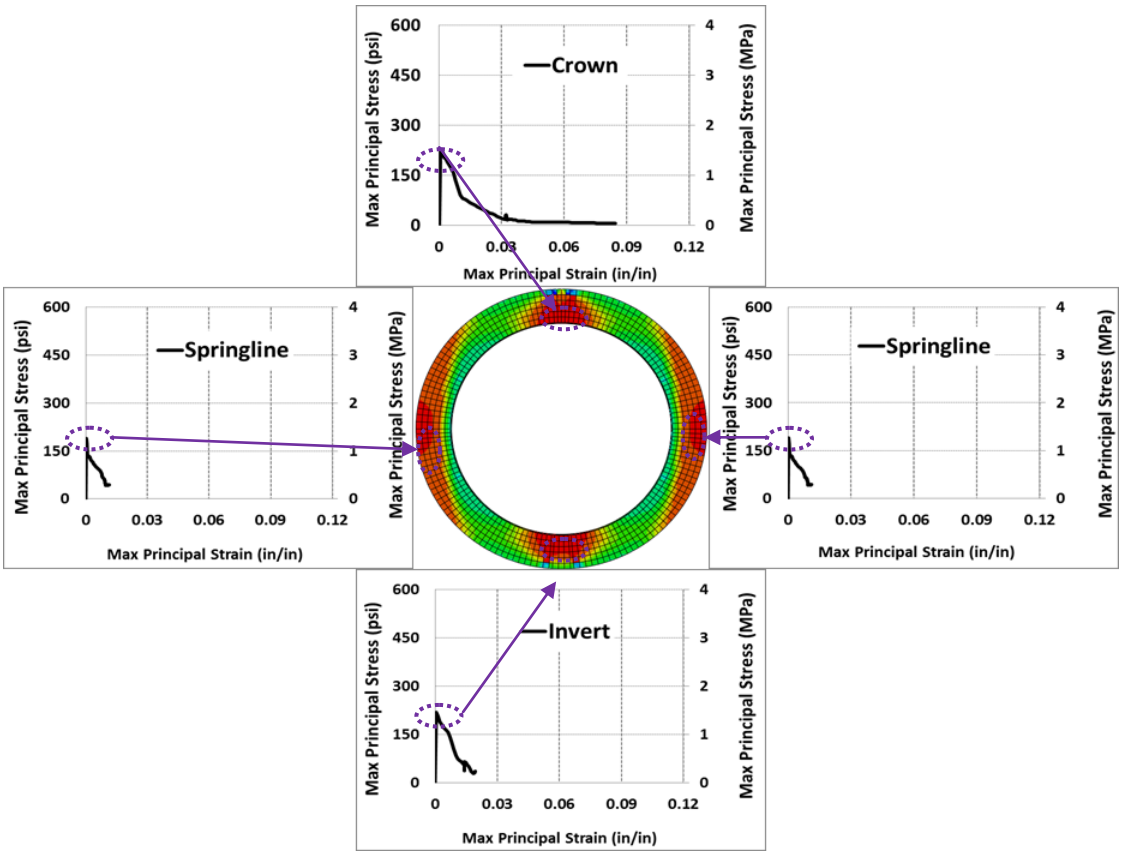

Figure G- 3 Maximum principal stress-strain relationship and stress distribution contours at ultimate stress in FEM 24-C-0.25-III Steel Fiber Reinforced Concrete Pipe

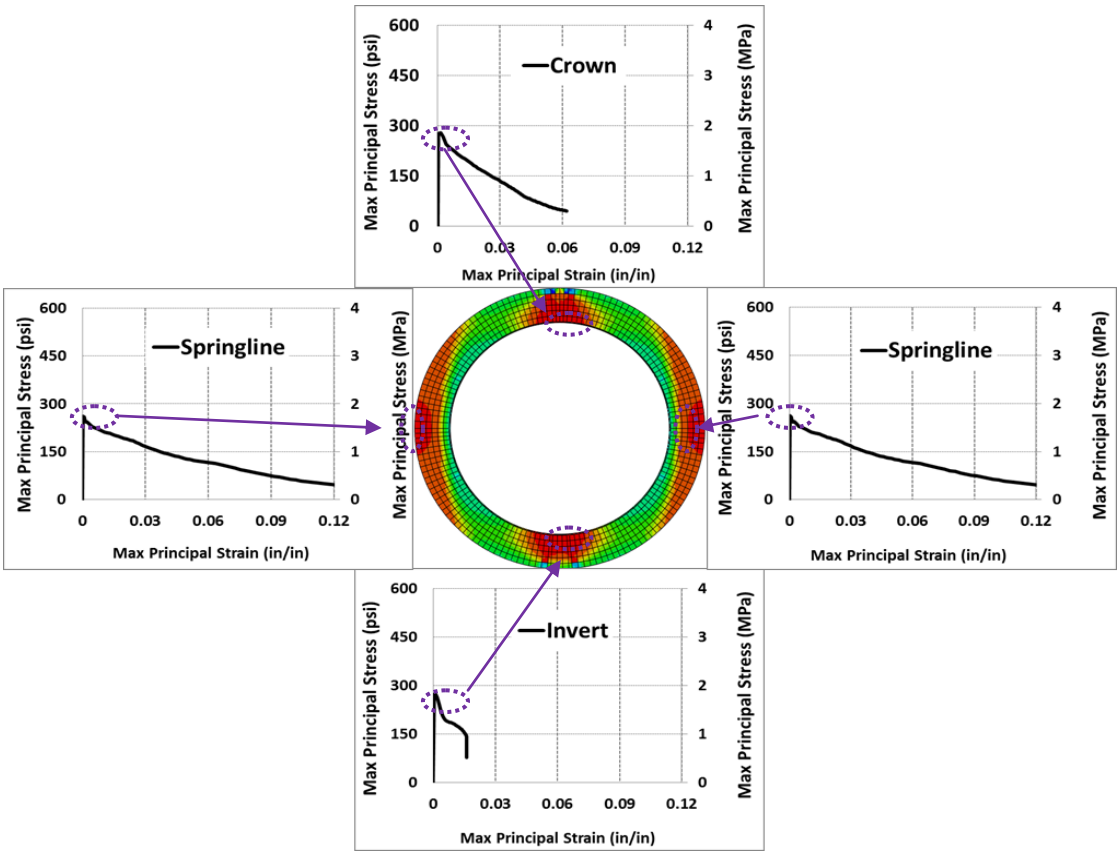

Figure G- 4 Maximum principal stress-strain relationship and stress distribution contours at ultimate stress in FEM 24-B-0.33-III Steel Fiber Reinforced Concrete Pipe

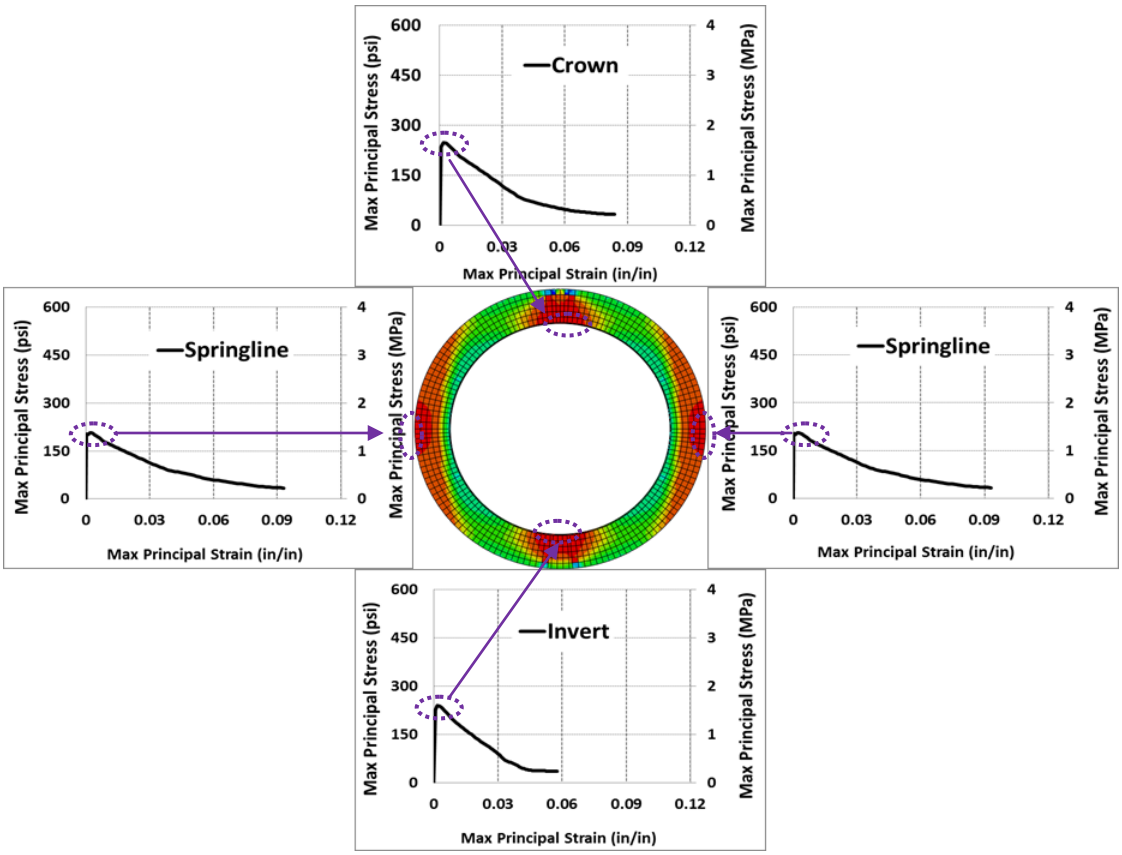

Figure G- 5 Maximum principal stress-strain relationship and stress distribution contours at ultimate stress in FEM 24-C-0.33-III Steel Fiber Reinforced Concrete Pipe

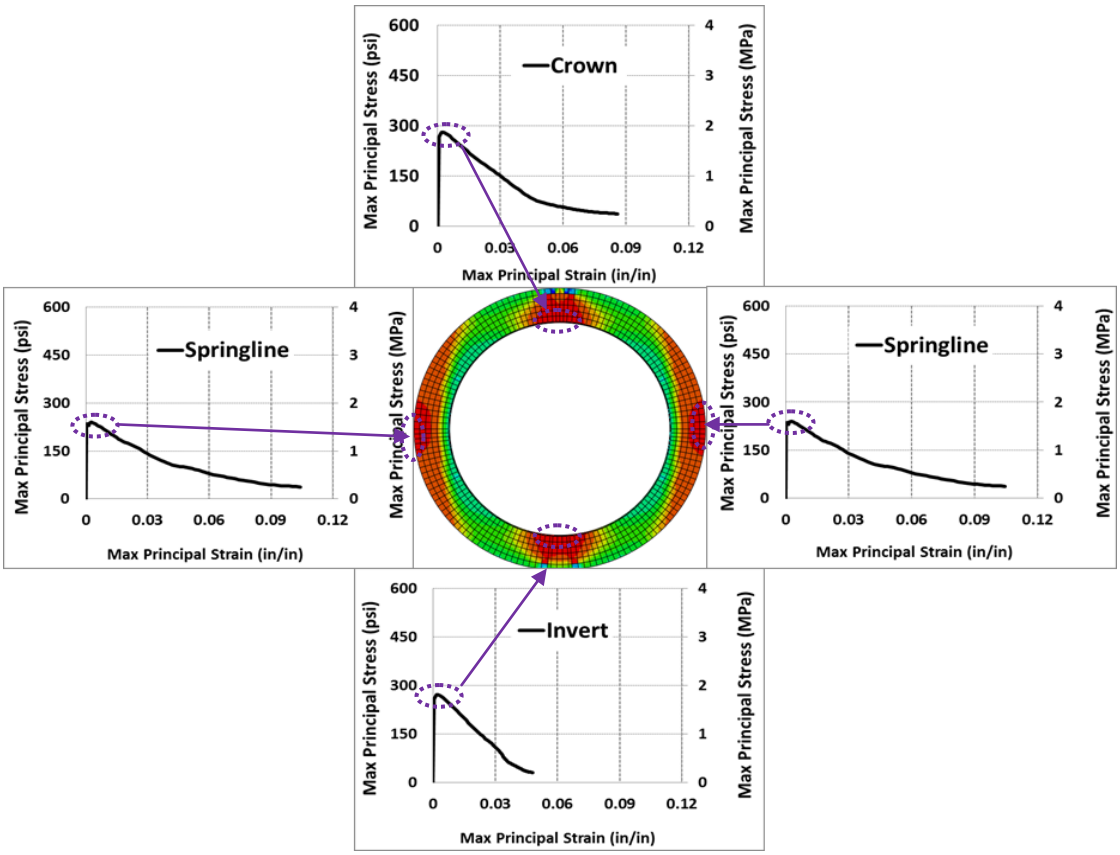

Figure G- 6 Maximum principal stress-strain relationship and stress distribution contours at ultimate stress in FEM 24-C-0.5-IV Steel Fiber Reinforced Concrete Pipe

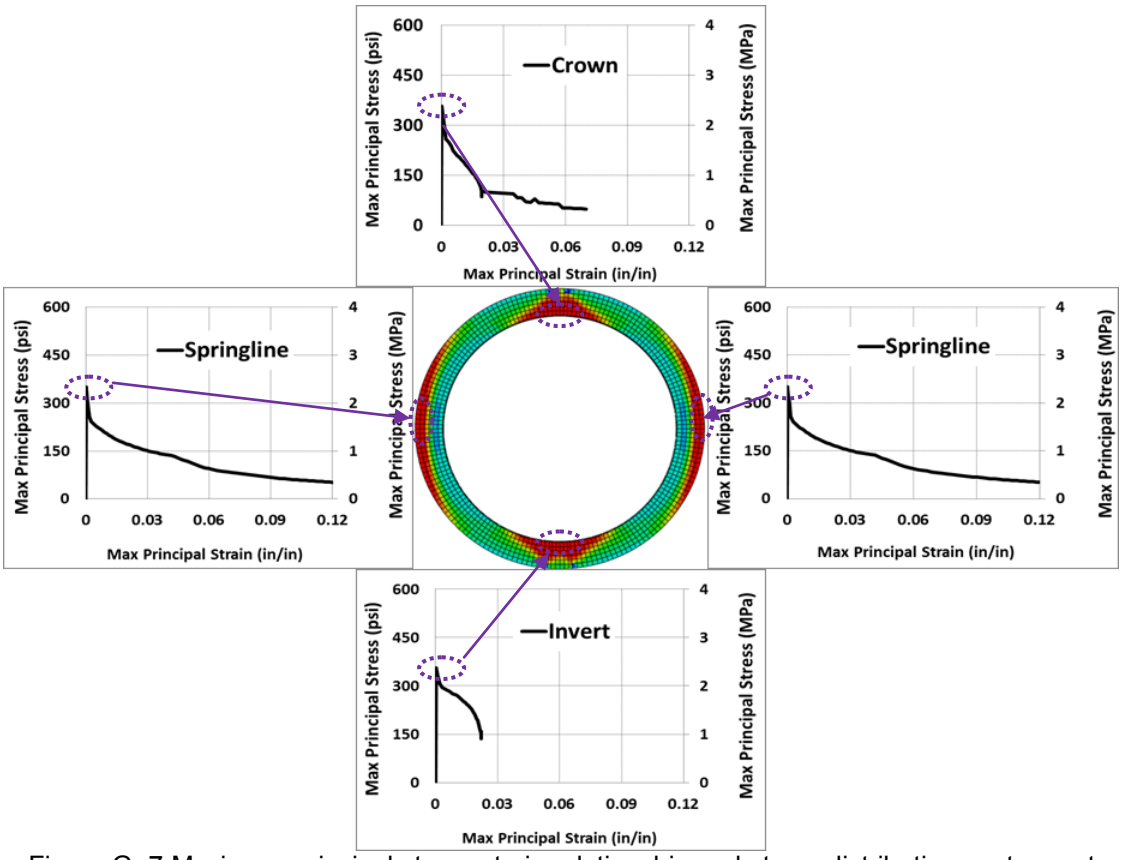

Figure G- 7 Maximum principal stress-strain relationship and stress distribution contours at ultimate stress in FEM 30-B-0.33-III Steel Fiber Reinforced Concrete Pipe

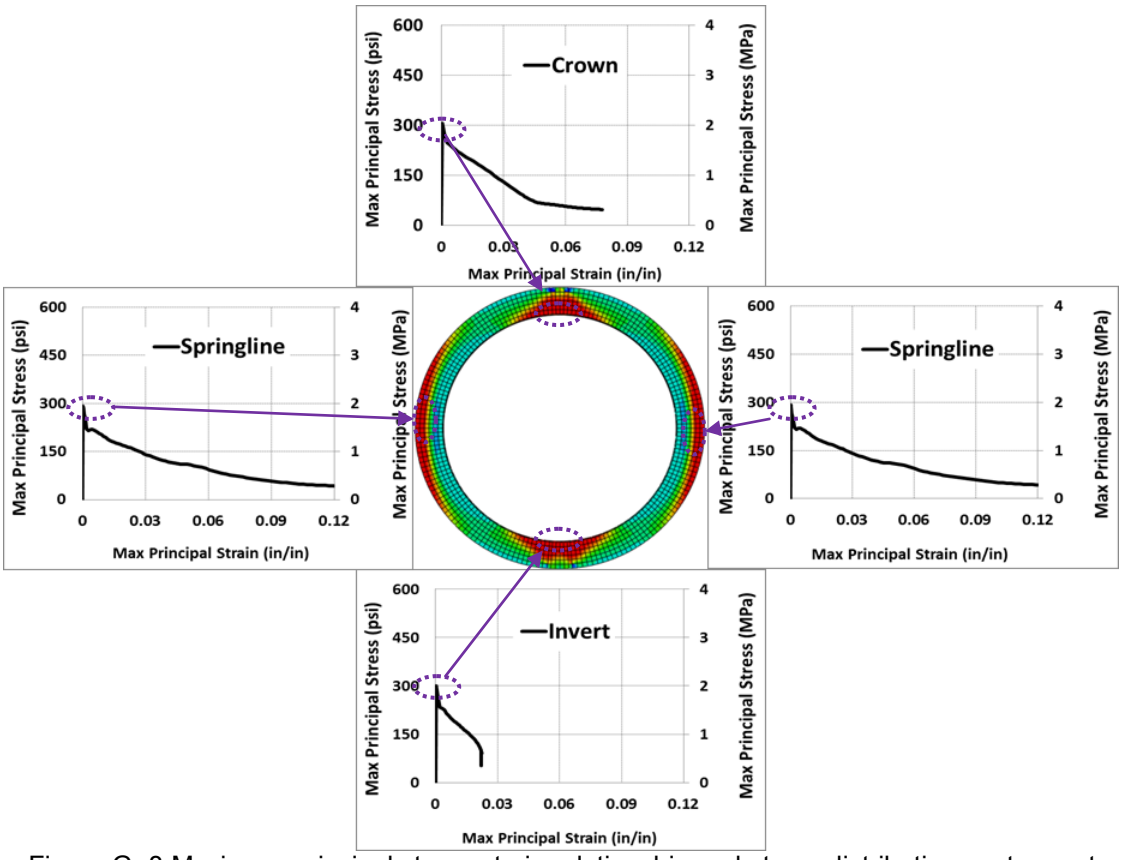

Figure G- 8 Maximum principal stress-strain relationship and stress distribution contours at ultimate stress in FEM 30-C-0.33-III Steel Fiber Reinforced Concrete Pipe

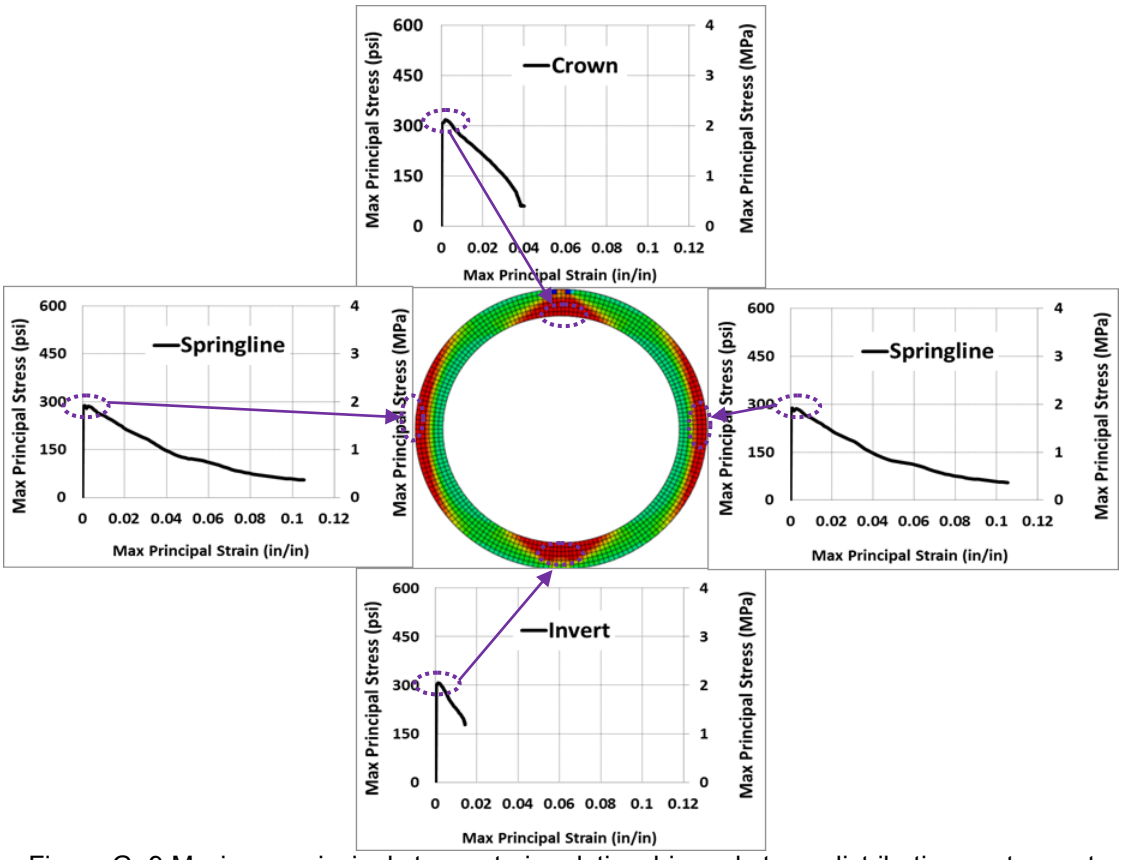

Figure G- 9 Maximum principal stress-strain relationship and stress distribution contours at ultimate stress in FEM 30-B-0.5-III Steel Fiber Reinforced Concrete Pipe

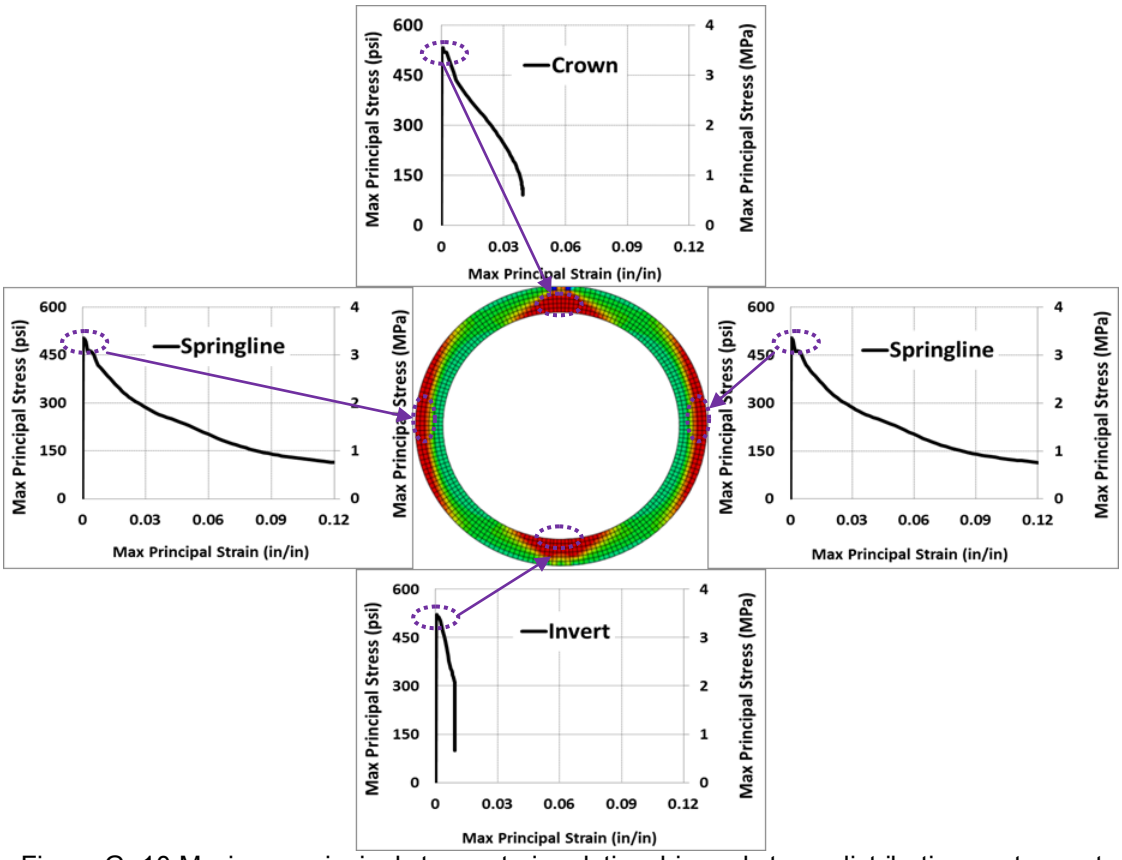

Figure G- 10 Maximum principal stress-strain relationship and stress distribution contours at ultimate stress in FEM 30-B-0.5-IV Steel Fiber Reinforced Concrete Pipe

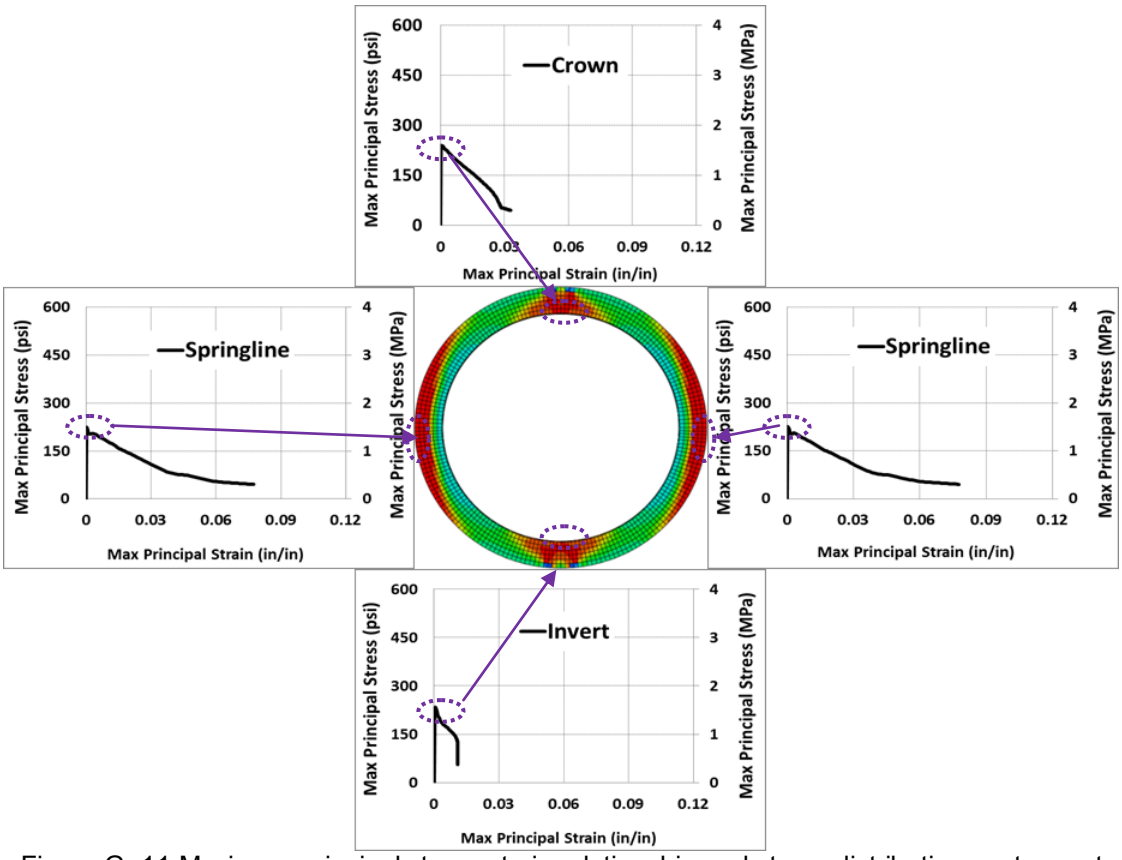

Figure G- 11 Maximum principal stress-strain relationship and stress distribution contours at ultimate stress in FEM 33-B-0.33-I Steel Fiber Reinforced Concrete Pipe

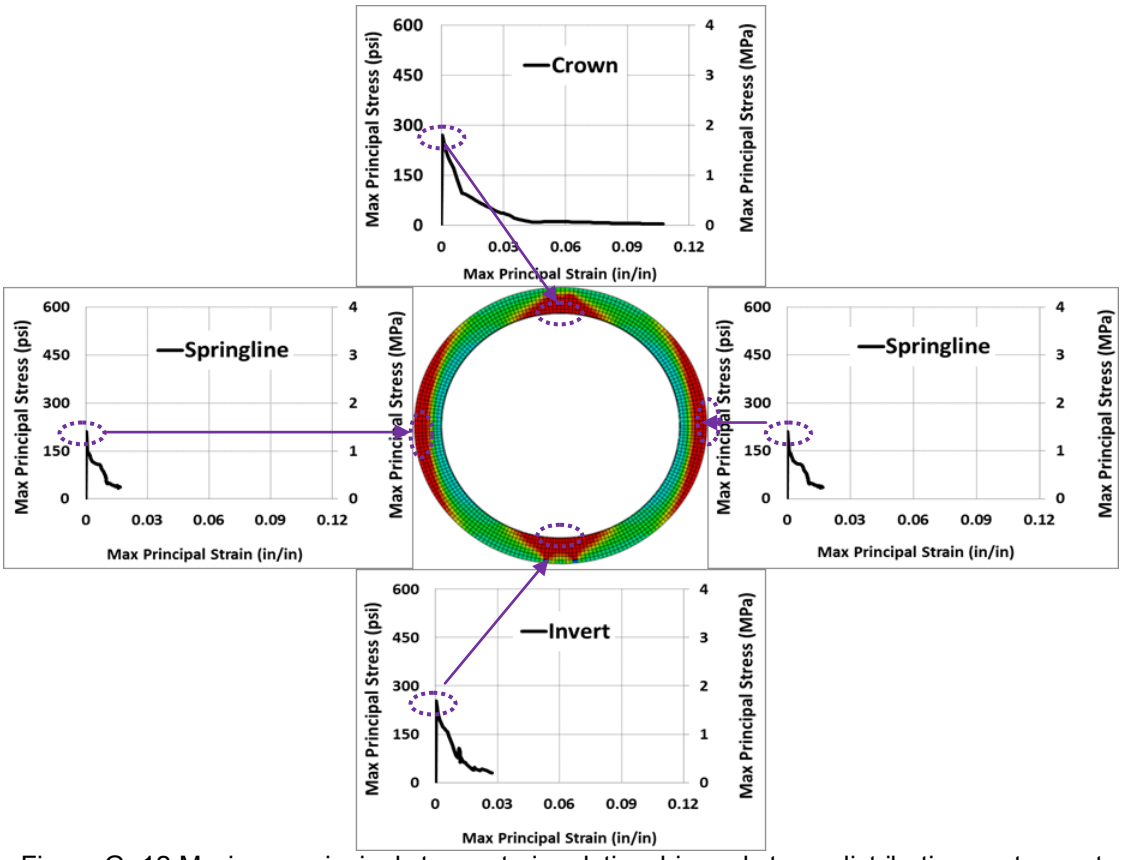

Figure G- 12 Maximum principal stress-strain relationship and stress distribution contours at ultimate stress in FEM 36-C-0.25-III Steel Fiber Reinforced Concrete Pipe

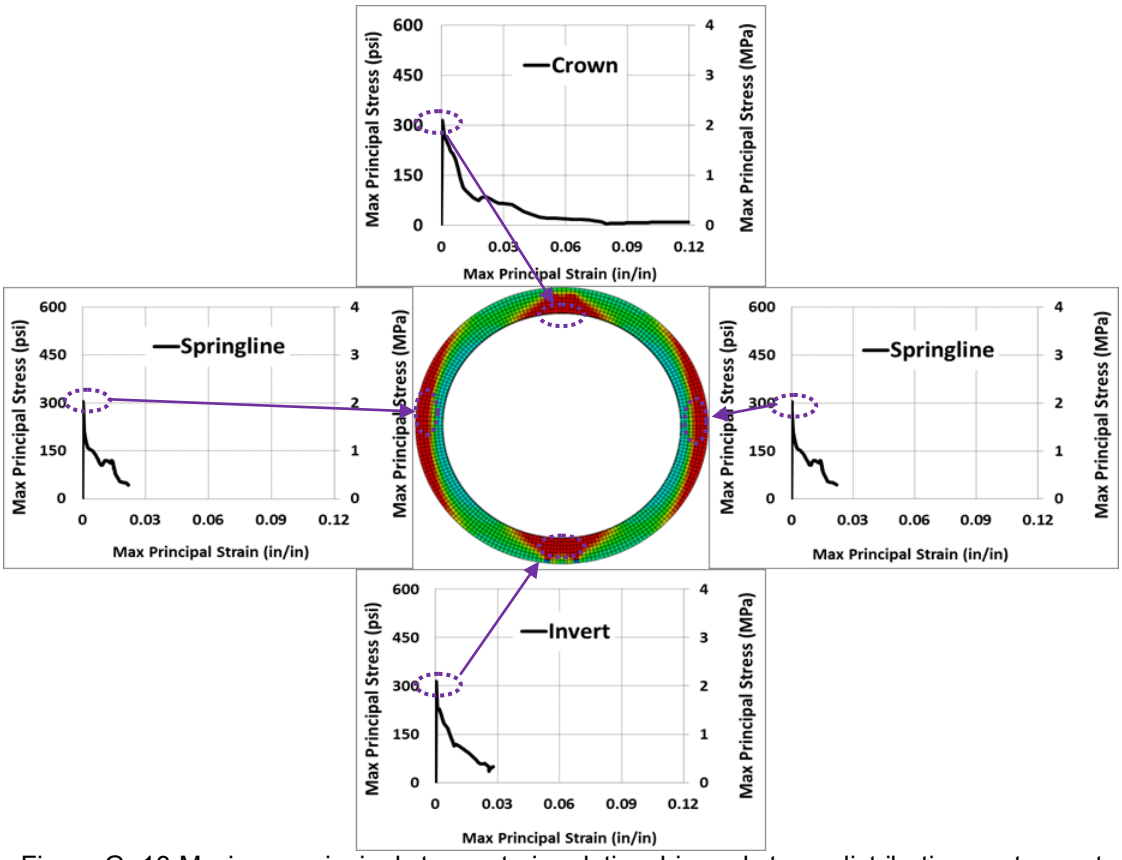

Figure G- 13 Maximum principal stress-strain relationship and stress distribution contours at ultimate stress in FEM 36-C-0.33-III Steel Fiber Reinforced Concrete Pipe

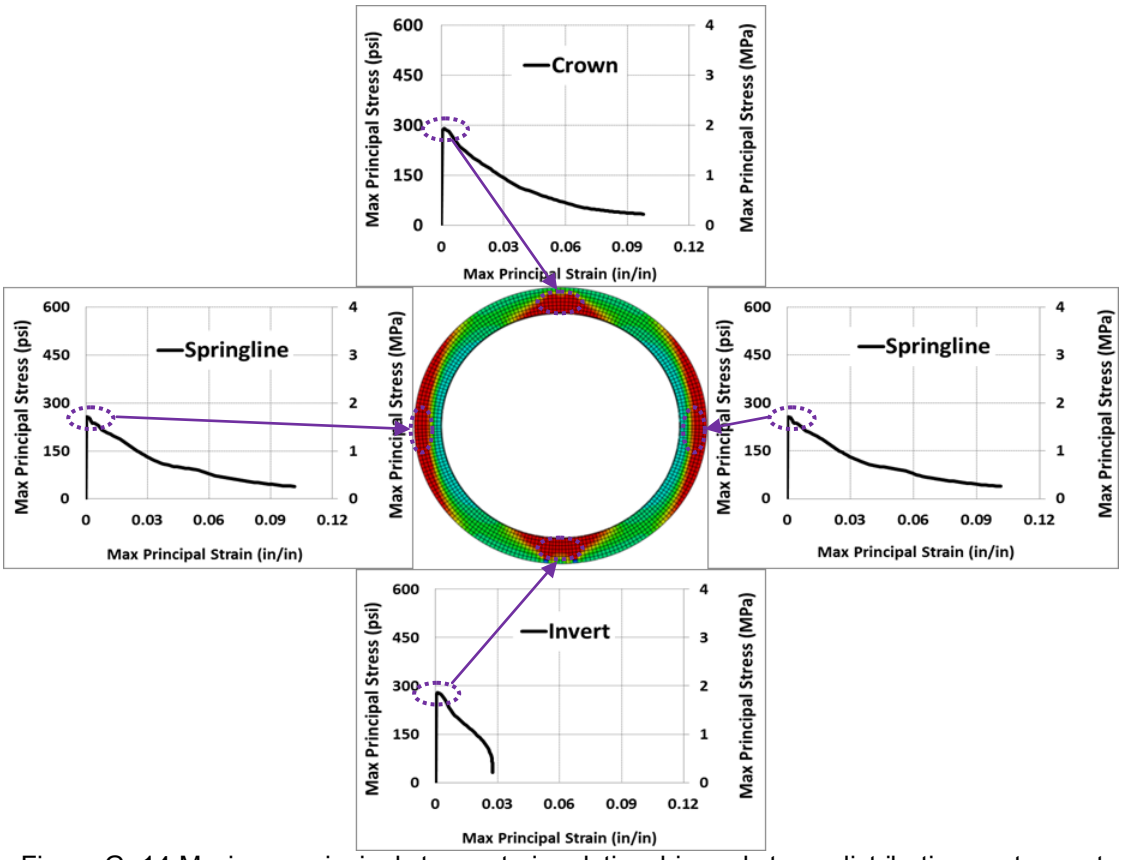

Figure G- 14 Maximum principal stress-strain relationship and stress distribution contours at ultimate stress in FEM 36-C-0.50-III Steel Fiber Reinforced Concrete Pipe

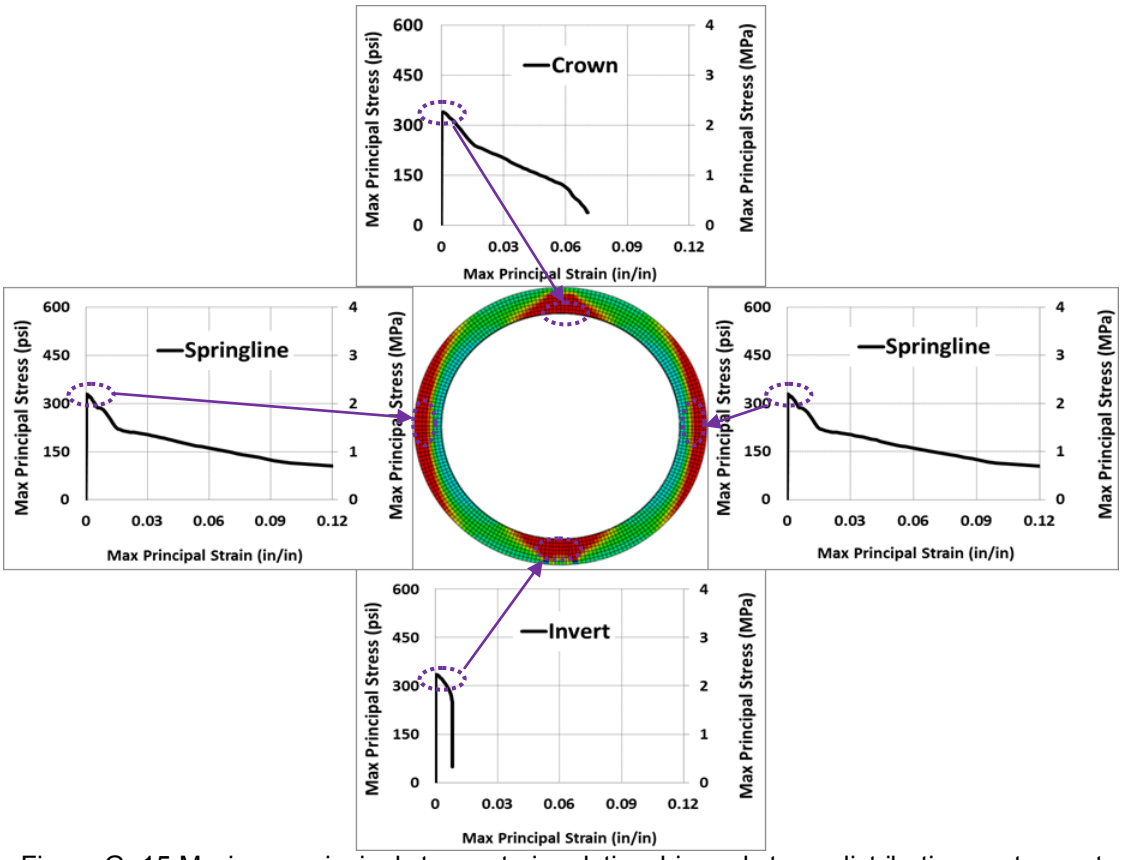

Figure G- 15 Maximum principal stress-strain relationship and stress distribution contours at ultimate stress in FEM 36-B-0.67-III Steel Fiber Reinforced Concrete Pipe

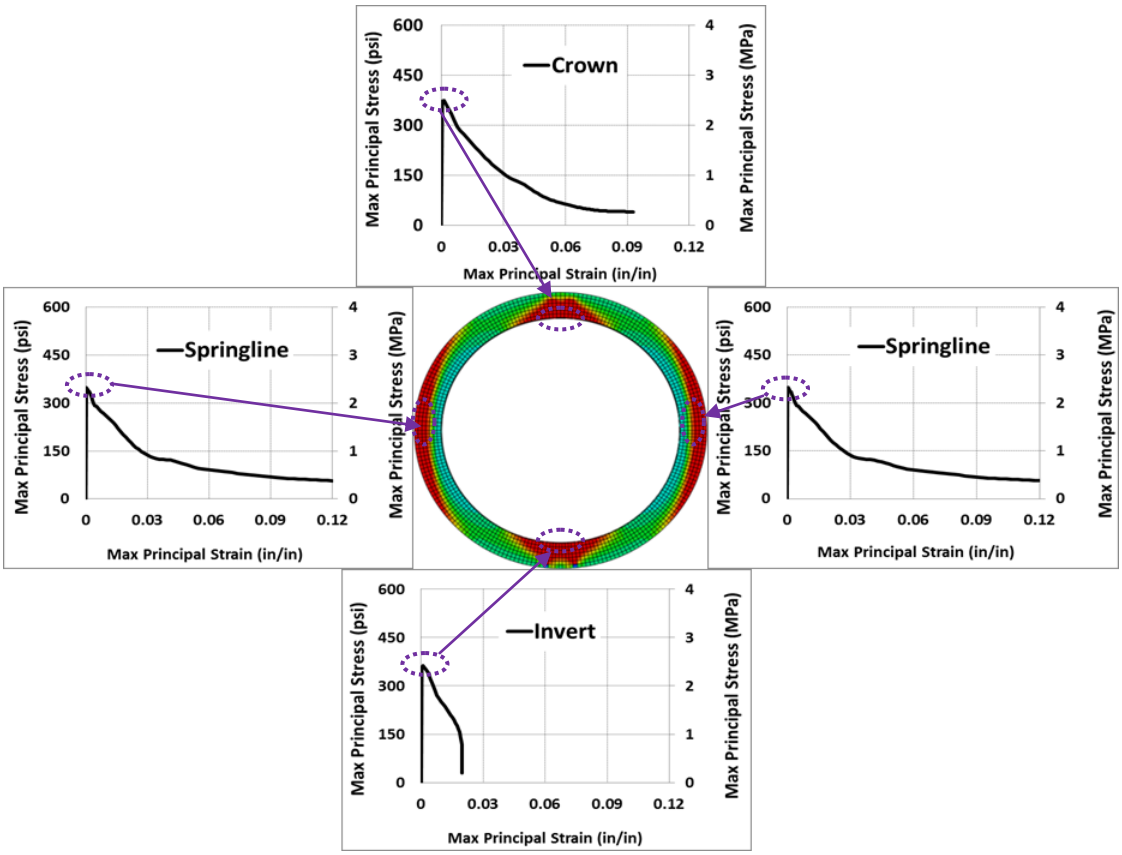

Figure G- 16 Maximum principal stress-strain relationship and stress distribution contours at ultimate stress in FEM 36-C-0.67-IV Steel Fiber Reinforced Concrete Pipe

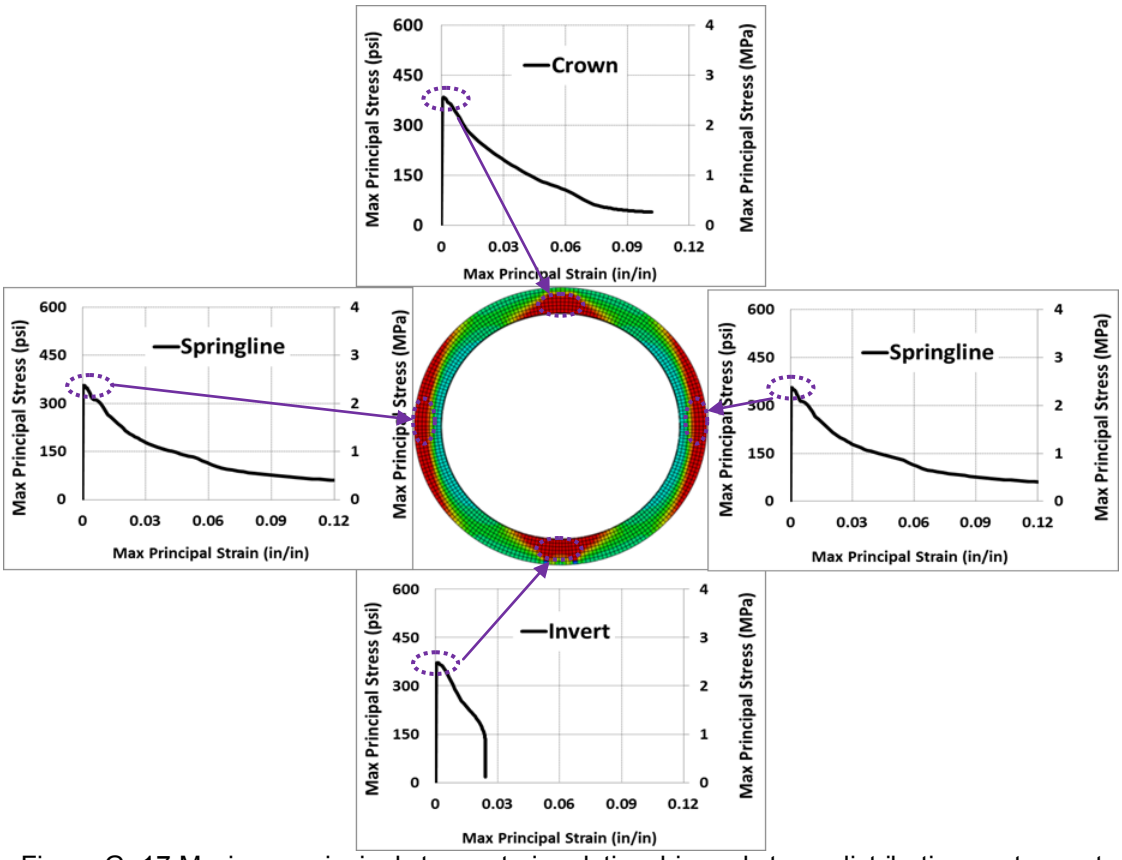

Figure G- 17 Maximum principal stress-strain relationship and stress distribution contours at ultimate stress in FEM 36-C-0.83-IV Steel Fiber Reinforced Concrete Pipe

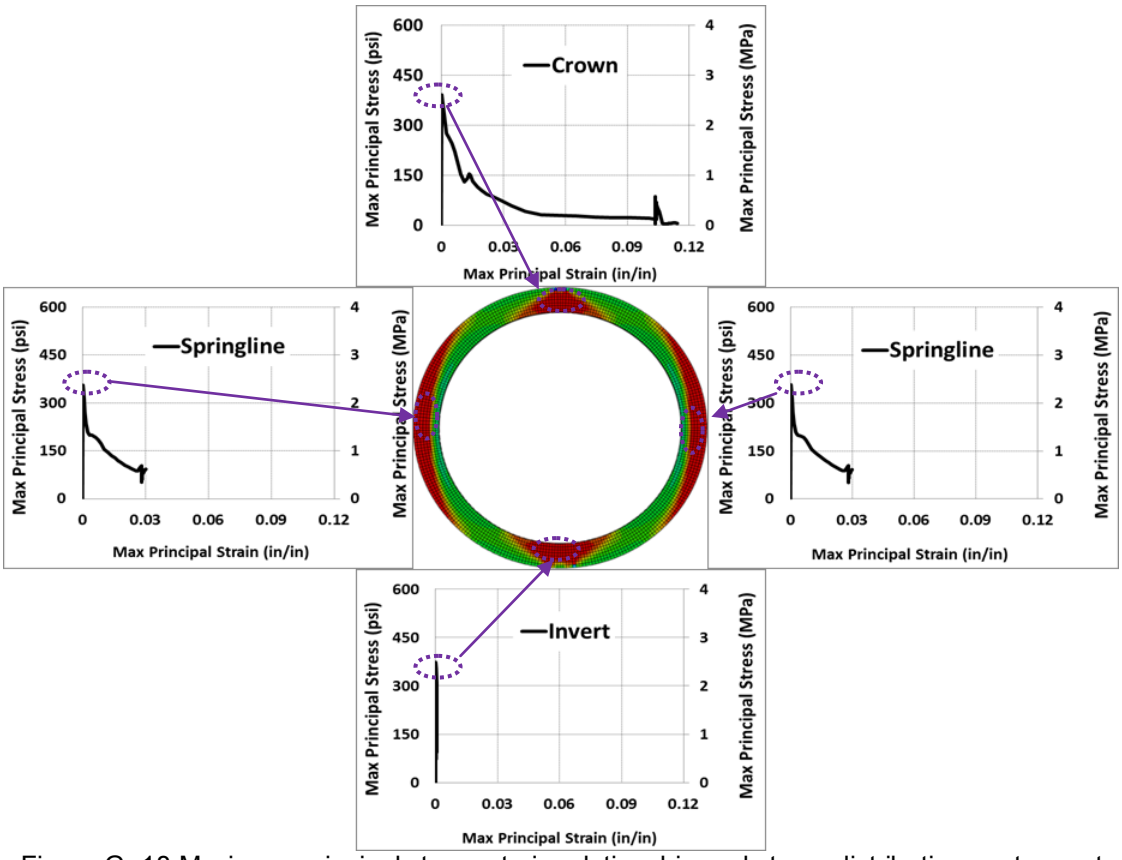

Figure G- 18 Maximum principal stress-strain relationship and stress distribution contours at ultimate stress in FEM 48-B-0.50-II Steel Fiber Reinforced Concrete Pipe

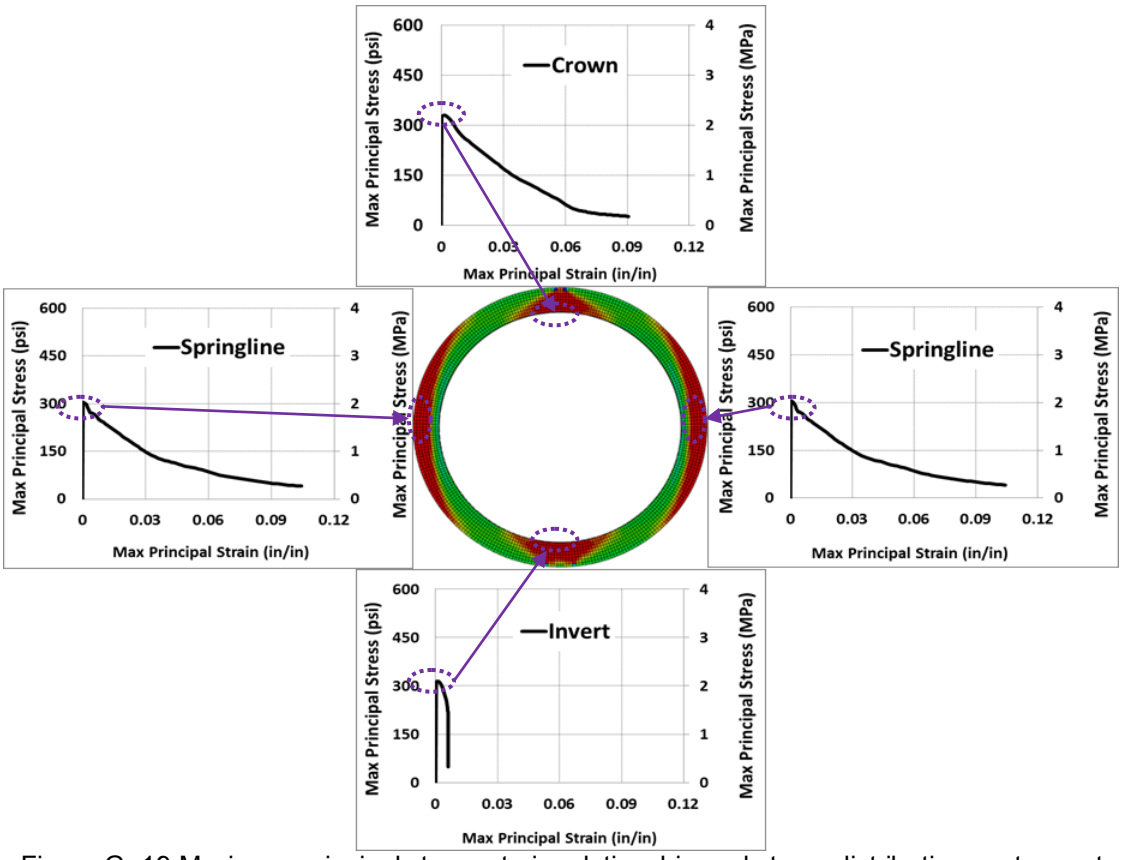

Figure G- 19 Maximum principal stress-strain relationship and stress distribution contours at ultimate stress in FEM 48-B-0.67-II Steel Fiber Reinforced Concrete Pipe

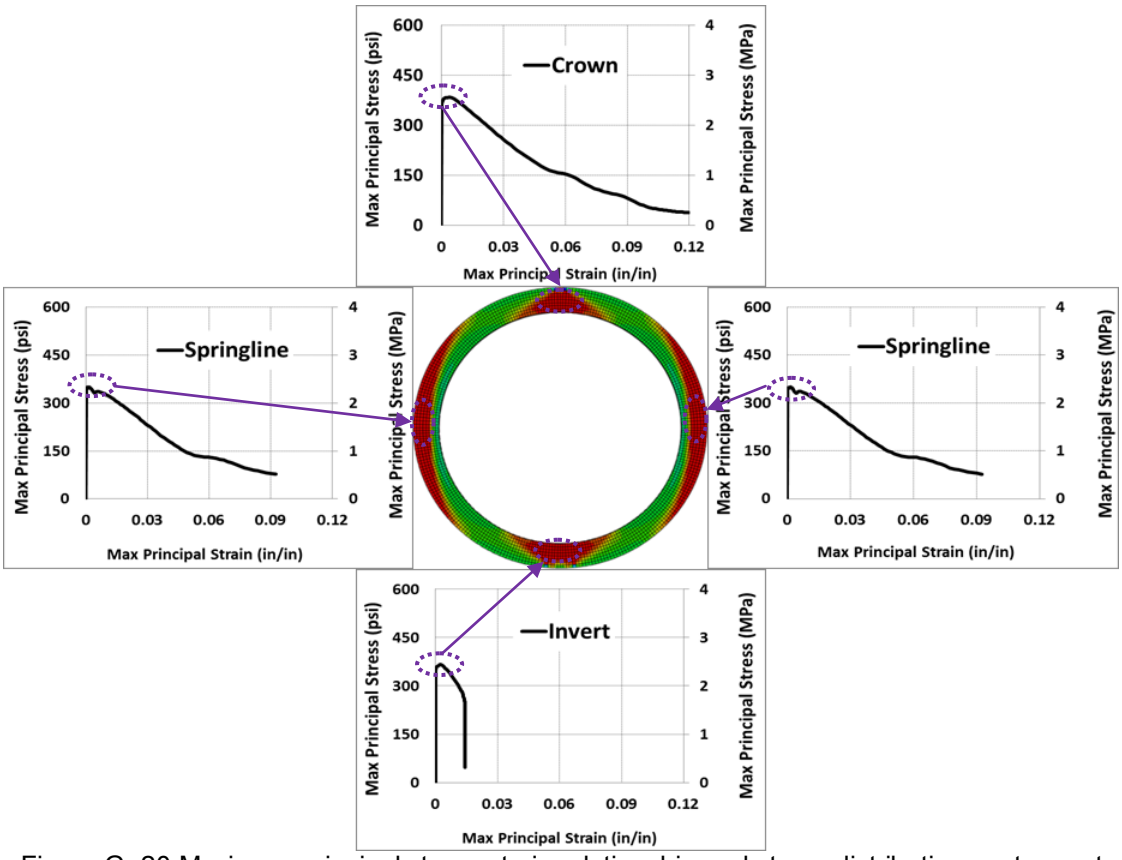

Figure G- 20 Maximum principal stress-strain relationship and stress distribution contours at ultimate stress in FEM 48-B-0.83-III Steel Fiber Reinforced Concrete Pipe

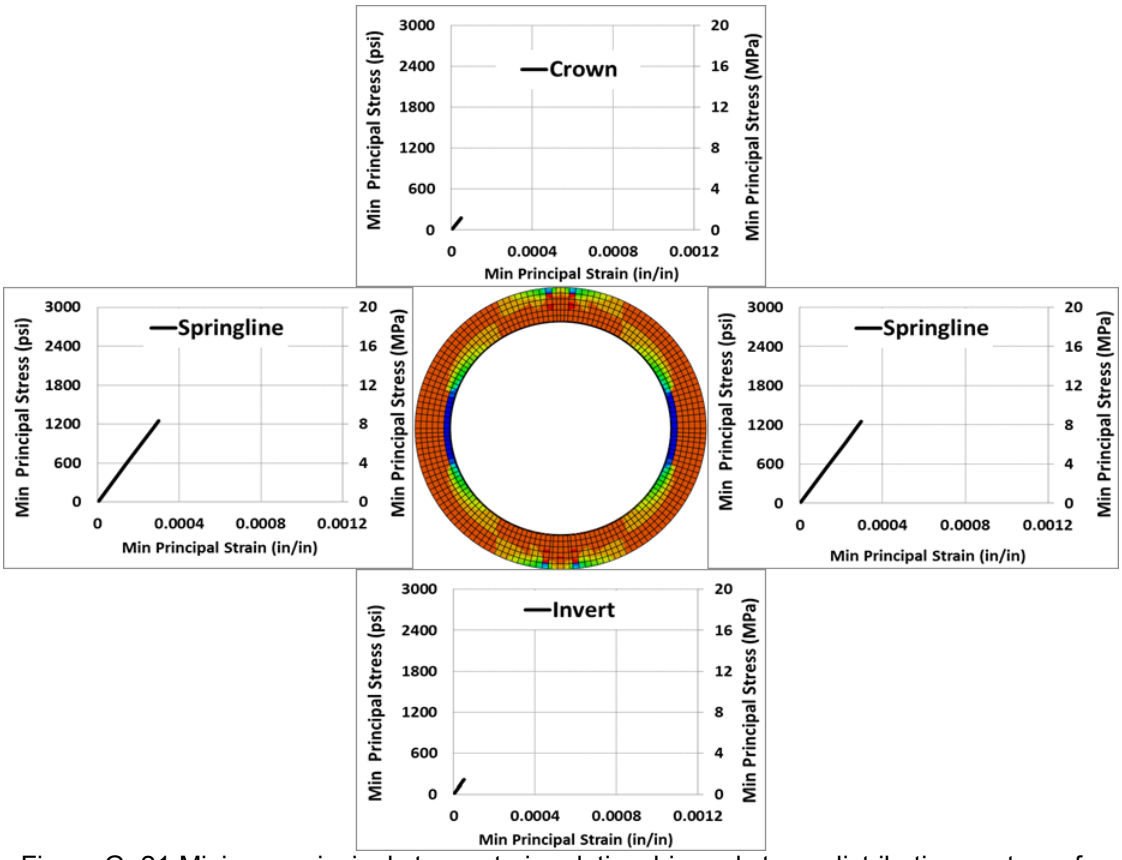

Figure G- 21 Minimum principal stress-strain relationship and stress distribution contours for ultimate stress in FEM 24-B-0.17-II Steel Fiber Reinforced Concrete Pipe

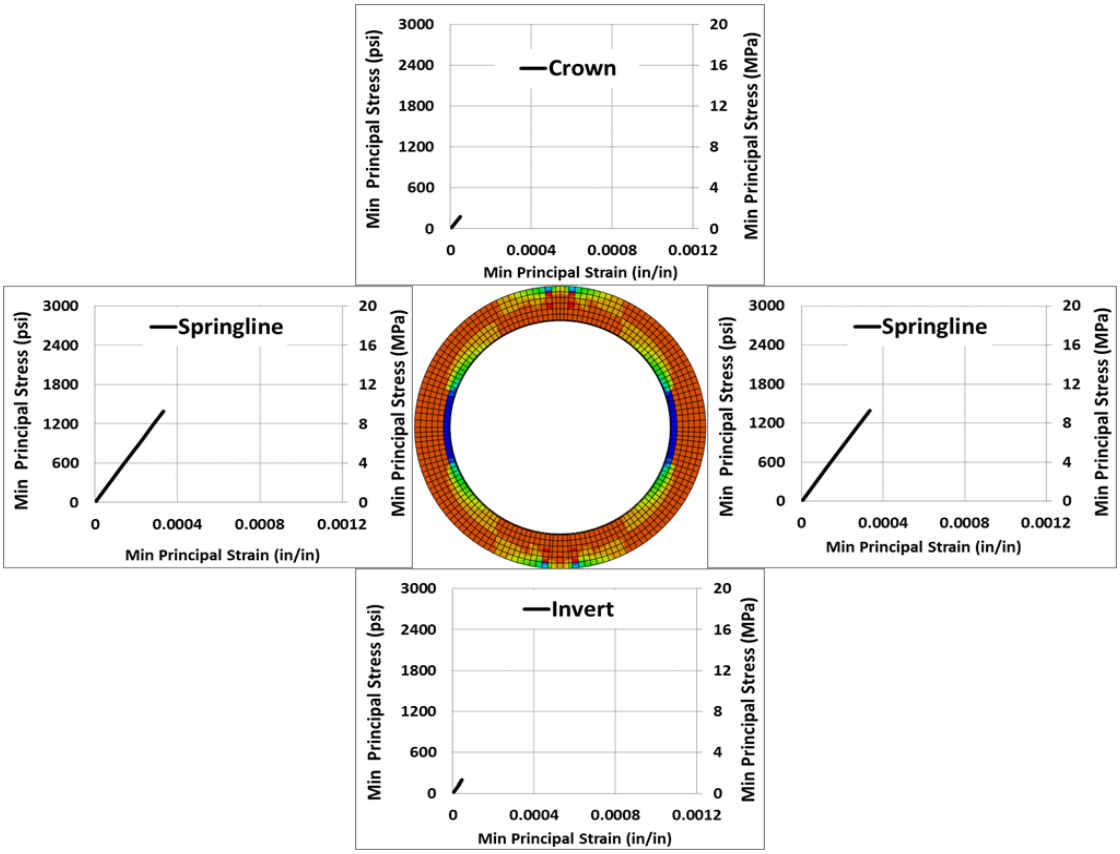

Figure G- 22 Minimum principal stress-strain relationship and stress distribution contours for ultimate stress in FEM 24-B-0.25-III Steel Fiber Reinforced Concrete Pipe

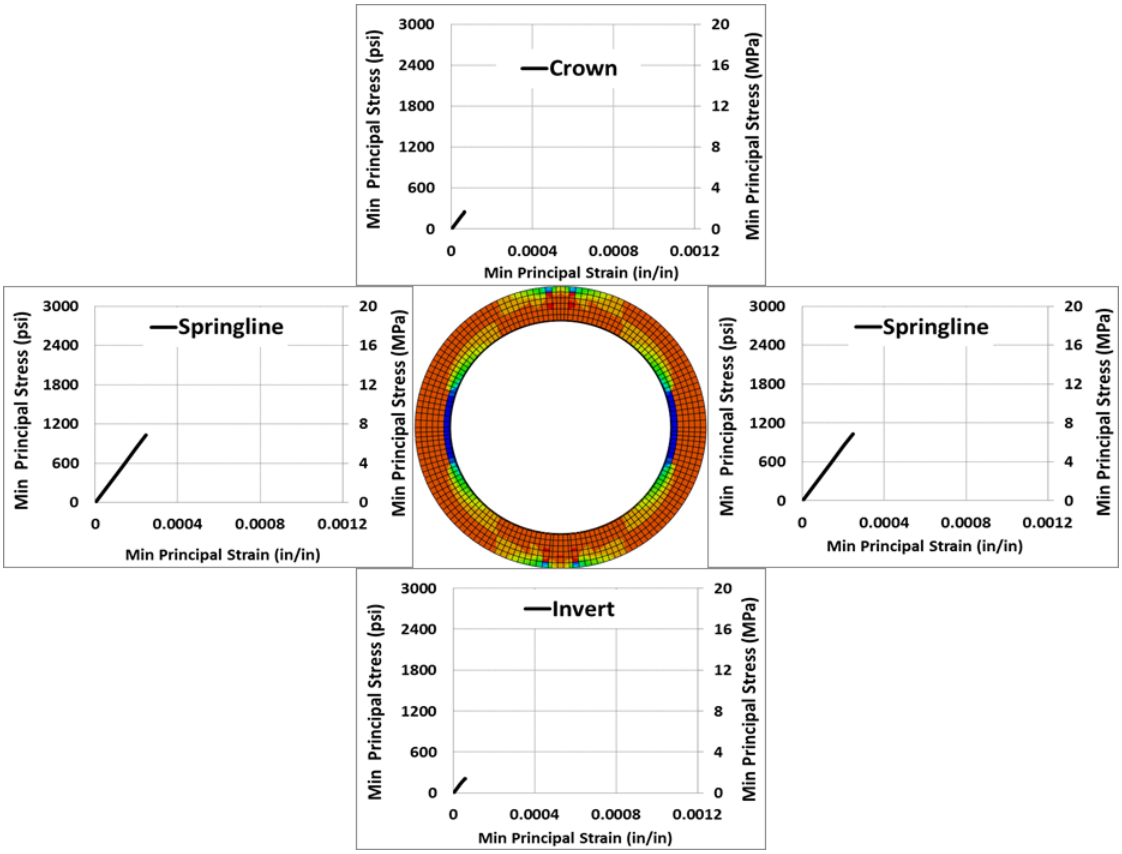

Figure G- 23 Minimum principal stress-strain relationship and stress distribution contours for ultimate stress in FEM 24-C-0.25-III Steel Fiber Reinforced Concrete Pipe

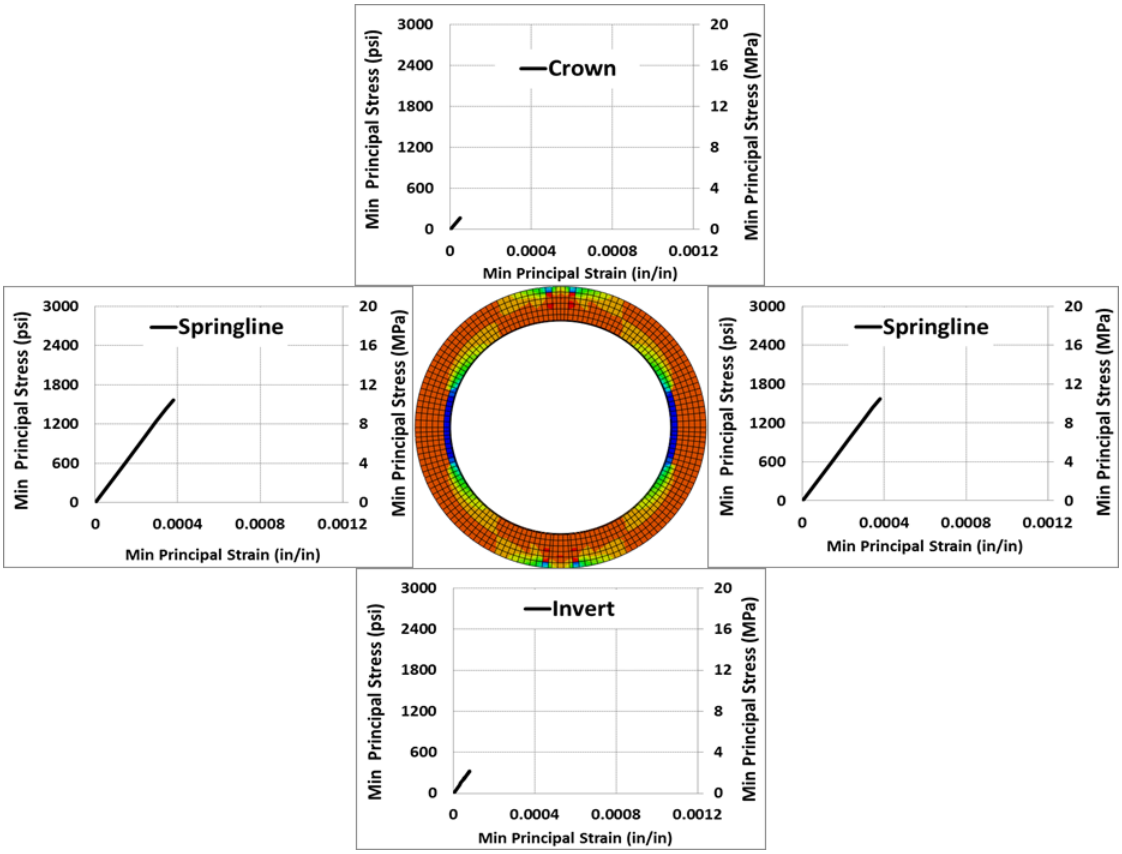

Figure G- 24 Minimum principal stress-strain relationship and stress distribution contours for ultimate stress in FEM 24-B-0.33-III Steel Fiber Reinforced Concrete Pipe

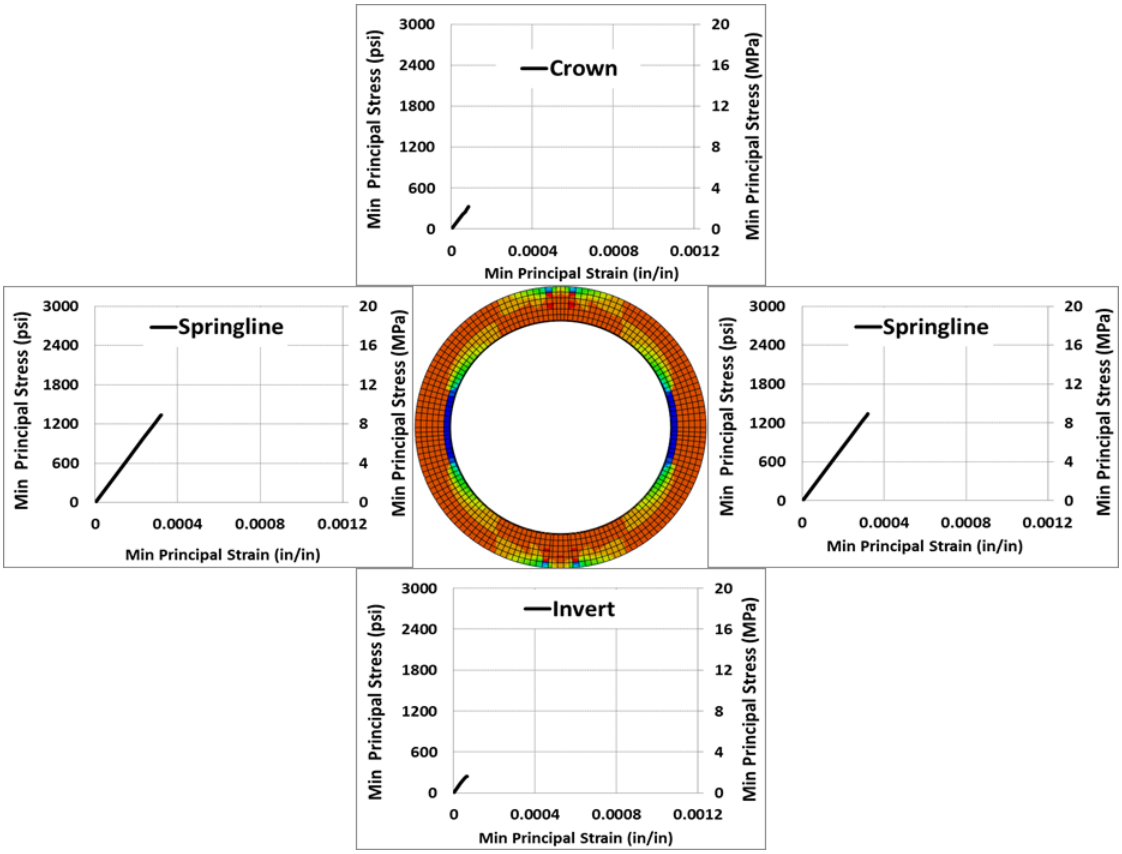

Figure G- 25 Minimum principal stress-strain relationship and stress distribution contours for ultimate stress in FEM 24-C-0.33-III Steel Fiber Reinforced Concrete Pipe

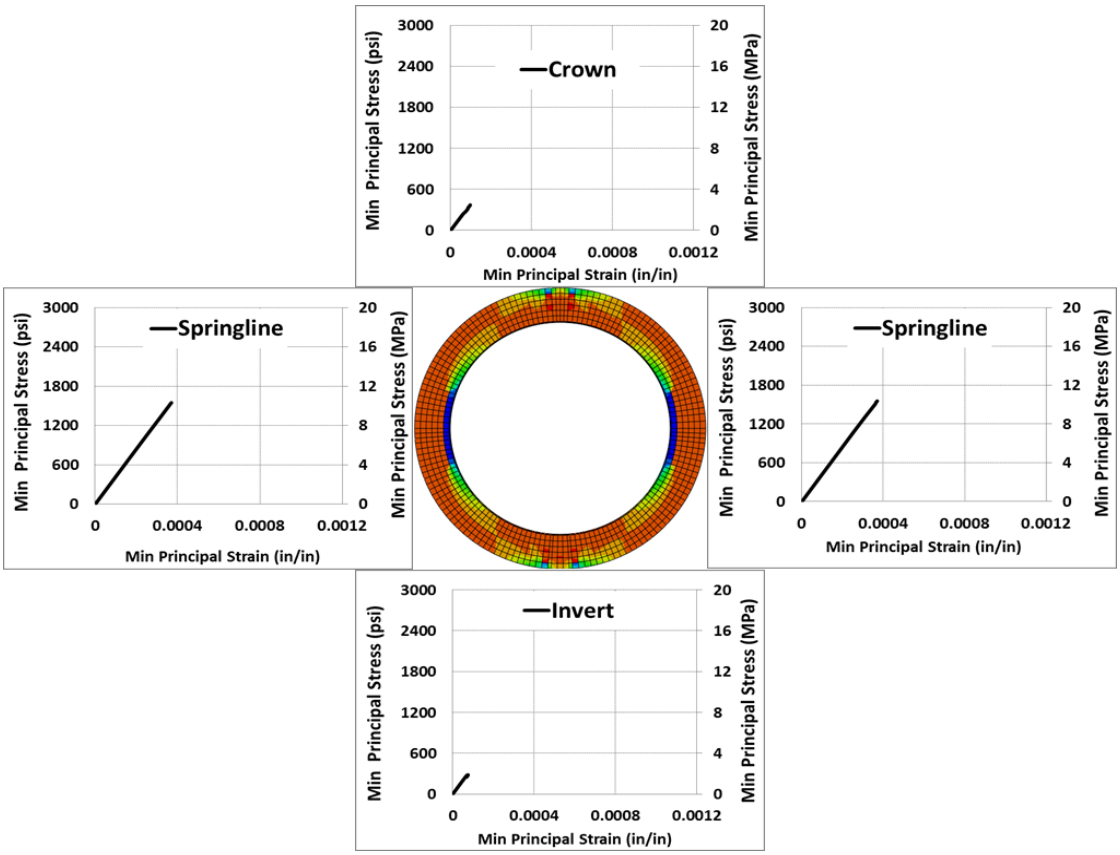

Figure G- 26 Minimum principal stress-strain relationship and stress distribution contours for ultimate stress in FEM 24-C-0.5-IV Steel Fiber Reinforced Concrete Pipe

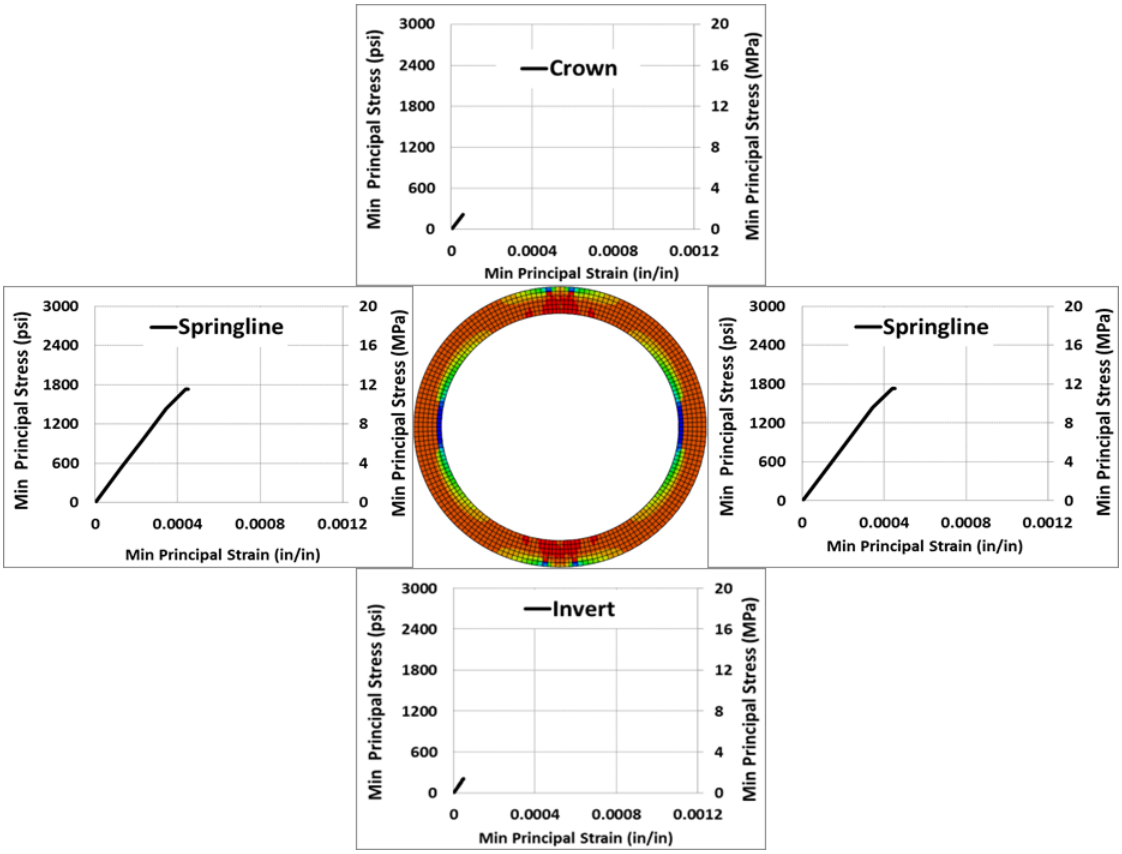

Figure G- 27 Minimum principal stress-strain relationship and stress distribution contours for ultimate stress in FEM 30-B-0.33-III Steel Fiber Reinforced Concrete Pipe

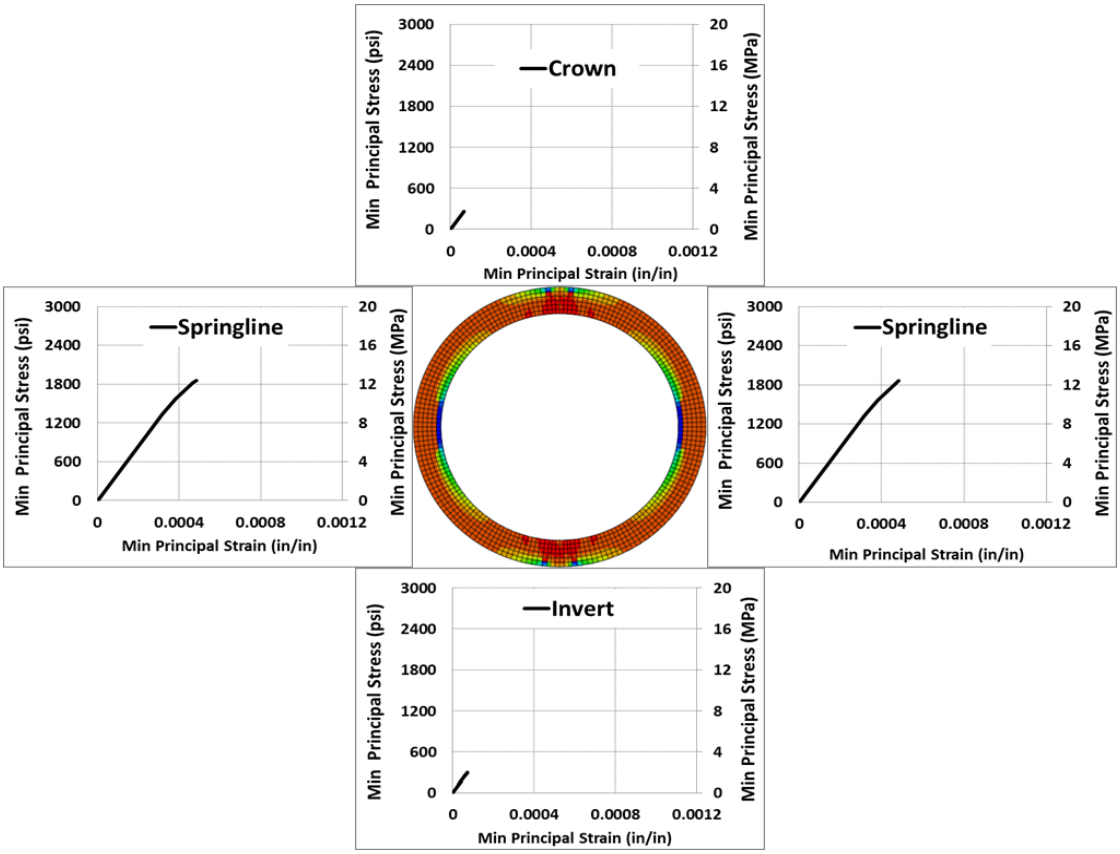

Figure G- 28 Minimum principal stress-strain relationship and stress distribution contours for ultimate stress in FEM 30-C-0.33-III Steel Fiber Reinforced Concrete Pipe

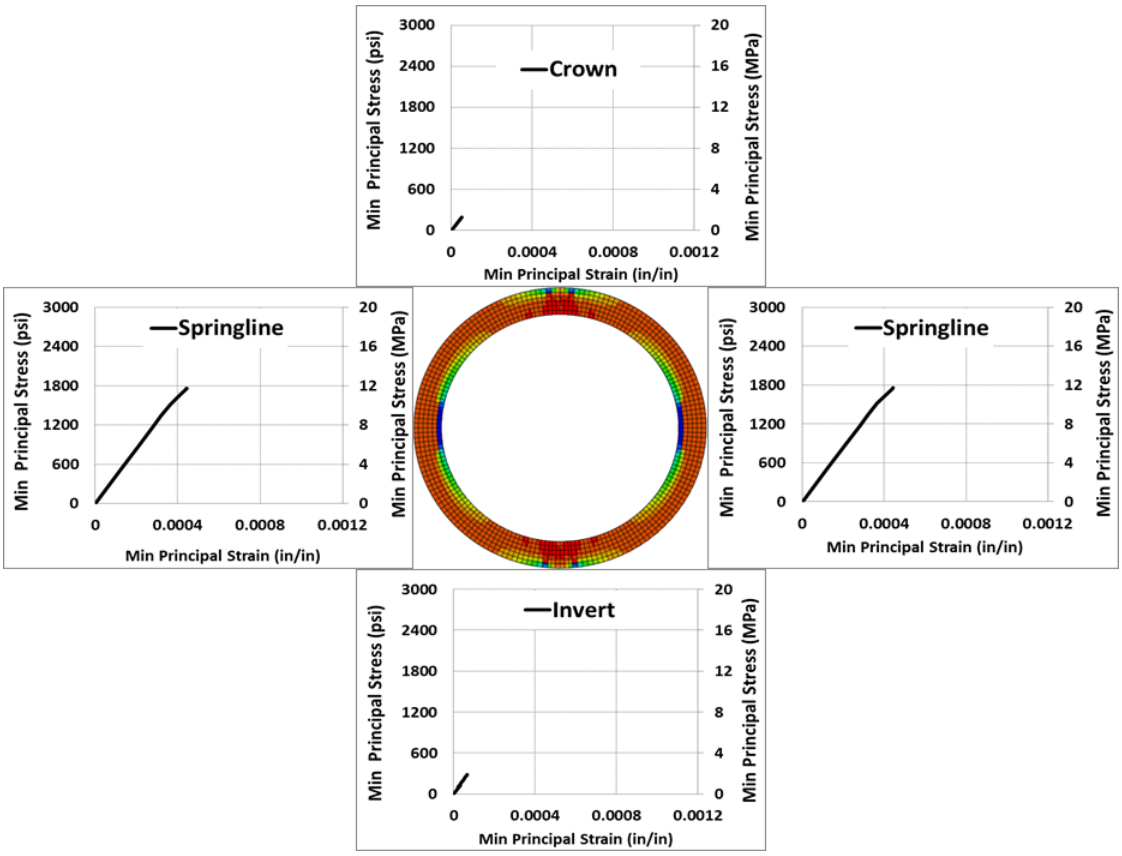

Figure G- 29 Minimum principal stress-strain relationship and stress distribution contours for ultimate stress in FEM 30-B-0.50-III Steel Fiber Reinforced Concrete Pipe

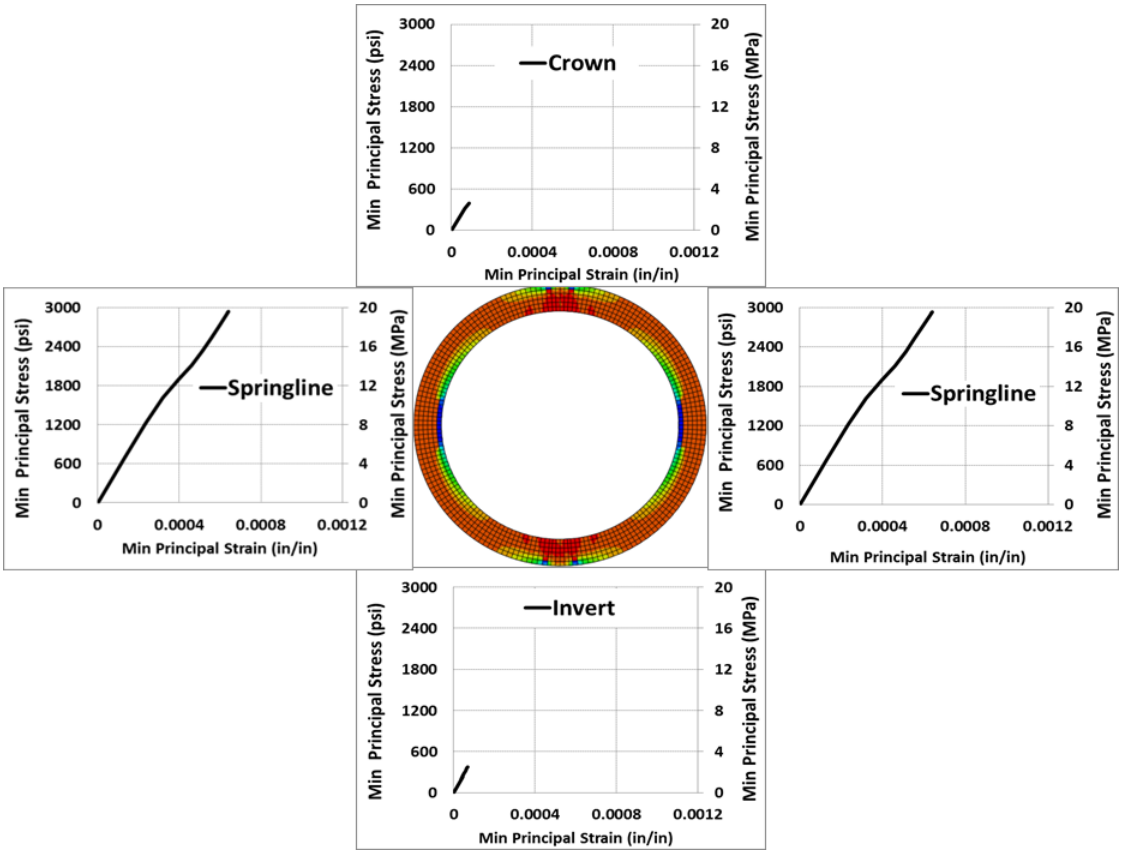

Figure G- 30 Minimum principal stress-strain relationship and stress distribution contours for ultimate stress in FEM 30-B-0.5-IV Steel Fiber Reinforced Concrete Pipe

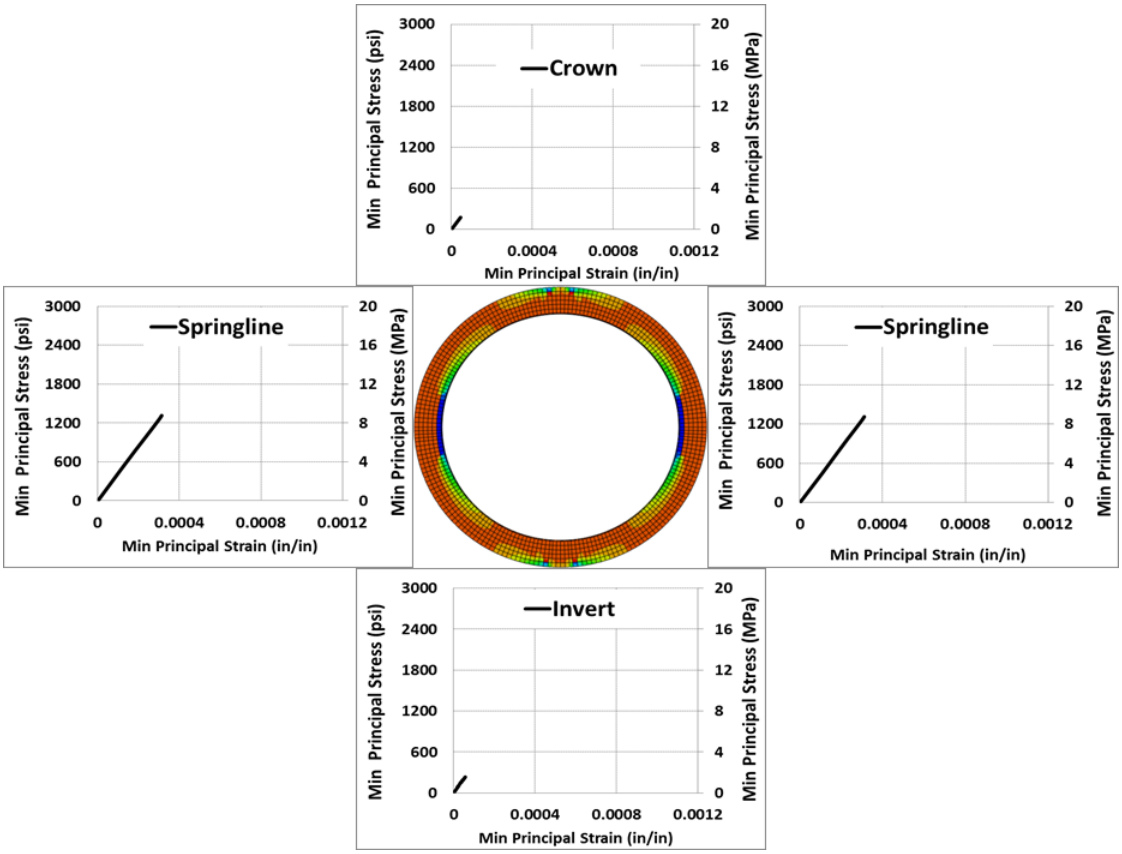

Figure G- 31 Minimum principal stress-strain relationship and stress distribution contours for ultimate stress in FEM 33-B-0.33-I Steel Fiber Reinforced Concrete Pipe

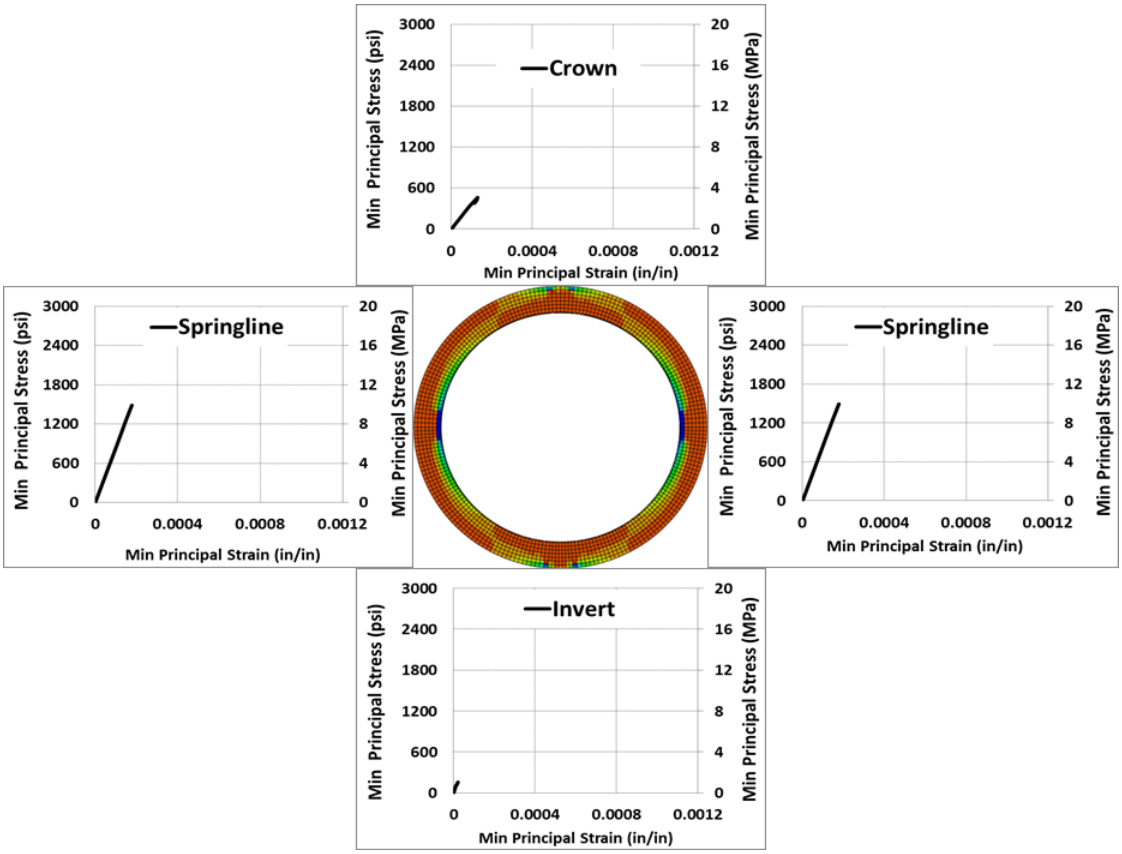

Figure G- 32 Minimum principal stress-strain relationship and stress distribution contours for ultimate stress in FEM 36-C-0.25-III Steel Fiber Reinforced Concrete Pipe

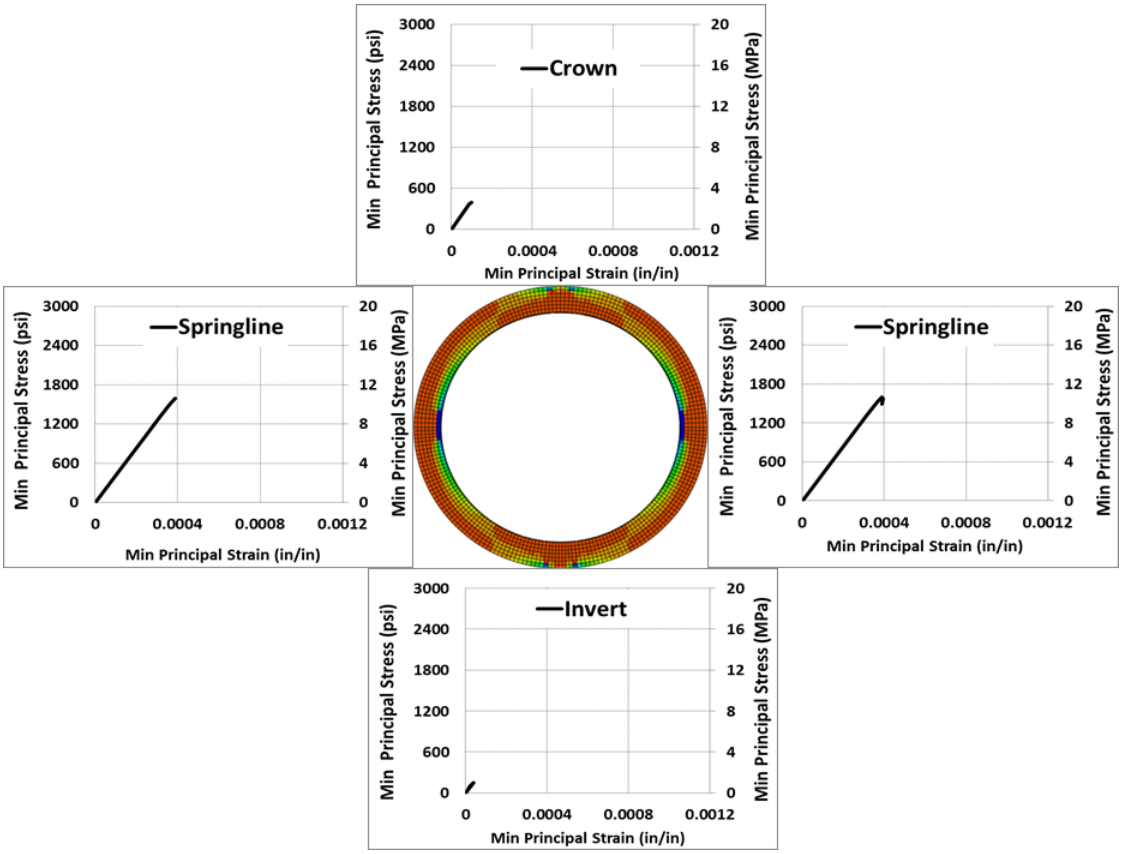

Figure G- 33 Minimum principal stress-strain relationship and stress distribution contours for ultimate stress in FEM 36-C-0.33-III Steel Fiber Reinforced Concrete Pipe

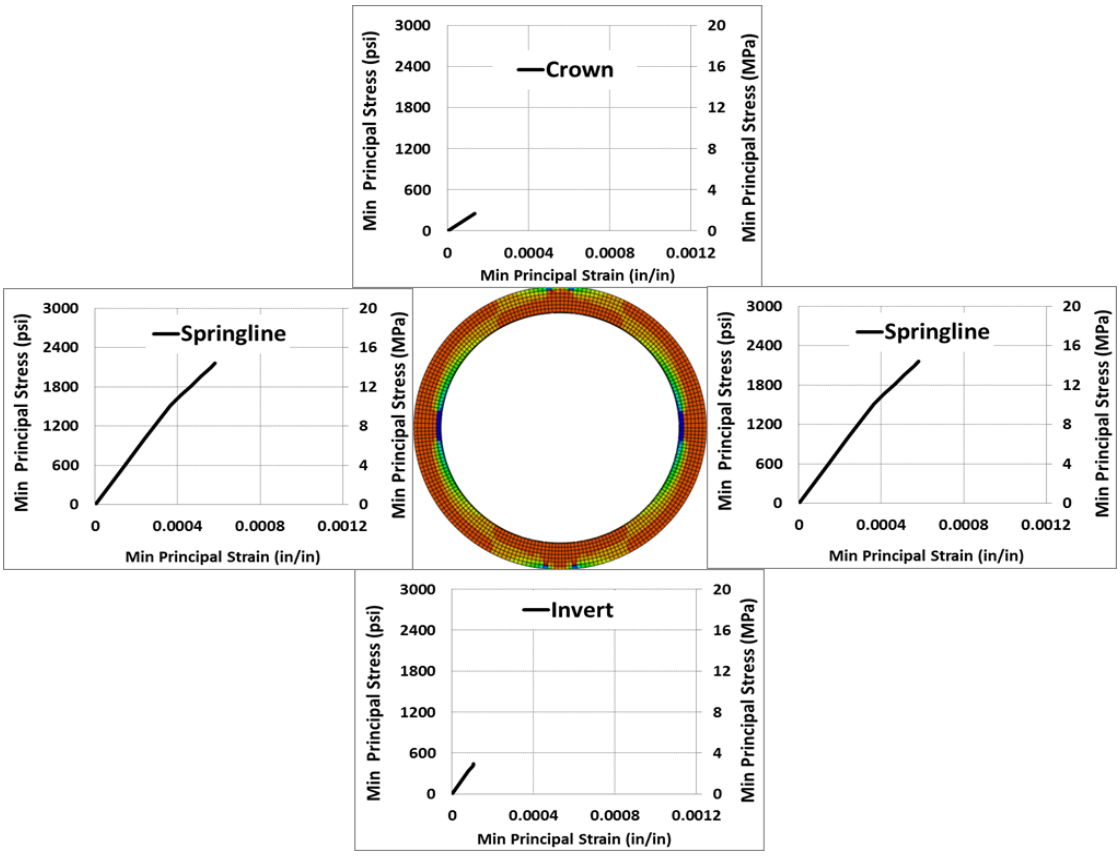

Figure G- 34 Minimum principal stress-strain relationship and stress distribution contours for ultimate stress in FEM 36-C-0.5-III Steel Fiber Reinforced Concrete Pipe

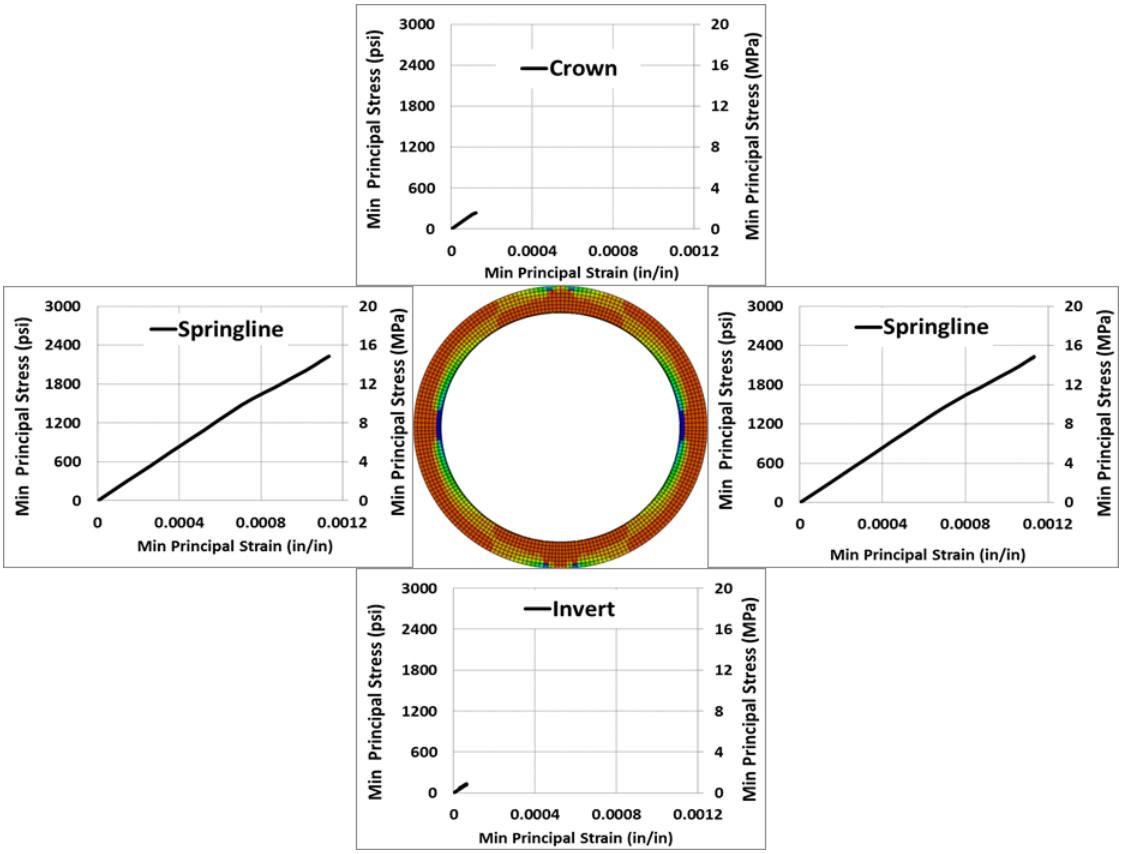

Figure G- 35 Minimum principal stress-strain relationship and stress distribution contours for ultimate stress in FEM 36-B-0.67-III Steel Fiber Reinforced Concrete Pipe

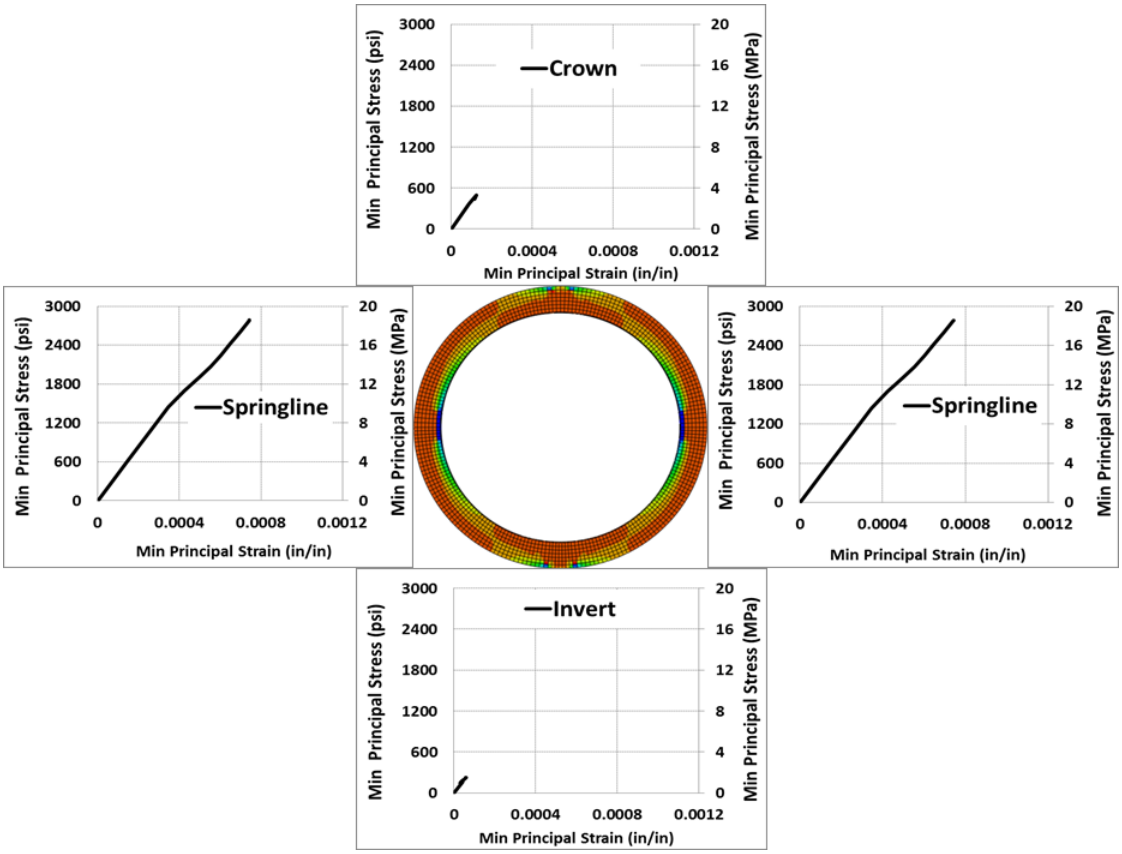

Figure G- 36 Minimum principal stress-strain relationship and stress distribution contours for ultimate stress in FEM 36-C-0.67-IV Steel Fiber Reinforced Concrete Pipe

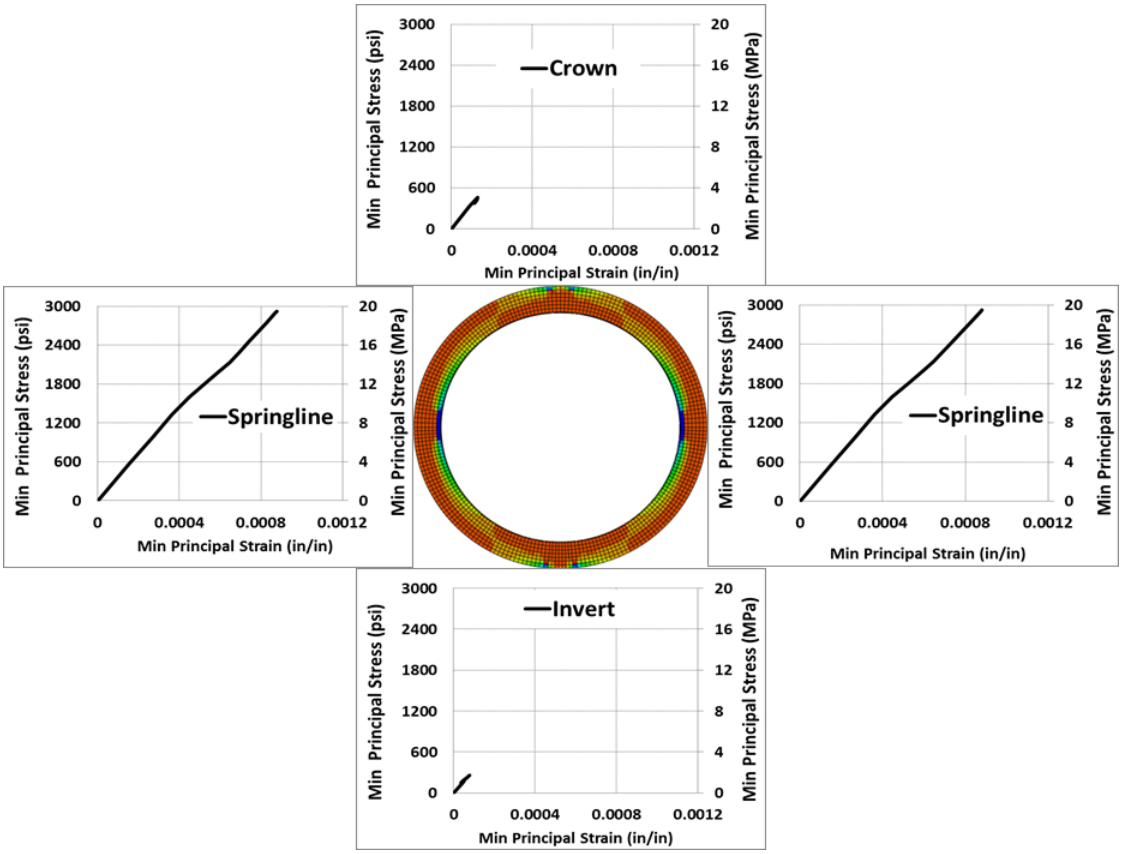

Figure G- 37 Minimum principal stress-strain relationship and stress distribution contours for ultimate stress in FEM 36-C-0.83-IV Steel Fiber Reinforced Concrete Pipe

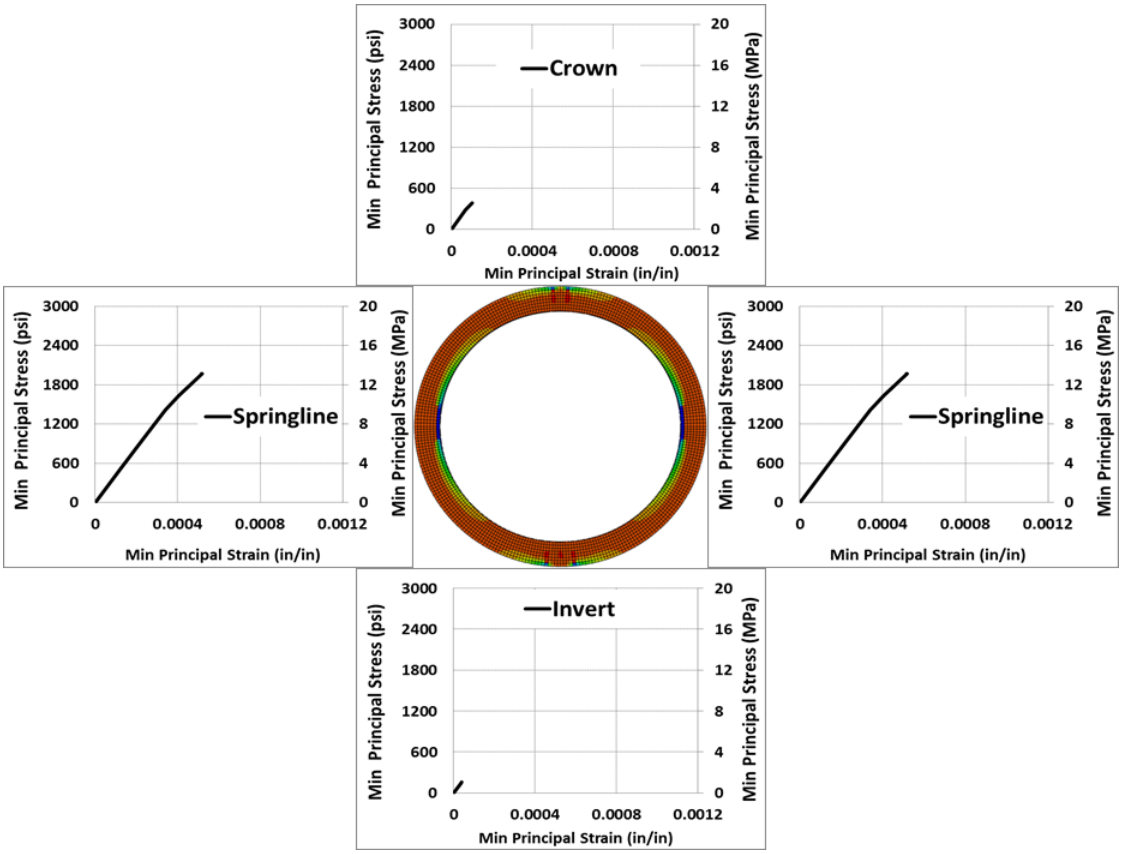

Figure G- 38 Minimum principal stress-strain relationship and stress distribution contours for ultimate stress in FEM 48-B-0.50-II Steel Fiber Reinforced Concrete Pipe

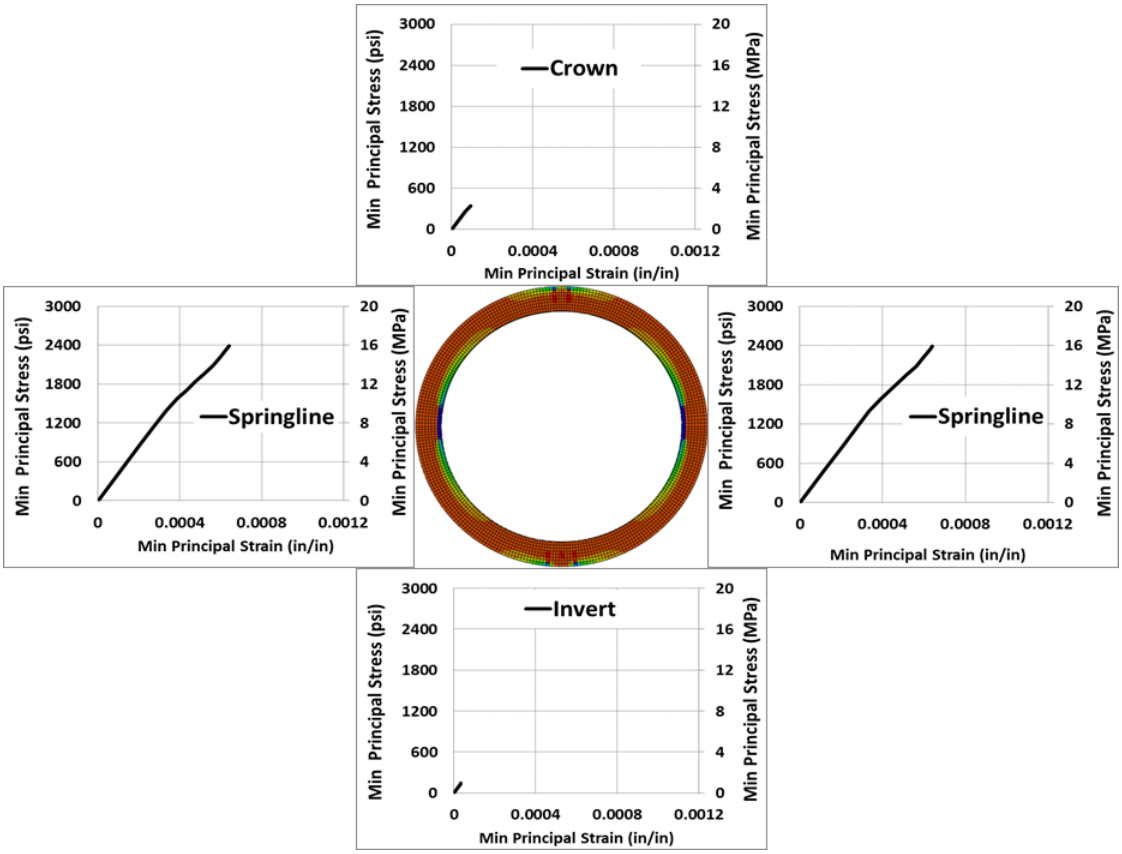

Figure G- 39 Minimum principal stress-strain relationship and stress distribution contours for ultimate stress in FEM 48-B-0.67-II Steel Fiber Reinforced Concrete Pipe

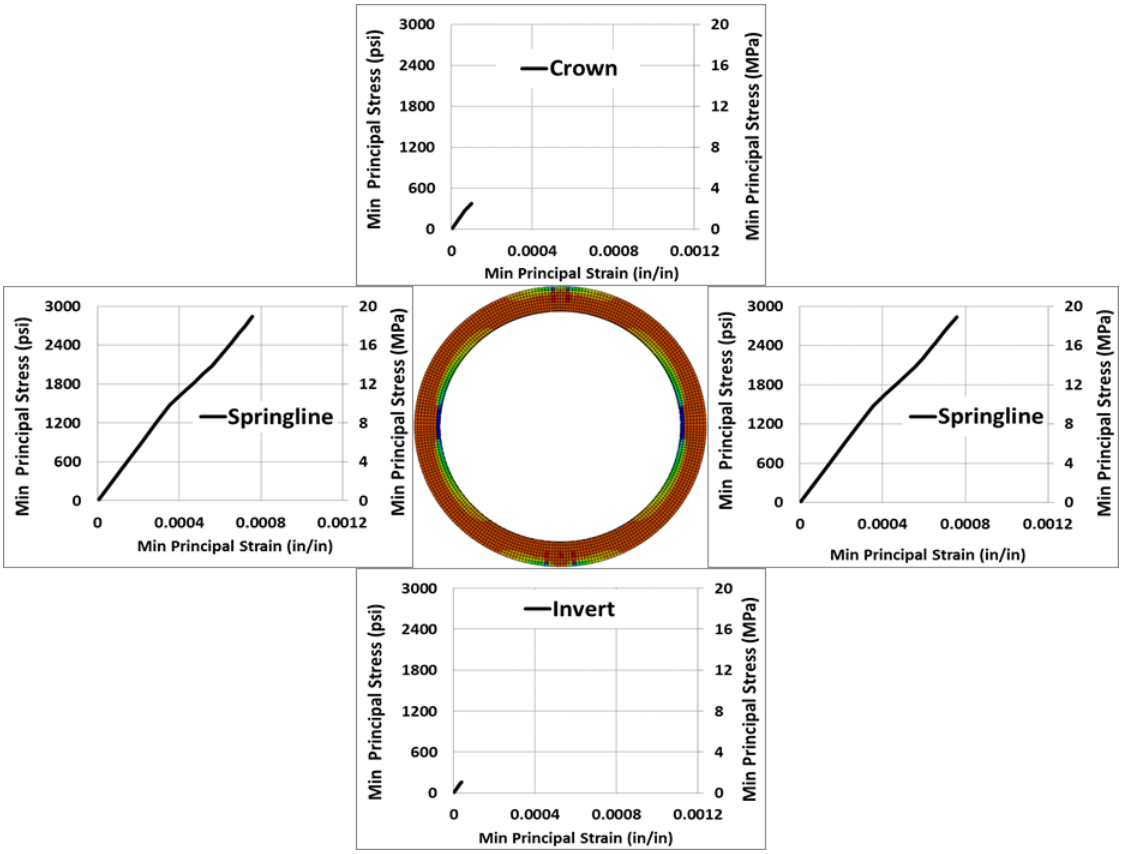

Figure G- 40 Minimum principal stress-strain relationship and stress distribution contours for ultimate stress in FEM 48-B-0.83-III Steel Fiber Reinforced Concrete Pipe

Appendix H

Prediction of Internal Forces with Finite Element Method in Steel Fiber Reinforced Concrete Pipe

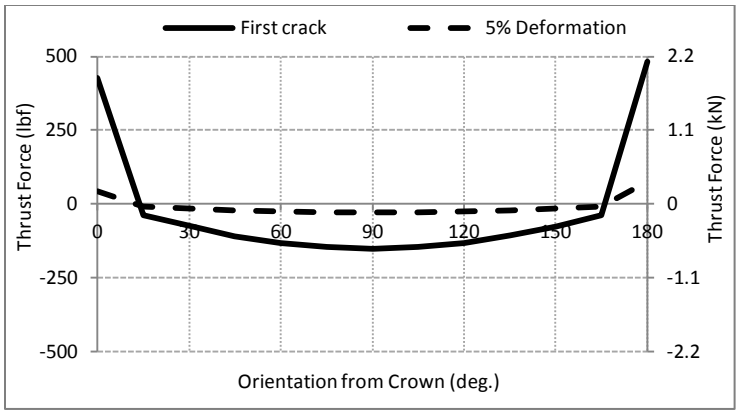

(a)

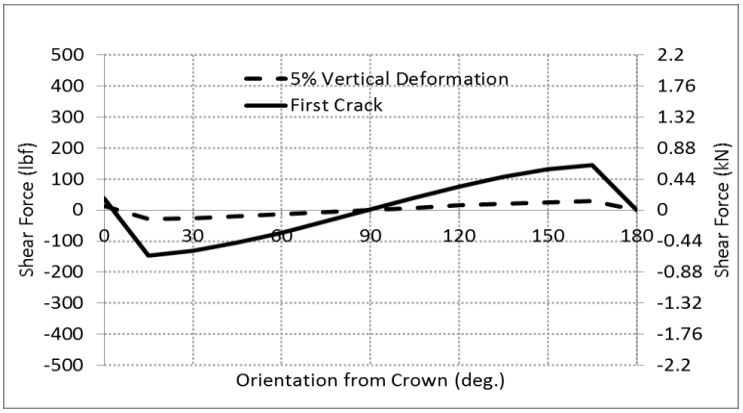

(b)

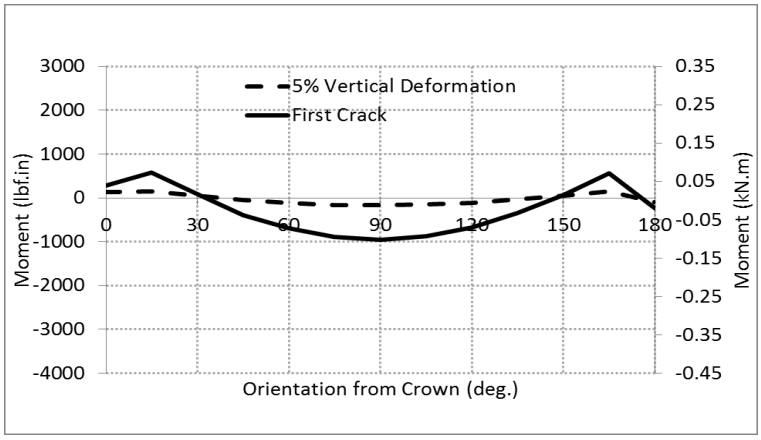

(c)

Figure H- 2 Variation of Internal Forces in 24-B-0.17-II SFRCP from crown to invert:

a) Thrust; b) Shear; and c) Moment

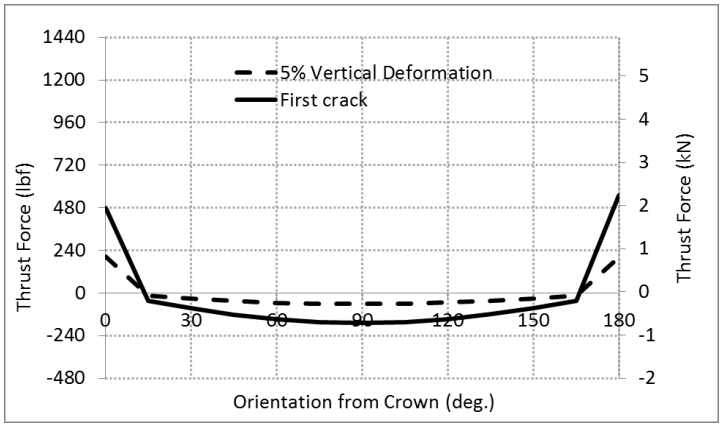

(a)

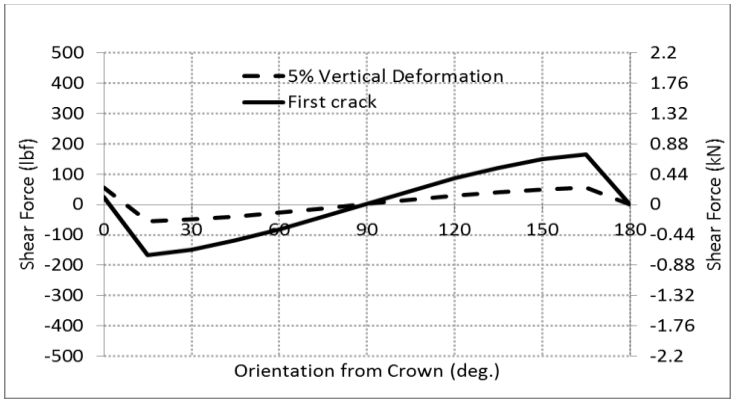

(b)

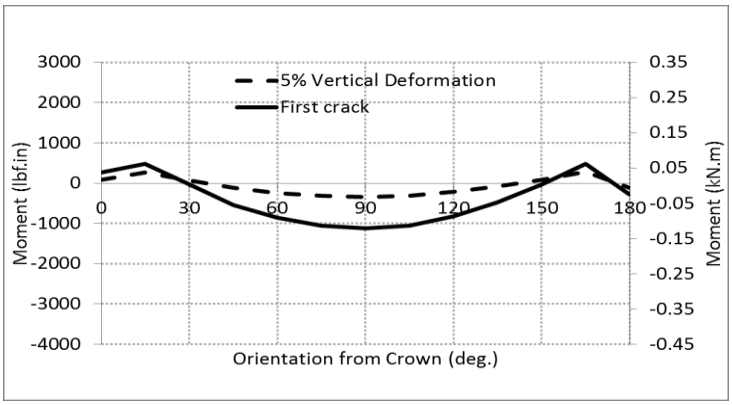

(c)

Figure H- 3 Variation of Internal Forces in 24-B-0.25-III SFRCP from crown to invert:

a) Thrust; b) Shear; and c) Moment

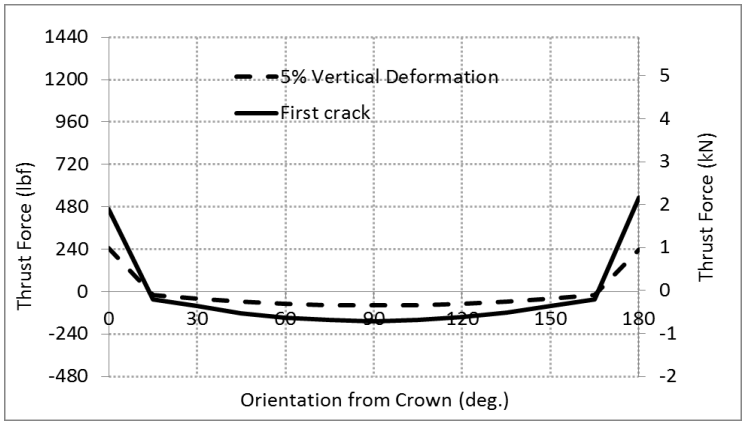

(a)

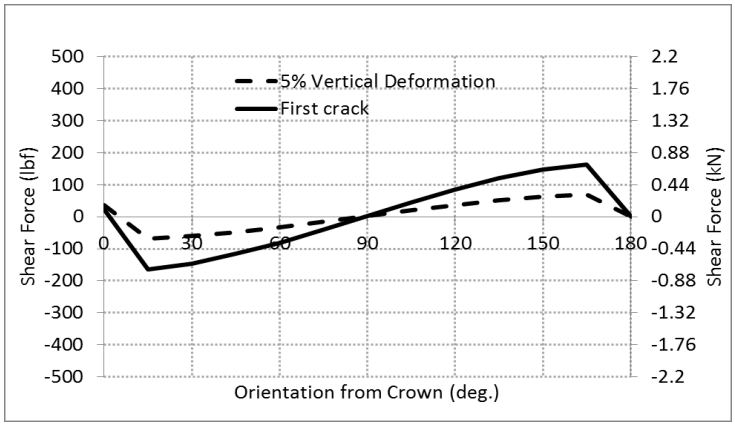

(b)

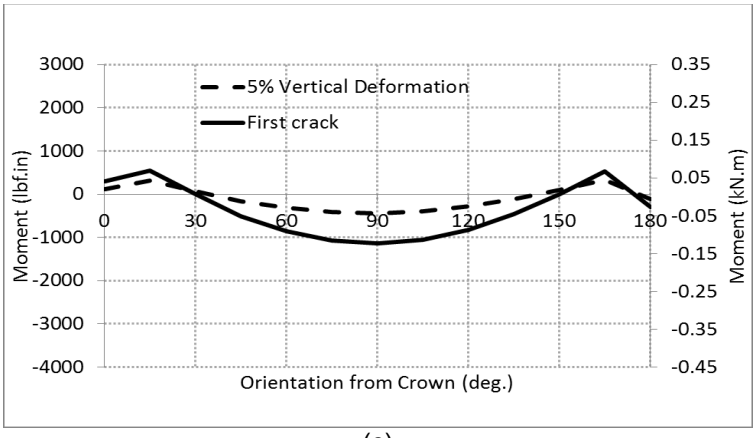

(c)

Figure H- 4 Variation of Internal Forces in 24-B-0.33-III SFRCP from crown to invert:

a) Thrust; b) Shear; and c) Moment

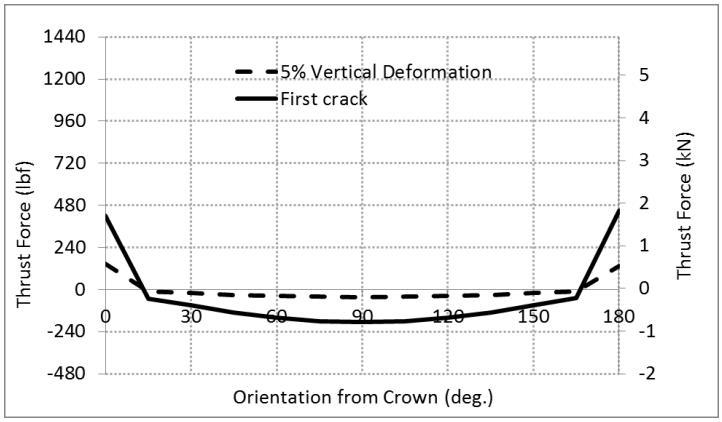

(a)

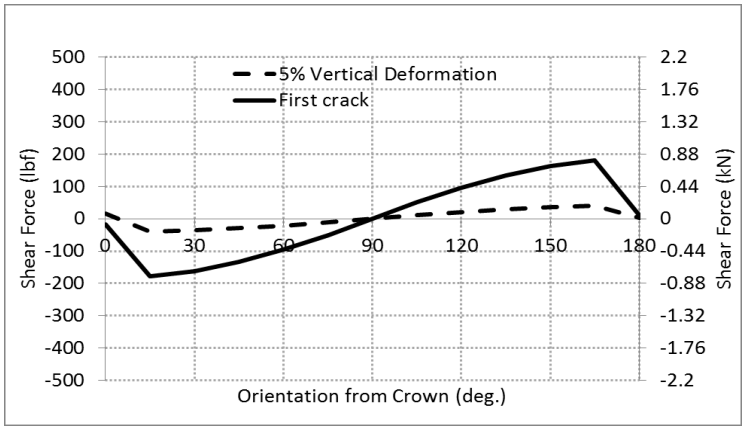

(b)

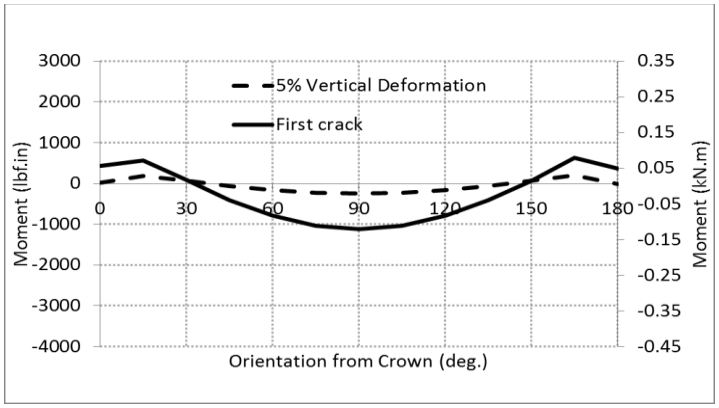

(c)

Figure H- 5 Variation of Internal Forces in 24-C-0.25-III SFRCP from crown to invert:

a) Thrust; b) Shear; and c) Moment

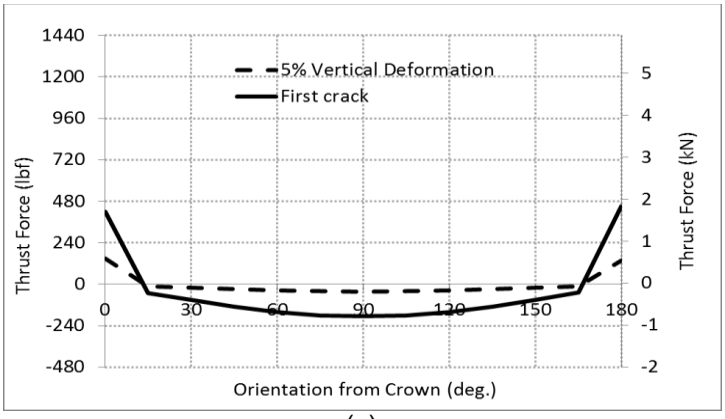

(a)

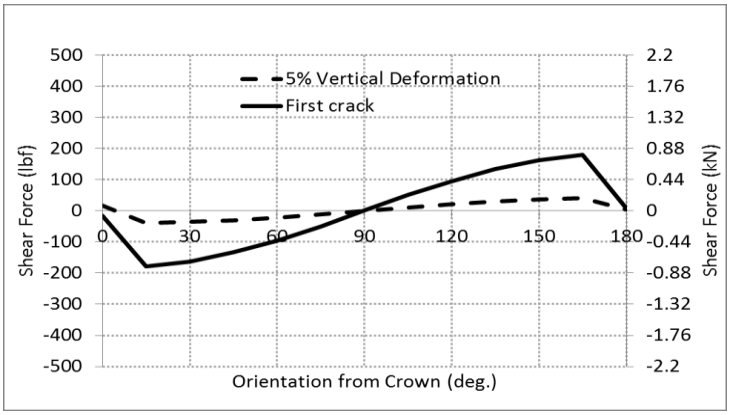

(b)

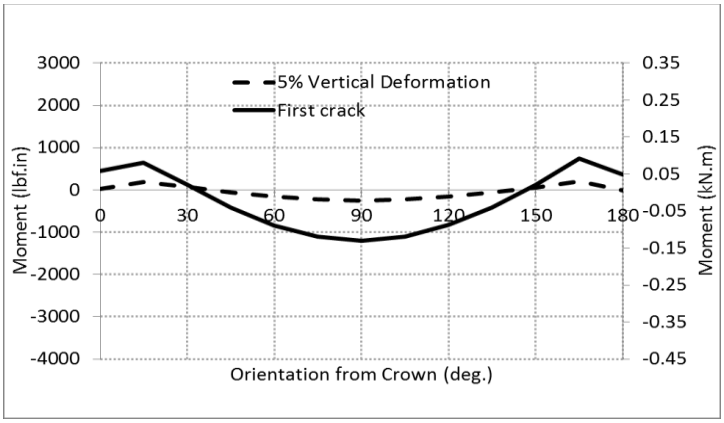

(c)

Figure H- 6 Variation of Internal Forces in 24-C-0.33-III SFRCP from crown to invert:

a) Thrust; b) Shear; and c) Moment

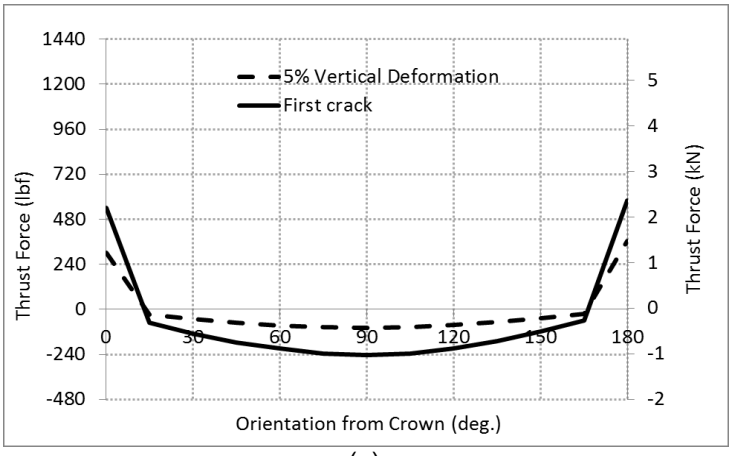

(a)

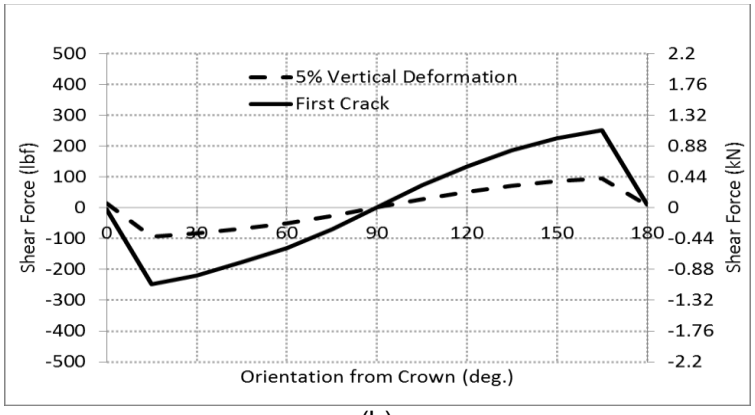

(b)

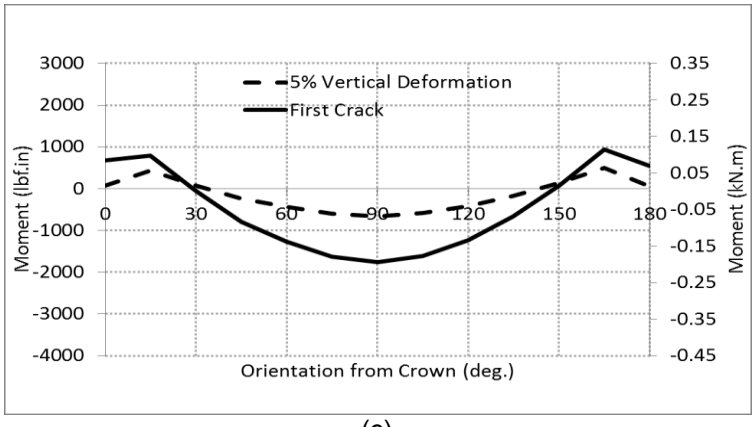

(c)

Figure H- 7 Variation of Internal Forces in 24-C-0.50-IV SFRCP from crown to invert:

a) Thrust; b) Shear; and c) Moment

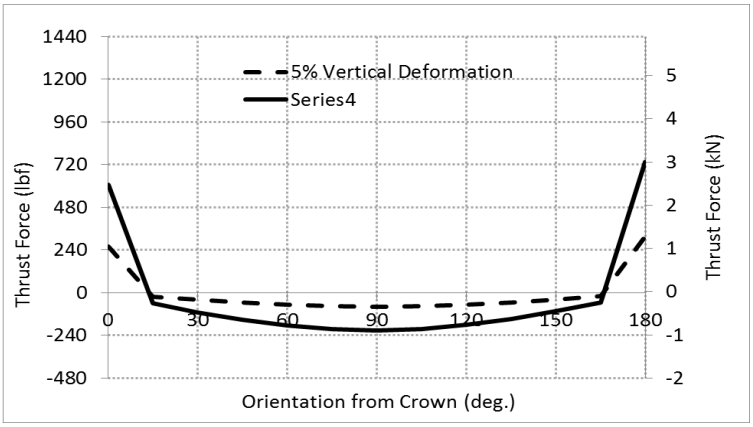

(a)

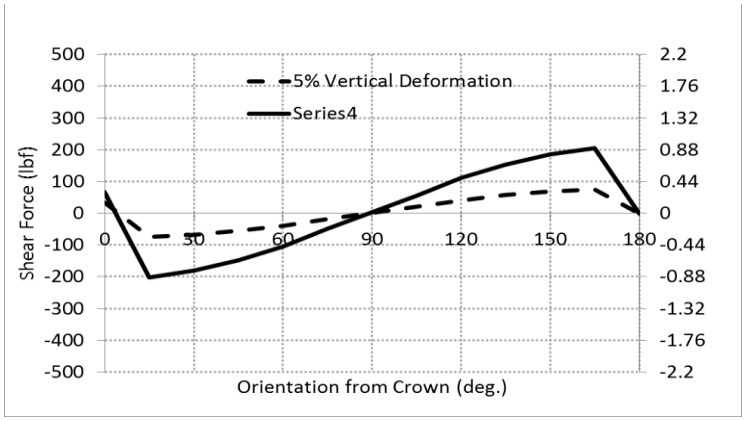

(b)

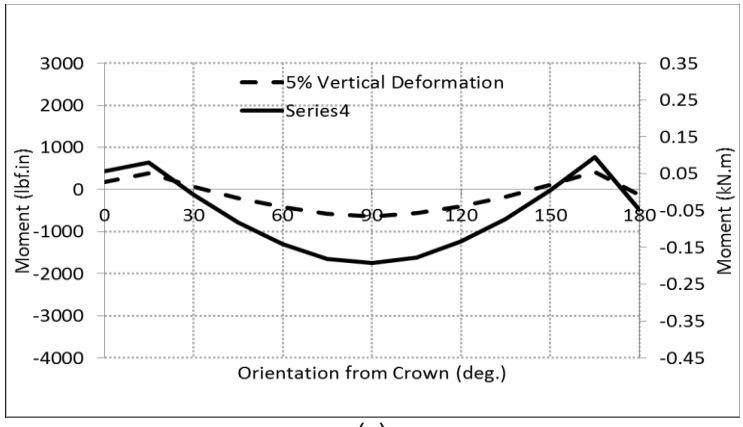

(c)

Figure H- 8 Variation of Internal Forces in 30-B-0.33-III SFRCP from crown to invert:

a) Thrust; b) Shear; and c) Moment

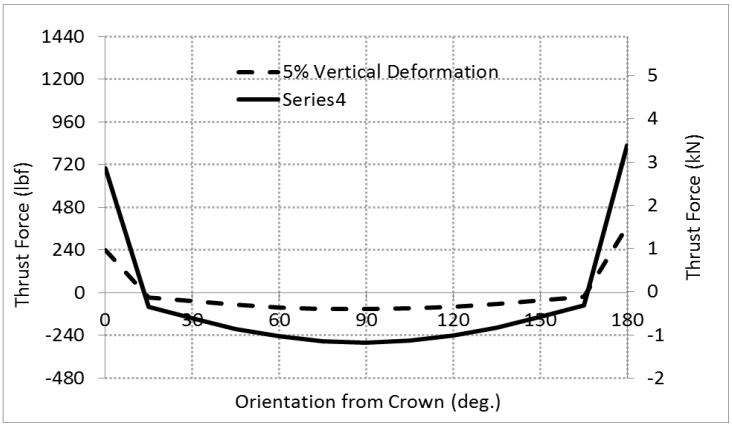

(a)

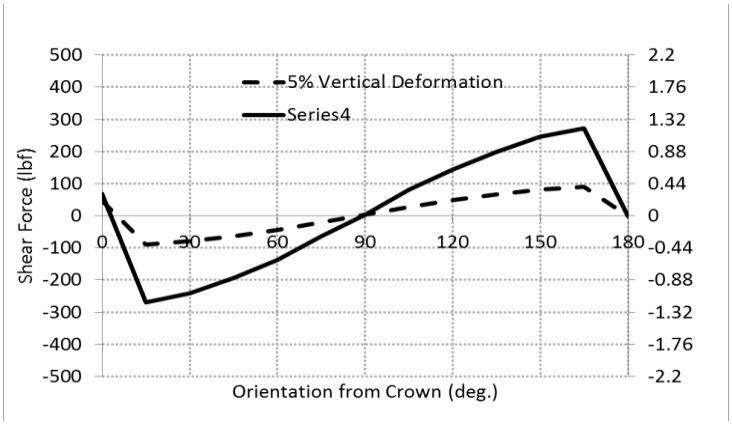

(b)

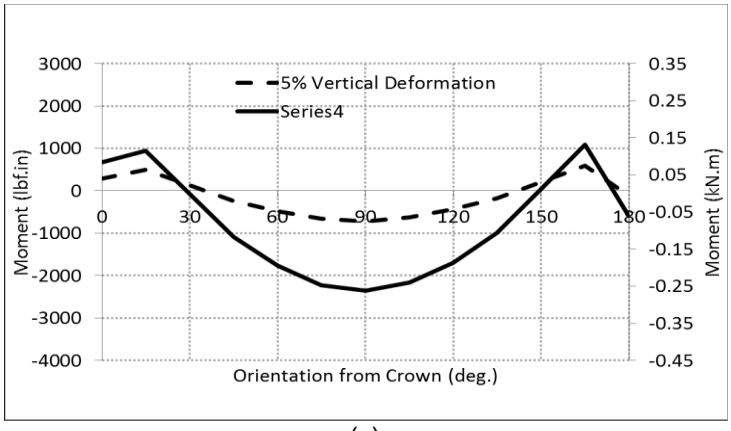

(c)

Figure H- 9 Variation of Internal Forces in 30-C-0.33-III SFRCP from crown to invert:

a) Thrust; b) Shear; and c) Moment

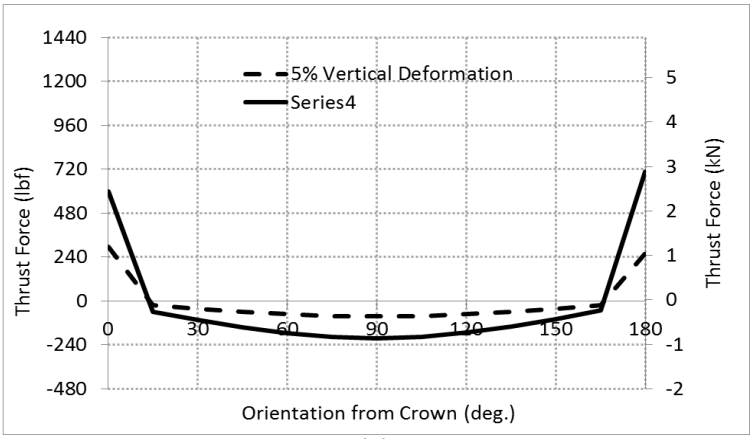

(a)

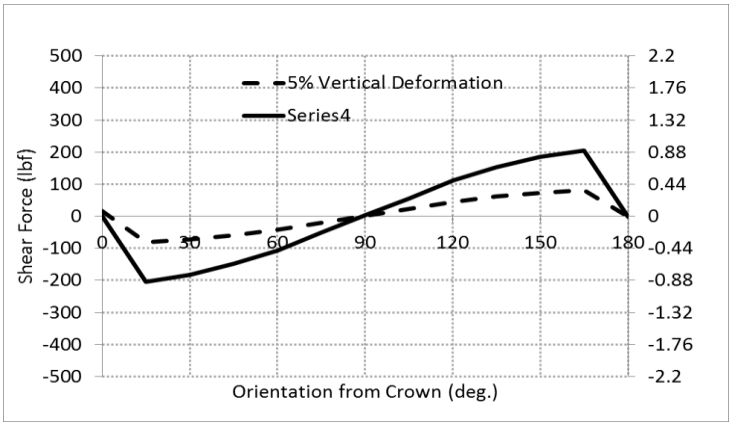

(b)

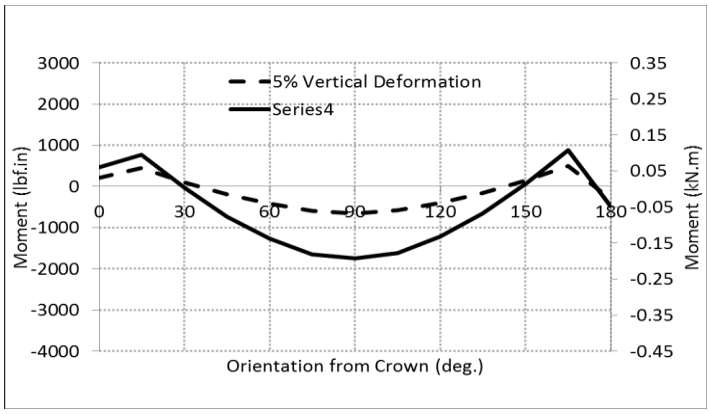

(c)

Figure H- 10 Variation of Internal Forces in 30-B-0.50-III SFRCP from crown to invert:

a) Thrust; b) Shear; and c) Moment

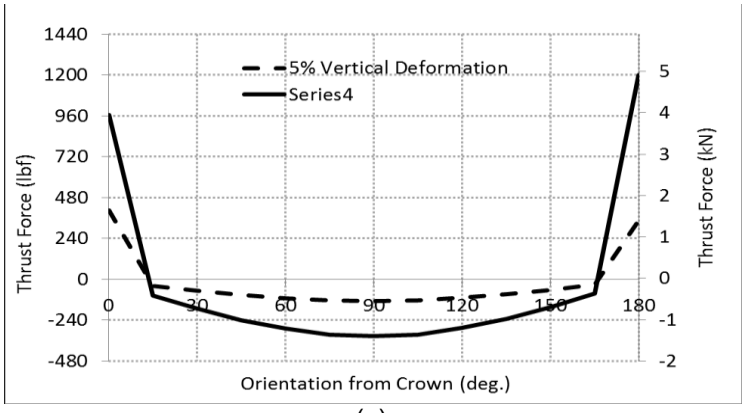

(a)

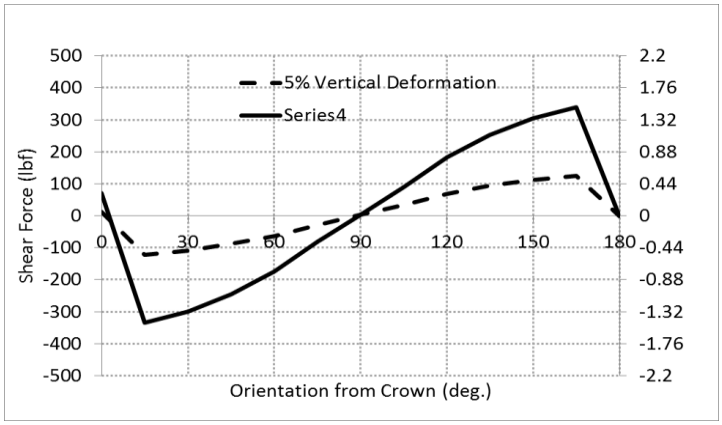

(b)

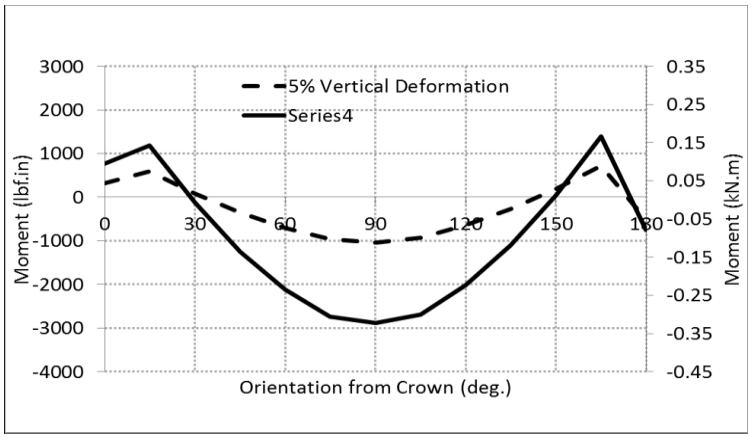

(c)

Figure H- 11 Variation of Internal Forces in 30-B-0.50-IV SFRCP from crown to invert:

a) Thrust; b) Shear; and c) Moment

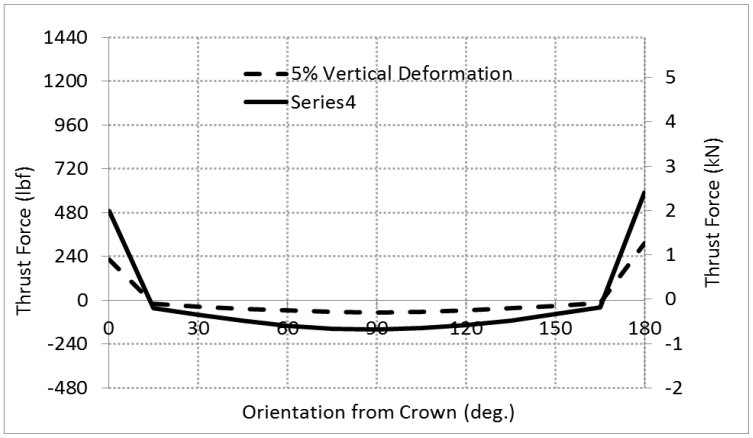

(a)

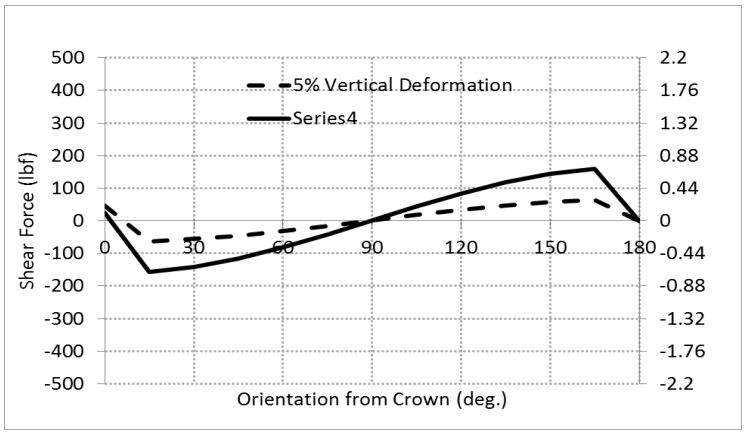

(b)

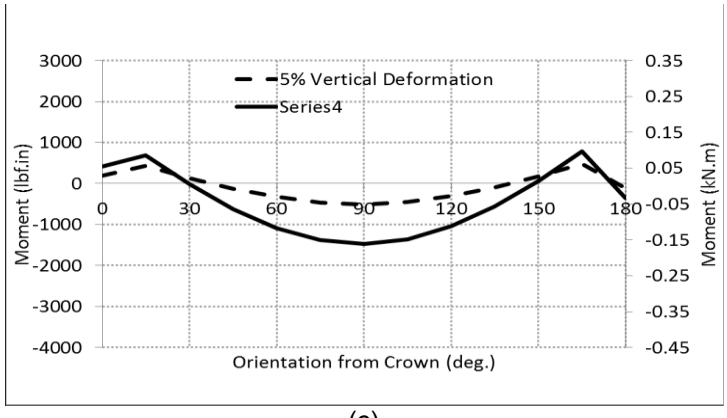

(c)

Figure H- 12 Variation of Internal Forces in 33-B-0.50-I SFRCP from crown to invert:

a) Thrust; b) Shear; and c) Moment

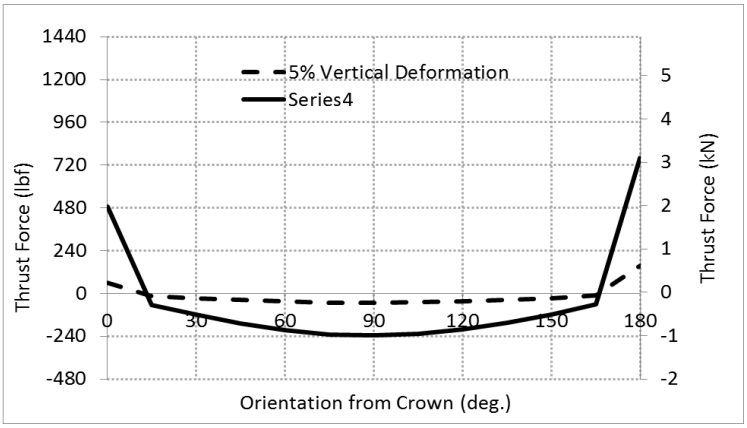

(a)

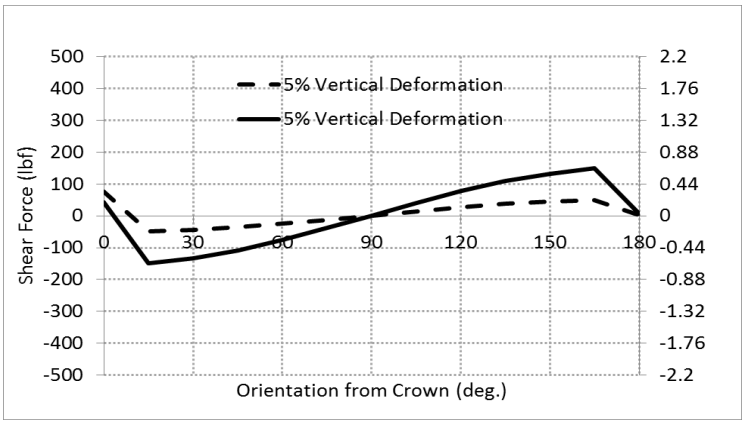

(b)

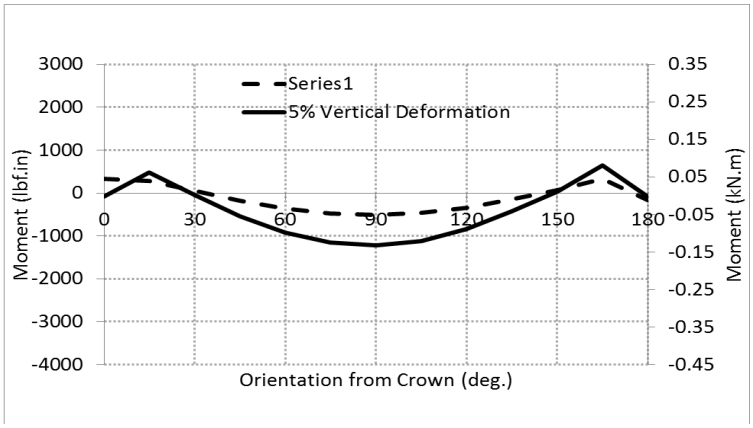

(c)

Figure H- 13 Variation of Internal Forces in 36-C-0.25-III SFRCP from crown to invert:

a) Thrust; b) Shear; and c) Moment

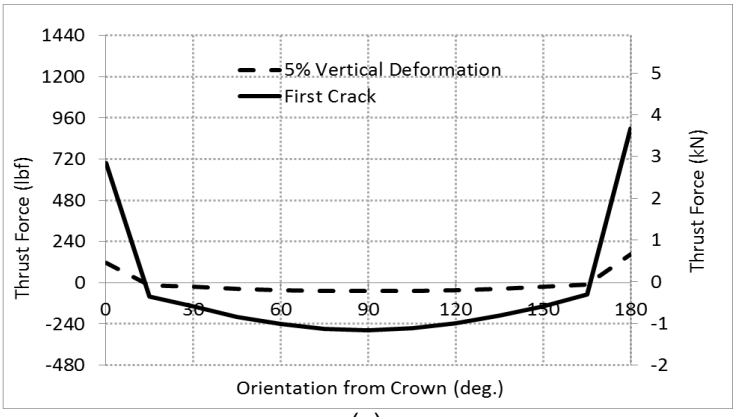

(a)

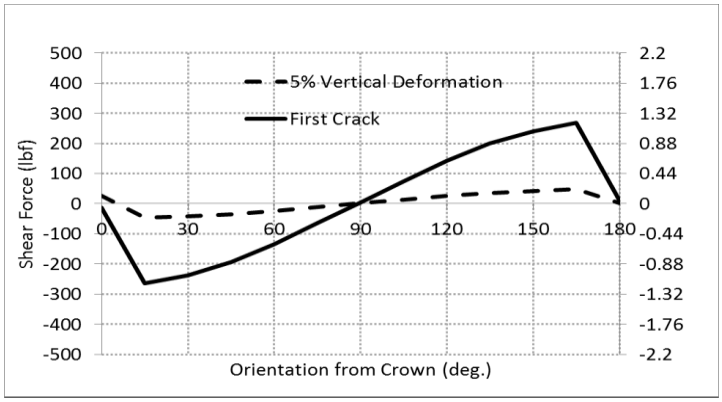

(b)

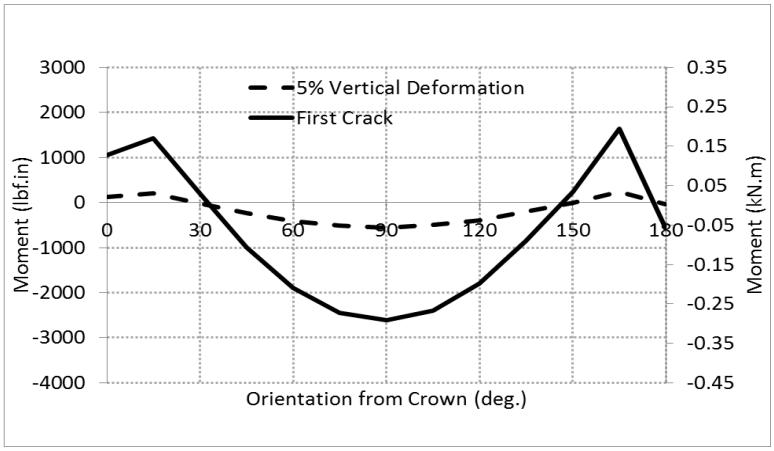

(c)

Figure H- 14 Variation of Internal Forces in 36-C-0.33-III SFRCP from crown to invert:

a) Thrust; b) Shear; and c) Moment

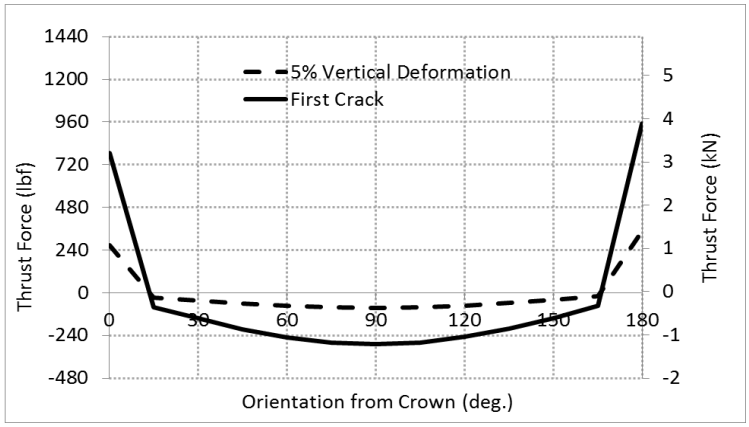

(a)

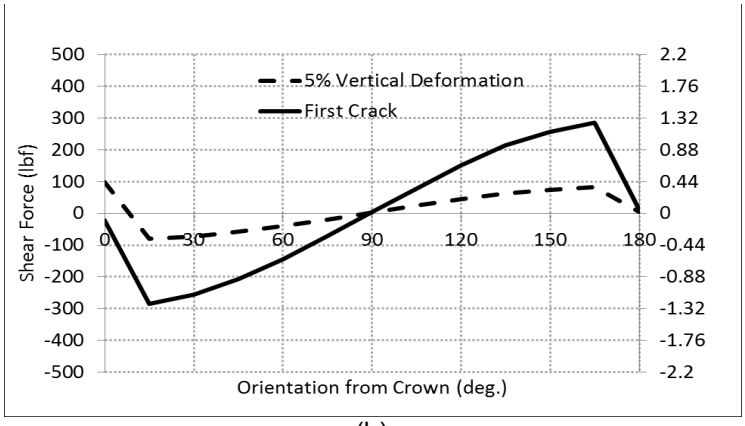

(b)

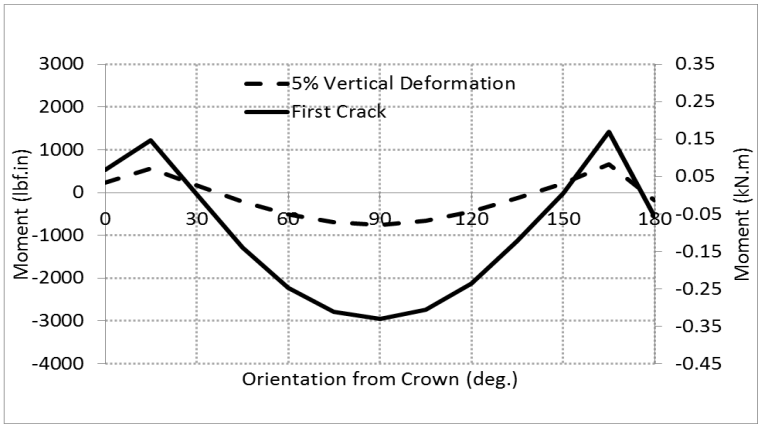

(c)

Figure H- 15 Variation of Internal Forces in 36-C-0.50-III SFRCP from crown to invert:

a) Thrust; b) Shear; and c) Moment

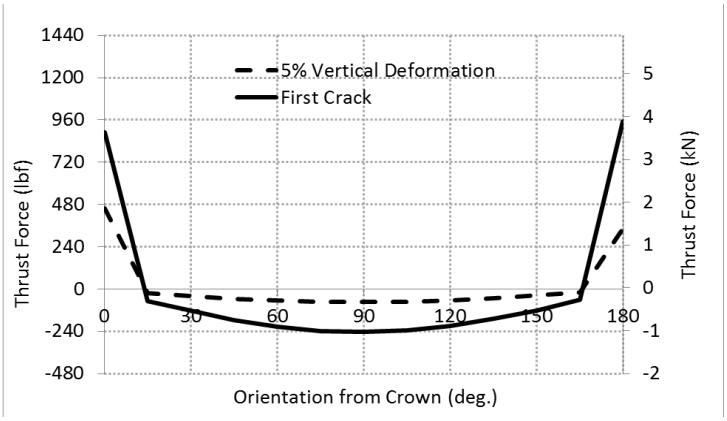

(a)

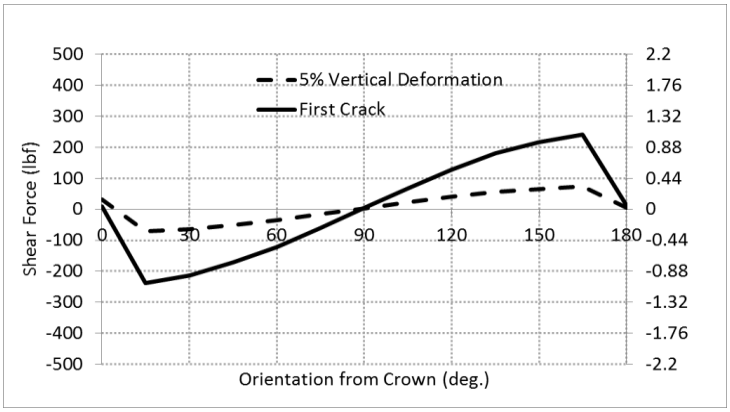

(b)

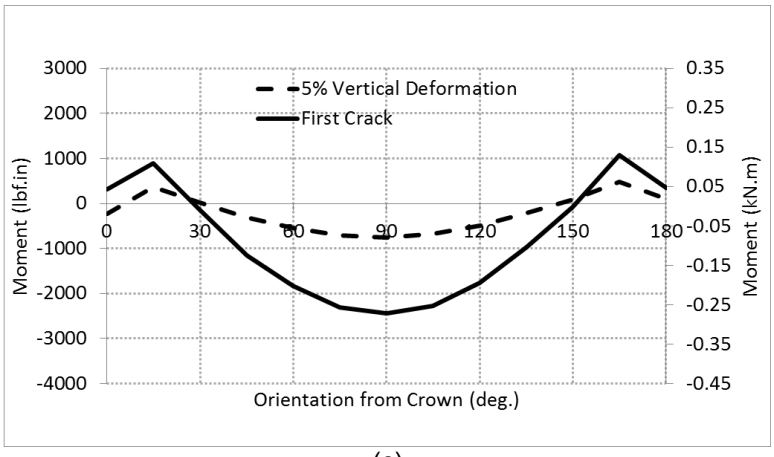

(c)

Figure H- 16 Variation of Internal Forces in 36-B-0.67-III SFRCP from crown to invert:

a) Thrust; b) Shear; and c) Moment

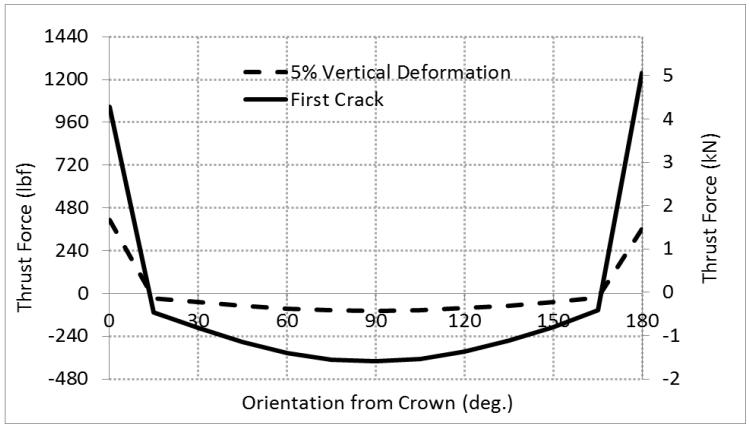

(a)

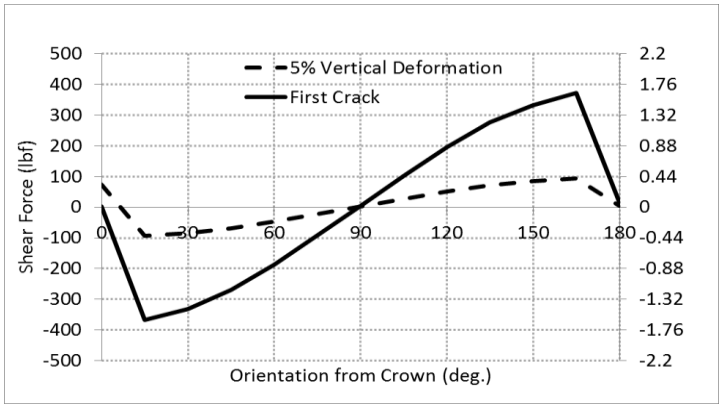

(b)

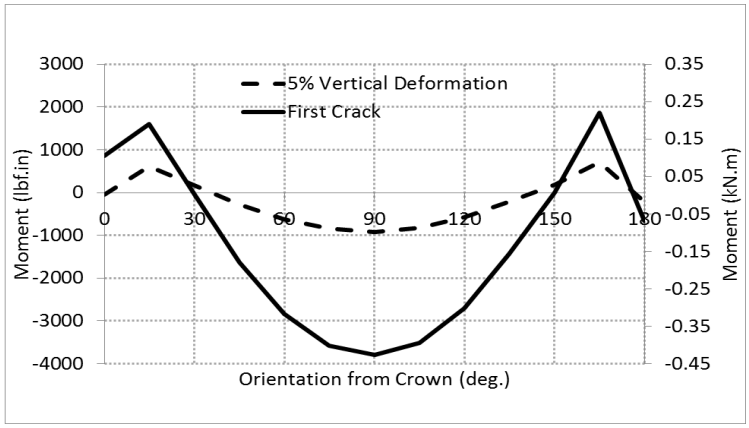

(c)

Figure H- 17 Variation of Internal Forces in 36-C-0.67-IV SFRCP from crown to invert:

a) Thrust; b) Shear; and c) Moment

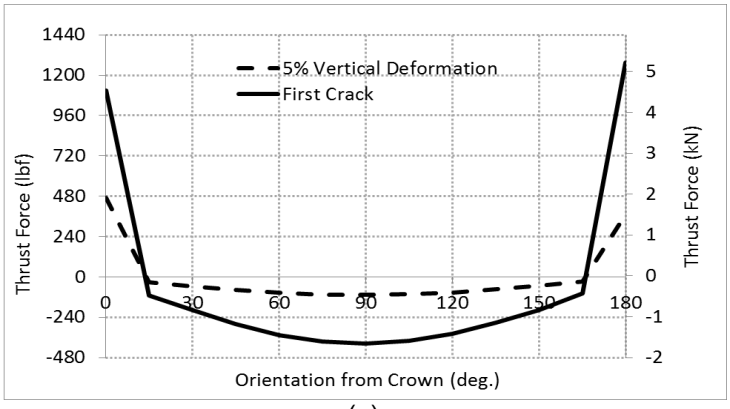

(a)

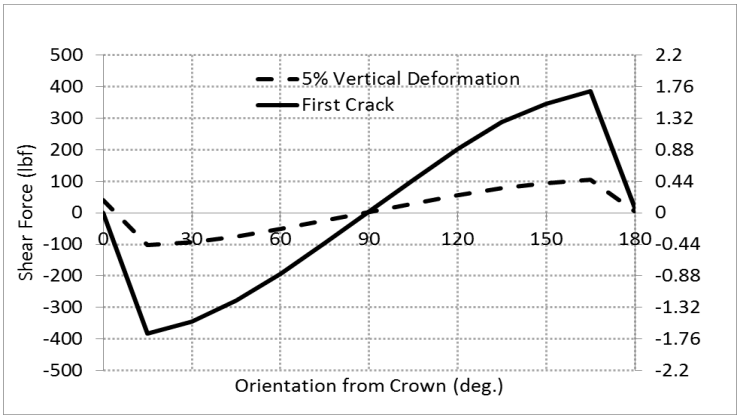

(b)

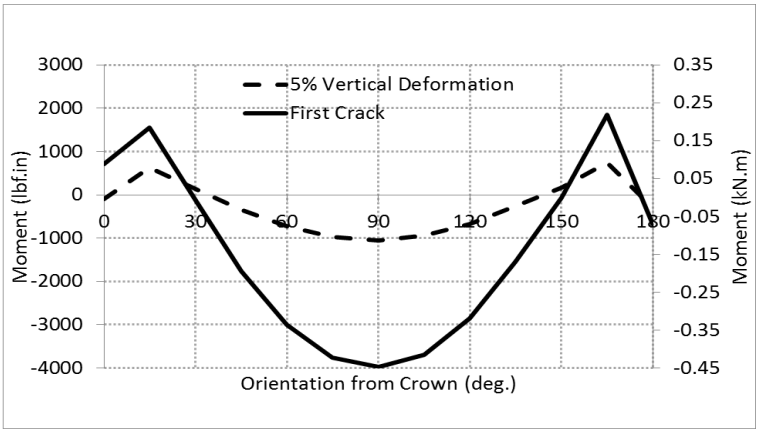

(c)

Figure H- 18 Variation of Internal Forces in 36-C-0.83-IV SFRCP from crown to invert:

a) Thrust; b) Shear; and c) Moment

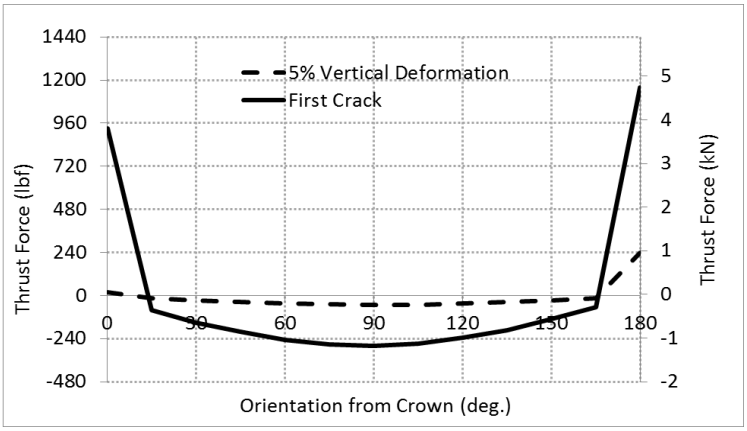

(a)

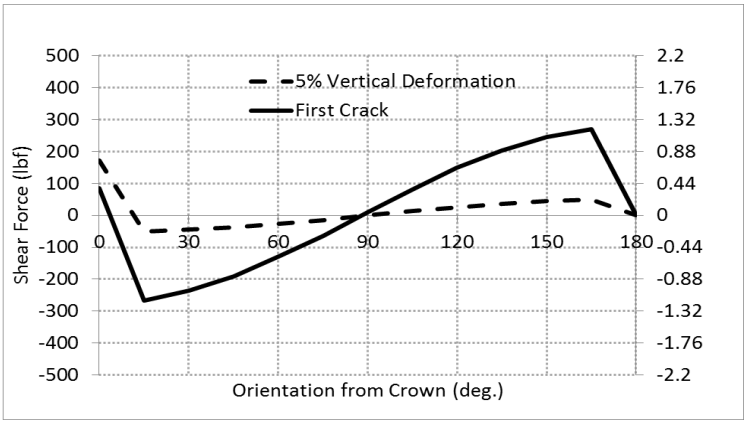

(b)

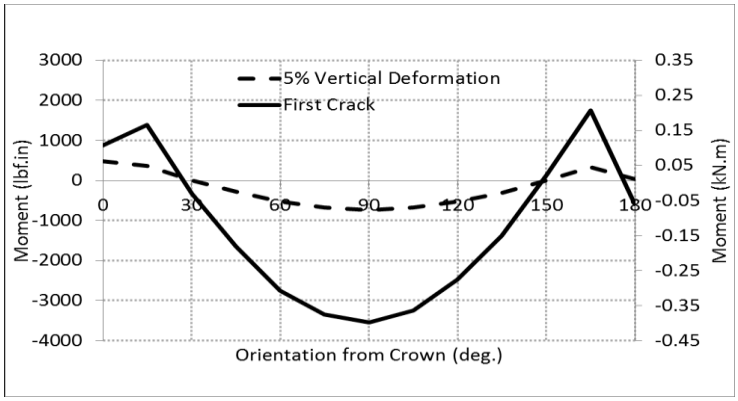

(c)

Figure H- 19 Variation of Internal Forces 48-B-0.50-II in SFRCP from crown to invert:

a) Thrust; b) Shear; and c) Moment

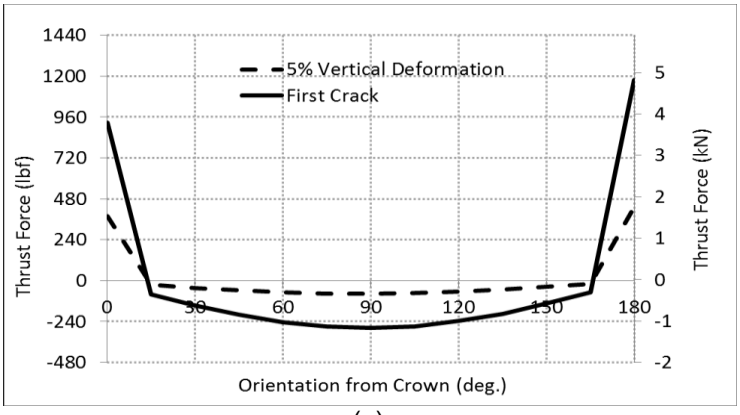

(a)

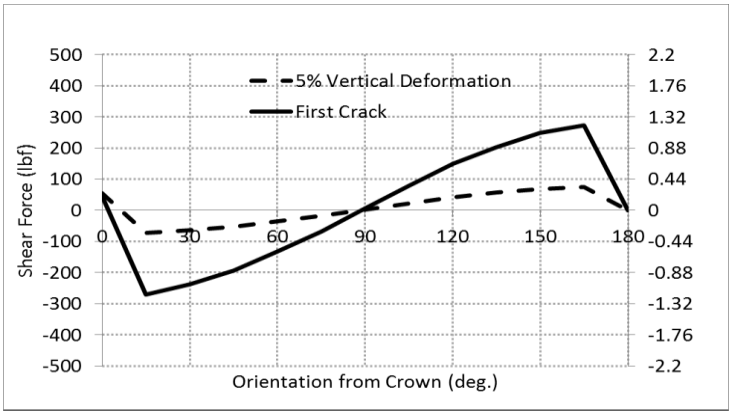

(b)

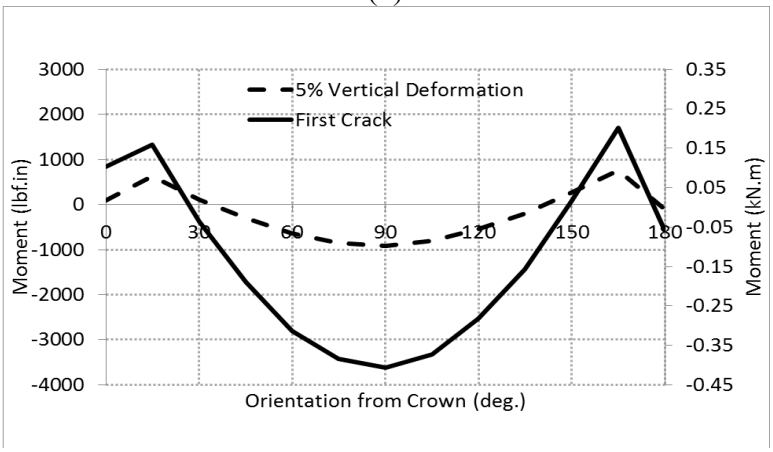

(c)

Figure H- 20 Variation of Internal Forces in 48-B-0.67-II SFRCP from crown to invert:

a) Thrust; b) Shear; and c) Moment

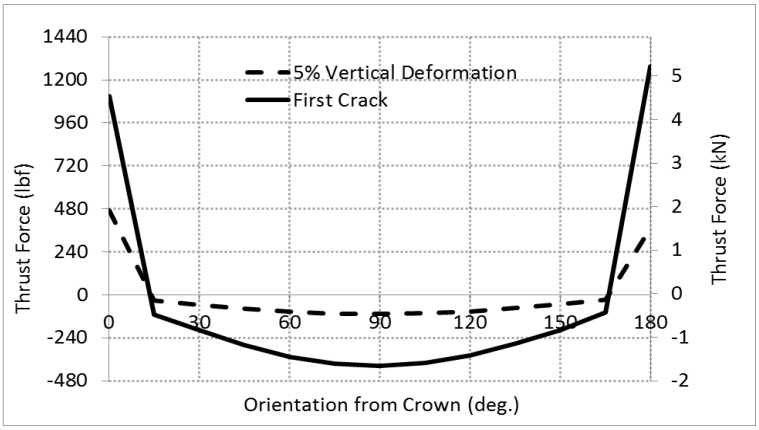

(a)

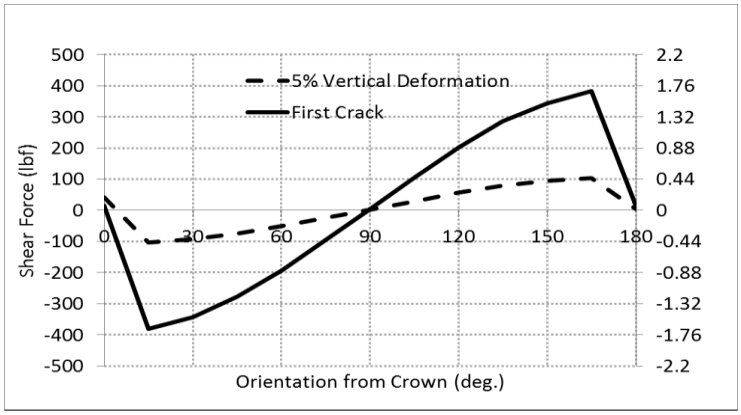

(b)

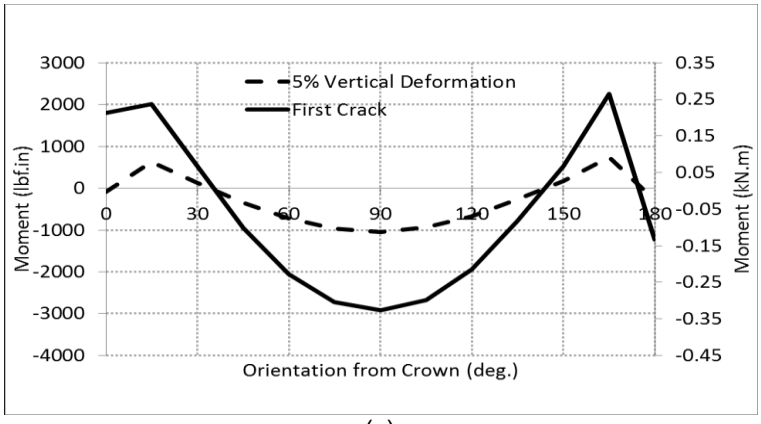

(c)

Figure H- 21 Variation of Internal Forces in 48-B-0.83-III SFRCP from crown to invert:

a) Thrust; b) Shear; and c) Moment

Appendix I

Fiber Distribution Study Results

Table I- 1 Parameters obtained with image processing analysis

Image Height (pix)	**Image Width (pix)**	**Total Area of the Surface (pix^2)**	**Total Area of the Fibers (pix^2)**	**Fiber Area Fraction (a_f)**
Specimen 1-ID-1				
446	444	155450	654	0.421
Specimen 1-ID-2				
599	599	281659	344	0.122

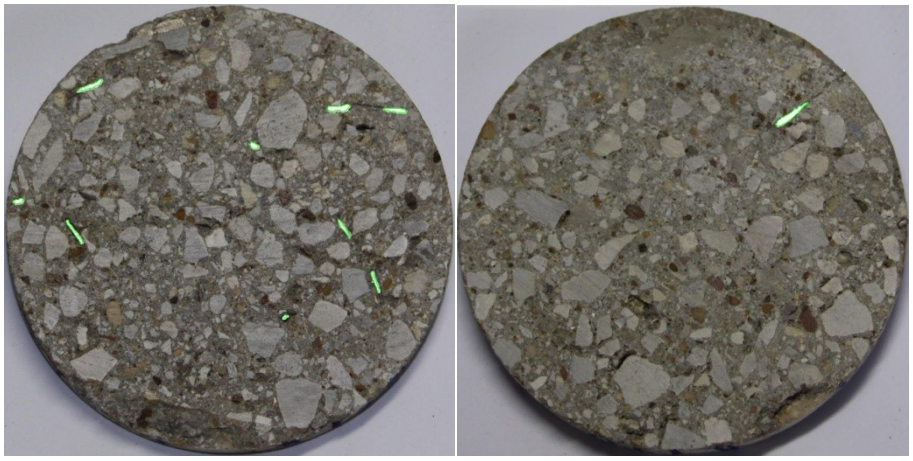

(a) (b)

Figure I- 1 Image of specimen 1-ID: (a) side 1; (b) side 2

Table I- 2 Parameters obtained with image processing analysis

Image Height (pix)	**Image Width (pix)**	**Total Area of the Surface (pix^2)**	**Total Area of the Fibers (pix^2)**	**Fiber Area Fraction (a_f)**
Specimen 1-M-1				
629	643	317529	1834	0.578
Specimen 1-M-2				
442	440	152668	712	0.466

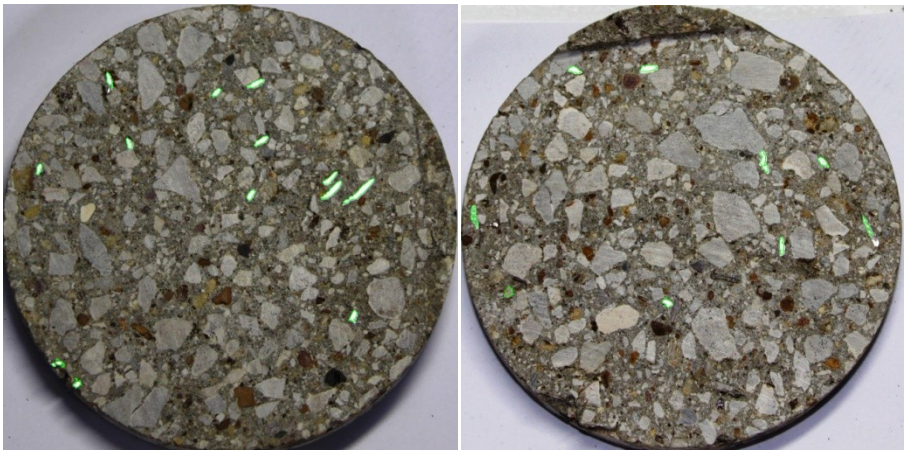

(a) (b)

Figure I- 2 Image of specimen 1-M: (a) side 1; (b) side 2

Table I- 3 Parameters obtained with image processing analysis

Image Height (pix)	**Image Width (pix)**	**Total Area of the Surface (pix^2)**	**Total Area of the Fibers (pix^2)**	**Fiber Area Fraction (a_f)**
Specimen 1-OD-1				
561	573	252369	507	0.201
Specimen 1-OD-2				
636	650	324557	1841	0.567

(a) (b)

Figure I- 3 Image of specimen 1-OD: (a) side 1; (b) side 2

Table I- 4 Parameters obtained with image processing analysis

Image Height (pix)	**Image Width (pix)**	**Total Area of the Surface (pix^2)**	**Total Area of the Fibers (pix^2)**	**Fiber Area Fraction (a_f)**
Specimen 2-ID-1				
645	645	326580	984	0.301
Specimen 2-ID-2				
652	657	336271	812	0.241

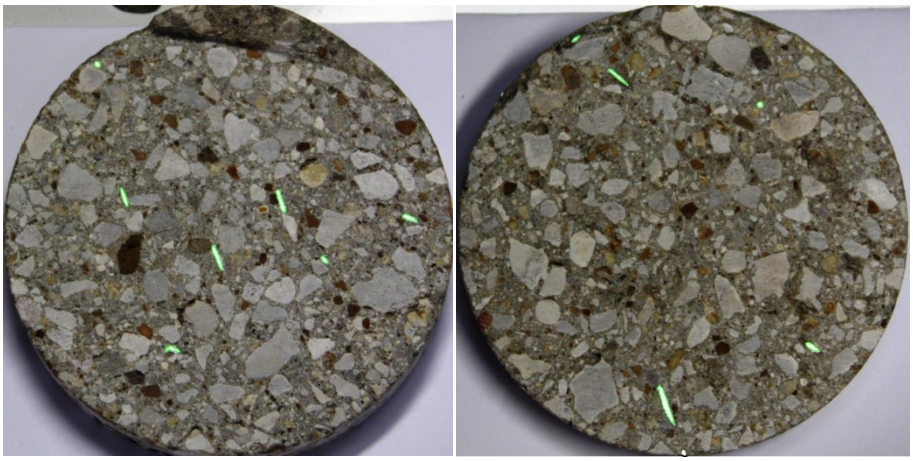

(a) (b)

Figure I- 4 Image of specimen 2-ID: (a) side 1; (b) side 2

Table I- 5 Parameters obtained with image processing analysis

Image Height (pix)	**Image Width (pix)**	**Total Area of the Surface (pix^2)**	**Total Area of the Fibers (pix^2)**	**Fiber Area Fraction (a_f)**
Specimen 2-M-1				
671	592	265442	1369	0.516
Specimen 2-M-2				
598	633	297390	1875	0.630

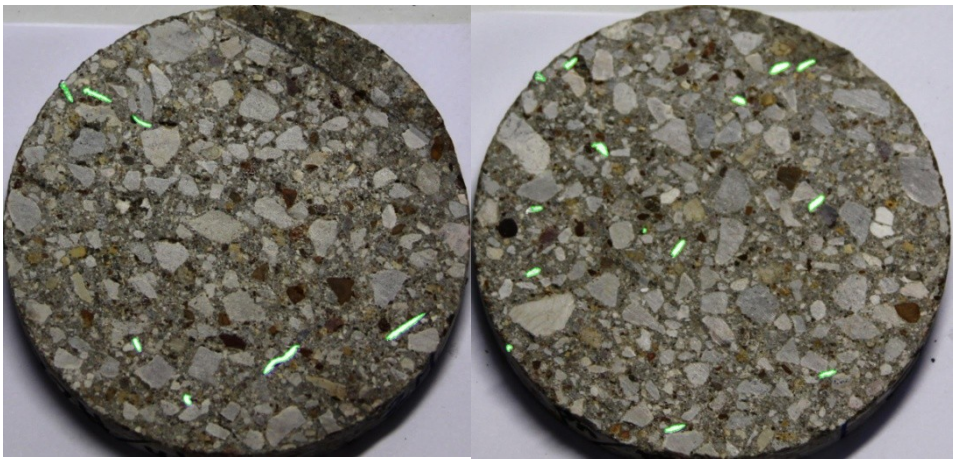

(a) (b)

Figure I- 5 Image of specimen 2-M: (a) side 1; (b) side 2

Table I- 6 Parameters obtained with image processing analysis

Image Height (pix)	**Image Width (pix)**	**Total Area of the Surface (pix^2)**	**Total Area of the Fibers (pix^2)**	**Fiber Area Fraction (a_f)**
Specimen 2-OD-1				
634	653	325062	2155	0.663
Specimen 2-OD-2				
444	455	158609	1071	0.675

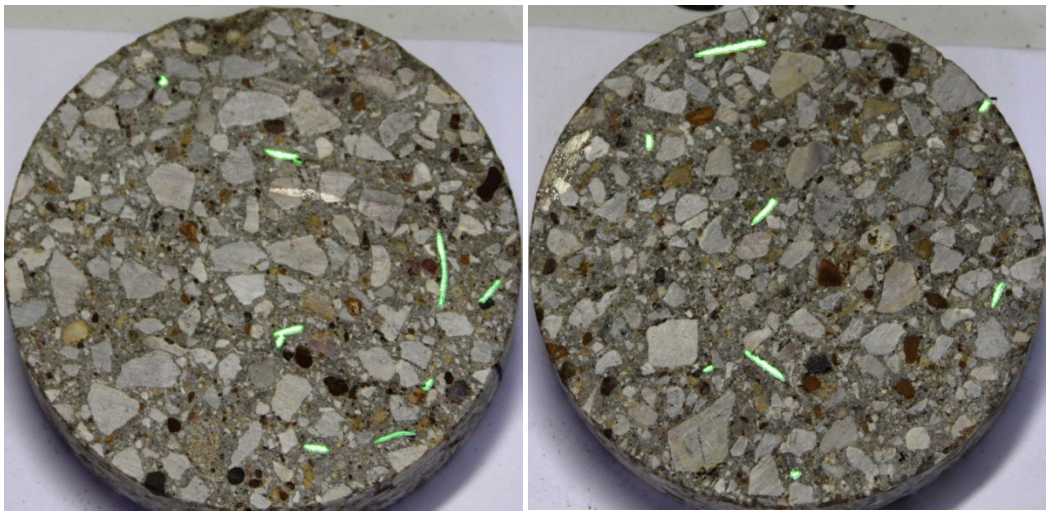

(a) (b)

Figure I- 6 Image of specimen 2-OD: (a) side 1; (b) side 2

Table I- 7 Parameters obtained with image processing analysis

Image Height (pix)	**Image Width (pix)**	**Total Area of the Surface (pix^2)**	**Total Area of the Fibers (pix^2)**	**Fiber Area Fraction (a_f)**
Specimen 3-ID-1				
580	606	276044	571	0.207
Specimen 3-ID-2				
625	654	321034	492	0.153

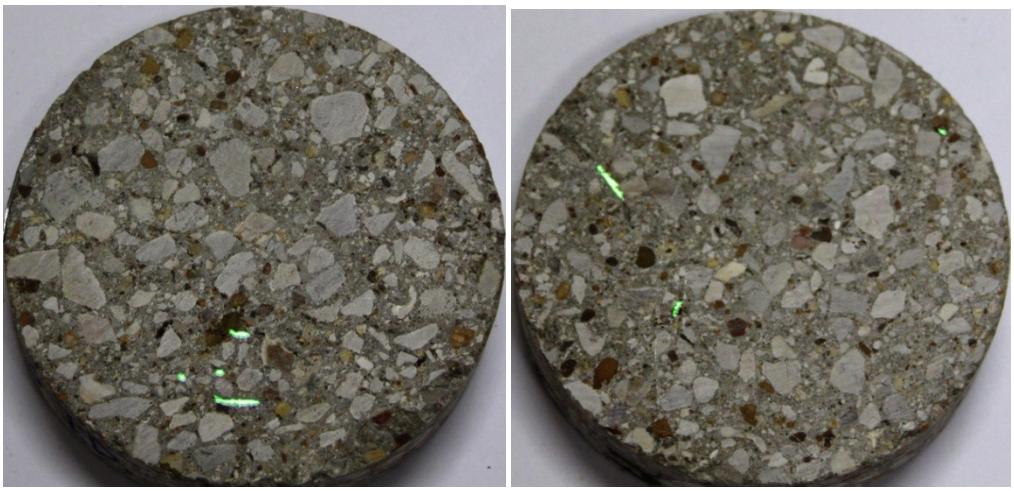

(a) (b)

Figure I- 7 Image of specimen 3-ID: (a) side 1; (b) side 2

Table I- 8 Parameters obtained with image processing analysis

Image Height (pix)	Image Width (pix)	Total Area of the Surface (pix^2)	Total Area of the Fibers (pix^2)	Fiber Area Fraction (a_f)
Specimen 3-M-1				
609	620	296424	971	0.328
Specimen 3-M-2				
501	520	204579	313	0.153

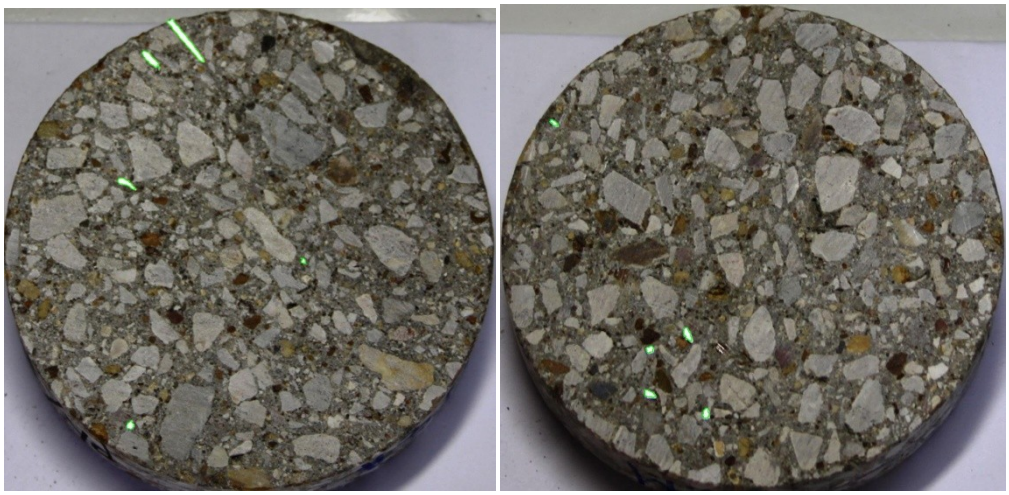

(a) (b)

Figure I- 8 Image of specimen 3-M: (a) side 1; (b) side 2

Table I- 9 Parameters obtained with image processing analysis

Image Height (pix)	**Image Width (pix)**	**Total Area of the Surface (pix^2)**	**Total Area of the Fibers (pix^2)**	**Fiber Area Fraction (a_f)**
Specimen 3-OD-1				
438	456	156850	40	0.026
Specimen 3-OD-2				
636	653	326073	217	0.067

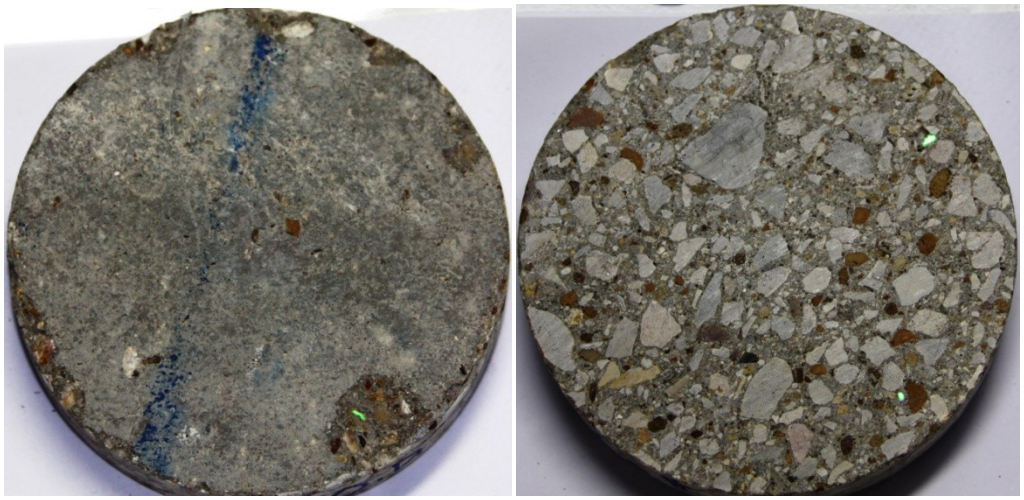

(a) (b)

Figure I- 9 Image of specimen 3-OD: (a) side 1; (b) side 2

Table I- 10 Parameters obtained with image processing analysis

Image Height (pix)	**Image Width (pix)**	**Total Area of the Surface (pix^2)**	**Total Area of the Fibers (pix^2)**	**Fiber Area Fraction (a_f)**
Specimen 4-ID-1				
451	453	160379	905	0.564
Specimen 4-ID-2				
627	638	314044	851	0.271

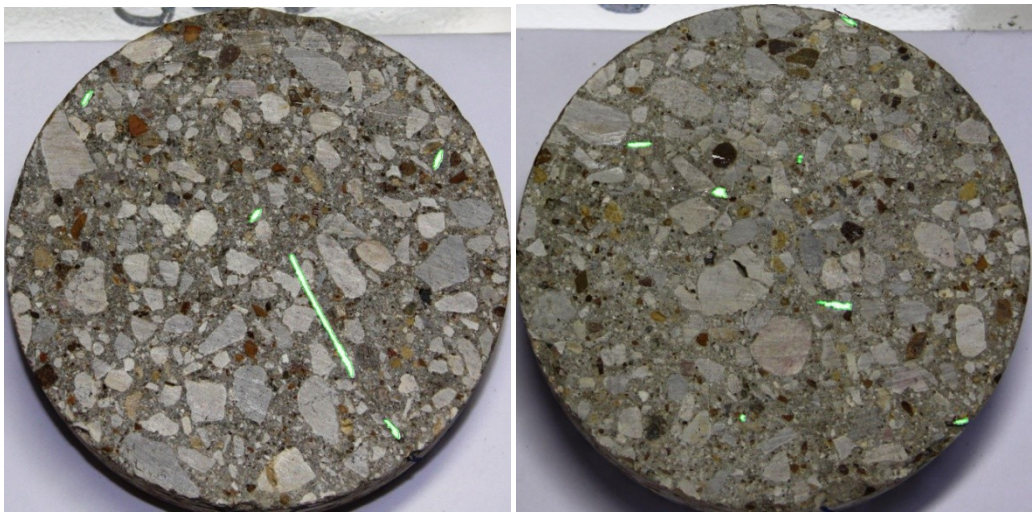

(a) (b)

Figure I- 10 Image of specimen 4-ID: (a) side 1; (b) side 2

Table I- 11 Parameters obtained with image processing analysis

Image Height (pix)	Image Width (pix)	Total Area of the Surface (pix^2)	Total Area of the Fibers (pix^2)	Fiber Area Fraction (a_f)
Specimen 4-M-1				
609	626	299325	1789	0.598
Specimen 4-M-2				
580	601	273722	559	0.204

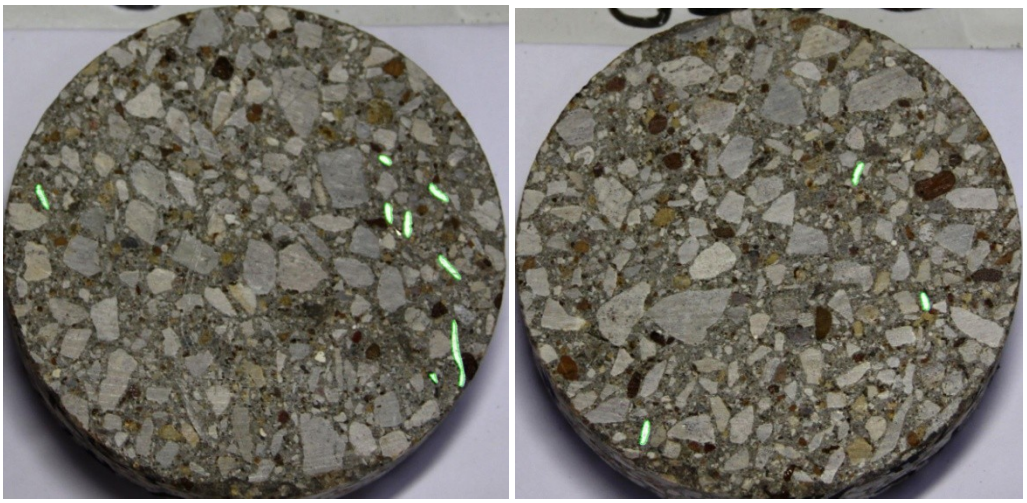

(a) (b)

Figure I- 11 Image of specimen 4-M: (a) side 1; (b) side 2

Table I- 12 Parameters obtained with image processing analysis

Image Height (pix)	**Image Width (pix)**	**Total Area of the Surface (pix^2)**	**Total Area of the Fibers (pix^2)**	**Fiber Area Fraction (a_f)**
Specimen 4-OD-1				
560	590	259541	616	0.237
Specimen 4-OD-2				
550	582	251479	1892	0.752

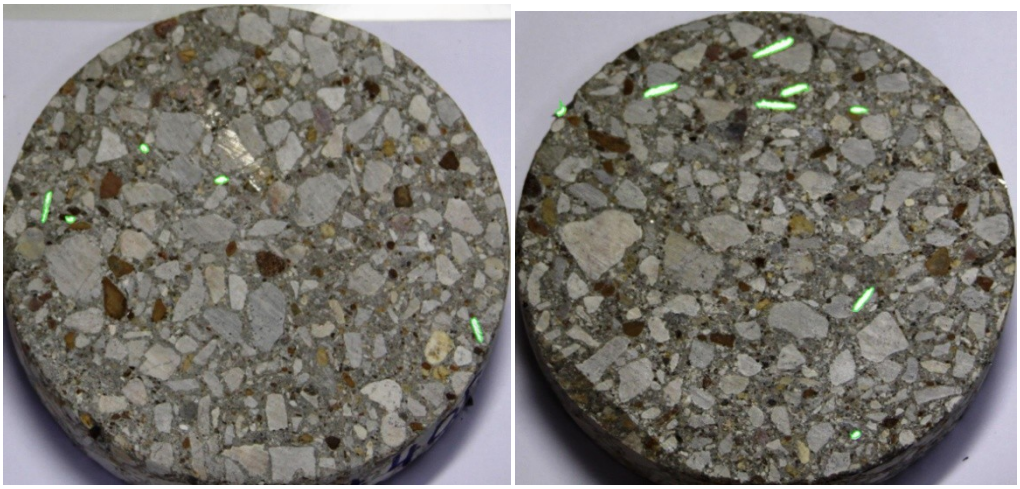

(a) (b)

Figure I- 12 Image of specimen 4-OD: (a) side 1; (b) side 2

Table I- 13 Parameters obtained with image processing analysis

Image Height (pix)	Image Width (pix)	Total Area of the Surface (pix^2)	Total Area of the Fibers (pix^2)	Fiber Area Fraction (a_f)
Specimen 5-ID-1				
580	613	279313	462	0.165
Specimen 5-ID-2				
567	600	267271	1070	0.400

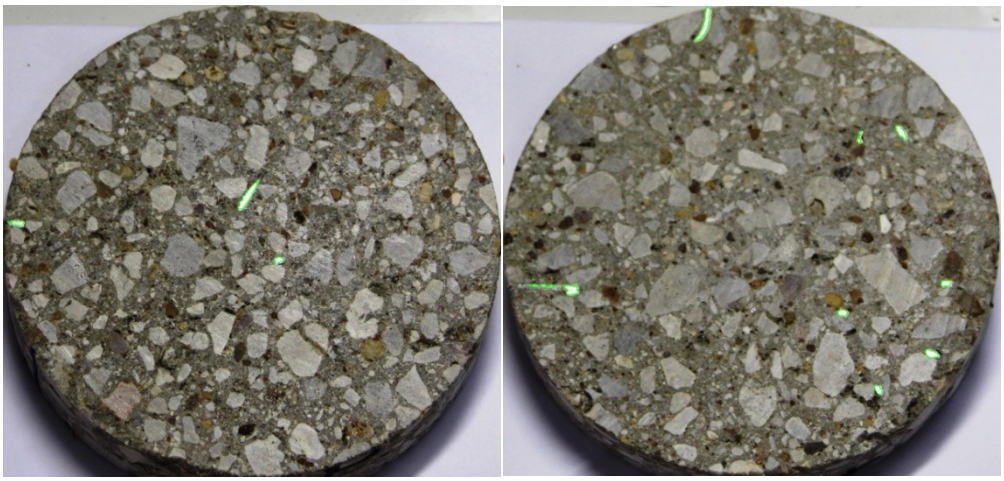

(a) (b)

Figure I- 13 Image of specimen 5-ID: (a) side 1; (b) side 2

Table I- 14 Parameters obtained with image processing analysis

Image Height (pix)	Image Width (pix)	Total Area of the Surface (pix^2)	Total Area of the Fibers (pix^2)	Fiber Area Fraction (a_f)
Specimen 5-M-1				
615	641	309591	266	0.086
Specimen 5-M-2				
555	577	251479	85	0.034

(a) (b)

Figure I- 14 Image of specimen 5-M: (a) side 1; (b) side 2

Table I- 15 Parameters obtained with image processing analysis

Image Height (pix)	Image Width (pix)	Total Area of the Surface (pix^2)	Total Area of the Fibers (pix^2)	Fiber Area Fraction (a_f)
Specimen 5-OD-1				
611	641	307623	1153	0.375
Specimen 5-OD-2				
432	460	156149	599	0.384

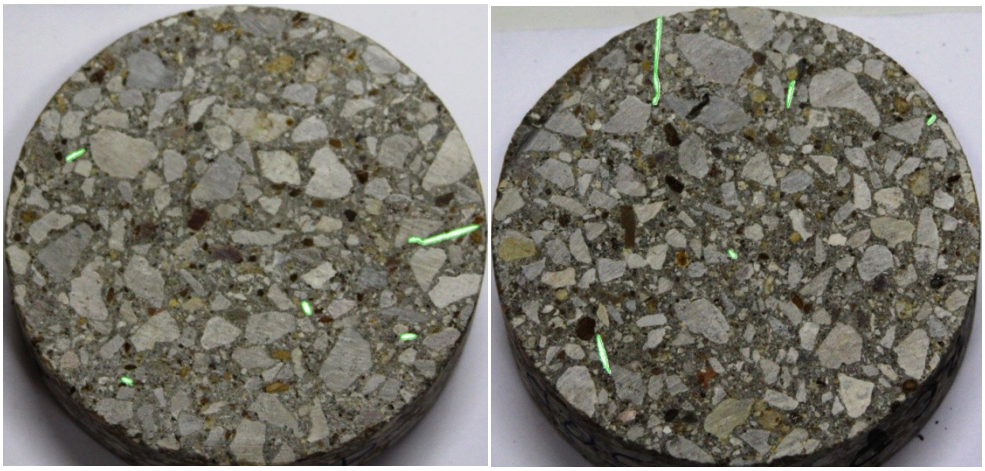

(a) (b)

Figure I- 15 Image of specimen 5-OD: (a) side 1; (b) side 2

Table I- 16 Parameters obtained with image processing analysis

Image Height (pix)	**Image Width (pix)**	**Total Area of the Surface (pix^2)**	**Total Area of the Fibers (pix^2)**	**Fiber Area Fraction (a_f)**
Specimen 6-ID-1				
449	461	166829	881	0.528
Specimen 6-ID-2				
461	502	181996	685	0.376

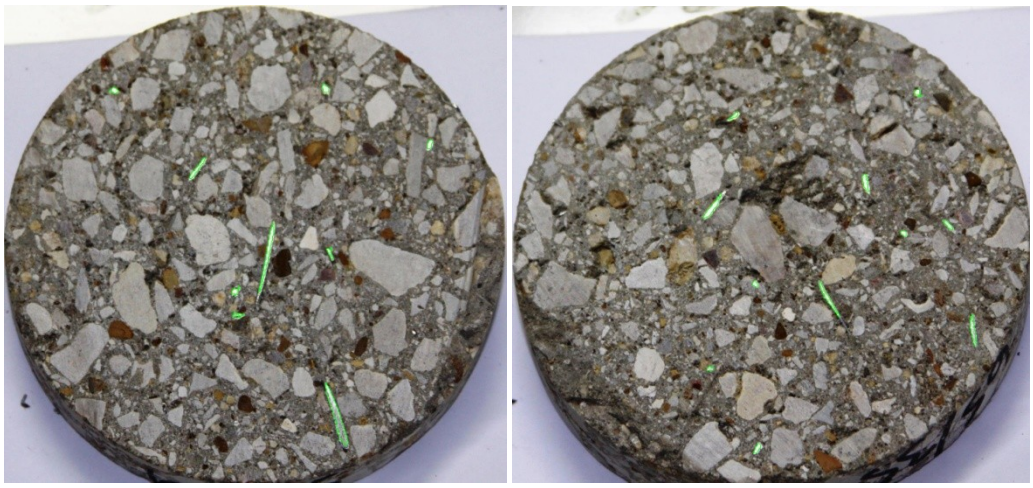

(a) (b)

Figure I- 16 Image of specimen 6-ID: (a) side 1; (b) side 2

Table I- 17 Parameters obtained with image processing analysis

Image Height (pix)	**Image Width (pix)**	**Total Area of the Surface (pix^2)**	**Total Area of the Fibers (pix^2)**	**Fiber Area Fraction (a_f)**
Specimen 6-M-1				
444	475	165745	1238	0.747
Specimen 6-M-2				
459	482	173776	980	0.564

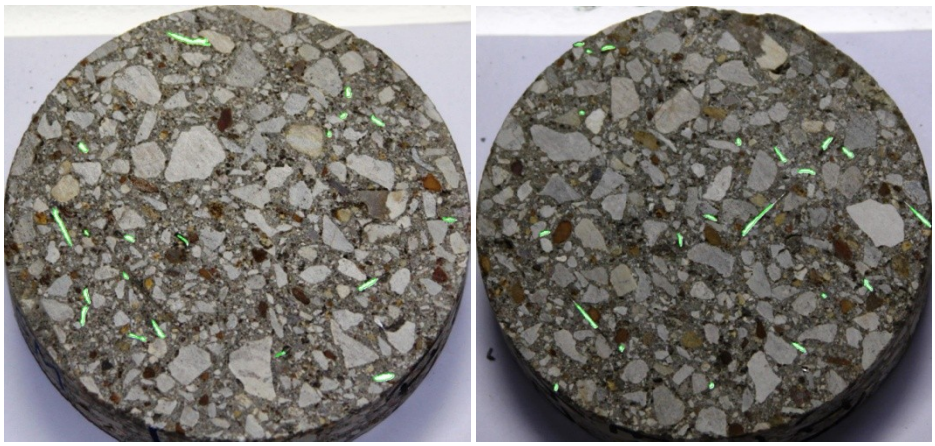

(a) (b)

Figure I- 17 Image of specimen 6-M: (a) side 1; (b) side 2

Table I- 18 Parameters obtained with image processing analysis

Image Height (pix)	**Image Width (pix)**	**Total Area of the Surface (pix^2)**	**Total Area of the Fibers (pix^2)**	**Fiber Area Fraction (a_f)**
Specimen 6-OD-1				
431	459	155450	312	0.200
Specimen 6-OD-2				
457	479	171934	734	0.427

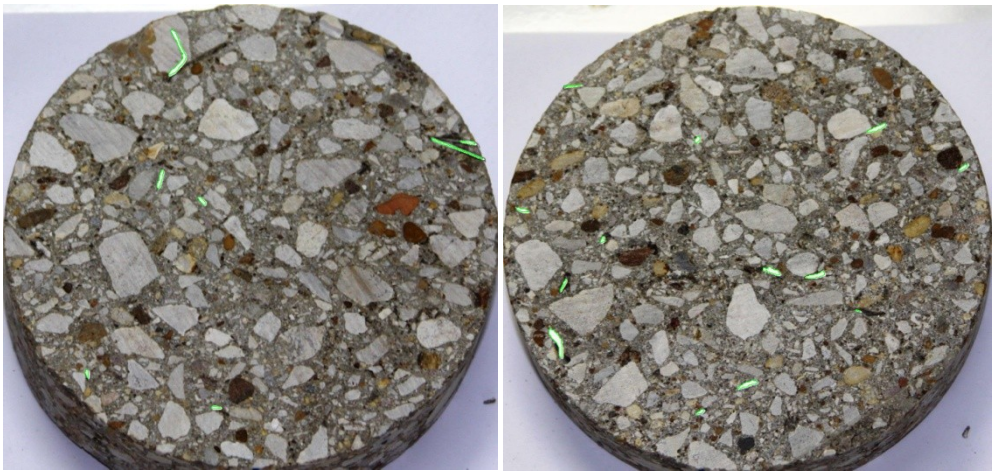

(a) (b)

Figure I- 18 Image of specimen 6-OD: (a) side 1; (b) side 2

Table I- 19 Parameters obtained with image processing analysis

Image Height (pix)	**Image Width (pix)**	**Total Area of the Surface (pix^2)**	**Total Area of the Fibers (pix^2)**	**Fiber Area Fraction (a_f)**
Specimen 7-ID-1				
641	659	331663	1152	0.347
Specimen 7-ID-2				
597	622	291620	538	0.184

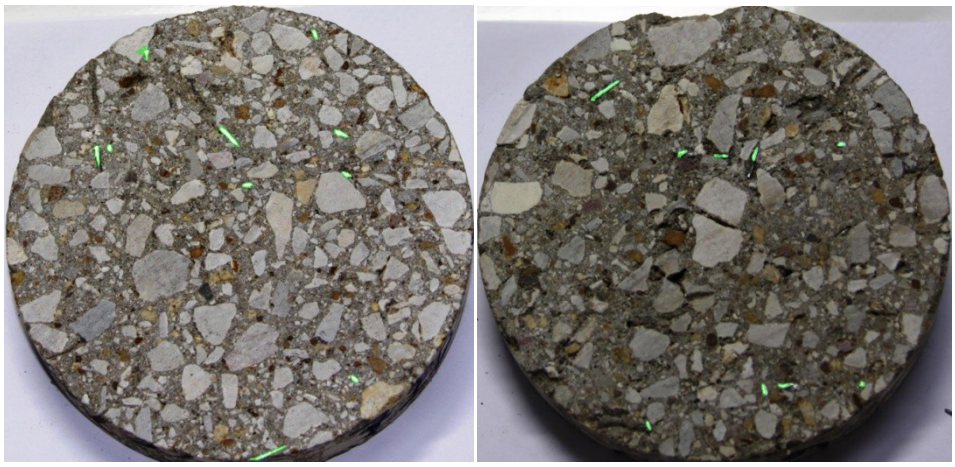

(a) (b)

Figure I- 19 Image of specimen 7-ID: (a) side 1; (b) side 2

Table I- 20 Parameters obtained with image processing analysis

Image Height (pix)	**Image Width (pix)**	**Total Area of the Surface (pix^2)**	**Total Area of the Fibers (pix^2)**	**Fiber Area Fraction (a_f)**
Specimen 7-M-1				
580	586	266813	712	0.267
Specimen 7-M-2				
610	621	297390	1028	0.346

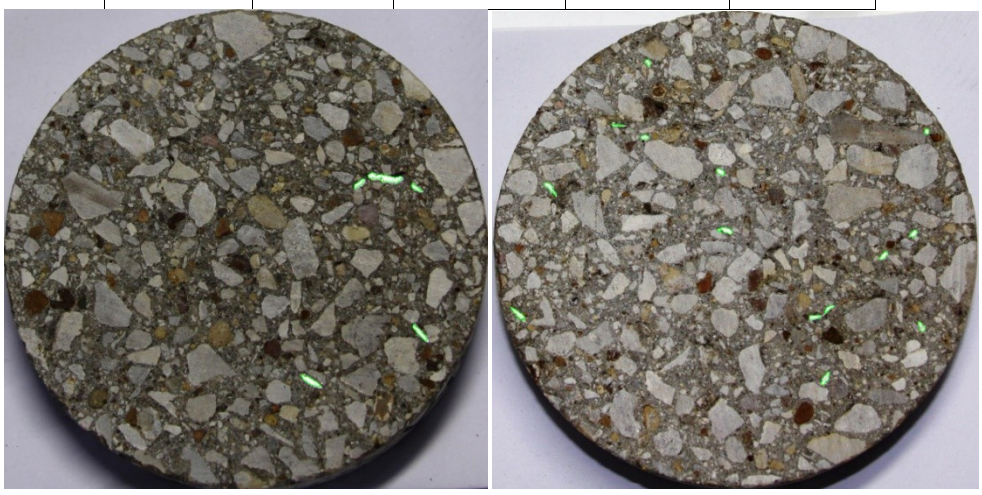

(a) (b)

Figure I- 20 Image of specimen 7-M: (a) side 1; (b) side 2

Table I- 21 Parameters obtained with image processing analysis

Image Height (pix)	Image Width (pix)	Total Area of the Surface (pix^2)	Total Area of the Fibers (pix^2)	Fiber Area Fraction (a_f)
Specimen 7-OD-1				
620	634	308606	1018	0.330
Specimen 7-OD-2				
610	629	301267	584	0.194

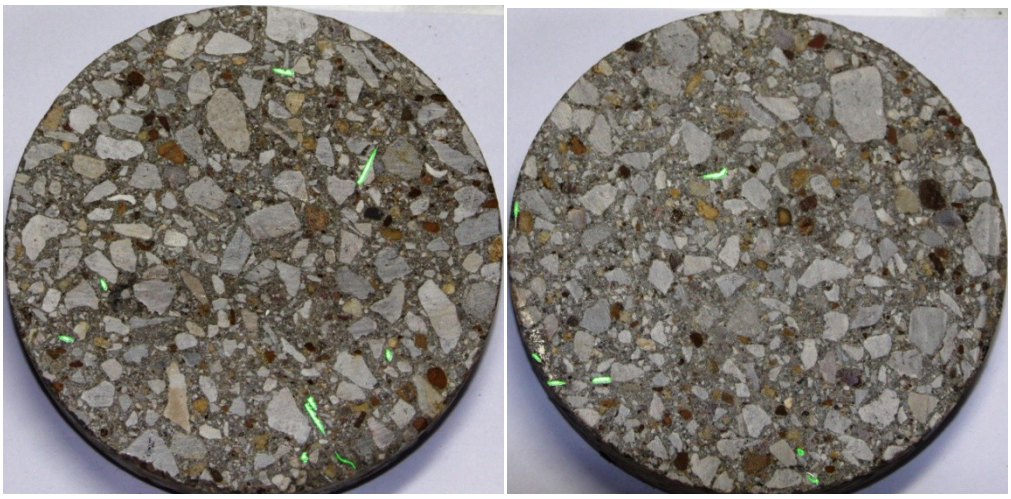

(a) (b)

Figure I- 21 Image of specimen 7-OD: (a) side 1; (b) side 2

Table I- 22 Parameters obtained with image processing analysis

Image Height (pix)	Image Width (pix)	Total Area of the Surface (pix^2)	Total Area of the Fibers (pix^2)	Fiber Area Fraction (a_f)
Specimen 8-ID-1				
629	629	310578	1656	0.533
Specimen 8-ID-2				
578	579	262710	0	0

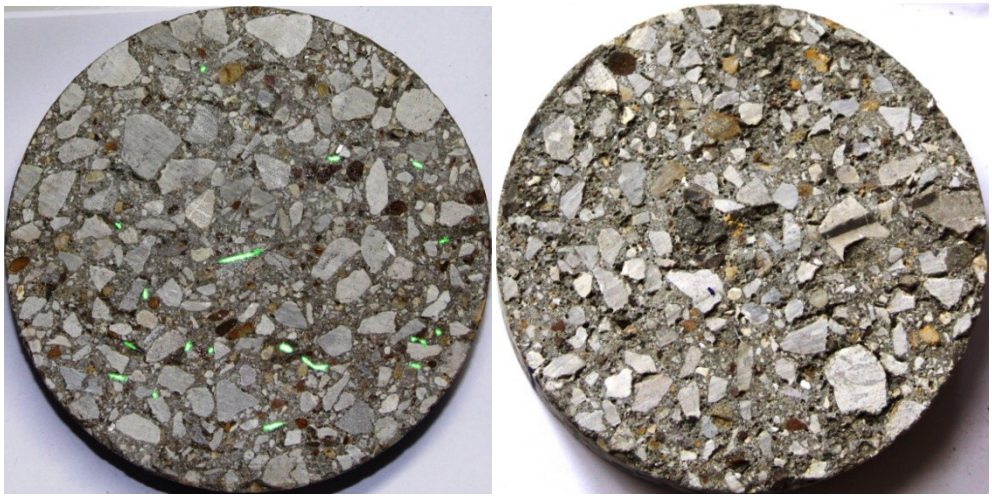

(a) (b)

Figure I- 22 Image of specimen 8-ID: (a) side 1; (b) side 2

Table I- 23 Parameters obtained with image processing analysis

Image Height (pix)	Image Width (pix)	Total Area of the Surface (pix^2)	Total Area of the Fibers (pix^2)	Fiber Area Fraction (a_f)
Specimen 8-M-1				
452	488	173407	838	0.483
Specimen 8-M-2				
480	523	197429	853	0.432

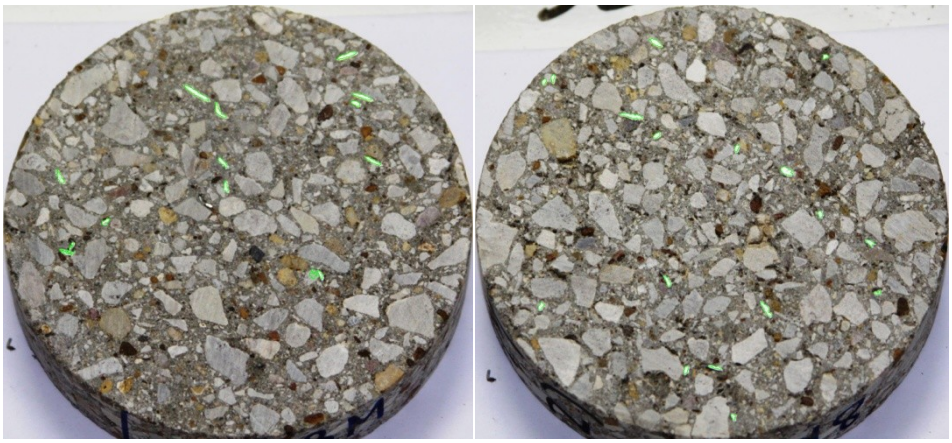

(a) (b)

Figure I- 23 Image of specimen 8-M: (a) side 1; (b) side 2

Table I- 24 Parameters obtained with image processing analysis

Image Height (pix)	**Image Width (pix)**	**Total Area of the Surface (pix^2)**	**Total Area of the Fibers (pix^2)**	**Fiber Area Fraction (a_f)**
Specimen 8-OD-1				
444	479	167191	723	0.432
Specimen 8-OD-2				
462	503	182753	891	0.488

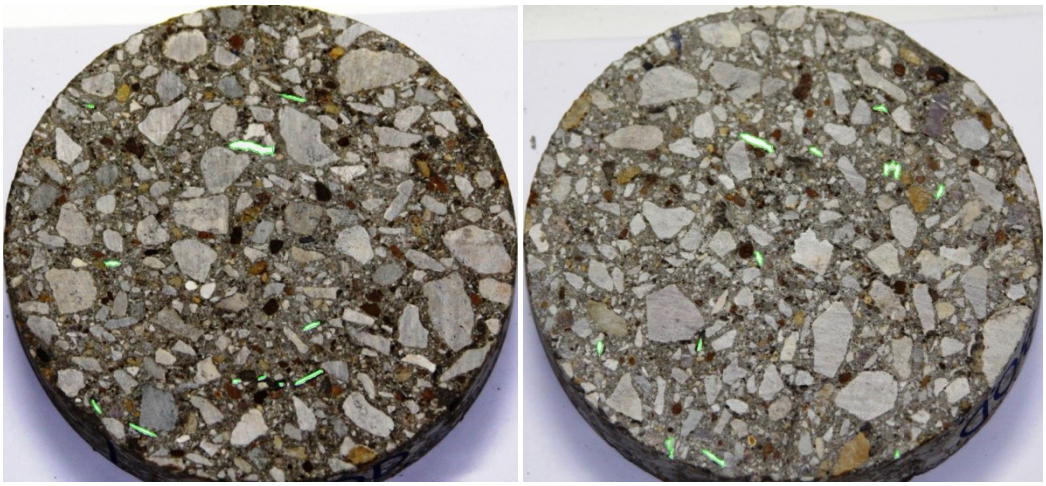

(a) (b)

Figure I- 24 Image of specimen 8-OD: (a) side 1; (b) side 2

Table I- 25 Parameters obtained with image processing analysis

Image Height (pix)	**Image Width (pix)**	**Total Area of the Surface (pix^2)**	**Total Area of the Fibers (pix^2)**	**Fiber Area Fraction (a_f)**
Specimen 9-ID-1				
435	461	157553	477	0.303
Specimen 9-ID-2				
449	483	170467	560	0.329

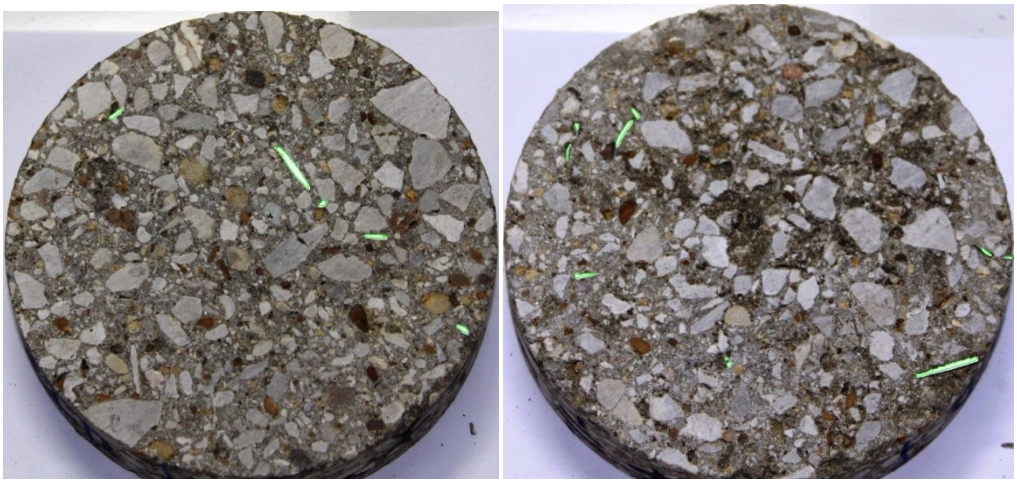

(a) (b)

Figure I- 25 Image of specimen 9-ID: (a) side 1; (b) side 2

Table I- 26 Parameters obtained with image processing analysis

Image Height (pix)	Image Width (pix)	Total Area of the Surface (pix^2)	Total Area of the Fibers (pix^2)	Fiber Area Fraction (a_f)
Specimen 9-M-1				
428	455	153014	402	0.263
Specimen 9-M-2				
645	654	331152	790	0.239

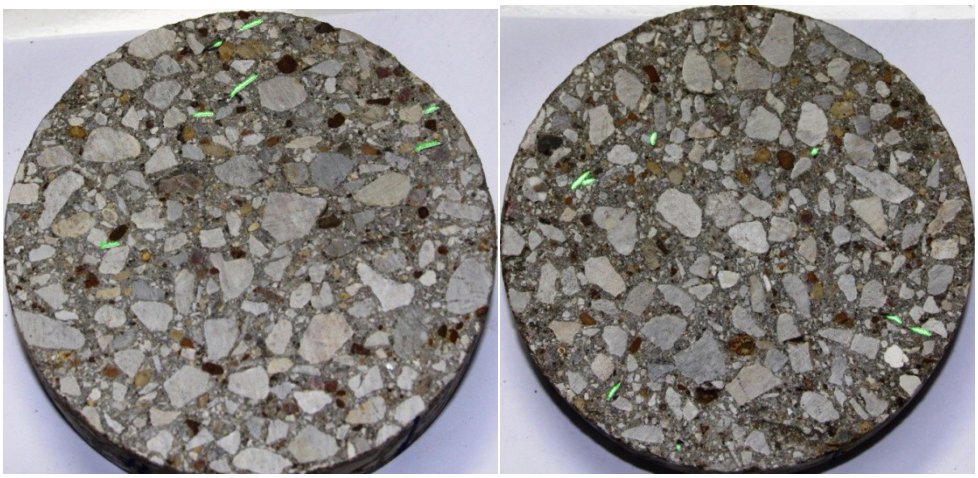

(a) (b)

Figure I- 26 Image of specimen 9-M: (a) side 1; (b) side 2

Table I- 27 Parameters obtained with image processing analysis

Image Height (pix)	Image Width (pix)	Total Area of the Surface (pix^2)	Total Area of the Fibers (pix^2)	Fiber Area Fraction (a_f)
Specimen 9-OD-1				
550	573	247497	134	0.054
Specimen 9-OD-2				
591	606	281189	629	0.224

(a) (b)

Figure I- 27 Image of specimen 9-OD: (a) side 1; (b) side 2

Table I- 28 Parameters obtained with image processing analysis

Image Height (pix)	Image Width (pix)	Total Area of the Surface (pix^2)	Total Area of the Fibers (pix^2)	Fiber Area Fraction (a_f)
Specimen 10-M-1				
614	634	305660	1971	0.645
Specimen 10-M-2				
649	663	337814	1741	0.515

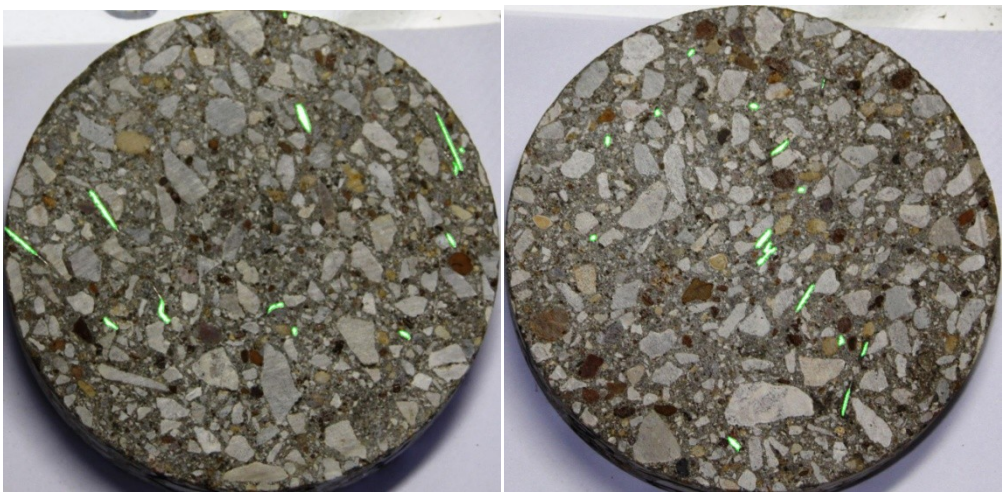

(a) (b)

Figure I- 28 Image of specimen 10-M: (a) side 1; (b) side 2

Table I- 29 Parameters obtained with image processing analysis

Image Height (pix)	**Image Width (pix)**	**Total Area of the Surface (pix^2)**	**Total Area of the Fibers (pix^2)**	**Fiber Area Fraction (a_f)**
Specimen 10-OD-1				
601	616	290664	1871	0.644
Specimen 10-OD-2				
613	626	301267	735	0.244

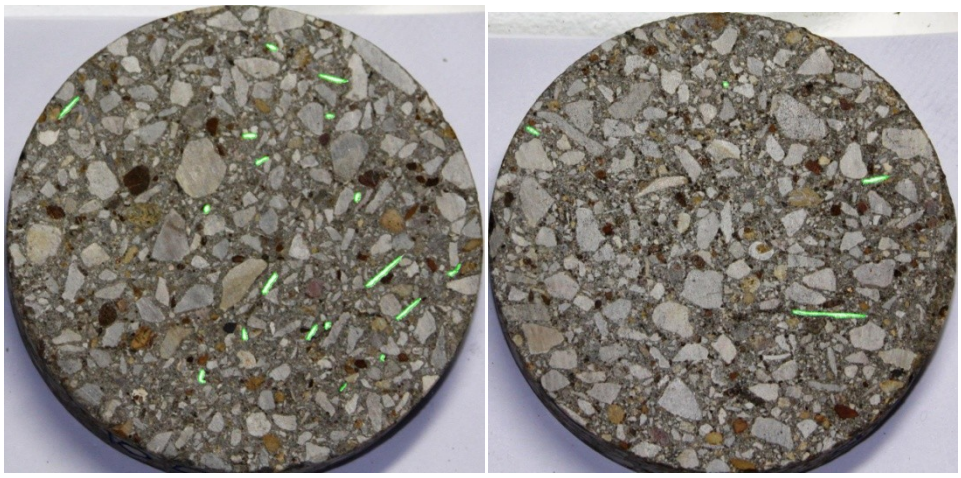

(a) (b)

Figure I- 29 Image of specimen 10-OD: (a) side 1; (b) side 2

Table I- 30 Parameters obtained with image processing analysis

Image Height (pix)	Image Width (pix)	Total Area of the Surface (pix^2)	Total Area of the Fibers (pix^2)	Fiber Area Fraction (a_f)
Specimen 10-ID-1				
589	607	280719	945	0.337
Specimen 10-ID-2				
594	592	276044	1281	0.464

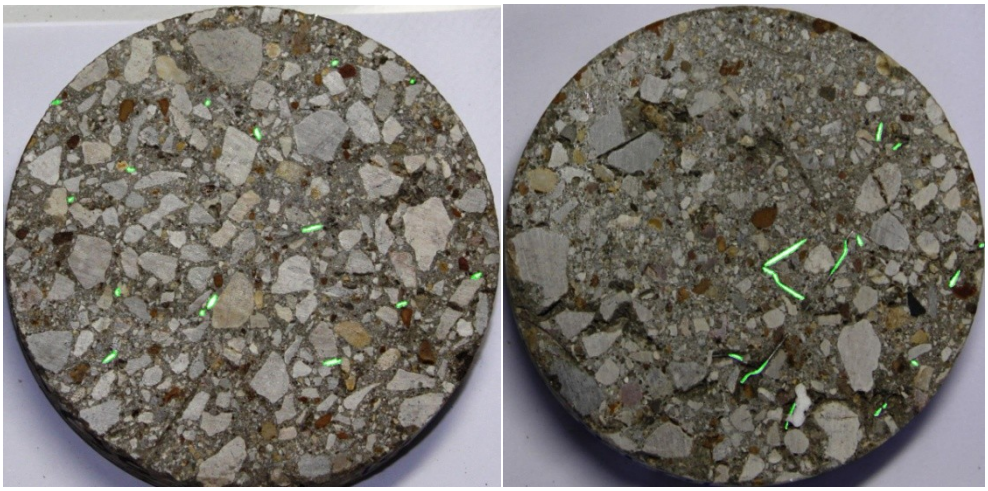

(a) (b)

Figure I- 30 Image of specimen 10-ID: (a) side 1; (b) side 2

Table I- 31 Parameters obtained with image processing analysis

Image Height (pix)	**Image Width (pix)**	**Total Area of the Surface (pix^2)**	**Total Area of the Fibers (pix^2)**	**Fiber Area Fraction (a_f)**
Specimen 11-ID-1				
585	617	283543	5811	2.049
Specimen 11-ID-2				
619	628	301754	2166	0.718

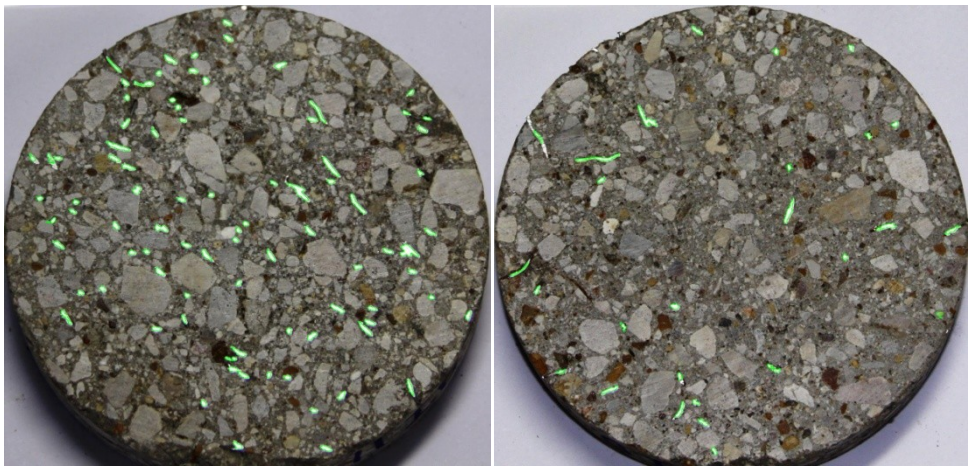

(a) (b)

Figure I- 31 Image of specimen 11-ID: (a) side 1; (b) side 2

Table I- 32 Parameters obtained with image processing analysis

Image Height (pix)	Image Width (pix)	Total Area of the Surface (pix^2)	Total Area of the Fibers (pix^2)	Fiber Area Fraction (a_f)
Specimen 11-M-1				
438	449	154403	1029	0.666
Specimen 11-M-2				
620	637	310085	5532	1.784

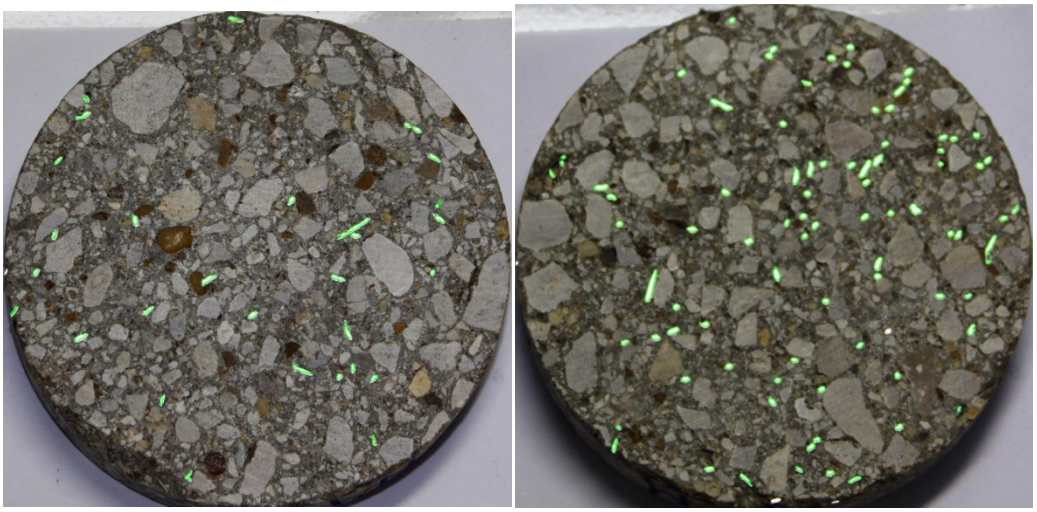

(a) (b)

Figure I- 32 Image of specimen 11-M: (a) side 1; (b) side 2

Table I- 33 Parameters obtained with image processing analysis

Image Height (pix)	Image Width (pix)	Total Area of the Surface (pix^2)	Total Area of the Fibers (pix^2)	Fiber Area Fraction (a_f)
Specimen 11-OD-1				
600	626	294979	783	0.265
Specimen 11-OD-2				
593	620	288756	2911	1.008

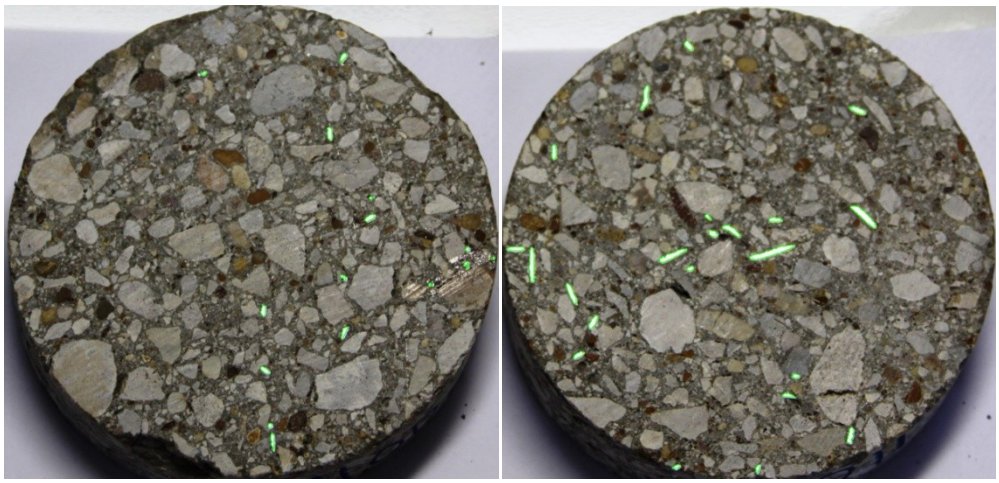

(a) (b)

Figure I- 33 Image of specimen 11-OD: (a) side 1; (b) side 2

Table I- 34 Parameters obtained with image processing analysis

Image Height (pix)	**Image Width (pix)**	**Total Area of the Surface (pix^2)**	**Total Area of the Fibers (pix^2)**	**Fiber Area Fraction (a_f)**
Specimen 12-ID-1				
435	457	156149	2817	1.804
Specimen 12-ID-2				
467	489	179360	1068	0.595

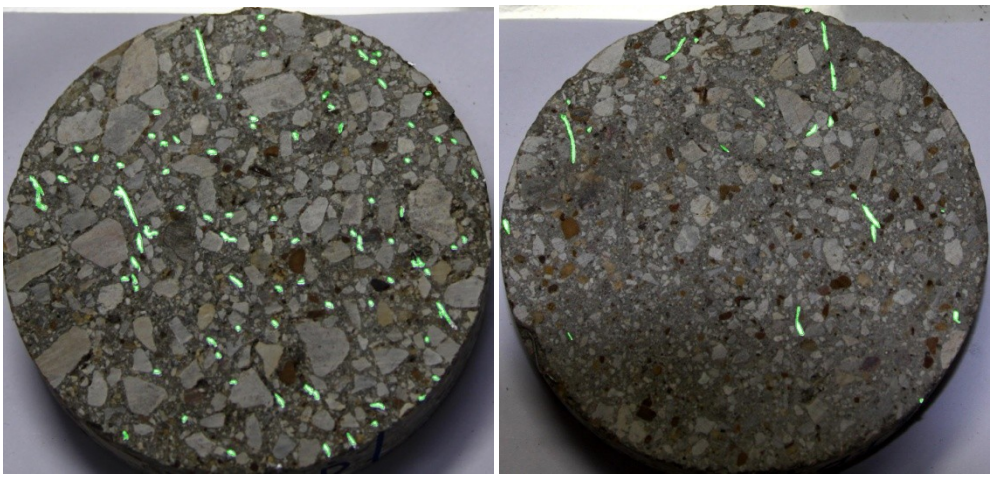

(a) (b)

Figure I- 34 Image of specimen 12-ID: (a) side 1; (b) side 2

Table I- 35 Parameters obtained with image processing analysis

Image Height (pix)	**Image Width (pix)**	**Total Area of the Surface (pix^2)**	**Total Area of the Fibers (pix^2)**	**Fiber Area Fraction (a_f)**
Specimen 12-M-1				
537	566	238760	2882	1.207
Specimen 12-M-2				
638	665	333195	3435	1.031

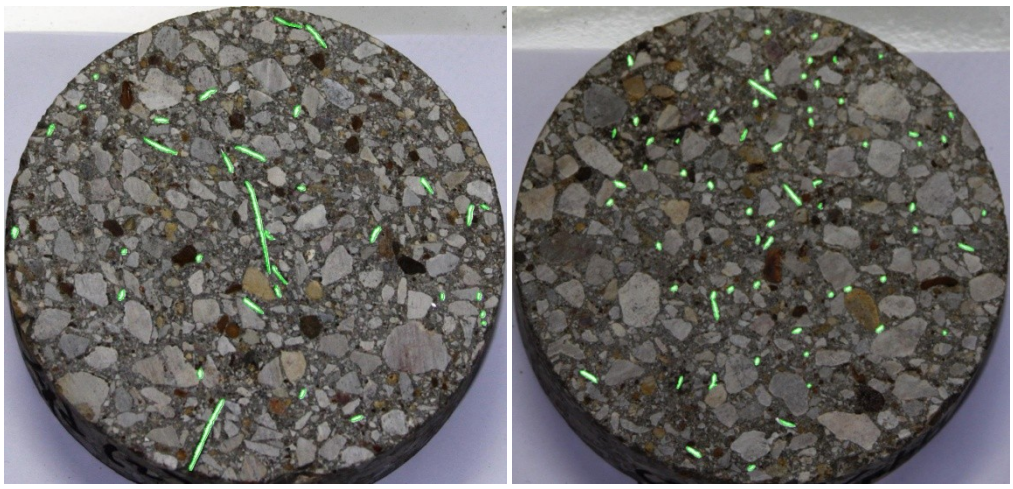

(a) (b)

Figure I- 35 Image of specimen 12-M: (a) side 1; (b) side 2

Table I- 36 Parameters obtained with image processing analysis

Image Height (pix)	Image Width (pix)	Total Area of the Surface (pix^2)	Total Area of the Fibers (pix^2)	Fiber Area Fraction (a_f)
Specimen 12-OD-1				
587	625	288280	2080	0.722
Specimen 12-OD-2				
579	609	276976	3328	1.202

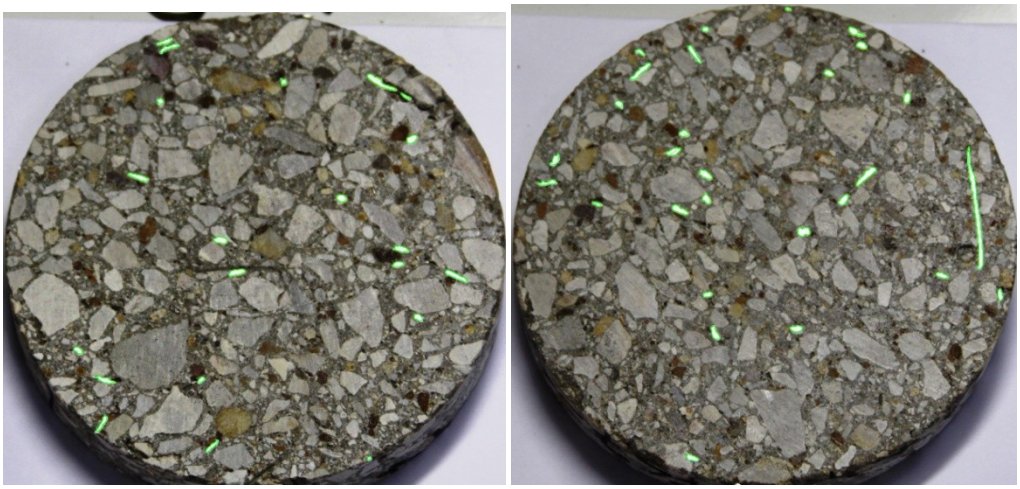

(a) (b)

Figure I- 36 Image of specimen 12-OD: (a) side 1; (b) side 2

Table I- 37 Parameters obtained with image processing analysis

Image Height (pix)	**Image Width (pix)**	**Total Area of the Surface (pix^2)**	**Total Area of the Fibers (pix^2)**	**Fiber Area Fraction (a_f)**
Specimen 13-ID-1				
580	603	274650	4295	1.564
Specimen 13-ID-2				
624	645	316033	1805	0.571

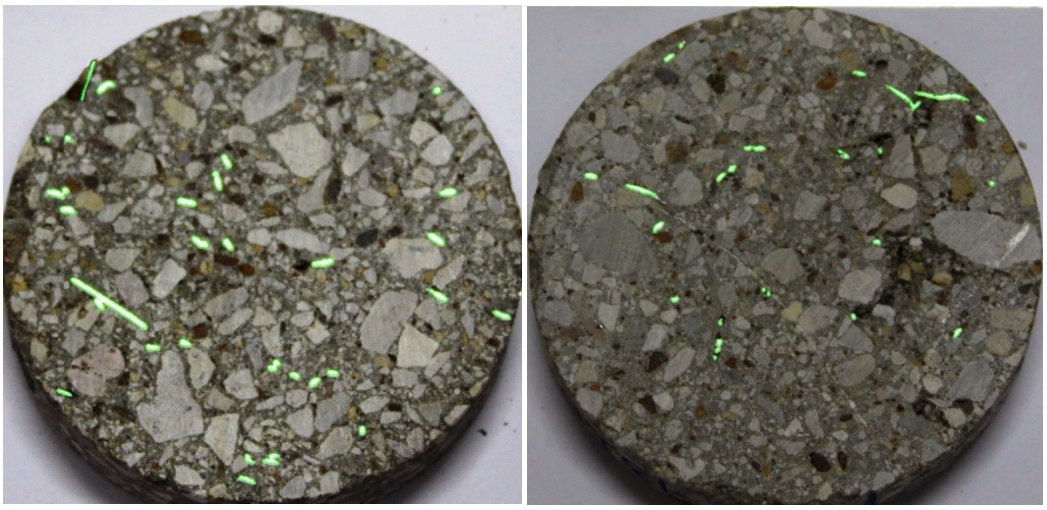

(a) (b)

Figure I- 37 Image of specimen 13-ID: (a) side 1; (b) side 2

Table I- 38 Parameters obtained with image processing analysis

Image Height (pix)	**Image Width (pix)**	**Total Area of the Surface (pix^2)**	**Total Area of the Fibers (pix^2)**	**Fiber Area Fraction (a_f)**
Specimen 13-M-1				
612	634	304681	4288	1.407
Specimen 13-M-2				
623	635	310578	2830	0.911

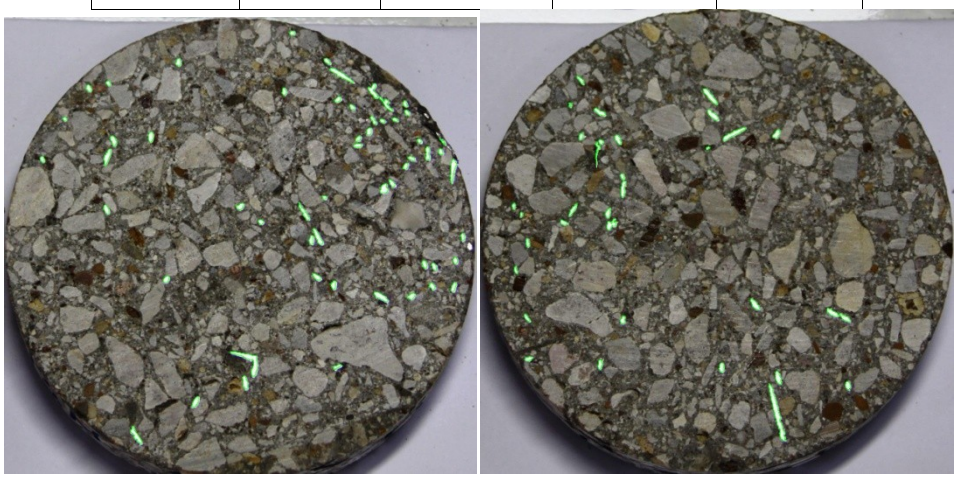

(a) (b)

Figure I- 38 Image of specimen 13-M: (a) side 1; (b) side 2

Table I- 39 Parameters obtained with image processing analysis

Image Height (pix)	**Image Width (pix)**	**Total Area of the Surface (pix^2)**	**Total Area of the Fibers (pix^2)**	**Fiber Area Fraction (a_f)**
Specimen 13-OD-1				
630	687	340393	2167	0.637
Specimen 13-OD-2				
576	630	285433	4837	1.695

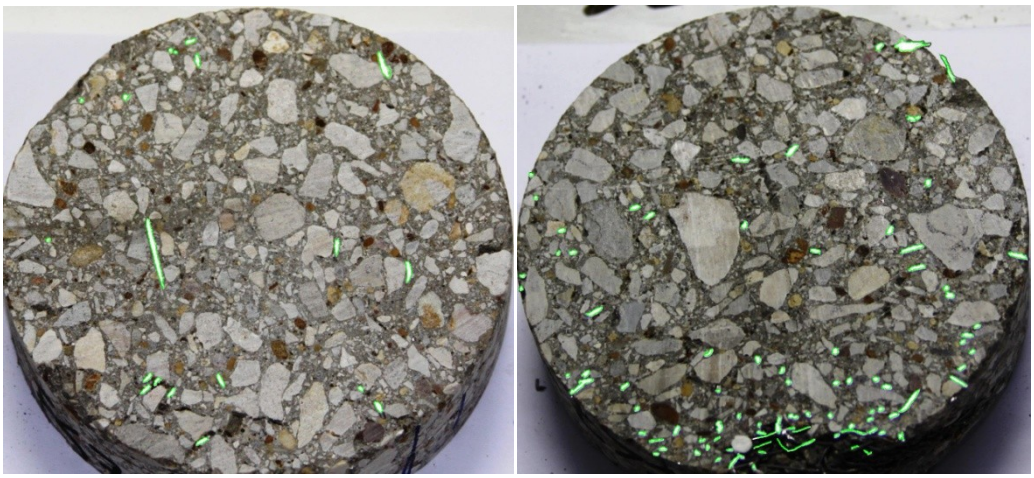

(a) (b)

Figure I- 39 Image of specimen 13-OD: (a) side 1; (b) side 2

Table I- 40 Parameters obtained with image processing analysis

Image Height (pix)	**Image Width (pix)**	**Total Area of the Surface (pix^2)**	**Total Area of the Fibers (pix^2)**	**Fiber Area Fraction (a_f)**
Specimen 14-ID-1				
439	465	160379	1063	0.663
Specimen 14-ID-2				
456	473	169372	1125	0.664

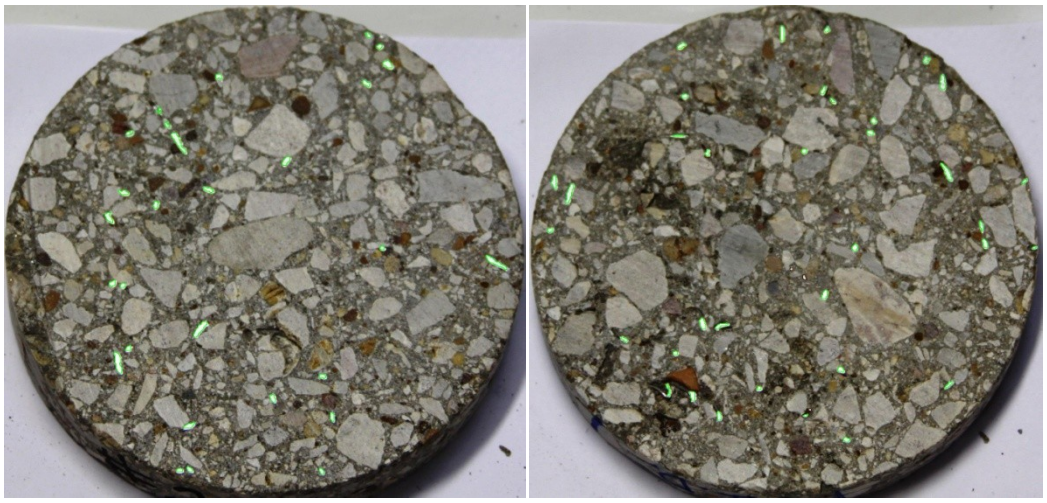

(a) (b)

Figure I- 40 Image of specimen 14-ID: (a) side 1; (b) side 2

Table I- 41 Parameters obtained with image processing analysis

Image Height (pix)	Image Width (pix)	Total Area of the Surface (pix^2)	Total Area of the Fibers (pix^2)	Fiber Area Fraction (a_f)
Specimen 14-M-1				
451	472	167191	1194	0.714
Specimen 14-M-2				
459	490	176743	2165	1.225

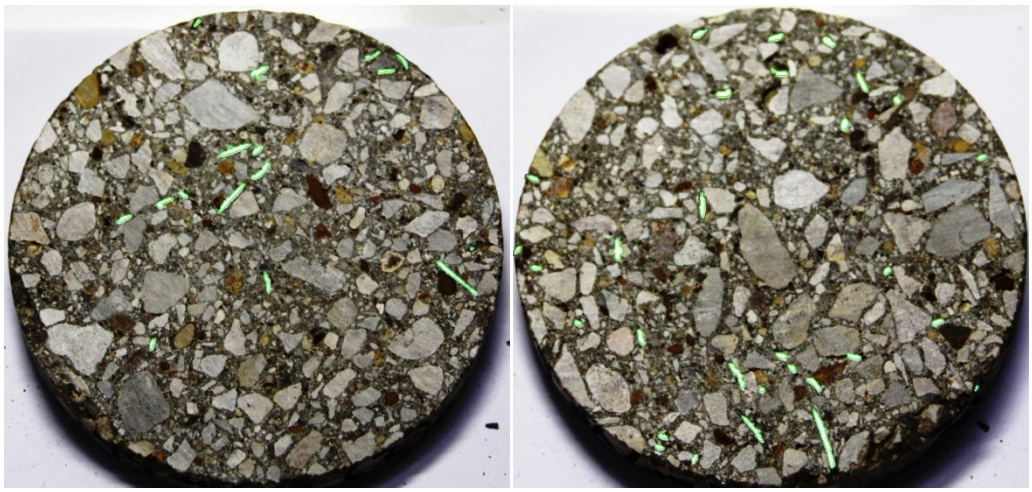

(a) (b)

Figure I- 41 Image of specimen 14-M: (a) side 1; (b) side 2

Table I- 42 Parameters obtained with image processing analysis

Image Height (pix)	Image Width (pix)	Total Area of the Surface (pix^2)	Total Area of the Fibers (pix^2)	Fiber Area Fraction (a_f)
Specimen 14-OD-1				
544	556	237463	1511	0.636
Specimen 14-OD-2				
501	528	207798	2228	1.072

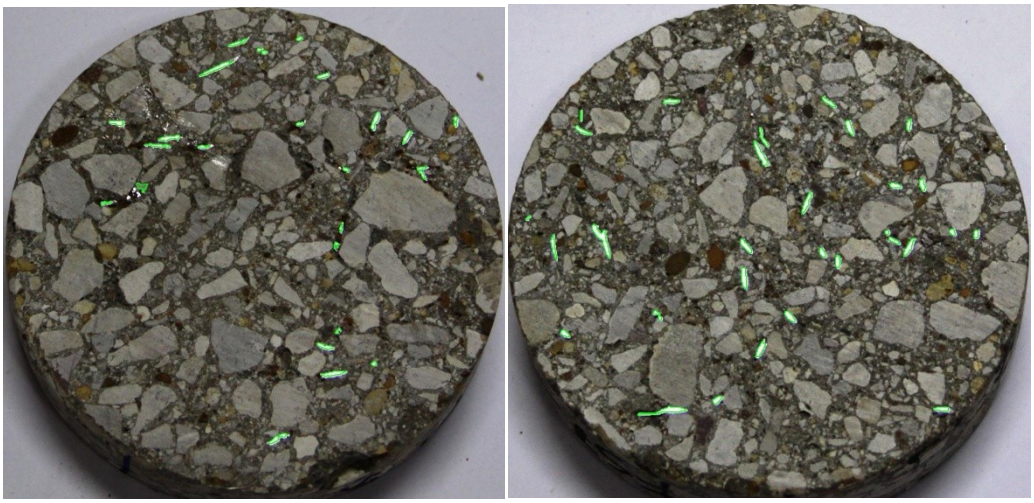

(a) (b)

Figure I- 42 Image of specimen 14-OD: (a) side 1; (b) side 2

Table I- 43 Parameters obtained with image processing analysis

Image Height (pix)	**Image Width (pix)**	**Total Area of the Surface (pix^2)**	**Total Area of the Fibers (pix^2)**	**Fiber Area Fraction (a_f)**
Specimen 15-ID-1				
673	694	366730	3183	0.868
Specimen 15-ID-2				
447	464	162872	959	0.589

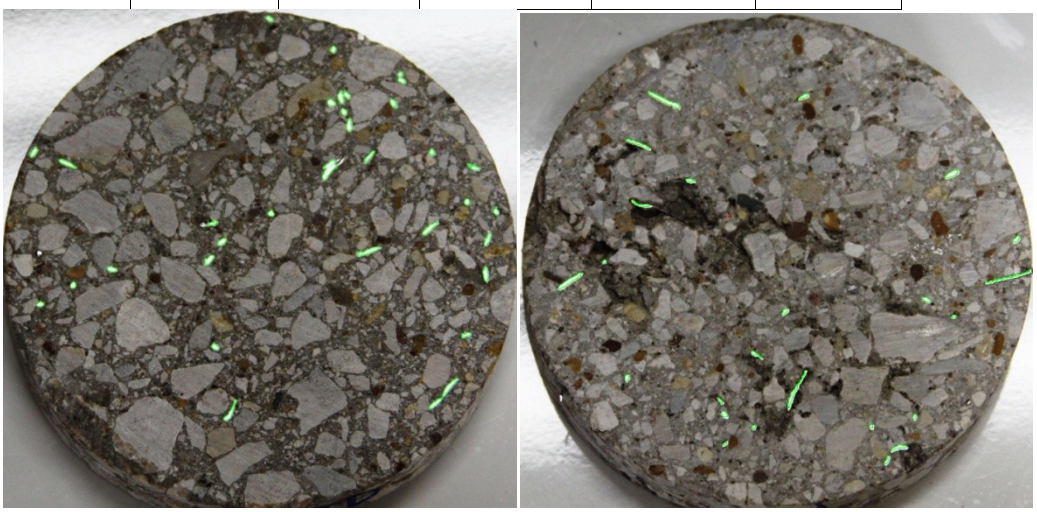

(a) (b)

Figure I- 43 Image of specimen 15-ID: (a) side 1; (b) side 2

Table I- 44 Parameters obtained with image processing analysis

Image Height (pix)	**Image Width (pix)**	**Total Area of the Surface (pix^2)**	**Total Area of the Fibers (pix^2)**	**Fiber Area Fraction (a_f)**
Specimen 15-M-1				
632	658	326580	2160	0.661
Specimen 15-M-2				
634	672	334731	5663	1.692

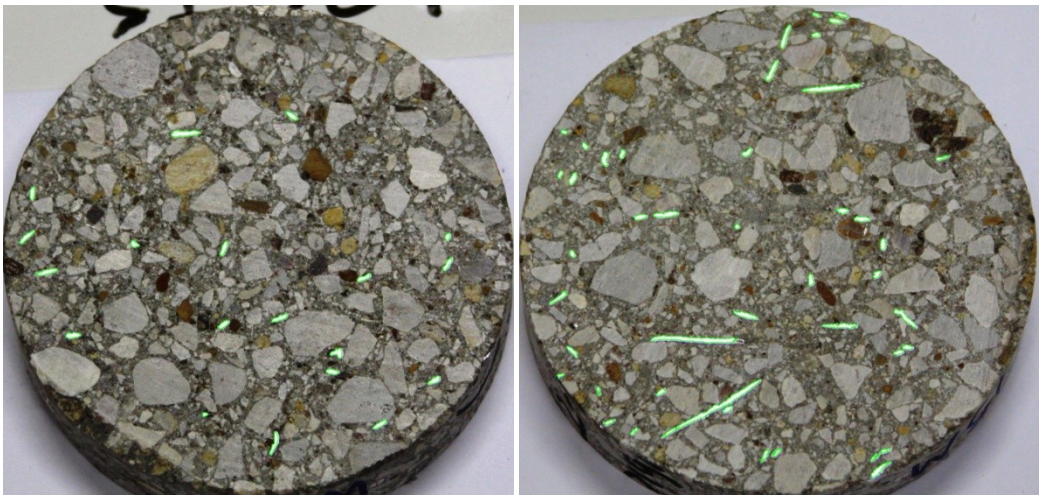

(a) (b)

Figure I- 44 Image of specimen 15-M: (a) side 1; (b) side 2

Table I- 45 Parameters obtained with image processing analysis

Image Height (pix)	**Image Width (pix)**	**Total Area of the Surface (pix^2)**	**Total Area of the Fibers (pix^2)**	**Fiber Area Fraction (a_f)**
Specimen 15-OD-1				
686	692	372656	4128	1.108
Specimen 15-OD-2				
629	670	331152	3741	1.130

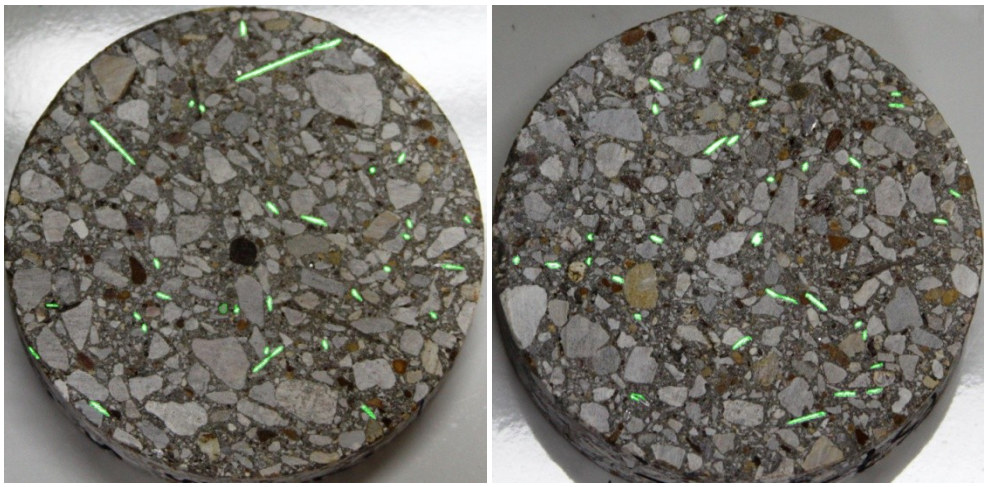

(a) (b)

Figure I- 45 Image of specimen 15-OD: (a) side 1; (b) side 2

Table I- 46 Parameters obtained with image processing analysis

Image Height (pix)	Image Width (pix)	Total Area of the Surface (pix^2)	Total Area of the Fibers (pix^2)	Fiber Area Fraction (a_f)
Specimen 16-ID-1				
586	596	274186	1949	0.711
Specimen 16-ID-2				
640	650	326580	4640	1.421

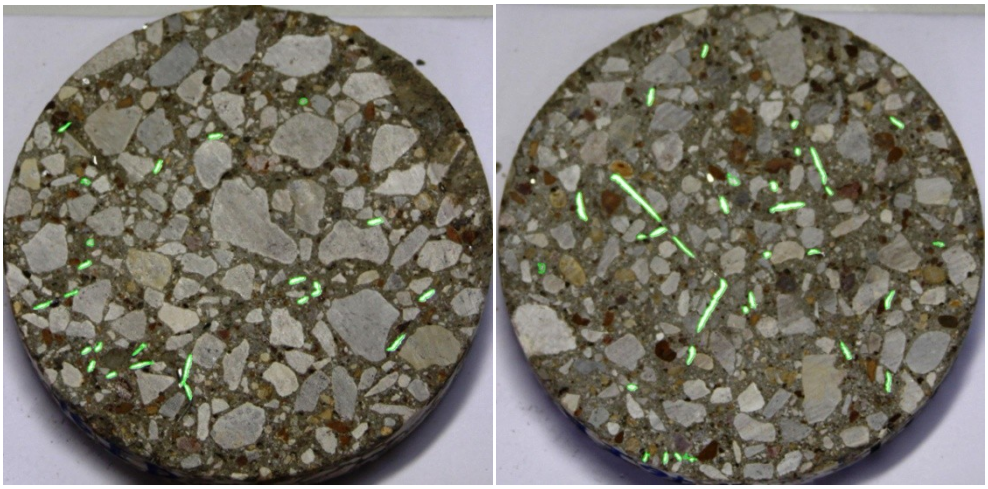

(a) (b)

Figure I- 46 Image of specimen 16-ID: (a) side 1; (b) side 2

Table I- 47 Parameters obtained with image processing analysis

Image Height (pix)	Image Width (pix)	Total Area of the Surface (pix^2)	Total Area of the Fibers (pix^2)	Fiber Area Fraction (a_f)
Specimen 16-M-1				
606	615	292578	1568	0.536
Specimen 16-M-2				
586	602	276976	1390	0.502

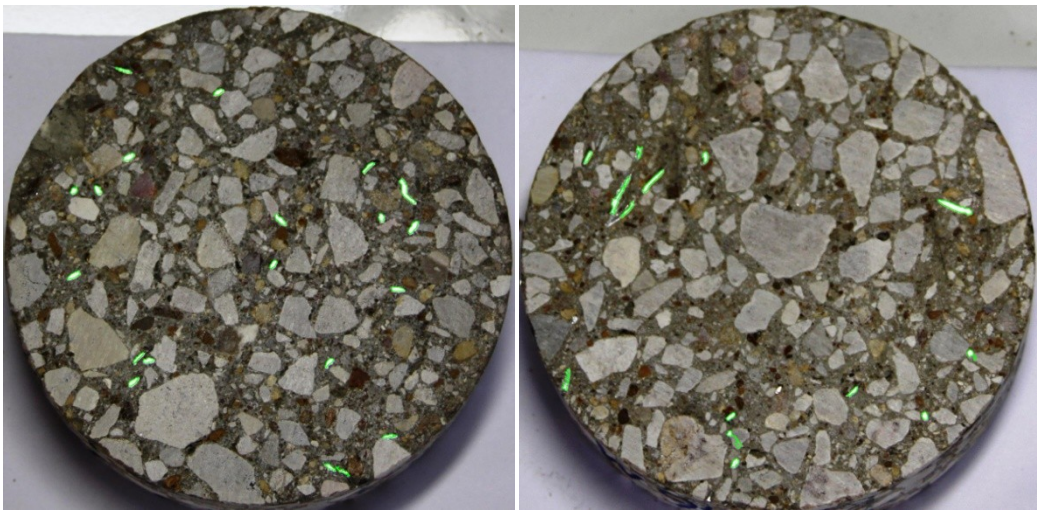

(a) (b)

Figure I- 47 Image of specimen 16-M: (a) side 1; (b) side 2

Table I- 48 Parameters obtained with image processing analysis

Image Height (pix)	Image Width (pix)	Total Area of the Surface (pix^2)	Total Area of the Fibers (pix^2)	Fiber Area Fraction (a_f)
Specimen 16-OD-1				
598	616	289232	3747	1.295
Specimen 16-OD-2				
584	584	267729	1587	0.593

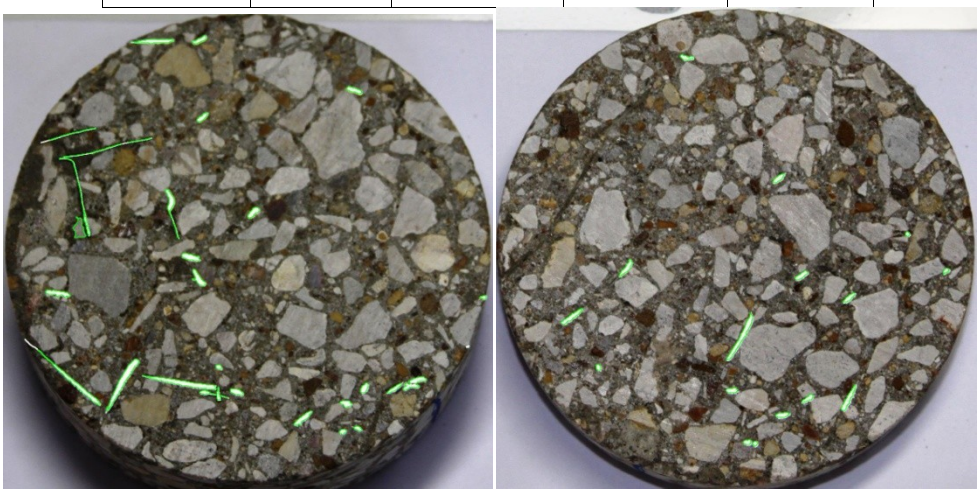

(a) (b)

Figure I- 48 Image of specimen 16-OD: (a) side 1; (b) side 2

Table I- 49 Parameters obtained with image processing analysis

Image Height (pix)	**Image Width (pix)**	**Total Area of the Surface (pix^2)**	**Total Area of the Fibers (pix^2)**	**Fiber Area Fraction (a_f)**
Specimen 17-ID-1				
601	605	285433	2875	1.007
Specimen 17-ID-2				
656	660	339877	1052	0.310

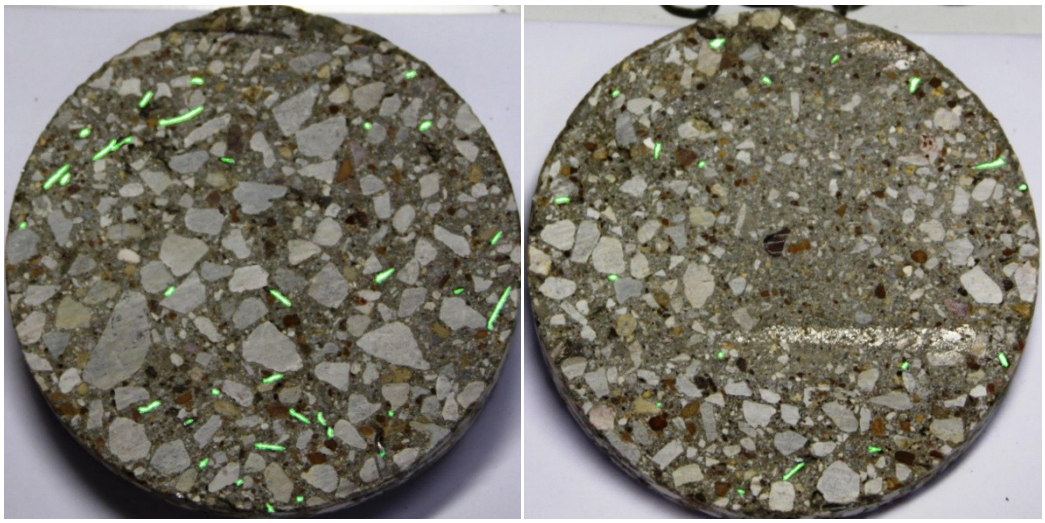

(a) (b)

Figure I- 49 Image of specimen 17-ID: (a) side 1; (b) side 2

Table I- 50 Parameters obtained with image processing analysis

Image Height (pix)	Image Width (pix)	Total Area of the Surface (pix^2)	Total Area of the Fibers (pix^2)	Fiber Area Fraction (a_f)
Specimen 17-M-1				
598	618	290186	2643	0.911
Specimen 17-M-2				
638	655	328100	1764	0.538

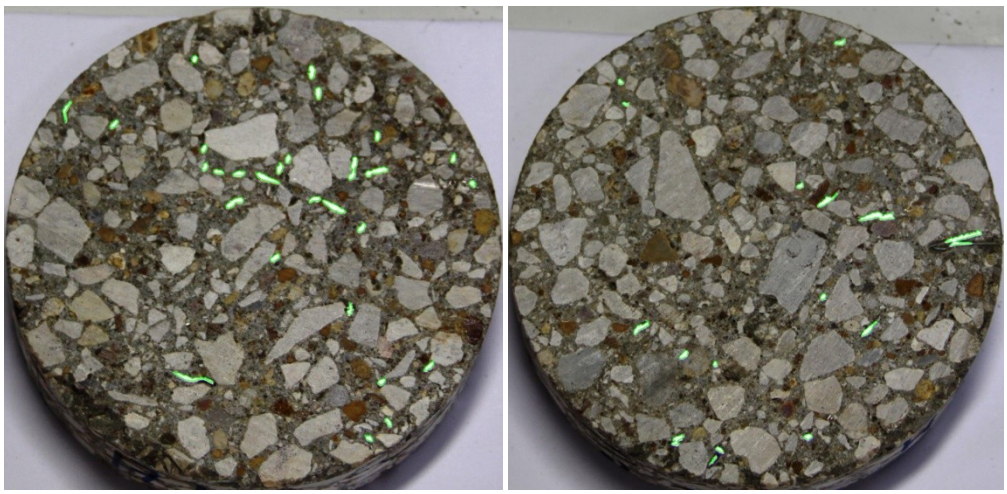

(a) (b)

Figure I- 50 Image of specimen 17-M: (a) side 1; (b) side 2

Table I- 51 Parameters obtained with image processing analysis

Image Height (pix)	**Image Width (pix)**	**Total Area of the Surface (pix^2)**	**Total Area of the Fibers (pix^2)**	**Fiber Area Fraction (a_f)**
Specimen 17-OD-1				
636	641	320031	2614	0.817
Specimen 17-OD-2				
608	617	294498	3106	1.055

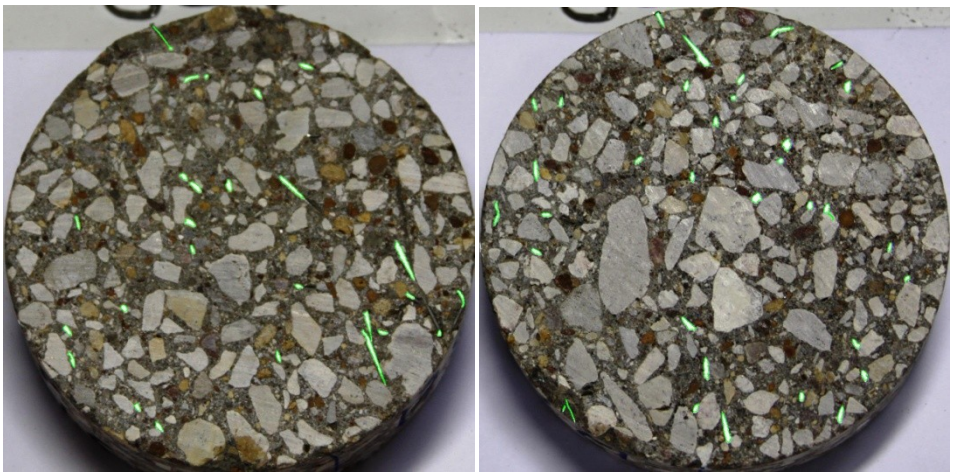

(a) (b)

Figure I- 51 Image of specimen 17-OD: (a) side 1; (b) side 2

Table I- 52 Parameters obtained with image processing analysis

Image Height (pix)	Image Width (pix)	Total Area of the Surface (pix^2)	Total Area of the Fibers (pix^2)	Fiber Area Fraction (a_f)
Specimen 18-ID-1				
664	670	349238	1372	0.393
Specimen 18-ID-2				
596	608	284487	2712	0.953

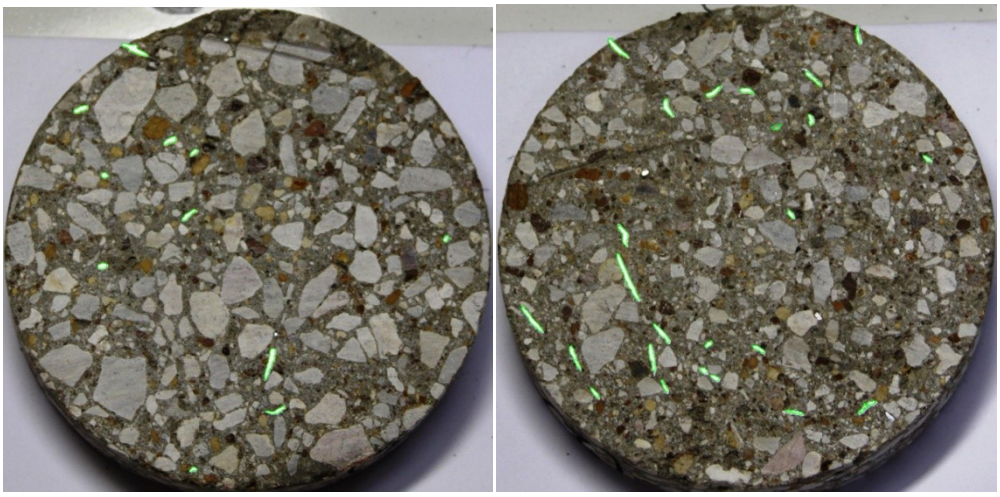

(a) (b)

Figure I- 52 Image of specimen 18-ID: (a) side 1; (b) side 2

Table I- 53 Parameters obtained with image processing analysis

Image Height (pix)	Image Width (pix)	Total Area of the Surface (pix^2)	Total Area of the Fibers (pix^2)	Fiber Area Fraction (a_f)
Specimen 18-OD-1				
582	593	270948	1151	0.425
Specimen 18-OD-2				
591	603	279781	3252	1.162

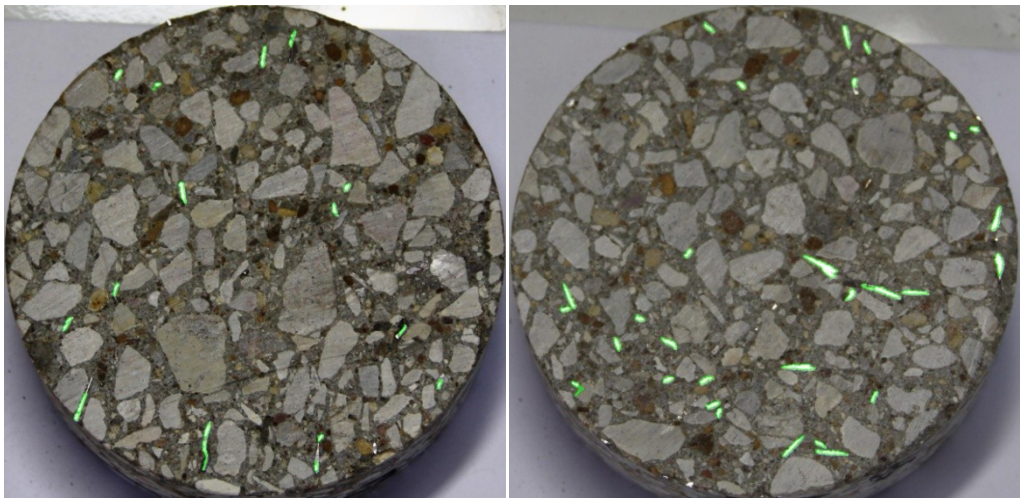

(a) (b)

Figure I- 53 Image of specimen 18-OD: (a) side 1; (b) side 2

Table I- 54 Parameters obtained with image processing analysis

Image Height (pix)	Image Width (pix)	Total Area of the Surface (pix^2)	Total Area of the Fibers (pix^2)	Fiber Area Fraction (a_f)
Specimen 18-M-1				
646	656	332684	2982	0.896
Specimen 18-M-2				
618	626	303704	2424	0.798

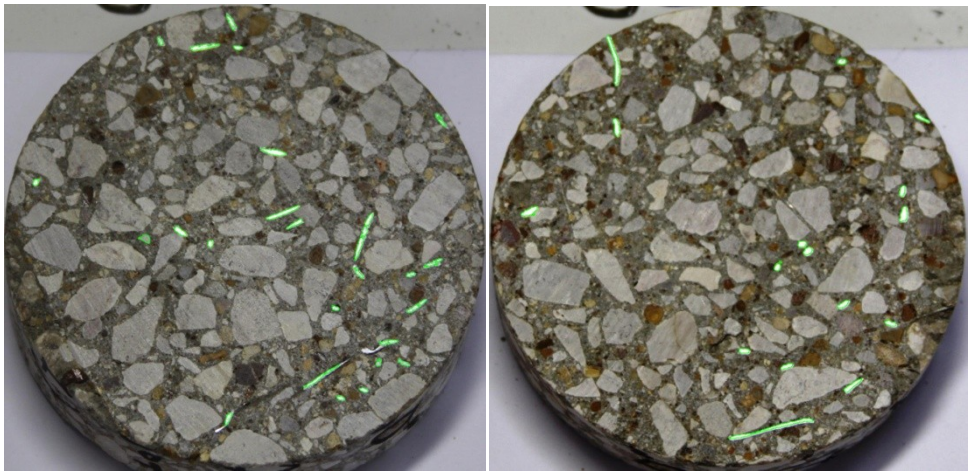

(a) (b)

Figure I- 54 Image of specimen 18-M: (a) side 1; (b) side 2

.

References

Abolmaali, A., et al. "Performance of Steel Fiber-Reinforced Concrete Pipes." *Transportation Research Record: Journal of the Transportation Research Board* 2313.1 (2012): 168-177.

Abolmaali, A., and Kararam A. "Nonlinear finite-element-based investigation of the effect of bedding thickness on buried concrete pipe." *Journal of Transportation Engineering* 136.9 (2009): 793-799.

ACI Committee 544.4R-88, Design Considerations for Steel Fiber Reinforced Concrete, *American Concrete Institute*, Detroit, Michigan, USA, 1988.

ACI Committee 544.1R-96, Report on Fiber Reinforced Concrete, *American Concrete Institute*, Detroit, Michigan, USA, 1996.

American Concrete Pipe Association, Chicago. *Concrete pipe handbook*. 1958.

ASTM, C1609 Standard Test Method for Flexural Performance of Fiber-Reinforced Concrete (Using Beam With Third-Point Loading). *American Society for Testing and Materials*, 2005.

ASTM, C1765 Standard Specification for Steel Fiber Reinforced Concrete Culvert, Storm Drain, and Sewer Pipe. *American Society for Testing and Materials*, 2013

Banthia, Nemkumar, et al. "Fiber-reinforced concrete in precast concrete applications: Research leads to innovative products." *PCI Journal* 57.3 (2012): 33.

Bathe, Klaus-Jürgen. *Finite element procedures*. Vol. 2. No. 3. Englewood Cliffs: Prentice hall, 1996.

Bazant Z. P and Oh, B. H., "Crack band theory for fracture of concrete." *Materials and Structures, January-February* (1983): 155-177.

Borst, Rene de, et al. "Discrete vs. smeared crack models for concrete fracture: bridging the gap." *International Journal for Numerical and Analytical Methods in Geomechanics* 28.7-8 (2004): 583-607.

De Borst, R. "Computation of post-bifurcation and post-failure behavior of strain-softening solids." *Computers & Structures* 25.2 (1987): 211-224.

Daigle, M., D. Fratta, and L. B. Wang. "Ultrasonic and X-ray tomographic imaging of highly contrasting inclusions in concrete specimens." *2005 GeoFrontier Conference*. 2005.

De Figueiredo, A. D., et al. "Steel fiber reinforced concrete pipes. Part 1: technological analysis of the mechanical behavior Tubos de concreto reforçado com fibras de aço. Parte 1: análise tecnológica do comportamento mecânico." (2012).

De Figueiredo, A. D. "Evaluation of the test method for crushing strength of steel fiber reinforced concrete pipes." *BEFIB 2008: 7th RILEM International Symposium on Fibre Reinforced Concrete*. Ed. R. Gettu. RILEM Publications SARL, 2008.

De La Fuente, Albert, et al. "Experimentation and numerical simulation of steel fibre reinforced concrete pipes."*Materiales de Construcción* 61.302 (2011): 275-288.

De La Fuente, Albert, et al. "A new design method for steel fibre reinforced concrete pipes." *Construction and Building Materials* 30 (2012): 547-555.

De La Fuente, A., et al. "Steel fibre reinforced concrete pipes. Part 2: Numerical model to simulate the crushing test Tubos de concreto reforçado com fibras de aço. Parte 2: Modelo numérico para simular o ensaio de compressão diametral." (2012).

Di Prisco, Marco, Giovanni Plizzari, and Lucie Vandewalle. "Fibre reinforced concrete: new design perspectives." *Materials and Structures* 42.9 (2009): 1261-1281.

European Standard, EN 1916 Concrete pipes and fittings, unreinforced, steel fibre and reinforced. *European Committee for Standardization*, 2002.

Fanella, David A., and Antoine E. Naaman. "Stress-strain properties of fiber reinforced mortar in compression." *ACI Journal proceedings*. Vol. 82. No. 4. ACI, 1985.

Gasser, Thomas C., and Gerhard A. Holzapfel. "3d crack propagation in unreinforced concrete.: A two-step algorithm for tracking 3d crack paths." *Computer Methods in Applied Mechanics and Engineering* 195.37 (2006): 5198-5219.

Gopalaratnam, V. S., and S. P. Shah. "Properties of steel fiber reinforced concrete subjected to impact loading." *ACI Journal Proceedings*. Vol. 83. No. 1. ACI, 1986.

Gribniak, Viktor, et al. "Deriving stress–strain relationships for steel fibre concrete in tension from tests of beams with ordinary reinforcement." *Engineering Structures* 42 (2012): 387-395.

Haktanir, Tefaruk, et al. "A comparative experimental investigation of concrete, reinforced-concrete and steel-fibre concrete pipes under three-edge-bearing test." Construction and Building Materials 21.8 (2007): 1702-1708.

Haktanir, Tefaruk, et al. "Effects of steel fibers and mineral filler on the water-tightness of concrete pipes." *Cement and Concrete Composites* 28.9 (2006): 811-816.

Heger, Frank J. "Structural Behavior of Circular Reinforced Concrete Pipe-Development of Theory." *ACI Journal Proceedings*. Vol. 60. No. 11. ACI, 1963.

Hibbitt, Karlsson, and Sorensen. *ABAQUS: Theory Manual*. Hibbitt, Karlsson & Sorensen, 1997.

Hillerborg, Arne, Mats Modéer, and P-E. Petersson. "Analysis of crack formation and crack growth in concrete by means of fracture mechanics and finite elements."*Cement and concrete research* 6.6 (1976): 773-781.

Johnston, Colin D. "Steel fiber reinforced mortar and concrete: a review of mechanical properties." *ACI Special Publication* 44 (1974).

Johnston, C. D., and Åke Skarendahl. "Comparative flexural performance evaluation of steel fibre-reinforced concretes according to ASTM C1018 shows importance of fibre parameters." *Materials and Structures* 25.4 (1992): 191-200.

Jindal, Roop L. "Shear and moment capacities of steel fiber reinforced concrete beams." *ACI Special Publication* 81 (1984).

Kang, Su Tae, et al. "The effect of fibre distribution characteristics on the flexural strength of steel fibre-reinforced ultra-high strength concrete." *Construction and Building Materials* 25.5 (2011): 2450-2457.

Karl, Kyoung-Wan, et al. "Revision on Material Strength of Steel Fiber-Reinforced Concrete." *International Journal of Concrete Structures and Materials* 5.2 (2011): 89-96

Kachanov, L. *Introduction to continuum damage mechanics*. Vol. 10. Springer, 1986.

Kupfer, Helmut, Hubert K. Hilsdorf, and Hubert Rusch. "Behavior of concrete under biaxial stresses." *ACI Journal Proceedings*. Vol. 66. No. 8. ACI, 1969.

Krenchel, H., “Fiber Reinforcement,” *Akademisk Forlag*, Copenhagen, Denmark, Eng. translation, 1964.

Lee, Jeeho, and Gregory L. Fenves. "Plastic-damage model for cyclic loading of concrete structures."*Journal of engineering mechanics*124.8 (1998): 892-900.

Lee, Seong-Cheol, Jae-Yeol Cho, and Frank J. Vecchio. "Diverse Embedment Model for Steel Fiber-Reinforced Concrete in Tension: Model Verification." *ACI Materials Journal* 108.5 (2011): 526-535.

Lubliner, J., et al. "A plastic-damage model for concrete." *International Journal of Solids and Structures* 25.3 (1989): 299-326.

MacDonald, C. N., and J. Trangsrud. "Steel Fiber Product Introduction through Pre-Cast Reinforced Concrete Pipe." *ACI Special Publication* 222 (2004).

Mansour, Farnoud Rahimi, Sasan Parniani, and Izni Syahrizal Ibrahim. "Experimental Study on Effects of Steel Fiber Volume on Mechanical Properties of SFRC." *Advanced Materials Research* 214 (2011): 144-148.

Manual, ABAQUS User's. "Version 6.12." *Hibbit, Karlsson & Sorensen* (2007).

Naaman, Antoine E. "Tensile strain-hardening FRC composites: Historical evolution since the 1960." *Advances in Construction Materials 2007*. Springer Berlin Heidelberg, 2007. 181-202.

Nataraja, M. C., N. Dhang, and A. P. Gupta. "Stress–strain curves for steel-fiber reinforced concrete under compression." *Cement and Concrete Composites* 21.5 (1999): 383-390.

Narayanan, R., and I. Y. S. Darwish. "Use of steel fibers as shear reinforcement." *ACI Structural Journal* 84.3 (1987).

Neter, John, William Wasserman, and Michael H. Kutner. *Applied linear statistical models*. Vol. 4. Chicago: Irwin, 1996.

Neves, Rui D., and JCO Fernandes de Almeida. "Compressive behaviour of steel fibre reinforced concrete." S*tructural concrete* 6.1 (2005): 1-8.

Ngo, D., and A. C. Scordelis. "Finite element analysis of reinforced concrete beams." *ACI Journal Proceedings*. Vol. 64. No. 3. ACI, 1967.

Prasad, M. V. K. V., and C. S. Krishnamoorthy. "Computational model for discrete crack growth in plain and reinforced concrete."*Computer methods in applied mechanics and engineering* 191.25 (2002): 2699-2725.

Romualdi, J.P., and Mandel, J.A., "Tensile Strength of Concrete Affected by Uniformly Distributed Closely Spaced Short Length of Wire Reinforcement," *ACI Journal*, June 1964.

Rots, J. G., et al. "Smeared crack approach and fracture localization in concrete." (1985).Saleh, A. L., and M. H. Aliabadi. "Crack growth analysis in concrete using boundary element method." *Engineering fracture mechanics* 51.4 (1995): 533-545.

Swaddiwudhipong, Somsak, and Puay Eng Constance Seow. "Modelling of steel fiber-reinforced concrete under multi-axial loads." *Cement and concrete research* 36.7 (2006): 1354-1361.

Stang, Henrik, and S. P. Shah. "Failure of fibre-reinforced composites by pull-out fracture." *Journal of materials science* 21.3 (1986): 953-957.

Swamy, R. N. "Deformation and ultimate strength in flexure of reinforced concrete beams made with steel fiber concrete." *ACI Journal Proceedings*. Vol. 78. No. 5. ACI, 1981.

Taqieddin, Ziad N. *Elasto-plastic and damage modeling of reinforced concrete*. Diss. 2008.

Wittmann, Folker H. *Fracture mechanics of concrete*. Elsevier. Distributors for the US and Canada, Elsevier Science Pub. Co., 1983.

Yang, Zhenjun, and Jianfei Chen. "Fully automatic modelling of cohesive discrete crack propagation in concrete beams using local arc-length methods." *International journal of solids and structures* 41.3 (2004): 801-826.

Zandi, Yousef, Metin Husem, and Selim Pul. "Effect of distribution and orientation of steel fiber reinforced concrete." *Proceedings of the 4th WSEAS international conference on Energy and development-environment-biomedicine*. World Scientific and Engineering Academy and Society (WSEAS), 2011.

Zhang, Jun, Christopher KY Leung, and Yuan Gao. "Simulation of crack propagation of fiber reinforced cementitious composite under direct tension." *Engineering Fracture Mechanics* 78.12 (2011): 2439-2454.

Biographical Information

Alena Mikhaylova has earned her Bachelor of Engineering Degree in Mechanical Engineering from the Gubkin's Russian State University of Oil and Gas in 2005. She received her Master of Engineering in Civil Engineering from the University of Texas at Arlington in 2009. Currently she is pursuing her degree in Doctor of Philosophy in Civil Engineering, in Structures and Applied Mechanics area from the University of Texas at Arlington.

While pursuing her degree, Ms. Mikhaylova worked as a teaching assistant for Finite Element Analysis course and a course instructor for Mechanics of Materials course in the Department of Civil Engineering at UTA. She also interned at a structural engineering firm, Gojer and Associates, Inc. before joining the program to pursue her Doctorate Degree.

Ms. Mikhaylova was a recipient of National Science Foundation award for East Asian and Pacific Summer Institutes in 2013. She also received a competitive Graduate Tuition Fellowship for 3 years from the University of Texas at Arlington.

Ms. Mikhaylova presented her research at international conference meetings and workshops, including Transportation Research Board Annual Meeting and American Society for Composites US-Japan conference, American Concrete Association Annual Meeting. Additionally Ms. Mikhaylova has published her research at Transportation Research Record Journal.

Ms. Mikhaylova's dissertation title, *Non-Linear Finite Element-Based Material Constitutive Law for Zero Slump Steel Fiber Reinforced Concrete Pipe Structures*, was supervised by Dr. Ali Abolmaali.